

University of Southampton Research Repository ePrints Soton

Copyright © and Moral Rights for this thesis are retained by the author and/or other copyright owners. A copy can be downloaded for personal non-commercial research or study, without prior permission or charge. This thesis cannot be reproduced or quoted extensively from without first obtaining permission in writing from the copyright holder/s. The content must not be changed in any way or sold commercially in any format or medium without the formal permission of the copyright holders.

When referring to this work, full bibliographic details including the author, title, awarding institution and date of the thesis must be given e.g.

AUTHOR (year of submission) "Full thesis title", University of Southampton, name of the University School or Department, PhD Thesis, pagination

UNIVERSITY OF SOUTHAMPTON

Faculty of

Natural and Environmental Sciences

Ocean and Earth Science

Assessing the Use of Non-Traditional Stable Isotopes as Tracers of Weathering Processes:

with Evidence from the Southern Alps, South Island, New Zealand

by

Sarah L. Wright

Thesis for the degree of Doctor of Philosophy

UNIVERSITY OF SOUTHAMPTON

Abstract

Faculty of Natural and Environmental Sciences, Ocean and Earth Science

Doctor of Philosophy

by Sarah L Wright

Concentrations of carbon dioxide (CO_2) in the Earth's atmosphere have increased by >100 ppm since pre-industrial times due to the burning of fossil fuels for energy and it is now clear that the consequent warming of the climate system will have widespread impacts on human and natural systems. Chemical weathering of silicate rocks draws down CO_2 from the atmosphere, but the significance of this process and the mechanisms which control weathering rates remain poorly constrained. New information with regards to chemical weathering processes, linkages to physical denudation rates, and the effects of certain rock types on global chemical budgets, are all required.

This study utilises elemental concentrations together with lithium ($\delta^7 \text{Li}$) and magnesium ($\delta^{26} \text{Mg}$) isotopic values of river waters and weathering products to determine the parameters that regulate weathering in a terrestrial environment, and assesses the influence of progressive metamorphism, glacial activity, rainfall patterns, rapid tectonic uplift, climate and geothermal fluid flow. Samples were collected from the Southern Alps on South Island, New Zealand. The Southern Alps represent a relatively pristine environment and a natural laboratory to examine the climatic and tectonic controls on chemical weathering of a largely lithologically homogenous metasilicate terrane with minor metamorphic carbonate, in a temperate, maritime environment.

Chemical weathering and atmospheric CO₂ consumption rates, calculated from riverine elemental data, demonstrate that CO₂ consumed by silicate weathering is relatively low compared to rivers globally. High overall chemical weathering rates (3.1 x 10⁷ g·km⁻²·yr⁻¹ in the west vs. 1.8 x 10⁷ g·km⁻²·yr⁻¹ in the east) are associated with high uplift and erosion rates, and high rainfall on the western side of the Southern Alps, where chemical erosion of metamorphic carbonates is more prevalent. However, higher rates of atmospheric CO₂ consumption due to silicate weathering were found on the eastern side of the Southern Alps (6.4 x 10⁴ mol·km⁻²·yr⁻¹ in the west vs. 7.7 x 10⁴ mol·km⁻²·yr⁻¹ in the east), where uplift and erosion rates are lower. This indicates that uplift accelerates weathering rates of metamorphic carbonates, but has little effect of rates of silicate weathering, which regulates CO₂ drawdown from the atmosphere on long timescales.

The mechanisms that moderate Li and Mg isotopic fractionation in the Southern Alps were thoroughly investigated. Protolith lithology and metamorphic grade have little effect upon the $\delta^7 \text{Li}$ and $\delta^{26} \text{Mg}$ composition of the bedrock. Secondary clay formation (e.g. illite, kaolinite and smectite) during weathering is the dominant process by which Li and Mg isotope fractionation occurs, and climate only has an indirect influence. The residence time of water-rock interaction imposes an important control upon the $\delta^7 \text{Li}$ composition of rivers. However, the effect of this control upon the $\delta^{26} \text{Mg}$ composition of rivers is less clear. The evidence for coupling between riverine $\delta^7 \text{Li}$ and $\delta^{26} \text{Mg}$ values during chemical weathering is weak with respect to results from this study and global studies. This suggests that the behaviour of these isotopes varies between different weathering environments, adding to the complexity of extrapolating local studies to global interpretations.

Declaration of Authorship

I, Sarah L. Wright declare that this thesis titled, 'Assessing the Use of Non-Traditional Stable Isotopes as Tracers of Weathering Processes: with Evidence from the Southern Alps, South Island, New Zealand' and the work presented in it are my own and has been generated by me as the result of my own original research.

I confirm that:

- 1. This work was done wholly or mainly while in candidature for a research degree at this University.
- 2. Where any part of this thesis has previously been submitted for a degree or any other qualification at this University or any other institution, this has been clearly stated.
- 3. Where I have consulted the published work of others, this is always clearly attributed.
- 4. Where I have quoted from the work of others, the source is always given. With the exception of such quotations, this thesis is entirely my own work.
- 5. I have acknowledged all main sources of help.
- 6. Where the thesis is based on work done by myself jointly with others, I have made clear exactly what was done by others and what I have contributed myself.
- 7. None of this work has been published before submission.

Signed:	 	 	
0			
Date:			

Acknowledgements

Firstly, I would like to thank Rachael James for being such a supportive supervisor over the past 3 and a half years. She has been a great teacher and mentor, and my writing style has forever changed for the better. This project has given me invaluable knowledge and experience in geochemistry, which I would not have been able to obtain were it not for advice and help given by Rachael and many others that I would like to thank below.

This project was made possible by Damon Teagle, who I have known since my undergraduate degree at the University of Southampton. My interest in the South Island, New Zealand, was first sparked by Damon with my Masters Project, and I have thoroughly enjoyed studying this area ever since.

I would like to say a big thank you to Catriona Menzies for all her help and support over the years. Her advice, both scientific and non-scientific, has been instrumental in helping me develop this thesis.

I would also like to thank the people who made the analysis of my samples possible, which include Andy Milton, Matt Cooper, Agnes Michalik and Ross Williams. I would also like to thank Chris Pearce for his advice with method development.

I would like to thank Carolyn Graves, Cathy Cole, Jessy Klar, Heather Goring-Harford and David Reading for being amazing office mates that I have had the pleasure of knowing over the years. Anything from discussing data to having a moan about the Neptune was invaluable and probably helped me keep my sanity.

Finally, I would like to thank my family and friends for all of their support. I would like to thank Tim, Mum, Dad, Mark, Carina, Steve, Ange, Karl, Sabrina, Hannah, Fran, and all of my other friends that have helped support me over the last few years.

Table of Contents

Abst	tract	•••••		iii
Decl	aration	of Aut	thorship	v
Ack	nowledg	gement	s	vii
Tabl	le of Co	ntents .		ix
List	of Figur	res		XV
List	of Table	es		xix
Cha	pter 1	•••••		1
1.1	Ration	ale		1
1.2	Weath	ering a	and the Carbon Cycle	2
1.3	Presen	t-day (CO ₂ Consumption by Weathering of Silicate Rocks	4
1.4	Assess	sing the	e Links Between Silicate Weathering and Climate	5
1.5	What (Contro	ls Chemical Weathering Rates?	6
	1.5.1	Lithe	ology	6
	1.5.2	Frac	turing	8
	1.5.3	Tem	perature	9
	1.5.4	Mete	eoric Precipitation	10
	1.5.5	Mou	ıntain Uplift	10
	1.5.6	Rive	erine Systems	11
	1.5.7	Glac	ciers	11
	1.5.8	Biol	ogy	12
	1.5.9	Sum	mary of the Controls on Weathering Rates	13
1.6	Coupli	ing bet	ween Physical Erosion and Chemical Weathering Rates	13
1.7	Clay N	/lineral	Formation and Classification	15
1.8	Isotope	e Syste	ems as Tracers of Continental Weathering Processes	16
	1.8.1	The	Sr Isotope System	17
	1.8.2	The	Li Isotope System	18
	1.	8.2.1	Secondary Mineral Formation	21
	1.	8.2.2	Variations in δ^7 Li of Seawater in the Past	22
	1.	8.2.3	Fractionation of Li Isotopes	23
	1.8.3	The	Mg Isotope System	24
	1.	8.3.1	Processes Fractionating Mg Isotopes	28
	1.	8.3.2	Variation in the δ^{26} Mg Composition of Seawater	29
	1.	8.3.3	Fractionation of Mg Isotopes	30

1.9	Weath	nering Studies on the Southern Alps, New Zealand	31
1.10	Aims	of this Study	31
1.11	Thesis	Outline	32
Char	oter 2		35
2.1		nent Terranes	
2.2		lpine Fault and the Modern Tectonic Setting of the Southern Alps	
2.3		ure of the Orogen	
2.4		ogy and Metamorphic Grade of the Haast Schist	
2.5		s of Rapid Uplift and Orogen Structure upon Climate and Erosion	
	2.5.1	Climate	42
	2.5.2	Glaciation	44
	2.5.3	Erosion	44
	2.5.4	Landslides	45
2.6	Why S	Study the Southern Alps?	46
Chap	ter 3		47
3.1	Sampl	e Collection and Preparation	47
3.2	Prepar	ration of Bedrock and Particulate Material	47
3.3	Eleme	ental Analysis of Bedrock and Particulate Material	49
	3.3.1	XRF (X-Ray Fluorescence) Analysis	49
	3.3.2	ICP-MS (Inductively-Coupled Plasma-Source Mass Spectrometry)	49
3.4	XRD	(X-Ray Diffraction) Analysis	53
	3.4.1	Separation of Clay from River Sand	53
	3.4.2	Clay Identification via XRD	53
3.5	Lithiu	m Isotope Analysis	54
	3.5.1	Separation of Li from the Sample Matrix	54
	3.5.2	Li Column Calibration	55
	3.5.3	MC-ICP-MS Analysis of δ7Li	57
3.6	Magn	esium Isotope Analysis	60
	3.6.1	Separation of Mg from the Sample Matrix	60
	3.6.2	Mg Column Calibration	
	3.6.3	MC-ICP-MS Analysis of δ^{26} Mg	64
Chap	oter 4		69
41	Introd	uction	69

4.2	Analyt	ical Me	ethods	70
4.3	Results	s		71
	4.3.1	Rive	r Waters and Rain Water	71
	4.3.2	Grou	ndwaters (Tartare Tunnels)	73
	4.3.3	Warı	n Springs	75
	4.3.4	Bedr	ock	76
	4.3.5	Mica	Mineral Separates	76
	4.3.6	Rive	r Sands	77
	4.3.7	Rive	rine Suspended Load	78
	4.3.8	Sprir	ng Suspended Load	78
4.4	Discus	sion		78
	4.4.1	Sprir	ng Water Input to River Waters	78
	4.4.2	Grou	ndwater Chemistry and Effect of Low Temperature Rock Reactions	80
	4.4.3	Cher	nistry of Glacial vs. Non-glacial River Waters	84
	4.4.4	Alter	ration of Bedrock, River Sands and Suspended Particulate Material	85
	4.4.5	Silica	ate vs. Carbonate Weathering	91
	4.	4.5.1	Source of Li and Mg	94
	4.4.6	Cher	nical Weathering and Atmospheric CO ₂ Consumption Rates	95
	4.	4.6.1	Comparison to Global Rivers	98
4.5	Summa	ary of t	he Weathering System in the Southern Alps	101
Cha	pter 5	•••••		103
5.1	Introdu	iction .		103
5.2	Metho	ds		104
5.3	Results	s		104
5.4	Discus	sion		107
	5.4.1	Bedr	ock δ ⁷ Li	107
	5.	4.1.1	Effect of Protolith Lithology	108
	5.4.1.2 Effect of Prograde Metamorphism		109	
	5.	4.1.3	Breakdown of Bedrock in the Weathering System	110
	5.4.2	Grou	ndwater (Tartare Tunnels) δ ⁷ Li	113
	5.4.3	Rive	r Water δ ⁷ Li	115
	5	4.3.1	Effect of Secondary Mineral Formation	115
	5.	4.3.2	Effect of Rainfall and Erosion	117
	5.	4.3.3	Effect of Glaciation	121

	5.4.4	Mine	eral Saturation States	123
	5.4.5	Asse	essing the Link between Riverine δ^7 Li and Silicate Weathering	127
	5.4.6	Li Is	otopes as a Proxy for Silicate Weathering Processes	130
5.5	Summ	ary		131
Cha	pter 6	•••••		133
6.1	Introdu	action		133
6.2	Metho	ds		134
6.3	Result	S		134
6.4	Discus	sion		137
	6.4.1	Bedr	·ock δ ²⁶ Mg	137
	6.	4.1.1	Effect of Protolith Lithology	138
	6.	4.1.2	Effect of Prograde Metamorphism	139
	6.	4.1.3	Breakdown of Bedrock in the Weathering System	140
	6.4.2	δ^{26} M	Ig Composition of River Waters	143
	6.	4.2.1	Effect of Primary Mineral Dissolution	143
	6.	4.2.2	Effect of Secondary Mineral Formation	144
	6.	4.2.3	Effect of Rainfall and Erosion	146
	6.	4.2.4	Effect of Biotic Activity	148
	6.	4.2.5	Effect of Glaciation	149
	6.4.3	Mine	eral Saturation States	151
	6.4.4	Asse	essing the Link between Riverine $\delta^{26}Mg$ and Silicate Weathering	154
	6.4.5	Beha	aviour of Mg vs. Li Isotopes during Weathering	158
6.5	Summ	ary		161
Cha	pter 7	•••••		165
7.1	Introdu	action		165
7.2	Hydro	therma	l Fluid Flow in the Southern Alps	166
7.3	Metho	ds		166
7.4	Result	s		167
	7.4.1	Meta	asedimentary-hosted Springs	168
	7.4.2	Ultra	amafic-hosted Springs	169
7.5	Discus	sion		170
	7.5.1	Effec	ct of Temperature	170
	7.5.2	Seco	ondary Mineral Formation	172

	7.5.3	Link between Spring Water δ^7 Li and Silicate Chemical Weathering	176	
	7.5.4	Coupled Mg and Li Isotopes in Spring Waters	178	
7.6	Summa	ary	179	
Chaj	pter 8		181	
8.1	Conclu	sions	181	
	8.1.1	Chemical Weathering and Atmospheric CO ₂ Drawdown in the Southe	rn Alps181	
	8.1.2	Li and Mg Isotopic Fractionation	182	
	8.1.3	Global Implications of δ ⁷ Li Values	182	
	8.1.4	Global Implications of δ ²⁶ Mg Values	183	
	8.1.5	Coupled Li and Mg Isotopic Systems	184	
8.2	Further	r Work	185	
	8.2.1	Further Sample Collection	185	
	8.2.2	Investigation of the Adsorption of Li and Mg onto Clays	185	
	8.2.3	Identification and Potential Quantification of the Processes Fractionati	ng Mg 186	
App	endix A		187	
A.1	Prepara	ation of Bedrock and Particulate Material	187	
	A.1.1	Rock Crushing	187	
	A.1.2	Splitting of River Sand Samples		
	A.1.3	Sieving River Sand Samples		
	A.1.4	Separation of Clay from Coarse Silt Fraction (for ICP-MS Analysis).	188	
	A.1.5	Suspended Load Removal from Filters	189	
	A.1.6	Mica Mineral Separate Picking	189	
	A.1.7	Dissolution of Bedrock and Particulate Material	189	
A.2	Elemei	ntal Analysis of Fluids	191	
	A.2.1	ICP-MS (Inductively-Coupled Plasma-Source Mass Spectrometry)	191	
	A.2.2	ICP-OES (Inductively-Coupled Plasma-Source Optical Emission Special)	ctrometry)	
	A.2.3	IC (Ion Chromatography)	192	
A.3	Spring	Contribution Calculations	192	
A.4		Chemical Weathering and Atmospheric CO ₂ Consumption Rates		
A.5		n and Rainfall Rates		
A.6		d Saturation States		
A.7		n Isotope Method Ticksheet		
A.8	Magnesium Isotope Method Ticksheet			

Appendix B	205
Appendix C	
Appendix C	231
List of References	233

List of Figures

1.1	Schematic diagram showing the major carbon reservoirs and the major carbon fluxes	3
1.2	Diagram highlighting the interactions between climate, tectonics, biology, geomorphology and weathering	6
1.3	Graphical representation of the lifetime of a 1 mm diameter mineral at pH 5 and 25 °C in solution	7
1.4	Dependence of chemical weathering on substrate age	8
1.5	Physical denudation rate against total chemical weathering rate	14
1.6	⁸⁷ Sr/ ⁸⁶ Sr against age (Myr)	17
1.7	Schematic of the Li oceanic budget	19
1.8	Lithium isotopic signature of different rock reservoirs	20
1.9	Lithium isotopic signature of different fluid reservoirs	20
1.10	Comparison of lithium reservoirs	21
1.11	Late Cretaceous to Holocene Li isotopic budget	23
1.12	Schematic of the Mg oceanic budget	25
1.13	Magnesium isotopic signature of different rock reservoirs	26
1.14	Magnesium isotopic signature of different fluid reservoirs	26
1.15	Comparison of magnesium reservoirs	27
1.16	Mg isotopic composition of seawater with depth	29
2.1	Simplified terrane map of South Island, New Zealand	36
2.2	Quaternary uplift and strike-slip rates along the Alpine Fault	38
2.3	Schematic model of the movements and stresses that formed the inboard and outboard zones of the Southern Alps	39
2.4	Map of the Southern Alps, showing the main lithologies that compose the Haast Schist	41
2.5	Map of the Southern Alps, showing the metamorphic facies that compose the Haast Schist	41
2.6	Map of the South Island, showing the topography, ice, major rivers, active faults, rainfall and erosion rates	42
2.7	Block diagram summarising the effects of Australian-Pacific plate transpression	43
2.8	Denudation rates and sediment discharges from catchments draining the Southern Alps to the west of the Main Divide	45
3.1	Li column calibration using a river water, a spring water and a bedrock sample	56
3.2	δ^7 Li external reproducibility of the standards	59
3.3	Mg column calibration using 2 M TD HNO ₃	61
3.4	Mg column calibration using 0.4 M TD HNO ₃	62
3.5	Mg column calibration using 0.4 M TD HNO ₃	63
3.6	Mg column calibration using 0.8 M TD HNO ₃ and 2 M TD HNO ₃	63
3.7	Effect of evaporation on Mg isotopic ratios during analyses on MC-ICP-MS.	65
3.8	δ^{25} Mg external reproducibility of the standards	67
3.9	δ^{26} Mg external reproducibility of the standards	68
- • -		\sim

4.1	Map showing the localities of samples analysed in this study	70
4.2	Ternary diagrams showing the major cation and anion composition of surface fluids from the Southern Alps	74
4.3	Bar charts showing the average major elements concentrations (Wt. %) in the solid phase	77
4.4	Schematic of the Tartare Tunnels	81
4.5	Elemental concentrations in the groundwater against depth of overburden.	83
4.6	Saturation index of calcite against pH in the dissolved load of the river waters	84
4.7	pH against TDS of the non-glacial river waters	85
4.8	Lithium concentration against CIA for the bedrock, micas, river sands and suspended load	87
4.9	Magnesium concentration against CIA for the bedrock, micas, river sands and suspended load	87
4.10	X-ray diffractograms of river sand clay fractions	90
4.11	Na-normalised mixing diagram between HCO ₃ ⁻ and Ca	92
4.12	Na-normalised mixing diagram of Ca and Mg	92
4.13	Calcium against alkalinity of the river waters	93
4.14	Lithium against alkalinity of the river waters	93
4.15	Histograms of the maximum proportion of dissolved lithium in river waters from silicate weathering	94
4.16	Graphical representation of weathering rates and atmospheric CO ₂ consumption rates.	100
5.1	δ^7 Li values of the fluid samples from the Southern Alps, with comparison to bedrock	105
5.2 5.3	Li concentration against δ^7 Li value of samples from the Southern Alps δ^7 Li signatures of the bedrock and weathering products of the Southern Alps	105 106
5.4	Li concentration against δ^7 Li value of the bedrock from the Southern Alps, with comparison to data from the literature	107
5.5	Li concentration against δ^7 Li value for the protolith lithologies of the Southern Alps bedrock	108
5.6	Li concentration and δ^7 Li value against metamorphic temperature	109
5.7	Metamorphic temperature against δ^7 Li value of the bedrock and the dissolved load of the rivers	110
5.8	Li concentration against δ^7 Li value of the bedrock and weathering products of the Southern Alps	111
5.9	CIA against δ^7 Li value of the bedrock and weathering products of the Southern Alps	112
5.10	Increasing tunnel overburden of the Tartare Tunnels against Li concentration and δ^7 Li value of groundwater samples	113
5.11		114
5.12	Li concentration against δ' Li value of the groundwaters	
5.13	Li concentration against δ^7 Li value of the groundwaters Li concentration against δ^7 Li value of the river waters	115
	Li concentration against δ' Li value of the groundwaters	115116

5.15	Li concentration against δ^7 Li value of rivers draining east and west of the Main Divide
5.16	Physical denudation rate against total chemical weathering rate, with focus on rivers east and west of the Southern Alps
5.17	Erosion rate and rainfall against δ^7 Li values in the riverine dissolved load east and west of the Main Divide
5.18	Li concentration against δ^7 Li value of the dissolved load in the glacial river waters
5.19	Relationship between Mg and Li for the river sands and riverine suspended load
5.20	Saturation indices of primary and secondary minerals against pH, temperature and δ^7 Li value in the dissolved load of the rivers
5.21	δ^7 Li value of the suspended load against δ^7 Li value of the dissolved load of the river waters
5.22 5.23	Silicate weathering rate against riverine $\delta^7 \text{Li}$ values
6.1 6.2	δ^{26} Mg and δ^{25} Mg values of all samples and standards
	δ^{26} Mg signatures of fluid samples from the Southern Alps, with comparison to the bedrock
6.3	Mg concentration against δ^{26} Mg value of fluid and bedrock samples
6.4	δ^{26} Mg value of the bedrock and weathering products
6.5	Mg concentration against δ^{26} Mg value of bedrock from the Southern Alps, with comparison to published data.
6.6	Mg concentration against δ^{26} Mg value for protolith lithologies of the Southern Alps bedrock
6.7 6.8	Mg concentration and δ^{26} Mg value against metamorphic temperature Metamorphic temperature against δ^{26} Mg value of the bedrock and the river waters
6.9	Mg concentration against δ^{26} Mg value of the bedrock and weathering products
6.10	CIA against δ^{26} Mg value of the bedrock and weathering products
6.11	Mg concentration against δ^{26} Mg value of the river waters
6.12	Ratios of Mg/Na in the dissolved load and Mg/Na in weathered rock against δ^{26} Mg value of the riverine dissolved load.
6.13	Mg concentration against δ^{26} Mg value of river waters draining east and west of the Main Divide.
6.14	Erosion rate and rainfall against δ^{26} Mg value in the dissolved load of rivers east and west of the Southern Alps.
6.15	Mg concentration against δ^{26} Mg value of glacial river waters
6.16	Ca/Na ratio against δ^{26} Mg value of the river waters
6.17	Saturation indices of primary and secondary minerals against δ^{26} Mg value of the river waters.
6.18	Saturation index of calcite against δ^{26} Mg value in the dissolved load of the river waters.
6.19	δ^{26} Mg value of the suspended load against δ^{26} Mg value of the dissolved load of the river waters
6.20	Silicate weathering rate against δ^{26} Mg value of the river waters
6.21	Mg/Na ratio against δ^{26} Mg value in the river waters
6.22	δ^7 Li value against δ^{26} Mg value in the river waters

6.23	δ^7 Li value against δ^{26} Mg value in the dissolved load and riverine suspended	
	load	160
7.1	Li concentration against δ^7 Li value of the spring waters	168
7.2	Mg concentration against δ^{26} Mg value of the spring waters	169
7.3	Measured spring water temperature and calculated silica equilibration	
	temperature against Li concentration and δ^7 Li value	171
7.4	Saturation indices of secondary minerals against pH, temperature and δ^7 Li	
	value for measured spring water temperature and silica equilibration	
	temperature	173
7.5	Saturation indices of secondary minerals against pH, temperature and δ^7 Li	
	value for silica equilibration temperature of the spring waters	175
7.6	Spring silica equilibration temperature against the lithium isotopic	
	fractionation factor	176
7.7	δ^7 Li value of the suspended load against δ^7 Li value of the dissolved load of	
	the spring waters	177
7.8	Li/Na against δ^7 Li value of the dissolved load of the springs	178
7.9	δ^7 Li value against δ^{26} Mg value in the dissolved load of the springs	179

List of Tables

1.1 1.2 1.3	CO ₂ consumption fluxes by carbonate and silicate weathering Effective rates of glacial erosion in various glacial environments Summary of clay mineral types	4 12 16
3.1 3.2 3.3	Precision of elemental analyses by ICP-MS	51 52 57
3.4 3.5	Average δ^7 Li values of analysed standards and external reproducibility Matrix elemental contributions from the Mg columns, as a % of the total Mg	58
3.6 3.7	loaded onto the columns	64 64
	reproducibility	66
4.1 4.2	TDS of the Southern Alps rivers, with comparison to global rivers	73
4.3	Hydrologic parameters, chemical weathering rates and atmospheric CO ₂ consumption rates of two rivers draining the Southern Alps	80 97
4.4	Comparison of hydrologic parameters, chemical weathering rates and atmospheric CO ₂ consumption rates of the Southern Alps rivers with comparison to global rivers	99
5.1	Mass balance defining the proportion of Li in the bedrock that is derived from micaceous minerals	111
6.1	Mass balance defining the proportion of Mg in the bedrock that is derived from micaceous minerals	141
A.1	Calculations of the minimum and maximum spring water contribution to river waters	194
A.2	Weathering and atmospheric CO ₂ consumption rates for global rivers	198
A.3	River water primary and secondary mineral saturation indices	202
A.4	Spring water secondary mineral saturation indices, calculated using measured temperature of the spring water	193 202
A.5	Spring water secondary mineral saturation indices, calculated using silica equilibrium temperature of the spring water	194 203
A.6	Spring water secondary mineral saturation indices (alternative assemblage), calculated using silica equilibrium temperature of the spring water	203

B.1	Chemical composition and isotopic data of the river waters, groundwaters	
	and rain waters	206
B.2	Chemical composition and isotopic data of the spring waters	211
B.3	Chemical composition and isotopic data of the bedrock	217
B.4	Chemical composition and isotopic data of the mica mineral separates	220
B.5	Chemical composition and isotopic data of the river sand size fractions	221
B.6	Chemical composition and isotopic data of the riverine and spring water	
	suspended load	224
B.7	Major element concentrations of the bedrock, mica separates, river sands,	
	riverine suspended load and spring suspended load in Wt. %	228

Chapter 1

Introduction

1.1 Rationale

The global carbon cycle balances the exchanges of carbon between different reservoirs on Earth. Recent studies show that atmospheric CO₂ is increasing, with subsequent effects on global climate (Canadell et al., 2007; Hansen et al., 2008). Weathering of silicate rocks is known to be a sink for atmospheric CO₂, but it is unclear how significant this sink may be with respect to the global carbon cycle (e.g. Walker et al., 1981; Berner et al., 1983; Molnar and England, 1990; Edmond, 1992; Raymo and Ruddiman, 1992, Gaillardet et al., 1999b). Mechanisms which moderate weathering processes and the weathering flux are poorly understood, leading to large uncertainties when modelling the global carbon budget. It is important to understand the dominant chemical weathering processes of an area, the spatial patterns of chemical denudation, and to determine whether small areas with complex lithologies can exert significant controls on global chemical budgets. Gaps in knowledge remain that continue to hinder our understanding of the links between weathering, erosion, uplift, climate, and the global carbon cycle.

This study focuses on the factors that affect weathering in a terrestrial environment and assesses the influence of metamorphism, glaciers, rainfall, rapid tectonic uplift, geothermal springs and climate. The aims of this study are to better constrain weathering regimes to improve our understanding of this aspect of the global carbon cycle. The Southern Alps on South Island, New Zealand, are the focus of this study, as they present a relatively pristine environment (e.g. little air and water pollution due to few industrial sources and low population) to systematically examine the climatic and tectonic controls on chemical weathering in a lithologically homogenous metasilicate terrane.

1.2 Weathering and the Carbon Cycle

Chemical weathering of both silicate and carbonate rocks affects the carbon cycle by removing carbon from the atmosphere and storing it in weathering products (short term) or as marine sediments (long term). Weathering of carbonate rocks (Eq. 1.1) results in the removal of one mole of atmospheric CO₂, which is converted to bicarbonate dissolved in river water (Walker et al., 1981). The subsequent precipitation of calcium carbonate in the oceans returns 1 mole of CO₂ to the atmosphere (Eq. 1.2). Therefore on long timescales, weathering of carbonate rocks has no impact on the CO₂ cycle.

In contrast, weathering of calcium and magnesium aluminosilicates results in the removal of 2 moles of CO₂ (Eq. 1.3), of which only one mole is returned to the atmosphere (Eq. 1.2) due to precipitation of carbonate in the oceans (Walker et al., 1981; Berner et al., 1983).

Carbonate weathering:

$$CO_2 + H_2O + CaCO_3 \rightarrow Ca^{2+} + 2HCO_3^{-}$$
 (Eq. 1.1)

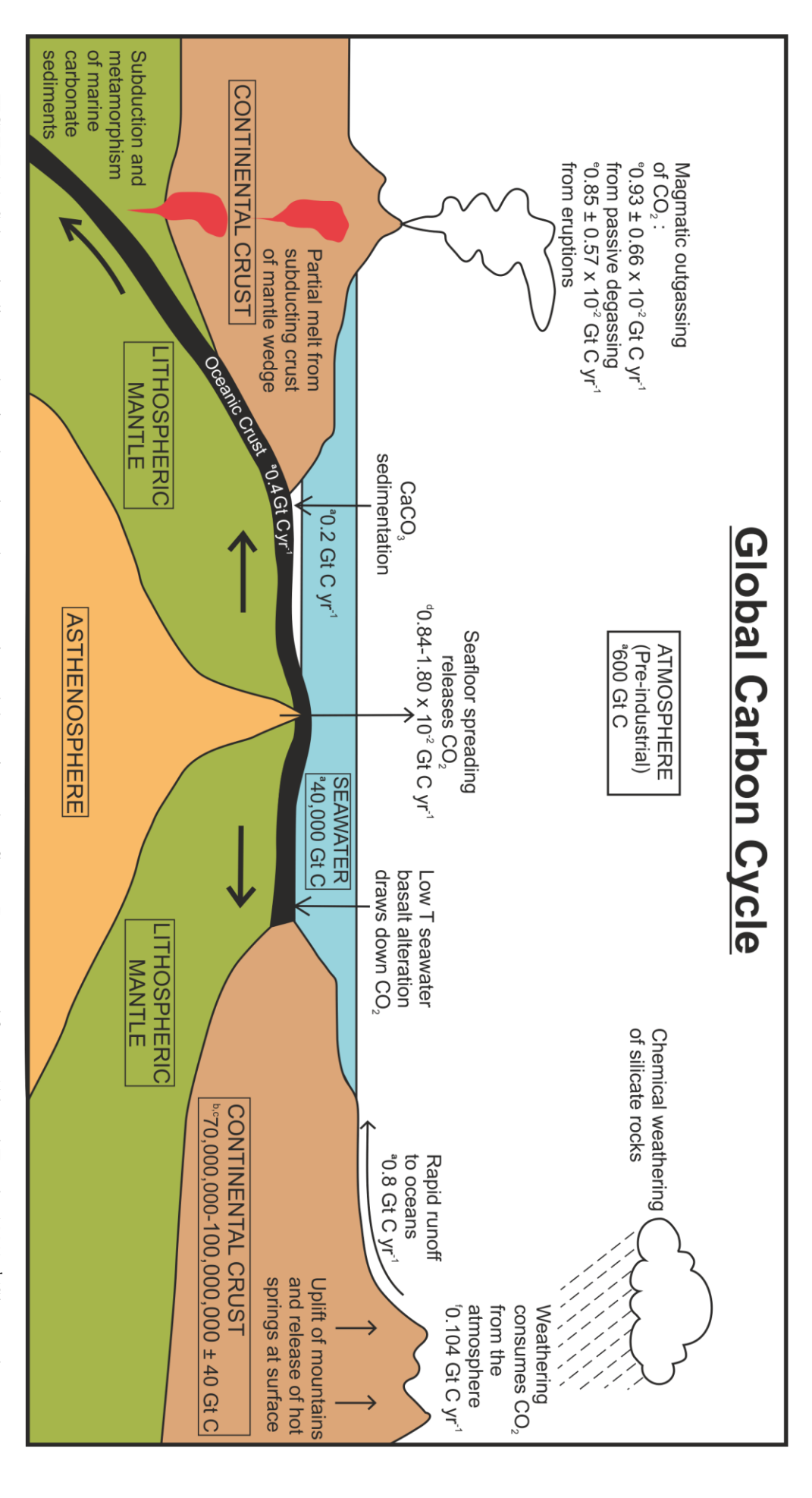
$$Ca^{2+} + 2HCO_3^{-} \rightarrow CaCO_3 + CO_2 + H_2O$$
 (Eq. 1.2)

Silicate weathering:

$$2CO_2 + 3H_2O + CaSiO_3 \rightarrow Ca^{2+} + 2HCO_3^{-} + H_4SiO_4$$
 (Eq. 1.3)

$$2CO_2 + 3H_2O + MgSiO_3 \rightarrow Mg^{2+} + 2HCO_3^- + H_4SiO_4$$
 (Eq. 1.4)

Thus, on long timescales, silicate weathering plays an important role on the regulation of levels of atmospheric CO₂ concentrations (Figure 1.1) and therefore global climate (Walker et al., 1981; Berner et al., 1983; Berner and Kothavala, 2001; Wallmann, 2001; Berner, 2004).



Munhoven, 2002; Amiotte-Suchet et al., 2003; Hartmann et al., 2009). Zahnle, 2001); (Hayes and Waldbauer, 2006); (Gerlach, 1991); (Williams et al., 1992); (Berner et al., 1983; Meybeck, 1987; Gaillardet et al., 1999b; FIGURE 1.1: Schematic diagram showing the major carbon reservoirs and the major carbon fluxes. Data sourced from: "(Alt and Teagle, 1999); (Sleep and

1.3 Present-day CO₂ Consumption by Weathering of Silicate Rocks

On a global scale, the amount of CO₂ consumed by rock weathering today is estimated to be between 0.133-0.154 Gt C yr⁻¹ for silicates and between 0.088-0.148 Gt C yr⁻¹ for carbonates (Table 1.1 and references therein). The range of estimates reflects differences in the geochemical models used in each study, as well as the uncertainties in the extrapolation of sparse measurements, which will be discussed below.

Two different approaches have been used to estimate global atmospheric CO₂ consumption: 1) reverse modelling using hydrochemical fluxes from large rivers, and 2) forward modelling using relationships between rock weathering rates of specific lithologies (Hartmann et al., 2009). Reverse modelling estimates the products of rock weathering using river chemical data (Berner et al., 1983; Meybeck, 1987; Gaillardet et al., 1999b), assuming that the weathering products are derived from specific lithologies. This method limits the spatial resolution of CO₂ consumption to a specific catchment area, and it has been suggested that these calculations often do not consider enough lithologies (Hartmann et al., 2009). Forward modelling identifies relationships between rock weathering rates of specific lithological classes and the major factors controlling them (Bluth and Kump, 1994; Amiotte-Suchet et al., 2003; Hartmann et al., 2009). Although the spatial resolution of forward modelling is not limited, it has not been determined if these lithological classes adequately represent the large variety of geochemical or mineralogical properties that could be observed (Hartmann et al., 2009).

The global contribution of carbonate sedimentary rocks to CO₂ consumption fluxes has been overestimated in older models (Table 1.1), which used the reverse model (Berner et al., 1983; Meybeck, 1987; Gaillardet et al., 1999b). Model results using the reverse method are sensitive to the chosen end-member chemical composition (Hartmann et al., 2009). Therefore, including additional rock end-members would result in a lower proportion of carbonate weathering to global CO₂ consumption using the reverse model approach (Amiotte-Suchet et al., 2003; Hartmann et

TABLE 1.1: CO₂ consumption fluxes by carbonate and silicate weathering in Gt C yr⁻¹.

	Berner et al., 1983 Rewrse model, used Ca & Mg containing silicates & carbonates		Reverse model, 16 major rock types		Gaillardet et al., 1999b Reverse model, granitoids and carbonates		Munhoven, 2002 Forward model 6 lithological classes		Amiotte-Suchet et al., 2003 Forward model, 6 lithological classes		Hartmann et al., 2009 Forward model, 15 lithological classes	
	Gt C yr ⁻¹	%	Gt C yr ⁻¹	%	Gt C yr ⁻¹	%	Gt C yr ⁻¹	%	Gt C yr ⁻¹	%	Gt C yr ⁻¹	%
Carbonates	0.142	50.7	0.144	48.8	0.148	51.4	0.088	39.7	0.104	40.1	0.088	37
Silicates	0.138	49.3	0.151^{b}	52.2	0.140^{a}	48.6	0.133	60.3	0.154	59.9	0.149	63
Flux Total	0.280		0.295 ^b		0.288		0.221		0.258		0.237	

^a Includes 8.7 x 10¹² mol C yr⁻¹ derived from continental rocks weathering + 3 x 10¹² mol C yr⁻¹ derived from weathering of volcanic rocks from oceanic islands and volcanic arcs.

^b These fluxes do not include the contribution of Na and K silicates.

al., 2009). In addition, more recent studies using the forward method also take into account spatial distribution of rock types (Amiotte-Suchet et al., 2003). It is apparent that simple modifications of model parameters can result in significant variations in the estimations of CO₂ consumption fluxes (Table 1.1).

1.4 Assessing the Links Between Silicate Weathering and Climate

The consumption of CO₂ by silicate weathering may stabilize global temperatures over geological timescales, because increases in atmospheric CO₂ increase temperature, which in turn increases the rate of silicate weathering, leading to enhanced drawdown of CO₂ (Walker et al., 1981). This idea has subsequently been extended to take into account other variables that affect CO₂, such as seafloor spreading rates, land area, and rock reservoir size, in the form of the 'BLAG' (Berner, Lasaga and Garrels, 1983) model, which attempts to simulate the variation in the atmospheric CO₂ concentration over the past 100 Myr (Berner et al., 1983).

The importance of silicate weathering-temperature feedback has been challenged, with the suggestion that climate cooling over the last 50 Myr is the result of uplift of the Himalayan and Andean mountain belts, with a consequent increase in chemical weathering rates, which draws down atmospheric CO₂, causing atmospheric cooling (Molnar and England, 1990; Edmond, 1992; Raymo and Ruddiman, 1992). A runaway Cenozoic "icehouse", due to increased weathering, is avoided by a reduction in the burial rate of organic carbon, and from weathering and precipitation of secondary minerals associated with submarine basalts (White and Brantley, 1995). Thus, in this model, increased weathering rates correlate with falling global temperatures, whereas in BLAG-type models, weathering rates increase as global temperature rises.

Long-term variations in weathering rates could also be driven by CO₂ produced by metamorphic decarbonation reactions during orogenesis (Bickle, 1996). Orogenesis will increase weathering rates by uplift, physical erosion and exposure of silicate minerals, and provide additional CO₂ from metamorphic decarbonation reactions to maintain the increased weathering rates (Bickle, 1996). Thus, the rate at which sediment is processed by orogenesis may be a major forcing factor for the rate at which chemical weathering increases and its effects on global climate.

1.5 What Controls Chemical Weathering Rates?

Chemical weathering can be separated into two different processes; chemical dissolution and chemical precipitation. Chemical weathering intensity is generally defined as the fraction of original bedrock dissolved during weathering. The rate of chemical weathering is controlled by various climatic, tectonic, biological and geomorphological processes (Figure 1.2). Climatic factors such as temperature and moisture availability are important because they directly control chemical kinetics, for example, wet and warm environments generally experience faster rates of chemical weathering (e.g. White et al., 1998). The removal of rock regolith by erosion may enhance or reduce weathering rates, depending on the environment (Drever, 1994), also the resistance of different lithologies and minerals to chemical weathering is variable (Figure 1.3). Tectonic factors can exert a significant control on chemical dissolution rate, for example, uplift can weaken rocks through faulting, which enhances mechanical erosion (Reed, 1964). These complex interlinkages make it difficult to isolate the impact of any one controlling factor on weathering rates.

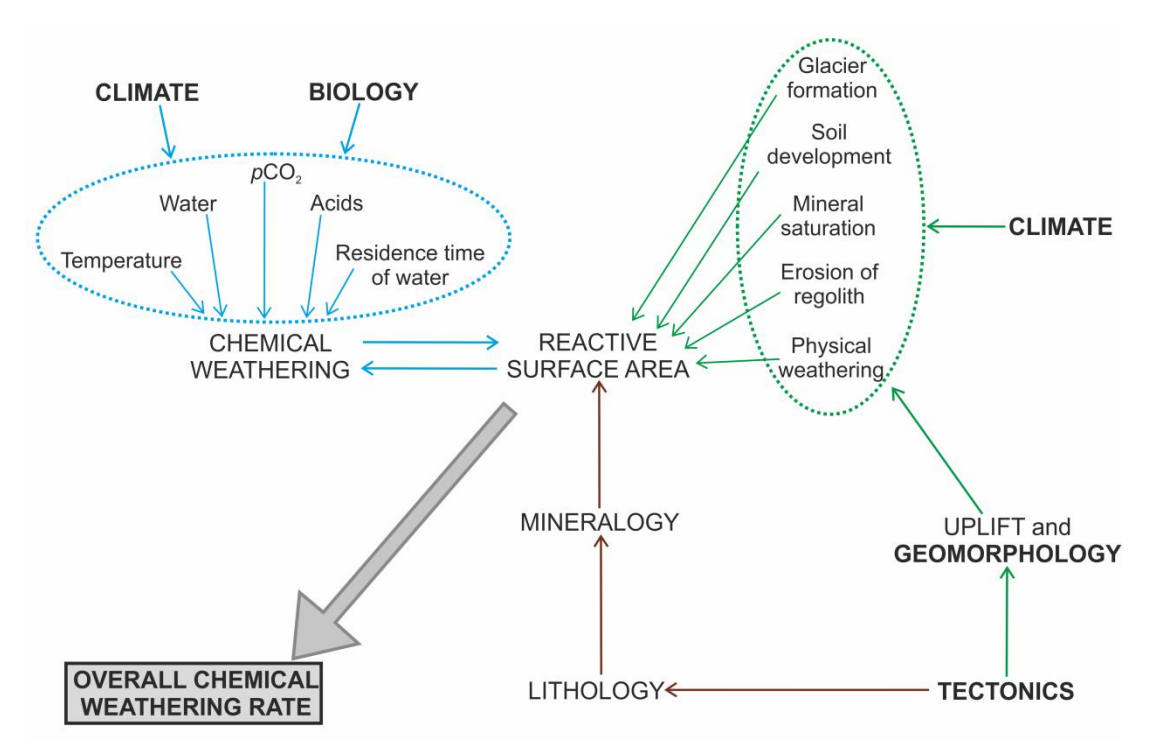


FIGURE 1.2: Diagram highlighting the interactions between climate, tectonics, biology, geomorphology and weathering. Adapted from Goudie and Viles (2012).

1.5.1 Lithology

Different minerals weather at different rates (Figure 1.3), and dissolution rates estimated in the field are usually reported to be 10 to 10^4 times slower than rates obtained in laboratory studies, due to the effects of climate and biota (Brantley and Chen, 1995; West et al., 2005), and the

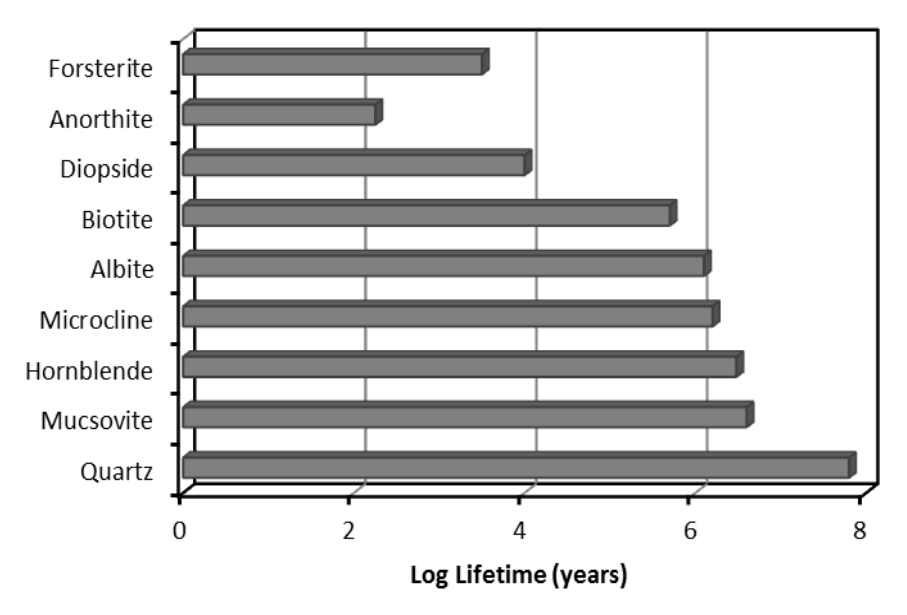


FIGURE 1.3: Graphical representation of the lifetime of a 1 mm diameter mineral at pH = 5 and 25 °C, in solution (Lasaga et al., 1994; Kump et al., 2000; White and Brantley, 2003). These values were calculated assuming far from equilibrium conditions and continuous contact with a sufficiently undersaturated solution. The time it takes for a crystal to dissolve completely is calculated, based on calculations of the dissolution of silica at 25 °C and pH = 5 (Lasaga et al., 1994).

accumulation of leached layers and precipitation of secondary products in the natural environment (White and Brantley, 2003).

Chemical dissolution rates also fall over time (Vance et al., 2009). Field and laboratory observations suggest that newly-eroded fine-grained material is highly reactive when initially exposed to chemical weathering agents, but with time, weathering rate decreases dramatically (Figure 1.4; Vance et al., 2009). The laboratory data conform to a power law relationship (shown by the solid line in Figure 1.4), with instantaneous weathering rate at any time subsequent to exposure (Vance et al., 2009). The slopes of the power law relationship between weathering rates and exposure times for different lithologies are similar (Taylor and Blum, 1995; White and Brantley, 2003; Porder et al., 2007; Vance et al., 2009). It is important to note that even though the lithologies differ, climatic regimes range from glacial to tropical, and there are variations in absolute weathering rates, the dependence of weathering rate on substrate age is the same (Vance et al., 2009).

In a study using hornblende crystals, the rate of release of Al, Fe and Mg was linear with respect to surface area (Zhang et al., 1993), although some have argued that dissolution rates may be independent of grain diameter (Anbeek, 1994). Surface area may also be increased by etching, although weathering of deep etches may become rate-limited by diffusion, such that dissolution rates are not linear with respect to surface area (Rimstidt and Dove, 1986). Micropores in naturally

occurring hornblende may actually dominate surface area, and may be more significant in the natural environment than laboratory etching (Anbeek, 1994).

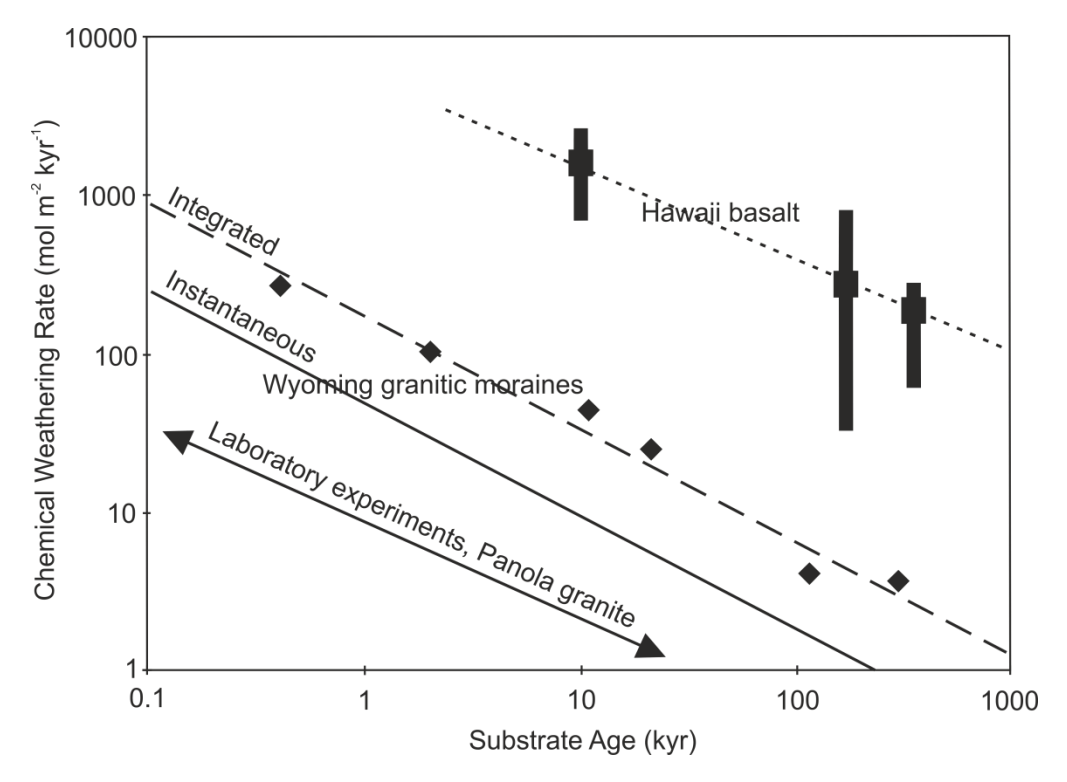


FIGURE 1.4: Dependence of chemical weathering on substrate age. Black diamonds represent measured chemical depletion rates for a sequence of soils of varying age, deposited by retreating glaciers/ice sheets in Wyoming (Taylor and Blum, 1995). Laboratory data on the weathering rate of Panola granite (White and Brantley, 2003), as well as data for a series of Hawaiian basaltic lavas (Porder et al., 2007) yield relationships between time-integrated weathering rate and substrate age that are very similar to the Wyoming data. Image from Vance et al. (2009).

Chemical dissolution of sheet silicates involves the dissolution of accessory phases, such as muscovite and biotite micas, and the nucleation and growth of authigenic phases, particularly clay minerals such as smectite and kaolinite (Nagy, 1995). Through dissolution, sheet silicates are a source of solutes in surface waters, but can also be a sink, through the processes of adsorption and precipitation (Nagy, 1995). Laboratory experiments involving sheet silicates have shown that they do not always dissolve congruently (Xie and Walther, 1992). In general, dissolution of sheet silicates is almost always initially incongruent, and with time, dissolution becomes congruent as chemical weathering intensity decreases (Nagy, 1995).

1.5.2 Fracturing

Fracturing is a slow process and an early stage contributor to the decomposition of bedrock, and converting silicate rocks into clastic constituents (Dove, 1995). During uplift of mountain belts, fractures and joints can form on many different scales and at different rates (Lorenz et al., 1991).

Important environmental implications can be influenced by fracturing, such as long-range groundwater transport patterns which are often dominated by the structure and arrangement of local and regional scale joint sets (Pollard and Aydin, 1988; Olson, 1993; Maréchal et al., 2004; Røyne et al., 2008). The dominant mechanism for fracture growth may be chemical stress corrosion or dissolution if materials are subjected to saturated and/or aggressive fluid environments (Kronenberg, 1994; Renshaw and Pollard, 1994). Many studies have documented that the kinetics of fracture growth are influenced by the chemical composition of fluids in contact with quartz (Atkinson and Meredith, 1981). Processes that govern subcritical crack growth of quartz include stress corrosion, diffusion, ion exchange, microplasticity and dissolution (Dove, 1995). In addition, frost weathering leads to the expansion of pore waters, inducing fracturing of rock (Walder and Hallet, 1986; Matsuoka, 2001).

1.5.3 Temperature

Chemical weathering is often considered to be primarily a function of temperature and runoff (Berner et al., 1983; Velbel, 1993; White and Blum, 1995; White et al., 1998; Dessert et al., 2001). In theory, the rate of mineral dissolution during weathering increases with temperature according to the Arrhenius equation (Eq. 1.5) (White and Blum, 1995; Dessert et al., 2003):

$$r_T = Ae^{(-Ea/RT)}$$
 (Eq. 1.5)

Where, *A* is a rate constant, *T* is the absolute temperature (kelvin), *Ea* is the activation energy (kJ mol⁻¹) required to overcome the energy barrier to chemical dissolution and *R* is the gas constant (Laidler, 1984). In practice this means that the rate of reaction doubles for every 10 °C rise in temperature, such that reaction rates in lowland humid tropical areas are faster by a factor of four compared to high latitude or high altitude locations (Thomas, 1994). However, field studies in eastern Siberia have shown that weathering rates and CO₂ uptake by weathering of aluminosilicate rocks are of a similar magnitude to that found in tropical shields (Huh and Edmond, 1999). These unexpectedly high weathering rates are attributed to exposure of fresh surfaces as a result of frost weathering; in tropical areas, weathering rates may be inhibited by thick, highly weathered (laterite) soils (Huh and Edmond, 1999). Thus, there is no simple Arrhenius-type temperature control on weathering rates, but rather that weathering rates are lower when temperature (and precipitation) is low, in the absence of uplift (Huh, 2003). The fundamental problem with trying to define a temperature dependence on weathering from field data at the watershed scale is the co-dependence of others factors that affect weathering, such as precipitation and evaporation, vegetation cover, and the extent of prior soil development and cation leaching (White et al., 1999).

Chapter 1

In addition, seasonality can significantly alter the weathering environment, resulting in seasonal variations in river chemistry (Tipper et al., 2006a).

Some success in assessing controls on weathering rates and fluxes has been achieved by carefully selecting small catchments and soil profiles (Riebe et al., 2001; France-Lanord et al., 2003; Jacobson and Blum, 2003; West et al., 2005). However, the importance of runoff and temperature in the long term remains uncertain (Riebe et al., 2001), as many studies only focus on short term climatic forcing effects. The mineral saturation state of a soil profile is also important to consider as it is directly affected by primary mineral dissolution and can determine the potential for secondary minerals to form.

1.5.4 Meteoric Precipitation

Chemical dissolution requires moisture and river flow to transport the weathered solutes to the ocean; in general, warm and wet catchments experience higher weathering rates (White and Blum, 1995). Studies of small river catchments indicate that rainfall can be important (Goldsmith et al., 2010), although the response of silicate weathering to increased runoff is not linear (Holland, 1978). In most rivers, the concentration of dissolved ions liberated by weathering decreases as river runoff increases, probably because of the increased contribution of groundwater inputs at low flows (Tipper et al., 2006a), and reduced water-rock contact time when runoff is high (Hornberger et al., 2001).

1.5.5 Mountain Uplift

Orogenic uplift leads to the development of high relief, and high rainfall produces steep slopes and rapid erosion rates, exposing fresh mineral surfaces which increases the potential for chemical dissolution (Gaillardet et al., 1995; Berner, 2004). Approximately 50% of CO₂ drawdown associated with silicate weathering occurs in the world's active mountain belts (Hilley and Porder, 2008). Mountains can also bring about enhanced rainfall due to orographic effects, resulting in greater flushing of rocks by water (Ruddiman et al., 1989). Thus, weathering of silicate minerals is expected to be higher during tectonic periods when high mountains were more extensive. For example, uplift rate in the eastern syntaxis of the Himalaya is high (up to 10 mm/yr; Burg et al., 1998), resulting in the removal of large volumes of rock and sediment through glacial erosion and massive landsliding and erosion. As a result, CO₂ consumption rates are high (~5.5 x 10⁵ mol·km²·yr⁻¹), relative to areas with lower rates of uplift (Hren et al., 2007). In the western Southern Alps of New Zealand, where uplift and erosion is rapid (125 x 10⁸ g·km²·yr⁻¹; Jacobson and Blum,

2003), the CO₂ consumption rate is ~2 times higher than it is on the eastern side ($14 \times 10^4 \text{ vs. } 6.9 \times 10^4 \text{ mol} \cdot \text{km}^{-2} \cdot \text{yr}^{-1}$; Jacobson and Blum, 2003).

However, controversies remain over the strength of uplift-erosion-weathering linkages (Goudie and Viles, 2012). For example, recent analyses of the chemical composition of Ganges, Brahmaputra, Indus and other river waters originating on the Qinghai-Tibet Plateau, suggest that this region only makes a small contribution (as little as 3.8%) to global atmospheric CO₂ drawdown derived from silicate weathering, despite high rates of uplift (Wu et al., 2008).

1.5.6 Riverine Systems

A large proportion of weathered material is transported to the oceans by rivers, which makes understanding the processes that occur during transportation critical to understanding of the signal that is transferred to the oceans by continental weathering. Lithology is a major factor in controlling the chemistry of rivers, as discussed previously. The chemical composition of rivers is generally dominated by Ca²⁺ and HCO₃-, but they can also have substantial concentrations of Mg²⁺, Na⁺, K⁺, Cl⁻ and SO₄²⁻ (Meybeck, 2003). Large rivers generally flow over a mixture of lithologies, and so determining exact lithological influences on river chemistry can be complex.

Easily weathered minerals (e.g. calcite) can have a disproportionate influence on river chemistry, thus the dissolved load of a river may not always reflect the chemistry of the bedrock (Anderson and Anderson, 2010). In addition, individual minerals themselves may not always dissolve congruently (Nagy, 1995). Some elements are also more easily mobilised during weathering, such as Na⁺, Ca²⁺ and Mg²⁺, than others, e.g. Fe²⁺ and Al³⁺ (Gislason et al., 1996). As a consequence, the river carries a proportionally higher dissolved load of mobile elements than the remaining weathered bedload, which is left with a higher proportion of immobile elements (Gaillardet et al., 2003). The congruency of chemical weathering increases as physical erosion intensifies, and dependence upon the chemical composition of the bedrock has less control over weathering susceptibilities.

1.5.7 Glaciers

The relationship between erosion and weathering rate becomes more complex when uplift causes a sufficient rise in surface elevation to facilitate glacial and periglacial conditions. Glacier formation is important with respect to weathering of mountain belts because glacial grinding on underlying bedrock enhances erosion, increasing mineral surface area, thus allowing more

Chapter 1

efficient chemical dissolution (Hallet et al., 1996), as shown by higher concentrations of solutes found in proglacial rivers (e.g. Jacobsen et al., 2003).

Effective rates of glacial erosion vary in different glacial environments. High latitude thin glaciers on resistant bedrock generally have low effective rates of glacial erosion (0.01-1 mm yr⁻¹; Table 1.2). Temperate glaciers at lower latitudes can produce much higher effective rates of glacial erosion, especially if the glaciers are rapid and located in tectonically active areas (>1-10 mm yr⁻¹; Table 1.2).

Table 1.2: Effective rates of glacial erosion in various glacial environments. Data taken from Hallet et al. (1996) and references therein.

Effective rate of glacial erosion (mm yr ⁻¹)	Glacial environment	Location
>0.01	Polar glaciers and thin temperate plateau glaciers on crystalline bedrock	Norway
>0.1	Temperate valley glaciers on resistant crystalline bedrock	Norway
>1	Small temperate glaciers on diverse bedrock	Swiss Alps, Southern Alps (New Zealand)
>10	Large and fast-moving temperate valley glaciers in tectonically active ranges	Southeast Alaska

1.5.8 Biology

Plants can physically affect weathering rates by increasing the residence time of water in soil systems, increasing evapotranspiration and increasing permeability in some soils, which indirectly affects chemical dissolution rates by creating fresh mineral surfaces (Kump et al., 2000). Vegetation, from land plants to microbiota, can also directly affect silicate chemical weathering rates and chemical fluxes in rivers through chemical effects (e.g. chelation of metal ions, changing pH through the increase of pCO_2 in the soil) (Drever, 1994; Moulton and Berner, 1998; Moulton et al., 2000; Derry et al., 2005). Where soils are thin and mineral dissolution limits weathering, plants can increase the chemical weathering rate due to increased surface area of minerals and contact time with water (Drever, 1994). Where mechanical erosion limits weathering, the precipitation of secondary alteration products and the development of a deep regolith (which is enhanced by plants) will decrease or have no effect upon chemical weathering rates (Drever, 1994). In addition, microbes can dramatically increase mineral dissolution rates, and can impact precipitation of secondary minerals and clay hydration reactions (Banfield et al., 1999).

1.5.9 Summary of the Controls on Weathering Rates

Controls on weathering rates are diverse and have complex interlinkages. The effects of these controls on weathering rates have been quantified where possible, but due to significant differences in laboratory and field studies, it is difficult to accurately define which controls are more substantial than others. Lithology is likely to be a major control on weathering rates due to different minerals weathering at different rates (Figure 1.3), but these rates are strongly dependent upon the climatic conditions (temperature and rainfall) that the weathering environment is subject to. Uplift of mountainous terranes and formations of glaciers have been shown to greatly increase weathering rates, however these processes only occur locally. The slow process of rock fracturing is difficult to quantitatively constrain accurately due to it occurring on a large scale and often at depth. Effect of biology is also difficult to quantify due to the broad range of biological processes that can possibly occur and the large number of factors that biology is affected by (e.g. temperature, rainfall, available soils and nutrients). All of the above factors can affect chemical weathering rates, but it can be difficult to define to what degree any one process is affecting the overall chemical weathering rate. In addition, the mineral saturation state of a soil profile can determine the potential for the formation of secondary phases.

1.6 Coupling between Physical Erosion and Chemical Weathering Rates

Rates of physical erosion and chemical weathering appear to be tightly coupled over time scales of soil formation and landscape evolution, and across diverse landscapes (Stallard and Edmond, 1983; Gaillardet et al., 1999b; Millot et al., 2002; Riebe et al., 2004; West et al., 2005; Hren et al., 2007; Dixon et al., 2009). Rapid uplift and erosion has resulted in some of the highest global riverine solute fluxes (Gaillardet et al., 1999b; Waldbauer and Chamberlain, 2005) and soil erosion rates (Riebe et al., 2001), which suggests that orogenic uplift increases the potential for chemical weathering by increasing the supply of fresh minerals. Although, rapid uplift may also limit chemical dissolution rates; as physical erosion rates increase, soil residence times decrease, and weatherable minerals do not have sufficient time to weather completely (Stallard and Edmond, 1983; Riebe et al., 2004; West et al., 2005).

There are two extreme end members on a spectrum of physical weathering regimes. In 'transport-limited' regimes, physical denudation develops when downward propagation of weathering outpaces erosional losses from a slope, resulting in the removal of material only being limited by the sediment transport rate (Carson and Kirkby, 1972; Stallard and Edmond, 1983). In 'weathering-limited' regimes at the other end of the spectrum, erosion develops when sediment transport matches the rate at which physically competent material loses its structural integrity,

resulting in erosional removal of material only being limited by how fast it is broken down by weathering (Carson and Kirkby, 1972; Stallard and Edmond, 1983). The concepts of 'transport-limited' and 'weathering-limited' regimes apply only to physical erosion rates, although these terms are often incorrectly used in discussions of chemical weathering fluxes (Riebe et al., 2011). When defining chemical weathering, the following two extreme end members in a spectrum of chemical erosion should be used. In 'supply-limited' chemical erosion regimes chemical weathering develops when physical erosion rates are slow enough (or soil residence times are long enough) that further chemical weathering of the regolith is not possible due to exhaustive depletion of reactive phases (Riebe et al., 2004; West et al., 2005). At the other end of the spectrum, 'kinetic-limited' chemical erosion develops when physical erosion is so rapid that chemical erosion can only partially deplete the regolith of its weatherable phases before they are removed from the slope (West et al., 2005).

The relationship between physical erosion and chemical weathering (Figure 1.5) has been modelled by Gabet and Mudd (2009), which effectively brackets field data collected from global rivers (West et al., 2005). At low rates of physical erosion (10⁰-10² t·km⁻²·yr⁻¹), conditions are 'supply-limited', and increases in denudation are matched by equivalent increases in chemical weathering rate (Figure 1.5; Gabet and Mudd, 2009). As physical erosion rates increase beyond 10² t·km⁻²·yr⁻¹, weathering enters the 'kinetically-limited' regime, and the relationship between denudation and chemical weathering becomes less than linear (Figure 1.5; Gabet and Mudd,

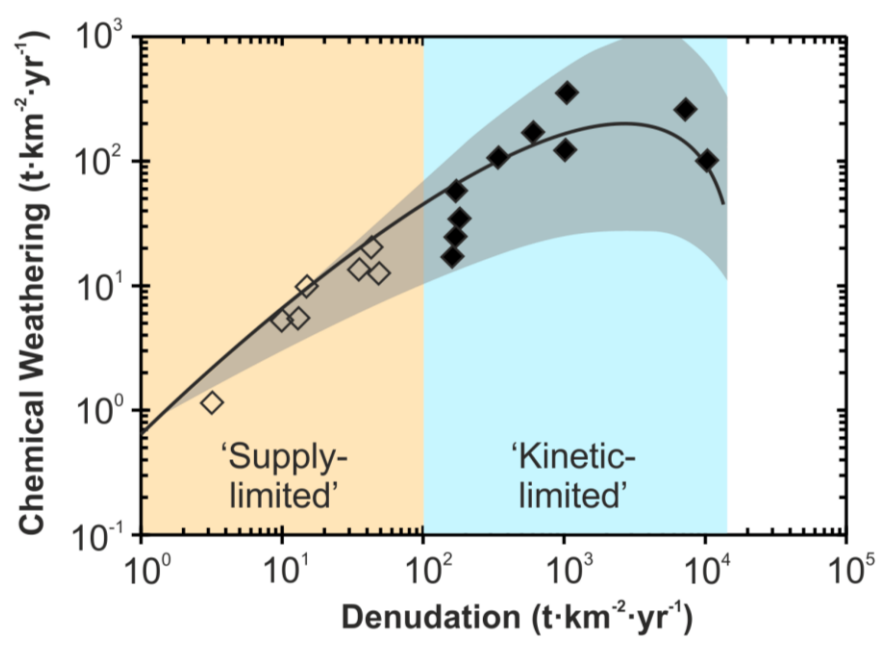


FIGURE 1.5: Physical denudation rate against total chemical weathering rate of climate-adjusted global river data compiled by West et al. (2005) and references therein. Solid data points are under 'kinetic-limited' conditions and hollow data points are under 'supply-limited' conditions. The solid black line represents the modelled trends for 'supply-limited' and 'kinetic-limited' environments and an order of magnitude increase or decrease in particle diameter size is shown by the grey band (Gabet and Mudd, 2009).

2009). This non-linear relationship is due to the positive effects of fresh minerals and the negative effects of thinner soils (Gabet and Mudd, 2009). Between physical erosion rates of 10³-10⁵ t·km²·yr⁻¹, chemical weathering rates reach a plateau, and then decline at the highest denudation rates (>10⁴ t·km⁻²·yr⁻¹). This suggests that the role of physical erosion and in situ chemical weathering becomes increasingly less significant in affecting global climate as denudation rates intensify (Gabet and Mudd, 2009). Instead, fine-grained unweathered minerals are transported to the lowlands, where they may undergo extensive chemical weathering, and have more significant influences upon global climate (Gaillardet et al., 1999b; Jacobsen et al., 2003; West et al., 2005; Gabet and Mudd, 2009).

1.7 Clay Mineral Formation and Classification

Continental chemical weathering reactions can transform primary minerals such as feldspars, phyllosilicates, amphiboles and pyroxenes to secondary minerals such as illites, smectites, vermiculites and chlorites (Nesbitt and Young, 1989). The rate of primary mineral dissolution and subsequent secondary mineral formation is controlled by the chemical weathering intensity, which is significantly affected by climatic effects (as discussed previously). Certain clay minerals preferentially adsorb certain elements into their structures, which subsequently affects the resultant chemistry in the rivers in which they are forming (Mackenzie and Garrels, 1966; Nesbitt and Young, 1989).

Layer types 1:1 or 2:1 are used as the main criterion for establishing divisions and layer charge of each division, for clay mineral classification (Bailey, 1980). Subgroups can then be made based on whether they are trioctahedral or dioctohedral (Table 1.3). These criterion work moderately well for mixed-layer clay minerals and for transitional boundaries between clays (Moore and Reynolds, 1997). Clay formation and alteration can be affected by diagenesis, which involves the addition and removal of material, transformation by dissolution and recrystallization or both, and by phase changes (Moore and Reynolds, 1997). Pedogenesis should also be considered as it involves the changes and formation of minerals in the soil environment (Moore and Reynolds, 1997). Other processes affecting mineral formation are neoformation (the new formation of minerals from a solution) and transformation (remodelling of an existing structure in which parts of the parent material are retained) (Moore and Reynolds, 1997).

Many clays that form as secondary products during weathering of primary minerals nucleate via a topotactic mechanism, which involves a structural change to a crystalline solid, resulting in the final lattice being related to that of the original structure (Banfield and Barker, 1994; Banfield et al., 1995; Moore and Reynolds, 1997). Topotactic nucleation occurs when the dissolving mineral

is leached of some cations, but retains partial structural integrity that provides the basic building blocks of clays (Nagy, 1995). Epitaxial nucleation occurs by nucleation of detrital clays (Banfield et al., 1991a; Banfield et al., 1991b) via a chemical and structural match of the new clay layer onto the templating surface, usually resulting in an overgrowth (Nagy, 1995; Moore and Reynolds, 1997).

TABLE 1.3: Summary of the different clay minerals types (Moore and Reynolds, 1997).

Layer Type	
1:1	Usually holds a very small or no layer charge.
	e.g. serpentinite minerals, berthierine, odinite, kaolin minerals,
	allophane and imogolite
2:1	Holds no charge. These minerals are generally soft, have
z = 0	excellent cleavage and exhibit varying degrees of stacking
	disorder.
2:1	A layer charge of -1 is neutralized by a univalent cation in the
z ~1	interlayer space. These micas can serve as precursors for
	other 2:1 layer silicates, especially illite and vermiculite.
	e.g. trioctahedral subgroup (phlogopite, biotite and annite) and
	the dioctohedral subgroup (muscovite and paragonite)
2:1	Although considered as different minerals, these types of clay
z < 1	are transitional to one another and are often interstratified.
	e.g. illite, glauconite, smectite, vermiculite and chlorite

1.8 Isotope Systems as Tracers of Continental Weathering Processes

Natural isotopes (both radiogenic and stable) have been used to study weathering and climate change, yielding both information on the mechanisms that control them and their timescales. Radiogenic isotope systems include Rb-Sr (Palmer and Edmond, 1989; Galy et al., 1999; Viers et al., 2000; McArthur et al., 2001; Chang et al., 2013) Sm-Nd (Vance and Burton, 1999; Liu et al., 2013), Lu-Hf (Van De Flierdt et al., 2002; Bayon et al., 2006; Chen et al., 2013), Re-Os (Levasseur et al., 1999; Peucker-Ehrenbrink and Ravizza, 2000; Peucker-Ehrenbrink and Ravizza, 2012) and the U-series (Riotte et al., 2003; Pogge von Strandmann et al., 2006; Keech et al., 2013). Stable isotope systems include Li (Chan et al., 1992; Huh et al., 1998a; Pistiner and Henderson, 2003; Teng et al., 2004; Hathorne and James, 2006; Vigier et al., 2008; Qiu et al., 2011), Ca (Blättler et al., 2011; Hindshaw et al., 2011; Moore et al., 2013), Mg (Young and Galy, 2004; Tipper et al., 2006c; Teng et al., 2010b; Wimpenny et al., 2011), Si (De La Rocha et al., 2000; Georg et al., 2007; Pogge von Strandmann et al., 2012) and B (Lemarchand and Gaillardet, 2006; Chetelat et al., 2009; Muttik et al., 2011).

1.8.1 The Sr Isotope System

Strontium is well mixed in the oceans and the Sr isotopic composition of seawater is determined by the balance of the input of radiogenic Sr from rivers (average ⁸⁷Sr/⁸⁶Sr = 0.711) (Spooner, 1976; Palmer and Edmond, 1989; Richter et al., 1992) and the input of non-radiogenic Sr from seafloor hydrothermal fluids (average ⁸⁷Sr/⁸⁶Sr = 0.7035) (Richter et al., 1992). For this reason, past changes in the ⁸⁷Sr/⁸⁶Sr composition of seawater, as recorded by marine carbonates, are usually attributed to changes in these input fluxes (Kump et al., 2000). The isotopic composition of hydrothermal strontium is not likely to vary through time, due to the relative constancy of the ⁸⁷Sr/⁸⁶Sr in mid-ocean ridge basalts, and the hydrothermal flux of Sr varies as a function of spreading rate (Bach and Humphris, 1999). On this basis, changes in seawater ⁸⁷Sr/⁸⁶Sr have been commonly used to assess how river fluxes, and therefore weathering rates, have changed over time (Palmer and Edmond, 1992).

The sharp increase in seawater ⁸⁷Sr/⁸⁶Sr at 40 Ma (Figure 1.6) is attributed to an increase in the ⁸⁷Sr/⁸⁶Sr value of the dissolved load in the Ganges-Brahmaputra river system from increased weathering of silicate minerals due to uplift of the Himalaya (Krishnaswami et al., 1992; Palmer and Edmond, 1992), although this interpretation is contested (Edmond, 1992). Crucially, recent studies have shown that carbonate rocks in the Lesser Himalaya have re-equilibrated with surrounding radiogenic silicate minerals that have high ⁸⁷Sr/⁸⁶Sr, which has dominated the Sr isotopic signal (Oliver et al., 2003). As more than 60% of the global riverine Sr flux (at the present day) is derived from weathering of these ancient carbonates, they presently account for a

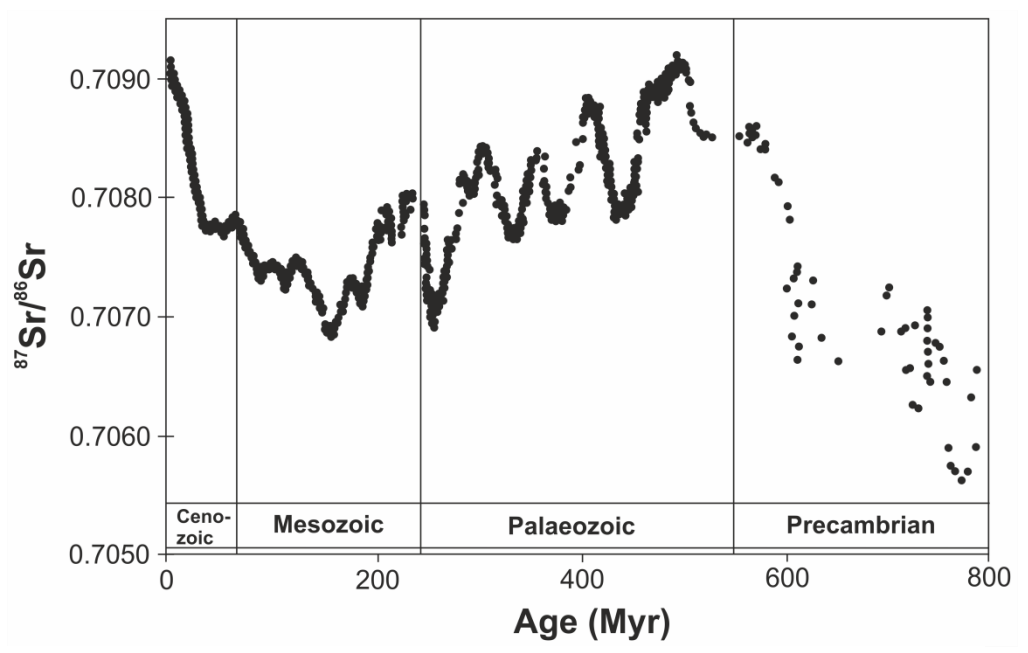


FIGURE 1.6: Plot of ⁸⁷Sr/⁸⁶Sr against age. Re-drawn from (McArthur et al., 2001). Data sourced from (Derry et al., 1989; Asmerom et al., 1991; Derry et al., 1992; Kaufman et al., 1993; Derry et al., 1994; Kaufman et al., 1996; Jacobsen and Kaufman, 1999; McArthur et al., 2001).

substantial component of the radiogenic Sr input to the oceans (Oliver et al., 2003). This results in a mixed signal and brings into question the reliability of Sr isotopes as a proxy for silicate weathering and highlights the need for other, independent measures of silicate weathering (English et al., 2000).

1.8.2 The Li Isotope System

Lithium isotopes have the potential to be effective tracers of weathering processes as they show significant fractionation due to the large relative mass difference between its isotopes (⁶Li ~7.5%; ⁷Li ~92.5%). In addition, lithium has only 1 redox state (+1 charge), and is therefore insensitive to changes in oxygen fugacity compared to Cr, Fe, Cu, Mo, etc (Latimer, 1952). Li is also not a nutrient, and so its elemental concentration and isotopic signature is not directly controlled by biological activity (Lemarchand et al., 2010). The benefit of using a stable isotope system, such as Li, is the isotopic compositions are dependent on both the composition of the underlying bedrock as well as the processes involved with weathering (e.g. Huh et al., 2001).

Lithium isotope data are reported as the per mil (‰) deviation from the NIST (National Institute of Standards and Technology, USA) standard LSVEC:

$$\delta^7 Li = \left(\frac{{}^7Li/{}^6Li_{SAMPLE}}{{}^7Li/{}^6Li_{LSVEC}} - 1\right) \times 1000$$
 (Eq. 1.6)

Lithium is conservative and well mixed in the oceans, with a residence time of ~1 Myr (Delaney and Boyle, 1986; Huh et al., 1998a), therefore the concentration and isotopic composition of Li in seawater is uniform ($\delta^7 \text{Li} = +31.5\%$; [Li] = 0.17 µg/g) (Tomascak, 2004; Hathorne and James, 2006). The lithium concentration and $\delta^7 \text{Li}$ signature of seawater is maintained by inputs of high-temperature hydrothermal fluids at oceanic ridges with an average $\delta^7 \text{Li} \sim +6.7\%$ (Bray et al., 2001), and dissolved lithium from rivers with an average $\delta^7 \text{Li} \sim +23\%$ (Huh et al., 1998a), and removal of lithium into oceanic basalts and marine sediments at low temperatures (Figure 1.7). The uptake of lithium into marine sediments occurs mainly by sorption onto clays (Zhang et al., 1998), as carbonates incorporate relatively little lithium (Hoefs and Sywall, 1997).

Isotopic fractionation during weathering leaves seawater enriched in ${}^{7}\text{Li}$ and continental crust becomes progressively depleted in ${}^{7}\text{Li}$ over time (Huh et al., 2001). This $\delta {}^{7}\text{Li}$ signature is imprinted upon the oceanic crust as it reacts with seawater (White, 2013). Oceanic crust is subducted and returned to the mantle, resulting in the mantle also becoming progressively enriched in ${}^{7}\text{Li}$ (White, 2013). This process has led to enrichment of $\delta {}^{7}\text{Li}$ in the mantle by 0.5-1‰, and depleted continental crust by 3‰ over geologic time (Elliott et al., 2004).

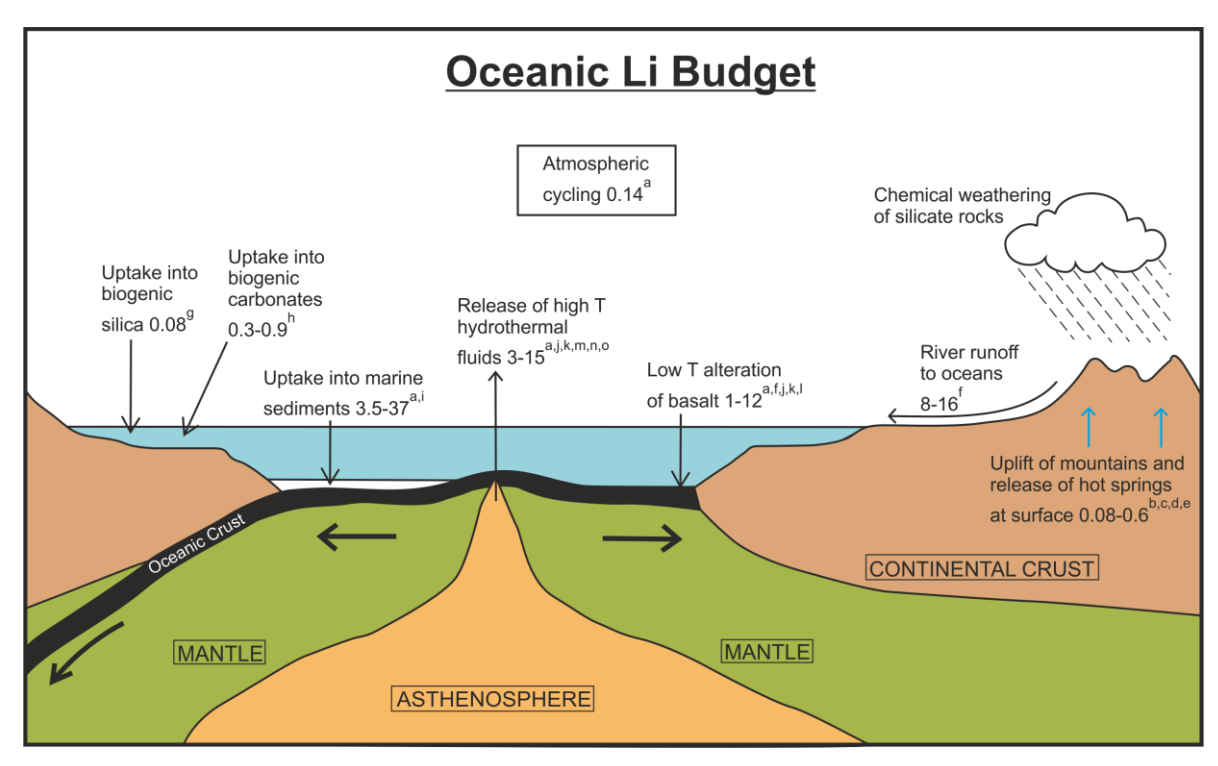


FIGURE 1.7: Schematic of the Li oceanic budget. Units in 10⁹ mol yr⁻¹. Data sourced from: ^a(Stoffyn-Elgi and MacKenzie, 1984), ^b(You et al., 1995), ^c(Chan and Kastner, 2000), ^d(Zhang et al., 1998), ^e(Scholz et al., 2010), ^f(Huh et al., 1998a), ^g(Chan et al., 2006), ^h(Hoefs and Sywall, 1997), ⁱ(Zhang et al., 1998), ^j(Mortimer, 1993), ^k(Chan et al., 2002), ^l(Wheat and Mottl, 2000), ^m(Chan et al., 1993), ⁿ(Elderfield and Schultz, 1996), ^o(Vigier et al., 2008).

There is generally little variation in the δ^7 Li signature of Li rock reservoirs (Figure 1.8). Although, saprolites have demonstrated a particularly light δ^7 Li signature (δ^7 Li values as low as -20%; Rudnick et al., 2004). Lithium isotopic signatures of fluid reservoirs show significantly more variability (Figure 1.9). Generally, seawater has the heaviest δ^7 Li signature and this signature is constant throughout the oceans. Rivers draining different types of weathering environment show a much wider range of δ^7 Li values, as do groundwater samples. Continental hydrothermal springs generally yield δ^7 Li values approaching that of the bedrock. The data displayed in Figures 1.8 and 1.9 is also shown in Figure 1.10, plotted as a function of lithium concentration. This plot shows why lithium isotopes are an effective tracer of weathering processes; lithium isotopes have a large relative mass difference, resulting in significant differences in lithium isotopic composition of natural surface reservoirs.

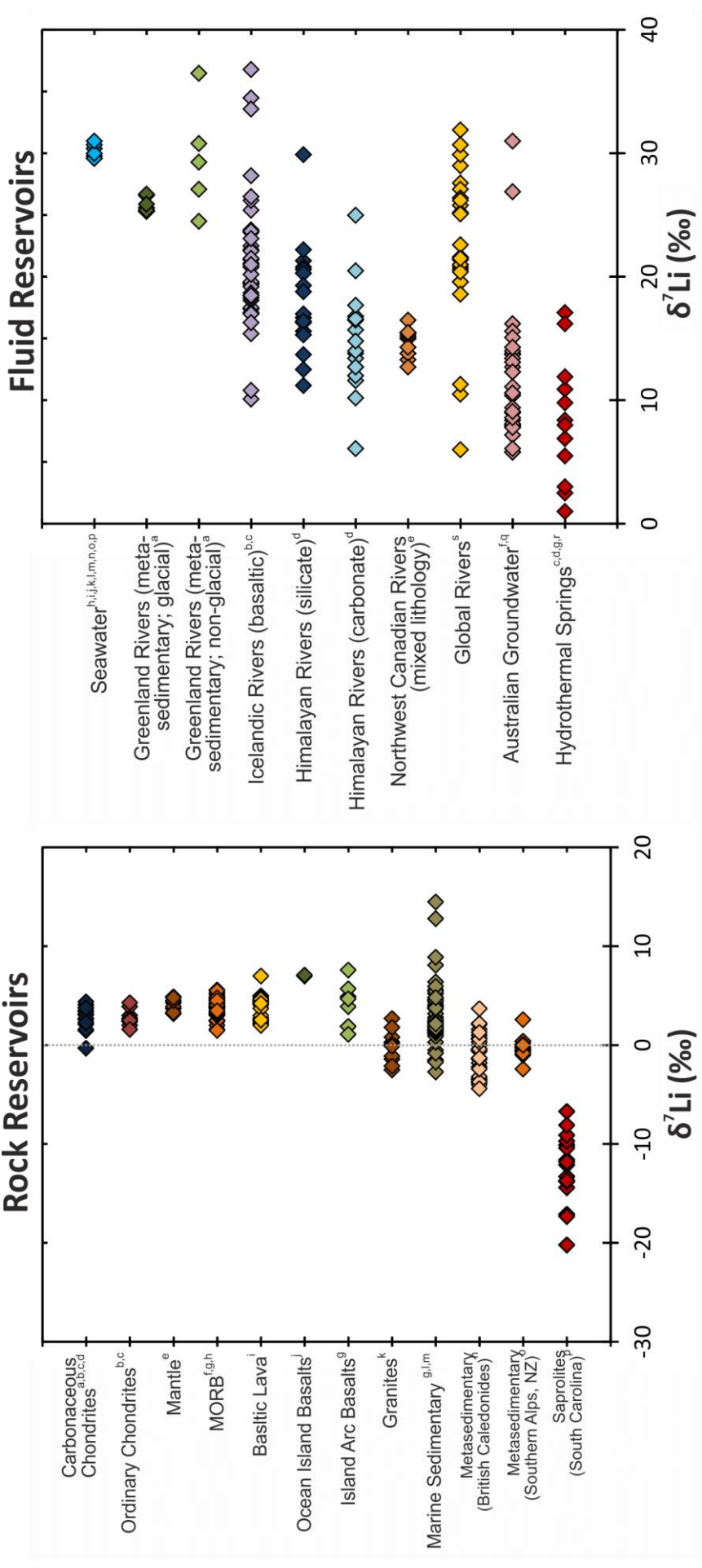


FIGURE 1.8: Lithium isotopic signature of different rock reservoirs. Data sourced from: ^a(Magna et al., 2006), ^b(Seitz et al., 2012), ^c(Pogge von Strandmann et al., 2011), ^d(Sephton et al., 2004), ^e(Jeffcoate et al., 2007), ^f(Tomascak et al., 2008), ^g(Moriguti and Nakamura, 1998a), ^h(Tomascak and Langmuir, 1999), [†](Chan and Frey, 2003), [†](Ryan and Kyle, 2004), ^k(Teng et al., 2004), [†](Bouman et al., 2004), ^m(Chan et al., 2006), ⁿ(Qiu et al., 2011), ^p(Rudnick et al., 2004).

FIGURE 1.9: Lithium isotopic signature of different fluid reservoirs. Data sourced from: ^a(Wimpenny et al., 2010b), ^b(Vigier et al., 2009), ^c(Pogge von Strandmann et al., 2006), ^d(Kısakűrek et al., 2005), ^e(Millot et al., 2010), ^f(Meredith et al., 2013), ^g(Pogge von Strandmann et al., 2010), ^h(Nishio and Nakai, 2002), ⁱ(Pistiner and Henderson, 2003), ^g(Bryant et al., 2003), ^k(Moriguti and Nakamura, 1998b), ^l(James and Palmer, 2000), ^m(Tomascak et al., 1999), ⁿ(You and Chan, 1996), ^o(Chan and Edmond, 1998), ^p(Millot et al., 2004), ^q(Pogge von Strandmann et al., 2014), ^r(Tomascak et al., 2003), ^s(Huh et al., 1998a). The range shown for the seawater lithium isotopic values is attributed to use of different analytical methods (i.e. TIMS and MC-ICP-MS) and differences in external precision.

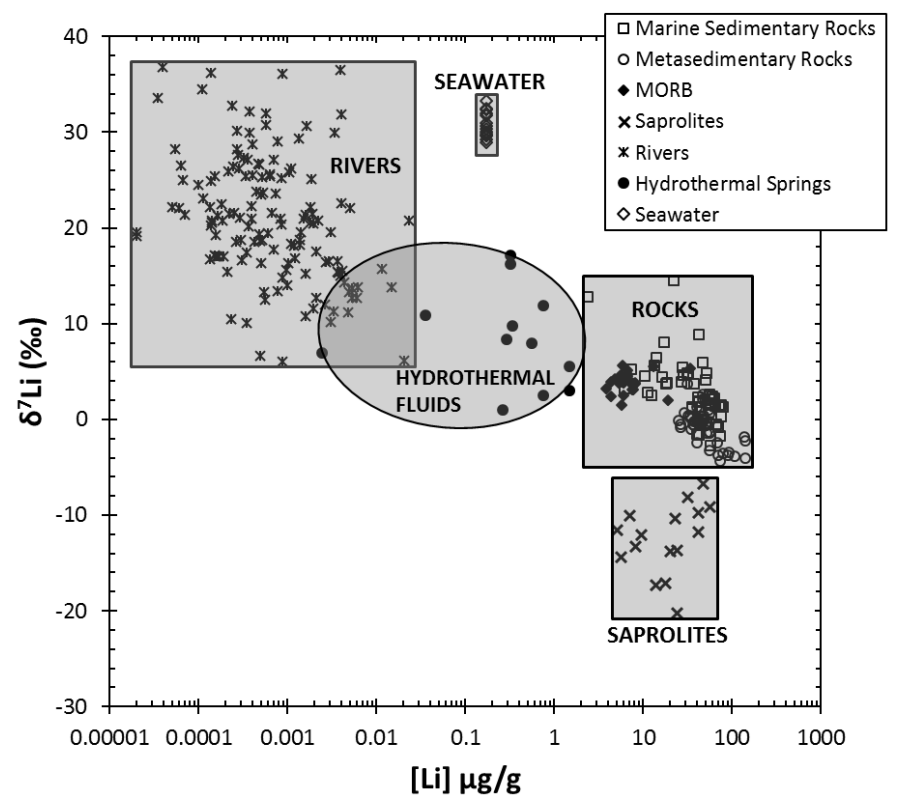


FIGURE 1.10: Comparison of lithium reservoirs showing lithium concentration plotted against lithium isotope signature. Data sourced from: rivers (Huh et al., 1998b; Huh et al., 2001; Kısakűrek et al., 2005; Pogge von Strandmann et al., 2006; Vigier et al., 2009; Millot et al., 2010; Pogge von Strandmann et al., 2010; Wimpenny et al., 2010b), hydrothermal fluids (Kısakűrek et al., 2005; Pogge von Strandmann et al., 2006; Pogge von Strandmann et al., 2010), rocks (Moriguti and Nakamura, 1998a; Tomascak and Langmuir, 1999; Bouman et al., 2004; Chan et al., 2006; Tomascak et al., 2008; Qiu et al., 2009; Qiu et al., 2011), saprolites (Rudnick et al., 2004), seawater (You and Chan, 1996; Chan and Edmond, 1998; Moriguti and Nakamura, 1998b; Tomascak et al., 1999; James and Palmer, 2000; Nishio and Nakai, 2002; Bryant et al., 2003; Pistiner and Henderson, 2003; Millot et al., 2004).

1.8.2.1 Secondary Mineral Formation

As bedrock disintegrates, secondary clays (e.g. smectite and illite) are formed. Lithium is incorporated in the clays along with Mg and Al whereas other elements (Na, Ca and K) are lost to solution (Huh et al., 2001). During weathering processes, dissolution of primary minerals results in no isotopic fractionation of Li (Pistiner and Henderson, 2003; Wimpenny et al., 2010a). However, during secondary mineral formation ⁶Li is preferentially retained in the newly formed minerals and ⁷Li is left in solution (Huh et al., 2001; Wimpenny et al., 2010a). Therefore, river Li concentration is dependent upon relative rates of primary mineral dissolution, and river lithium isotopic signature is dependent upon secondary mineral formation. It should be pointed out that the term 'incorporation' of Li into clays is being used as a catch-all phrase in this thesis, and may also include adsorption, as at this time distinction between these two processes is not possible.

The average diffusion rate of the lighter isotope in solution is faster (8% for ⁶Li) (Giletti and Shanahan, 1997), and as Li has higher diffusion rates than other alkali cations, diffusion is expected to be an important mode of transport and of fractionation of Li during the weathering process (Huh et al., 2001). The bonds bearing the lighter Li isotope have higher vibrational energies, and during a chemical reaction molecules containing the lighter isotope will react more readily, enriching the reaction product in the lighter isotope (Huh et al., 2001). The above kinetic isotope effects suggest that ⁶Li-containing bonds will preferentially break and diffuse (Huh et al., 2001). However, the hydration effect of water on Li is very strong. Due to the high vibrational frequency of water (1600-3900 cm⁻¹) compared to common minerals (<1000 cm⁻¹), water has a tendency to incorporate the heavy isotope preferentially in order to lower the free energy of the system (O'Neil, 1986). Thus, ⁶Li is preferentially retained in the secondary solid phase and ⁷Li remains in solution. During cation exchange chromatography, a similar effect can be observed, where ⁶Li is preferentially retained (via adsorption) on the resin phase regardless of the type of cation exchanger and the counter ion in the solution phase (Taylor and Urey, 1938; Oi et al., 1991).

1.8.2.2 *Variations in* δ^7 *Li of Seawater in the Past*

Changes in the amount of lithium and the $\delta^7 Li$ signature of seawater can be expected to provide information about past changes in weathering processes. In the last 60 Myr, a 9‰ increase in $\delta^7 Li_{seawater}$ has been observed (Figure 1.1), which is likely to be linked to increased chemical weathering rates and the $\delta^7 Li_{river}$ signature delivered to the oceans (Misra and Froelich, 2012). This is consistent with the $^{87}Sr/^{86}Sr$ record.

In seawater, Li and Li isotopes show some useful trends, but it is clear that the processes that regulate the Li and Li isotopic composition of river water need to be better constrained in order to accurately interpret seawater records.

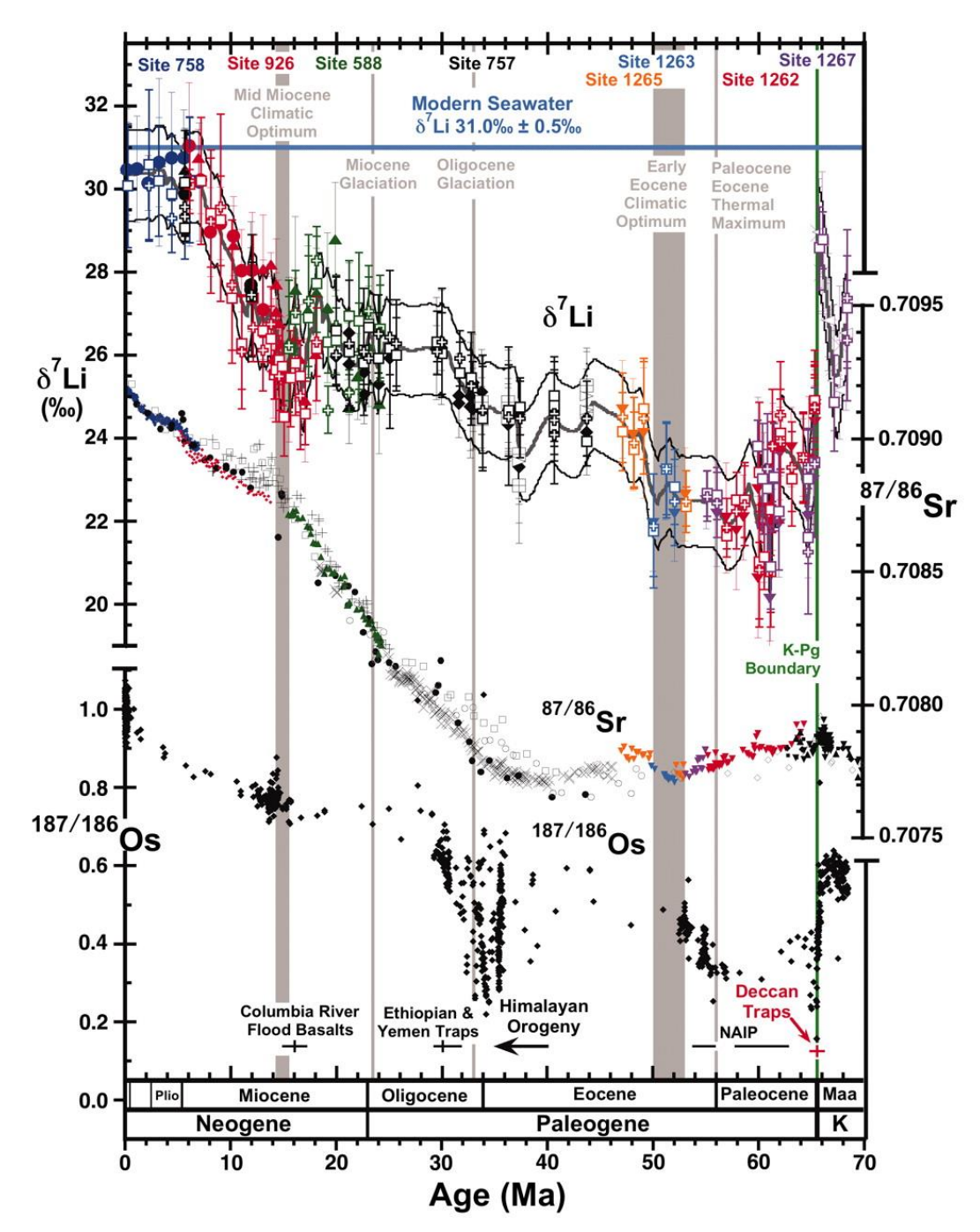


FIGURE 1.11: Late Cretaceous to Holocene Li isotope record, with comparison to published seawater records for ⁸⁷Sr/⁸⁶Sr and ¹⁸⁷OS/¹⁸⁶Os (Misra and Froelich, 2012). The data for the Li, Sr and Os isotopic records is sourced from Misra and Froelich (2012) and references therein.

1.8.2.3 Fractionation of Li Isotopes

Isotopic fractionation of lithium between two components, A and B, is given by the fractionation factor α_{A-B} :

$$\propto_{A-B} = \left({^{7}Li}/{^{6}Li} \right)_{A}/\left({^{7}Li}/{^{6}Li} \right)_{B}$$
 (Eq. 1.7)

Lithium isotopic fractionation can be on the order of a few per mil, so may also be described by the approximation:

$$10^3 \ln \propto_{A-B} \approx \delta^7 L i_A - \delta^7 L i_B = \Delta^7 L i_{A-B}$$
 (Eq. 1.8)

An example of this equation can be shown by the most significant process that controls lithium isotopic fractionation during continental weathering, which is the preferential loss of ⁷Li to solution during secondary mineral formation (e.g. Huh et al., 2001):

$$10^{3} ln \propto_{clay-river\ water} \approx \delta^{7} Li_{clay} - \delta^{7} Li_{river\ water} = \Delta^{7} Li_{clay-river\ water}$$
 (Eq. 1.9)

1.8.3 The Mg Isotope System

A primary long term sink of atmospheric CO₂ is the chemical weathering of Ca-Mg silicates (Walker et al., 1981; Berner et al., 1983; Berner, 2004), therefore Mg isotopes may provide information on weathering processes as magnesium is directly involved in the carbon cycle. In a weathering system, the main controls on magnesium isotopic composition are lithology, secondary mineral alteration and biotic uptake, which potentially make Mg isotopes effective tracers of weathering processes. Magnesium has three naturally occurring isotopes: ²⁴Mg (78.99%), ²⁵Mg (10.00%) and ²⁶Mg (11.01%). The variation seen between the relative abundances of Mg isotopes is expected to be a result of physiochemical processes due to the large relative mass differences between ²⁵Mg and ²⁶Mg (4%) and ²⁶Mg and ²⁴Mg (8%) (Young and Galy, 2004).

Magnesium isotopes are reported as the per mil (‰) deviation from the pure Mg standard DSM-3 (Dead Sea Magnesium) (Galy et al., 2003):

$$\delta^{26} Mg = \left(\frac{^{26} Mg^{/24} Mg_{sample}}{^{26} Mg^{/24} Mg_{DSM-3}} - I\right) x 1000$$
 (Eq. 1.10)

Much like lithium, magnesium is conservative and well mixed in the oceans, with a long residence time of ~13 Myr (Broecker and Peng, 1982) and a homogeneous δ^{26} Mg signature (δ^{26} Mg = -0.8 \pm 0.1%; see caption for Figure 1.14). The magnesium concentration and δ^{26} Mg composition of seawater is maintained by inputs of dissolved magnesium transported in rivers (e.g. Berner and Berner, 1996), and removal of magnesium into oceanic basalts at high temperature (Kadko et al., 1995; Elderfield and Schultz, 1996; Higgins and Schrag, 2015) and low temperature (Elderfield and Schultz, 1996; Higgins and Schrag, 2015), dolomitization (Drever, 1974; Higgins and Schrag, 2015), and clay formation (Drever, 1974) at low temperatures (Figure 1.12).

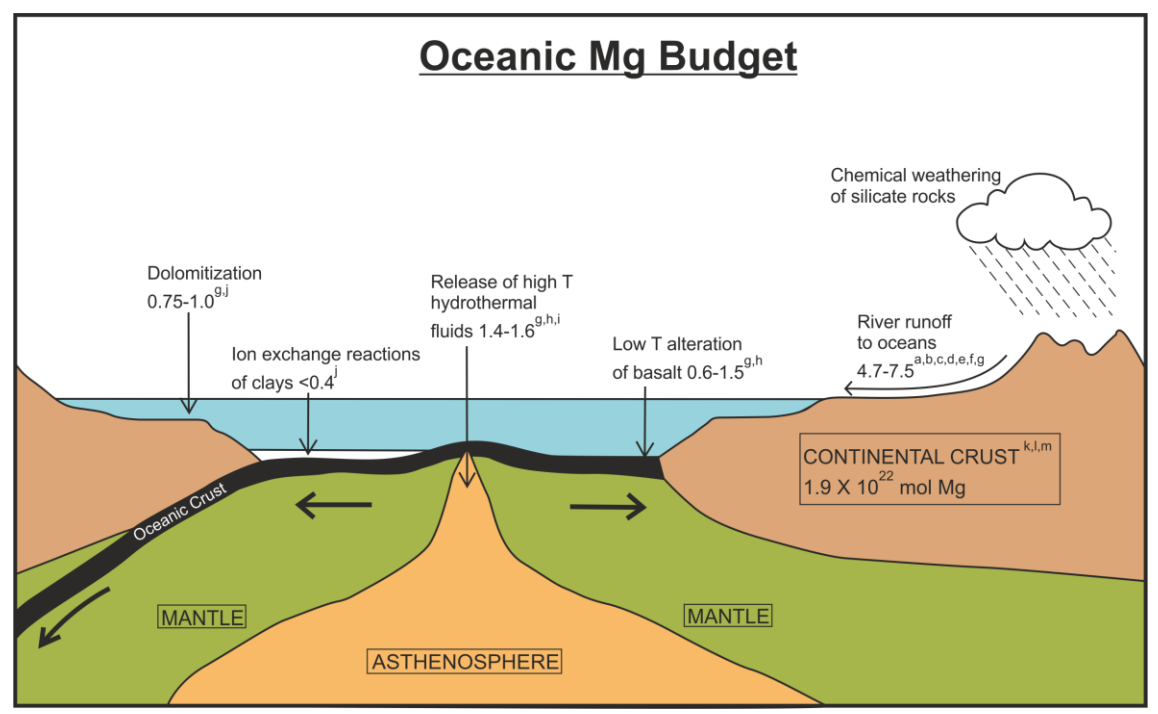


FIGURE 1.12: Schematic of the Mg oceanic budget. Units in 10¹² mol yr⁻¹. Data sourced from: ^a(Berner et al., 1983), ^b(Berner and Berner, 1996), ^c(Drever and Maynard, 1988), ^d(Holland, 1978), ^e(Wolery and Sleep, 1976), ^f(Wolery and Sleep, 1988), ^g(Higgins and Schrag, 2015), ^h(Elderfield and Schultz, 1996), ⁱ(Kadko et al., 1995), ^j(Drever, 1974), ^k(Krauskopf, 1967), ¹(Heydemann, 1969), ^m(Albarède and Michard, 1986).

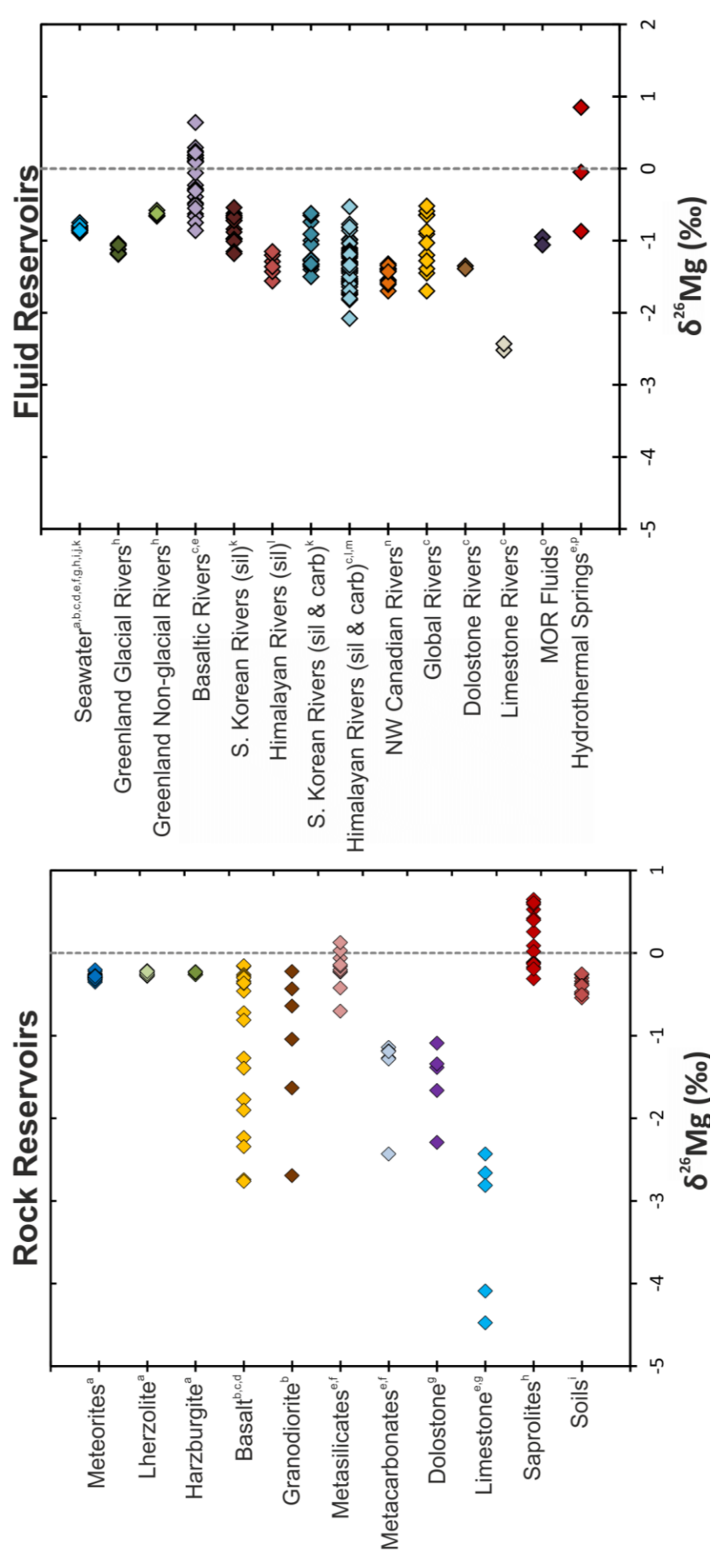


FIGURE 1.13: Magnesium isotopic signature of different rock reservoirs. Data sourced from: ^a(Teng et al., 2010a), ^b(Tipper et al., 2008b), ^c(Young and Galy, 2004), ^d(Teng et al., 2007), ^e(Lee et al., 2014), ^f(Tipper et al., 2006b), ^g(Galy et al., 2002), ^h(Teng et al., 2010b), ⁱ(Pogge von Strandmann et al., 2012).

FIGURE 1.14: Magnesium isotopic signature of different fluid reservoirs. Data sourced from: ^a(Chang et al., 2003), ^b(Young and Galy, 2004), ^c(Tipper et al., 2006c), ^d(Pearson et al., 2006), ^e(Pogge von Strandmann et al., 2008), ^f(Hippler et al., 2010), ^g(Immenhauser et al., 2010), ^h(Wimpenny et al., 2011), ⁱ(Choi et al., 2012), ^j(Pogge von Strandmann et al., 2012), ^k(Lee et al., 2014), ^l(Tipper et al., 2006b), ⁿ(Tipper et al., 2008b), ⁿ(Tipper et al., 2008a).

There has been much debate as to whether the Earth has a chondritic Mg isotopic composition or not. It was concluded in some studies that the δ^{26} Mg signature of the Earth is on average ~0.3‰ higher than that of chondrites, suggesting that the Earth has a non-chondritic δ^{26} Mg composition (Wiechert and Halliday, 2007; Young et al., 2009). However, recent high-precision magnesium isotopic studies have suggested that the Earth and chondrites have identical δ^{26} Mg compositions (Teng et al., 2007; Chakrabarti and Jacobsen, 2009; Handler et al., 2009; Yang et al., 2009; Dauphas et al., 2010; Teng et al., 2010a). This suggests a little variation in the δ^{26} Mg composition of the Earth's mantle has occurred since the Archaean (Teng et al., 2010a). Carbonate rocks and foraminifera have consistently lower δ^{26} Mg values than seawater by several per mil (Figure 1.13 and 1.14). Carbonate rocks are also consistently lower in δ^{26} Mg values than dolomite values.

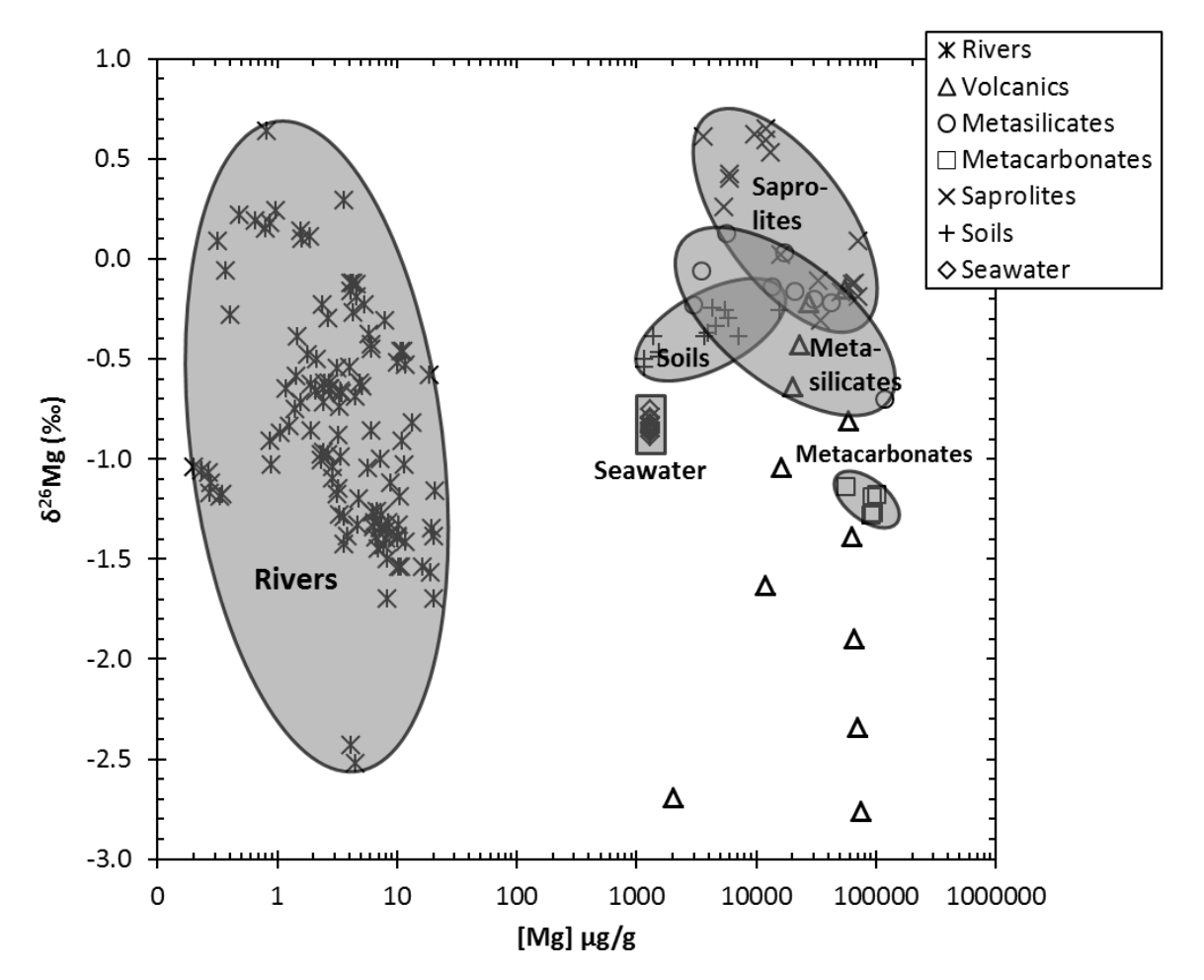


FIGURE 1.15: Comparison of magnesium reservoirs showing magnesium concentration plotted against magnesium isotopic signature. Data sourced from: rivers (Ming-Hui et al., 1982; Stallard and Edmond, 1983; Edmond et al., 1996; Gaillardet et al., 1997; Louvat and Allègre, 1997; Huh et al., 1998b; Gaillardet et al., 1999a; Galy and France-Lanord, 1999; Gaillardet et al., 2003; Millot et al., 2003; Tipper et al., 2006c; Pogge von Strandmann et al., 2008; Wimpenny et al., 2011; Pogge von Strandmann et al., 2012; Tipper et al., 2012; Lee et al., 2014), seawater (Chang et al., 2003; Young and Galy, 2004; Pearson et al., 2006; Tipper et al., 2006c; Pogge von Strandmann et al., 2008; Hippler et al., 2009; Wombacher et al., 2009; Immenhauser et al., 2010; Wimpenny et al., 2011; Choi et al., 2012; Pogge von Strandmann et al., 2012; Lee et al., 2014), saprolites (Gardner et al., 1981; Teng et al., 2010b), soils (Pogge von Strandmann et al., 2012).

These data show that heavier Mg isotopes partition to water relative to carbonate minerals, which is similar to the isotopes of Ca (Gussone et al., 2003; Schmitt et al., 2003). There is a clear mineralogical control on Mg isotopes and possibly a weak dependence on temperature at low temperature values (Galy et al., 2002; Young and Galy, 2004).

Magnesium isotopic signatures of rivers show less variability than rock suites (Figure 1.14), although global rivers display a large range in Mg concentration (Figure 1.15). Continental hydrothermal springs show a large range in δ^{26} Mg values (-0.9 to +0.9 %; Figure 1.14; Pogge von Strandmann et al., 2008; Tipper et al., 2008). It is apparent that δ^{26} Mg signatures of river waters are influenced by catchment lithology, as rivers draining limestone catchments have particularly light δ^{26} Mg values and rivers draining basaltic rivers generally have heavier δ^{26} Mg values (Figure 1.14).

The Mg isotopic signature of silicate rocks is relatively uniform (Teng et al., 2010a), although carbonate rocks generally display lighter δ^{26} Mg values (Galy et al., 2002; Lee et al., 2014). Thus, a significant control on the Mg isotopic signature of rivers waters is the proportion of carbonate rocks to silicate in the host catchment (Tipper et al., 2006b; Tipper et al., 2006c; Pogge von Strandmann et al., 2008; Tipper et al., 2008a). However, Mg is usually only found as a trace element in limestones, but it is a major element in silicate minerals such as biotite, chlorite and clays (Le Fort, 1975), therefore silicate mineral dissolution generally has a dominant control upon the dissolved Mg concentration and δ^{26} Mg value.

The δ^{26} Mg value range for global rivers waters extends from -2.5 to +0.9‰ (Tipper et al., 2006c; Pogge von Strandmann et al., 2008), which is about half of the range observed for terrestrial rocks (-4.5 to +0.7‰; Galy et al., 2002; Teng et al., 2010b). Therefore, to better understand the effects of weathering processes upon dissolved δ^{26} Mg values, studies should involve mono-lithological terrains (Pogge von Strandmann et al., 2008).

1.8.3.1 Processes Fractionating Mg Isotopes

During weathering, bedrock disintegrates and secondary clays (such as smectite and illite) are formed. Dissolution of primary minerals by chemical weathering has been suggested to cause some Mg isotopic fractionation, as light Mg is preferentially lost to solution (Tipper et al., 2006b; Wimpenny et al., 2010a). Secondary mineral formation has also been suggested to cause Mg isotopic fractionation. However, this process has been shown to preferentially retain the heavy Mg isotope (Tipper et al., 2006b; Pogge von Strandmann et al., 2008; Teng et al., 2010b) and the light Mg isotope (Pogge von Strandmann et al., 2008; Wimpenny et al., 2010a). In addition, secondary carbonates are always isotopically light with regards to the waters from which they

precipitate (Galy et al., 2002; Chang et al., 2004). Therefore, riverine Mg concentration and δ^{26} Mg signature is dependent upon both primary mineral dissolution and secondary mineral formation. It should be pointed out that the term 'incorporation' of Li into clays is being used as a catch-all phrase in this thesis, and may also include adsorption, as at this time distinction between these two processes is not possible.

Magnesium is also important to both the chlorophyll molecule and to the function of ATP in biological systems (Shaul, 2002). Mg isotopic fractionation is associated with the uptake of Mg into chlorophyll-a and into higher plants, although, like secondary mineral formation, this fractionation can preferentially retain both the light and heavy Mg isotopes (Black et al., 2006; Bi et al., 2007; Ra and Kitagawa, 2007; Bolou-Bi et al., 2010).

1.8.3.2 Variation in the δ^{26} Mg Composition of Seawater

Magnesium has a residence time in the oceans of $\sim 10^7$ years (Berner and Berner, 1996; Lemarchand et al., 2002), and should therefore be well mixed and behave conservatively. Samples

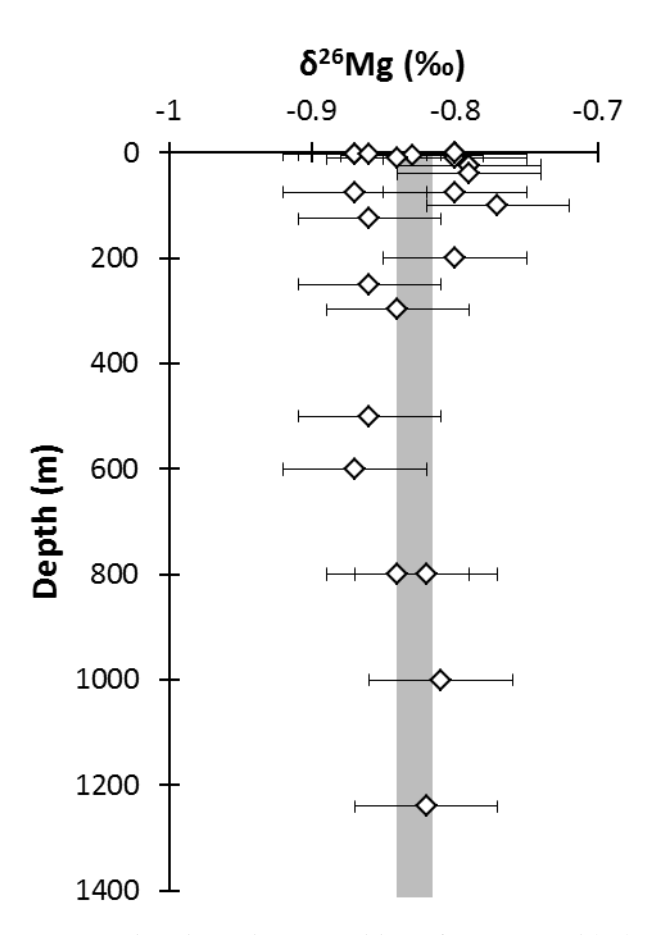


FIGURE 1.16: Magnesium isotopic composition of seawater with depth. The error bars represent the external precision at 95% confidence based on repeat measurements of a seawater in-house standard. The vertical grey bar reflects the mean value ± 2 s.e. Re-drawn from Foster et al. (2010).

collected from various depths throughout the oceans (Figure 1.6) demonstrate that $\delta^{26}Mg$ is relatively constant with depth and the oceans are relatively homogenous with regards to Mg isotopic composition (Foster et al., 2010).

1.8.3.3 Fractionation of Mg Isotopes

The relationships between ²⁵Mg/²⁴Mg and ²⁶Mg/²⁴Mg are indicative of kinetic fractionation and equilibrium fractionation (Young and Galy, 2004). The three isotopes of Mg define two fractionation factors:

$$\alpha_{25/24} = \frac{\binom{25}{Mg}\binom{24}{Mg}_a}{\binom{25}{Mg}\binom{24}{Mg}_b}$$
 and $\alpha_{26/24} = \frac{\binom{26}{Mg}\binom{24}{Mg}_a}{\binom{26}{Mg}\binom{24}{Mg}_b}$ (Eq. 1.11)

Where *a* and *b* refer to either two different conditions or two different materials (Young and Galy, 2004). At equilibrium, the two fractionation factors can be shown by the following expression:

$$\frac{\ln \alpha_{25/24}}{\ln \alpha_{26/24}} = \frac{\left(\frac{1}{m_1} - \frac{1}{m_2}\right)}{\left(\frac{1}{m_1} - \frac{1}{m_3}\right)}$$
(Eq. 1.12)

Where m_1 is the atomic mass of ²⁴Mg (23.985042), m_2 is the atomic mass of ²⁵Mg (24.985837), and m_3 is the atomic mass of ²⁶Mg (25.982593) (Hulston and Thode, 1965; Matsuhisa et al., 1978; Weston, 1999; Young et al., 2002). The above equation can be rearranged to give:

$$\alpha_{25/24} = (\alpha_{26/24})^{\beta}$$
 (Eq. 1.13)

Where the exponent is:

$$\beta = \frac{\left(\frac{1}{m_1} - \frac{1}{m_2}\right)}{\left(\frac{1}{m_1} - \frac{1}{m_2}\right)}$$
 (Eq. 1.14)

Equation 1.14 is a high temperature limit for the exponent in the equilibrium fractionation law, that is a good indication of the true equilibrium value (Young et al., 2002). The exponent (β) value obtained from the atomic masses of the Mg isotopes is 0.521 (Young and Galy, 2004).

A quality control can be applied to the data as follows:

$$\Delta^{25}$$
Mg' = δ^{25} Mg' - 0.521 δ^{26} Mg' (Eq. 1.15)

Where 0.521 refers to the equilibrium value for the exponent β .

1.9 Weathering Studies on the Southern Alps, New Zealand

Few studies have been carried out that use non-traditional stable isotopes (e.g. Li, Mg, Ca) to investigate the relationship between uplift, metamorphism and weathering. The behaviour of lithium isotopes during metamorphism has been investigated in the Otago Schists by Qui et al. (2011). They show that δ^7 Li signatures are relatively constant across all metamorphic grades, with average δ^7 Li = -0.2 ± 2.2 % (Qiu et al., 2011). These values are similar to the δ^7 Li value of upper continental crust (δ^7 Li = +0.3 ± 2 %) (Teng et al., 2004) and pelitic sedimentary rocks (δ^7 Li = -1.6 to +5 %) (Chan et al., 2006), suggesting that metamorphism has no measureable effect on δ^7 Li and that lithology is the main control on δ^7 Li rather than the degree of metamorphism (Qiu et al., 2011).

Silicate weathering affects long term climate, whereas carbonate weathering does not. Therefore, tracing the contributions of each to the dissolved load of rivers in an actively uplifting mountain belt allows for constraints to be placed on the global carbon cycle. This has been assessed by measuring the calcium isotopic composition ($\delta^{44/40}$ Ca) of rivers, rocks and soils in the Southern Alps, which are dominantly silicate in lithology but contain small amounts of disseminated calcite (Moore et al., 2013). However, $\delta^{44/40}$ Ca values show limited variation between the carbonate and silicate end members (Moore et al., 2013). Nonetheless, it is apparent that calcium in the dissolved load of rivers from this rapidly uplifting region is dominantly sourced from carbonates, and the proportion of Ca derived from carbonate weathering increases under higher uplift rates (Moore et al., 2013).

The role of calcite weathering has also been investigated in the Southern Alps using an analytical model to evaluate the contribution of Sr from calcite veins (Chamberlain et al., 2005). Results of this suggest that as much as 60% of the total Sr released during weathering is sourced from calcite (Chamberlain et al., 2005). In addition, the ⁸⁷Sr/⁸⁶Sr of weathered material is relatively constant over a range of effective surface ages, which indicates that even a small amount of disseminated calcite can have a significant effect on the Sr composition of weathered material (Chamberlain et al., 2005).

1.10 Aims of this Study

This study will characterise the chemistry of the weathering system of the Southern Alps on the South Island, New Zealand, and also examine the processes controlling lithium and magnesium isotopic fractionation within the weathering system. Isotopic signatures are used to examine the climatic and tectonic controls upon Li and Mg concentration and Li and Mg isotopes during weathering processes. The Southern Alps are relatively pristine and are affected by differing

climatic regimes and differing rates of uplift and erosion (Adams, 1980; Whitehouse, 1986; Koons, 1989; Koons, 1990; Beaumont et al., 1992; Koons, 1994). Moreover, the Southern Alps are mainly composed of variably metamorphosed siliciclastic sediments, with a relatively uniform bulk composition, as well as trace amounts of calcite (Mackinnon, 1983; Grapes and Watanabe, 1984; Roser and Korsch, 1986; Mortimer and Roser, 1992). Rapid uplift and exhumation has exposed rocks with a higher metamorphic grade to the west, with metamorphic grade decreasing eastwards (Norris et al., 1990; Craw et al., 1999).

1.11 Thesis Outline

Chapter 2

A brief geological history of the South Island, New Zealand, with a focus on the Southern Alps is described in this chapter. This summary describes the basement terranes, the modern tectonic setting of the Southern Alps, with regards to the Alpine Fault, the structure of the orogen, and the lithology and metamorphic grade of the Haast Schist. The processes affecting continental weathering in this region are discussed, such as climate, uplift rates, erosion rates, glacier formation and landsides.

Chapter 3

An outline of the methods used to determine elemental concentrations in this study and in previous studies, and also the methods used to determine Li and Mg isotopic values. Descriptions of sample collection and preparation are also given. The accuracy and precision for the data analysed in this study are reported in this chapter, with comparison to published values. More detailed methods used in this study are outlined in the Appendix.

Chapter 4

The chemical composition of the weathering products of the Southern Alps are compared to the bedrock to examine the processes that regulate weathering and the sources of Li and Mg in the weathering system. Chemical weathering rates and atmospheric CO₂ consumption rates are calculated for the Southern Alps, and compared to global data. This chapter summarises the processes occurring in the weathering system of the Southern Alps.

A discussion on the Li isotopic signature of Li reservoirs in the weathering system of the Southern Alps. Various processes taking place in this weathering system and how they affect Li isotopic fractionation are discussed, and mineral saturation states are modelled to determine the secondary minerals that may form during chemical weathering. The link between riverine Li isotopic signature and silicate weathering is assessed. Finally, the utility of Li isotopes as a proxy for silicate weathering is discussed.

Chapter 6

In this chapter, the Mg isotopic signature of Mg reservoirs in the weathering system of the Southern Alps are determined. The processes occurring in this weathering system and how they affect Mg isotopic fractionation are discussed. The link between riverine Mg isotopic signature and silicate weathering is assessed, and the utility of Mg isotopes as a proxy for silicate weathering is discussed. The coupling of riverine Li and Mg isotopes in their behaviour is assessed, with comparison to data from Chapter 5.

Chapter 7

The behaviour of Li isotopes in hydrothermal fluids emanating from the Southern Alps. The effect on these fluids under high temperature conditions is assessed, and mineral saturation states are modelling for both temperatures at surface conditions and temperatures at depth. The processes by which Li isotopes fractionate in the spring fluids are discussed. The behaviour of coupled spring water Li and Mg isotopes is determined and compared to the behaviour observed in rivers draining the Southern Alps.

Geological Setting

The tectonic history of New Zealand consists of three main phases. During the Rangitata Orogeny (Palaeozoic and Mesozoic), much of New Zealand was formed by accretion of crustal fragments onto the Gondwana plate margin (Bishop, 1985; Mortimer et al., 1999b). In the Late Cretaceous and Cenozoic, seafloor spreading caused continental rifting and subsidence, which brought about the deposition of widespread cover sequences (Molnar et al., 1975; Cox and Sutherland, 2007). By the Late Tertiary, the onset of compression across the previously purely strike-slip Australian-Pacific plate boundary marked the start of the present day Kaikoura Orogeny (Landis and Coombs, 1967; Cooper et al., 1987; Cox and Sutherland, 2007). This period of transpression uplifted mountain ranges high enough to form glaciers, developed a strongly asymmetrical climate producing high erosion rates, and exposing a variety of basement rocks and cover sequences.

2.1 Basement Terranes

The basement geology of New Zealand is composed of a series of terranes and igneous suites (Figure 2.1) (Mortimer, 2004; Cox and Sutherland, 2007). The South Island basement terranes can be divided into the Western and the Eastern Province (Landis and Coombs, 1967; Bishop, 1985; Mortimer, 2004). These have distinct geological histories and they are separated by a long-lived (375-110 Ma), subduction-related batholith called the Median Tectonic Zone (MTZ) (Mortimer et al., 1999a; Mortimer et al., 1999b; Cox and Sutherland, 2007). The MTZ represents ~250 Myr of magmatism along the southern Gondwana margin (Mortimer et al., 1999b). The basement terranes of South Island consist of: the Brook Street Terrane (layered ultramafic-gabbro sequences, diorites and

volcaniclastic sediments); the Murihiku and Maitai Terranes (Permian to Triassic volcanogenic sandstone, siltstone and tuff); the Dun Mountain Ophiolite Belt (a Permian ophiolite); the Caples Terrane (Permian to Triassic/Jurassic volcaniclastic marine flysch); the Torlesse Terrane (Permian to Middle and Late Triassic turbiditic quartzofeldspathic sandstones and argillites); the Waipapa Terrane (volcaniclastic marine flysch); and the Median Tectonic Zone (MTZ; pre-Cenozoic subduction-related I-type plutonic, volcanic and sedimentary rocks) (Figure 2.1) (Gray and Foster, 2004). The MTZ consists of more than 70 rock units and has a wide range of protoliths, crystallisation ages and internal deformation (Mortimer et al., 1999b). Generally, more than 90% of the MTZ is made up of calc-alkaline, I-type plutonic rocks (Mortimer et al., 1999b). The MTZ underlies a ~10,200 km² area, which intrudes into the Brook Street and Takaka Terranes (both Eastern and Western Provinces), and it has been displaced by ~460 km by transcurrent movement on the Alpine Fault (Figure 2.1) (Mortimer et al., 1999b).

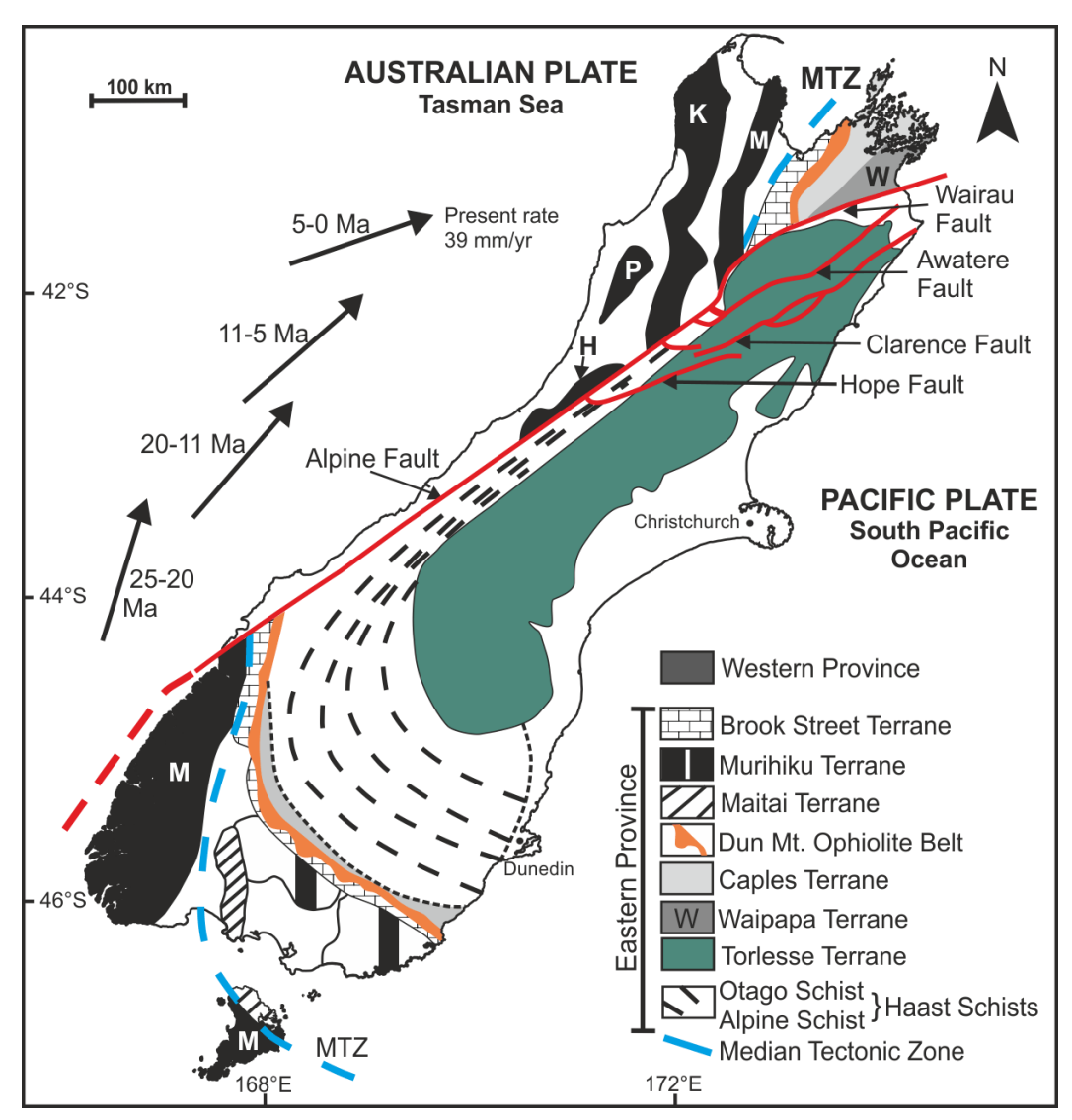


FIGURE 2.1: Simplified terrane map of South Island, New Zealand. The various batholiths are as follows: M – Median Batholith; H – Hononu Batholith; P – Paparoa Batholith; E – Karamea Batholith. The arrows show how plate motions have changed over time (Craw, 2002) and the basement terrane map was re-drawn by Menzies (2012) from Pitcairn (2004).

The Rangitata Orogeny involved the accretion of crustal fragments onto the Gondwana plate margin, forming the majority of New Zealand (Bishop, 1985; Mortimer, 2004). During this time, collision of the Caples and Torlesse Terranes resulted in metamorphism of the Haast Schists (Fleming, 1969; Coombs et al., 1976; Adams et al., 1985). Ar-Ar dating of micas indicate that the schists were uplifted and eroded to a low level surface by the Mid-Late Cretaceous (Gray and Foster, 2004).

The Alpine Fault was initiated in the late Tertiary (23-25 Ma) and is a major dextral strike-slip plate boundary (Kamp, 1986; Cooper et al., 1987). It took on a component of compression between 12 and 5 Ma (Kamp et al., 1989; Kamp and Tippett, 1993; Sutherland, 1996; Kamp, 1997; Walcott, 1998; Batt et al., 2004; Cande and Stock, 2004), and subsequently, 90 ± 20 km of shortening has occurred, forming the >3000 m high Southern Alps (Walcott, 1998). The Kaikoura Orogeny ensued and the higher grade Alpine Schists were uplifted (Norris et al., 1990). The Alpine Schists form a 10-20 km wide area to the southeast of the Alpine Fault, and the Otago and Alpine Schists form the Haast Schist of South Island New Zealand (Mortimer, 2000).

2.2 The Alpine Fault and the Modern Tectonic Setting of the Southern Alps

The Alpine Fault marks the present-day Pacific-Australian transpressional plate boundary through the South Island. The fault is ~400 km in length and can be traced from Milford Sound in the south to Arthur's Pass in the north, where it joins the Marlborough Fault Zone (Sutherland et al., 2000). The Alpine Fault has undergone ~460 km of strike-slip motion and >20 km of vertical motion (Norris et al., 1990; Sutherland, 1996).

Alpine Fault strike-slip rates are high $(21-29 \pm 6 \text{ mm/yr})$ along the Southern section of the Alpine Fault (from Lake McKerrow to Kakapotahi River) (Norris and Cooper, 2000; Sutherland et al., 2006), but are substantially lower north of the Hope Fault ($\geq 6.2 \pm 2 \text{ mm/yr}$) as strain is partitioned onto the Marlborough Fault System (Figure 2.2) (Norris and Cooper, 2000). Uplift rates vary significantly along the length of the Alpine Fault (0 to >10 mm/yr), with the highest rates (>12 mm/year) in the central segment near Franz Josef and Fox Glaciers (Figure 2.2) (Bull and Cooper, 1986; Norris and Cooper, 2000).

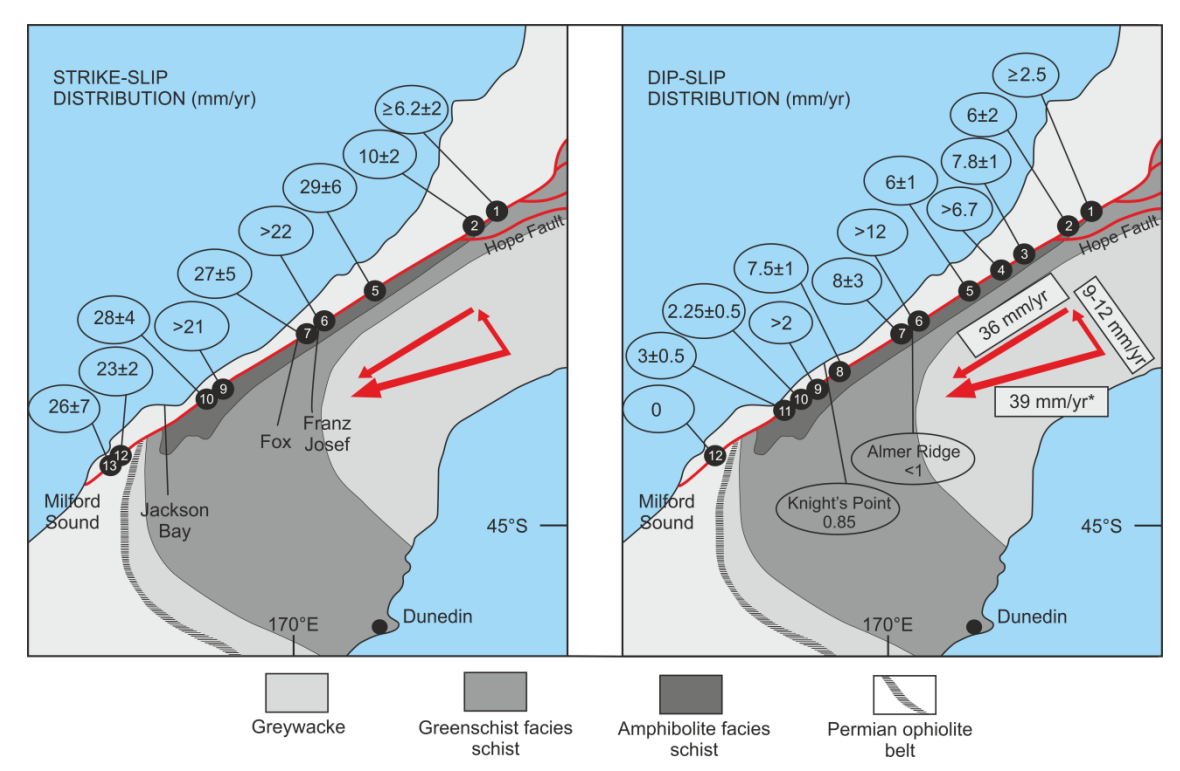


FIGURE 2.2: Quaternary uplift and strike-slip rates vary significantly along the Alpine Fault. These rates are derived from measurements of the offsets of Quaternary units (Norris et al., 1990; Cooper and Kostro, 2006; Sutherland et al., 2006) and dating of uplifted hydrothermal minerals (Teagle et al., 1998). The plate vector with an * is taken from the NUVEL-1A plate motion (DeMets et al., 1994) and the resolution of this vector was deciphered using GPS measurements (Beavan et al., 1999). The numbers in the black circles represent localities: 1 - Haupiri River; 2 – Inchbonni; 3 - Toaroha River; 4 - Kaka Creek; 5 - Kakapotahi River; 6 - Gaunt Creek; 7 - Waikukupa River; 8 - Paringa River; 9 - Haast River, north bank; 10 - Haast River, south bank; 11 - Okuru River; 12 - Hokuri Creek; 13 - Lake McKerrow. Figure modified from Norris and Cooper (2000), by Menzies (2012).

No large earthquakes have been recorded on the central section of the Alpine Fault since European settlement in 1840 AD, but the last three ruptures have been dated at 1717 AD, 1600 AD and 1430 AD (Sutherland et al., 2007). A record of fault ruptures in the Haast Schist area and Hokuri Creek has revealed that the southern section of the Alpine Fault has ruptured 24 times over the last 8000 years, with a mean recurrence interval of 329 ± 68 years (Berryman et al., 2012a; Berryman et al., 2012b). Lake sediments recording the post-seismic landscape has indicated that earthquakes are responsible for a significant amount of the sediment flux in the Southern Alps (Howarth et al., 2012).

In collisional orogens with rapid uplift rates, advection of hot rock occurs faster than the heat can be conducted and this produces thermal anomalies in the shallow crust (Koons, 1987). In the Southern Alps, rapid uplift, along with effective removal of rock by strong physical erosion, has raised the brittle-ductile transition zone, which may lie only 6-8 km below the surface proximal to the Alpine Fault in the areas of highest uplift rates (Koons, 1987; Craw, 1997; Leitner et al., 2001; Sutherland et al., 2012). This has produced high geothermal gradients estimated between 40-200 °C/km in the upper crust (Allis et al., 1979; Koons, 1987; Allis and Shi, 1995; Shi et al., 1996; Craw, 1997; Batt and Braun, 1999; Toy et al., 2010). The Deep Fault Drilling Project (DFDP-1) drilled a ~150 m

borehole at Gaunt Creek, and measured a geothermal gradient of 62.6 ± 2.1 °C/km (Sutherland et al., 2012). More recent findings from the DFDP-2 drilling project on the Alpine Fault has suggested that the geothermal gradient is >100 °C/km, and may even be as high as 140-150 °C/km in the upper 1 km of the crust (DFDP-2, unpublished data).

2.3 Structure of the Orogen

During continental collision in regions with strong weather asymmetry (e.g. prevailing winds), a two-sided orogen (Figure 2.3) consisting of opposite facing, asymmetrical wedges is produced by convergence of continental plates of approximately the same thickness (Koons, 1990; Norris et al., 1990; Koons, 1994; Koons and Henderson, 1995). The two wedges which make up the collisional orogen are the steep inboard wedge facing the indentor, which is separated by the Main Divide from the outboard wedge (Koons, 1990; Norris et al., 1990; Koons, 1994). The narrow belt that forms the steep inboard wedge was formed by movement of material up the basal thrust from a décollement at depth (Koons, 1990). The broad region to the east forms the outboard wedge, which grows by thrusting away from the indentor over undisturbed crust, and is thickened by antithetic and synthetic faulting (Koons, 1990). The inboard wedge has high rates of uplift, rainfall and erosion, and the

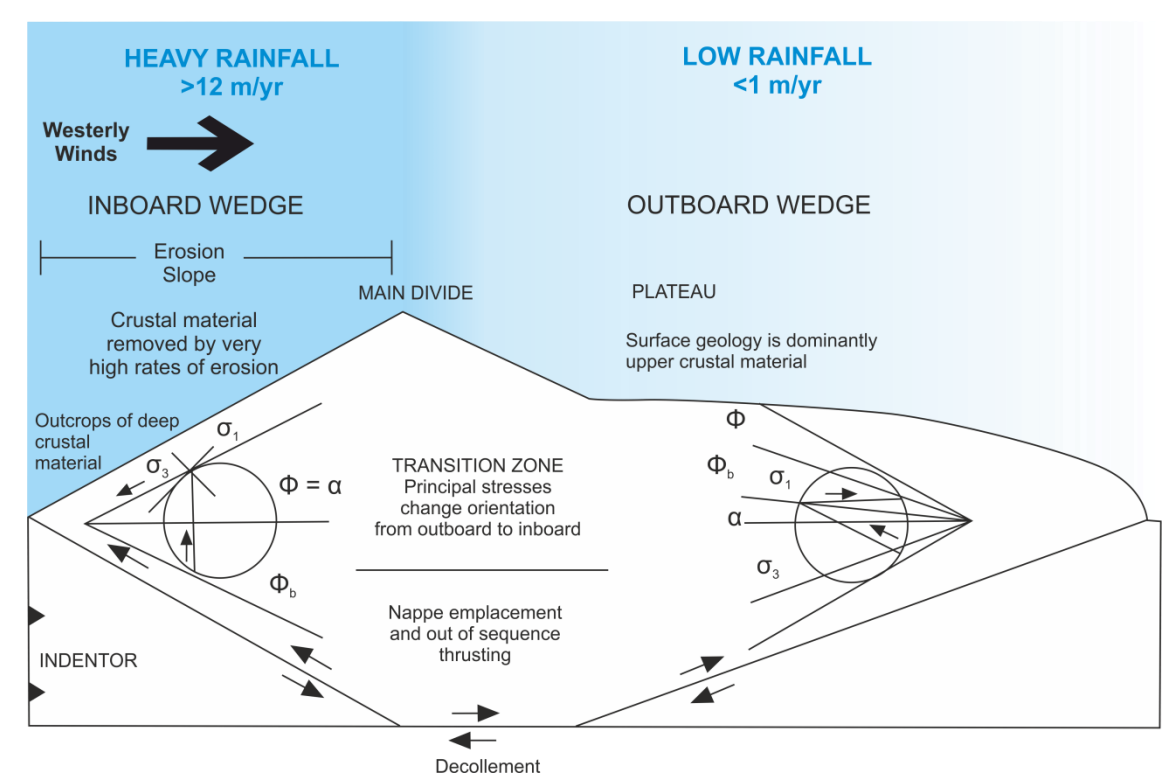


FIGURE 2.3: Schematic model of the movements and stresses that formed the inboard and outboard zones, two opposite facing wedges. Mohr Circles show orientations of principal stresses in each wedge (Lehner, 1986). The arrows show slip directions and coupled vectors show relative senses of shear at the base of the orogen. This figure was re-drawn by Menzies (2012) from Koons (1990). The rainfall rates were sourced from the literature (Griffiths and McSaveney, 1983; Henderson and Thompson, 1999; Woods et al., 2006).

outboard wedge has low rates of uplift, rainfall and erosion (Adams, 1980; Whitehouse, 1986; Koons, 1989; Koons, 1990; Beaumont et al., 1992; Koons, 1994).

2.4 Lithology and Metamorphic Grade of the Haast Schist

The Haast Schist (Figure 2.1) is composed of the Alpine Schist (high metamorphic grade Amphibolite Facies rocks uplifted adjacent to the Alpine Fault) and the Otago Schist (lower metamorphic grade Greenschist Facies rocks that extend to the east) (Wood, 1963). The Otago Schist forms a 150 km-wide northwest-trending schist belt across southern New Zealand that ranges in metamorphic grade from Prehnite-Pumpellyite Facies either side and Greenschist Facies rocks exposed in the middle (Mortimer, 1993; Mortimer, 2000). The northern portion of the Otago Schist is derived from the Torlesse Terrane and the southern portion is derived from the Caples Terrane (Mortimer and Roser, 1992). The Torlesse Terrane is largely made up of quartzofeldspathic greywackes and grey/black mudstones, with minor conglomerates and red/green mudstones (Mackinnon, 1983). The Caples Terrane consists of volcaniclastic greywackes and argillites (Bishop et al., 1976). The Caples greywackes are mainly derived from an active intraoceanic magmatic arc (Mackinnon, 1983; Roser and Korsch, 1986; Mortimer and Roser, 1992). Hydrothermal calcite and quartz veins are prevalent across the Southern Alps, especially in the higher metamorphic grade regions (Grapes and Watanabe, 1984; Holm et al., 1989).

In the Southern Alps, the Torlesse Terrane show increasing metamorphic grade from east to west (Figure 2.5). Unmetamorphosed greywackes are found in the east along with the lowest metamorphic grade rocks (weakly cleaved Prehnite-Pumpellyite Facies greywackes and argillites), which grade to recrystallized and deformed upper Greenschist Facies psammitic and pelitic schists (Norris et al., 1990; Craw et al., 1999). The Alpine Schist consist of higher grade garnet-oligoclase grade Amphibolite Facies rocks adjacent to the Alpine Fault, which contain multiple generations of metamorphic fabrics, folds, and metamorphic quartz veins (Cox and Rattenbury, 2006; Cox and Sutherland, 2007; Little et al., 2007; Wightman and Little, 2007). Away from the Alpine Fault, metamorphic grade decreases eastwards to Prehnite-Pumpellyite Facies (Norris et al., 1990; Grapes and Watanabe, 1992; Grapes, 1995; Cox and Sutherland, 2007).

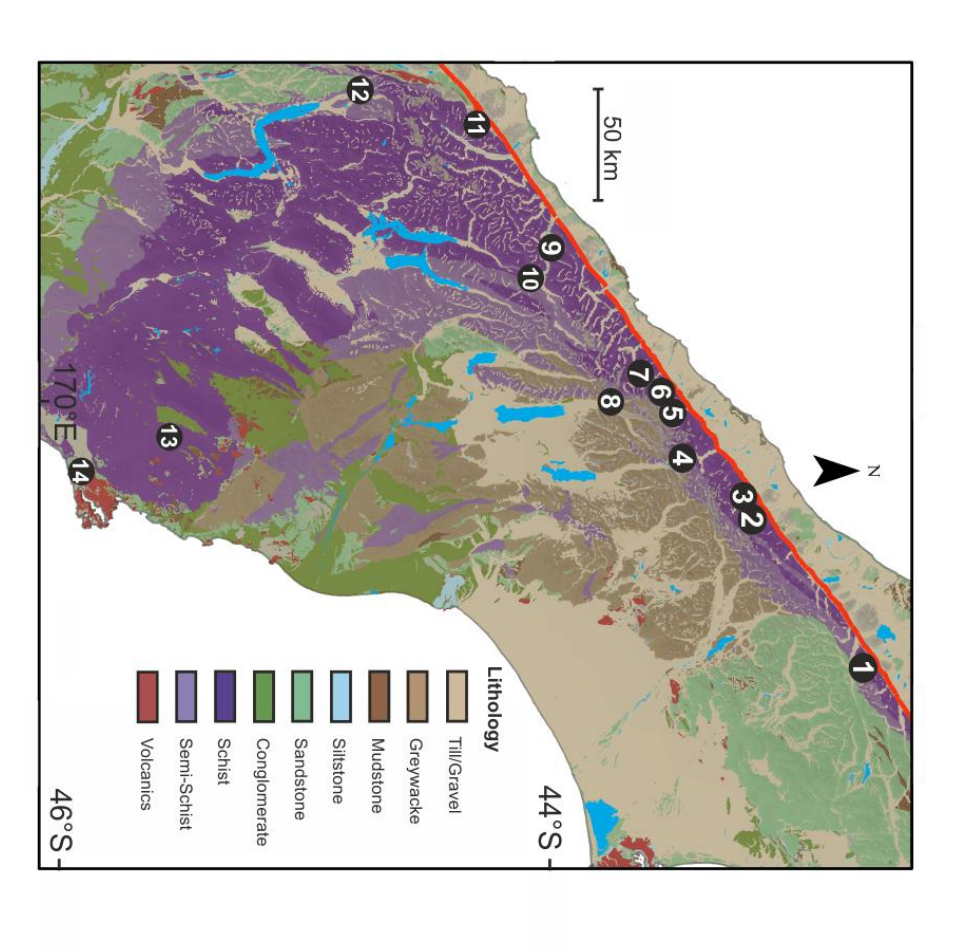


FIGURE 2.4: Map of the Southern Alps, South Island, New Zealand, showing the main lithologies that compose the Haast Schist. The red line represents the Alpine Fault. Localities in black circles: 1 – Mingha River, 2 – Morgan's Gorge, 3 – Wanganui, 4 – Butler Junction, 5 – Franz Josef, 6 – Fox Glacier, 7 – Copland, 8 – Hooker Glacier, 9 – Haast river, 10 – Thunder Creek, 11 – Cascade, 12 – Chinaman's Bluff, 13 – Macraes, 14 – Dunedin. GIS data from Simon Cox (Cox and Rattenbury, 2006).

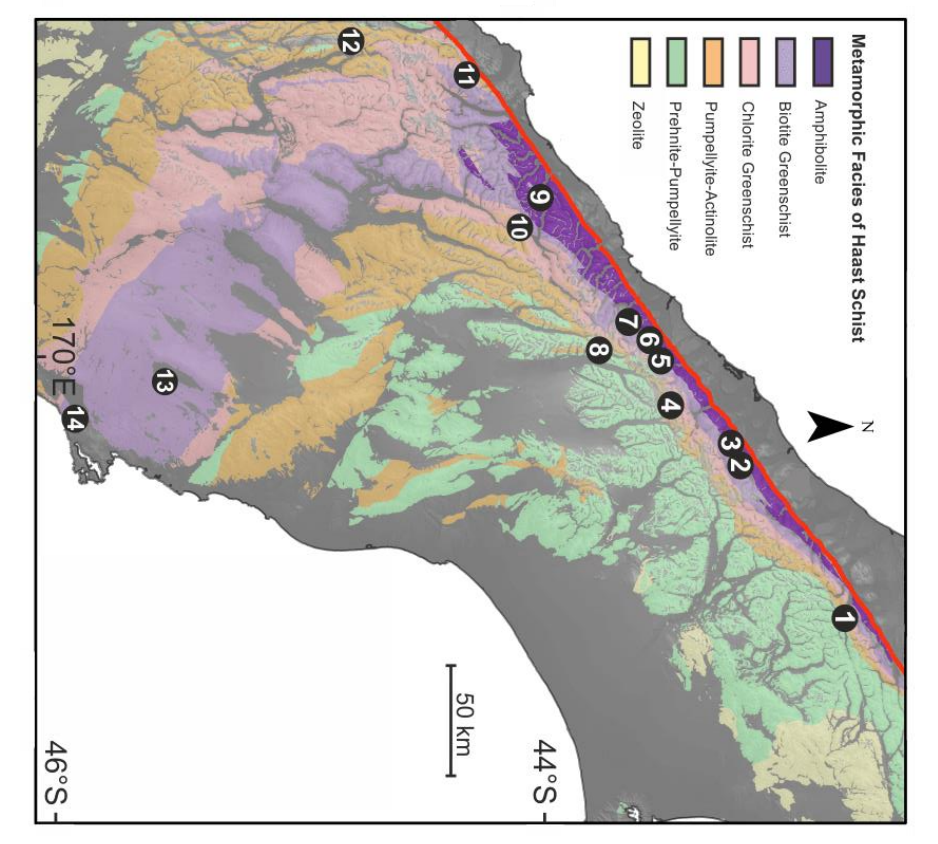


FIGURE 2.5: Map of the Southern Alps, South Island, New Zealand, showing the metamorphic facies that compose the Haast Schist. The red line represents the Alpine Fault. Localities in black circles: 1 – Mingha River, 2 – Morgan's Gorge, 3 – Wanganui, 4 – Butler Junction, 5 – Franz Josef, 6 – Fox Glacier, 7 – Copland, 8 – Hooker Glacier, 9 – Haast river, 10 – Thunder Creek, 11 – Cascade, 12 – Chinaman's Bluff, 13 – Macraes, 14 – Dunedin. GIS data from Simon Cox (Cox and Rattenbury, 2006).

2.5 Effects of Rapid Uplift and Orogen Structure upon Climate and Erosion

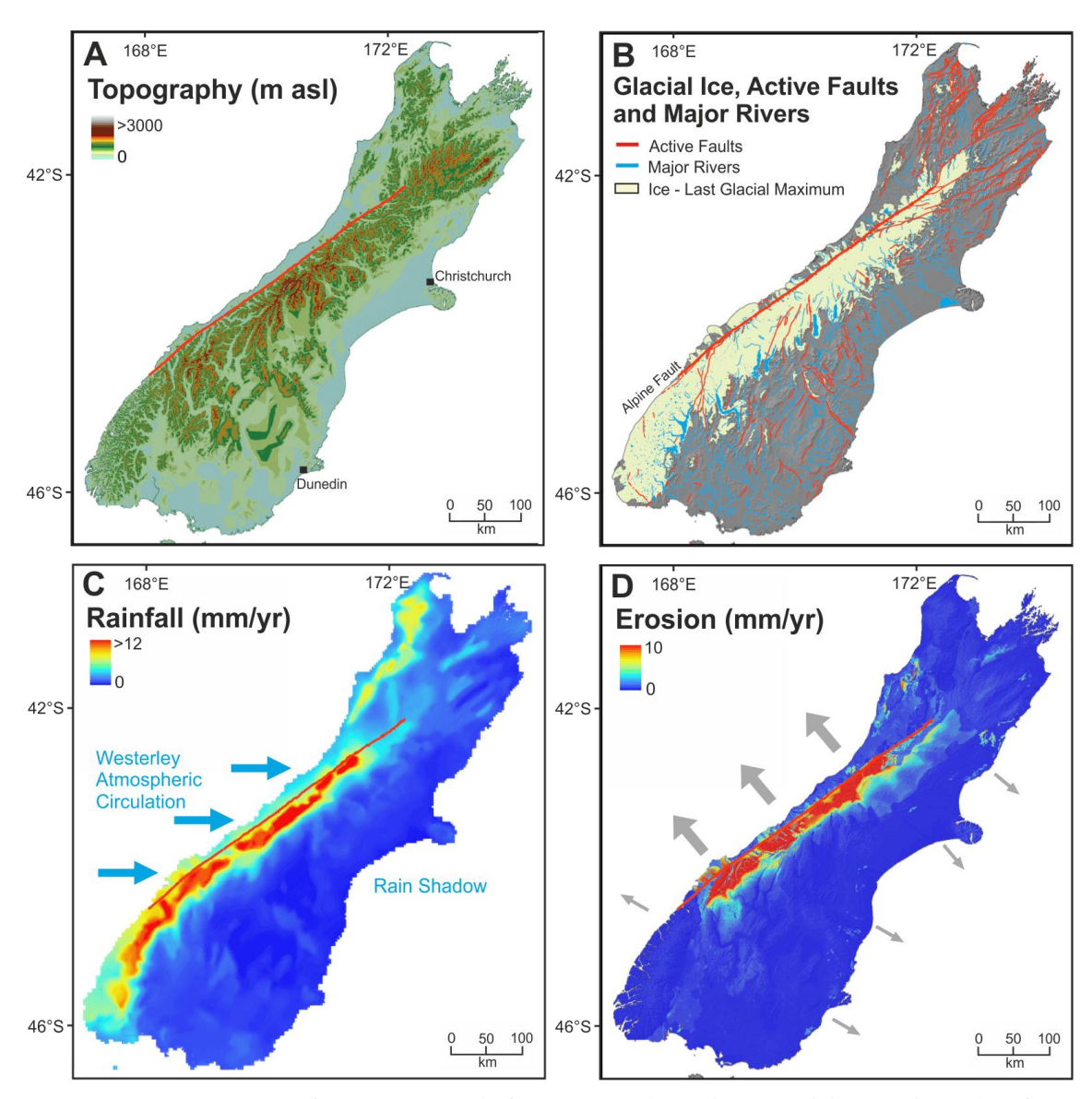


FIGURE 2.6: Maps of the South Island of New Zealand showing: (A) digital terrain model of topography in metres above sea level; (B) extent of ice at the last glacial maximum (Barrell, 2011), major rivers and active faults with known evidence for rupture in the past 120 kyr (GNS Science, Active Faults Database 2011); (C) mean annual rainfall, modelled from the period 1971-2000 (Tait et al., 2006); (D) erosion rate, calculated as a mean ground lowering from a suspended sediment yield model (Hicks et al., 1996), assuming an average crustal density of 2.65 t/m³. This image was adapted from (Cox et al., 2012).

2.5.1 Climate

The Southern Alps form a barrier to the prevailing westerly winds, which travel uninterrupted for ~2000 km across the Southern Ocean, onshore onto the western side of the island (Figure 2.7) (Henderson, 1993; Mosley and Pearson, 1997; Jacobson et al., 2003; Williams et al., 2005). As a result, rainfall west of the Main Divide is intense (>12 m/yr), and the area to the east of the Main Divide receives considerably less rain (<1 m/yr) (Griffiths and McSaveney, 1983; Henderson and Thompson, 1999; Woods et al., 2006). To the west of the Main Divide, steep gradients and high

runoff (from high rainfall and snow/glacial melt) produce flash streams with a coarse and boulder-strewn bedload that feed large rivers; but to the east, gentle gradients and lower rainfall produce braided rivers and lakes with silt and gravel-sized bedloads which drain glaciated catchments (Jacobson et al., 2003). The South Island has a temperate climate. On the east of the island, summer temperatures are 18-26 °C (can be as high as 30 °C) and winter temperatures are 7-14 °C (NIWA Climate Database). On the west of the island, summer temperatures are 17-22 °C (rarely exceed 25 °C) and winter temperatures are 10-14 °C (NIWA Climate Database). This, along with the high altitude of the Southern Alps, results in maritime glaciers, which form the warm and wet maritime end member of the glacier response scale (Fitzharris et al., 1999). High rainfall to the west supports dense, temperate montane rainforest and sub-alpine shrub ecosystems that grow on <1 m thick soils formed from highly fractured schist bedrock (Griffiths and McSaveney, 1983; Tonkin and Basher, 1990; Clarke and Burbank, 2011).

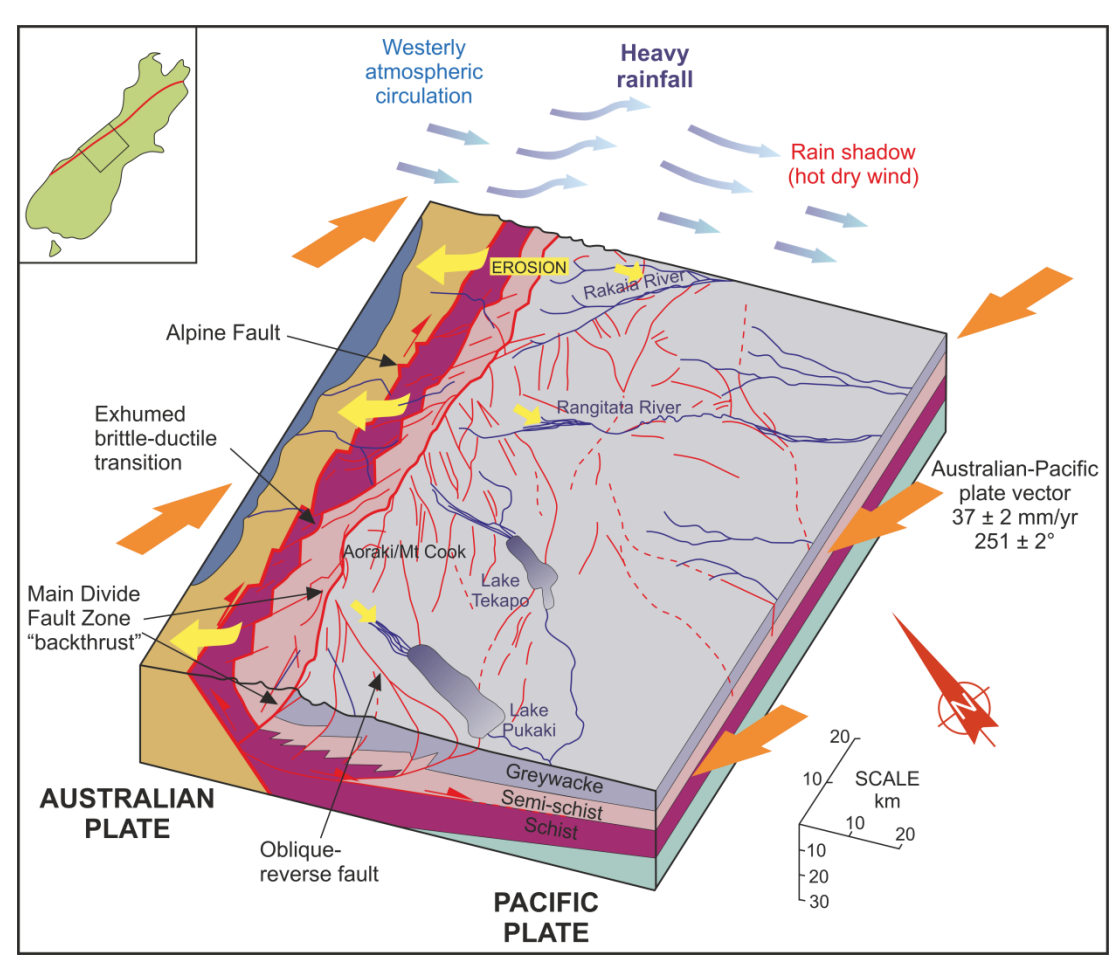


FIGURE 2.7: Block diagram showing the effects of Australian-Pacific plate transpression. Summarises the dominant climatic pattern, erosion, geology, structure and tectonics of the Southern Alps. Figure from Cox and Sutherland (2007).

2.5.2 Glaciation

Around 5% of South Island is currently covered with ice and there are more than 3000 glaciers ranging from small (10⁴ m²) snowfields to the largest (10⁸ m²) Tasman Glacier (Chinn, 2001). The net gains/losses of snow and ice are influenced by New Zealand's humid maritime climate and the strength of westerly atmospheric circulation (Fitzharris et al., 1992; Chinn, 1995; Shulmeister et al., 2004). Glacier response time is the amount of time taken for a glacier to adjust its geometry to a new steady state after a change in the glacier mass balance (Bahr et al., 1998). This change in glacier morphology varies across the Southern Alps. Highly active glaciers on steep slopes to the west respond rapidly (5-8 years) to climatic events, whereas larger, gentler sloping glaciers to the east have slower (up to 100 years) response times (Gellatly et al., 1988; Chinn, 2001). For steep glaciers in the west (such as the Franz Josef and Fox Glaciers), high mass turnover coupled with the maritime climate of the South Island, results in increased velocities (up to ~5 m d⁻¹) (Herman et al., 2011). Whereas, low-angled and debris covered glaciers in the east (such as the Tasman Glacier) are lower velocity (Herman et al., 2011).

2.5.3 Erosion

Sediment production rates across the Southern Alps are among the highest in the world (Hales and Roering, 2005). Rapid uplift and heavy rainfall in the west has increased mechanical erosion rates by a factor of ~13, compared to the eastern side of the Southern Alps which has lower rates of uplift and less rainfall (125 x 10⁸ vs. 9.4 x 10⁸ g·km²·yr⁻¹; Jacobson and Blum, 2003).

The presence of glaciers in the Southern Alps can lead to glacial grinding, which also increases physical erosion, and can lead to higher concentrations of solutes in glacial rivers relative to those draining non-glaciated terranes (Anderson et al., 1997).

In addition, mechanical erosion is enhanced near fault-weakened areas; close to the Alpine Fault, cataclasites and fractured mylonites crop out (Reed, 1964). Cataclasites are fault products formed by grain size reduction in the brittle portion of the crust (Scholz, 1988; Snoke et al., 1998). Cataclasites and other brittle fault products have a high surface area available for chemical weathering, although these minerals are largely altered already. Potentially active faults have also been mapped in the Southern Alps, evidence of which is erased by rapid erosion, and they could be a potential source of seismic activity and further erosion (Cox et al., 2012).

2.5.4 Landslides

Gravitational mass wasting is widespread and frequent in the Southern Alps, particularly in areas where the bedrock has been weakened by faulting (Whitehouse and Griffiths, 1983; Cox and Findlay, 1995; McSaveney, 2002; Korup, 2004). In the central Southern Alps, almost 2% (414 km²) of the total land area is affected by landsliding (Allen et al., 2011). In general, processes such as rock-mass dilation, ice wedging, glacier retreat, snow level recession, and the reduction in ice-binding of rock material combine to lower the resistance of rock masses to gravitational failure (Wegmann et al., 1998; Davies et al., 2001; Gruber and Haeberli, 2007). For the Southern Alps, extremely heavy rainfall to the west and earthquakes are also an important control on landsliding (Korup, 2004). Landslide mapping across the central region of South Island has shown that the majority of landslides have occurred from steep slopes along the Main Divide (Allen et al., 2011). The regional denudation rate for the western side of the Southern Alps attributed to landsliding has been calculated to account

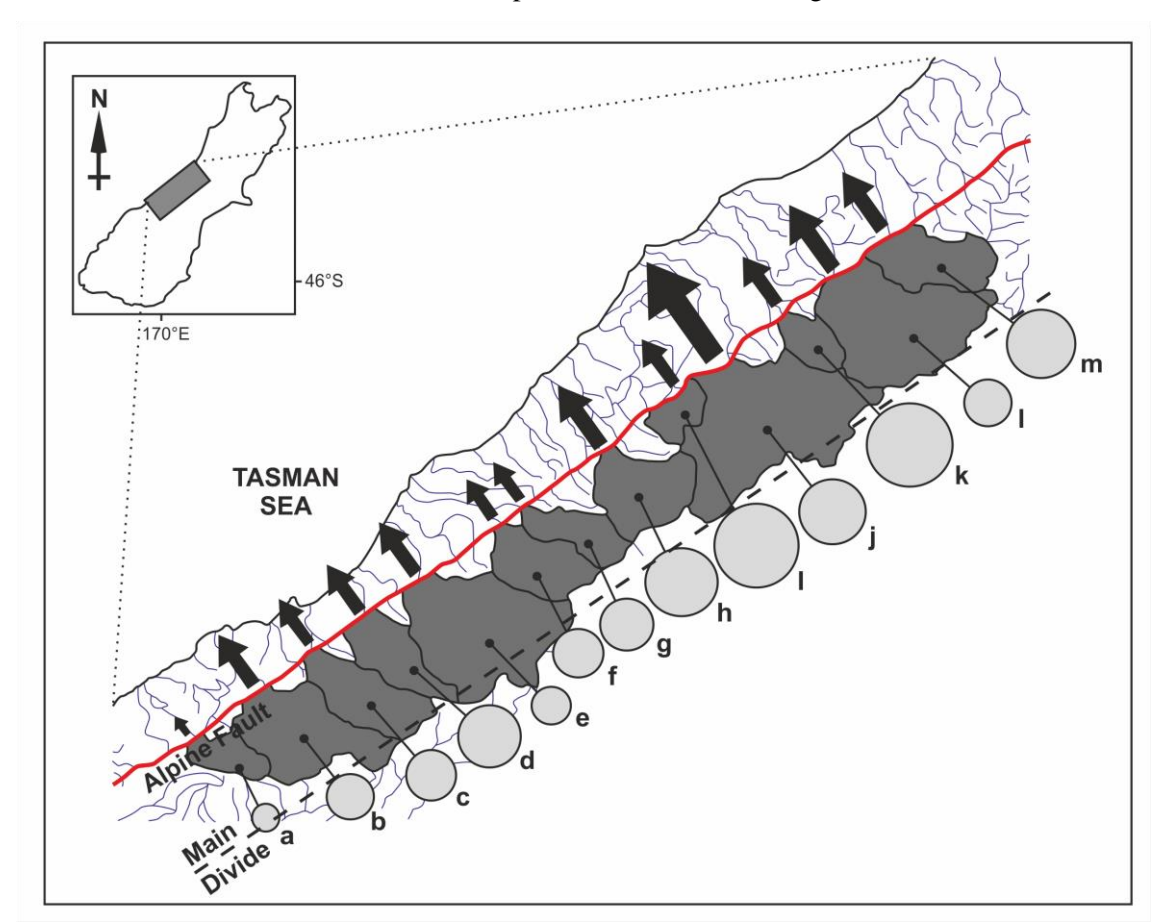


FIGURE 2.8: Collection of denudation rates and sediment discharges from catchments draining the Southern Alps, to the west of the Main Divide, calculated from a 60 year landslide record. Denudation rates (E) are shown by circles and sediment discharges (D) are shown by black arrows, the size of which are proportional to each estimate. Catchments: (a) Moeraki: E = 1.8 mm/yr, $D = 1.2 \times 10^5 \text{ m}^3/\text{yr}$; (b) Paringa: E = 5.5 mm/yr, $D = 1.3 \times 10^6 \text{ m}^3/\text{yr}$; (c) Mahitahi: E = 6.3 mm/yr, $D = 9.8 \times 10^5 \text{ m}^3/\text{yr}$; (d) Makawhio: E = 9.9 mm/yr, $D = 1.1 \times 10^6 \text{ m}^3/\text{yr}$; (e) Karangarua: E = 3.7 mm/yr, $D = 1.3 \times 10^6 \text{ m}^3/\text{yr}$; (f) Cook: E = 5.8 mm/yr, $D = 7.9 \times 10^5 \text{ m}^3/\text{yr}$; (g) Fox: E = 7.5 mm/yr, $D = 7.1 \times 10^5 \text{ m}^3/\text{yr}$; (h) Waiho: E = 12.2 mm/yr, $D = 2.0 \times 10^6 \text{ m}^3/\text{yr}$; (i) Waitangitaona: E = 18.1 mm/yr, $D = 1.1 \times 10^6 \text{ m}^3/\text{yr}$; (j) Whataroa: E = 11.4 mm/yr, $D = 5.1 \times 10^6 \text{ m}^3/\text{yr}$; (k) Poerua: E = 18.1 mm/yr, $D = 1.2 \times 10^6 \text{ m}^3/\text{yr}$; (l) Wanganui: E = 6.1 mm/yr, $D = 2.1 \times 10^6 \text{ m}^3/\text{yr}$; (m) Waitaha: E = 11.6 mm/yr, $D = 1.7 \times 10^6 \text{ m}^3/\text{yr}$. Adapted image and data from Hovius et al. (1997).

for 9 ± 4 mm/yr downwasting (Figure 2.8), which indicates that the majority of sediment discharge in the west may be sourced from landslide-derived material (Hovius et al., 1997).

2.6 Why Study the Southern Alps?

The Southern Alps on South Island, New Zealand, are the focus of this study because they present a relatively pristine environment to systematically examine the climatic and tectonic controls on chemical weathering in a dominantly metasilicate terrain. The reasons why the Southern Alps have been chosen as the study area for this project include:

- The Southern Alps are subject to little air and water pollution due to few industrial sources and a low population.
- The Southern Alps are almost entirely composed of metasilicates, which include mostly metasediments and some metabasalts, with minor disseminated calcite.
- The South Island has been subject to rapid uplift and exhumation of high grade metamorphic rocks adjacent to the Alpine Fault, with a transition from high grade metamorphic rocks in the west to lower grade rocks in the east.
- Warm springs are present in the Southern Alps, which allow the investigation of water-rock reactions at depth. There is no magmatic activity occurring in this orogen, which leaves only two possible fluid end members for these fluids (metamorphic and meteoric fluids).
- The structure of this orogen has led to differing patterns of climate and erosion to the east and west of the Main Divide:
 - The asymmetry of this orogen has resulted in heavy rainfall to the west and created a rain shadow to the east.
 - The high elevation of this mountain belt has led to the formation of glaciers along the Main Divide.
 - Uplift rates vary along the length of the Alpine Fault, but uplift is generally higher to the west of the Main Divide than the east.
 - Landslides are more frequent in the west where rapid uplift rates have led to increased bedrock weakening by faulting.
 - The above factors have led to a high erosion rate west of the Main Divide and a lower erosion rate to the east.

Sampling and Analytical Methodology

3.1 Sample Collection and Preparation

This study involves the analysis of river waters, groundwaters, spring waters, bedrock, mica mineral separates, river sands and suspended particles from the rivers and springs. The bedrock samples were collected by Ian Pitcairn from the Otago and Alpine Schists on the South Island of New Zealand between January and April 2001 (Pitcairn, 2004). Each sample collected was large enough (1-2 kg) to ensure that all weathered faces could be removed completely (Pitcairn, 2004).

The river waters, groundwaters (collected from the Tartare Tunnels), spring waters and river sands were collected by Catriona Menzies, Damon Teagle, Simon Cox and Rachael James, between 2009 and 2011 (Menzies, 2012). The groundwaters were collected from the drips/streams of fluid issuing from the roof of the Tartare Tunnels (Menzies, 2012). Temperature, conductivity and pH were measured in the field. The fluid samples were filtered at $0.2 \mu m$, and collected in 1 L acid-cleaned HDPE bottles for cation analysis and in Milli-Q (18.2 M Ω H₂O) washed 60 ml bottles for anion analysis (Menzies, 2012). Alkalinity was determined by titration with 0.1 M TD (thermally-distilled) HNO₃ for the spring samples and 0.01 M TD HNO₃ for the river water samples within 24 hours of sample collection. Detailed methods regarding the fluid samples are outlined in Menzies (2012).

3.2 Preparation of Bedrock and Particulate Material

Large bedrock samples were first cut using a water-lubricated diamond saw and then the surfaces were ground to remove any unwanted material from the saw. The samples were then crushed using a hardened pure-iron fly-press. A range of different micas then were selected (biotite, chlorite and

muscovite) for picking from different bedrock samples. Approximately 30 mg of mica was picked to a high degree of purity for each sample and then crushed using a mortar and pestle.

River sand samples were sieved to separate different size fractions: 2 mm (granules), 1 mm (very coarse sand), 0.5 mm (coarse sand), 0.25 mm (medium sand), 0.125 mm (fine sand), 0.0625 mm (very fine sand) and <0.0625 mm (coarse silt). The weight of the different size fractions was totalled and the loss of sample throughout this procedure was calculated. The river sediment clay fraction was separated from the coarse silt fraction by suspension in Milli-Q water.

To ensure sample homogeneity, samples were crushed to a fine powder ($<75 \mu m$). This degree of fineness in essential for ensuring maximum grain-acid contact during acid digestion (Potts, 1987). Semi-crushed bedrock and river sand samples were crushed to a fine powder ($<75 \mu m$) in a hardened pure-iron Tema pot.

The river water and spring water samples were filtered at time of sampling (Menzies, 2012). The particulate material that remained on the filters is the suspended load and this was removed. The filters were completely submerged in Milli-Q and ultrasonicated for 2 hours or until the material had re-suspended. The filters were removed and rinsed with Milli-Q to remove as much of the suspended load as possible. The mixture was then dried on a hotplate (130 °C) and the mass of the particles was determined. The uncertainty in the mass of the dried particles is ± 0.0005 g (due to very small sample sizes and problems with static), which means that the uncertainty in the elemental concentration of the samples may be up to $\pm 10\%$.

The bedrock, mica mineral separates, river sand size fractions and suspended load samples were dissolved via a HF-HNO₃-HCl digestion. Approximately 75 mg of each bedrock, bulk river sand fraction and fine river sand fraction was accurately weighed and placed into a weighed acid-cleaned Teflon pot. Insufficient material was collected for the mica mineral separates and the clay river sand fraction, and so the whole sample was digested (after being accurately weighed). The suspended load samples were kept in the same Teflon pots for digestion as the sample sizes were very small, and removal of the particulate material from inside of the Teflon vials would have been difficult, and would have resulted in loss of sample. To each sample, 1 drop of 15 M TD HNO₃ per 10 mg of powdered rock was added to make a slurry, and then 0.75 ml of Aristar HF was added. The samples were left to reflux on a hot plate at 130 °C for at least 12 hours and then the samples were dried. Once dry, the samples were carefully removed from the hotplate and sufficient 6 M TD HCl was added to dissolve the samples (>2 ml). The samples were left to reflux on a hot plate at 130 °C for at least 12 hours and then the samples were dried. If undissolved sample remained, the sample was dried down and 6 M TD HCl was added again and left to reflux. If undissolved material still remained, the samples were dried down and repeated attacks of 15 M TD HNO3 and 12 M TD HCl were carried out. Once fully dissolved in 6 M TD HCl, the lids were removed and the samples were placed on a hotplate to dry, and then sufficient 6 M TD HCl was added and left to dissolve for at least 2 hours. The samples were transferred to acid-cleaned bottles and the Teflon pots were thoroughly rinsed with 6 M TD HCl and Milli-Q to make the solution up to an approximate volume (~30 ml).

Dilution factors of the mother solutions were calculated (usually on the order of ~400). At least one laboratory blank accompanied each batch of samples, which underwent the same digestion procedure as the rock samples, but without the addition of any rock powder. At least one rock standard was also digested along with every batch of samples; usually JB-2 and/or BCR-2 as these rock reference materials are well characterised in the literature.

3.3 Elemental Analysis of Bedrock and Particulate Material

3.3.1 XRF (X-Ray Fluorescence) Analysis

X-ray fluorescence uses a primary X-ray beam to excite fluorescent radiation from the material being analysed. This can be used as a non-destructive chemical analytical technique. XRF was one of the techniques used to analyse the chemical composition of the Southern Alps bedrock samples (Pitcairn, 2004). A suite of samples were analysed at the University of Leicester for major and trace elements using XRF. Chemical analysis was performed on fused glass beads for major elements and pressed powder pellets for some trace elements on a PW1400 X-ray spectrometer using a Rh-tube and the Compton scattering method (Harvey, 1989; Pitcairn, 2004). Precision was estimated for each element from multiple analyses of USGS reference materials, which is quoted in Pitcairn (2004).

3.3.2 *ICP-MS* (*Inductively-Coupled Plasma-Source Mass Spectrometry*)

The Thermo X-Series II ICP-MS was used to analyse major and trace elements in the river sand fractions, mica mineral separates and suspended sediments. To achieve this, two dilutions were made from the mother solutions; a 4000 fold dilution for trace elements and an 80000 fold dilution for major elements. With every analysis, 9 rock standards and a control blank were analysed to check the accuracy of the analyses. Dilutions of standards and samples were made using 3% TD HNO₃. A beryllium and indium internal standard was also used to assess the internal precision of the machine.

Before each analysis, the instrument was tuned using a 1 ppb multi-element standard (Co, Y, In, La, Re, Bi and U). The tuning parameters can be used to obtain optimum sensitivity and stability (ideally better than <2%). Elements that form common oxides were analysed in CCT mode, which uses a mixture of hydrogen and helium, which lowers the sensitivity, but removes interferences from oxides. The samples were run in a random order with 6 calibration standards and an acid blank at the

start and end of each run, and at the very end of the run, several blanks were analysed to constrain detection limits.

For the whole rocks, the international standard JA-2 was used to text for accuracy, and this standard, as well as internal standards BAS206 and BRR-1, were used to assess precision. Precision and accuracy of measurements are shown in Tables 3.1 and 3.2. Internal precision was monitored by measuring each sample four times and calculating the percentage relative standard deviation (%RSD) which is expressed as the standard deviation of the mean as a percentage of the mean. Data with RSD of >10% were rejected.

Trace element analysis using the Thermo X-Series II ICP-MS was also carried out on the bedrock samples (Pitcairn, 2004). Precision and accuracy for these analyses can be found in Pitcairn (2004).

TABLE 3.1: Precision of elemental analyses by ICP-MS calculated from 3 separate analyses of rock standards.

		Preci		
Element	BRR-1	BAS206	JA-2	Average
	%RSD	%RSD	%RSD	%RSD
Na	3.6	1.8	3.4	2.9
Mg	3.1	1.8	3.1	2.7
Al	3.1	1.5	3.2	2.6
K	14	3.6	3.0	6.9
Ca	2.8	1.7	3.2	2.6
Mn	1.0	1.5	2.1	1.6
Fe	2.0	0.9	2.1	1.7
Li	1.2	1.3	1.2	1.2
P	9.7	4.5	4.8	6.3
Sc	0.5	0.6	0.9	0.7
Ti	0.5	0.7	0.8	0.7
V	0.8	0.8	0.7	0.8
Cr	1.5	1.7	0.8	1.4
Co	1.0	1.0	0.6	0.9
Ni	0.8	1.0	0.6	0.8
Cu	0.8	0.8	1.4	1.0
Zn	0.8	0.8	1.1	0.9
Rb	2.9	1.2	0.8	1.7
Sr	0.7	0.8	0.7	0.7
Y	0.8	0.5	0.9	0.7
Zr	0.6	0.5	0.5	0.5
Nb	1.3	0.7	0.7	0.9
Mo	5.7	2.1	3.1	3.6
Sn	2.4	2.3	1.2	2.0
Cs	8.1	3.0	0.8	4.0
Ba	0.9	1.0	0.8	0.9
La	0.9	0.8	0.8	0.8
Ce	0.9	0.6	0.8	0.8
Pr Na	1.0	0.7	0.8	0.8
Nd Sm	1.0	1.2	1.1	1.1
Sm	1.8	1.8	1.8	1.8
Eu Cd	1.4	1.3	2.3	1.7
Gd Th	2.0	1.3	1.9	1.7
Tb Dec	2.3	1.6	1.0	1.6
Dy	2.3	1.8	1.6	1.9
Ho	2.0	1.6	1.0	1.5
Er	1.2	2.1	1.3	1.5
Tm	1.3	0.8	1.2	1.1
Yb	0.7	1.0	1.7	1.1
Lu	1.1	1.3	1.0	1.1
Hf –	1.1	1.0	1.2	1.1
Ta	2.9	1.0	1.2	1.7
Pb	2.4	1.4	0.9	1.5
Th	2.7	2.4	1.1	2.1
U	4.1	2.2	1.3	2.5

TABLE 3.2: Accuracy of element concentration analysis by ICP-MS. Certified values for JA-2 are sourced from the GeoReM online database (Jochum et al., 2005).

	_			JA-2			Average Accuracy
	Element	Cert. Value	Run 1	Run 2	Run 3	Average	%
Na	μg/g	23100	23100	23400	23000	23200	0.4
Mg	$\mu g/g$	45800	43000	43600	44200	43600	5.0
Al	μg/g	81600	82000	82700	82400	82400	0.9
K	μg/g	15000	16200	16800	16500	16500	9.0
Ca	μg/g	45000	44300	45000	44800	44700	0.7
Mn	μg/g	852	_	797	830	814	4.7
Fe	μg/g	43700	42400	50900	45600	46300	5.6
Li	μg/g	29.1	28.4	28.8	29.0	28.8	1.2
P	μg/g	637	666	696	700	687	7.3
Sc	μg/g	18.4	17.8	18.1	18.6	18.2	1.4
Ti	$\mu g/g$	4170	3900	3980	4040	3970	5.0
V	μg/g	122	116	123	113	117	4.1
Cr	$\mu g/g$	465	396	393	395	395	18
Co	μg/g	27.0	27.1	27.4	28.2	27.5	1.9
Ni	μg/g	134	122	125	126	124	8.1
Cu	μg/g	27.9	29.5	30.0	30.7	30.0	7.1
Zn	μg/g	65.0	62.0	64.2	63.8	63.4	2.6
Rb	$\mu g/g$	71.0	75.7	76.7	77.3	76.6	7.3
Sr	μg/g	250	243	246	247	245	2.0
Y	μg/g	18.1	17.2	17.4	17.5	17.4	4.2
Zr	μg/g	112	117	119	119	118	5.1
Nb	μg/g	9.00	8.80	8.94	9.00	8.9	1.0
Mo	μg/g	0.60	0.51	0.52	0.50	0.5	18
Sn	μg/g	1.68	1.50	1.49	1.50	1.5	12
Cs	μg/g	4.90	5.15	5.14	5.21	5.2	5.2
Ba	μg/g	315	318	319	317	318	1.0
La	μg/g	16.1	15.9	15.9	16.0	15.9	1.0
Ce	μg/g	33.7	33.5	33.5	33.2	33.4	0.9
Pr	μg/g	3.70	3.82	3.81	3.76	3.80	2.6
Nd	μg/g	14.2	14.6	14.5	14.4	14.5	2.0
Sm	μg/g	3.10	3.09	3.08	3.06	3.08	0.7
Eu	μg/g	0.91	0.91	0.89	0.92	0.90	0.6
Gd	μg/g	3.00	3.09	3.07	3.08	3.08	2.6
Tb	μg/g	0.48	0.48	0.48	0.49	0.48	0.7
Dy	μg/g	2.90	2.94	2.95	3.00	2.96	2.1
Но	μg/g	0.61	0.60	0.61	0.62	0.61	0.1
Er	μg/g	1.70	1.72	1.71	1.77	1.73	2.0
Tm	$\mu g/g$	0.26	0.26	0.25	0.26	0.26	1.0
Yb	μg/g	1.68	1.67	1.70	1.74	1.70	1.4
Lu	μg/g	0.25	0.26	0.26	0.26	0.26	3.1
Hf	μg/g	2.93	2.95	2.92	2.95	2.94	0.3
Ta	μg/g	0.70	0.74	0.71	0.74	0.73	3.9
Pb	μg/g	19.3	21.9	21.7	21.8	21.8	11
Th	μg/g	5.00	4.90	4.86	4.83	4.86	2.8
U	μg/g	2.20	2.26	2.26	2.23	2.25	2.2

3.4 XRD (X-Ray Diffraction) Analysis

3.4.1 Separation of Clay from River Sand

- 1. The sieved coarse silt fraction was placed into clean glass beakers. Milli-Q (containing 1 g to 5 L MgCl₂) was added to each sample and placed in an ultrasonic bath for 20 minutes.
- 2. ~10 ml of Calgone (10% sodium hexa-meta-phosphate) was added. The samples were then stirred and left to settle for ~3 hours.
- 3. The <2 µm fraction was poured off into centrifuge tubes and topped up with Milli-Q.
- 4. ~10 ml MgCl₂ (10%) was added. MgCl₂ causes the sample to flocculate and Mg bonds to the cation sites.
- 5. The samples were centrifuged for ~20 minutes, and the clear liquid was poured off.
- 6. Milli-Q (containing a small amount of MgCl₂) was added to the samples and centrifuged for ~20 minutes, and then poured off.
- 7. The clay residue was then smeared evenly over a glass slide.

3.4.2 Clay Identification via XRD

Clay identification was carried out using X-ray diffraction (XRD). For clay mineral analysis using XRD, it is important to obtain maximum intensity, even if some resolution has to be sacrificed (Moore and Reynolds, 1997). Clay minerals have broad peaks that cannot be improved by highly refining the optics, as finer slits would diminish the intensity making it harder to identify clay mineral peaks (Moore and Reynolds, 1997).

The identification of clay minerals is a qualitative procedure, and begins by searching for a mineral that best explains the strongest peak(s). This choice is then confirmed by locating the positions of weaker peaks for the same mineral. These identified peaks are then eliminated from consideration and the process is repeated to locate the next mineral; this process continues until all peaks have been identified. Quartz can be useful in this process as its structure tolerates no significant atomic substitutions, and so its peak positions do not change (Moore and Reynolds, 1997). Thus, the quartz spectra can be used as a built-in internal standard, against which accuracy and precision of peak positions for the other phases present can be estimated (Moore and Reynolds, 1997). Peak position is determined from Bragg's Law (Bragg, 1933):

$$n\lambda = 2d\sin\theta$$
 (Eq. 3.1)

Quantitative analysis of XRD patterns can be carried out by calculating the relative proportions of each clay mineral in a sample using Biscaye's method (Biscaye, 1965). However, this method is not particularly robust; major constituents can have an error of ~10% and minor constituents can have an error of ~20%. To achieve an accurate analysis, it is important that sample thickness is uniform,

which may be difficult to achieve. If a sample is too thin, the intensities produced would be too weak to be useful for identification and quantification (Moore and Reynolds, 1997). It is preferable to make the sample as thick as possible. However, if a sample is not flat, it can result in sample misalignment.

The XRD analysis carried out for clay identification used 4 different methods to produce 4 patterns of XRD spectra:

- **E:** Addition of ethylene glycol and placed in a humidifier at 55 °C overnight. This replaces water in swelling clays.
- **A:** Air-dried at ambient temperature overnight.
- **3:** Placed in an oven overnight at 375 °C. This method is used for completeness.
- **5:** Placed in an oven overnight at 550 °C. This is used to check for the presence of chlorite.

3.5 Lithium Isotope Analysis

All Li isotope work was carried out in an over-pressurized clean laboratory (Class 100) at the NOC, Southampton. PTFE (Savillex) columns and vials were cleaned in 50% TD HNO₃ at 110 °C overnight, and the vials then refluxed with 12 M HCl at 110 °C overnight. Acids were thermally distilled (TD) in Teflon stills, and regularly checked for purity. Dilute acids were prepared from the TD acids by dilution with 18.2 M Ω Milli-Q, and standardised by titration against NaOH.

3.5.1 Separation of Li from the Sample Matrix

In order to make accurate and precise measurements of the lithium isotopic composition of natural samples, Li must first be separated from the rest of the sample matrix. This was done by cation exchange chromatography. Acid-cleaned PTFE columns (6 mm in diameter, 30 ml reservoir, PTFE frit) were loaded with pre-cleaned AG50W-X12 (Bio-RadTM) cation exchange resin (James and Palmer, 2000), to a height of 8.5 cm in 0.2 M TD HCl. The column procedure is as follows:

- 1. The columns were cleaned with 15 ml 6 M TD HCl and rinsed with 8 ml Milli-Q.
- 2. The columns were equilibrated with 8 ml 0.2 M TD HCl and resin height was measured to check it was 8.5 cm.
- 3. Samples containing 20 ng Li were dissolved in 200 μ l of 0.2 M TD HCl and carefully loaded onto the columns.
- 4. The samples were washed in with $2 \times 500 \mu l$ aliquots of 0.2 M TD HCl.
- 5. 22 ml of 0.2 M TD HCl was discarded (for rock samples 18 ml of 0.2 M TD HCl was discarded).

- 6. The Li fraction was collected in 18 ml of 0.2 M TD HCl in Savillex vials (for rock samples 26 ml of 0.2 M TD HCl was collected).
- 7. The Li fraction was dried down on a hotplate at \sim 130 °C.
- 8. The columns were cleaned with 30 ml 6 M TD HCl and rinsed with 30 ml Milli-Q.
- 9. The columns were stored in 0.05 M TD HCl.

The total procedural Li blank associated with the column chemistry is 10 ± 3 pg, which is <0.1% of the amount of Li loaded onto the columns, and thus has a negligible effect on δ^7 Li.

3.5.2 Li Column Calibration

To get a representative column calibration, a spring water sample, a river water sample and an acid-digested bedrock sample were used for this procedure. Each sample contained 20 ng of Li, to which 2 μ g of Li (2 μ l of a synthetic 1000 ppm Li ICP-MS standard solution) was added, and then dried down.

- The columns were preconditioned by gently adding 4 ml of Milli-Q and re-suspending the resin, equilibrated by adding 8 ml of 0.2 M TD HCl, and then the resin height was checked to be 8.5 cm.
- 2. The samples were re-dissolved in 100 µl of 0.2 M TD HCl and loaded onto the column.
- 3. The samples were washed in with 2 x 500 µl 0.2 M TD HCl.
- 4. 15 ml of 0.2 M TD HCl was added to the columns and then discarded.
- 5. The next 16 ml of 0.2 M TD HCl was collected in 2 ml fractions in separate vials.
- 6. The remaining cations were eluted with 30 ml of 6 M TD HCl and then rinsed with 30 ml Milli-Q.
- 7. Each 2 ml column fraction was made up to 5 ml with 0.2 M TD HCl for ICP-OES analysis.
- 8. Synthetic multi-element standards were prepared, which contained Li (Aristar, 1000 ppm), Mg (VWR Prolabo, 10000 ppm) and Na (Inorganic Ventures, 10000 ppm) ICP-MS standards. A range of concentrations were used to bracket the upper and lower end of the suspected concentration.
- 9. ICP-OES analysis of Li, Mg and Na was conducted. A wash solution of 0.2 M TD HCl was used.

The columns achieved good separation of Li from Na and Mg. The yield of Li from the columns is $99.1 \pm 1\%$.

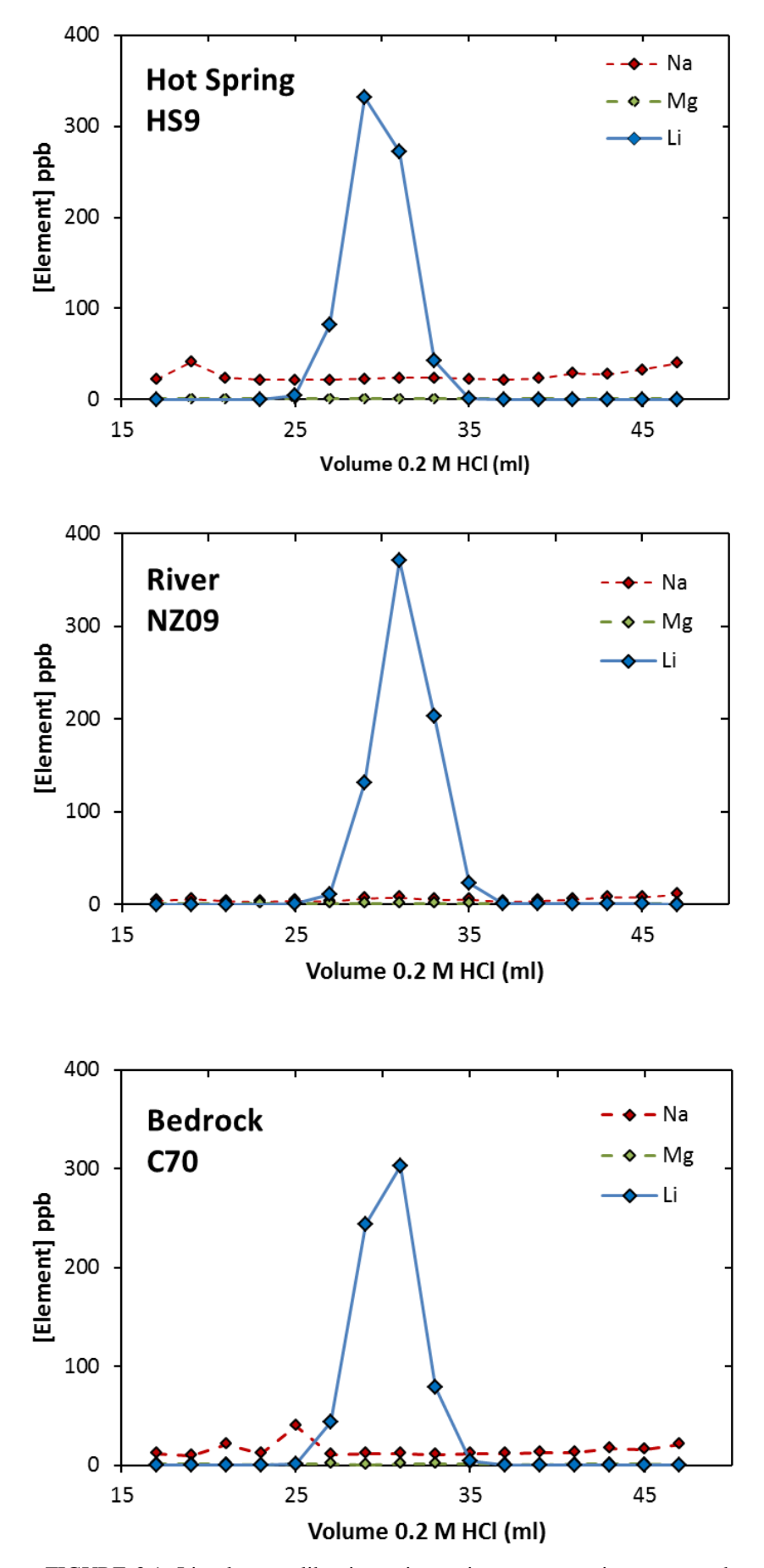


FIGURE 3.1: Li column calibration using a river water, spring water and bedrock sample. Volume of acid eluted is plotted against element concentration in ppb.

3.5.3 MC-ICP-MS Analysis of δ7Li

The lithium isotopic ratio measurements were determined by multi-collector inductively-coupled plasma-source mass spectrometry (MC-ICP-MS; Thermo Scientific Neptune), at the National Oceanography Centre, Southampton. The Li fractions purified by cation exchange chromatography were re-dissolved in 4 ml of 3% TD HNO₃ to produce a solution with a concentration of 5 ppb Li. Aliquots of 600 µl were taken from each sample for analysis. The samples were analysed using a sample-standard bracketing technique (Albarède and Beard, 2004), whereby the mass bias is determined from analysis of the ⁷Li/⁶Li ratio measured on the LSVEC tuning solution, which is analysed before and after each sample. The ⁷Li and ⁶Li intensity of the 3% TD HNO₃ blank solution was determined prior to analysis of each sample and standard, and then subtracted. If the ⁷Li intensity of the blank solution became higher than 100 mV, then the analytical run was stopped and the cones were cleaned. This typically reduced the blank ⁷Li intensity to 30-40 mV. This set-up was used for the river samples (low lithium concentration), using a CETAC Aridus IITM desolvating nebuliser system. Spring water and bedrock samples have much higher concentrations of lithium, and so could be analysed using a ThermoFinnigan stable introduction system (SIS). This system provided more stability to the signal than the Aridus, but 150 ng of Li (instead of 20 ng of Li) was required to be passed through the columns, so this method could only be used for samples with high concentrations of Li. The river sands, suspended load and mica mineral separates were analysed at Bristol University on a Thermo Scientific Neptune and CETAC Aridus ITM.

Typical parameters for Li isotopic analyses are shown in Table 3.3. With the Aridus set-up, the Ar sweep gas was usually the most influential tuning parameter, but with the SIS set-up it was the sample gas. δ^7 Li analyses carried out at Bristol University used the Aridus set-up, and the parameters used were very similar to those used at the University of Southampton, although a lower sweep gas (3-4 L/min) was used.

TABLE 3.3: Settings applied during Li isotope analysis on the Neptune, at the National Oceanography Centre, Southampton.

Parameter/Hardware	Aridus Set-up	SIS Set-up	
Average Blank	<50	< 500	mV
Sample and Standard Li Concentration	5	150	ppb
Nebuliser Aspiration Rate	75	75	μl/min
Ar sweep gas	6-8	0	L/min
No. of measurements	20	20	
Integration time	8.389	8.389	seconds
Idle time	3	3	seconds
Extraction voltage	-2000	-2000	V
Wash solution	3% HNO ₃	3% HNO ₃	
Wash time after sample	7	7	minutes
Wash time after blank	1	1	minutes
Cones	X	Н	Nickel

The combined uncertainty on the ${}^{7}\text{Li}/{}^{6}\text{Li}$ ratio of the two bracketing standards (u_{LSVEC1} and u_{LSVEC2}) is:

$$u_{LSVEC} = \frac{\sqrt{(u_{LSVEC1})^2 + (u_{LSVEC2})^2}}{2}$$
 (Eq. 3.2)

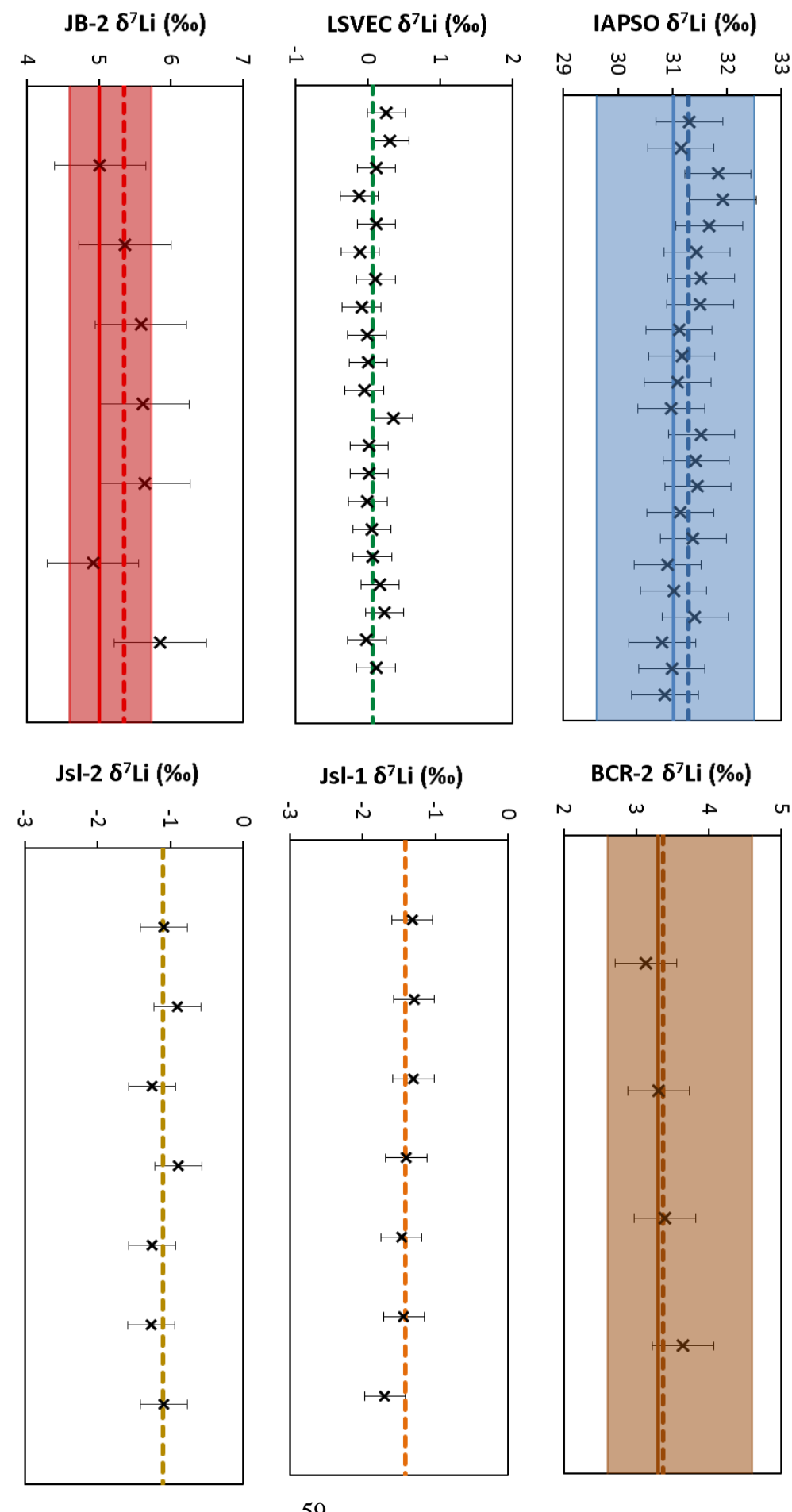
The combined uncertainty on the δ^7 Li value of the sample is:

$$u_{combined} = \frac{{}^{7}_{Li/} {}^{6}_{Li_{SAMPLE}}}{{}^{7}_{Li/} {}^{6}_{Li_{LSVEC}}} \times \sqrt{\left(\frac{u_{SAMPLE}}{{}^{7}_{Li/} {}^{6}_{Li_{SAMPLE}}}\right)^{2} + \left(\frac{u_{LSVEC}}{{}^{7}_{Li/} {}^{6}_{Li_{LSVEC}}}\right)^{2}}$$
(Eq. 3.3)

Where $u_{combined}$ is the internal reproducibility of the $\delta^7 Li$ value. The typical internal reproducibility was 0.1-0.2‰. To verify that no Li isotopic fractionation occurred during column chemistry and to access the external reproducibility of the $\delta^7 Li$ values of samples subject to column chemistry, LSVEC (a pure Li standard), IAPSO (a seawater standard), JB-2 and BCR-2 (basaltic rock standards), and JSl-1 and JSl-2 (metasedimentary rock standards) were also passed through the cation exchange columns and analysed within each instrument run. These $\delta^7 Li$ values were within range of previously published data for these standards (Table 3.4 and Figure 3.2).

TABLE 3.4: The average $\delta^7 \text{Li}$ values of the standards analysed within the instrumental analyses, and external reproducibility (2 σ).

Standard	δ ⁷ Li (‰)	2σ	n
IAPSO	31.3	0.61	23
LSVEC	0.07	0.27	21
JB-2	5.36	0.64	7
BCR-2	3.37	0.43	4
JSI-1	-1.42	0.28	7
JSI-2	-1.11	0.32	7



of average values from the literature. The published values are sourced from: IAPSO (James and Palmer, 2000; Bryant et al., 2003; Pistiner and Henderson, 2003; Millot et al., represent the external reproducibility (2σ) for each particular standard from this study. values taken from the literature are after 2004. This is due to increased consistency in the methods and machines used in recent times to obtain $\delta^7 \text{Li}$ values. The error bars al., 2006; Hippler et al., 2009; Košler et al., 2009; Janoušek et al., 2010; Pogge von Strandmann et al., 2011; John et al., 2012; Penniston-Dorland et al., 2012). Note, the IAPSO Millot et al., 2010; Négrel et al., 2010; Nishio et al., 2010; Tang et al., 2010; Magna et al., 2011; Pogge von Strandmann et al., 2011; John et al., 2012) and BCR-2 (Jochum et 2004; Vigier et al., 2009; Huang et al., 2010; Pogge von Strandmann et al., 2010; Wimpenny et al., 2010; Murphy et al., 2014), JB-2 (Hippler et al., 2009; Vigier et al., 2009; The dashed lines show average for the measured values from this study. The solid lines represent the average for values from the literature and the faded boxes show the range FIGURE 3.2: δ^7 Li external reproducibility of the standards. The measured δ^7 Li values for the standards passed through cation exchange columns are shown as black crosses.

3.6 Magnesium Isotope Analysis

All Mg isotope work was completed in an over-pressurized clean laboratory (Class 100) at the NOC, Southampton. PTFE (Savillex) columns and vials were cleaned in 50% TD HNO₃ at 100 °C overnight, and the vials then refluxed with 12 M TD HCl at 110 °C overnight. Dilute acids were prepared from the TD acids by dilution with 18.2 M Ω Milli-Q, and standardised by titration against NaOH.

3.6.1 Separation of Mg from the Sample Matrix

In order to make accurate and precise measurements of the magnesium isotopic composition of natural samples, Mg must first be separated from the rest of the sample matrix. This was done by cation exchange chromatography. The method used in this study for complete Mg separation was adapted from techniques similar to those described previously (e.g. Pogge von Strandmann et al., 2008; Pogge von Strandmann et al., 2012). Acid-cleaned PTFE columns (6 mm in diameter, 30 ml reservoir, PTFE frit) were loaded with pre-cleaned AG50W-X12 (Bio-RadTM) cation exchange resin, to a height of 8.5 cm in 0.8 M TD HNO₃. Due to problems with separation of the K and Mg peaks during elution from the column, a long wash-out of a weak acid (0.8 M TD HNO₃) was eluted and then discarded prior to collection of the Mg fraction. This was based upon *Kd* (distribution coefficients) values obtained for cations passed through AG50W-X8 (Bio-RadTM) cation exchange resin in different strengths of nitric acid (Strelow et al., 1965). With a weaker acid, the difference in *Kd* values between Mg and K is greatest, therefore a weaker acid was more efficient at achieving a better separation of Mg and K. The column procedure is as follows:

- 1. The columns were cleaned with 4 ml 6 M TD HCl and rinsed with 4 ml Milli-Q.
- 2. The columns were equilibrated with 4 ml 0.8 M TD HNO₃ and resin height was measured to check it was 8.5 cm.
- 3. Samples containing 2000 ng Mg were dissolved in 200 μl of 0.8 M TD HNO₃ and carefully loaded onto the columns.
- 4. The samples were washed in with 2 x 500 μl aliquots of 0.8 M TD HNO₃.
- 5. 50 ml of 0.8 M TD HNO₃ was discarded.
- 6. The Mg fraction was collected in 20 ml of 2 M TD HNO₃ in Savillex vials.
- 7. The Mg fraction was dried down on a hotplate at ~130 °C.
- 8. The columns were cleaned with 30 ml 6 M HCl and rinsed with 30 ml Milli-Q.
- 9. The columns were stored in 0.05 M TD HCl.

3.6.2 Mg Column Calibration

To ensure complete recovery of Mg and to minimise contamination of elements that cause isobaric interferences with Mg, several Mg column calibrations were carried out, until the Mg yield was near 100% and all other elements were <1% of the Mg concentration. Each column calibration used either BCR-2 (basaltic rock standard) or IAPSO (seawater) containing 1500 ng Mg.

The first column calibration was based upon methods used previously (e.g. Pogge von Strandmann et al., 2008; Pogge von Strandmann et al., 2012). In this method, 9 ml of 2 M TD HNO₃ was eluted and discarded, and then 11 ml 2 M TD HNO₃ was collected for the Mg fraction. The 20 ml of 2 M

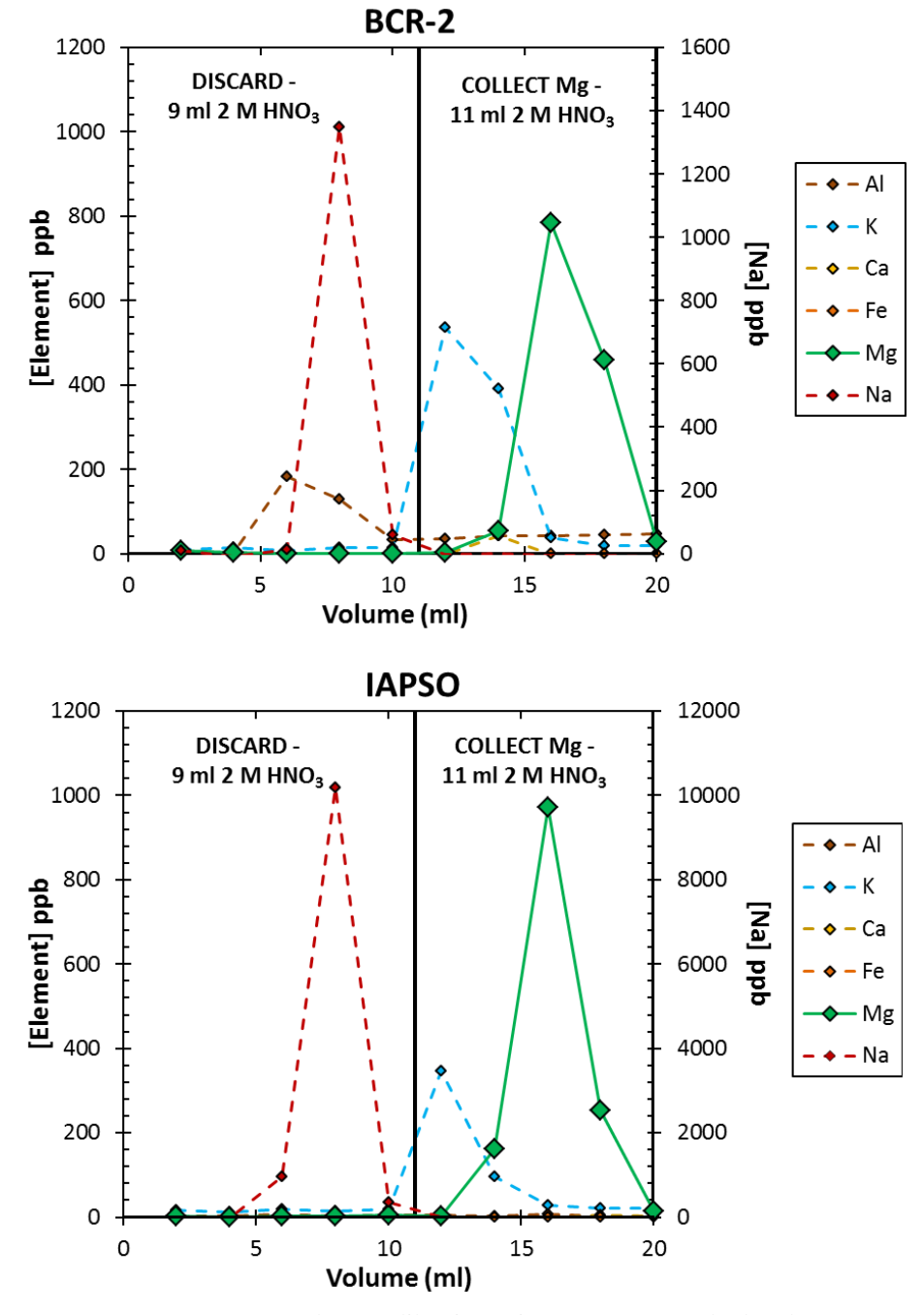


FIGURE 3.3: Mg column calibration using a BCR-2 standard and an IAPSO standard, with volume of acid eluted against element concentration.

TD HNO₃ eluted for this method was collected in 2 ml fractions (Figure 3.3). This method resulted in a crossover of the K and Mg peaks, which led to a significant amount of K contamination in the Mg fractions.

The second column calibration involved the elution of a much weaker acid to observe which elements were eluted. With a weaker acid, the difference in *Kd* values between Mg and K is greater, therefore a weaker acid would be more efficient at achieving a better separtion of Mg and K (Strelow et al., 1965). In this calibration, 40 ml 0.2 M TD HNO₃ was eluted and collected in 4 ml fractions. No element peaks were observed with this elution. This acid strength was too weak to successfully remove elements with isobaric interferences from the column prior to Mg collection.

The third column calibration involved the elution of a slightly stronger acid. 60 ml 0.4 M TD HNO₃ was eluted and collected in 4 ml fractions (Figure 3.4). A complete Na peak was collected, the K peak was completely collected but it is wide, and the Ti peak was not fully collected with this strength acid.

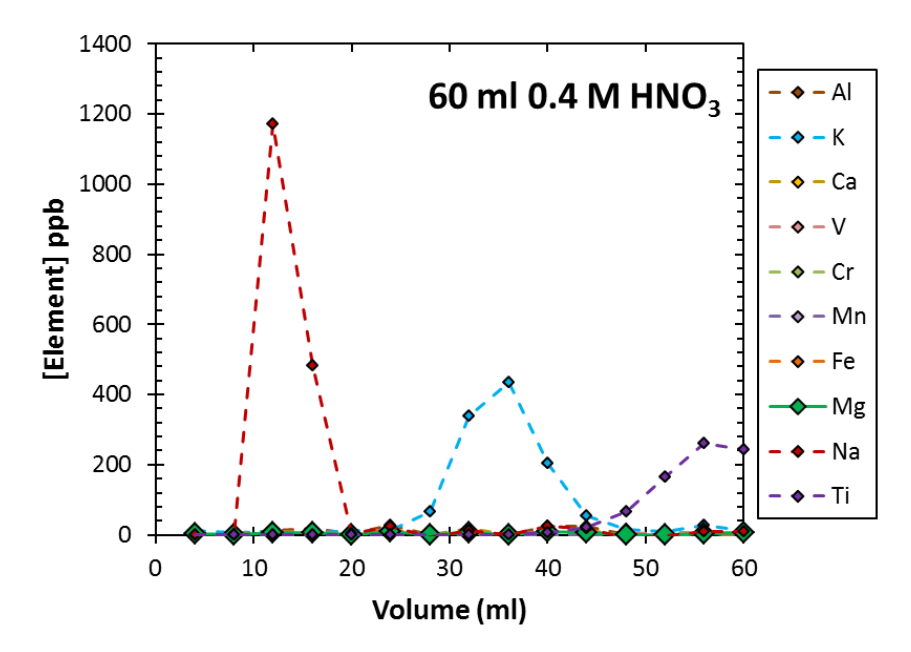


FIGURE 3.4: Mg column calibration using a BCR-2 standard, with volume of acid eluted against element concentration.

The fourth column calibration involved the elution of a stronger acid: 60 ml 0.8 M TD HNO₃ was eluted and collected in 4 ml fractions (Figure 3.5). A complete Na peak was collected, as were the Ti and K peaks, which have a much narrower collection at this acid strength. In addition, no Mg was eluted at this strength acid.

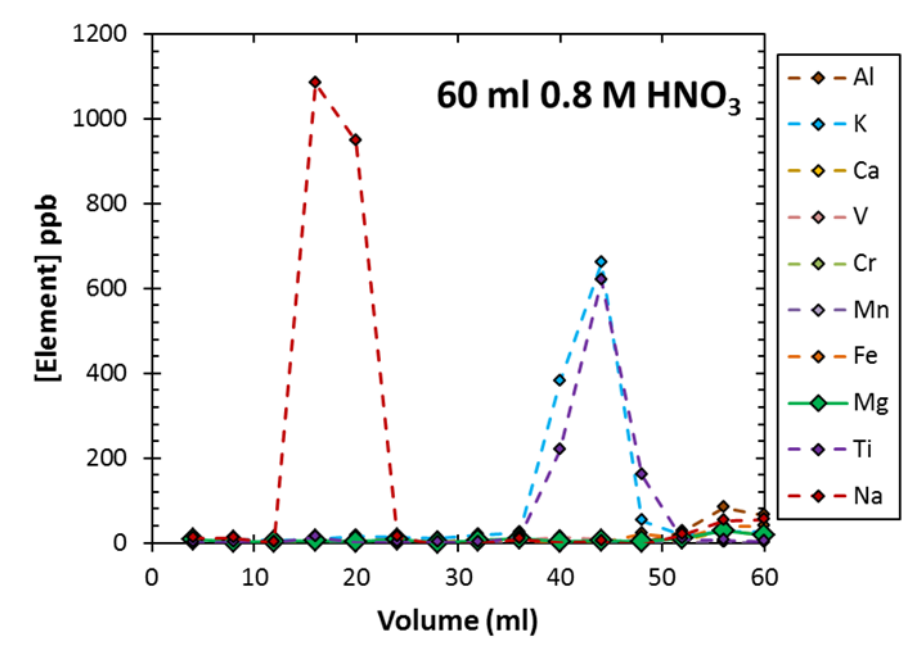


FIGURE 3.5: Mg column calibration using a BCR-2 standard, with volume of acid eluted against element concentration.

The final column calibration consisted of a 50 ml 0.8 M TD HNO₃ 'discard' (collected in 4 ml fractions) and a 20 ml 2 M TD HNO₃ 'Mg collection' (collected in 3 ml fractions). This method ensured a better separation of all other elements from the Mg collection, while ensuring complete recovery of Mg (Figure 3.6). To ensure a complete separation from all other elements (all elements <1% of the Mg concentration), a double column pass was carried out for each sample and standard.

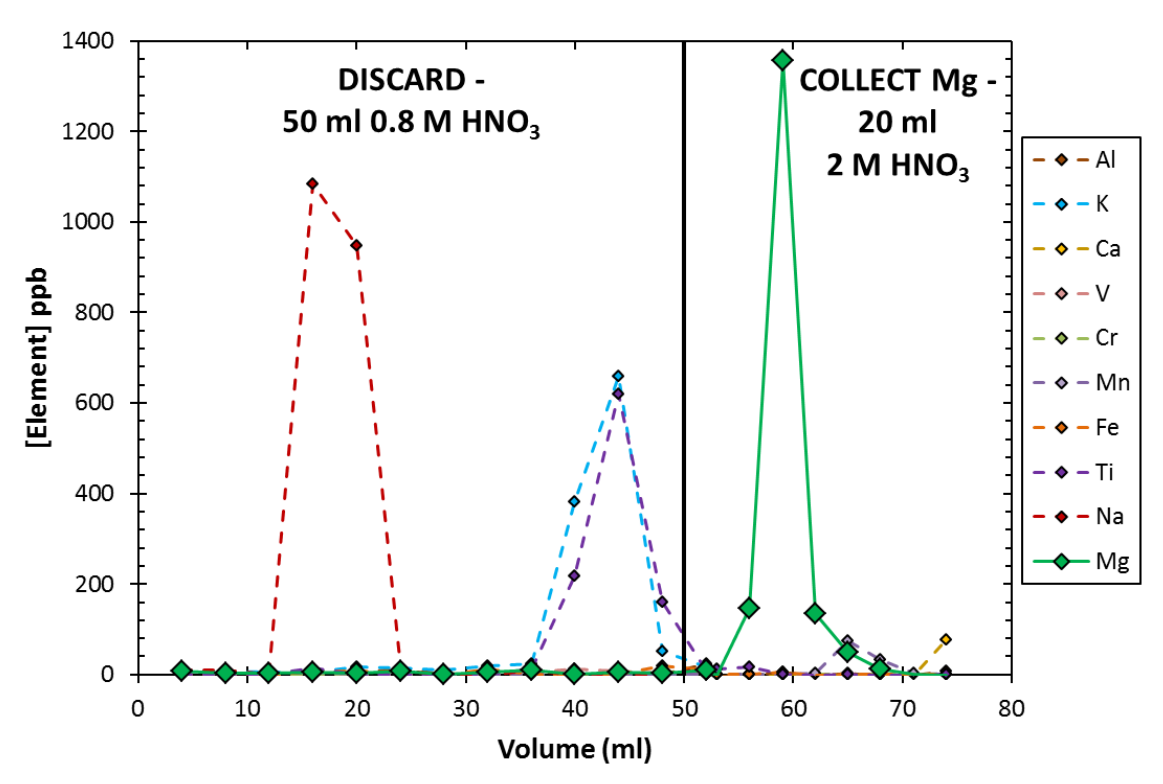


FIGURE 3.6: Mg column calibration using a BCR-2 standard, with volume of acid eluted against element concentration.

The columns achieved a Mg yield of $99 \pm 5\%$ and matrix elemental contributions did not exceed 1% (Table 3.5). The total Mg procedural blank associated with the column chemistry is <10 ng Mg, which represents <0.5% of the total Mg loaded onto the columns, and thus has a negligible effect upon the δ^{26} Mg value of samples.

TABLE 3.5: Matrix elemental contributions from the columns, shown as a percentage of the total Mg loaded onto the columns.

Matrix Element	% of Total Mg Concentration		
Na	0.62 ± 0.3		
Al	0.03 ± 0.0		
K	0.41 ± 0.1		
Ca	0.48 ± 0.2		
Ti	0.07 ± 0.0		
V	0.01 ± 0.0		
Cr	0.00 ± 0.0		
Mn	0.02 ± 0.0		
Fe	0.09 ± 0.1		
Rb	0.00 ± 0.0		
Sr	0.01 ± 0.0		

3.6.3 MC-ICP-MS Analysis of δ^{26} Mg

The magnesium isotopic ratio measurements were determined by multi-collector inductively-coupled plasma-source mass spectrometry (MC-ICP-MS; Thermo Scientific Neptune), at the National Oceanography Centre, Southampton. The Mg fractions, purified by cation exchange chromatography, were re-dissolved in 3 ml of 3% TD HNO₃, to produce a solution with a concentration of 600 ppb Mg. Evaporation significantly affects the Mg isotopic ratio, as shown in Figure 3.7). Therefore, large aliquots of 800 µl were taken from each sample for analysis, and

TABLE 3.6: Settings applied during Mg isotope analysis on the Neptune.

Parameter/Hardware	SIS Set-up	
Average Blank	<40	mV
Sample and Standard Concentration	600	ppb
Nebuliser Aspiration Rate	75	μLmin
Sample gas	~1	L/min
Integration time	8.389	seconds
Idle time	3	seconds
Extraction voltage	-2000	V
Wash solution	3% HNO ₃	
Wash time after sample	4	minutes
Wash time after blank	1	minutes
Cones	Н	Nickel

samples were not placed into autosampler vials until 5 minutes prior to their analysis to ensure minimal evaporation.

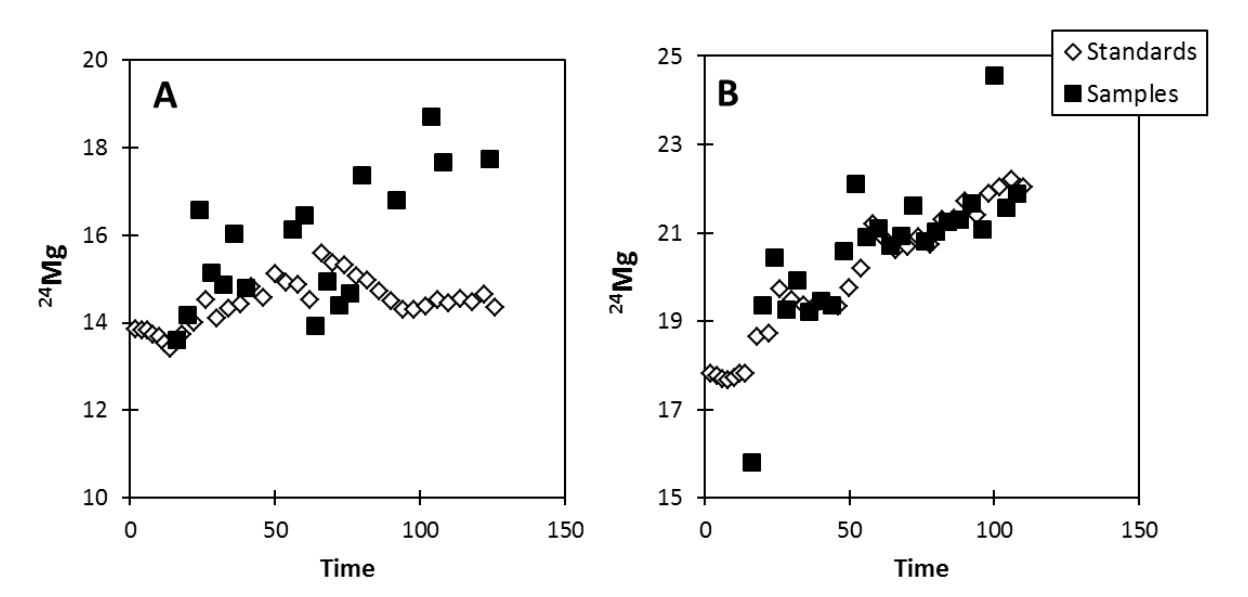


FIGURE 3.7: Experiments showing the effect of evaporation upon the magnesium isotopic ratio, using DSM-3 tuning solution. 'Samples' represent tuning solution analysed as samples and 'standards' represents the larger bottle of tuning solution (~20 ml). A) Samples were pipetted prior to the start of the run, and evaporation has resulted in significant excursion in ²⁴Mg from the tuning solution standard values. B) All samples and standards were pipetted prior to the start of the run. Consistent evaporation results in no significant excursion in ²⁴Mg values.

These samples were all tested for Mg concentration prior to analysis to ensure that sample Mg concentration was within 10% of the tuning solution Mg concentration, which minimises the potential influences of isobaric interferences. The isobaric interferences that can affect the Mg mass spectrum include ⁴⁸Ti²⁺, ⁵⁰Ti²⁺, ⁴⁸Ca²⁺, ⁵⁰Cr²⁺, ⁵²Cr²⁺ and CN⁺. The effects of nitrogen are rendered negligible by avoiding N₂ gas during analysis (Young and Galy, 2004). The effects of other elements are removed by analysing pure Mg solutions (see Section 3.6.2).

The samples were analysed using a sample-standard bracketing technique (Albarède and Beard, 2004), whereby the mass bias is determined from analysis of the ²⁶Mg/²⁴Mg ratio measured on the DSM-3 tuning solution, which is analysed before and after each sample. The ²⁶Mg and ²⁴Mg intensity of the 3% TD HNO₃ blank solution was determined prior to analysis of each sample and standard, and then subtracted. If the ²⁴Mg intensity of the blank solution became higher than 100 mV, then the analytical run was stopped and the cones were cleaned. This typically reduced the blank ²⁴Mg intensity to 20-40 mV. All samples were analysed using a ThermoFinnigan stable introduction system (SIS). Typical parameters for Mg isotopic analyses are shown in Table 3.6.

The combined uncertainty on the $^{26}\text{Mg}/^{24}\text{Mg}$ ratio of the two bracketing standards (u_{DSM1} and u_{DSM2}) is:

$$u_{DSM} = \frac{\sqrt{(u_{DSM1})^2 + (u_{DSM2})^2}}{2}$$
 (Eq. 3.4)

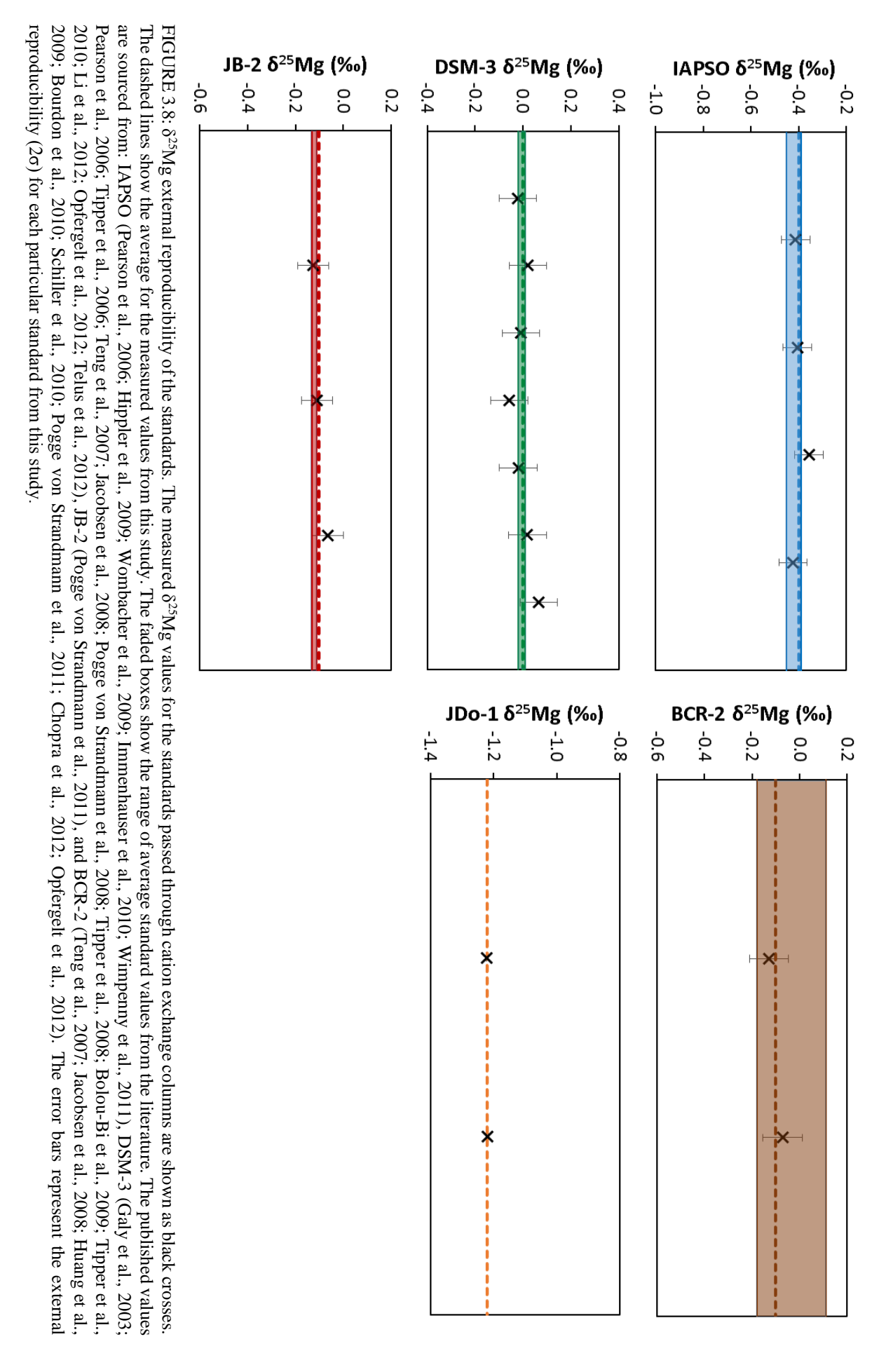
The combined uncertainty on the δ^{26} Mg of the sample is:

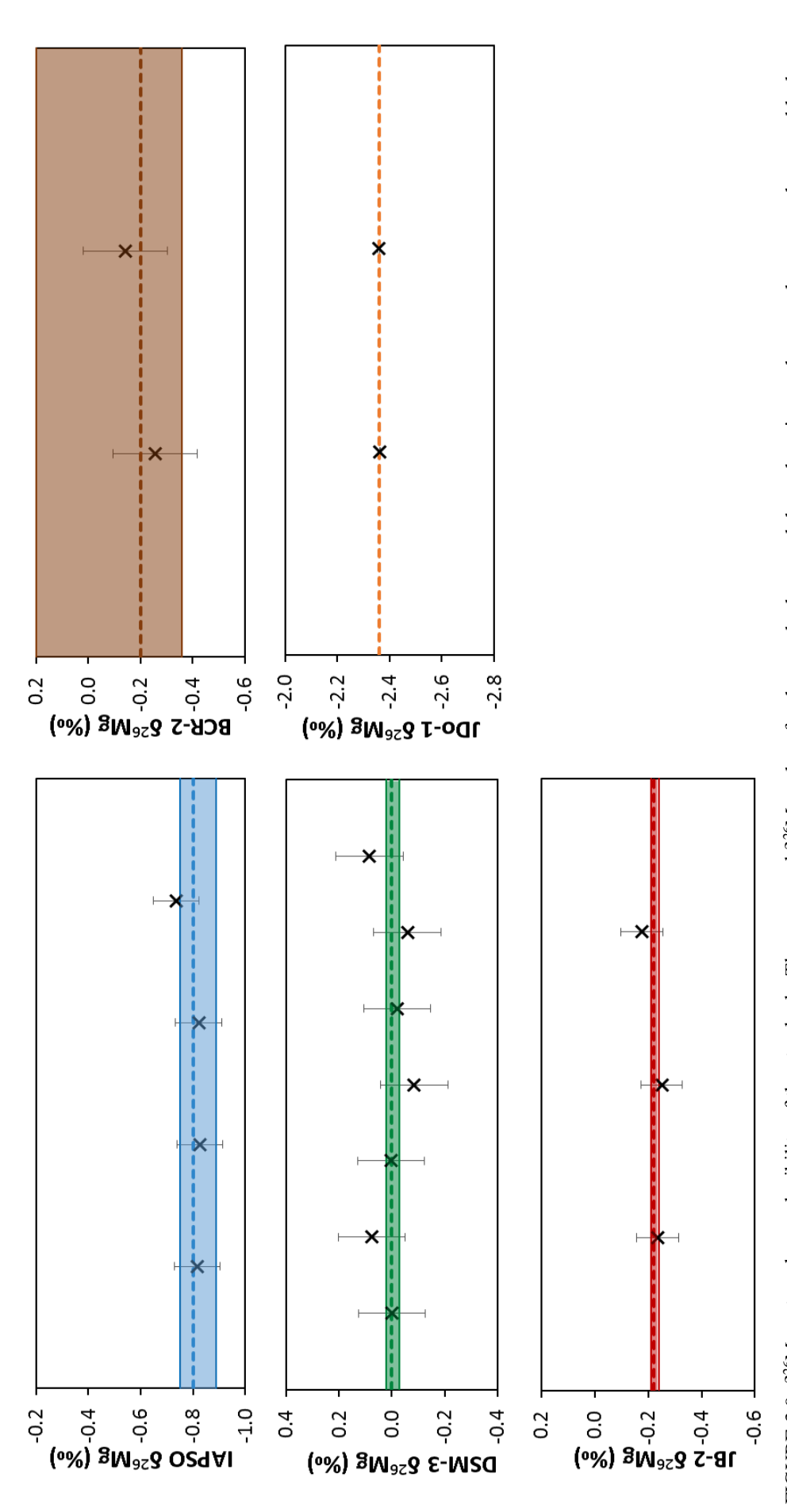
$$u_{\text{combined}} = \frac{x_{\text{Mg}/^{24}\text{Mg}_{\text{SAMPLE}}}}{x_{\text{Mg}/^{24}\text{Mg}_{\text{DSM}}}} \times \sqrt{\left(\frac{u_{\text{SAMPLE}}}{x_{\text{Mg}/^{24}\text{Mg}_{\text{SAMPLE}}}}\right)^2 + \left(\frac{u_{\text{DSM}}}{x_{\text{Mg}/^{24}\text{Mg}_{\text{DSM}}}}\right)^2}$$
(Eq. 3.5)

Where X refers to either 25 or 26 and $u_{combined}$ is the internal reproducibility of the $\delta^{25}Mg$ or $\delta^{26}Mg$ value. The typical internal reproducibility of the $\delta^{26}Mg$ measurements was better than 0.06‰, and better than 0.05‰ for the $\delta^{25}Mg$ measurements. To verify that no Mg isotopic fractionation occurred during column chemistry and to access the external reproducibility of the $\delta^{25}Mg$ and $\delta^{26}Mg$ values of samples subject to column chemistry, DSM-3 (a pure Mg standard), IAPSO (a seawater standard), JB-2 and BCR-2 (basaltic rock standards) and JDo-1 (a dolomite rock standard) were also passed through the cation exchange columns and analysed within each instrument run. These $\delta^{25}Mg$ and $\delta^{26}Mg$ values are within range of previously published data for these standards (Table 3.7 and Figures 3.8 and 3.9).

TABLE 3.7: The average δ^{25} Mg and δ^{26} Mg values of the standards analysed within the instrumental analyses, and external reproducibility (2 σ).

Standard	δ^{25} Mg (‰)	2σ	δ ²⁶ Mg (‰)	2σ	n
IAPSO	-0.40	0.06	-0.80	0.09	7
DSM-3	0.00	0.08	0.00	0.13	4
JB-2	-0.10	0.07	-0.22	0.08	3
BCR-2	-0.10	0.08	-0.20	0.16	2
JDo-1	-1.30	0.00	-2.36	0.01	2





The dashed lines show the average for the measured values from this study. The faded boxes show the range of average standard values from the literature. The published values FIGURE 3.9: δ^{26} Mg external reproducibility of the standards. The measured δ^{26} Mg values for the standards passed through cation exchange columns are shown as black crosses. are sourced from: IAPSO (Chang et al., 2003; Young and Galy, 2004; Pearson et al., 2006; Tipper et al., 2006; Pogge von Strandmann et al., 2008; Wombacher et al., 2009; Immenhauser et al., 2010; Wimpenny et al., 2011; Choi et al., 2012; Pogge von Strandmann et al., 2012; Lee et al., 2014), DSM-3 (Galy et al., 2003; Pearson et al., 2006; Tipper et al., 2006; Teng et al., 2007; Jacobsen et al., 2008; Pogge von Strandmann et al., 2008; Tipper et al., 2008; Bolou-Bi et al., 2009; Tipper et al., 2010; Choi et al., 2012; Li et al., 2012; Opfergelt et al., 2012; Telus et al., 2012), JB-2 (Pogge von Strandmann et al., 2008; Pogge von Strandmann et al., 2011), and BCR-2 (Teng et al., 2007; Jacobsen et al., Huang et al., 2009; Bourdon et al., 2010; Schiller et al., 2010; Huang et al., 2011; Pogge von Strandmann et al., 2011; Choi et al., 2012; Chopra et al., 2012; Opfergelt et al., 2012; Pogge von Strandmann et al., 2012). The error bars represent the external reproducibility (20) for each particular standard from this study

Chemical Composition of Bedrock and its Weathering Products in the Southern Alps, New Zealand

4.1 Introduction

The Southern Alps on South Island, New Zealand, are a relatively pristine environment, which makes them an ideal study area to examine the processes that regulate continental weathering. They are composed of metamorphosed silicate rocks and are relatively monolithological (Mackinnon, 1983). The South Island has been subject to rapid uplift and exhumation of high grade metamorphic rocks adjacent to the Alpine Fault, and a gradation from high grade metamorphic rocks in the west to lower grade rocks in the east is observed (Norris et al., 1990; Grapes and Watanabe, 1992; Grapes, 1995; Cox and Sutherland, 2007). The structure of this orogen has led to differing patterns of climate and erosion to the east and west of the Main Divide (the highest point along the mountain chain): 1) the asymmetry of the orogen has resulted in high rainfall to the west and lower rainfall to the east (Griffiths and McSaveney, 1983; Henderson and Thompson, 1999), 2) the high elevation of this mountain belt has led to the formation of glaciers along the Main Divide (Chinn, 2001), 3) uplift rates are much higher in the west than in the east (Bull and Cooper, 1986; Norris and Cooper, 2000), and 4) landslides are more frequent in the west where rapid uplift has led to increased bedrock weakening by faulting (Whitehouse and Griffiths, 1983; Cox and Findlay, 1995; McSaveney, 2002; Korup, 2004). These factors have led to a high erosion rate in the west and a lower erosion rate in the east (Jacobson and Blum, 2003).

To examine the continental weathering system of the Southern Alps, the chemical composition of the bedrock, and its weathering products (river waters, groundwaters, river sands and suspended particulate material), has been determined. Samples were collected both to the east and west of the Main Divide; sample localities are shown on Figure 4.1.

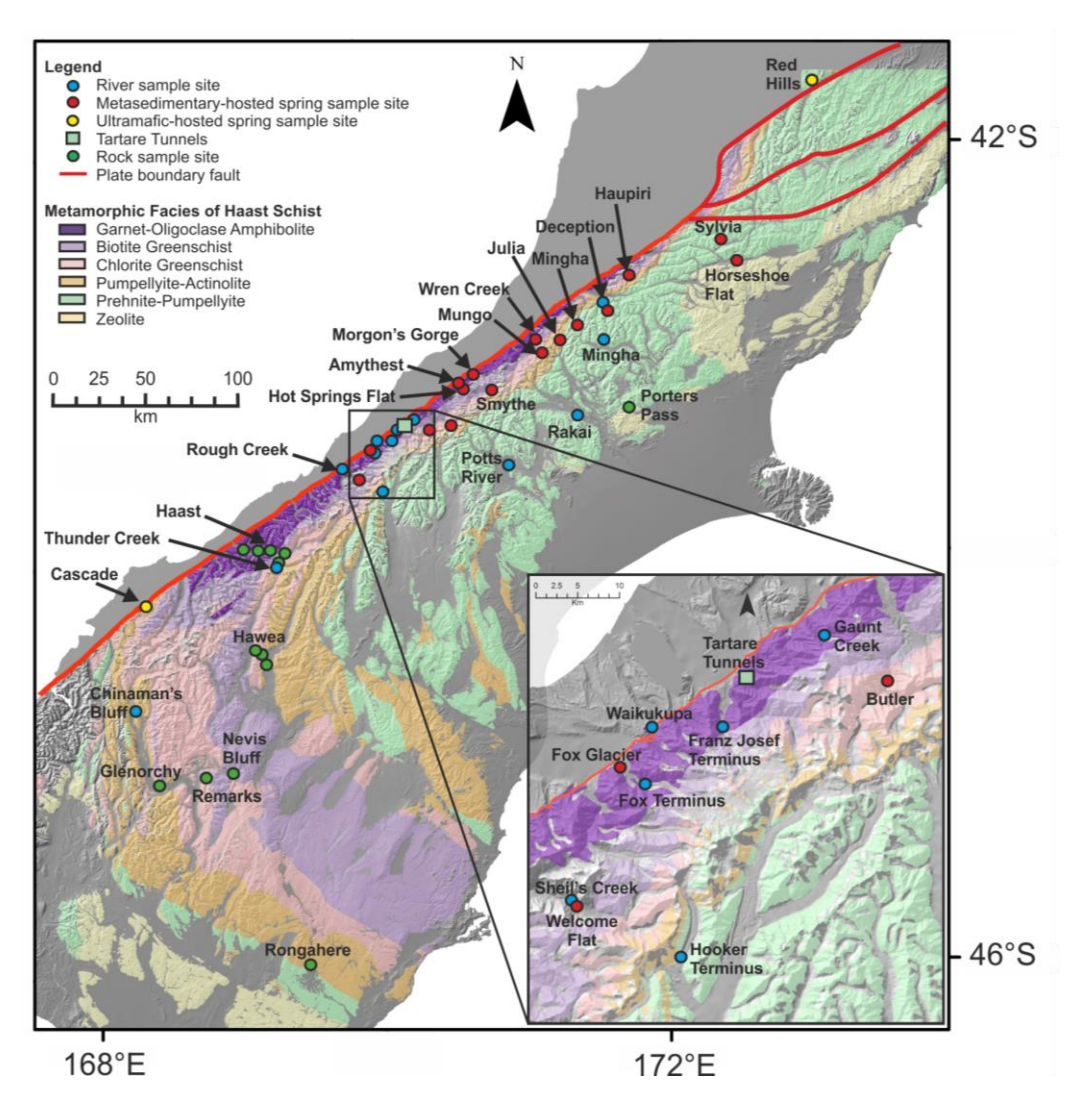


FIGURE 4.1: Locations of samples analysed in this study. Also shown is the metamorphic grade of the underlying bedrock. GIS data from Simon Cox (Cox and Rattenbury, 2006).

4.2 Analytical Methods

The chemical compositions of the river water, groundwater, rainwater and spring water fluids are reported in Menzies (2012), and trace element analyses of the bedrock samples are reported in Pitcairn (2004).

Full details of analyses of the chemical composition of riverine suspended particulate material, river sands, and mineral separates, conducted as part of this study, can be found in Chapter 3. Briefly, suspended particulate material was removed from the filters by ultrasonicating with Milli-Q water,

in pre-weighed Teflon vials for 2 hours, or longer if material remained on the filters. Once all material had been removed, the mixture was dried on a hotplate and the mass of the particles was determined. The particles were then dissolved in a mixture of HNO₃-HF-HCl. The uncertainty in the mass of the dried particles is ± 0.0005 g, which means that the uncertainty in the elemental concentration of the samples may be $\pm 10\%$. River sand samples were sieved and separated into 3 size fractions: <2 mm (the 'bulk' fraction), <125 μ m (the 'fine' fraction), and < 2 μ m (the 'clay' fraction). Note that no disaggregating agent was used to separate the clay fraction, as this would contaminate the analysis of trace elements. This means that the clay fraction may include small quantities of fine rock material, including glacial 'flour', where present. The river sands were also dissolved in a mixture of HNO₃-HF-HCl.

Finally, as concentrations of Li and Mg are known to be relatively high in micas, and micas are abundant minerals in Southern Alps bedrock, a number of different mica minerals were picked to a high degree of purity from crushed bedrock samples. The mica mineral separates were also dissolved in a mixture of HNO₃-HF-HCl.

The chemical composition of the resultant solutions was determined by inductively coupled plasma mass spectrometry (Thermo X-Series ICP-MS) at the National Oceanography Centre, Southampton. The reproducibility of the analyses was on average $\langle \pm 1.7\% \rangle$ for all elements, and the measured concentrations of a certified standard reference material (JA-2) were on average within $\pm 4.0\%$ of the certified values (Table 3.1 and Table 3.2).

4.3 Results

4.3.1 River Waters and Rain Water

The abundance of cations and anions in the sample of rain water from the west coast is very low; this sample was collected during a storm, which may mean that it is atypically dilute (Table B.1 in Appendix B; Menzies, 2012). Rainwater collected to the east of the Main Divide has far higher concentrations of cations and anions, and it has a much higher proportion of sodium and potassium (Table B.1 in Appendix B; Figure 4.2A; Jacobsen et al., 2003).

As the chemical composition of river waters reflects both atmospheric and weathering inputs, the atmospheric input must be removed to evaluate the effects of weathering. As the rain water sample collected from the west coast was extremely dilute, and concentrations of many elements were below detection limit (Menzies, 2012), the atmospheric input to the west coast rivers is assumed to be derived from seawater (as westerly prevailing winds are onshore; Williams et al., 2005), and a correction is applied as follows (Berner and Berner, 2012):

$$[M]_{corrected} = [Cl]_{measured} X \left(\frac{[M]_{seawater}}{[Cl]_{conveter}}\right)$$
 (Eq. 4.1)

Where $[M]_{corrected}$ is the river water concentration of chemical species M corrected for atmospheric input, $[Cl]_{measured}$ is the concentration of Cl measured in the river water sample, and $[M]_{seawater}$ and $[Cl]_{seawater}$ are the concentrations of M and Cl in seawater, taken from (Millero, 2006). Applying this correction indicates that the overall atmospheric contribution to river waters west of the Main Divide is 10-33% for Si (average = 15%), 19-47% for Na⁺ (average = 27%), 0.2-1.1% for Ca²⁺ (average = 0.5%), 4.9-17% for Mg²⁺ (average = 11%), 11-56% for SO₄²⁻ (average = 29%) and 1.3-16% for K⁺ (average = 5.4%), which is in good agreement with previous work in the Southern Alps (Jacobson et al., 2003).

As rainwater collected to the east of the Main Divide contains non-negligible concentrations of dissolved salts, the atmospheric contribution to the river waters is corrected as follows (Stallard and Edmond, 1981; Jacobson et al., 2003):

$$[M]_{corrected} = [Cl]_{measured} X \left(\frac{[M]_{rainwater}}{[Cl]_{rainwater}}\right)$$
 (Eq. 4.2)

Applying this correction shows that the overall atmospheric contribution to river waters east of the Main Divide is 6.8-22% for Si (average = 13%), 14-55% for Na⁺ (average = 36%), 2.4-4.9% for Ca²⁺ (average = 3.6%) and 3.8-13% for Mg²⁺ (average = 9.6%), which is in good agreement with previous work in the Southern Alps (Jacobson et al., 2003). The corrected river water values are given in Table B.1 in Appendix B. The concentration of SO_4^{2-} and K^+ in the rain waters collected by Jacobsen et al. (2003) were higher than those of some of the rivers from this study. Therefore, it was not possible to apply a correction for rainwater input for these ions for the rivers to the east of the Main Divide.

The total dissolved solids (TDS) are calculated from the measured concentrations of the major elements in the river waters as follows:

TDS (mg/L) =
$$SiO_2 + HCO_3^- + Cl^- + SO_4^{2-} + Na^+ + Ca^{2+} + Mg^{2+} + K^+$$
 (Eq. 4.3)

TDS in the non-glacial rivers draining the Southern Alps show a broader range (29-86 mg/L) than the glacial rivers (28-55 mg/L). These values are low compared to North American, European, African and Asian rivers, but within range of South American rivers (Table 4.1). The glacial river water temperatures are low and range from 0.3-5.0 °C and the pH is generally high (8.7-9.8). The non-glacial river water temperatures are more variable and range from 8.6-19.6 °C, and pH ranges from near neutral to slightly alkaline (7.5-8.6). Little difference in temperature, pH or TDS is observed between river waters to the east and west of the Main Divide.

Locality	TDS (mg/L)	References
Global Rivers		
North Americas Average	301	1,2
South American Average	60	1,4,5
European Average	207	1,3
African Average	102	1,6
Asian Average	183	1,7,8,9,10,11
Southern Alps		
Non-glacial Rivers	29-86	This study
Glacial Rivers	28-55	This study

TABLE 4.1: Total dissolved solids (TDS) of river waters draining the Southern Alps compared to global rivers. Global river data from: ⁽¹⁾(Martin and Meybeck, 1979), ⁽²⁾(Livingstone, 1963), ⁽³⁾(Zobrist and Stumm, 1981), ⁽⁴⁾(Stallard, 1980), ⁽⁵⁾(Meybeck, 1980), ⁽⁶⁾(Probst et al., 1992), ⁽⁷⁾(Sarin et al., 1989), ⁽⁸⁾(Zhang et al., 1990), ⁽⁹⁾(Gaillardet et al., 1999a), ⁽¹⁰⁾(Gordeev and Siderov, 1993), ⁽¹¹⁾(Telang et al., 1991).

On an average molar basis, Ca^{2+} is the most abundant major cation in the river waters (73%), followed by Na^{+} (12%), K^{+} (9.1%) and Mg^{2+} (5.9%) (Menzies, 2012). The chemical composition of the river waters sampled in this study is similar to that reported by Jacobsen et al. (2003). Although the rivers drain predominantly silicate catchments, their chemistry is similar to the average composition of rivers that drain predominantly carbonate bedrock, as they have a large proportion of calcium (Figure 4.2A). HCO_3^{-} is the most abundant anion in the river waters (72%), followed by SO_4^{2-} (20%), CI^{-} (8.3%) and F^{-} (0.25%) (Figure 4.2B; Menzies, 2012).

4.3.2 Groundwaters (Tartare Tunnels)

Groundwater samples were collected from the Tartare Tunnels, which were cut through the hangingwall schist of the Alpine Fault, near Franz Josef, in the early 20th Century as part of an alluvial mining operation (Menzies, 2012). The Tartare Tunnels cut through quartzofeldspathics (Amphibolite Facies) and metavolcanics (garnet zone Greenschist Facies). The fluids infiltrate at low temperature to reach fractures in the roof of the tunnels, and the fluid flow from these fractures is higher during rain storms (Menzies, 2012). The groundwater samples were collected at increasing distances from the tunnel entrance to observe any variation there might be deeper into the tunnel.

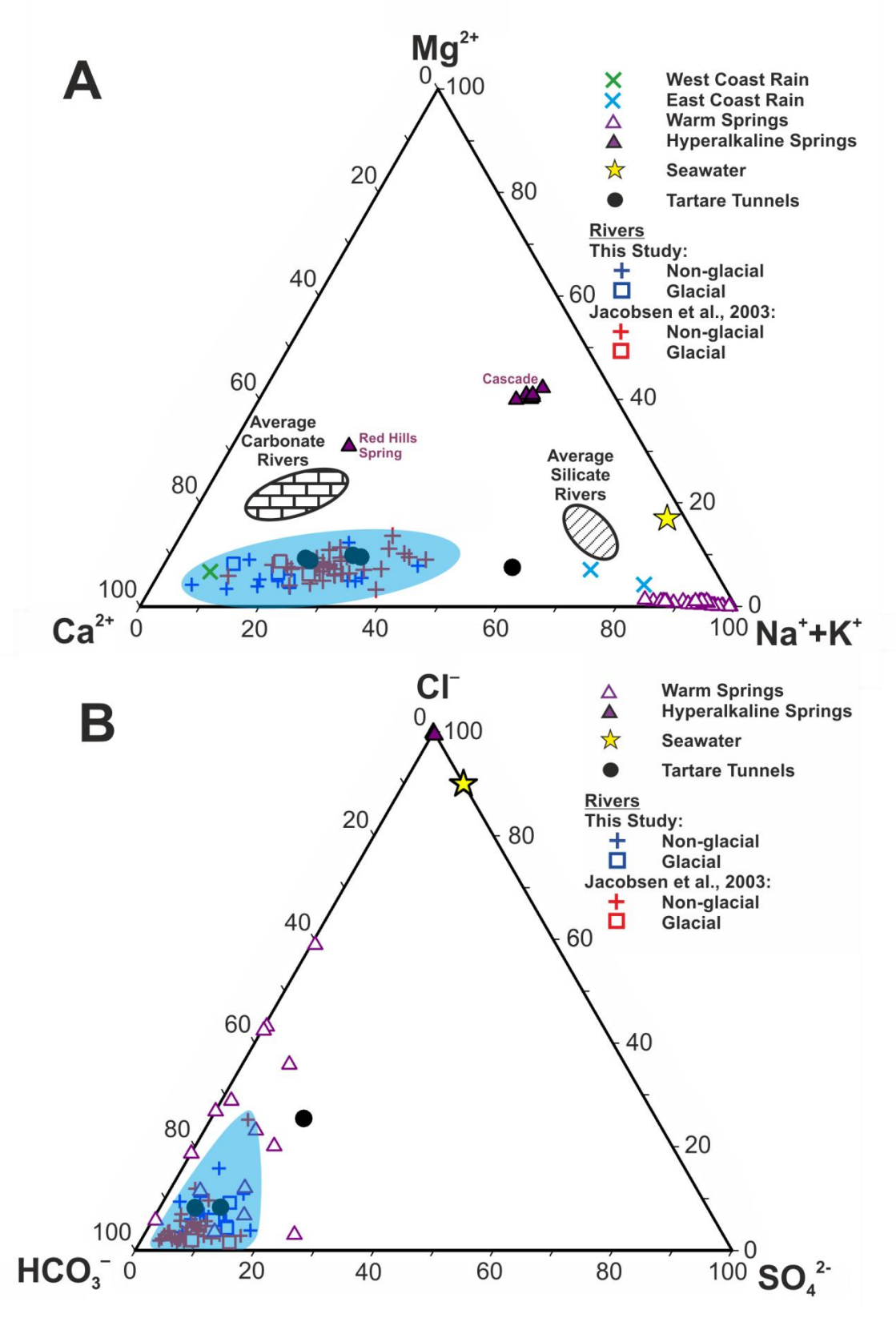


FIGURE 4.2: Ternary diagrams showing: (A) major cation composition and (B) major anion composition, of surface fluids from the Southern Alps. Also shown are: global average of silicate rivers (Meybeck, 1987; Gislason et al., 1996; Gaillardet et al., 1999a); global average of carbonate rivers (Galy and France-Lanord, 1999; Chen et al., 2002; Han and Liu, 2004); seawater and east coast rain water (Jacobson et al., 2003). The river waters draining the Southern Alps from this study have been corrected for atmospheric inputs.

Temperatures of the Tartare Tunnels fluids range from 10.0-11.5 °C and pH ranges from 6.8-7.9 (Table B.1 in Appendix B). On an average molar basis, Ca²⁺ is the most abundant cation in the Tartare Tunnels waters (54%), followed by K⁺ (20%), Na⁺ (19%) and Mg²⁺ (8.2%) (Figure 4.2A; Menzies, 2012). HCO₃⁻ is the most abundant anion (75%), followed by SO₄²⁻ (28%), Cl⁻ (26%) and F⁻ (0.83%) (Figure 4.2B; Menzies, 2012). The average sulphate concentration in the Tartare tunnels (64.8 μmol/L) is similar to river waters (44.0 μmol/L), as is total alkalinity (river waters average 434 μmol/L and Tartare Tunnels fluids average 485 μmol/L), except for the groundwater sample collected at 94 m along the tunnel (123 μmol/L) (Table B.1 in Appendix B). Concentrations of Cl⁻, Na⁺, Ca²⁺, Mg²⁺, Si, K⁺, Li, Ba, Y and most rare earth elements (REEs) are up to 2 times higher in the Tartare Tunnels fluids than the river waters, except for the fluids collected at 94 m into the tunnel, which have lower concentrations of Ca²⁺ and Li than the river waters (Table B.1 in Appendix B). By contrast, concentrations of Al and Mn are >5 times higher and Fe and Rb are > 2 times higher in the river waters.

4.3.3 Warm Springs

The majority of the springs analysed from the Southern Alps are hosted within metasediments, ranging from unmetamorphosed greywackes to high-grade garnet oligoclase amphibolites. Spring water temperatures range from 20.3-60.0 °C, conductivity ranges from 0.0-2.1 S/m and the fluids have pH values of 5.8-9.5 (Table B.2 in Appendix B).

The chemical composition of the spring waters varies considerably. The springs are highly concentrated in most elements compared to the river waters of the Southern Alps; the average TDS of the spring waters (14400 mg/L) is >100 times higher than the river water average (46 mg/L). Compared to river waters, elemental concentrations in the spring waters are >100 times higher in Na and Li, ~100 times higher in Cl⁻, >10 times higher in F⁻, Si, K, HCO₃⁻ and Fe, ~3 times higher in Ca, and ~2 times higher in Mg. Al concentrations are similar for river waters and spring waters (Table B.2 in Appendix B). Spring water SO_4^{2-} concentration is highly variable, with values that range from 8.44 µmol/L (~5 times lower than average river water) to 939 µmol/L (~20 times higher than average river water). On an average molar basis, Na⁺ is the most abundant major cation in metasedimenthosted spring waters (91%), followed by $Ca^{2+}(5.7\%)$, $K^+(2.6\%)$ and $Mg^{2+}(0.5\%)$ (Figure 4.2A), and HCO_3^- is the most abundant anion (57%), followed by $Cl^-(32\%)$, $SO_4^{2-}(7.8\%)$ and $F^-(3.3\%)$ (Figure 4.2B; Menzies, 2012).

The Permian Dun Mountain Ophiolite Belt has been separated by ~460 km of strike-slip movement on the Alpine Fault (Norris et al., 1990; Sutherland, 1996), and springs hosted in these areas have interacted with peridotites (Red Hills in the north and Cascade in the south). These spring waters are hyperalkaline, and absorb atmospheric CO₂ and precipitate calcite on emergence at the surface

(Menzies, 2012). The hyperalkaline spring water temperatures range from 10.6-17.1 °C, conductivity ranges from 0.2-0.6 S/m and the fluids have high pH (9.7-11.8; Table B.2 in Appendix B).

The hyperalkaline springs are more dilute than the metasedimentary-hosted springs (average TDS = 2220 mg/L). Compared to river waters, elemental concentrations in the hyperalkaline springs are >10 times higher in Cl⁻ and Na, ~5 times higher in Li, ~3 times higher in Mg and Fe, and ~2 times higher in Ca (Table B.2 in Appendix B). K concentrations in the hyperalkaline springs are similar to those of the river waters. The peridotite-hosted springs have no HCO_3^- until they absorb it from the atmosphere, as these waters are highly undersaturated in CO_2 and so rapidly absorb it on exposure at the surface, precipitating calcite; alkalinity is instead made up OH^- (Menzies, 2012). Although the hyperalkaline springs are enriched in some elements, relative to the rivers, SO_4^{2-} and Al are >10 times lower, and Si is ~3 lower in the spring waters. Na⁺ is the most abundant major cation (56%), followed by Ca^{2+} (37%), Mg^{2+} (5.1%) and K^+ (1.4%) (Figure 4.2A), and Cl^- is the most abundant anion (>99%), followed by SO_4^{2-} (0.3%), HCO_3^- (0.1%) and F^- (0.1%) (Figure 4.2B; Menzies, 2012).

4.3.4 Bedrock

The bedrock samples encompass a range of lithologies (metasediments and metavolcanics), and varying degrees of metamorphism (from unmetamorphosed greywackes to garnet-oligoclase amphibolites) with metamorphic temperatures that range from 0-600 °C (Mortimer, 1993; Mortimer, 2000; Pitcairn, 2004). After SiO₂ (65%), Al₂O₃ (16%) is most abundant in the metasediments, followed by Fe₂O₃ (5.3%), Na₂O (4.2%), K₂O (2.8%), CaO (1.9%), MgO (1.6%), TiO₂ (0.7%), P₂O₅ (0.1%) and MnO (>0.1%) (Pitcairn, 2004; Table B.7 in Appendix B). In metabasalts, the most abundant element is SiO₂ (48%), followed by Fe₂O₃ (13%), Al₂O₃ (12%), MgO (7.8%), CaO (6.8%), TiO₂ (3.4%), K₂O (1.6%), Na₂O (1.3%), P₂O₅ (0.63%) and MnO (0.20%) (Pitcairn, 2004; Table B.7 in Appendix B). The metabasalts from the Southern Alps have lower proportions of SiO₂, Al₂O₃, K₂O and Na₂O than the metasediments, but have higher proportions of all other major metal oxides. Li concentration in the bedrock ranges from 22-92 ppm, with an average of ~47 ppm (Table B.3 in Appendix B).

4.3.5 Mica Mineral Separates

Biotite, chlorite and muscovite micas were picked from bedrock samples to a high degree of purity. Compared to the bedrock, the mica mineral separates have higher proportions of Al₂O₃ (21-29 Wt. % higher), Fe₂O₃ (37-56 Wt. % higher, except for muscovite), K₂O (~18 Wt. % higher, except for chlorite) and MgO (~6 Wt. % higher, except for muscovite) (Table B.7 in Appendix B). CaO and Na₂O are ~2-4 Wt. % lower in the mica mineral separates compared to the bedrock (Figure 4.3). The

Li concentration of the mica mineral separates ([Li] = \sim 210 ppm) is more than 4 times that of the bedrock ([Li] = \sim 47 ppm), except for muscovite which has a Li concentration of 69 ppm (Table B.4 in Appendix B).

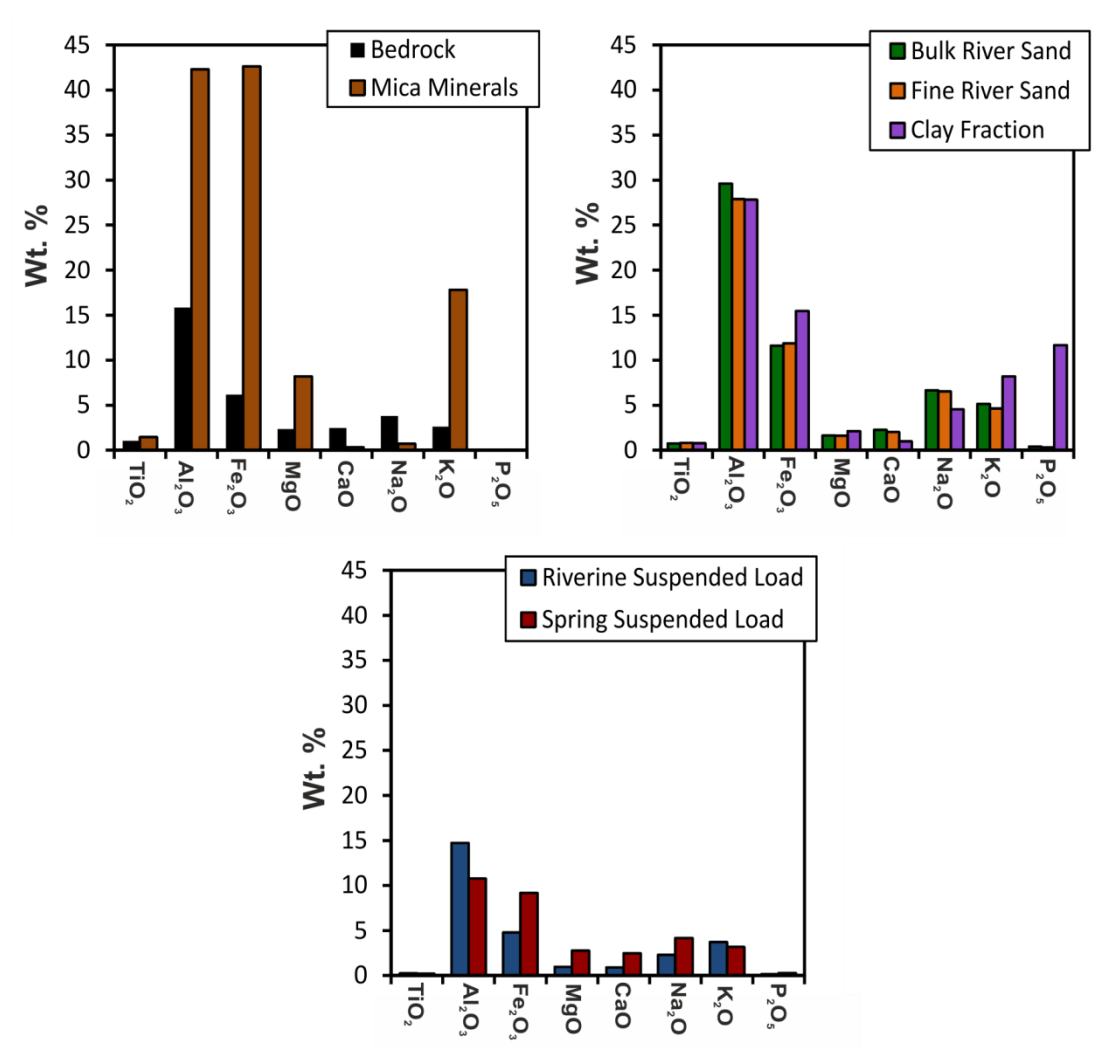


FIGURE 4.3: Bar charts showing the average major element concentrations (Wt. %) for the bedrock, mica mineral separates, river sand size fractions, and river and spring suspended particles.

4.3.6 River Sands

The river sands were sieved to different size fractions, and a bulk sub-sample (<2 mm), a fine sand fraction (<125 µm) and a clay fraction (<2 µm) were analysed from each sample. The bulk river sand and fine river sand size fractions have near identical chemical compositions, which are similar to the bedrock, although the river sands have around twice as much Al_2O_3 and ~5 Wt. % more Fe_2O_3 (Table B.7 in Appendix B). Compared to the bulk and fine river sand, the clay fractions of the river sand samples generally have ~4 Wt.% more Fe_2O_3 and K_2O_3 and K_2O_4 Wt. % more P_2O_5 , ~1 Wt. % more MgO, and $\sim1-2$ Wt. % less CaO and Na_2O_4 (Figure 4.3; Table B.7 in Appendix B). There is less Li in the bulk and fine river sand size fractions ([Li] = ~40 ppm) than the bedrock ([Li] = ~47 ppm), but

there is more Li in the clay fraction ([Li] = \sim 78 ppm; Table B.5 in Appendix B). It is important to note that no disaggregate was added during the clay separation procedure (as this would have contaminated the sample), therefore the clay fraction may also include fine rock material.

4.3.7 Riverine Suspended Load

The riverine suspended load is similar in chemical composition to the bedrock (Figure 4.3), although TiO_2 , Al_2O_3 , MgO, CaO and Na_2O are lower by ~1 Wt. %, Fe_2O_3 is lower by ~2 Wt. %, and K_2O is higher by ~1 Wt. % in the suspended sediments (Figure 4.3; Table B.7 in Appendix B). The Li concentration in the suspended load is generally around half ([Li] = ~25 ppm) of that of the bedrock ([Li] = ~47 ppm; Table B.6 in Appendix B).

4.3.8 Spring Suspended Load

The suspended load of the spring waters is similar in chemical composition to the bedrock (Figure 4.3), although Al_2O_3 is lower by ~5 Wt. % and Fe_2O_3 is higher by ~3 Wt. % in the suspended sediments. Compared to the riverine suspended sediments, the spring suspended sediments are ~2 Wt. % higher in MgO, CaO and Na₂O, ~5 Wt. % higher in Fe_2O_3 , and ~4 Wt. % lower in Al_2O_3 (Figure 4.3; Table B.7 in Appendix B). The Li concentration of the spring suspended load varies significantly between metasedimentary-hosted ([Li] = ~75 ppm) and peridotite-hosted ([Li] = ~1.6 ppm) springs (Table B.6 in Appendix B).

4.4 Discussion

4.4.1 Spring Water Input to River Waters

Across the Southern Alps, warm springs can be found issuing at varying flow rates, generally near to the Alpine Fault or other faults, and in deeply incised valleys (Barnes et al., 1978). The springs are thought to be meteoric in origin, as δD and $\delta^{18}O$ values of the warm springs lie on the meteoric water line (Menzies et al., 2014). There is no magmatic activity occurring in the Southern Alps, therefore the springs are heated by the elevated upper (2-3 km) crustal geothermal gradient (60-150 °C/km; Sutherland et al., 2012; DFDP-2 unpublished data), caused by rapid uplift of crustal material along the Alpine Fault. Hydrothermal inputs have been shown to be an important contributor to stream chemistry in other tectonic environments, such as the Himalaya (Evans et al., 2001). However, flow rates of the springs in the Southern Alps are estimated to be fairly low, on the order of ~3 L/min

(Reyes et al., 2010). The contribution of the springs to the chemical composition of the river waters can be calculated as follows:

Spring Water Contribution (%)=
$$\left(\frac{\text{Flux of M from Springs (mg/s)}}{\text{Flux of M from Rivers (mg/s)}}\right) \times 100$$
 (Eq. 4.6)

Table 4.2 summarises the minimum, maximum and average spring water contribution to the river waters (see Section A.3 in Appendix A for a detailed explanation). The minimum spring water contribution utilises the highest measured discharge value for the Haast River, and the lowest measured spring flow rate. The maximum spring water contribution utilises the lowest measured discharge value for the Haast River, and the highest measured spring flow rate. The minimum spring water contribution to the rivers is $\leq 0.005\%$ for all elements, except Cs, which has a minimum contribution of 0.011%. The maximum spring water contribution to the rivers is generally 0.1%, except for Na (0.17%), Li (0.58%), B (0.89%) and Cs (2.0%). This suggests that the contribution of hydrothermal inputs to river waters is generally much lower than 1%, and therefore, the springs are unlikely to have any effect upon the river water chemistry in the Southern Alps.

TABLE 4.2: Minimum, maximum and average possible spring water contribution to the river waters.

Element		MINIMUM	MAXIMUM	AVERAGE
HCO ₃	%	<0.001	0.017	0.017
F	%	<0.001	0.017	0.017
r Cl	% %	<0.001	0.085	0.085
Br	% %	0.001	0.083	0.083
SO ₄	%	<0.001	0.005	0.005
Li D	%	0.003	0.580	0.290
B	%	0.005	0.890	0.450
Na M	%	0.001	0.170	0.085
Mg	%	<0.001	0.004	0.004
Al	%	<0.001	0.001	0.001
Si	%	<0.001	0.020	0.020
K	%	<0.001	0.014	0.014
Ca	%	<0.001	0.003	0.003
Mn	%	0.001	0.093	0.047
Fe	%	< 0.001	0.015	0.015
Rb	%	<0.001	0.056	0.056
Sr	%	< 0.001	0.012	0.012
Cs	%	0.011	2.000	1.000
Ba	%	< 0.001	0.014	0.014
Y	%	< 0.001	0.022	0.022
La	%	< 0.001	0.002	0.002
Ce	%	< 0.001	0.004	0.004
Pr	%	< 0.001	0.003	0.003
Nd	%	< 0.001	0.003	0.003
Sm	%	< 0.001	0.004	0.004
Eu	%	< 0.001	0.006	0.006
Gd	%	< 0.001	0.005	0.005
Tb	%	< 0.001	0.008	0.008
Dy	%	< 0.001	0.011	0.011
Ho	%	<0.001	0.014	0.014
Er	%	<0.001	0.016	0.016
Tm	%	<0.001	0.018	0.018
Yb	%	<0.001	0.020	0.020
Lu	%	<0.001	0.019	0.019
Pb	%	<0.001	0.003	0.003
U	%	< 0.001	< 0.001	< 0.001

4.4.2 Groundwater Chemistry and Effect of Low Temperature Rock Reactions

Groundwater flow emanating from the Tartare Tunnels is higher during rain storms and stable isotopes (δD and $\delta^{18}O$) lie on the meteoric water line, which would suggest that these fluids are meteoric in origin (Menzies, 2012; Sims, 2013). Groundwater samples were collected in 2009 and 2010 from 46 m, 94 m, 279 m and 290 m along the tunnel (Figure 4.4). The flow of these fluids emanating from the roof of the tunnel was estimated to be low (\sim 0.4 L/min; Menzies 2012).

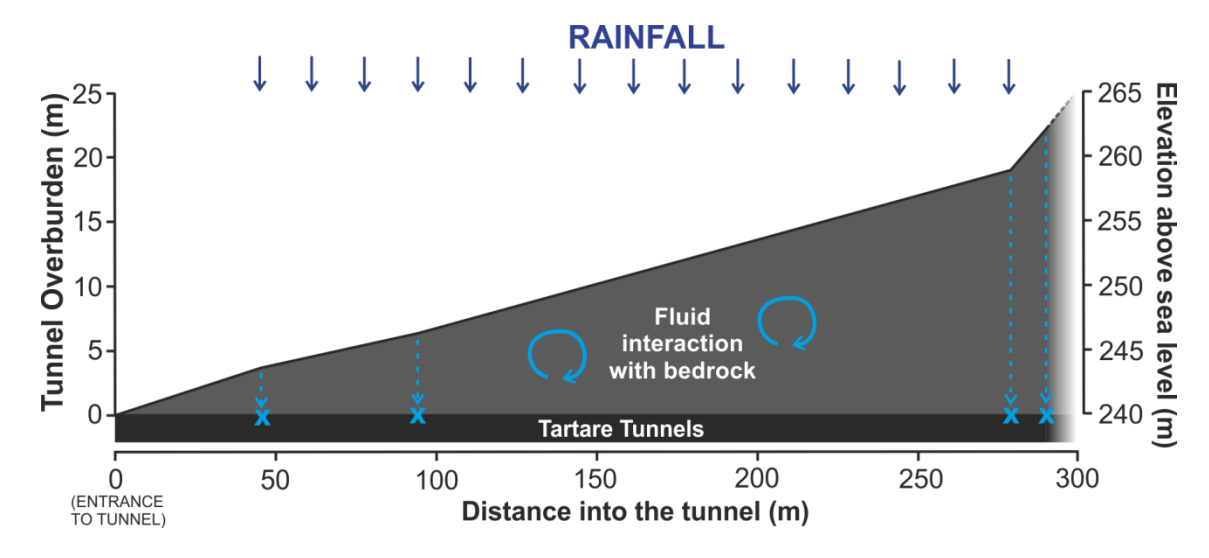


FIGURE 4.4: Schematic of the Tartare tunnels. The blue crosses mark the location of where the Tartare Tunnels fluids were sampled along the tunnel. The vertical axes are at a 4 fold vertical exaggeration to the horizontal axis.

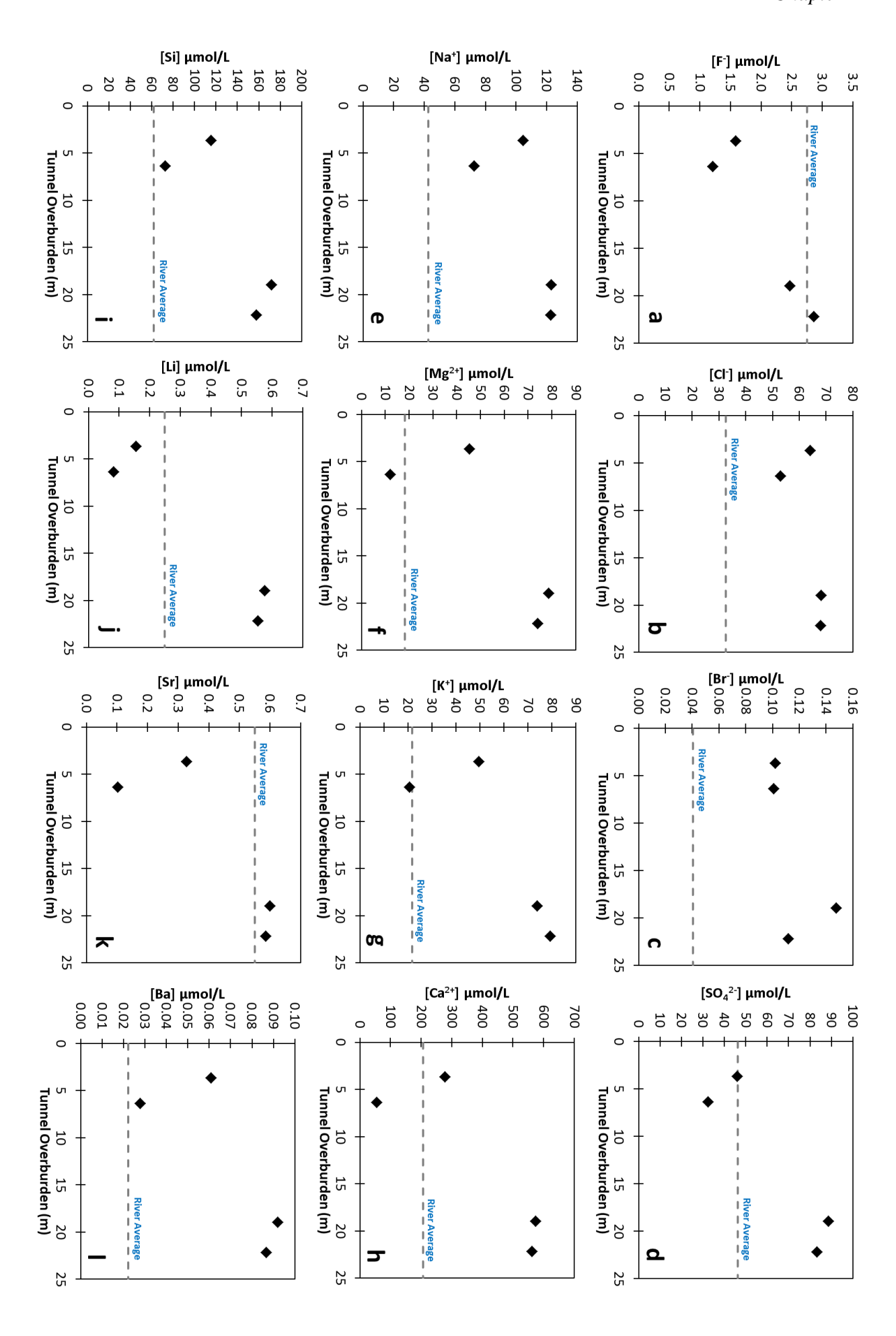
The distance into the tunnel from the tunnel entrance where each groundwater sample was collected was measured on collection (Menzies, 2012). The tunnel overburden was calculated by using ArcGIS to identify the elevation above sea level of the sample localities, and using the distances from the entrance of the tunnel to locate the entrance (zero tunnel overburden). The elevation above sea level of the entrance to the Tartare Tunnels was used to calculate the tunnel overburden for each sample (Figure 4.4). This conclusion makes the assumption that: (i) the tunnel was flat, and (ii) the tunnel was straight. Note that this is a simplified model, as water flows along fractures that are rarely vertical in the bedrock (Sims, 2013), and so tunnel overburden is unlikely to correspond directly to fluid-rock interaction time. Nonetheless, as shown below, the chemistry of these groundwater fluids still provides useful insights into fluid interaction with bedrock.

With increasing tunnel overburden, the groundwater fluids have to travel through a greater amount of bedrock, extending the rock-fluid interaction time. Concentrations of most of the major anions (F, Cl, Br, SO₄) and major and minor cations (Na, Mg, K, Ca, Si, Li, Sr, Ba) increase with increasing tunnel overburden (Figure 4.5), suggesting that increased distance for fluids to travel through increases groundwater interaction with the surrounding rock. Some elements show more significant increases in concentration with increasing overburden depth than others: Cl, Br, Na, F and Si increase by less than a factor of 2; SO₄, K, Mg, Ba and Sr increase by a factor of more than 2; Ca increases by a factor of more than 3; Li increases by a factor of more than 4. High calcium concentrations can be explained by the high dissolution rate of disseminated calcite, which can also be observed in river waters where calcium dominates the river chemistry. The high sulphate concentration in the groundwater fluids is due to the oxidation of sulphide minerals in the surrounding bedrock, which also increases the acidity of the groundwaters and promotes dissolution of calcite. This is supported by the lower pH of the Tartare Tunnels fluids (6.8-7.9) compared to the pH of the river waters

draining the Southern Alps (7.5-9.8), and the higher calcium content of the Tartare Tunnels fluids (average $Ca = 366 \mu mol/L$) compared to the river waters ($Ca = 206 \mu mol/L$).

This interpretation is further supported by the fact that most elemental concentrations in the groundwater are higher than the average value for river waters of the Southern Alps (except for F and Sr). This indicates that the groundwaters have interacted more extensively with the bedrock, which has altered their chemical composition from the surface, down to the roof of the Tartare Tunnels. Although, some elements (B, Al, Mn, Fe, Rb) are lower in concentration in the Tartare Tunnels groundwaters than the average for the river waters and also show a decrease in elemental concentration with increasing overburden. This would suggest that these elements are lost from solution due to precipitation of clay minerals and oxides.

FIGURE 4.5 (Next page): Concentrations of (a) F⁻, (b) Cl⁻, (c) Br⁻, (d) SO₄²⁻, (e) Na⁺, (f) Mg²⁺, (g) K⁺, (h) Ca²⁺, (i) Si, (j) Li, (k) Sr, and (l) Ba in groundwater samples from the Tartare Tunnels, plotted as a function of the depth of overburden. The dashed lines represent the average concentration value for the river waters of the Southern Alps. Groundwater and river water elemental concentrations are from Menzies (2012).



4.4.3 Chemistry of Glacial vs. Non-glacial River Waters

The geology of the watershed and the original source of the water determine the initial pH of river waters. The pH of natural waters is subsequently modified by: 1) consumption of protons during weathering of silicate rocks which increases pH, 2) production of protons by atmospheric CO₂ entering solution or the oxidation of sulphides which lowers pH (Galy et al., 1999). In the Southern Alps, the glacial river waters have higher pH (8.7-9.8) than the non-glacial rivers (7.5-8.6). This is likely due to sub-glacial dissolution processes during weathering, which can increase pH to >9 due to the hydrolysis of carbonate and silicate minerals (Tranter, 2003).

The saturation rates of calcite were calculated using the geochemical modelling software Geochemist's Workbench, which estimates mineral stability (degree of oversaturation or undersaturation) in terms of Gibbs free energy (kJ). A mineral with SI values of >0 is oversaturated and has the potential to precipitate, and a mineral with SI values of <0 is undersaturated and will dissolve. Hydrolysis of carbonates results in a solution that is near saturation (SI = 0) at the highest measured pH values (Figure 4.6). Non-glacial river waters from the Southern Alps become increasingly undersaturated with respect to calcite as pH decreases, and glacial rivers (which have the highest pH values) are near saturation with respect to calcite.

The production of protons by the sub-glacial oxidation of sulphides may mediate this effect (Galy et al., 1999) and lower the pH, but there is no evidence for significant oxidation of sulphides under the ice, as SO_4 concentration in the glacial rivers (30.7-81.3 μ mol/L) is no higher than the non-glacial

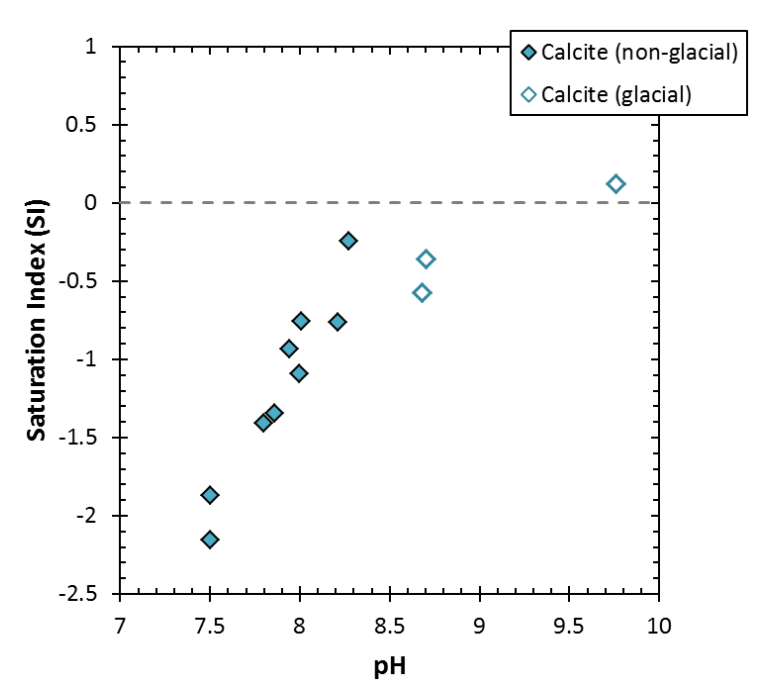


FIGURE 4.6: Saturation index (SI) of calcite against pH in the dissolved load of the river waters draining the Southern Alps. The estimated overall uncertainty on the saturation indices for calcite is 0.5 SI units, as the thermodynamics of calcite are well understood.

rivers (9.23-126 μmol/L). As there is no evidence for pH lowering via oxidation of sulphides, this would explain the high pH of the glacial river waters draining the Southern Alps.

The pH of the non-glacial river waters appears to reflect the extent of chemical dissolution, as increasing pH correlates with increasing TDS (Figure 4.7). This indicates that proton consumption during dissolution weathering reactions is occurring, and driving the pH to more alkaline values. As silicate dissolution during chemical weathering occurs, bicarbonate (HCO₃-) ions are released (Eq. 1 and Eq. 2), which raises the pH level of the solution. Formation of clays such as illite and smectite would be likely to form under alkaline conditions, however, this process would not necessarily lower the pH of the weathering environment. The effect of silicate dissolution upon the chemistry of the system would be several orders of magnitude higher than secondary clay formation. Therefore, the high pH of the Southern Alps rivers raises the potential for the formation of clays such as illite and smectite, however, this mineral formation would not necessarily lower the pH of the weathering system.

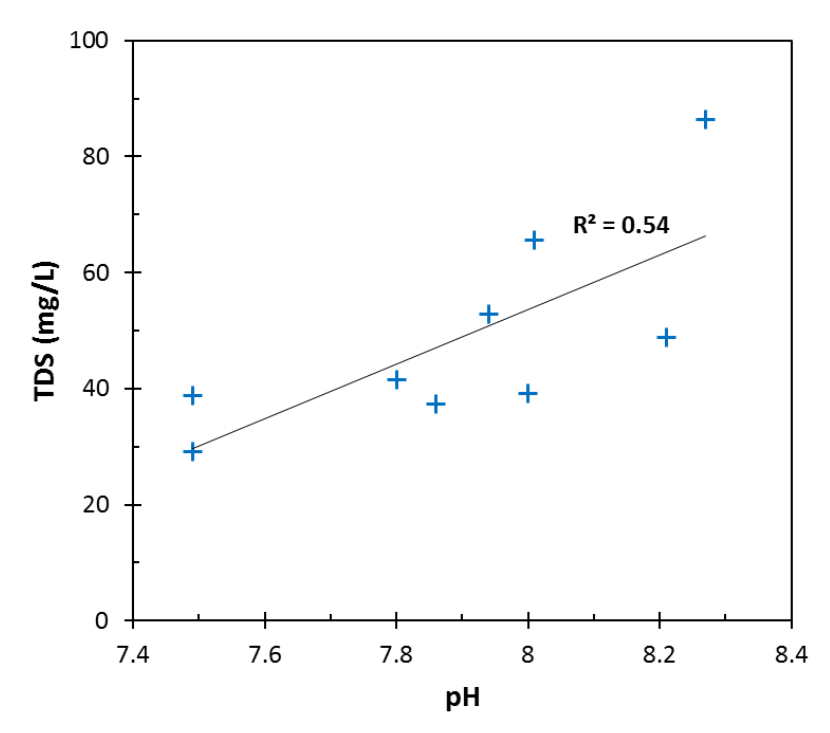


FIGURE 4.7: pH against TDS of the non-glacial river waters draining the Southern Alps.

4.4.4 Alteration of Bedrock, River Sands and Suspended Particulate Material

Feldspars are the most abundant of the reactive (labile) minerals in the Southern Alps and the dominant process during continental chemical weathering is the degradation of feldspars and the subsequent formation of clay minerals. Generally, Ca, Na and K are removed from feldspars by interaction with water and soil solutions, which results in the proportion of aluminium to alkalis

increasing in the weathered product (Nesbitt and Young, 1982). The Chemical Index of Alteration (CIA) can be used to quantify the degree of chemical weathering (Nesbitt and Young, 1982):

$$CIA = [Al_2O_3/(Al_2O_3 + CaO + Na_2O + K_2O)] \times 100$$
 (Eq. 4.7)

In general, the higher the CIA, the higher the weathering intensity. CIA values for the bedrock, river sands and suspended particulate material analysed in this study are given in Table B.7 in Appendix B, and are plotted with respect to Li and Mg concentration in Figures 4.8 and 4.9.

Metasedimentary bedrock, bulk river sand and fine river sand all have similar CIA values and plot close together. On average, the CIA of the river sands and riverine suspended load (CIA = \sim 67) is only slightly higher than that of the bedrock (CIA = 64), which would suggest that they are not particularly weathered compared to the bedrock. This would suggest that chemical weathering in the Southern Alps is low, as these CIA values are at the lower end of the range for intermediate silicate weathering intensity (Selvaraj and Chen, 2006). The clay fraction of the river sands generally have high CIA values, although one clay sample (from Copland River) has a much lower CIA value due to a larger proportion of Na₂O.

There is generally a positive relationship between Li and Mg concentration and CIA (Figure 4.8 and 4.9), with the clay fraction of the river sands generally having the highest CIA values and Li and Mg concentrations. This indicates that Li and Mg are retained in secondary mineral phases during the weathering process. Micaceous minerals are an abundant constituent of the Southern Alps bedrock, and due to high elemental concentrations of Li and Mg, biotite and chlorite are likely to be the main sources of Li and Mg to the weathering system.

Authigenic clay minerals have developed in the Southern Alps due to ground water alteration of non-marine sedimentary sequences formed during the Late Cretaceous to Quaternary (Chamberlain et al., 1999). Alteration occurs as groundwater passes through the sediments (Craw, 1984; Craw, 1994), resulting in the formation of authigenic minerals by direct replacement of primary minerals and in pore spaces during degradation of primary minerals (Chamberlain et al., 1999). To further explore the idea that Li and Mg are retained in secondary clays, XRD analyses were conducted on the clay ($<2~\mu m$) fraction of the river sands. XRD analysis of the river sand clays shows that the vast majority of clay in the Southern Alps is composed of illite and chlorite, with possible minor kaolinite and sepiolite (Figure 4.10). The relative proportions of different clay minerals in each sample, also shown in Figure 4.10, was estimated using the Biscaye Method (Biscaye, 1965); note, however, that this method is semi-quantitative.

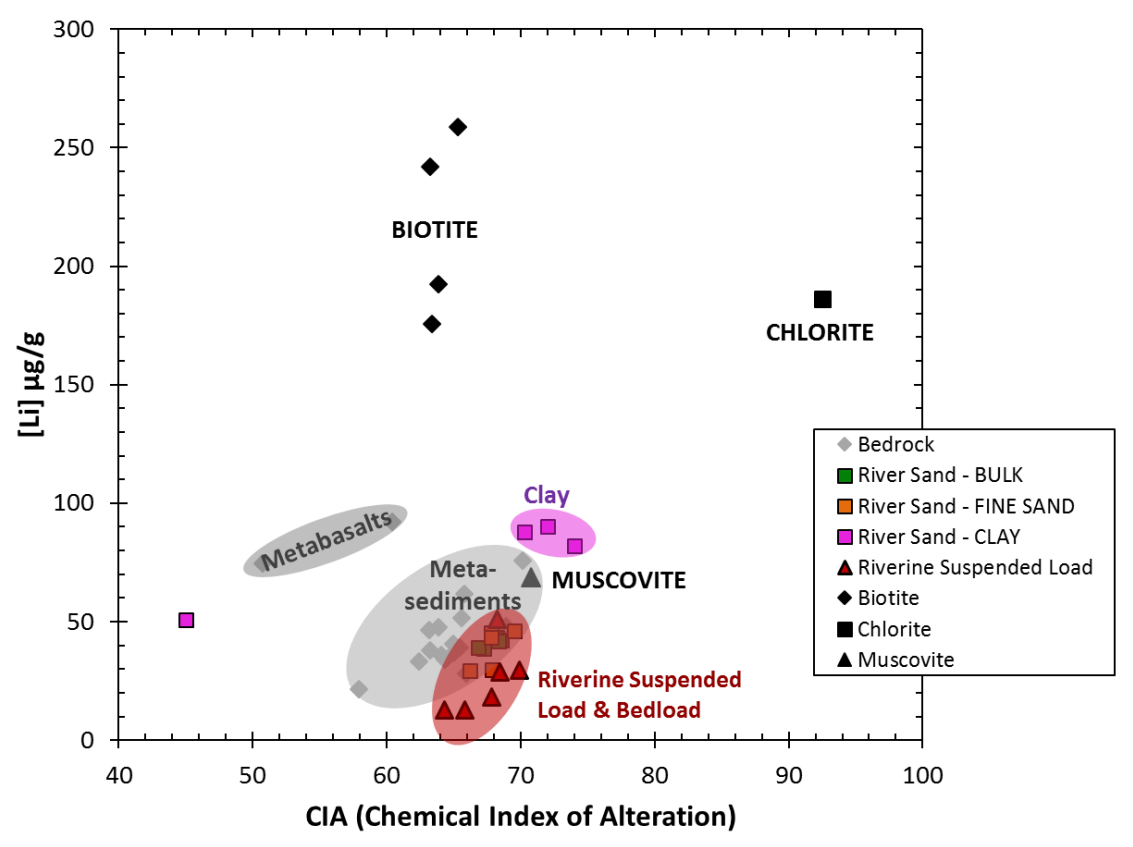


FIGURE 4.8: Lithium concentration against CIA (Chemical Index of Alteration) for the bedrock, mica mineral separates, river sands and suspended load of the Southern Alps. The bedrock data are from Pitcairn (2004).

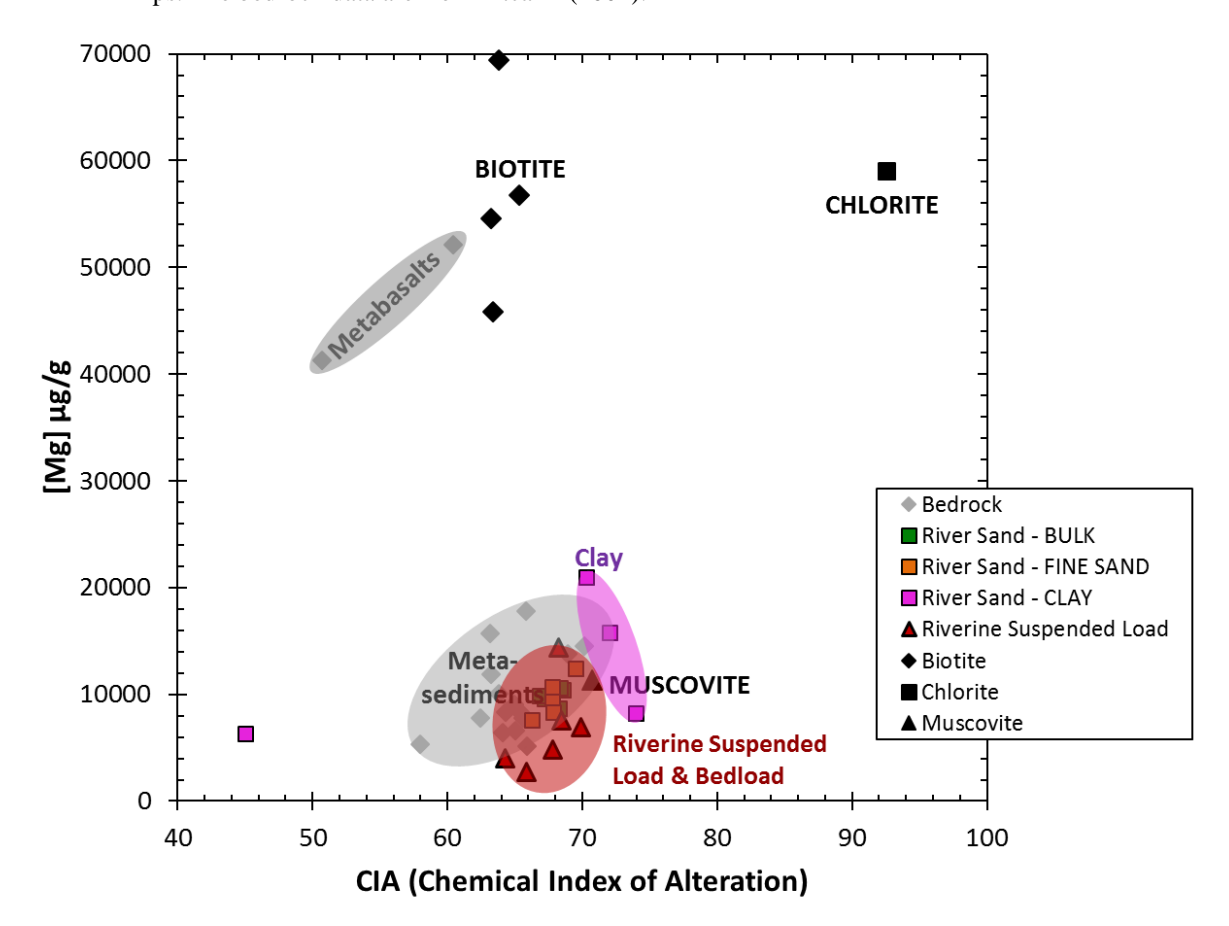


FIGURE 4.9: Magnesium concentration against CIA (Chemical Index of Alteration) for the bedrock, mica mineral separates, river sands and suspended load of the Southern Alps. The bedrock data are from Pitcairn (2004).

Li⁺ often substitutes for Mg²⁺ in octahedral sites of clay minerals, due to the similarity of their ionic radius (Shannon, 1976), and their geochemical cycles are thought to be closely related (Stoffyn-Elgi and MacKenzie, 1984). However, there is no simple correlation in the behaviour between Li and Mg concentrations in solid phases and there is little data on the partitioning of Li between Mg-clays and water (Decarreau et al., 2012). Li⁺ ions have been shown to have been structurally incorporated into the octahedral sheet of smectites, substituting for an Mg²⁺ ion, which results in a charged layer (Decarreau et al., 2012). This charged layer is compensated for by a non-structural exchangeable ion, such as Na⁺, but can also possibly be Mg²⁺ or Li⁺ (Decarreau et al., 2012). Secondary Mg-bearing smectite can incorporate significant amounts of structural Li during water-rock interaction, but only minor Li adsorption into the interlayer sites occurs at the temperatures observed in natural waters, such as rivers (Decarreau et al., 2012). Smectites are efficient sinks for Li in the weathering system (Decarreau et al., 2012), however, few studies have been carried out on the efficiency of Li uptake in other secondary clays and the rate at which uptake occurs.

Illite is one of the major clay components identified in the river sands of the Southern Alps. It is formed by several mechanisms: weathering of silicate rocks (primarily feldspar), the alteration of other clay minerals, and the degradation of biotite and muscovite (Fordham, 1990; Deer and Zussman, 2003). In metamorphic terranes (>100-150 $^{\circ}$ C), smectite reacts to form illite during sediment burial, which is a common diagenetic reaction (Meunier et al., 2000). Illite is a non-expanding micaceous mineral, and it is similar in structure to muscovite, but on average generally has more Si, Mg, Fe and H₂O (Bailey, 1980).

Illite:
$$(K,H_3O)(Al,Mg,Fe)_2(Si,Al)_4O_{10}[(OH)_2,(H_2O)]$$
 (Eq. 4.8)

Chlorite is another major clay component identified in the river sands. It is a phyllosilicate mineral and is commonly found in metamorphic rocks and is usually indicative of low grade metamorphism of the Greenschist Facies (Bishop, 1972; Zane et al., 1998). Chlorite is likely to have been sourced from physical weathering of the bedrock and is therefore considered to be detrital. Chlorite can have a variety of chemical formulae, but for clinochlore/chamosite (common varieties of chlorite) it is typically:

Chlorite:
$$(Mg,Fe)_3(Si,Al)_4O_{10}(OH)_2 \cdot (Mg,Fe)_3(OH)_6$$
 (Eq. 4.9)

Kaolinite is a possible minor clay component identified in the river sands. It is a layered silicate mineral and is generally found in weathering profiles as a product of hydrothermal alteration and in sedimentary rocks (Deer et al., 1992). Kaolinite most commonly forms from the breakdown of feldspar, biotite and muscovite during early diagenesis (Ahn and Peacor, 1987; Nagy et al., 1990) and/or chlorite may react to form some kaolinite (Craw, 1984; Craw, 1994). Muscovite that has altered to illite may also react to form kaolinite (Chamberlain et al., 1999) and albite alteration can

lead to the formation of kaolinite after significant weathering of the bedrock (Craw, 1984; Craw, 1994).

Kaolinite:
$$Al_2Si_2O_5(OH)_4$$
 (Eq. 4.10)

Another possible minor clay component identified in the river sands by XRD is sepiolite. It is a complex hydrous magnesium silicate and occurs as a secondary mineral associated with serpentine (Acimovic et al., 2003). Sepiolite is sedimentary in origin and generally occurs as a precipitate in arid environments and can be associated with dolomite and opal (Dixon and Weed, 1989).

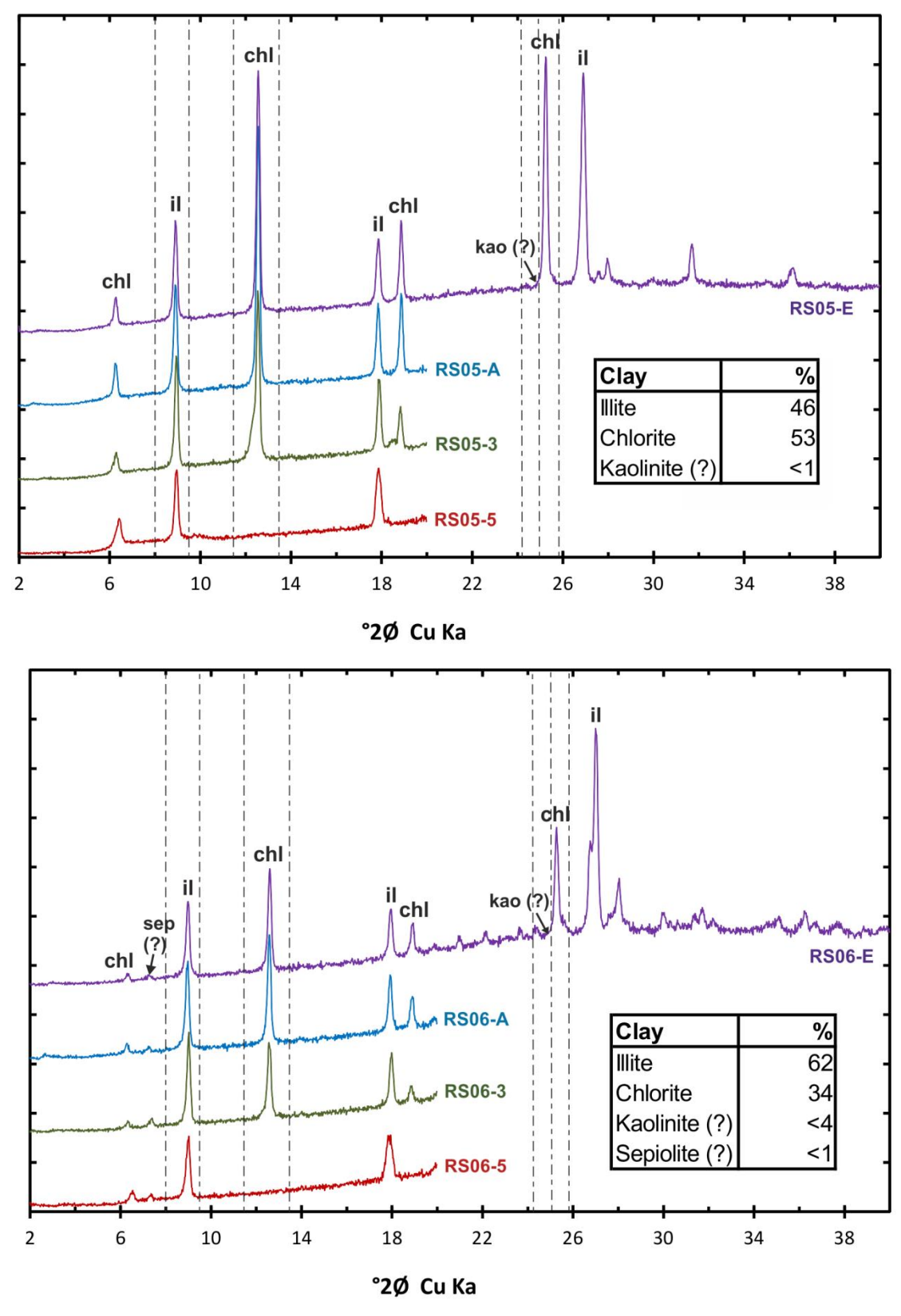


FIGURE 4.10: X-ray diffractograms of river sand clay fractions from Chinaman's Bluff (RS05) and Hooker Terminus (RS06). The dashed lines represent the area used to calculate the relative proportions of each clay mineral using Biscaye's Method (Biscaye, 1965). This method is only semi-quantitative; the uncertainty is at least $\pm 10\%$. il = illite, chl = chlorite, kao = kaolinite and sep = sepiolite.

However, it is likely that the possible minor sepiolite observed in XRD analysis (Figure 4.10) is simply an artefact caused by background noise. Sepiolite generally forms in lacustrine and perimarine environments (Birsoy, 2002), and so it would be unlikely that this clay would form in the Southern Alps. The bedrock of the Southern Alps also generally has a relatively high Al content, which would make the formation of sepiolite unlikely (Weaver and Beck, 1972).

Sepiolite:
$$Mg_4Si_6O_{15}(OH)_2 \cdot 6H_2O$$
 (Eq. 4.11)

Although it was not shown by these XRD analyses, smectite is also present along the Alpine Fault zone, and is formed as a secondary mineral under low temperature alteration (<120 °C) of muscovite/chlorite (Warr and Cox, 2001; Boulton et al., 2012). Smectite may then further alter into kaolinite (Boulton et al., 2012).

4.4.5 Silicate vs. Carbonate Weathering

Both carbonate and silicate weathering remove CO₂ from the atmosphere, but only silicate weathering stores atmospheric CO₂ over long time scales, and thus regulates levels of atmospheric CO₂ and global climate (Walker et al., 1981; Berner et al., 1983; Berner and Kothavala, 2001; Wallmann, 2001; Berner, 2004). Therefore, it is important to quantify the relative importance of silicate versus carbonate weathering in a weathering system.

Mixing diagrams using sodium normalised cation and anion ratios can enable us to observe the range of chemical compositions of different natural reservoirs. In a sodium-normalised mixing diagram of calcium and bicarbonate, the river waters draining the Southern Alps show a strong positive correlation and plot close to the carbonate river end member, although the rivers are slightly offset by a high bicarbonate concentration (Figure 4.11).

Despite a very low abundance of calcite measured in the bedload (Jacobson et al., 2003), Ca²⁺ dominates river water chemistry. This is likely due to the very rapid weathering rate of calcite, which weathers at ~10⁴-10⁵ times faster than plagioclase at neutral pH (Chou et al., 1989; Blum and Stillings, 1995). An abundance of Ca²⁺ in river waters (due to preferential release during weathering of trace carbonates) would suggest that it is the most mobile element, although Na⁺ is generally considered to be the most mobile major cation during weathering of silicate minerals (Gislason et al., 1996; Gaillardet et al., 1999a; Gaillardet et al., 1999b). The high mobility of Na⁺ means that it will preferentially enter solution, and as weathering intensity increases, element ratios normalised to Na⁺ will also rise, which can be observed in a sodium-normalised mixing diagram of calcium over magnesium (Figure 4.12) in the bedrock samples. The river data plotted on Figure 4.12 indicate that carbonate weathering is dominant.

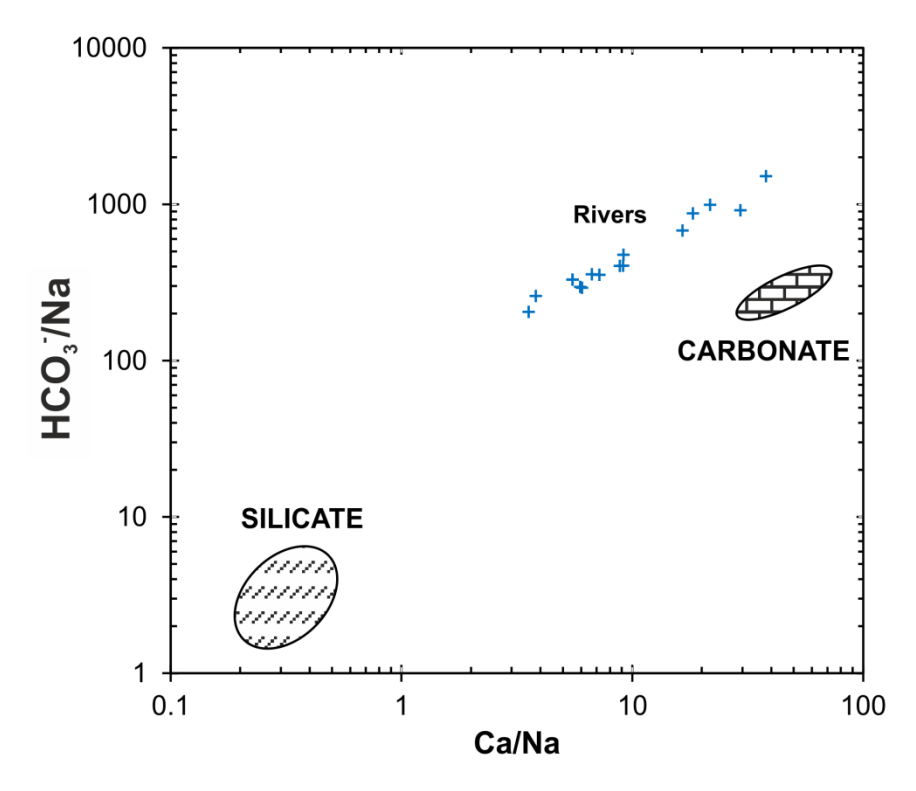


FIGURE 4.11: Sodium-normalised mixing diagram between HCO₃⁻ and Ca. Silicate and carbonate river end members were estimated using data from small rivers draining one single lithology from multiple locations (Gaillardet et al., 1999b).

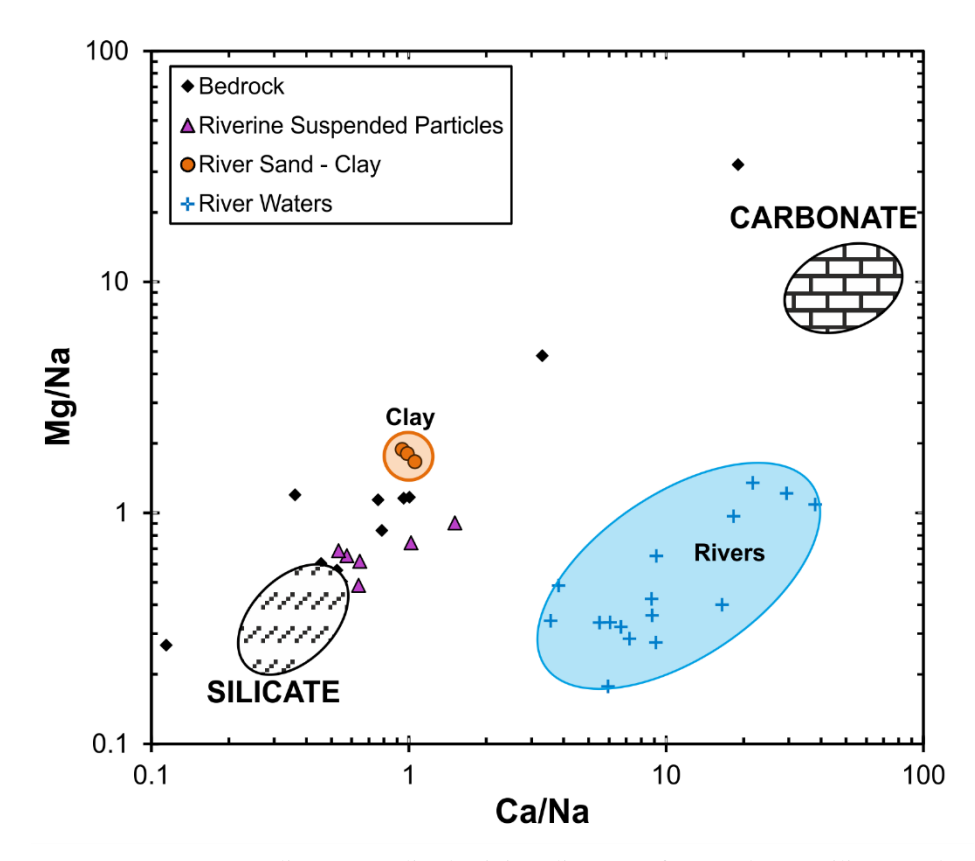


FIGURE 4.12: Sodium-normalised mixing diagram of Ca and Mg. Silicate and carbonate river end members were estimated using data from small rivers draining one single lithology from multiple locations (Gaillardet et al., 1999b).

The river waters have a lower magnesium content than the carbonate rivers end member (Figure 4.12; Gaillardet et al., 1999b), which is likely due to magnesium uptake during the formation of secondary minerals.

A measure of the importance of carbonate weathering on river chemistry can also be assessed by plotting calcium versus alkalinity. The strong positive trend suggests that the calcium content of the rivers draining the Southern Alps is regulated by carbonate weathering ($R^2 = 0.71$; Figure 4.13). Alkalinity is also affected by silicate weathering, whereby dissolution releases cations and consumes protons, therefore increasing HCO_3^- . However, this is not the case for the lithium content of the rivers, as little correlation is seen between lithium concentration and alkalinity (Figure 4.14).

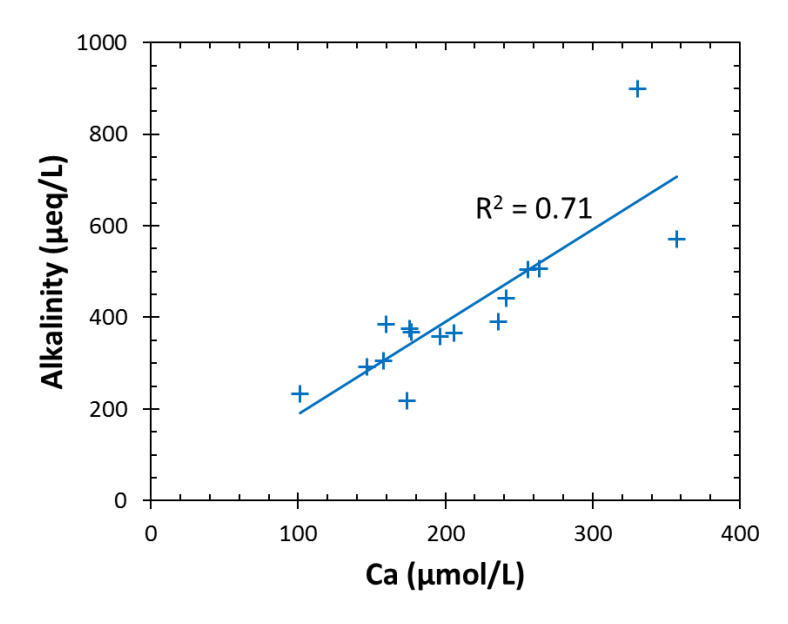


FIGURE 4.13: Calcium against alkalinity of the river waters draining the Southern Alps.

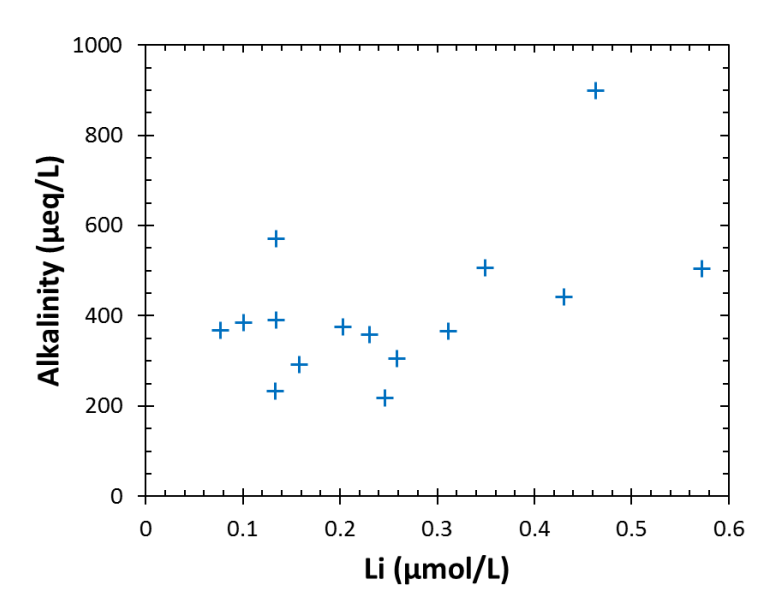


FIGURE 4.14: Lithium against alkalinity of the river waters draining the Southern Alps.

4.4.5.1 Source of Li and Mg

Although carbonates generally have low lithium concentrations compared to silicates, they have much higher dissolution rates, making them a potentially significant source of Li (Millot et al., 2010). The proportions of dissolved lithium in river waters derived from silicate (f_{sil}) and carbonate (f_{carb}) weathering can be determined as follows:

$$(Ca/Li)_{river} = f_{carb} (Ca/Li)_{carb} + (f_{sil}) \times (Ca/Li)_{sil}$$
 (Eq. 4.12)

Where $f_{carb} + f_{sil} = 1$. $(Ca/Li)_{river}$ is calculated from the river data from this study, $(Ca/Li)_{carb}$ is calculated from a carbonate rock end member (Turekian and Wedepohl, 1961), and $(Ca/Li)_{sil}$ is calculated from a silicate rock end member (Wedepohl, 1995). This becomes:

$$(Ca/Li)_{river} = f_{carb} \left[(Ca/Li)_{carb} - (Ca/Li)_{sil} \right] + (Ca/Li)_{sil}$$
 (Eq. 4.13)

This can then be rearranged to calculate the minimum % of dissolved lithium in river waters derived from carbonate weathering:

%Li from Carbonates =
$$\frac{(Ca/Li)_{river} - (Ca/Li)_{sil}}{(Ca/Li)_{carb} - (Ca/Li)_{sil}} \times 100$$
 (Eq. 4.14)

These values can then be used to calculate the maximum proportion of dissolved lithium in river waters derived from silicate weathering. To this end, we find that more than 90% of the dissolved lithium in rivers draining the Southern Alps is sourced from silicate weathering, which is consistent with other studies (Figure 4.15; Millot et al., 2010). This source of Li is likely to be in the micaceous mineral phases, as analyses of mica mineral separates (Section 4.3.5) show that biotite and chlorite (common mica minerals in the Southern Alps) contain around 4 times as much Li as the bedrock.

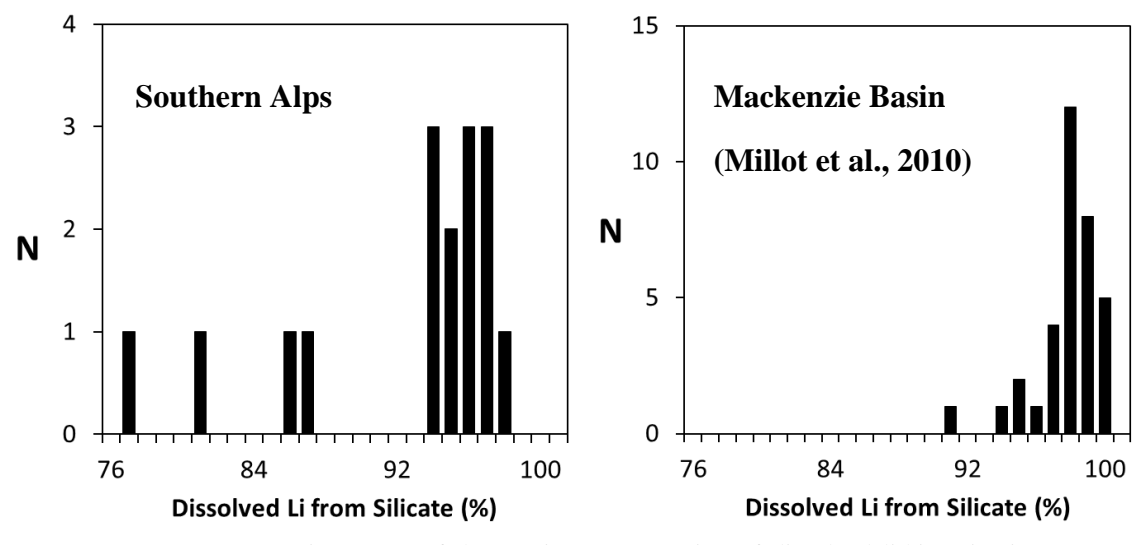


FIGURE 4.15: Histograms of the maximum proportion of dissolved lithium in river waters from silicate weathering (%) in the river waters draining the Southern Alps, with comparison to the Mackenzie Basin, northwest Canada (Millot et al., 2010).

Detrital micas in the Southern Alps (biotite, chlorite and muscovite) are not as weatherable as plagioclase feldspar, but much more easily weathered than quartz (Velbel, 1985).

The only carbonate material thought to be present in the Southern Alps is disseminated calcite, therefore it is likely that Mg is sourced from the weathering of silicates. Mg is a significant component of biotite and chlorite minerals, which have \sim 6 Wt. % more MgO than the bedrock (Section 4.3.5), suggesting that micas are the main source of Mg to the weathering system of the Southern Alps. When attempting to use equations 4.11-4.13 to calculate the proportion of dissolved magnesium derived from silicate and carbonate weathering, the values produced are unrealistic, which is likely to be because Mg is a major element. The Ca/Mg values for the rivers draining the Southern Alps are generally too high to calculate realistic f_{carb} values. This would indicate that Mg is being removed from solution via secondary mineral formation. In addition, unlike Li, Mg is a major element, which may make it more difficult to observe variations in the proportions of dissolved Mg from silicate and carbonate sources. Mg is also involved in more processes than Li; for example Mg is utilised in biotic processes.

4.4.6 Chemical Weathering and Atmospheric CO₂ Consumption Rates

Silicate and carbonate weathering rates along with atmospheric CO₂ consumption rates can be calculated using major cation concentration data along with catchment area size and runoff rates. Information regarding the hydrologic parameters was sourced from the National Institute of Water and Atmospheric Research Limited in Christchurch, New Zealand (NIWA). The runoff is the calculated mean annual value. The river water samples were collected during a single time period, and therefore do not account for possible seasonal variations. Following Jacobsen et al. (2003) and Jacobsen and Blum (2003), Ca²⁺ was apportioned between silicate (Ca²⁺sil) and carbonate (Ca²⁺carb) weathering as follows:

$$Ca_{sil}^{2+} = (Ca/Na)_{plag} \times Na_{sil}^{+}$$
 (Eq. 4.15)

$$Ca_{carb}^{2+} = Ca_{tot}^{2+} - Ca_{sil}^{2+}$$
 (Eq. 4.16)

Where $(Ca/Na)_{plag}$ represents the molar ratio of sodium in the bedrock plagioclase (~0.32), Na^{+}_{sil} is the riverine concentration of sodium (after correction for atmospheric inputs), and Ca^{2+}_{tot} is the total riverine concentration of calcium. Total chemical weathering rates (W_{chem}), silicate weathering rates (W_{sil}) and carbonate weathering rates (W_{carb}) are calculated as follows (Jacobson and Blum, 2003):

$$W_{\text{chem}} = (Ca^{2+} + Mg^{2+} + Na^{+} + K^{+} + Si) \times R$$
 (Eq. 4.17)

$$W_{\text{sil}} = (Ca_{\text{sil}}^{2+} + Na^{+} + K^{+} + Si) \times R$$
 (Eq. 4.18)

$$W_{\text{carb}} = (Ca_{\text{carb}}^{2+} + Mg^{2+}) \times R$$
 (Eq. 4.19)

Where the units of W resolve to $g \cdot \text{km}^2 \cdot \text{yr}^{-1}$, when the sum of the riverine solute concentrations (ΣC_i) has units of $\mu g/L$ and runoff (R) has units of $\mu m/\text{yr}$.

Long term atmospheric CO_2 consumption rates attributed to silicate weathering ($W_{sil-CO2}$) are calculated as follows (Jacobson and Blum, 2003):

$$W_{\text{sil-CO}_2} = 2 \times \text{Ca}_{\text{sil}}^{2+} \times R$$
 (Eq. 4.20)

Where the units of $W_{\text{sil-CO2}}$ are $\text{mol} \cdot \text{km}^2 \cdot \text{yr}^{-1}$, when $\text{Ca}^{2+}_{\text{sil}}$ has units of μ mol/L and R has units of mm/yr. The factor of 2 is derived from the stoichiometry of the reaction between carbonic acid and plagioclase (Jacobson and Blum, 2003). Atmospheric CO₂ consumption rates attributed to carbonate weathering ($W_{\text{carb-CO2}}$) are given by (Jacobson and Blum, 2003):

$$W_{\text{carb-CO}_2} = \left(\text{Ca}_{\text{carb}}^{2+} + \text{Mg}^{2+} \right) \times R$$
 (Eq. 4.21)

Where the units of $W_{\text{carb-CO2}}$ are mol·km²·yr⁻¹, when (Ca²⁺carb + Mg²⁺) has units of µmol/L and R has units of mm/yr. To calculate $W_{\text{carb-CO2}}$, the factor of 2 is not used, as only half of the alkalinity derived from the reaction between carbonic acid and carbonate-bearing minerals is from dehydrated atmospheric CO₂ (Jacobson and Blum, 2003).

A drawback of this set of equations from Jacobsen and Blum (2003) is the omission of Mg content in the silicate weathering rate equation and the atmospheric CO₂ drawdown via silicate weathering equation. Mg is a major component of silicate rocks, and the bedrock of the Southern Alps typically contains ~14000 ppm Mg. Mg is also affected by secondary clay formation, which occurs during silicate weathering processes.

Due to a lack of hydrological data for the river localities in this study, only two river catchments were selected, which are representative of the east and of the west of the Main Divide. The River Haast is a large river west of the Main Divide. It is subject to high rates of uplift, rainfall and mechanical erosion. The River Rakai is a large river east of the Main Divide and is subject to lower rates of uplift, rainfall and mechanical erosion. The results from these calculations are shown in Table 4.3, with comparison to results from Jacobsen and Blum (2003). The variation in runoff values between this study and Jacobsen and Blum (2003) is due to the differing sampling points along these rivers. The error on the weathering calculations summarised in Table 4.3 is largely affected by the variation in annual runoff values, and is on the order of $\pm 10\%$.

TABLE 4.3: Hydrologic parameters, chemical weathering rates and atmospheric CO₂ consumption rates of two rivers draining the Southern Alps, either side of the Main Divide. River catchment area and runoff data from NIWA.

		This Study		Jacobsen & Blum, 2003	
		Haast (NZ04)	Rakai (NZ27)	Haast	Rakai
Area	km^2	1020	2560	1020	2560
Runoff	mm/yr	2990	801	5787	2723
$W_{ m chem}$	$\times 10^7 \text{ g}\cdot\text{km}^{-2}\cdot\text{yr}^{-1}$	3.1	1.8	8.1	3.6
$W_{ m sil}$	$\times 10^7 \text{ g}\cdot\text{km}^{-2}\cdot\text{yr}^{-1}$	0.9	0.8	2.2	1.3
$W_{ m carb}$	$\times 10^7 \text{ g}\cdot\text{km}^{-2}\cdot\text{yr}^{-1}$	2.1	1.0	6.0	2.4
$W_{ m sil ext{-}CO2}$	x 10 ⁴ mol·km ⁻² ·yr ⁻¹	6.4	7.7	7.4	10
$W_{ m carb ext{-}CO2}$	x 10 ⁵ mol·km ⁻² ·yr ⁻¹	5.6	2.8	15	6.0

Variations between the chemical weathering and atmospheric CO₂ consumption rates calculated in this study, and those reported in Jacobsen and Blum (2003) are most likely due to differences in the correction of atmospheric inputs, seasonal and annual variations in the chemical composition of the river waters, and exact locations of river water samples. Nevertheless, the results from this study (Table 4.3) are generally in good agreement with Jacobsen and Blum (2003). Although, W_{chem} for the River Haast calculated in this study (3.1 x 10⁷g·km²·yr⁻¹) is lower than the previous estimate (8.1 x 10⁷g·km²·yr⁻¹; Jacobsen and Blum, 2003). In general, all of the values calculated in this study are lower than those calculated in Jacobsen and Blum (2003). It was noted that there is a large difference in magnitude between silicate weathering rate and atmospheric CO2 consuption rate via silicate weathering between the two datasets; the difference in magnitude bettwen these two values is twice as large in the dataset from this study. This can be attributed to the Haast river water sample from this study having around half the Na content and around a quarter of the K content with comparison to the Haast river water sample from Jacobsen and Blum (2003). The lower concentration values for Na and K resulted in a lower silicate weathering rate value (0.9 x 10⁷ g·km⁻²·yr⁻¹). In addition, the atmospheric CO₂ consumption rate attributed to carbonate weathering in this study is lower for the Haast river (5.6 x 10⁵ mol·km⁻²·yr⁻¹) than previously quoted in Jacobsen and Blum (2003) (15 x 10⁵ mol·km⁻²·yr⁻¹). The source of this discrepancy is the much lower runoff rate used in this study for this river, and the sample also a lower Mg concentration (20.1 µmol/L) than the sample used in Jacobsen and Blum (2003) (27.2 µmol/L).

Chemical weathering rates are much higher west of the Main Divide $(3.1 \times 10^7 \text{ g·km}^{-2} \cdot \text{yr}^{-1})$ than in the east $(1.8 \times 10^7 \text{ g·km}^{-2} \cdot \text{yr}^{-1})$. This is likely due to the higher uplift and erosion rates and a higher amount of rainfall in the west (>12 m/yr), compared to the east (<1 m/yr) (Griffiths and McSaveney, 1983; Henderson and Thompson, 1999). Little variation in silicate weathering rate is observed between the west and the east of the Main Divide $(0.9 \times 10^7 \text{ g·km}^{-2} \cdot \text{yr}^{-1} \text{ and } 0.8 \times 10^7 \text{ g·km}^{-2} \cdot \text{yr}^{-1}$, respectively). Carbonate weathering rates are twice as high in the west $(2.1 \times 10^7 \text{ g·km}^{-2} \cdot \text{yr}^{-1})$ as in the east $(1.0 \times 10^7 \text{ g·km}^{-2} \cdot \text{yr}^{-1})$, which can be attributed to increased calcite weathering. Hydrothermal

disseminated calcite is present throughout the bedrock of the Southern Alps, but with higher rate of uplift, erosion and rainfall in the west, the rate of dissolution of calcite is higher. Atmospheric CO₂ consumption attributed to carbonate weathering is almost twice as high in the west (5.6 x 10⁵ mol·km⁻²·yr⁻¹) than the east (2.8 x 10⁴ mol·km⁻²·yr⁻¹). However, atmospheric CO₂ consumption attributed to silicate weathering is higher in the east (7.7 x 10⁴ mol·km⁻²·yr⁻¹) where uplift and erosion rates are low, compared to the west (6.4 x 10⁴ mol·km⁻²·yr⁻¹). Although silicate weathering leads to long term drawdown of atmospheric CO₂, carbonate weathering does not. This would suggest that, although high rates of uplift, rainfall and erosion have led to high carbonate weathering rates in the west, more long term atmospheric CO₂ consumption occurs in the east. The majority of the rivers draining the western side of the Southern Alps are relatively short, resulting in a weathering-limited regime where chemical weathering intensity is reduced, as there are few lowlands/deltas for significant chemical weathering to take place.

4.4.6.1 Comparison to Global Rivers

In Table 4.4 and Figure 4.16, it can be seen that chemical weathering rate in the Southern Alps (1.8-3.1 x 10⁷ g·km⁻²·yr⁻¹) is around twice as high as rivers measured in North America (0.6-1.5 x 10⁷ g·km⁻²·yr⁻¹), South America (0.5-1.2 x 10⁷ g·km⁻²·yr⁻¹) and Africa (0.2-0.5 x 10⁷ g·km⁻²·yr⁻¹). A much wider range is shown for Europe (0.4-6.3 x 10⁷ g·km⁻²·yr⁻¹), and Asia (0.3-11 x 10⁷ g·km⁻²·yr⁻¹). Atmospheric CO₂ consumption rates attributed to silicate weathering in the Southern Alps (6.4-7.7 x 10⁴ mol·km⁻²·yr⁻¹) are relatively low compared to many rivers across all other continents (up to 69 x 10⁴ mol·km⁻²·yr⁻¹), except for Africa (1.2-6.4 x 10⁴ mol·km⁻²·yr⁻¹). However, atmospheric CO₂ consumption rates attributed to carbonate weathering in the Southern Alps are high (2.8-5.6 x 10⁵ mol·km⁻²·yr⁻¹) compared to North America (0.4-2.7 x 10⁵ mol·km⁻²·yr⁻¹), South America (0.1-0.8 x 10⁵ mol·km⁻²·yr⁻¹) and Africa (0.1-0.2 x 10⁵ mol·km⁻²·yr⁻¹), and are at the higher end of the range of values shown by rivers in Europe (0.1-6.8 x 10⁵ mol·km⁻²·yr⁻¹) and Asia (0.1-21.6 x 10⁵ mol·km⁻²·yr⁻¹). For further information on the global rivers used for this comparison, see Section A.4 in Appendix A.

The atmospheric CO₂ consumption attributed to silicate weathering in the Southern Alps of New Zealand is relatively low compared to rivers globally. This demonstrates that rapid tectonic uplift in the Southern Alps accelerates chemical weathering, but does not greatly enhance the rate of long-term atmospheric CO₂ consumption, as rapid uplift seems to increase dissolution of carbonates disproportionately to silicates.

TABLE 4.4: Hydrologic parameters, chemical weathering rates and atmospheric CO_2 consumption rates of global rivers. The global river data are summarised by Gaillardet et al. (1999b).

River Basin	Runoff	TDS	$W_{ m chem}$	$W_{\rm sil}$	$W_{\rm carb}$	W sil-CO2	W _{carb-CO2}
	mm/yr	mg/L	$x 10^{7}$	$x 10^{7}$	$x 10^{7}$	$x 10^4$	$x 10^{5}$
		J	g·km ⁻² ·yr ⁻¹	g·km ⁻² ·yr ⁻¹	g·km ⁻² ·yr ⁻¹		mol·km ⁻² ·yr ⁻¹
New Zealand			<u> </u>	8) .	g j .	1110111111	11.01 III.1 J1
Haast	2990	37.5	3.10	0.90	2.10	6.40	5.60
Rakai	801	39.1	1.80	0.80	1.00	7.70	2.80
N. America	•						
Mississippi	195	216	1.19	0.71	0.48	11.3	1.18
Mackenzie	172	209	0.89	0.41	0.48	6.87	1.19
Yukon	236	183	0.94	0.25	0.69	3.23	1.70
Columbia	353	115	1.14	0.63	0.51	9.28	1.25
Nelson	79	236	0.56	0.39	0.18	6.66	0.43
Fraser	509	92	1.25	0.54	0.72	7.77	1.77
Kuskokwim	487	145	1.52	0.44	1.07	5.66	2.65
S. America							
Amazon	1078	44	1.17	0.85	0.32	10.4	0.78
Parana	204	86	0.51	0.47	0.05	5.71	0.11
Orinoco	1032	25	0.79	0.67	0.12	8.00	0.30
Tocantins	491	42	0.59	0.47	0.12	4.88	0.29
Uruguay	604	60	1.10	0.81	0.29	9.00	0.70
Europe							
Danube	253	428	2.97	1.33	1.64	22.6	4.01
Yenisei	239	112	0.70	0.44	0.26	6.54	0.65
St. Lawrence	330	168	1.35	0.59	0.76	9.55	1.88
Lena	211	112	0.63	0.32	0.31	5.01	0.75
Magdalena	1009	118	3.57	2.95	0.62	44.1	1.52
Ob	135	126	0.43	0.23	0.20	3.76	0.49
N. Dvina	316	173	1.32	0.51	0.81	8.30	2.00
Rhone	565	339	4.46	2.02	2.44	33.6	6.05
Po	667	354	6.25	3.51	2.75	59.0	6.77
Elbe	154	698	4.22	4.16	0.06	69.3	0.12
Dnepr	103	274	0.75	0.44	0.31	7.60	0.77
Kolima	200	74	0.37	0.21	0.16	2.95	0.39
Pechora	404	70	0.73	0.40	0.33	6.36	0.80
Khatanga	234	96 402	0.79	0.71	0.09	12.0	0.20
Seine	164	493	2.07	1.11	0.96	18.3	2.39
Nemunas Asia	200	447	2.25	0.96	1.30	16.6	3.19
	513	221	2.50	0.91	1.59	13.8	3.92
Changjiang Xijiang	831	161	3.04	0.91	2.12	11.8	5.25
Brahmaputra	879	101	2.09	0.92	1.14	9.69	2.80
Ganges	470	182	2.23	1.51	0.72	23.7	1.77
Godavari	335	193	1.52	1.04	0.72	14.3	1.77
Amur	185	55	0.30	0.18	0.48	2.82	0.29
Huanghe	55	460	0.30	0.18	0.12	15.8	0.29
Shatt el Arab	85	400	1.12	0.91	0.04	13.9	0.76
Hong He	1025	147	4.93	3.74	1.20	60.0	2.89
Fly	2311	116	5.42	2.22	3.19	28.3	7.92
Sepik	1525	114	4.09	2.14	1.95	28.1	4.80
Purari	2749	126	7.64	3.82	3.82	46.3	9.44
Mahanadi	500	147	2.27	1.67	0.59	26.8	1.42
Kikori	3035	177	10.6	1.88	8.71	20.9	21.6
Africa	3033	1//	10.0	1.00	0.71	20.7	21.0
Limpopo	59	238	0.47	0.41	0.07	6.40	0.16
Congo-Zaire	324	35	0.47	0.33	0.07	3.77	0.10
Zambese	77	80	0.23	0.33	0.05	2.19	0.12
Niger	128	59	0.19	0.17	0.06	1.21	0.15

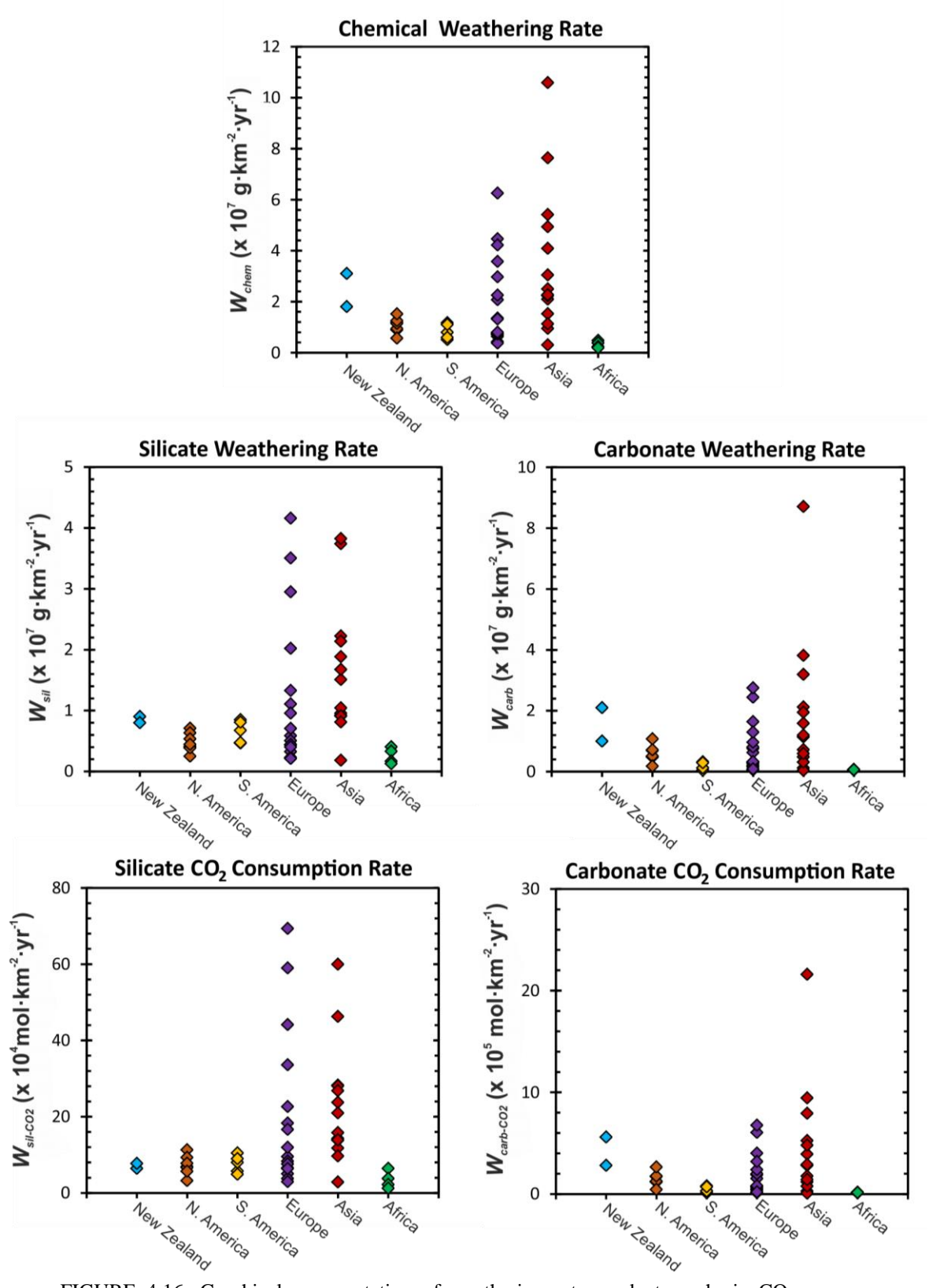


FIGURE 4.16: Graphical representation of weathering rates and atmospheric CO_2 consumption rates. Summarised from Table 4.4

4.5 Summary of the Weathering System in the Southern Alps

- The river waters draining the Southern Alps are relatively dilute (non-glacial river TDS = 29-86 mg/L; glacial river TDS = 28-55 mg/L) compared to most global rivers. Although the river catchments in the Southern Alps are underlain primarily by metasediments, the rivers draining the Southern Alps have an abundance of Ca²⁺ (most abundant major cation = 73%), which would suggest a carbonate weathering source is present, which is likely to be in the form of disseminated calcite.
- The glacial river waters have higher pH (8.7-9.8) than the non-glacial rivers (7.5-8.6), which is likely to be due to high degrees of sub-glacial weathering, which can increase pH to >9 due to the hydrolysis of carbonate and silicate minerals. In the non-glacial river waters, increasing pH correlates with increasing TDS, indicating that proton consumption during weathering is occurring.
- The groundwater samples collected from varying distances along the Tartare Tunnels are generally similar to river water chemistry in sulphate concentration and total alkalinity, although the Tartare Tunnels fluids have higher concentrations of Cl, Na, Ca, Mg, Si and Li than the river waters. With increasing tunnel overburden, most major anion (F, Cl, Br, SO₄) and major and minor cation (Na, Mg, K, Ca, Si, Li, Sr, Ba) concentrations increase, indicating the low temperature fluid-rock interaction is occurring in the Southern Alps. This is further supported by the fact that most element concentrations in the groundwater are higher than the average value for river waters draining the Southern Alps.
- The hydrothermal springs located within the Southern Alps generally have much higher elemental concentrations than the river waters; average TDS of the spring waters (14400 mg/L) is >100 times higher than the river waters (46 mg/L). Although, the ultramafic-hosted hyperalkaline springs (average TDS = 2220 mg/L) are ~100 times more dilute than the metasedimentary-hosted springs. However, due to low flow rates, the maximum possible spring water contribution to the river waters is generally much less than 1%, and therefore the springs are likely to have a negligible effect upon the river water chemistry.
- The elemental chemistry of the bedrock shows little variation across the Southern Alps. The riverine suspended load is similar in chemical composition to the bedrock, as are the bulk and fine sand size fractions of the river sands (although Al₂O₃ is higher in the bedload). The average CIA of the bedload and riverine suspended load (CIA = ~67) is similar to the bedrock (CIA = ~64), implying that chemical weathering is relatively low in the Southern Alps.

- The main clays present in river sands are illite and chlorite. The chlorite present is likely to be detrital, whereas illite is formed by alteration of muscovite and biotite.
- Carbonate weathering dominates the river chemistry of the Southern Alps, although the majority
 of dissolved lithium (generally >90%) is sourced from silicate weathering.
- Disseminated calcite is the only carbonate material thought to be present in the Southern Alps bedrock. Therefore, it is likely that the source of Mg is the weathering of silicate rocks. This is further supported by the high MgO content of micaceous minerals (biotite and chlorite), which have ~6 Wt. % more MgO than the bedrock. This would suggest that micaceous minerals in the bedrock are the main source of Mg to the weathering system of the Southern Alps.
- Overall chemical weathering rates, carbonate weathering rates, and to a lesser extent silicate
 weathering rates in the Southern Alps are relatively high compared to rivers globally.
 Atmospheric CO₂ consumption rates attributed to carbonate weathering are also high compared
 to rivers globally, however atmospheric CO₂ consumption rates attributed to silicate weathering
 are relatively low.
- Rapid uplift and erosion rates along with heavy rainfall west of the Main Divide have led to high overall chemical weathering rates, carbonate weathering rates and atmospheric CO₂ consumption rates attributed to carbonate weathering. There is little observed difference in silicate weathering rates east and west of the Main Divide. However, atmospheric CO₂ consumption rates attributed to silicate weathering are higher east of the Main Divide. This indicates that although uplift in the Southern Alps may accelerate chemical weathering, it does not necessarily enhance the rate of long term atmospheric CO₂ consumption.

Lithium Isotopes as a Tracer of Weathering Processes in the Southern Alps

5.1 Introduction

Lithium isotopes have a large relative mass difference, resulting in significant variations in the lithium isotopic signature (δ^7 Li) of natural reservoirs. Lithium isotopes are effective tracers of weathering processes as the isotopic compositions in river waters are dependent on the composition of the underlying bedrock and the processes involved with weathering. Generally, there is little variation in δ^7 Li values of different rock reservoirs (Figure 1.8), and rivers tend to be highly fractionated from rocks and have heavier δ^7 Li values (Figure 1.9). It is widely accepted that lithium isotopic fractionation during weathering is associated with the formation of secondary alteration products (Huh et al., 2001; Kısakűrek et al., 2005; Pogge von Strandmann et al., 2006; Vigier et al., 2009; Millot et al., 2010; Pogge von Strandmann et al., 2010; Wimpenny et al., 2010b). Little or no lithium isotopic fractionation occurs during the weathering and dissolution of primary silicate minerals (Pistiner and Henderson, 2003; Wimpenny et al., 2010a). Hence, riverine δ^7 Li signatures are controlled by the rate of Li release into solution by dissolution of primary minerals, and by the rate of Li removal from solution by secondary mineral precipitation.

In order to fully utilize Li isotopes as geochemical tracers of weathering processes, the δ^7 Li signatures of different geological reservoirs need to be characterised, and the dominant processes controlling Li isotopic fractionation and the extent of fractionation need to be determined. In this chapter, the Li isotopic composition of river waters and other weathering products collected from the Southern Alps on South Island, New Zealand, will be used to interpret the weathering system. These samples include river waters, groundwaters, spring waters, bedrock, river sands and suspended load.

5.2 Methods

Full details of the methods used for the determination of Li isotope compositions are given in Chapter 3 (Section 3.5). Briefly, lithium was separated from the sample matrix using cation exchange chromatography. Acid-cleaned PTFE columns were loaded with AG50W-X12 cation exchange resin to a height of 8.5 cm in 0.2 M TD HCl, and the lithium fraction was eluted with 0.2 M TD HCl. A column calibration was carried out to ascertain the volume of 0.2 M TD HCl needed to collect the whole Li elution curve to ensure complete collection of Li. For rock samples, a larger elution volume was collected to account for matrix effects. Lithium isotopic analyses were carried out on a Thermo Scientific Neptune MC-ICP-MS at the National Oceanography Centre, Southampton. Both a CETAC Aridus IITM and a ThermoFinnigan sample introduction system (SIS) were used depending upon the lithium concentration in the samples. A CETAC Aridus ITM was also used alongside a Thermo Scientific Neptune MC-ICP-MS at the University of Bristol for one batch of samples. The Li isotopic values are expressed as $\delta^7 \text{Li}$, the per mil (‰) deviation of the $^7 \text{Li}/^6 \text{Li}$ ratio from the international NIST standard LSVEC. To ensure that no isotopic fractionation occurred during column chemistry, LSVEC, IAPSO seawater and a series of certified rock reference materials (JB-2, BCR-2, JSl-1 and JS1-2) were passed through the cation exchange columns and analysed within each instrument analysis. The external reproducibility of the δ^7 Li values of the fluid samples from this study is $\pm 0.61\%$, and $\pm 0.64\%$ for rock samples (Table 3.4). The external reproducibility for the δ^7 Li analyses is given as twice the standard deviation (2σ) throughout this chapter.

5.3 Results

Results of $\delta^7 Li$ analyses are reported in Figure 5.1 and Figure 5.2. The river waters and groundwaters (Tartare Tunnels fluids) sampled from the Southern Alps have higher $\delta^7 Li$ values than the bedrock, whereas the $\delta^7 Li$ composition of the spring waters is less fractionated from the bedrock, with some spring water samples approaching bedrock $\delta^7 Li$ values. The lithium concentration of the bedrock ranges from 21.6 $\mu g/g$ to 75.6 $\mu g/g$, and show a narrow range of $\delta^7 Li$ values, from -1.6% to +1.4%. The concentration of Li in the glacial rivers ranges from 0.23 μ mol/L to 0.35 μ mol/L, and the $\delta^7 Li$ values range from +12.0% to +14.5%. In the non-glacial rivers, the concentration of Li ranges from 0.10 μ mol/L to 0.46 μ mol/L, and the $\delta^7 Li$ values have a large range from +11.8% to +26.1%.

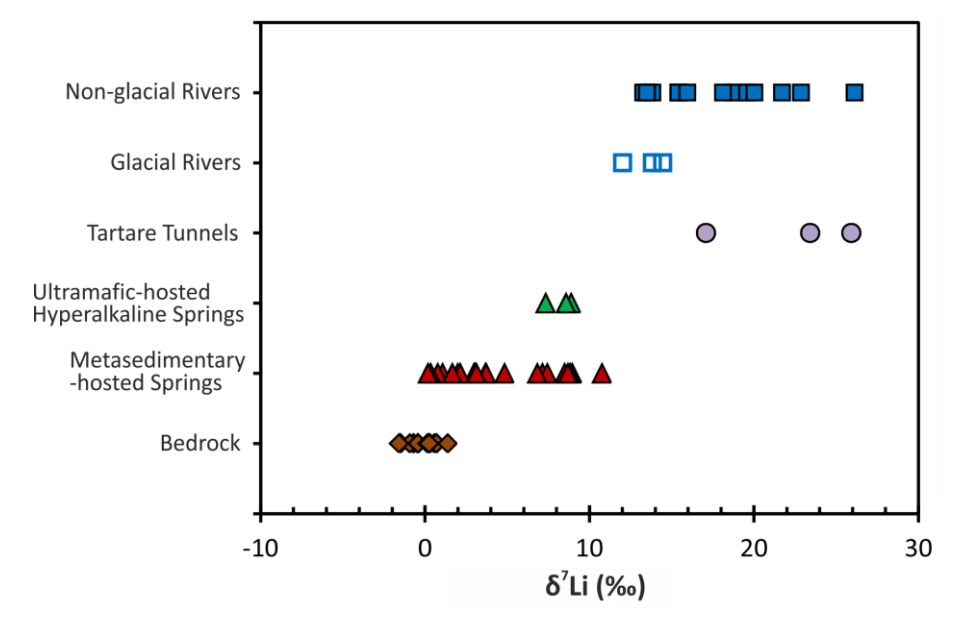


FIGURE 5.1: δ^7 Li values of fluid samples (river water, groundwater and spring water) from the Southern Alps, with comparison to the bedrock. The external reproducibility of the δ^7 Li analyses is smaller than the size of the symbols.

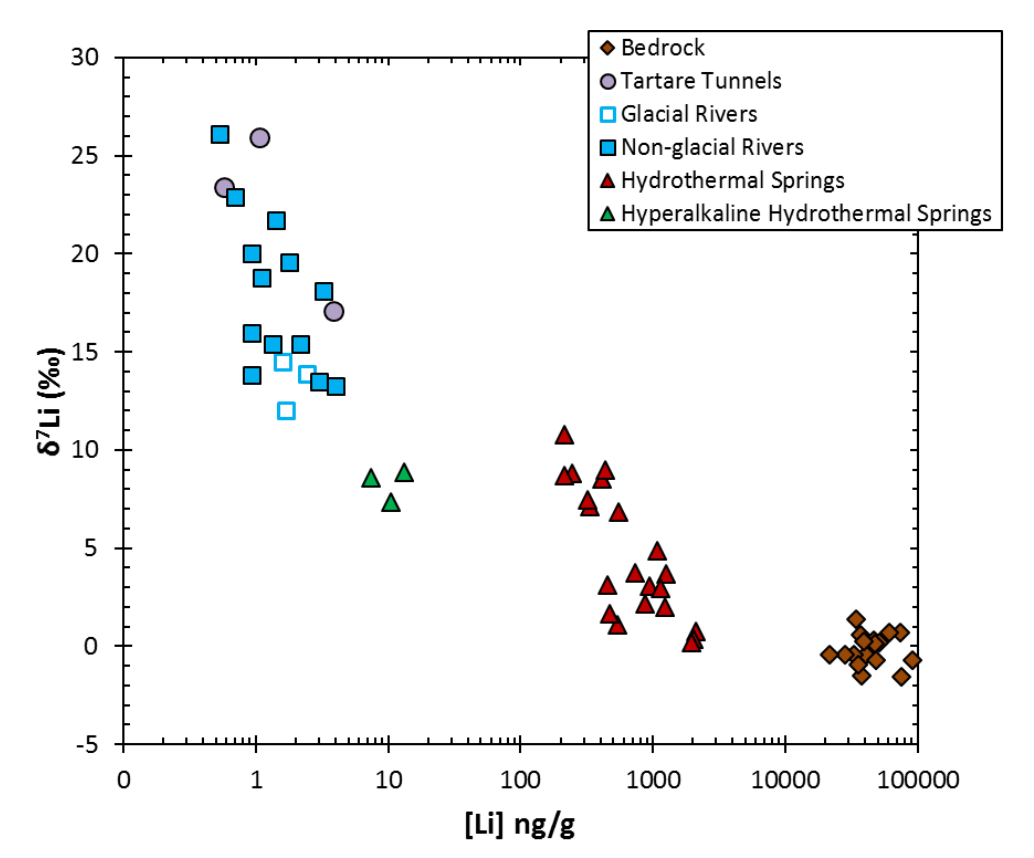


FIGURE 5.2: Lithium concentration against $\delta^7 Li$ value of samples from the Southern Alps. The external reproducibility of the $\delta^7 Li$ analyses is smaller than the size of the symbols.

The Tartare Tunnels fluids have a lithium concentration range of 0.08 μ mol/L to 0.55 μ mol/L and a δ^7 Li signature range of +17.1 to +25.9‰. The metasedimentary-hosted spring waters have a high concentration of Li, which ranges from 30.6 μ mol/L to 303 μ mol/L, and the δ^7 Li values display a wide range from +0.2‰ (bedrock δ^7 Li values) to +10.8‰. The concentration of Li in the ultramafic-hosted hyperalkaline spring waters is much lower than it is in the metasedimentary-hosted spring waters, and ranges from 1.06 μ mol/L to 1.90 μ mol/L, and the δ^7 Li values range from +7.4‰ to +8.9‰. Due to low flow rates, the maximum possible spring water input into the rivers is generally significantly less than 1% for most elements, including lithium, and therefore the spring waters will have a negligible effect upon the lithium isotopic signature of the rivers (see Section 4.4.1). Thus, the spring waters will not be considered when interpreting the weathering system of the Southern Alps in this chapter. The δ^7 Li signature and processes controlling isotopic fractionation of the spring waters will be further discussed in Chapter 7.

There is little variation in $\delta^7 \text{Li}$ value of rock reservoirs compared to fluid reservoirs of the Southern Alps (Figure 5.3). The mica mineral separates, likely to be the source of the majority of Li in the bedrock ([Li] = 68.8-258 µg/g), have $\delta^7 \text{Li}$ signatures that are similar to the bulk bedrock. All river sand size fractions also have similar $\delta^7 \text{Li}$ values to the bedrock, although the clay river sand fraction is at the lower end of this range ($\delta^7 \text{Li}$ = -2.6% to +0.1%). The riverine suspended load is also similar to the bedrock, but again, sits at the lower end of the range of $\delta^7 \text{Li}$ values ($\delta^7 \text{Li}$ = -2.5% to +0.7%). The spring water suspended load shows more variation in $\delta^7 \text{Li}$ value, with samples ranging from -

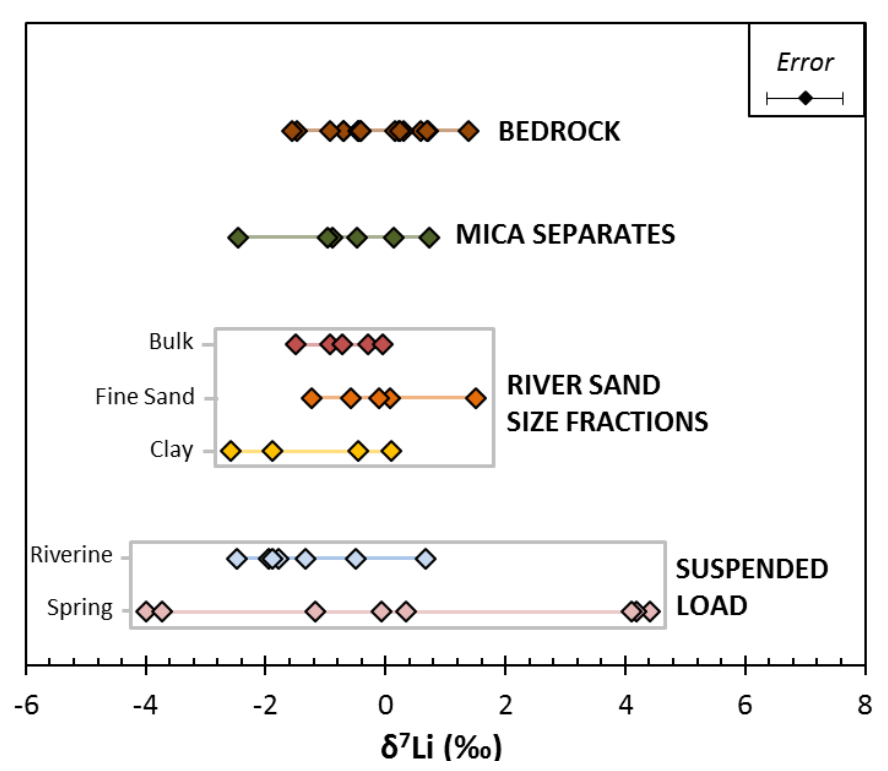


FIGURE 5.3: $\delta^7 \text{Li}$ signatures of the bedrock and weathering products of the Southern Alps. The external reproducibility of the $\delta^7 \text{Li}$ analyses is shown in the top right hand corner of the plot (2σ) .

4.0 to +4.4%, which would suggest that there are processes occurring at depth at higher temperatures that are not affecting rocks at the surface. Due to the negligible contribution of the spring waters to the river chemistry, the spring water suspended load will not be considered when interpreting the weathering system of the Southern Alps in this chapter (see Section 4.4.1). The δ^7 Li of the spring water suspended load will be further discussed with the spring waters in Chapter 7.

5.4 Discussion

5.4.1 Bedrock δ^7 Li

The δ^7 Li composition of bedrock samples collected from the Southern Alps in this study (δ^7 Li = -1.6 to +1.4%; Figure 5.4) are consistent with bedrock analysed from the Southern Alps by Qui et al. (2011) (δ^7 Li = -2.4 to +2.6%). There is little variation in δ^7 Li signature of the bedrock samples. There appears to be no relationship between δ^7 Li signature of the bedrock and Li concentration (Figure 5.4), which is also in agreement with Qiu et al. (2011). Low grade metavolcanics and metasediments from China (Teng et al., 2004) have similar Li concentrations and δ^7 Li signatures to the

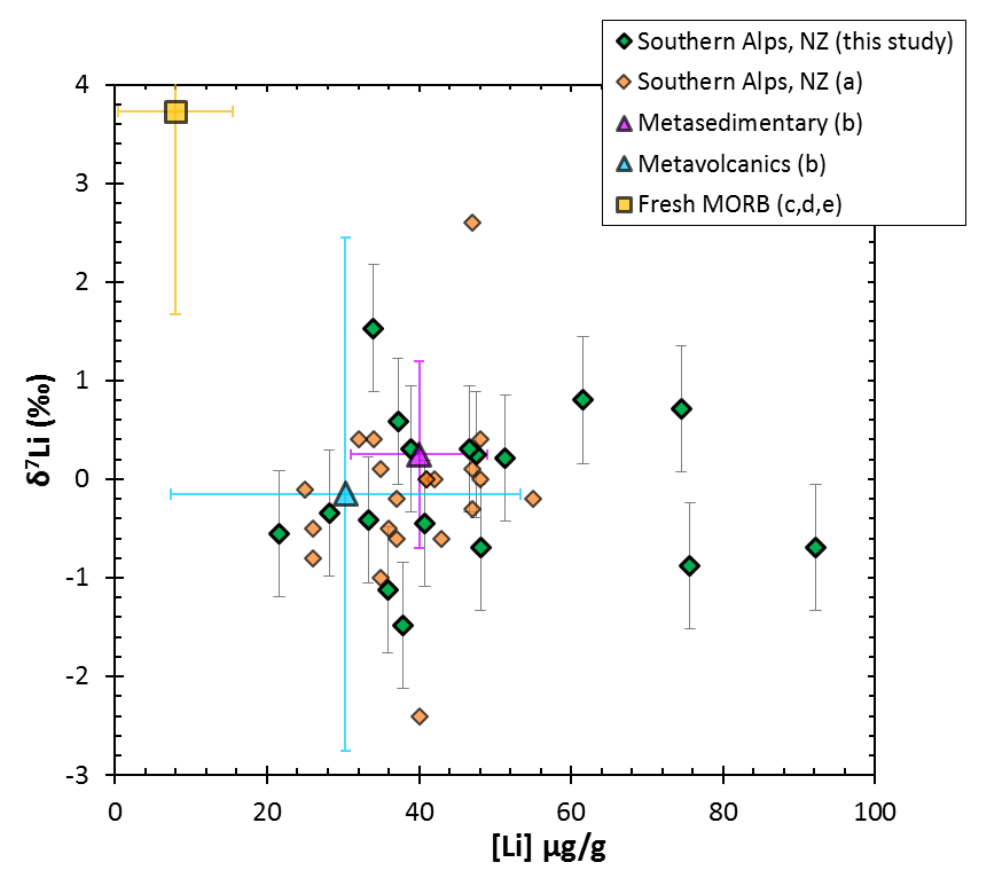


FIGURE 5.4: Lithium concentration against $\delta^7 Li$ value of bedrock from the Southern Alps. Published data sourced from: ^(a)(Qiu et al., 2011), ^(b)(Teng et al., 2004), ^(c)(Moriguti and Nakamura, 1998), ^(d)(Tomascak et al., 1999), ^(e)(Tomascak et al., 2008). The external reproducibility on the $\delta^7 Li$ values from this study is 2σ .

metasedimentary bedrock samples from the Southern Alps. Fresh MORB is more enriched in the heavier lithium isotope and the average δ^7 Li signature is +3.7‰ (Moriguti and Nakamura, 1998; Tomascak et al., 1999; Elliott et al., 2006; Tomascak et al., 2008). This is likely due to the mineralogical composition of the particular lithology. The metasediments of the Southern Alps are rich in biotite and chlorite which generally have δ^7 Li values of ~0‰ (Figure 5.3; Table B.4 in Appendix B). MORB is sourced from the undepleted upper mantle, which has an estimated δ^7 Li signature of approximately +3.5‰, obtained from studies of bulk rock, pyroxene and olivine from mantle xenoliths (Brooker et al., 2004; Seitz et al., 2004; Jeffcoate et al., 2007)

5.4.1.1 Effect of Protolith Lithology

The δ^7 Li signature of the bedrock does not show any variation with differing protolith lithology across the Southern Alps (Figure 5.5). Protolith lithologies show a wide range of lithium concentrations, with metabasalts having the highest concentration of lithium ([Li] = 74.5-92.2 μ g/g). For silicate rocks, these Li concentrations are high compared to fresh basalt ([Li]_{basalt} = ~5-10 μ g/g; Moriguti and Nakamura,1998; Tomascak et al., 1998; Tomascak et al., 1999; Chan and Frey, 2003). The high Li concentration in the metabasalts of the Southern Alps is likely due to hydrothermal alteration through the infiltration of fluids during metamorphism. The quartzofeldspathic metasediments are the most variable of the protolith lithologies in Li concentration (21.6-75.6 μ g/g) and δ^7 Li value (-1.6 to +1.4‰) and are the most common in the Southern Alps (Figure 5.5). The Li

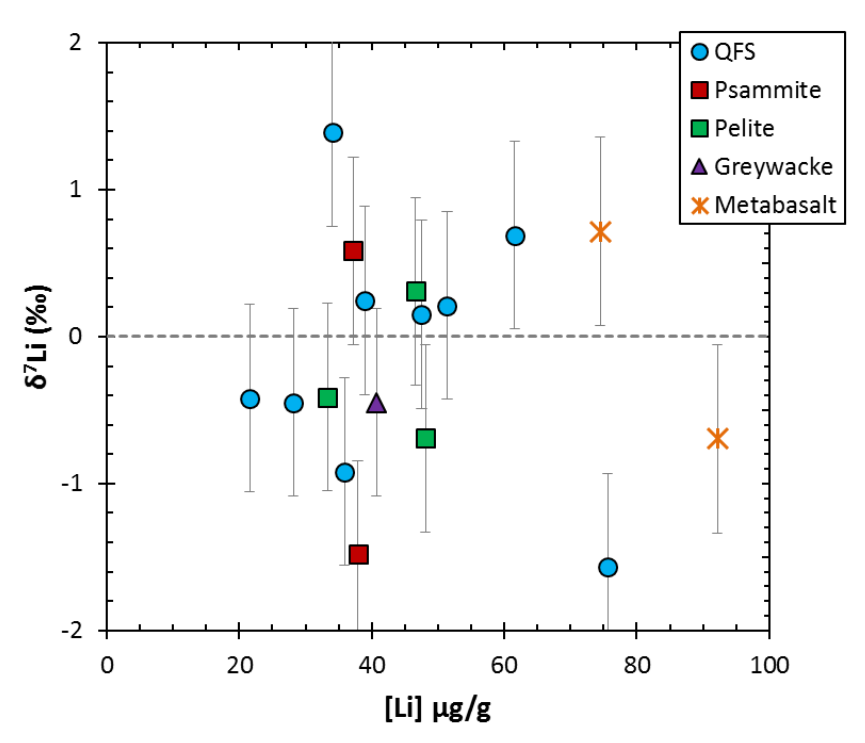


FIGURE 5.5: Lithium concentration against $\delta^7 \text{Li}$ value for various protolith lithologies of the Southern Alps bedrock. QFS = quartzofeldspathic. The external reproducibility on the $\delta^7 \text{Li}$ values is 2σ .

concentration and $\delta^7 Li$ signature of psammite, pelite and greywacke protolith lithologies are all within the range of quartzofeldspathic metasediments. There is no significant heterogeneity in protolith elemental concentration in the bedrock samples analysed from the Southern Alps (see Section 4.3.4), which would explain why little variation is observed in lithium concentration and $\delta^7 Li$ signature across this suite of samples.

5.4.1.2 Effect of Prograde Metamorphism

The lithium concentration and δ^7 Li signature of the bedrock show no variation with metamorphic grade (from unmetamorphosed greywacke to garnet-oligoclase Amphibolite Facies schist) (Figure 5.6). Most prograde metamorphic reactions in metapelites release H₂O, into which Li preferentially partitions over minerals (Brenan et al., 1998), which would suggest that Li concentration should decrease in the bedrock as metamorphic grade increases. However, this effect is not observed in the Southern Alps (Figure 5.6), although it has been observed in a contact aureole under Greenschist Facies conditions (Teng et al., 2007).

Removal of Li from metapelites via Rayleigh distillation during progressive metamorphic dehydration has been suggested to result in only minor Li isotopic fractionation (Wunder et al., 2005), although a shift in δ^7 Li value with increasing metamorphism is not observed in the bedrock of the Southern Alps (Figure 5.6). Thus, low-grade metamorphism has little effect upon bedrock δ^7 Li signatures; similarly, prograde metamorphism, from unmetamorphosed rocks up to eclogite facies, has been observed to only account for a δ^7 Li decrease of $\leq 3\%$ (Marschall et al., 2007).

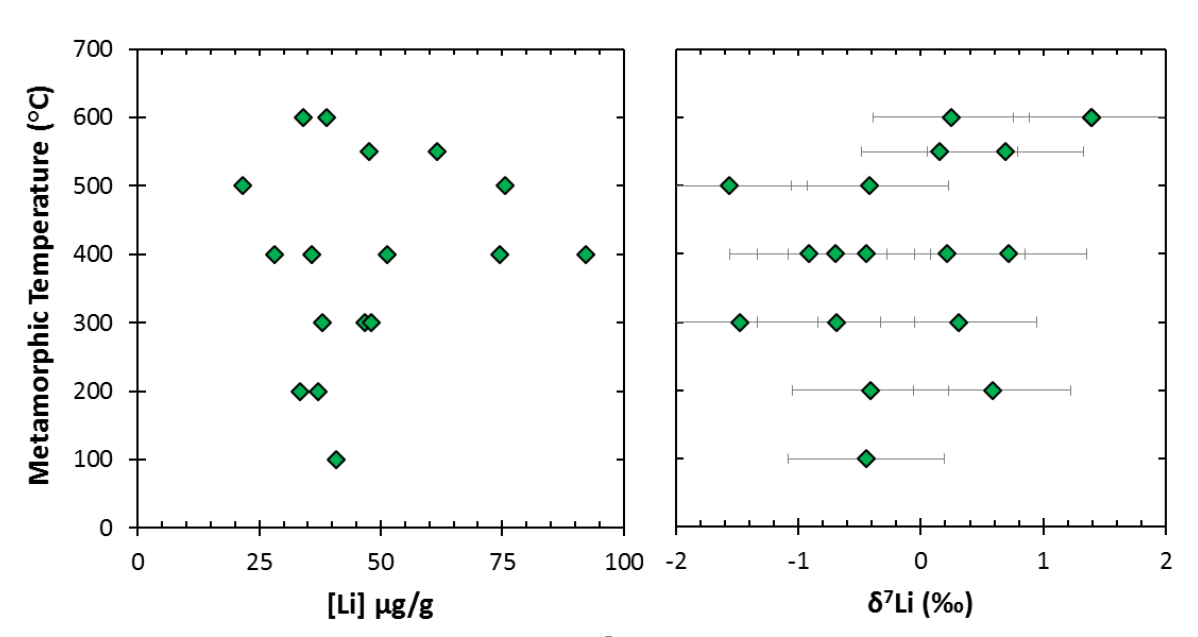


FIGURE 5.6: Lithium concentration and $\delta^7 \text{Li}$ value verses increasing metamorphic temperature of the Southern Alps bedrock. The theoretical metamorphic temperature of the metamorphic grade has been estimated in previously published work (Mortimer, 1993; Mortimer, 2000; Pitcairn, 2004), with an error of ± 50 °C. The external reproducibility on the $\delta^7 \text{Li}$ values is 2σ .

To explore the effect of catchment bedrock upon the δ^7 Li signature of the rivers draining the Southern Alps, the metamorphic grade of the bedrock can be plotted against δ^7 Li signature for the bedrock and river water samples (Figure 5.7). There is no observed relationship between δ^7 Li signature of the river waters with increasing metamorphic grade of the bedrock. Thus, in the Southern Alps, catchment lithology and metamorphic grade do not appear to have any effect upon the δ^7 Li value of the river waters.

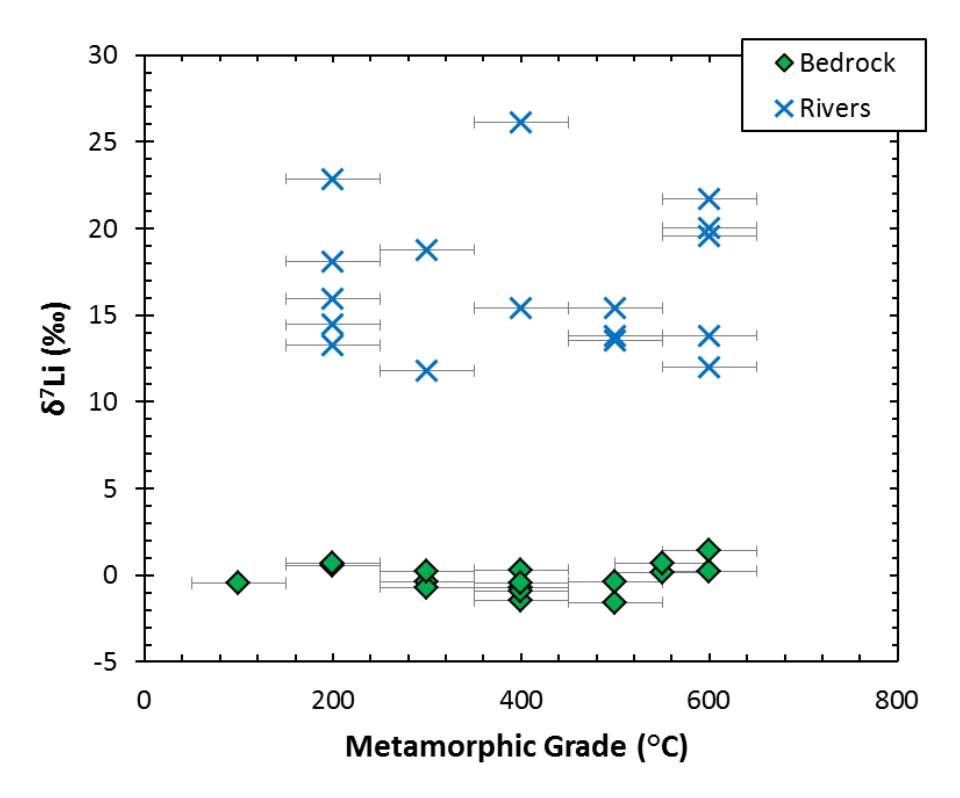


FIGURE 5.7: Theoretical metamorphic temperature against $\delta^7 Li$ value of the bedrock and the dissolved load in the river waters of the Southern Alps. The metamorphic grade of the river catchments was estimated by using ArcGIS to determine the location of the catchment and the dominant metamorphic grade. The theoretical metamorphic temperature of the metamorphic grade has been estimated in previously published work (Mortimer, 1993; Mortimer, 2000; Pitcairn, 2004), with an error of ± 50 °C. The external reproducibility of the $\delta^7 Li$ analyses is smaller than the size of the symbols.

5.4.1.3 Breakdown of Bedrock in the Weathering System

The relationship between Li concentration and δ^7 Li value for the rock particulates analysed in this study (river sand size fractions, riverine suspended loads and mica mineral separates from the bedrock) and the bedrock of the Southern Alps can be seen in Figure 5.8. Bulk river sand and fine river sand all plot within range of the bedrock.

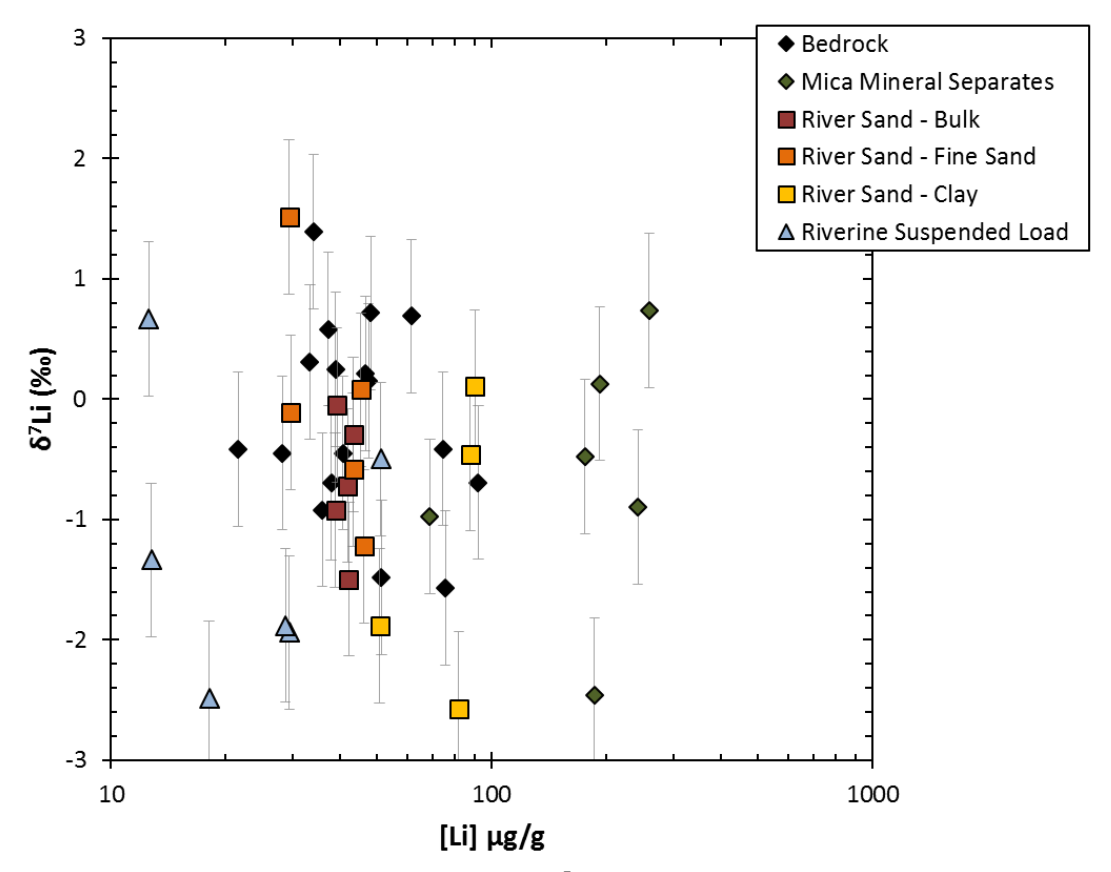


FIGURE 5.8: Li concentration against $\delta^7 \text{Li}$ value of the bedrock and weathering products of the Southern Alps weathering system. The external reproducibility on the $\delta^7 \text{Li}$ values is 2σ .

TABLE 5.1: A mass balance defining the proportion of lithium in the bedrock that is derived from mica minerals. The Li concentration values for biotite, muscovite and chlorite are from this study. The Li concentration values for quartz (Dennen, 1966; Vorontsov and Lin, 1966; Dennen, 1967) and plagioclase (Bindeman et al., 1998) were sourced from the literature. The major mineral proportions in the bedrock were estimated for a high metamorphic grade quartzofeldspathic rock of the Otago/Alpine schist of Greenschist to Amphibolite Facies (Craw, 1984; Mortimer and Roser, 1992; Pitcairn, 2004; Menzies et al., 2014).

	Li Concentration (µg/g)	Mineral in Rock (%)	Li from Mineral (µg/g)	Li in Rock from Mineral (%)
Bulk Bedrock	42.6	100		
Biotite	217	10	21.7	51.0
Muscovite	68.8	10	6.88	16.2
Chlorite	186	3	5.58	13.1
Quartz	12.5	60	7.50	17.6
Plagioclase	5.00	17	0.85	2.00
SUM		100	42.5	99.8

The mica minerals separated from bedrock samples of the Southern Alps have a high concentration of Li (68.8-259 μ g/g), but generally fall within the same range of δ^7 Li values as the bulk bedrock (except for chlorite which has a light δ^7 Li value of -2.5‰; Figure 5.8). A mass balance was used to define the proportion of lithium in the bedrock that is derived from each of the major mineral constituents (Table 5.1). Around 80% of lithium in the bedrock is sourced from micaceous minerals, and as there is little difference between the δ^7 Li value of the bedrock and micas, this would suggest that micas have a significant influence upon the δ^7 Li composition of the bedrock.

In sediments that are clay-rich, lithium is predominantly hosted in smectite, illite and chlorite clay minerals (Chan et al., 1994; Chan and Kastner, 2000). The clay fraction of the river sand has relatively high concentrations of Li (50.8-90.3 µg/g) compared to the bedrock ([Li] = 21.6-75.6 µg/g), and the range of δ^7 Li values are slightly lower (-2.6 to +0.1‰) than that of the bedrock (-1.6 to +1.4‰). It would be expected that if these clays were the product of secondary mineral formation, they would have low δ^7 Li values, as the formation of secondary minerals during weathering preferentially sequesters ⁶Li (Huh et al., 1998; Huh et al., 2001). However, only one clay fraction (from Sheil's Creek) falls well below the δ^7 Li range for the Southern Alps bedrock (δ^7 Li = -2.6‰). This may indicate that the other clay fractions included very fine rock material (as no disaggregate was used to separate the clays; see Section 3.2), and/or some of the clays present are detrital.

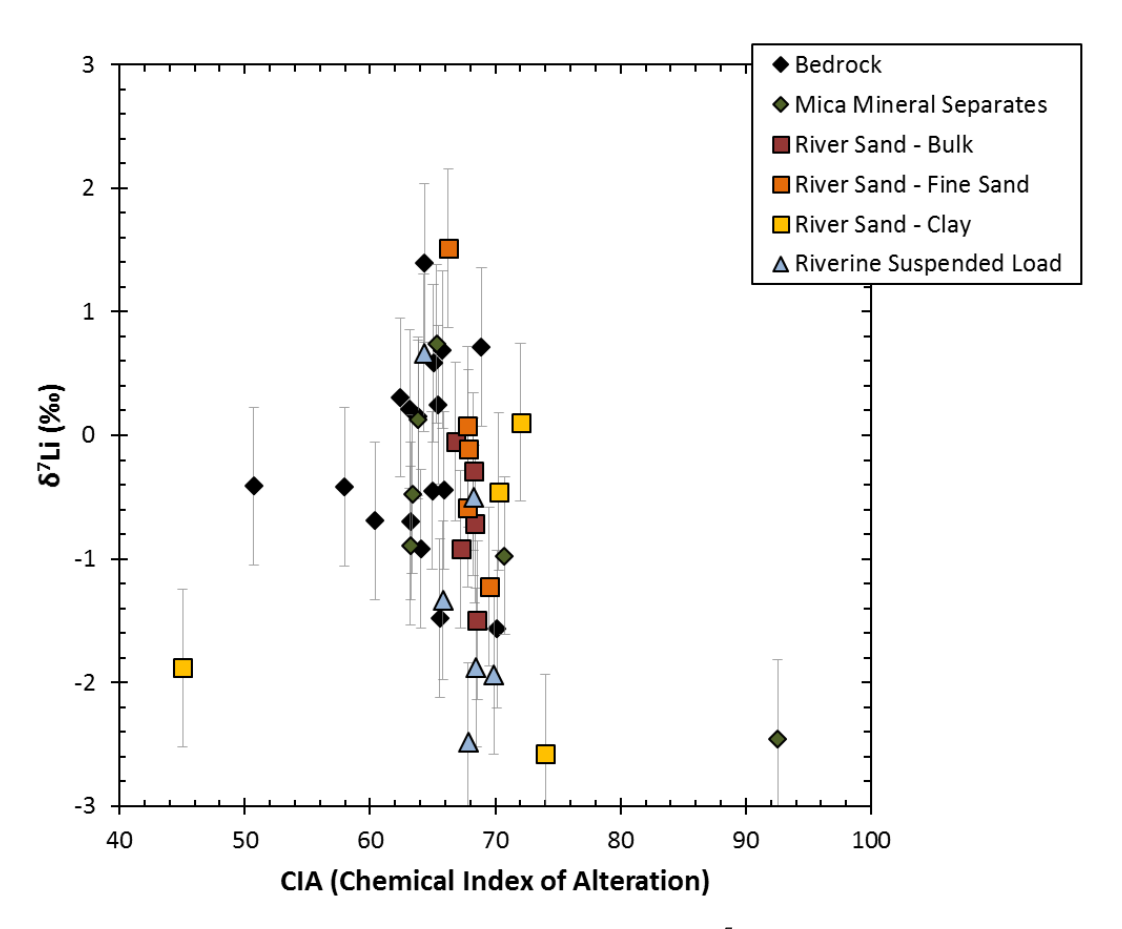


FIGURE 5.9: CIA (chemical index of alteration) against δ^7 Li value of the bedrock and weathering products of the Southern Alps. The external reproducibility on the δ^7 Li values is 2σ .

The riverine suspended load has a large variation in Li concentration (12.6-51.1 μ g/g). The suspended load samples are slightly isotopically lighter (δ^7 Li = -2.5 to +0.7‰) than the bedload (δ^7 Li = -1.5 to +0.0‰), which is consistent with previous work (Kısakűrek et al., 2005; Pogge von Strandmann et al., 2006; Pogge von Strandmann et al., 2010). This reflects the preferential uptake of 6 Li into secondary alteration products, which are a component of the suspended load.

CIA (chemical index of alteration; detailed in Chapter 4) values can be calculated to ascertain the degree of weathering that has taken place; high CIA values are usually indicative of greater weathering (Nesbitt and Young, 1982). The CIA of the bedrock and various rock particulate samples from this weathering system do not correlate with δ^7 Li values (Figure 5.9), which suggests that chemical weathering is insufficient to cause any significant change in the δ^7 Li composition of the rocks. However, the degree of chemical weathering does have an effect upon the Li isotopic composition of the river waters; this will be discussed in Section 5.4.3.

5.4.2 Groundwater (Tartare Tunnels) $\delta^7 Li$

The groundwater fluids have infiltrated through the bedrock at low temperature to reach fractures in the roof of the Tartare Tunnels (Menzies, 2012). The groundwaters have a similar lithium concentration range (0.08-0.55 μ mol/L) and δ^7 Li range (δ^7 Li = +17.1 to +25.9‰) to the river waters of the Southern Alps. There is evidence for lithium concentration increasing with increasing tunnel overburden, which likely reflects increased water-rock residence time (Figure 5.10 A). However, with only 3 data points, this relationship can only be speculated upon.

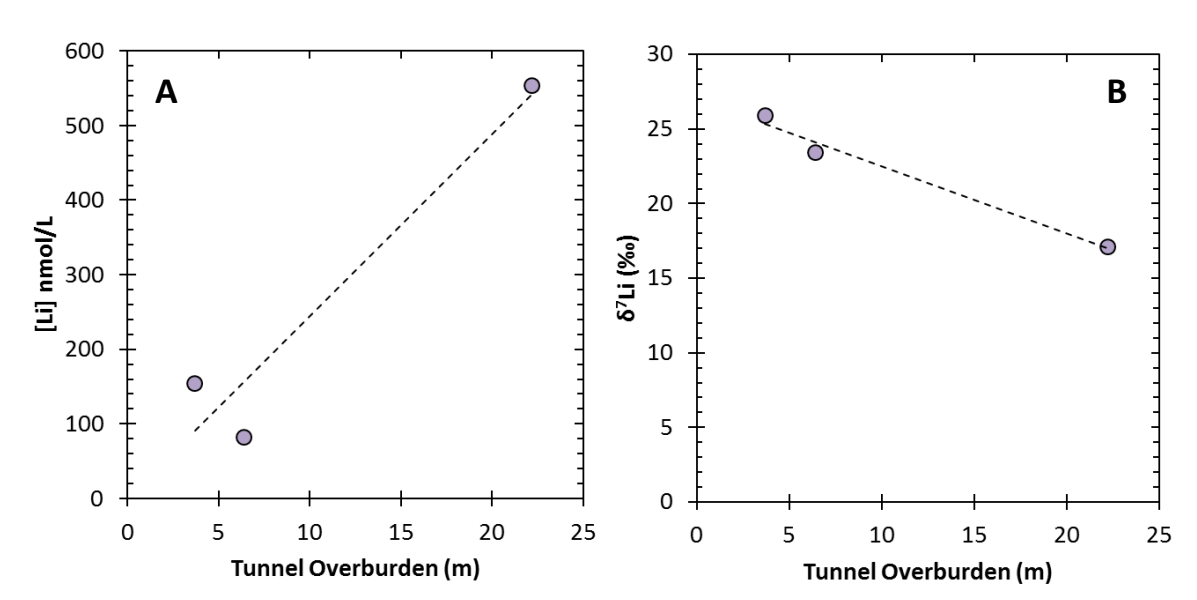


FIGURE 5.10: Increasing tunnel overburden of the Tartare Tunnels against Li concentration (A) and $\delta^7 Li$ value (B) of groundwater samples collected from the Tartare Tunnels. The external reproducibility of the $\delta^7 Li$ analyses is smaller than the size of the symbols.

Reactions at low temperature include the formation of secondary alteration products in the form of clays. This process isotopically fractionates Li, as 6 Li preferentially goes into the secondary alteration products and 7 Li remains in solution (Huh et al., 2001), resulting in heavy δ^7 Li signatures of the groundwaters. Groundwater δ^7 Li values decrease with increasing tunnel overburden (Figure 5.10 B), which suggests that weathering becomes more congruent, as increased water/rock interaction results in the groundwaters becoming oversaturated with respect to secondary phases, inhibiting the formation of secondary minerals. In addition, it is possible that secondary phases are being chemically dissolved and this process is releasing 6 Li into solution.

The groundwater sample that travelled through the highest amount of tunnel overburden (i.e. longest flow path) is the only sample from the Tartare Tunnels that plots within range of other groundwater studies (Négrel et al., 2012; Meredith et al., 2013; Pogge von Strandmann et al., 2014; Liu et al., 2015), as shown in Figure 5.11. The other groundwater samples from the Tartare Tunnels that infiltrated through much less bedrock plot closer to the average for world rivers ([Li] = \sim 0.35 μ mol/L; δ 7Li = \sim 22.4‰; Huh et al., 1998).

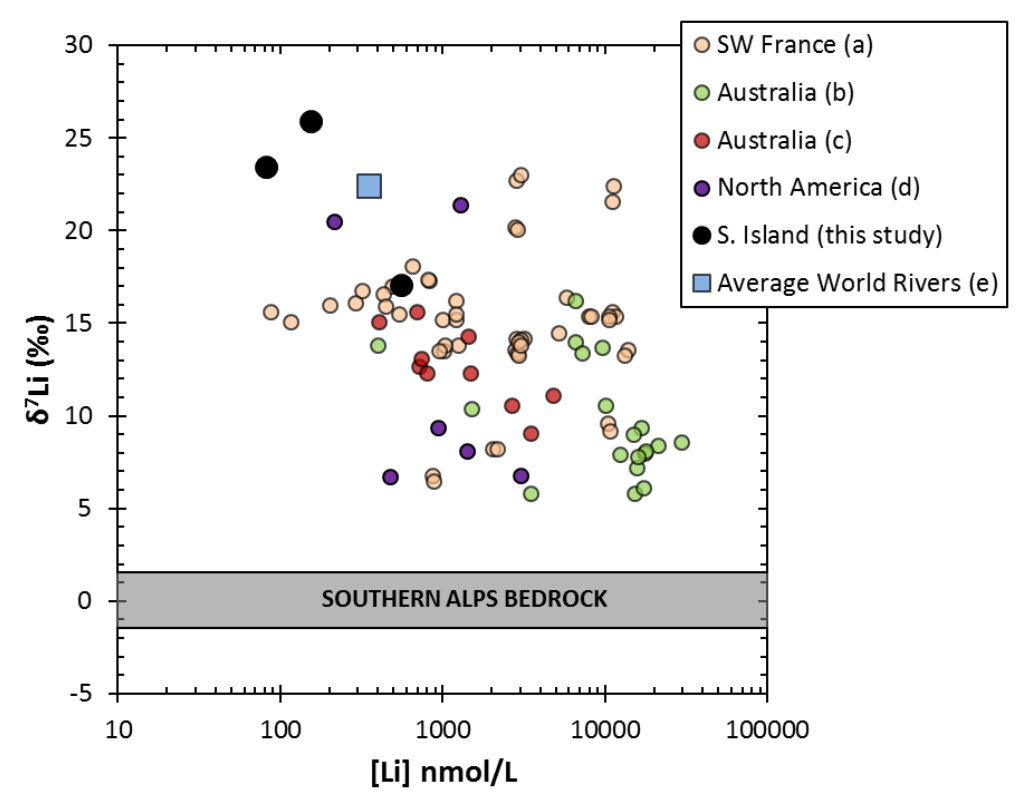


FIGURE 5.11: Lithium concentration against $\delta^7 Li$ value of the dissolved load in the groundwater samples collected from the Tartare Tunnels, with comparison to global published data. Data sourced from: ^(a)(Négrel et al., 2012), ^(b)(Meredith et al., 2013), ^(c)(Pogge von Strandmann et al., 2014), ^(d)(Liu et al., 2015), ^(e)(Huh et al., 1998). The grey band represents the range of bedrock $\delta^7 Li$ values across the Southern Alps. The external reproducibility of the $\delta^7 Li$ analyses is smaller than the size of the symbols.

5.4.3 River Water $\delta^7 Li$

The river waters draining the Southern Alps are within range of lithium concentration and $\delta^7 Li$ value observed for global rivers in previously published work (Figure 5.12). However, the Southern Alps river waters are at the higher end of lithium concentration ([Li] = 0.10-0.46 μ mol/L) and the lower end of the $\delta^7 Li$ range ($\delta^7 Li = +11.8$ to +26.1%).

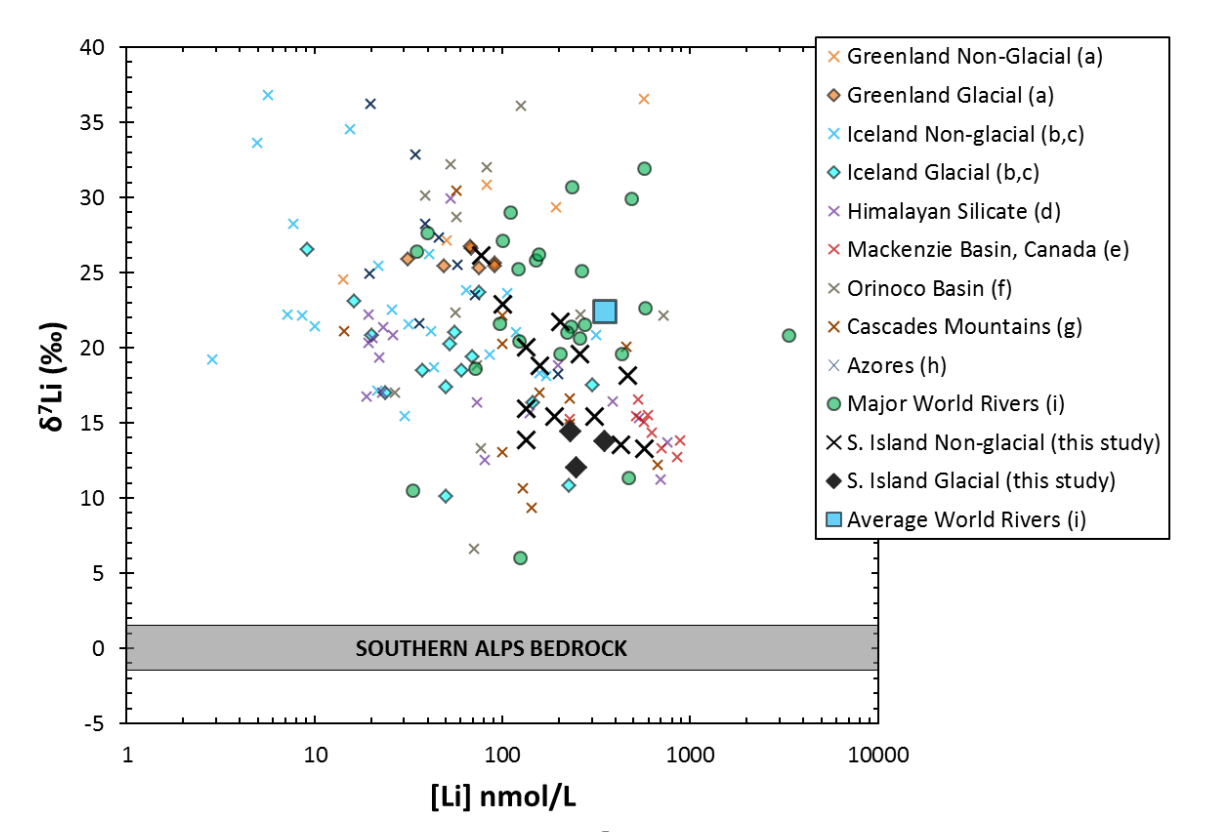


FIGURE 5.12: Lithium concentration against $\delta^7 Li$ value of the dissolved load in the river waters draining the Southern Alps, with comparison to global published river data. Data sourced from: ^(a)(Wimpenny et al., 2010b), ^(b)(Vigier et al., 2009), ^(c)(Pogge von Strandmann et al., 2006), ^(d)(Kısakűrek et al., 2005), ^(e)(Millot et al., 2010), ^(f)(Huh et al., 2001), ^(g)(Liu et al., 2015), ^(h)(Pogge von Strandmann et al., 2010), ⁽ⁱ⁾(Huh et al., 1998). The grey band represents the range of bedrock $\delta^7 Li$ values across the Southern Alps. The external reproducibility of the $\delta^7 Li$ analyses is smaller than the size of the symbols.

5.4.3.1 Effect of Secondary Mineral Formation

During weathering, bedrock disintegrates and dissolution of primary minerals occurs, followed by the formation of secondary alteration products. Lithium is a fluid-mobile element and is incorporated into these secondary products, which results in fractionation of lithium isotopes. This process preferentially retains the light 6 Li isotope in secondary minerals and leaves the heavy 7 Li isotope in solution (Huh et al., 2001). To determine the degree of retention of Li in secondary minerals, the relationship between ratios of Li/Na of the dissolved load and Li/Na of weathered rock particulates against δ^7 Li value of the river waters can be used as an index of Li mobility in relation to Na, which

is rarely retained in secondary minerals (Figure 5.13; Millot et al., 2010). The fraction of Li remaining in solution relative to Na (f_{Li}) is defined by:

$$f_{\text{Li}} = \frac{\text{(Li/Na)}_{\text{dissolved}}}{\text{(Li/Na)}_{\text{rock}}}$$
 (Eq. 5.1)

Both bedload and suspended load samples were used to determine the Li/Na ratio of the rock. If $f_{\rm Li}$ = 1, then chemical weathering is congruent (Millot et al., 2010). However, the river waters that have $\delta^7 {\rm Li}$ values of >17‰ all have $f_{\rm Li}$ values of less than 1, which indicates that Li is retained in secondary minerals (Figure 5.13). XRD analysis (discussed in Chapter 4) shows that illite, chlorite and minor kaolinite clay minerals are present in river sand clays sampled from the rivers draining the Southern Alps, which all readily incorporate lithium. Experimental data indicates that Li isotopic fractionation during clay mineral formation is caused by surface complexation reactions associated with a change in Li coordination chemistry or by Li substitution into crystal lattices (Zhang et al., 1998; Pistiner and Henderson, 2003; Vigier et al., 2008).

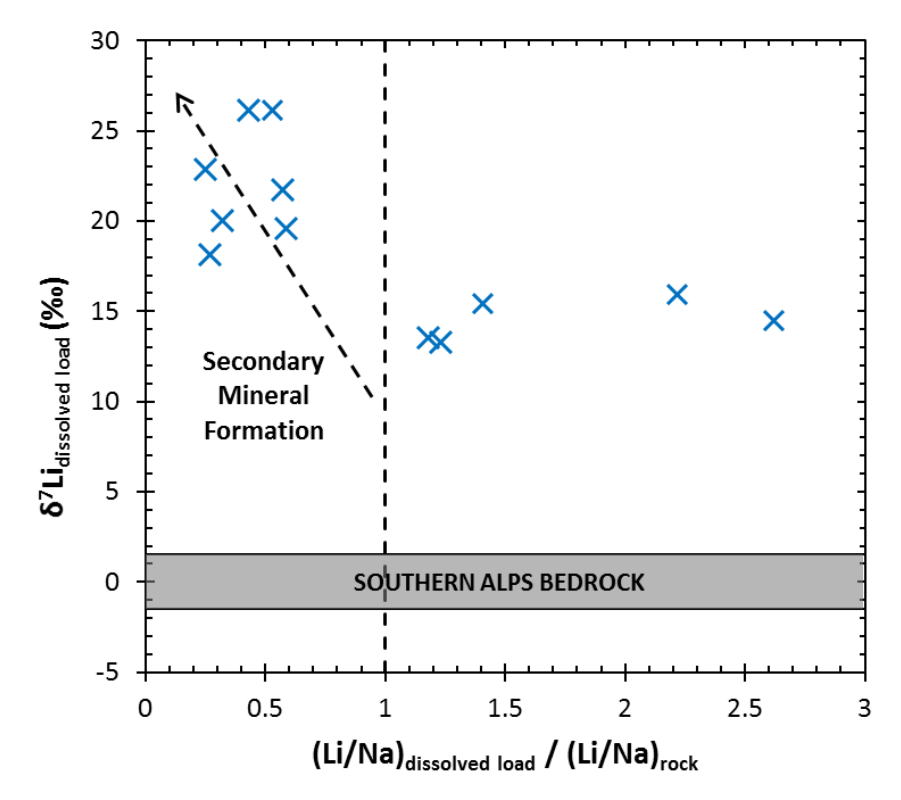


FIGURE 5.13: Ratios of Li/Na in the dissolved load and Li/Na in weathered rock particulates was calculated and plotted against $\delta^7 Li$ value of the dissolved load in the Southern Alps. The grey band represents the range of $\delta^7 Li$ values for bedrock across the Southern Alps. The external reproducibility of the $\delta^7 Li$ analyses is smaller than the size of the symbols.

Some river waters (glacial and non-glacial) draining the Southern Alps have f_{Li} values greater than 1. There does not appear to be any viable reason as to why these rivers have f_{Li} values greater than 1, other than that they have the highest Li/Na ratios in the dissolved load. This is unexpected, and

may indicate that these river waters are not in equilibrium with the suspended particles or bedload, meaning that they are not representative of the river water sample collected. There is little variation in the chemical composition or $\delta^7 \text{Li}$ signature of the bedrock and its weathering products, and so variations in Li/Na_{rock} are unlikely to cause the $f_{\text{Li}} > 1$ values (Figure 5.13). In addition, a single-spot measurement of bedload/suspended sediment is unlikely to always be representative of a river water sample that may have travelling a long distance downstream to reach the sampling location. When $f_{\text{Li}} = 1$ (i.e. when chemical weathering should be congruent), riverine $\delta^7 \text{Li}$ should be 0%, however this is not evident in Figure 5.13. This is because chemical weathering is rarely truly congruent, and congruent weathering is not observed in the Southern Alps in this study. It is possible that $f_{\text{Li}} = 1$ in tropical watersheds with thick and heavily chemically weathered soils, where chemical weathering is more congruent.

5.4.3.2 Effect of Rainfall and Erosion

Lithium concentration and δ^7 Li composition of river waters is dependent upon chemical weathering intensity and formation of secondary alteration products during weathering and transport (Stallard and Edmond, 1981; James and Palmer, 2000; Kısakűrek et al., 2005). The overall chemical weathering intensity is strongly affected by climatic effects, such as temperature and meteoric precipitation (e.g. White and Blum, 1995). These factors can also affect the erosion rate; mechanical breakdown of the bedrock increases surface area, leading to increased potential for chemical weathering. Rapid mountain uplift, which can lead to the development of high relief and glacier formation, can also lead to rapid erosion rates, creating new weathered surfaces and increasing the potential for chemical weathering.

Studies focusing on the relationship between physical erosion and chemical weathering rates, and the subsequent effect upon riverine $\delta^7 Li$ values, have drawn different conclusions. An increase in seawater $\delta^7 Li$ over the last 40 Myr has been attributed to increased denudation from the Himalayan uplift and increased incongruent weathering (formation of secondary minerals) in the rapidly eroding mountain belt (Misra and Froelich, 2012). Several problems have been noted with this interpretation. First of all, the use of 'weathering-limited' and 'transport-limited' regimes are used in connection with chemical weathering, when these terms are strictly only applied to physical erosion rates. Chemical erosion fluxes should be described in terms of 'supply-limited' and 'kinetic-limited' regimes (see Section 1.6 for further definition of these terms). Secondly, Misra and Froelich (2012) suggest that incongruent weathering (incomplete weathering and the formation of secondary minerals; high riverine $\delta^7 Li$ values) is occurring in 'kinetically-limited' regimes, and that congruent weathering (complete weathering with no secondary mineral formation; low riverine $\delta^7 Li$ values) is occurring in 'supply-limited' regimes. However, rivers draining the Himalayas have $\delta^7 Li$ values lower than the riverine global average (Kısakűrek et al., 2005), implying that Himalayan weathering

is more congruent, which should have resulted in Himalayan uplift driving seawater δ^7 Li to lower values rather than higher (Pogge von Strandmann and Henderson, 2015).

The Southern Alps form an asymmetric mountain belt, which provides a barrier to the prevailing westerly winds, producing a rain shadow to the east (Henderson, 1993; Mosley and Pearson, 1997). The Main Divide forms the highest point along this mountain chain, separating the eastern and western climatic regimes. Rainfall is extremely heavy west of the Main Divide (~12 m/yr) and low to the east (<1 m/yr; Griffiths and McSaveney, 1983; Henderson and Thompson, 1999). Pogge von

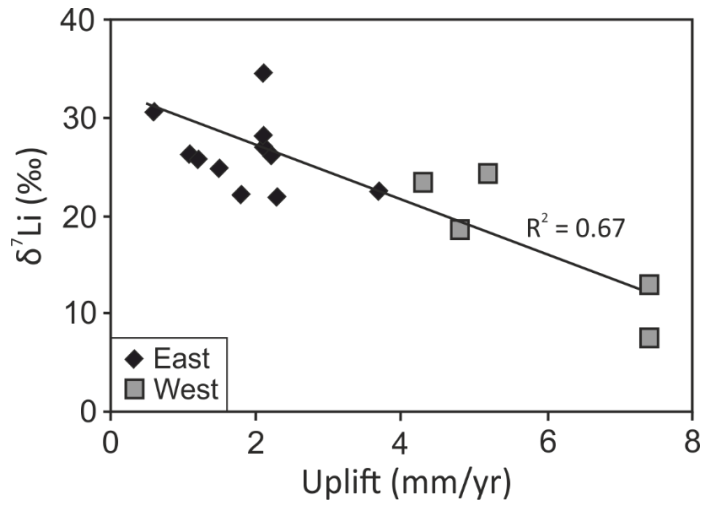


FIGURE 5.14: Riverine $\delta^7 \text{Li}$ values against uplift rates for rivers draining the Southern Alps on South Island, New Zealand (Pogge von Strandmann and Henderson, 2015). Uplift rates for each sample were taken from a digital elevation model of the Southern Alps (Robinson et al., 2004).

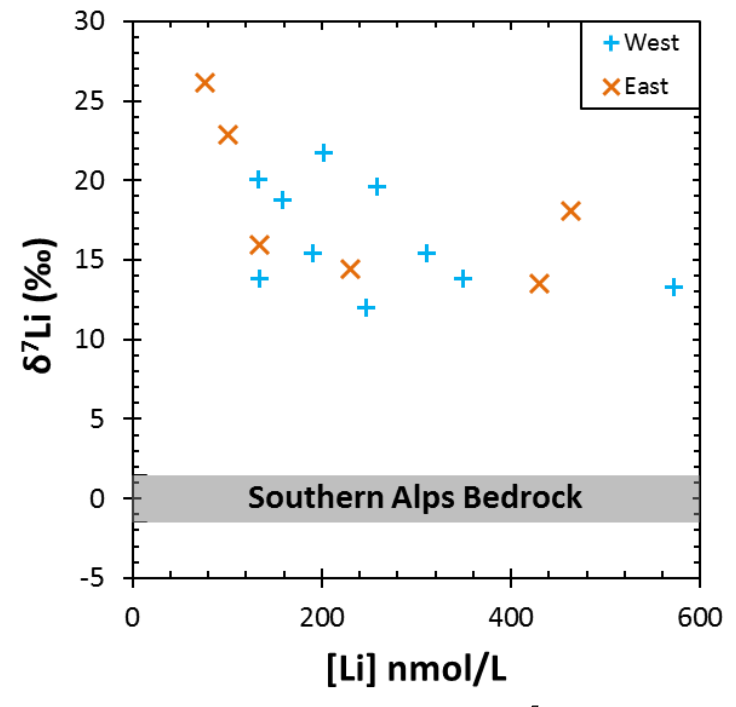


FIGURE 5.15: Lithium concentration against $\delta^7 Li$ value of river waters draining the east and west of the Main Divide. The grey band represents the range of bedrock $\delta^7 Li$ values across the Southern Alps. The external reproducibility of the $\delta^7 Li$ analyses is smaller than the size of the symbols.

Strandmann and Henderson (2015) assessed the relationship between riverine $\delta^7 Li$ values and uplift rate (Figure 5.14), using data from the Southern Alps on South Island, New Zealand, which indicated that there is a negative correlation between riverine $\delta^7 Li$ values and increasing uplift rates. This suggests that weathering is more incongruent (more secondary mineral formation driving $\delta^7 Li$ to higher values) in the lowlands than in the rapidly uplifting and eroding mountainous regions, where secondary mineral formation is relatively inhibited. This is consistent with the relatively low $\delta^7 Li$ values of the Himalayan rivers (Kısakűrek et al., 2005). As it is known that seawater $\delta^7 Li$ has risen over the last 40 Myr (Misra and Froelich, 2012), which coincides with the uplift of the Himalayas, it was suggested that the dominant effect upon seawater $\delta^7 Li$ is instead Li isotopic fractionation occurring in the floodplains (significant retention of Li by clays), and it is possible that this process is linked to the increased supply of material transported in rivers due to rapid uplift and erosion (Pogge von Strandmann and Henderson, 2015). Thus, it was suggested that Li isotopes are a record of the efficiency of continental weathering in driving CO_2 removal, instead of a measure of the total amount of CO_2 removal (Pogge von Strandmann and Henderson, 2015).

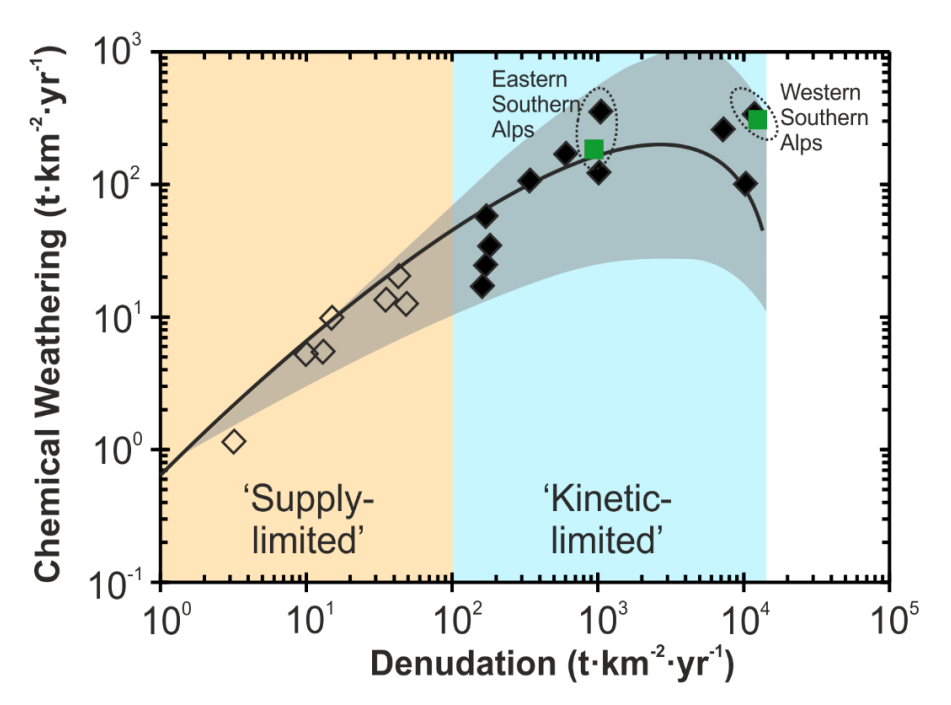


FIGURE 5.16: Physical denudation rate against total chemical weathering rate of climate-adjusted global river water data. The black symbols represent data compiled by West et al. (2005) and the green symbols represent data from this study using physical denudation rates for the Southern Alps from Jacobsen and Blum (2003). The solid black line represents the modelled trends for 'supply-limited' and 'kinetic-limited' regimes, and an order of magnitude increase or decrease in particle diameter size for this model is shown by the grey band (Gabet and Mudd, 2009).

However, the data from this study does not support the findings of Pogge von Strandmann and Henderson (2015), as no clear difference in riverine δ^7 Li signature is observed east and west of the Main Divide (Figure 5.15). Rivers on South Island, New Zealand, are short and have little in the way of floodplains, and therefore chemical weathering is unlikely to have been high enough to drive δ^7 Li

to significantly higher values. In addition, physical erosion may be lower in the east than the west, but it is still high on a global scale (Figure 5.16). Rivers in the west have been subject to rapid uplift and erosion, which should inhibit secondary mineral formation ('kinetic-limited'), leading to lower riverine δ^7 Li values. However, the δ^7 Li values of rivers to the west do not approach that of the bedrock, which may be due to very high rainfall rates (Griffiths and McSaveney, 1983; Henderson and Thompson, 1999), which would promote leaching. Calculations have also shown that silicate chemical weathering rates are similar east and west of the Main Divide (see Section 4.4.6). In addition, secondary clays have been found in both eastern and western rivers (see Section 4.4.4), indicating that secondary mineral formation (incongruent weathering) has occurred on both sides of the Main Divide. A negative correlation between riverine δ^7 Li and uplift rate should be observed, suggesting more dissolution of primary rock is occurring relative to secondary mineral formation (Pogge von Strandmann and Henderson, 2015), but this relationship cannot be observed from rivers on the South Island analysed in this study due to the nature of the weathering environment in the Southern Alps.

The precision of the uplift rates used to plot against δ^7 Li values (Pogge von Strandmann and Henderson, 2015; Figure 5.14) is limited (Robinson et al., 2004). Although this model acts as a good guide to the relative uplift rate in the region, it is a simplified representation of the complex tectonic deformation of the South Island (Robinson et al., 2004). The riverine δ^7 Li values are really plotted against exhumation and denudation, and there is also a time dependence that needs to be considered (Lamb and Bibby, 1989; Ota et al., 2010). In addition, a significant amount of sediment delivery is landslide/debris flow derived, which is driven by rainfall and earthquake ground shaking (Hovius et al., 1997; Bull and Brandon, 1998; Korup et al., 2004).

Thus, it would be more appropriate to instead observe the relationship between $\delta^7 \text{Li}$ values and erosion rate and rainfall (Figure 5.17). The rainfall data is based on the period 1971-2000 (Tait et al., 2006), and was recorded by NIWA (National Institute of Water and Atmospheric Research Limited in Christchurch, New Zealand). The erosion rate is derived from a grid of suspended sediment yield (recorded by NIWA), calculated as a mean ground lowering rate, assuming an average crustal density of 2.65 t/m³ (Cox et al., 2012). Atmospheric inputs to the elemental concentration of the rivers draining the Southern Alps were applied in Section 4.3.1. Although we know the $\delta^7 \text{Li}$ composition of seawater, we do not know the $\delta^7 \text{Li}$ composition of the rain water over the Southern Alps. Therefore, it would not be appropriate in this case to apply an atmospheric input $\delta^7 \text{Li}$ correction to the river waters in this study.

Although rivers east of the Main Divide generally have lower erosion rates and amounts of rainfall, which is what would be expected, the riverine $\delta^7 \text{Li}$ values appear to show little correlation with rainfall and erosion rate (Figure 5.17). High mechanical erosion rates should inhibit the formation of secondary minerals, resulting in lower riverine $\delta^7 \text{Li}$ values. However, the highest erosion rates are in

the west where rainfall is very high (up to 8 m/yr; Figure 5.17), which would increase the potential for chemical weathering by increasing leaching. The relationships shown in Figure 5.17 are not linear, thus suggesting that climate has an indirect influence upon Li isotopic fractionation.

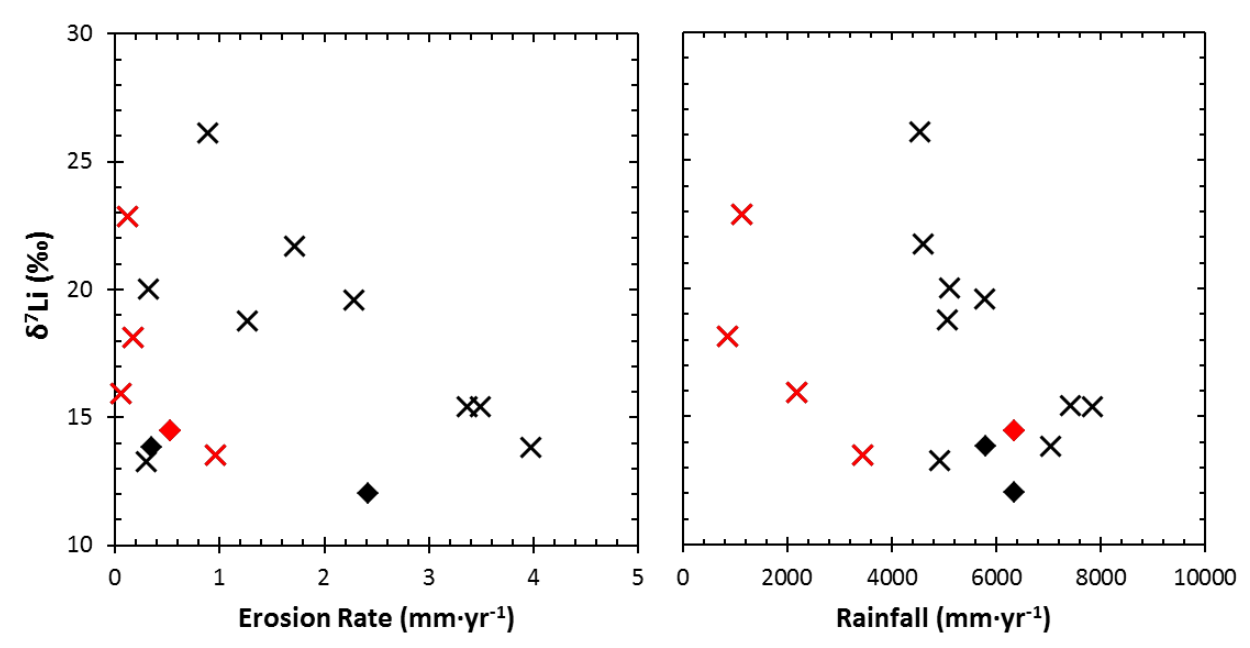


FIGURE 5.17: Erosion rate and rainfall against $\delta^7 Li$ values in the dissolved load of the Southern Alps. The crosses represent the non-glacial rivers and the diamonds represent the glacial rivers. The black symbols represent rivers west of the Main Divide and the red symbols represent rivers east of the Main Divide. The rainfall data was recorded by NIWA (Tait et al., 2006) and the erosion rates were calculated using sediment yield values recorded by NIWA (Cox et al., 2012). The external reproducibility of the $\delta^7 Li$ analyses is smaller than the size of the symbols.

5.4.3.3 Effect of Glaciation

The rivers draining temperate glaciers in the Southern Alps have distinctly lower $\delta^7 \text{Li}$ values than glacial rivers at higher latitudes (Figure 5.18). The glacial rivers in the Southern Alps have lower $\delta^7 \text{Li}$ signatures ($\delta^7 \text{Li} = +12.0$ to +14.5%) than glacial rivers in Iceland ($\delta^7 \text{Li} = +16.3$ to +36.8%; Pogge von Strandmann et al., 2006) and Greenland ($\delta^7 \text{Li} = +25.3$ to +26.7%; Wimpenny et al., 2010; Figure 5.18). The chemical dissolution rate underneath the glaciers in the Southern Alps must be significantly higher than in Iceland and Greenland, as the glacial river waters in the Southern Alps are oversaturated with respect to secondary mineral phases (Section 5.4.4). By contrast, XRD analyses show little evidence for the formation of clay minerals in glacial rivers in Greenland (Wimpenny et al., 2010b). Instead, the lithium isotopic fractionation observed in these glacial rivers was attributed to the formation of Fe-oxyhydroxides, as result of sulphide oxidation under the ice (Wimpenny et al., 2010b). This process is not occurring under the glaciers of the Southern Alps, as these glacial rivers do not have high SO_4^{2-} concentrations, with respect to Cl⁻. This suggests that oxidation of sulphides, and subsequent Fe-oxyhydroxide formation, is not an important mechanism of Li isotopic fractionation in the glacial river waters draining the Southern Alps.

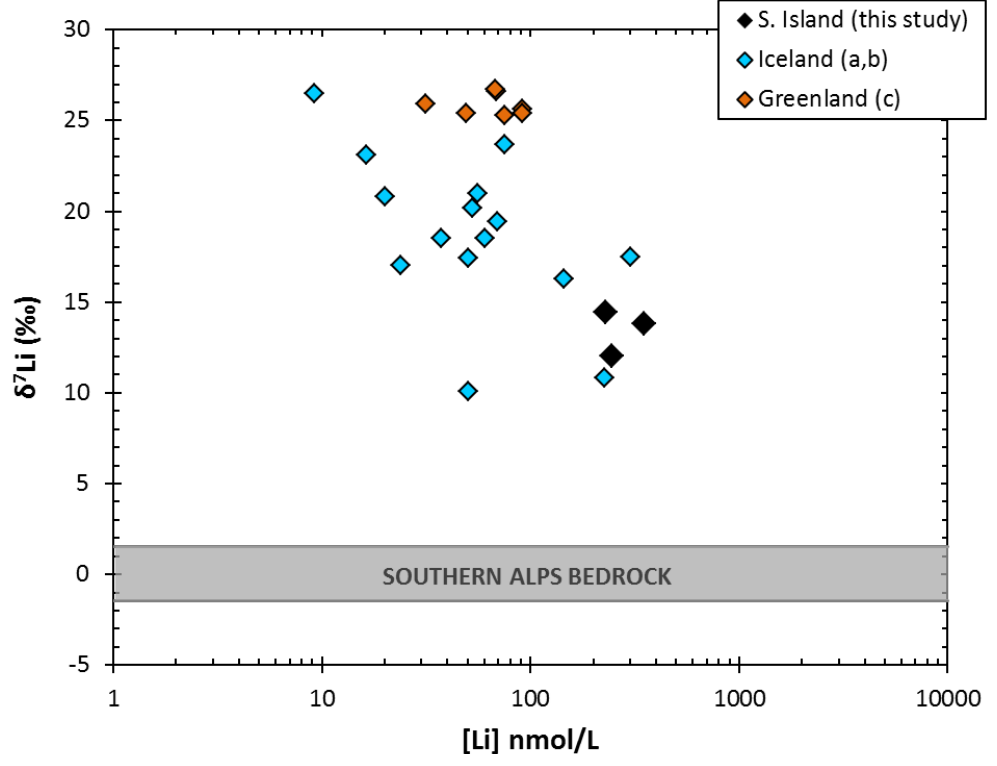


FIGURE 5.18: Lithium concentration against $\delta^7 Li$ value of the dissolved load in the glacial river waters draining the Southern Alps, with comparison to published data. Data sourced from: ^(a)(Pogge von Strandmann et al., 2006), ^(b)(Vigier et al., 2009) and ^(c)(Wimpenny et al., 2010b). The grey band represents the range of bedrock $\delta^7 Li$ values across the Southern Alps. The external reproducibility of the $\delta^7 Li$ analyses from this study is smaller than the size of the symbols.

The light $\delta^7 \text{Li}$ signatures of the glacial rivers in the Southern Alps may be attributed to the rapid advance/retreat of these glaciers (Franz Josef and Fox Glaciers), which greatly increases physical weathering rates from glacial grinding. The glaciers in the Southern Alps are warm-based maritime glaciers and they have experienced recurrent periods of dynamic advance and retreat (Fitzharris et al., 1999). In addition, the maritime climate and high mass turnover of these glaciers means that the velocities are very high for the Franz Josef and Fox Glaciers, at up to ~5 m per day (Herman et al., 2011). Precipitation is evenly distributed throughout the year in this region so that at high altitudes, substantial amounts of snow can be deposited, even in summer (Fitzharris et al., 1999). Due to the mid-latitude, maritime locations of these glaciers, high summer solar radiation levels also mean that there are high volumes of melt (Fitzharris et al., 1999). With high velocity glaciers and high degrees of melting, it is likely that these glacial river waters are affected by high levels of mechanical erosion, increasing reactive surface area, resulting in more congruent weathering and lower $\delta^7 \text{Li}$ values in these glacial rivers (Figure 5.18).

5.4.4 Mineral Saturation States

River water chemistry is strongly influenced by primary mineral dissolution and secondary mineral formation during weathering (Gislason and Arnorsson, 1993; Gislason et al., 1996; Sophocleous, 2002; Gislason et al., 2006; Maher et al., 2009; Zhu and Lu, 2009). Therefore, secondary mineral precipitation can potentially deplete surface waters in the elements derived from the dissolution of primary minerals, which consequently continue to dissolve (Pogge von Strandmann et al., 2010). Mineral saturation states are important with respect to lithium because during mineral synthesis, lithium replaces Mg in micas, pyroxenes and amphiboles (Huh et al., 2004). Lithium is retained in secondary clays as its ionic radius is well-matched to the octahedral cavity in these minerals (Huh et al., 2004). Primary mineral dissolution in the Southern Alps is significantly affected by rapid uplift and subsequent rapid erosion (Jacobson and Blum, 2003), resulting in greatly enhanced physical weathering. High elevation through uplift and erosion has also led to the development of steep slopes (increasing the potential for landslides) and the formation of glaciers (leading to glacial grinding), which further enhance physical weathering.

The Li/Mg ratio is high in the clay fraction of the river sand, compared to bulk river sand, fine river sand and riverine suspended load from the Southern Alps (Figure 5.19). This would suggest that the clay fraction is preferentially retaining Li, which is what would be expected, as the clay fraction of the bedload would be largely composed of secondary alteration products.

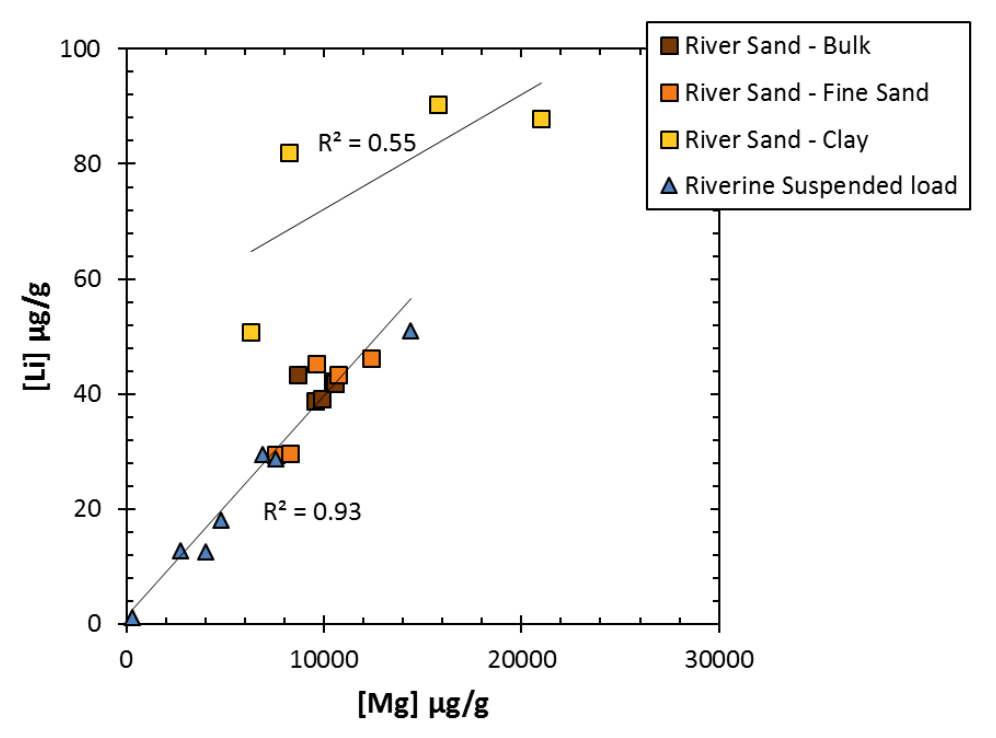


FIGURE 5.19: Correlation between Mg and Li concentration for the river sand size fractions and suspended riverine sediments sampled from rivers draining the Southern Alps.

Primary and secondary mineral saturation rates were calculated using the geochemical modelling software Geochemist's Workbench, which estimates mineral stability (degree of oversaturation or undersaturation) in terms of Gibbs free energy (kJ). The results are given as a Saturation Index (SI):

SI values > 0 Mineral is oversaturated in solution

SI values < 0 Mineral is undersaturated in solution

If a mineral has an SI value of <0 it will dissolve, and if it has a value of >0 it has the potential to precipitate. A value of 0 would indicate that the mineral is in equilibrium with the solution. To calculate these values, in situ pH and temperature measurements, along with total alkalinity and measured anion and cation concentrations were used. The overall uncertainty on the calculated SI values is estimated to be 1-2 SI units (Stefansson and Gislason, 2001). See Section A.5 for tables of mineral saturation indices and further details on mineral saturation state modelling. It is important to note that while saturation state modelling may suggest the presence of certain minerals, XRD analyses may not confirm the presence of all of them. It is also important to note that geochemical modelling of mineral saturation states focuses on 'brand new' formation of minerals, and not absorption on neo-formed minerals.

Biotite (primary mineral) is a major constituent of the Southern Alps bedrock and is a major source of Li; \sim 65% of Li in the bedrock is sourced from biotite (Table 5.1). Biotite has a broad range of SI values, from undersaturated (SI = -7) to oversaturated (SI = +3) in the river waters draining the Southern Alps (Figure 5.20 A). SI values show a weak positive correlation with pH for biotite.

Illite, kaolinite and smectite (secondary minerals) are all oversaturated (SI = 0 to +4; Figure 5.20 A), indicating potential formation and precipitation of these secondary minerals. XRD analyses (see Section 4.4.4) support the presence of clays (illite and kaolinite) indicated by these geochemical modelling results. With increasing pH in the non-glacial rivers, illite, kaolinite and smectite become less oversaturated by 2-3 SI units and approach equilibrium. This would suggest that these minerals would become undersaturated and may dissolve at higher pH, which has been demonstrated in Icelandic basaltic rivers (Gislason et al., 1996; Pogge von Strandmann et al., 2006). There is also a negative correlation between pH and SI value of secondary minerals in the glacial rivers, and the SI values become less oversaturated by ~3 SI units as pH increases.

With the relatively narrow temperature range (0-20 $^{\circ}$ C) of the rivers draining the Southern Alps, no correlation can be seen between temperature and the saturation index of primary minerals or secondary minerals (Figure 5.20 B). It is possible that the rate of dissolution of primary minerals and the rate of secondary mineral formation does not vary significantly between the small temperature range (0-20 $^{\circ}$ C) observed in these rivers.

The δ^7 Li signature of the dissolved load shows no relationship with the SI values for biotite (Figure 5.20 C). This is what would be expected, as Li is not isotopically fractionated by the dissolution of primary minerals during weathering (Pistiner and Henderson, 2003; Wimpenny et al., 2010a). A weak correlation between the δ^7 Li value of the dissolved load and SI value of illite, kaolinite and smectite (secondary minerals) can be observed in the rivers draining the Southern Alps (Figure 5.20 C). Some authors (Pogge von Strandmann et al., 2006) have suggested that δ^7 Li should increase with decreasing SI values, as high SI promotes more rapid precipitation of secondary minerals, which results in less isotope fractionation. However, higher saturation of secondary phases in river waters should lead to more ⁶Li preferentially taken up in the formation of secondary minerals, leaving the residual lithium in solution increasingly enriched in ⁷Li (Huh et al., 2001).

Large variations in riverine δ^7 Li have been attributed to the formation of different secondary phases that have different fractionation factors with water (Millot et al., 2010; Wimpenny et al., 2010b). However, this cannot explain the variations in δ^7 Li in rivers draining the Southern Alps, as geochemical modelling of mineral saturation indices (Figure 5.20) suggests that all of the rivers draining the Southern Alps are saturated with the same secondary mineral assemblage.

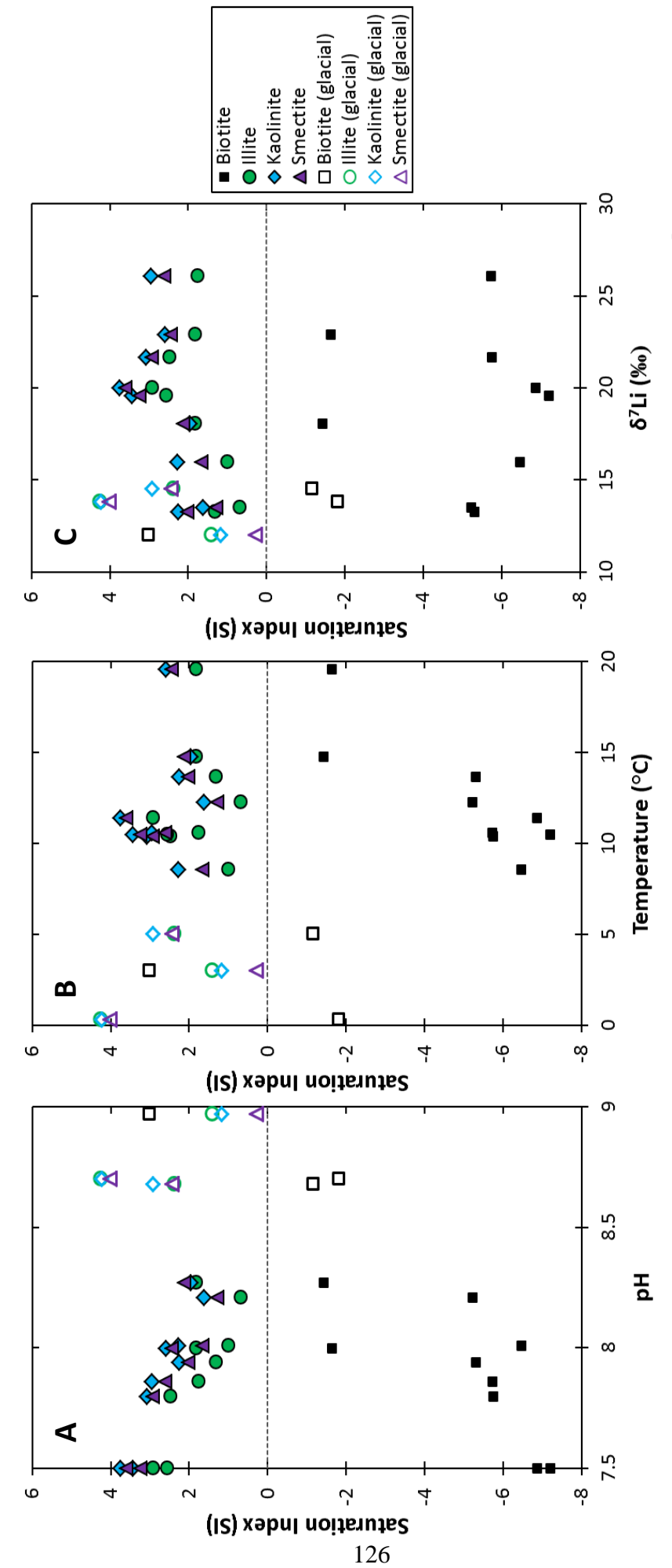


FIGURE 5.20: Saturation indices (SI) of biotite (primary mineral) and illite, kaolinite and smectite (secondary minerals) against pH, temperature and δ 7Li value The external reproducibility of the δ ^{TL} analyses is smaller than the size of the symbols. The overall uncertainty on the saturation indices is 1-2 SI units of the dissolved load of the rivers draining the Southern Alps. The closed symbols represent non-glacial rivers and the open symbols represent glacial rivers. (Stefansson and Gislason, 2001).

5.4.5 Assessing the Link between Riverine δ^7 Li and Silicate Weathering

The difference between the δ^7 Li signature of river waters and the δ^7 Li signature of suspended sediments (Δ^7 Li) is given by:

$$\Delta^7 \text{Li}_{\text{suspended-dissolved}} = \delta^7 \text{Li}_{\text{suspended}} - \delta^7 \text{Li}_{\text{dissolved}}$$
 (Eq. 5.2)

 $\Delta^7 \text{Li}_{\text{suspended-dissolved}}$ is always <0, which indicates that $^6 \text{Li}$ is preferentially retained in secondary minerals while $^7 \text{Li}$ goes into solution (Huh et al., 1998; Huh et al., 2001). Carbonate weathering is essentially complete (so $\Delta = 0$). $\Delta^7 \text{Li}_{\text{suspended-dissolved}}$ values <0 must result from the formation of secondary minerals during weathering of silicate minerals. The average $\Delta^7 \text{Li}_{\text{suspended-dissolved}}$ for river waters draining the Southern Alps is -20.5‰, which is within range of global rivers ($\Delta^7 \text{Li}_{\text{suspended-dissolved}} = \sim 18.5 \pm 10\%$) (Kısakűrek et al., 2005; Pogge von Strandmann et al., 2006; Pogge von Strandmann et al., 2010; Wimpenny et al., 2010b).

The isotopic fractionation factor (α) can be calculated from $\Delta^7 \text{Li}_{\text{suspended-dissolved}}$ values as follows:

$$\alpha = e^{\Delta/1000}$$
 (Eq. 5.3)

River water Li isotopic fractionation factors in the Southern Alps range from 0.973 to 0.987. This is similar to values calculated between fluids and vermiculite, kaolinite and suspended sediments from the Mississippi River ($\alpha = 0.972$ -0.979; Zhang et al., 1998) and values calculated between the dissolved load and suspended sediments from the Himalayas (average $\alpha = \sim 0.976$; Kisakűrek et al., 2005).

On a plot of δ^7 Li signature of the dissolved load and δ^7 Li signature of the suspended load, the data from the Southern Alps from this study plots within range of global data (Figure 5.21). This shows that rivers have consistently heavier δ^7 Li signatures than (and are highly fractionated from) the suspended load. This confirms that heavy riverine δ^7 Li values are mainly due to Li isotope fractionation occurring during silicate weathering (e.g. Huh et al., 2001; Pogge von Strandmann et al., 2006; Pogge von Strandmann et al., 2010).

A decrease in silicate weathering intensity does not necessarily mean that a decrease in silicate weathering rate is observed (Wan et al., 2012). Chemical weathering intensity is defined as the degree of chemical depletion of silicate rocks (Wan et al., 2012). Chemical weathering rate is the lost amount of soluble mass per unit area per unit time of the bedrock due to chemical weathering (White and Blum, 1995). The chemical weathering rate is influenced by physical erosion, as high physical erosion rates result in the rapid production of fresh mineral surfaces, which potentially leads to rapid chemical weathering rates (West et al., 2005).

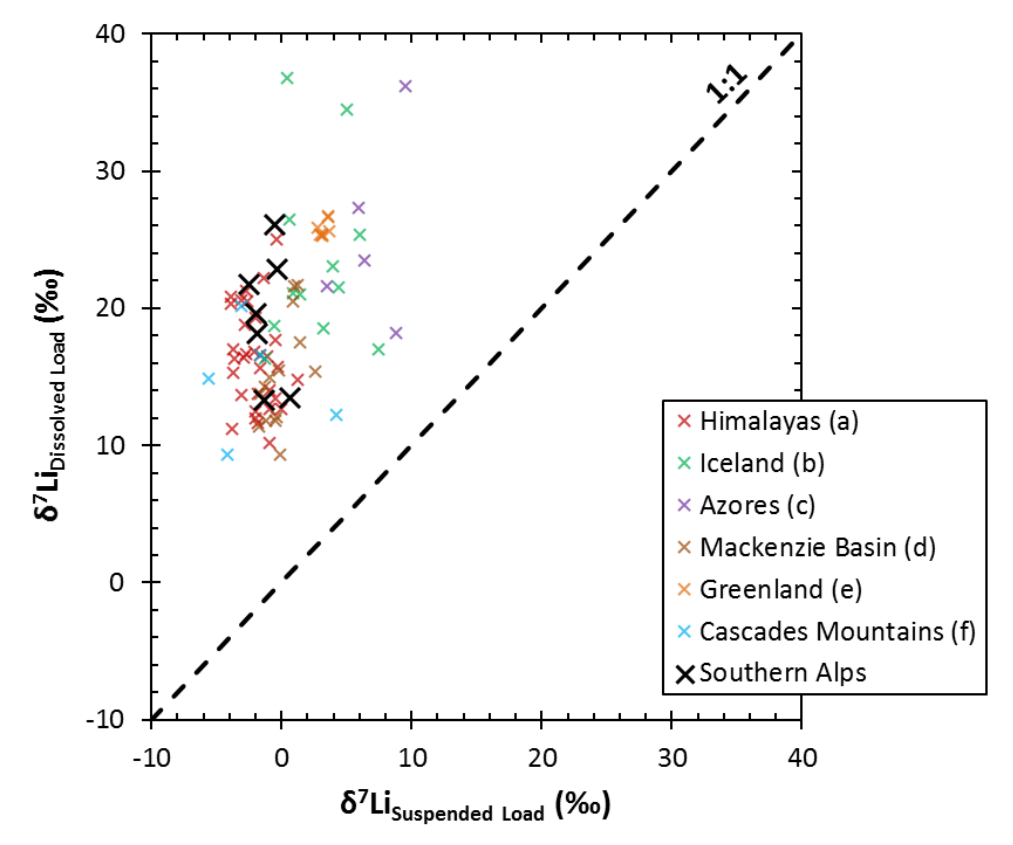


FIGURE 5.21: $\delta^7 \text{Li}$ value of the suspended load against the $\delta^7 \text{Li}$ value of the dissolved load of rivers draining the Southern Alps, with comparison to global published river data. Data sourced from: ^(a)(Kısakűrek et al., 2005), ^(b)(Pogge von Strandmann et al., 2006), ^(c)(Pogge von Strandmann et al., 2010), ^(d)(Millot et al., 2010), ^(e)(Wimpenny et al., 2010b), ^(f)(Liu et al., 2015). The external reproducibility of the $\delta^7 \text{Li}$ analyses from this study is smaller than the size of the symbols.

Observations have suggested that there may be a link between the rate of silicate weathering and δ^7 Li signature of river waters. Vigier et al. (2009) observed a negative correlation between δ^7 Li value and silicate weathering rates for Icelandic Rivers, and an empirical law linking δ^7 Li value and silicate weathering rate for the Icelandic river waters was deduced (Figure 5.22 A; Vigier et al. 2009). Vigier et al. (2009) further suggest that this law can be applied to other rivers that have a silicate weathering rate of less than 100 t·km⁻²·yr⁻¹. However, when these data are considered together with the data from this study for the Southern Alps, and other global river water data (from the Amazon, Ganges, Brahmaputra, Lena, Orinoco and Kolyma rivers), no correlation is observed (Figure 5.22 B). This is consistent with other compiled data (Wanner et al., 2014). The collection of global rivers and the river waters draining the Southern Alps all display high δ^7 Li values and low chemical erosion rates (<18 t·km⁻²·yr⁻¹). Figure 5.22 B would imply that these rivers do not follow the trend defined by Icelandic rivers (Vigier et al., 2009). These findings would suggest that there is not a direct link between silicate weathering rate and riverine δ^7 Li composition. Thus, the relationship between silicate weathering rate and riverine δ^7 Li shown by Vigier et al. (2009) is unlikely to be representative of silicate weathering at a larger scale, and is not particularly useful in deciphering the effect of other rock types and other climatic regimes. In addition, silicate weathering rate is only referring to chemical dissolution of silicates, and is not representative of secondary mineral formation, which would explain why no correlation is observed with riverine δ^7 Li values.

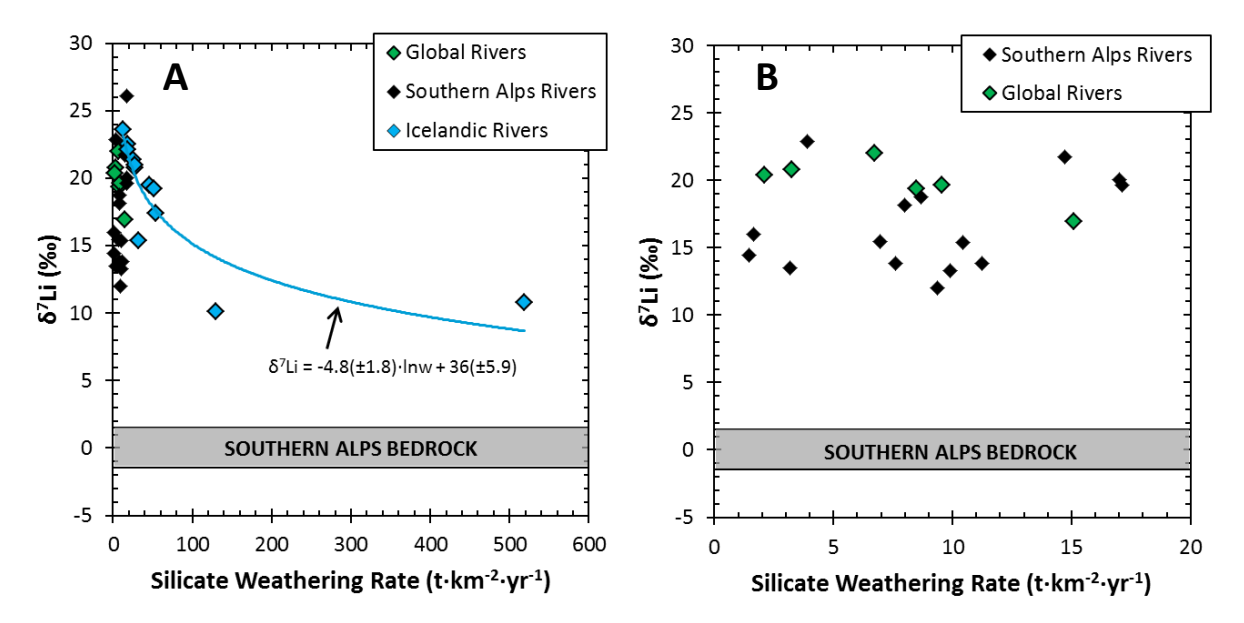


FIGURE 5.22: Silicate weathering rates, estimated from runoff and flux of dissolved elements transported by rivers, against $\delta^7 Li$ value of river waters. The black symbols represent the river water samples from this study. Data sourced from the literature: global rivers (Huh et al., 1998; Gaillardet et al., 1999) and Icelandic rivers (Vigier et al., 2006; Vigier et al., 2009). The silicate weathering rates for the rivers draining the Southern Alps were calculated in Chapter 4. An empirical law for the Icelandic river data set was inferred (Vigier et al., 2009). See text for more details. The grey band represents the range of bedrock $\delta^7 Li$ values across the Southern Alps. The external reproducibility of the $\delta^7 Li$ analyses from this study is smaller than the size of the symbols.

The rivers draining the Southern Alps show a negative correlation between $\delta^7 \text{Li}$ value and Li/Na (Figure 5.23), which agrees well with global river draining silicate catchments (Kısakűrek et al., 2005; Pogge von Strandmann et al., 2006; Vigier et al., 2009; Pogge von Strandmann et al., 2010; Liu et al., 2015). This reflects the incorporation of Li into secondary minerals, whereas Na remains in solution, which means that Li/Na is an excellent indicator of the residence time in the hydrological cycle, as Na concentration in the dissolved load is generally at least 3 orders of magnitude higher than Li, and is therefore not as strongly affected by small amounts of secondary mineral formation (Liu et al., 2015). The negative correlation observed between δ^7 Li and Li/Na in the dissolved load implies that residence time has a major effect upon the δ^7 Li signature of rivers.

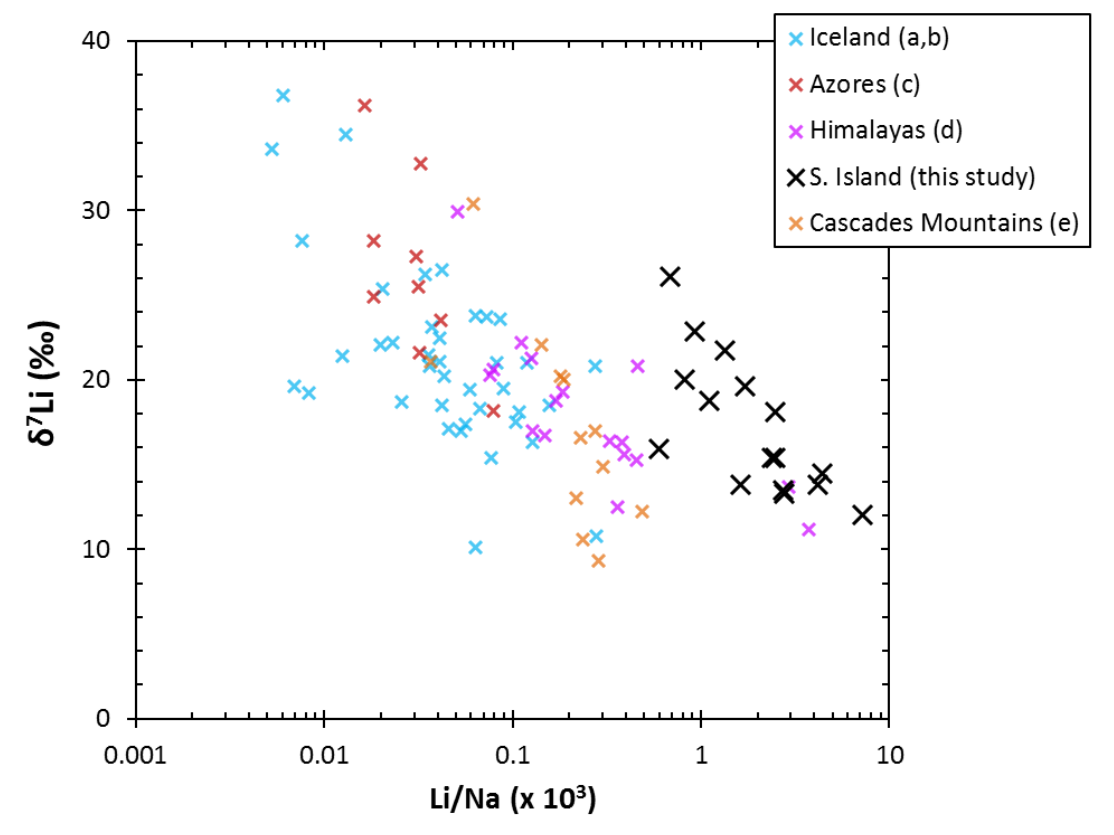


FIGURE 5.23: $\delta^7 \text{Li}$ value plotted against Li/Na in the dissolved load of the rivers draining the Southern Alps, with comparison to global published river data draining monolithological silicate catchments. Data sourced from: ^(a)(Vigier et al., 2009), ^(b)(Pogge von Strandmann et al., 2006), ^(c)(Pogge von Strandmann et al., 2010), ^(d)(Kısakűrek et al., 2005), ^(e)(Liu et al., 2015). The external reproducibility of the $\delta^7 \text{Li}$ values from this study is smaller than the size of the symbols.

5.4.6 Li Isotopes as a Proxy for Silicate Weathering Processes

There is no clear variation in riverine $\delta^7 \text{Li}$ value between rivers east and west of the Main Divide, and there is no correlation between riverine $\delta^7 \text{Li}$ value and erosion rate and amount of rainfall (Figure 5.15 and 5.17). Although, in a similar study in an area of heavy precipitation, significant variations in rainfall in the winter and summer months resulted in large variations in riverine $\delta^7 \text{Li}$ values, which suggests an indirect control of climate upon riverine $\delta^7 \text{Li}$ values (Liu et al., 2015). Thus, climatic conditions appear to have little effect upon riverine $\delta^7 \text{Li}$ values.

In this chapter, it has been demonstrated that in rivers draining monolithological silicate catchments, $\delta^7 \text{Li}$ values are negatively correlated with Li/Na (Figure 5.23), which suggests that this relationship could be used to indicate the extent of chemical weathering occurring in rivers. Therefore, we can surmise that riverine $\delta^7 \text{Li}$ can be a robust tracer of silicate chemical weathering, as Li isotopic fractionation is linked to the degree of water-rock interaction and the precipitation of secondary minerals. Generally, the heavier the riverine $\delta^7 \text{Li}$ value, the more water-rock interaction has occurred, which is in agreement with previous studies (Wanner et al., 2014; Liu et al., 2015).

Assuming the rise in seawater δ^7 Li signature over the past 60 Myr (Misra and Froelich, 2012) is primarily controlled by changing riverine input, this study suggests that the seawater δ^7 Li composition reflects increased continental physical weathering processes, which is likely to be due to increased tectonic uplift resulting in increased water-rock interaction. In addition, climate only appears to have an indirect influence upon riverine δ^7 Li values.

5.5 Summary

- There is little variation in δ^7 Li values of bedrock samples from the Southern Alps (δ^7 Li = -1.6 to -1.4‰). Protolith lithology and metamorphic grade has little influence upon the Li concentration or the δ^7 Li value of the bedrock. Li concentrations in the bedrock are regulated by Greenschist Facies metamorphism along with mass addition. Consistent with previous studies, low grade metamorphism has only a negligible effect on the lithium isotopic composition of the bedrock.
- Little variation is observed in lithium concentration or δ^7 Li signature of weathered particulate material. Bulk river sand and fine river sand are within range of the bedrock. The clay fraction of the river sand has δ^7 Li signatures that range from bedrock values to slightly lighter values (δ^7 Li = -2.6 to +0.1‰). This may suggest that the clay fraction also contains very fine rock material and/or some of the clays may be detrital.
- Mass balance calculations have shown micas to be the main source of Li in the bedrock (~80%), as they have very high Li concentrations (68.8-258 μ g/g). However, there is little difference in the δ^7 Li signature of the bedrock and the δ^7 Li signature of the mica mineral separates. This suggests that the δ^7 Li signature of the bedrock is strongly influenced by the δ^7 Li composition of micas present in the bedrock.
- The hydrothermal spring waters across the Southern Alps generally have higher $\delta^7 \text{Li}$ values than that of the bedrock (+0.2 to +10.8%), but lighter $\delta^7 \text{Li}$ values than the river waters (+11.8 to +26.1%). However, the maximum possible Li contribution from spring waters into rivers is <1%, and so the $\delta^7 \text{Li}$ signature of the spring waters is unlikely to affect that of the river waters.
- The groundwaters emanating from the roof of the Tartare Tunnels fall within the range of Li concentration and δ^7 Li signature of the rivers draining the Southern Alps. Compared to global groundwater studies, the shallowest groundwater samples from the Southern Alps have a lower Li concentration and a heavier δ^7 Li signature, but the sample that has the highest tunnel overburden plots within range of other groundwater studies.

- The rivers draining the Southern Alps are within the range of Li concentration and δ^7 Li values observed for global rivers in previously published work. However, the Southern Alps river waters are at the higher end of Li concentration and the lower end of the δ^7 Li range. Rivers draining the Southern Alps have relatively low δ^7 Li values (average δ^7 Li = +17.2‰), relative to rivers globally (average δ^7 Li = +23‰; Huh et al., 1998). Although, the river waters are still enriched in δ^7 Li relative to the bedrock (δ^7 Li_{bedrock} = -1.6 to +1.4‰).
- Secondary mineral formation during weathering is the dominant control on lithium isotopic
 fractionation in river waters draining the Southern Alps, which is consistent with global studies.
 Geochemical modelling of saturation states of minerals shows that secondary alteration products
 (illite, kaolinite and smectite) are oversaturated (0 to +4) in river waters and have the potential
 to precipitate.
- Differing patterns in rainfall and erosion appear to have little effect upon the δ^7 Li value in rivers draining the Southern Alps. This suggests that climate does not have a direct control upon riverine δ^7 Li values.
- The glacial rivers draining the Southern Alps have low $\delta^7 \text{Li}$ values ($\delta^7 \text{Li} = +12.0$ to +14.5%) compared to glacial rivers in Greenland and Iceland ($\delta^7 \text{Li} = +16.3$ to +36.8%). The glaciers in the Southern Alps are high velocity and are subject to a high degree of melting, which leads to high levels of mechanical erosion, resulting in more congruent weathering, explaining the lower glacial river $\delta^7 \text{Li}$ values.
- A direct relationship between silicate weathering rate and δ^7 Li signature cannot be seen in the rivers draining the Southern Alps, which is consistent with global river studies. Rather, the δ^7 Li signature of river waters appears to be controlled by residence time of water-rock interaction (as shown by a plot of Li/Na vs. δ^7 Li), which makes Li isotopes useful tracers of silicate chemical weathering.
- Assuming the rise in seawater δ⁷Li signature during the Cenozoic is primarily due to riverine input, the results from this study suggest that this increase may be related to tectonic uplift, which resulted in increased chemical weathering due to the increase in physical weathering and the decrease in weathering intensity. Climate appears to have at most only an indirect effect upon riverine δ⁷Li values.

Magnesium Isotopes as a Tracer of Weathering Processes in the Southern Alps

6.1 Introduction

The variation in the Mg isotopic composition of natural reservoirs is believed to be a result of physiochemical processes due to the large relative mass differences between 25 Mg and 24 Mg (4%) and 26 Mg and 24 Mg (8%) (Young and Galy, 2004). Silicate rock reservoirs have relatively uniform δ^{26} Mg values (Figures 1.13), although carbonate rocks generally have lighter δ^{26} Mg values (Galy et al., 2002; Lee et al., 2014). Therefore, a major control on the δ^{26} Mg signature of rivers is the proportion of carbonate to silicate rocks in the host catchment (Tipper et al., 2006a; Tipper et al., 2006b; Pogge von Strandmann et al., 2008; Tipper et al., 2008a). The δ^{26} Mg signature of rivers is also dependent upon Mg isotopic fractionation caused by secondary mineral formation during chemical weathering (Galy et al., 2002; Tipper et al., 2006a; Pogge von Strandmann et al., 2008; Tipper et al., 2010; Wimpenny et al., 2010a), and by biotic activity (Black et al., 2006; Ra and Kitagawa, 2007; Bolou-Bi et al., 2010).

The processes controlling Mg isotopic fractionation make Mg isotopes potential tracers of weathering processes, thus the δ^{26} Mg compositions of different geological reservoirs need to be characterised, and the dominant processes controlling Mg isotopic fractionation and the extent of fractionation need to be determined. In this chapter, the δ^{26} Mg composition of rivers and other weathering products collected from the Southern Alps on South Island, New Zealand, will be used to interpret this weathering system. These samples include river waters, spring waters, bedrock, river sands and suspended load.

6.2 Methods

Full details of the methods used to determine the Mg isotopic composition of river waters, springs, and solid phases, are given in Section 3.6. Briefly, magnesium was separated from the sample matrix using cation exchange chromatography. Acid-cleaned PTFE columns were loaded with AG50W-X12 cation exchange resin to a height of 8.5 cm (in 0.8 M TD HNO₃), unwanted elements were discarded with a wash of 0.8 M TD HNO₃, and the complete Mg fraction was eluted with 2 M TD HNO₃. Several column calibrations were carried out to ascertain the volume and strength of acid required for effective separation of Mg from K and Ti, and the volume and strength of acid required to ensure complete collection of Mg (see Section 3.6.2). This column procedure was carried out twice on all samples and standards to ensure complete separation of Mg from all other elements. Magnesium isotopic analyses were carried out on a Thermo Scientific Neptune MC-ICP-MS, using a ThermoFinnigan sample introduction system (SIS), at the National Oceanography Centre, Southampton. The Mg isotopic values are expressed as δ^{26} Mg, the per mil (‰) deviation from the pure Mg standard DSM-3 (Dead Sea Magnesium). To ensure that no isotopic fractionation occurred during column chemistry, DSM-3, IAPSO and rock standards (JB-2, BCR-2 and JDo-1) were passed through the cation exchange columns and analysed within each analytical run (see Table 3.7). The external reproducibility for the $\delta^{26}Mg$ and $\delta^{25}Mg$ analyses was determined by repeated analyses of standards that have well constrained magnesium isotopic values in the literature, and is given as 2σ (where σ is the standard deviation). The external reproducibility for the rock samples was determined by repeated analyses of JB-2 (n = 3), and is $\pm 0.08\%$ for δ^{26} Mg and $\pm 0.07\%$ for δ^{25} Mg. The external reproducibility for the fluid samples was determined by repeated analyses of IAPSO (n = 7), and is $\pm 0.09\%$ for δ^{26} Mg and $\pm 0.06\%$ for δ^{25} Mg.

6.3 Results

The $\delta^{26}Mg$ and $\delta^{25}Mg$ values of all samples and standards measured in this study define a line with a slope of 0.525 ± 0.011 ($R^2 = 0.995$) on a $\delta^{26}Mg$ versus $\delta^{25}Mg$ plot (Figure 6.1). This is close to the slope of the terrestrial equilibrium mass fractionation line defined by Young and Galy (2004), which gave a slope of 0.521.

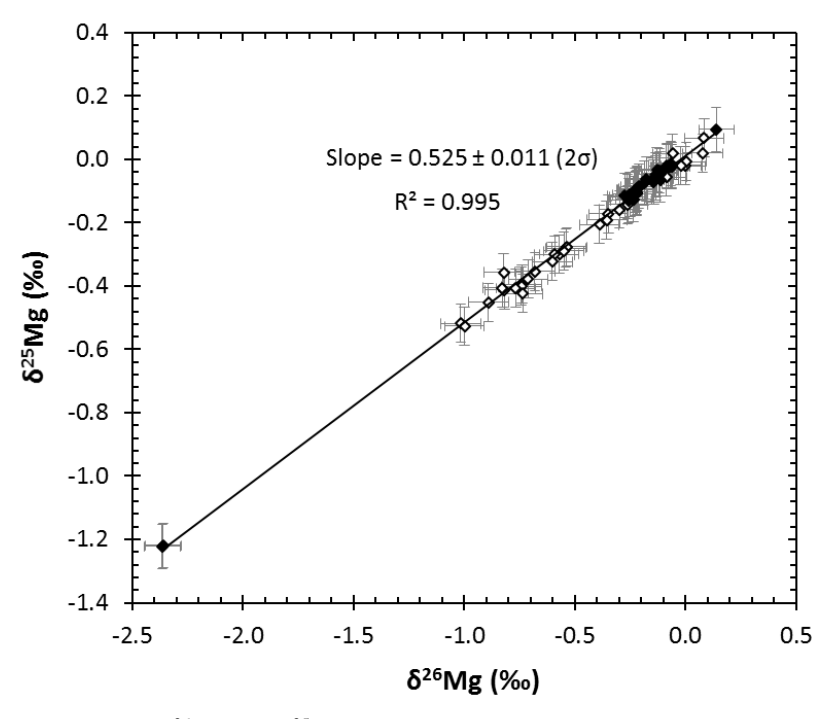


FIGURE 6.1: δ^{26} Mg and δ^{25} Mg values of all samples and standards analysed in this study. The fluid samples and standards are shown by the open black symbols and the rock samples and standards are shown by the solid black symbols. The external reproducibility on the δ^{26} Mg and δ^{25} Mg analyses is 2σ .

The δ^{26} Mg values of river waters and spring waters sampled from the Southern Alps are lower than the δ^{26} Mg values of the bedrock (Figure 6.2 and Figure 6.3). The magnesium concentration of the bedrock ranges from 5910 µg/g to 52500 µg/g, and the δ^{26} Mg values range from -0.26‰ to +0.14‰. Generally, the range of bedrock δ^{26} Mg values is very narrow (-0.26 to -0.06‰), although one bedrock sample from Haast (C56) has a heavier δ^{26} Mg value of +0.14‰. However, there is no analytical

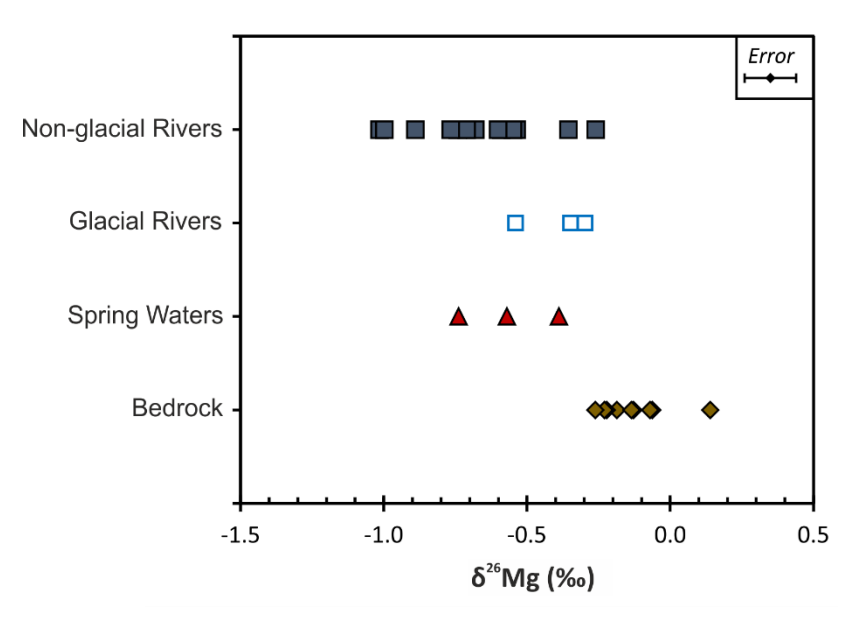


FIGURE 6.2: δ^{26} Mg signatures of fluid samples (river water and spring water) from the Southern Alps, with comparison to bedrock. The external reproducibility of the δ^{26} Mg analyses is shown in the top right hand corner of the plot (2σ).

problem (i.e. no problems associated with the column chemistry or during isotopic analysis) with this data point and the chemistry of this bedrock sample is very similar to all other Southern Alps bedrock samples analysed in this study. The concentration of Mg in the glacial rivers ranges from 11.9 μ mol/L to 23.0 μ mol/L, and the δ^{26} Mg values range from -0.54‰ to -0.30‰. The concentration of Mg in the non-glacial rivers ranges from 7.21 μ mol/L to 69.3 μ mol/L, and the δ^{26} Mg values display a wide range from -1.02‰ to -0.26‰. The spring waters have a Mg concentration range of 50 μ mol/L to 190 μ mol/L, and δ^{26} Mg values fall within range of river waters of the Southern Alps (δ^{26} Mg = -0.74 to -0.39‰). Due to low flow rates, the maximum possible spring water input into the rivers is generally significantly less than 1% for most elements, including magnesium, and therefore the spring waters have a negligible effect upon the δ^{26} Mg composition of the rivers draining the Southern Alps (see Section 4.4.1).

The rock reservoirs of the Southern Alps show near identical δ^{26} Mg signatures (Figure 6.4). The mica mineral separates, a significant source of Mg in the bedrock ([Mg] = 11300-59000 µg/g), have a δ^{26} Mg range of -0.27‰ to -0.09‰. All river sand size fractions have similar δ^{26} Mg values to the bedrock (δ^{26} Mg_{river sand} = -0.23‰ to -0.06‰; δ^{26} Mg_{bedrock} = -0.26‰ to +0.14‰). The riverine suspended load also falls within range of bedrock δ^{26} Mg values (-0.22‰ to -0.09‰).

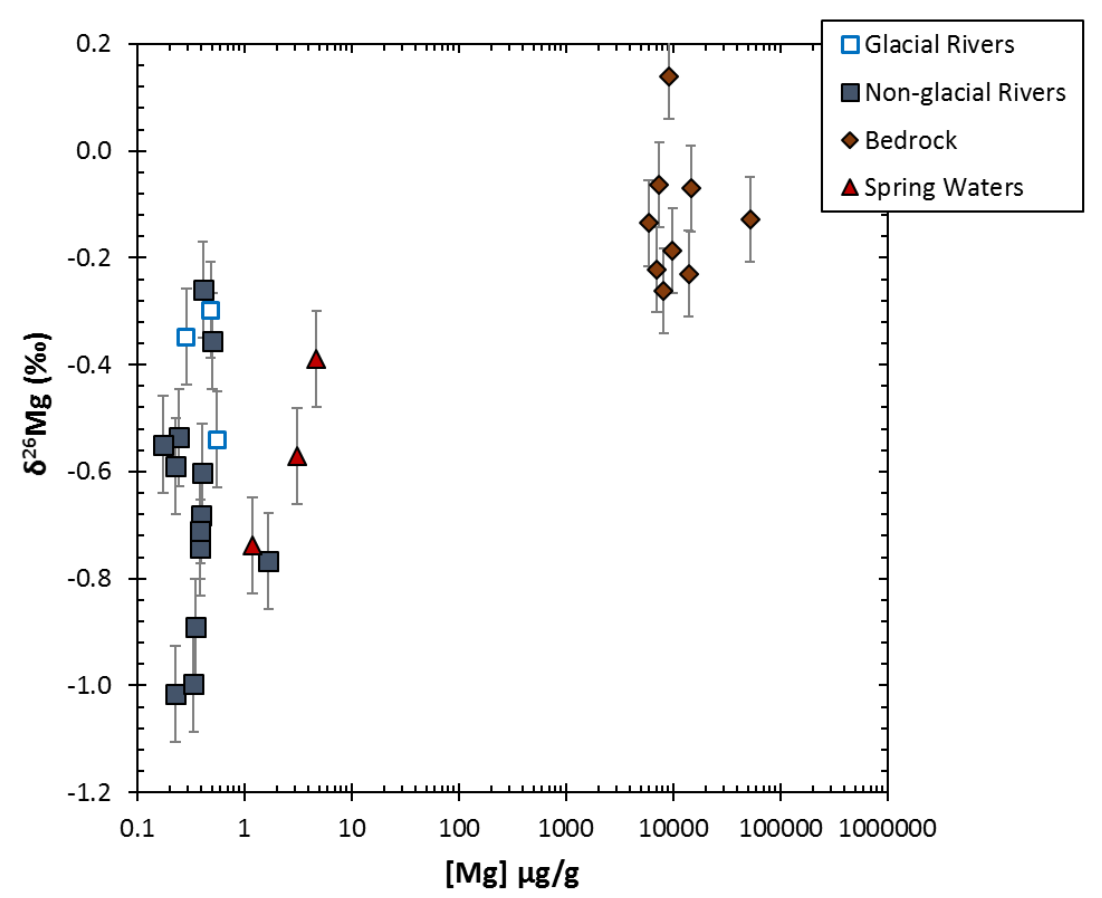


FIGURE 6.3: Magnesium concentration against $\delta^{26}Mg$ value of samples across the Southern Alps. The external reproducibility of the $\delta^{26}Mg$ values is 2σ .

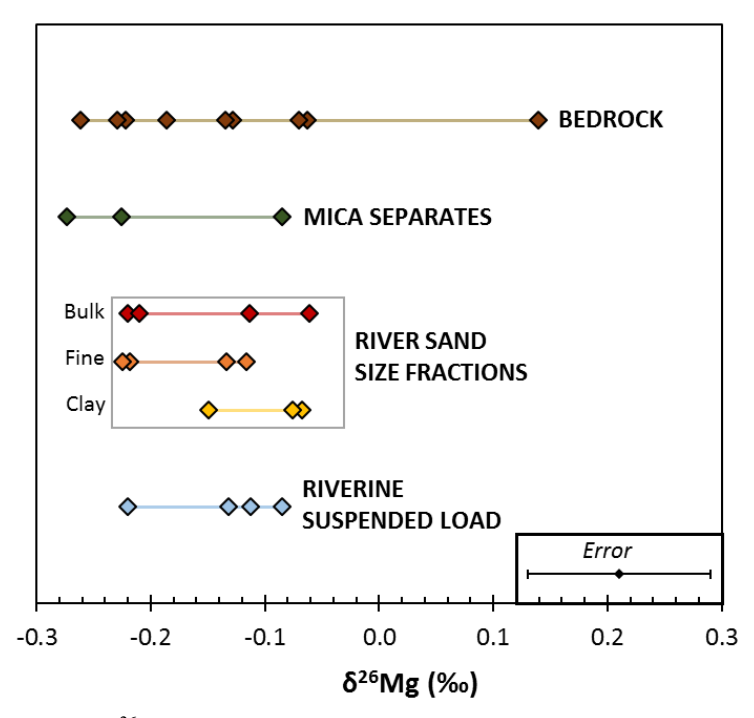


FIGURE 6.4: $\delta^{26}Mg$ value of the bedrock and weathering products of the Southern Alps. The external reproducibility of the $\delta^{26}Mg$ values is shown in the bottom right hand corner pf the plot (2σ) .

6.4 Discussion

6.4.1 Bedrock $\delta^{26}Mg$

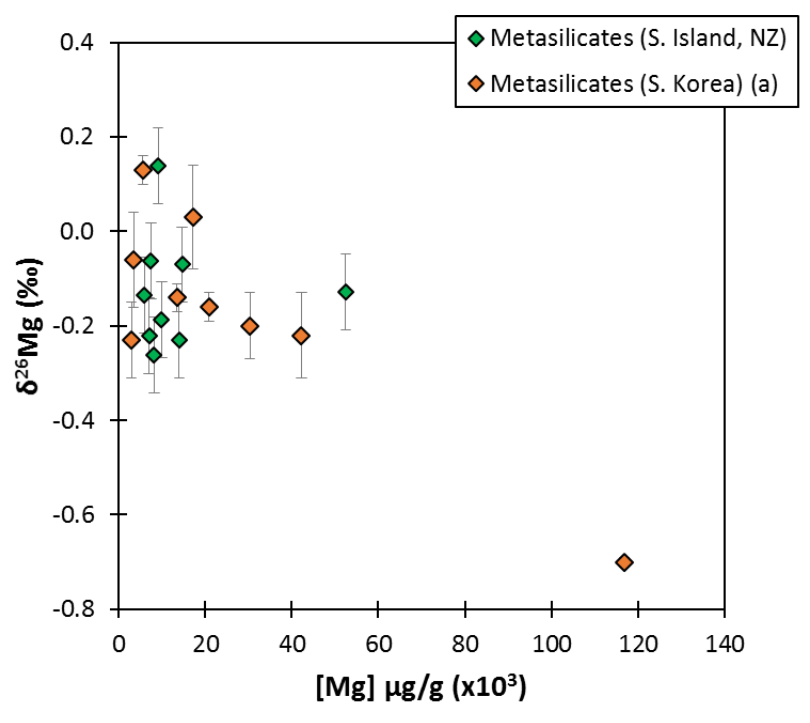


FIGURE 6.5: Magnesium concentration against $\delta^{26}Mg$ value of bedrock from the Southern Alps, with comparison to published data. Published data sourced from: ^a(Lee et al., 2014). The external reproducibility of the $\delta^{26}Mg$ values from this study is 2σ .

The range of δ^{26} Mg values (-0.26‰ to +0.14‰) and Mg concentration (5910-52500 µg/g) of bedrock samples collected from the Southern Alps on South Island, New Zealand, are within range of δ^{26} Mg signature (-0.70‰ to +0.13‰) and Mg concentration (3000-120000 µg/g) of metasilicates collected from South Korea (Figure 6.5) (Lee et al., 2014). Metasilicates have a heavier δ^{26} Mg signature than carbonates (Galy et al., 2002; Tipper et al., 2006a; Lee et al., 2014) and volcanic rocks (Young and Galy, 2004; Teng et al., 2007; Tipper et al., 2008b), but generally have similar δ^{26} Mg values to meteorites (Teng et al., 2010a) (Figure 1.13). The metasilicates of the Southern Alps are rich in micas (biotite, chlorite and muscovite), which generally have δ^{26} Mg values within range of the bedrock (Figure 6.4; Table B.4 in Appendix B).

6.4.1.1 Effect of Protolith Lithology

The δ^{26} Mg signature of the bedrock does not show any variation with differing protolith lithology across the Southern Alps (Figure 6.6), although metabasalts have much higher Mg concentrations than the metasediments ([Mg]_{metabasalts} = 52500 µg/g; [Mg]_{average metasedimentary bedrock} = 5910-14700 µg/g). The δ^{26} Mg value of most metasilicate samples from the Southern Alps are within analytical uncertainty of each other, except for a high metamorphic grade sample from Haast (δ^{26} Mg = +0.14‰). There is no significant protolith heterogeneity in the elemental chemistry of the bedrock of the Southern Alps (see Section 4.3.4), which would explain why little variation is observed in Mg concentration and δ^{26} Mg value across this suite of samples.

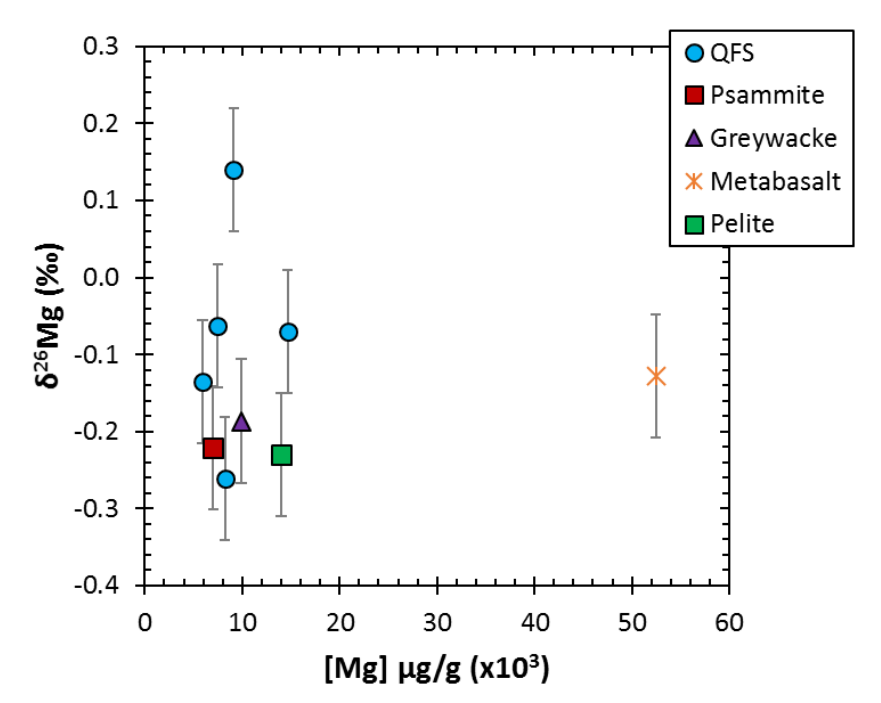


FIGURE 6.6: Magnesium concentration against δ^{26} Mg value for various protolith lithologies of the Southern Alps. The external reproducibility of the δ^{26} Mg values is 2σ .

6.4.1.2 Effect of Prograde Metamorphism

Many prograde reactions in metapelites release H₂O, into which Mg should readily partition, as it is a fluid-mobile element (Brenan et al., 1998; Pearson et al., 2006). This would suggest that Mg concentration should decrease in the bedrock with increasing metamorphic grade. However, Mg depletion due to increasing metamorphism and metasomatism is not observed in the Southern Alps, thus no correlation is observed between the Mg concentration of the bedrock and metamorphic grade (which increases from unmetamorphosed greywacke to garnet-oligoclase Amphibolite Facies schist) (Figure 6.7).

In a study examining metasomatised peridotites, kinetic isotope fractionation has been suggested to be occurring during transport of mantle xenoliths (Pogge von Strandmann et al., 2011). It was proposed that diffusion of Mg into the xenoliths is coupled to hydrogen loss from anhydrous minerals following degassing (Pogge von Strandmann et al., 2011). However, the δ^{26} Mg value of the Southern Alps bedrock appears to show no correlation with increasing metamorphic grade. If Mg was depleted in the bedrock with increasing metamorphism via diffusion, light Mg should be lost to solution and the δ^{26} Mg value of the bedrock would become higher.

To explore the effect of catchment lithology upon the $\delta^{26}Mg$ signature of the rivers draining the Southern Alps, the metamorphic grade of the bedrock can be plotted against $\delta^{26}Mg$ values of the bedrock and river water samples (Figure 6.8). No relationship can be observed between the $\delta^{26}Mg$ composition of the rivers waters with increasing metamorphic grade of the bedrock. Thus, in the Southern Alps, catchment lithology and metamorphic grade do not appear to have any effect upon the $\delta^{26}Mg$ value of the river waters.

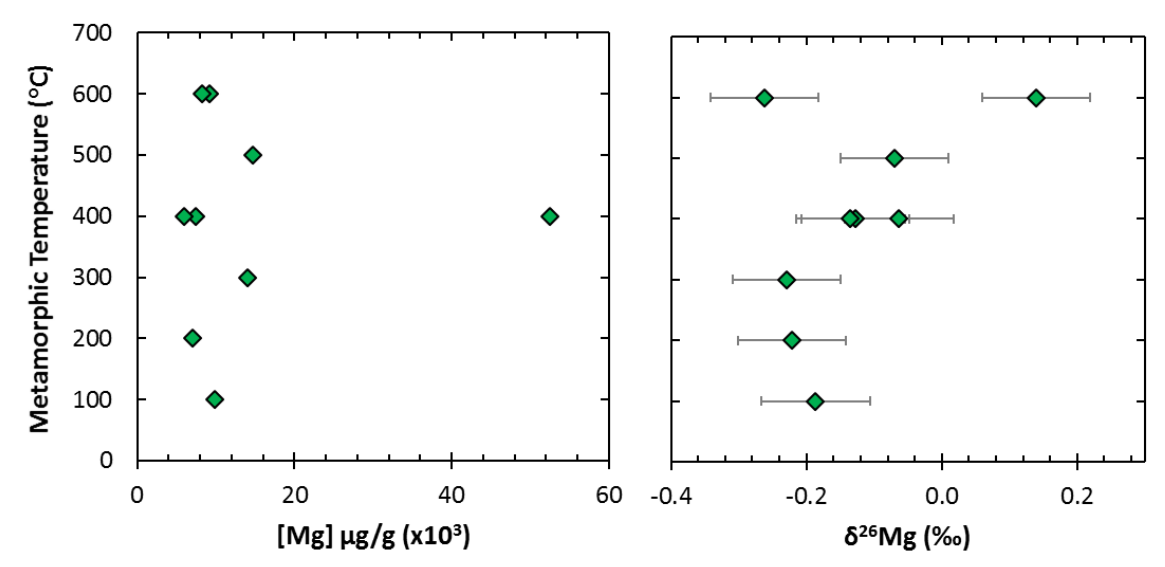


FIGURE 6.7: Magnesium concentration and $\delta^{26} Mg$ value versus metamorphic temperature of the Southern Alps bedrock. Metamorphic temperature is estimated from the metamorphic grade, following (Mortimer, 1993; Mortimer, 2000; Pitcairn, 2004) and the estimated uncertainty of these values is ± 50 °C. The external reproducibility of the $\delta^{26} Mg$ values is 2σ .

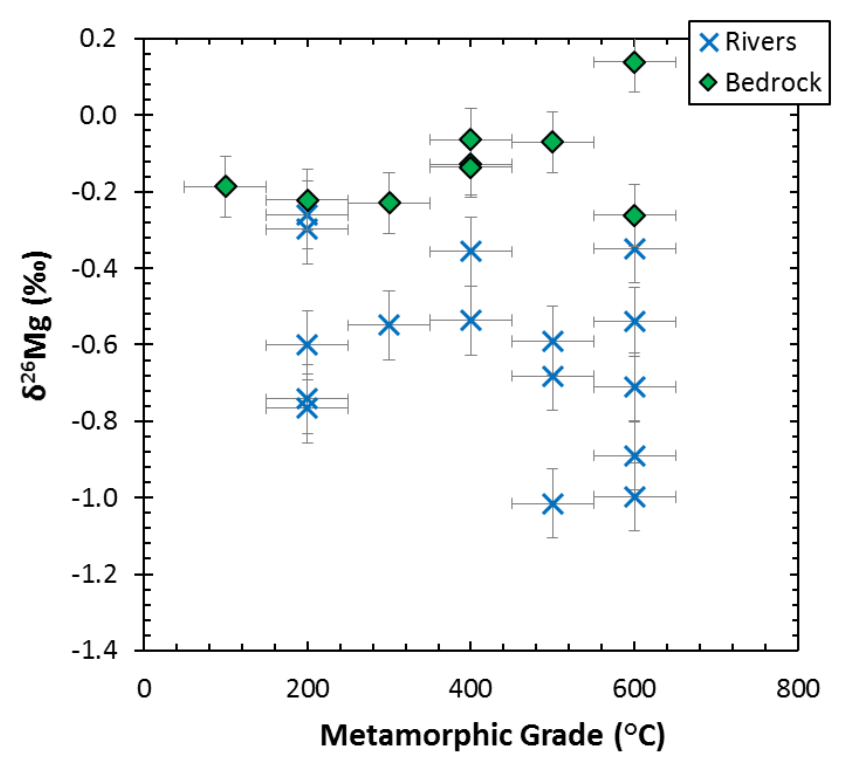


FIGURE 6.8: Theoretical metamorphic temperature against $\delta^{26} Mg$ value of the bedrock and the dissolved load in the river waters of the Southern Alps. Metamorphic temperature is estimated from the metamorphic grade, following (Mortimer, 1993; Mortimer, 2000; Pitcairn, 2004) and the estimated uncertainty of these values is ± 50 °C. The metamorphic grade of the river catchments was estimated using ArcGIS. The external reproducibility of the $\delta^{26} Mg$ values is 2σ .

6.4.1.3 Breakdown of Bedrock in the Weathering System

The rock particulates analysed in this study (river sand size fractions, riverine suspended loads and mica mineral separates from the bedrock) have been plotted with Mg concentration and δ^{26} Mg value, with the bedrock of the Southern Alps included for reference (Figure 6.9). The bulk river sand, fine river sand, clay fraction of the river sand and mica mineral separates all plot within range of the bedrock. The riverine suspended load typically has a similar range of Mg concentration values to the bedrock ([Mg]_{suspended load} = 2800-14000 μ g/g; [Mg]_{metasilicate bedrock} = 5900-14700 μ g/g; [Mg]_{metabasalt bedrock} = 53000 μ g/g), and falls within range of the bedrock.

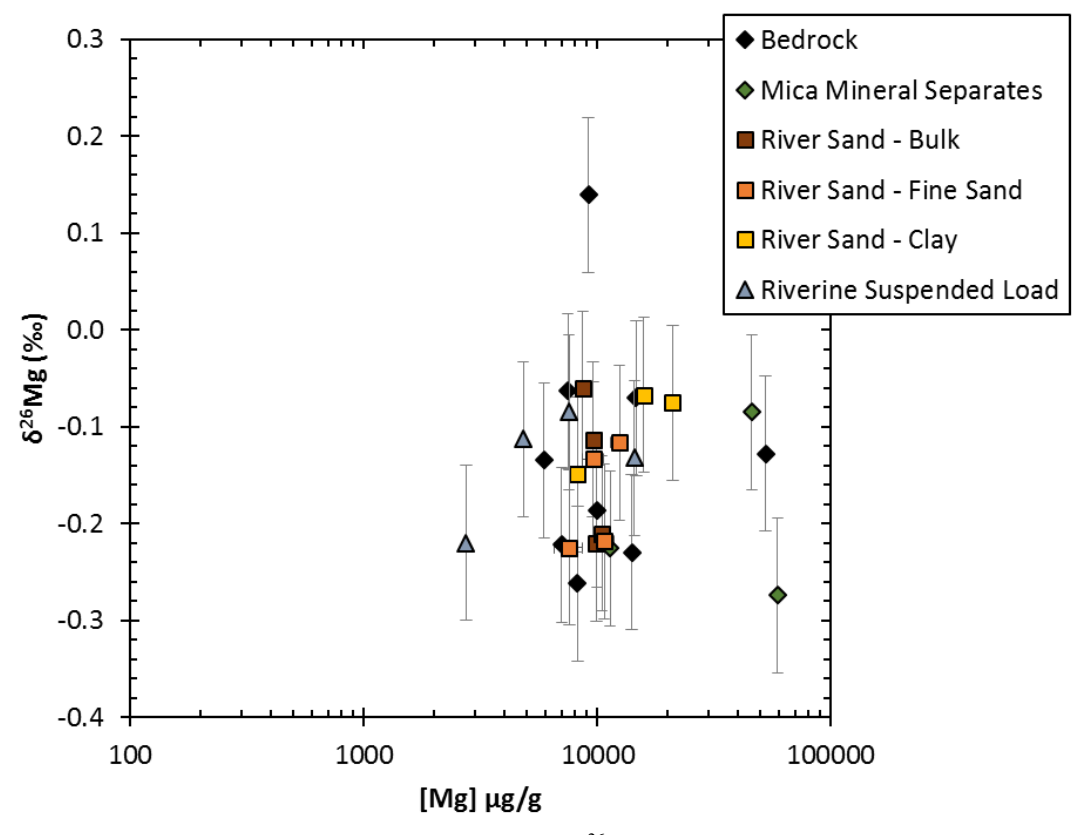


FIGURE 6.9: Mg concentration against $\delta^{26}Mg$ value of the bedrock and weathering products of the Southern Alps weathering system. The external reproducibility of the $\delta^{26}Mg$ values is 2σ .

TABLE 6.1: A mass balance defining the proportion of magnesium in the bedrock that is derived from mica minerals. The Mg concentration values for biotite, muscovite and chlorite are from this study. The Mg concentration values for quartz (Dennen, 1967) and plagioclase (Bindeman et al., 1998) were sourced from the literature. The major mineral proportions in the bedrock were estimated for a quartzofeldspathic rock of the Otago/Alpine schist of Greenschist Facies (Craw, 1984; Mortimer and Roser, 1992; Pitcairn, 2004; Menzies et al., 2014).

	Mg Concentration	Mineral in Rock	Mg from Mineral	Mg in Rock from Mineral
	(μg/g)	(%)	(μg/g)	(%)
Bulk Bedrock	9550	100		
Biotite	45900	10	4590	48.1
Muscovite	11300	10	1130	11.8
Chlorite	59000	3	1770	18.5
Quartz	1090	60	654	6.85
Plagioclase	882	17	150	1.57
SUM		100	8290	86.8

The mica minerals separated from the bedrock samples of the Southern Alps have a high concentration of Mg (11300-59000 μ g/g), but generally fall within the same range of δ^{26} Mg values as the bedrock (Figure 6.9). A mass balance calculation was used to define the proportion of Mg in the bedrock that is derived from each of the major mineral constituents (Table 6.1). Around 78% of magnesium in the bedrock is sourced from micaceous minerals, and as there is little difference between the δ^{26} Mg value of the bedrock and micas, this would suggest that micas have a significant influence upon the δ^{26} Mg composition of the bedrock. The calculated total of Mg in the rock amounted to ~87% of the total Mg, which suggests that other minor minerals are also sources of Mg in the bedrock.

The δ^{26} Mg signature of the clay fraction of the river sand (δ^{26} Mg_{average} = -0.10‰) and the riverine suspended load (δ^{26} Mg_{average} = -0.13‰) is slightly heavier than that of the bedrock (δ^{26} Mg_{average} = -0.16‰) (Figure 6.10), although this generally falls within analytical uncertainty. In addition, the CIA (degree of chemical weathering) values of the clay fraction of the river sand (average CIA = 72) and the riverine suspended load (average CIA = 68) are higher than the bedrock (average CIA = 65), which suggests that river sand clay and the suspended load are more weathered than the bedrock. However, there is no observable pattern between CIA and δ^{26} Mg signature of the bedrock or the weathering products of the Southern Alps.

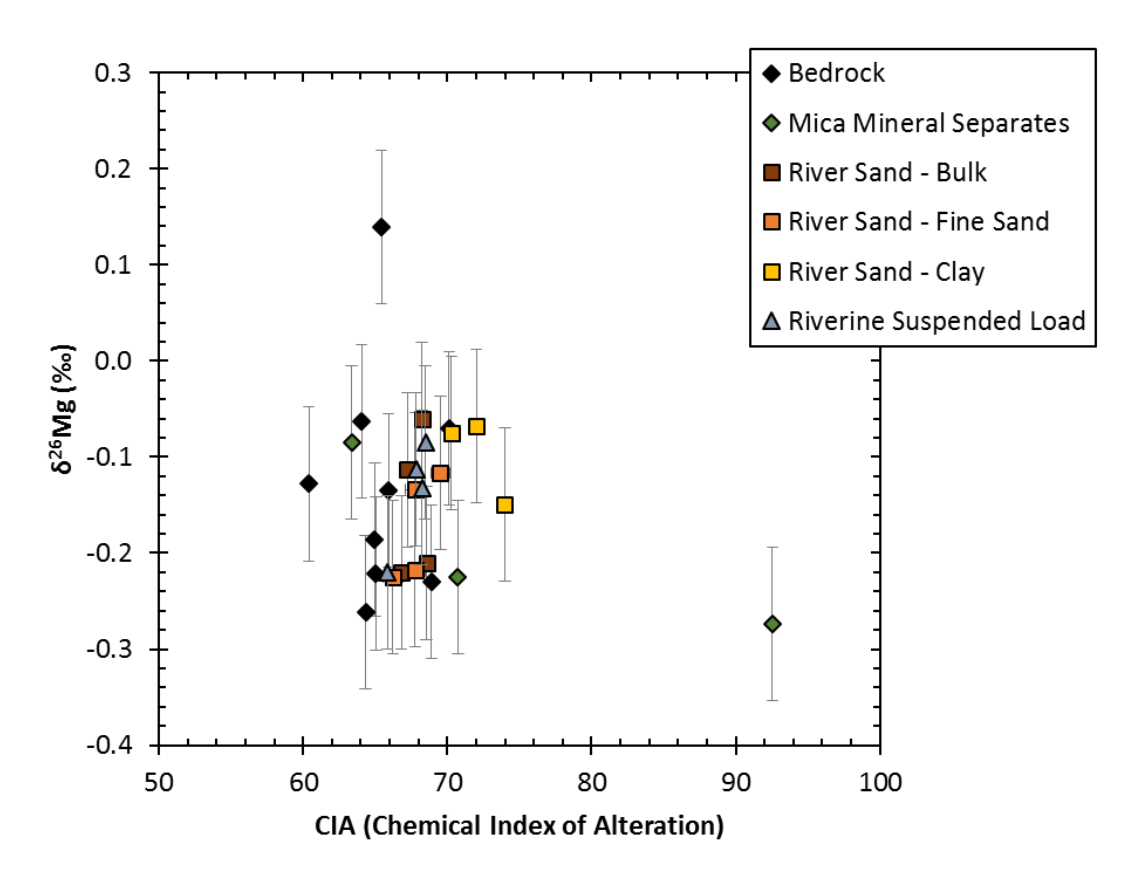


FIGURE 6.10: CIA (chemical index of alteration) against δ^{26} Mg value of the bedrock and weathering products of the Southern Alps. The external reproducibility of the δ^{26} Mg values is 2σ .

6.4.2 δ^{26} Mg Composition of River Waters

The δ^{26} Mg composition of natural waters is controlled by the mixing of waters with distinct δ^{26} Mg signatures reflecting the diversity of bedrock, as well as fractionation during weathering (e.g. Tipper et al., 2008a). The river waters draining the Southern Alps are within the range of Mg concentrations and δ^{26} Mg values observed for global rivers in previously published work (Figure 6.11). Although, the Southern Alps river waters are at the lower end of the magnesium concentration range ([Mg] = 7.21-69.3 μ mol/L), compared to rivers globally ([Mg] = 8.28-850 μ mol/L).

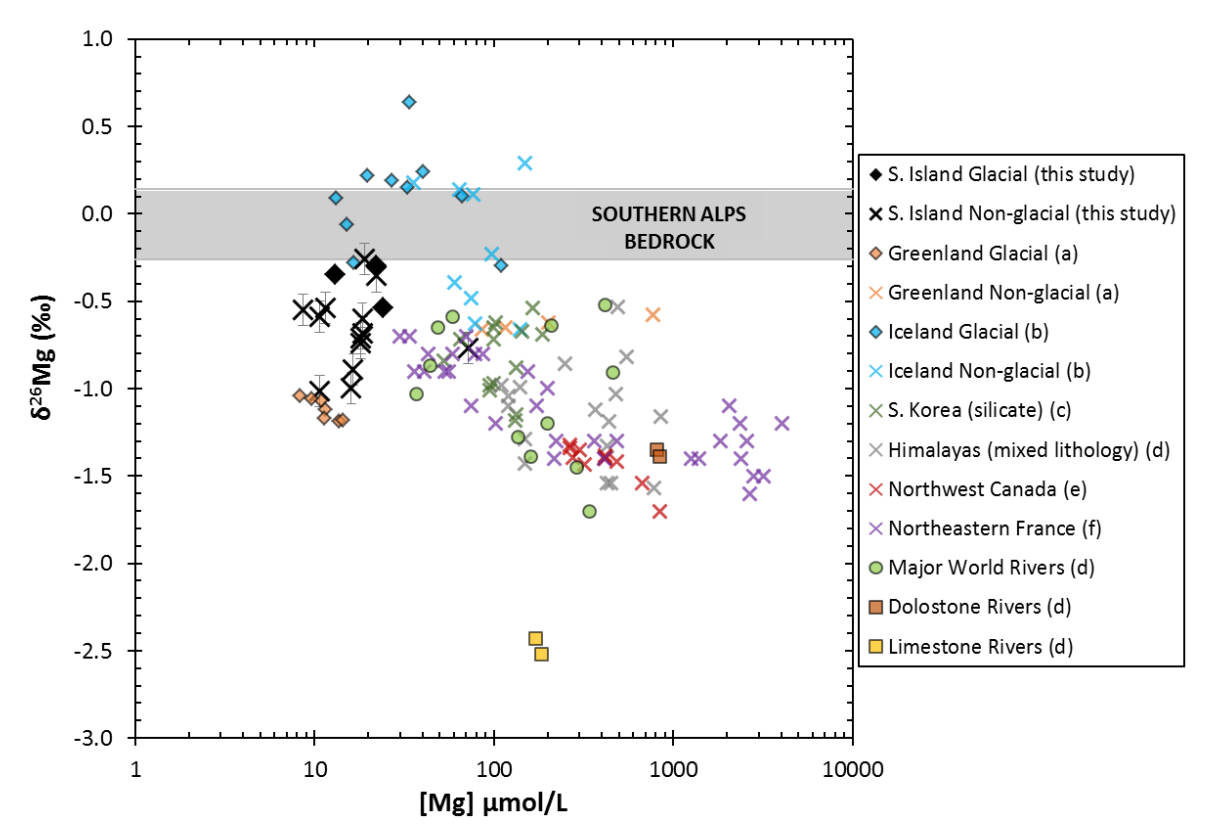


FIGURE 6.11: Mg concentration against $\delta^{26}Mg$ value of the dissolved load in the rivers draining the Southern Alps, with comparison to global published river data. Isotopic data sourced from: ^a(Wimpenny et al., 2011), ^b(Pogge von Strandmann et al., 2008), ^c(Lee et al., 2014), ^d(Tipper et al., 2008a), ^e(Tipper et al., 2012), ^f(Brenot et al., 2008). Concentration data sourced from: ^d(Gaillardet et al., 1999; Galy and France-Lanord, 1999). The grey band represents the range of bedrock $\delta^{26}Mg$ values across the Southern Alps. The external reproducibility of the $\delta^{26}Mg$ analyses from this study is 2σ .

6.4.2.1 Effect of Primary Mineral Dissolution

Primary mineral dissolution has been suggested to cause some Mg isotope fractionation, due to the preferential loss of light Mg to the fluid phase, resulting in lower δ^{26} Mg values in solution (Tipper et al., 2006a; Wimpenny et al., 2010a). The rivers draining the Southern Alps have lower δ^{26} Mg values than the bedrock (δ^{26} Mg_{dissolved} = -1.02 to -0.26‰; δ^{26} Mg_{bedrock} = -0.26 to +0.14‰; Figure 6.2). The large range of riverine δ^{26} Mg values could suggest preferential dissolution of certain primary phases, but it was shown in Figure 6.6 that there is little evidence for significant Mg isotopic heterogeneity

among the lithological protoliths of the Southern Alps. Thus, this suggests that the range observed in riverine δ^{26} Mg values does not simply relate to the δ^{26} Mg signature from primary dissolution in the Southern Alps, but is also affected by a secondary process (e.g. formation of secondary minerals or biotic activity; Pogge von Strandmann et al., 2008).

6.4.2.2 Effect of Secondary Mineral Formation

During weathering, bedrock disintegrates and dissolution of primary minerals occurs, which is associated with the formation of secondary alteration products. Magnesium is a fluid-mobile element and is incorporated into these secondary minerals, which is one of the mechanisms by which Mg isotopes fractionate during weathering. This process has been shown to preferentially retain the heavy 26 Mg isotope in minerals such as chlorite and smectite (Tipper et al., 2006a; Pogge von Strandmann et al., 2008; Teng et al., 2010) and the light 24 Mg isotope in minerals such as allophane and forsterite (Pogge von Strandmann et al., 2008; Wimpenny et al., 2010a), Thus, the nature, and extent of δ^{26} Mg isotopic fractionation is dependent upon what minerals are formed, implying that fractionation of Mg isotopes during silicate secondary mineral precipitaion may be mineral specific.

To determine the degree of Mg retention in secondary minerals, the relationship between ratios of Mg/Na of the dissolved load and Mg/Na of weathered rock particulates against the δ^{26} Mg value of the river waters can be used as an index of Mg mobility in relation to Na, which is rarely retained in secondary minerals (Figure 6.12). The fraction of Mg remaining in solution relative to Na (f_{Mg}) is defined by:

$$f_{\text{Mg}} = \frac{(\text{Mg/Na})_{\text{dissolved}}}{(\text{Mg/Na})_{\text{rock}}}$$
 (Eq. 6.1)

Both bedload and suspended load samples were used to determine the Mg/Na ratio of the rock. If $f_{\rm Mg}$ = 1, then chemical weathering is congruent (Millot et al., 2010). However, most of the river waters have $f_{\rm Mg}$ values of less than 1, and $\delta^{26}{\rm Mg}$ values of \leq -0.6‰, which indicates that heavy Mg is retained in secondary minerals (Figure 6.12) (Tipper et al., 2006b; Brenot et al., 2008; Pogge von Strandmann et al., 2008; Teng et al., 2010). XRD analyses (see Section 4.4.4) have shown the presence of clays in the river sands from the rivers draining the Southern Alps. A similar relationship was also shown between ratios of Li/Na of the dissoved load and Li/Na of weathered rock against riverine $\delta^7{\rm Li}$ values (see Section 5.4.3.1).

River waters with the highest δ^{26} Mg values (-0.36 to -0.26‰) have f_{Mg} values greater than 1. There does not appear to be any obvious reason as to why these rivers have f_{Mg} values greater than 1, but it may indicate that these river waters are not in equilibrium with the suspended particles or bedload,

meaning that they are not representative of the river water sample collected. There is little variation in the chemical composition or δ^{26} Mg signature of the bedrock and its weathering products, and so variations in Mg/Na_{rock} are unlikely to cause the $f_{\rm Mg} > 1$ values (Figure 6.12). In addition, a single-spot measurement of bedload/suspended sediment is unlikely to always be representative of a river water sample that may have travelling a long distance downstream to reach the sampling location. When $f_{\rm Mg} = 1$ (i.e. when chemical weathering should be congruent), riverine δ^{26} Mg should be the same as bedrock δ^{26} Mg values, however this is not evident in Figure 6.12. This is because chemical weathering is rarely truly congruent, and congruent weathering is not observed in the Southern Alps in this study. It is possible that $f_{\rm Mg} = 1$ in tropical watersheds with thick and heavily chemically weathered soils, where chemical weathering is more congruent.

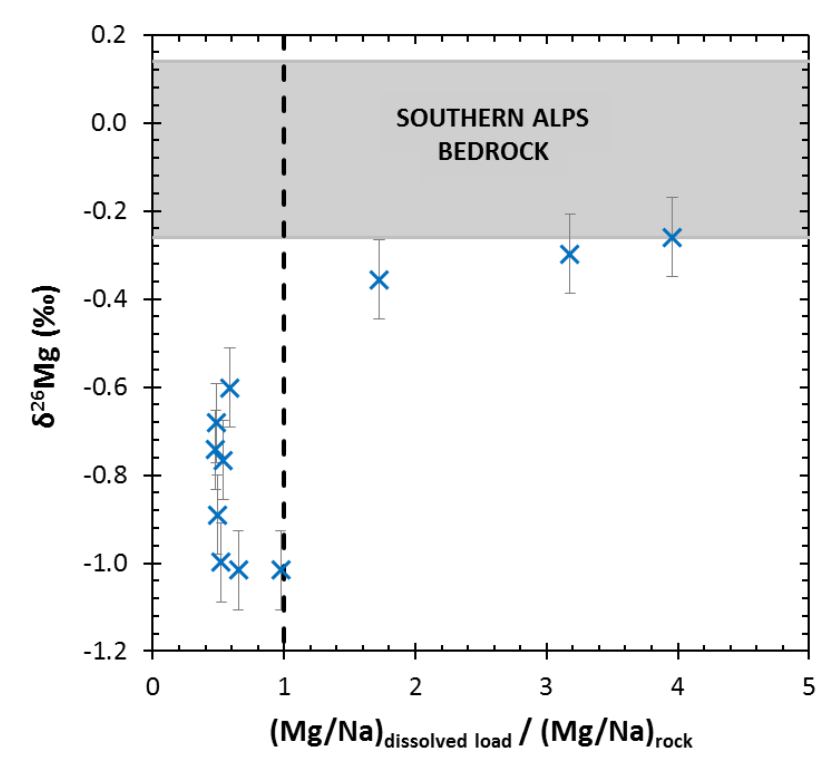


FIGURE 6.12: Ratios of Mg/Na in the dissolved load and Mg/Na in rock particulates was calculated and plotted against δ^{26} Mg value of the dissolved load in the Southern Alps. The grey band represents the range of bedrock δ^{26} Mg values across the Southern Alps. The external reproducibility on the δ^{26} Mg values is 2σ .

The δ^{26} Mg signature of the clay fraction of the river sand (average δ^{26} Mg = -0.10‰) and the riverine suspended load (average δ^{26} Mg = -0.13‰) is slightly heavier than that of the bedrock (average δ^{26} Mg = -0.16‰), and thus river waters are more highly fractionated from the weathering products than the bedrock (Figure 6.10). River sand clay and the riverine suspended load are also compositionally distinct from the bedrock (higher CIA values), suggesting that they have been subject to a higher degree of weathering and contain secondary phases (Figure 6.10). This would indicate that the formation of secondary minerals is a significant control upon Mg isotopic fractionation and riverine δ^{26} Mg values.

6.4.2.3 Effect of Rainfall and Erosion

Mg isotopic fractionation is directly affected by the intensity of chemical weathering, which can preferentially retain the heavy ²⁶Mg isotope (Tipper et al., 2006a; Pogge von Strandmann et al., 2008; Teng et al., 2010) or the light ²⁴Mg isotope (Pogge von Strandmann et al., 2008; Wimpenny et al., 2010a) in secondary products, depending on what minerals are being formed, implying that fractionation of Mg isotopes during silicate secondary mineral precipitation may be mineral specific. The overall intensity of chemical weathering is significantly affected by climatic effects, such as temperature and meteoric precipitation. These factors can affect the physical erosion rate; mechanical breakdown of the bedrock increases the available surface area, leading to increased potential for chemical weathering. Rapid orogenic uplift and erosion, which can lead to high relief and glacier formation, can also lead to rapid physical weathering, creating new weathered surfaces and increasing the potential for chemical weathering.

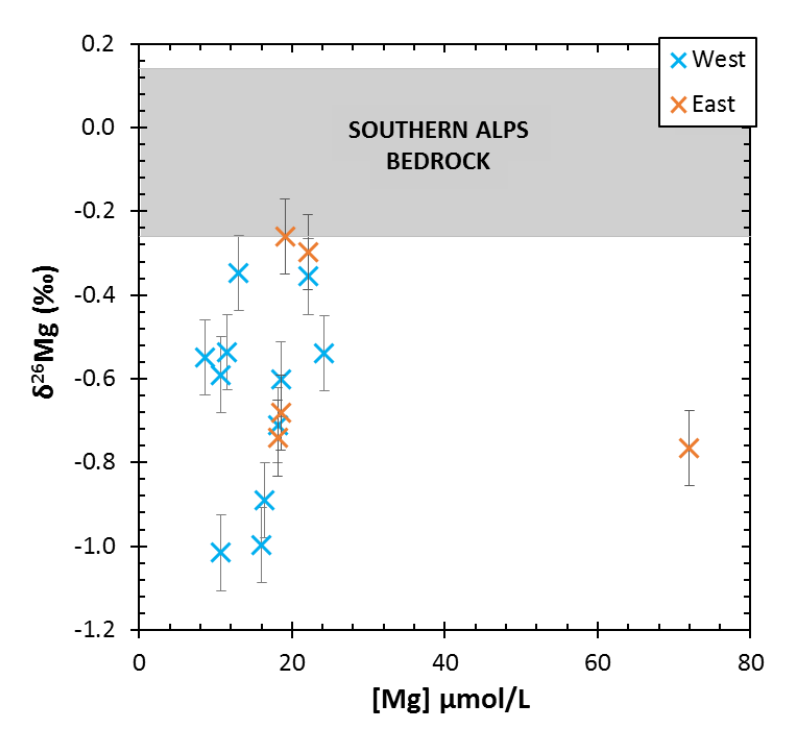


FIGURE 6.13: Mg concentration against δ^{26} Mg value of river waters draining the east and west of the Main Divide. The grey band represents the range of bedrock δ^{26} Mg values across the Southern Alps. The external reproducibility on the δ^{26} Mg values is 2σ .

The Southern Alps form an asymmetric mountain belt, which forms a barrier to the prevailing westerly winds, producing a rain shadow to the east (Henderson, 1993; Mosley and Pearson, 1997). The Main Divide forms the highest point along this mountain chain, separating the eastern and western climatic regimes. Rainfall is extremely heavy west of the Main Divide (~12 m/yr) and low to the east (<1 m/yr; Griffiths and McSaveney, 1983; Henderson and Thompson, 1999). This should lead to more incongruent weathering and higher chemical weathering intensity in the east, and less incongruent weathering (potential for secondary mineral formation is relatively inhibited due to rapid

uplift and erosion) and lower chemical weathering intensity in the west (see Section 5.4.3.2). Thus, lower δ^{26} Mg values should be observed in the east and higher δ^{26} Mg values should be observed in the west (approaching bedrock δ^{26} Mg values). However, little variation in δ^{26} Mg value can be observed between rivers east and west of the Main Divide (Figure 6.13). In addition, little variation can be observed in Mg concentration of the rivers draining the Southern Alps, although one river sample from a tributary of the Rakai River (NZ27) has a high Mg concentration ([Mg]_{Rakai} = 72 μ mol/L; [Mg]_{river average} = 20 μ mol/L). The higher Mg concentration measured in this river is likely due to the farming that occurs in this region.

Atmospheric inputs to the elemental concentration of the rivers draining the Southern Alps were applied in Section 4.3.1 (eastern river Mg input = 9.6% from rain water; western river Mg input = 11% from seawater). Although we know the δ^{26} Mg composition of seawater, we do not know the δ^{26} Mg composition of the rain water over the Southern Alps. Therefore, it would not be appropriate in this case to apply an atmospheric input δ^{26} Mg correction to the river waters in this study.

As discussed in Chapter 5, both regions east and west of the Main Divide are subject to 'kinetic-limited' weathering regimes (Figure 5.16). Rivers on South Island, New Zealand, are short and have little in the way of floodplains, and although physical erosion may be lower in the east than the west, it is still high on a global scale. This can explain why δ^{26} Mg values in the rivers to the east were not driven to lower values through high chemical weathering intensity. The δ^{26} Mg values of the rivers to the west are fractionated from the bedrock, even though secondary mineral formation should be

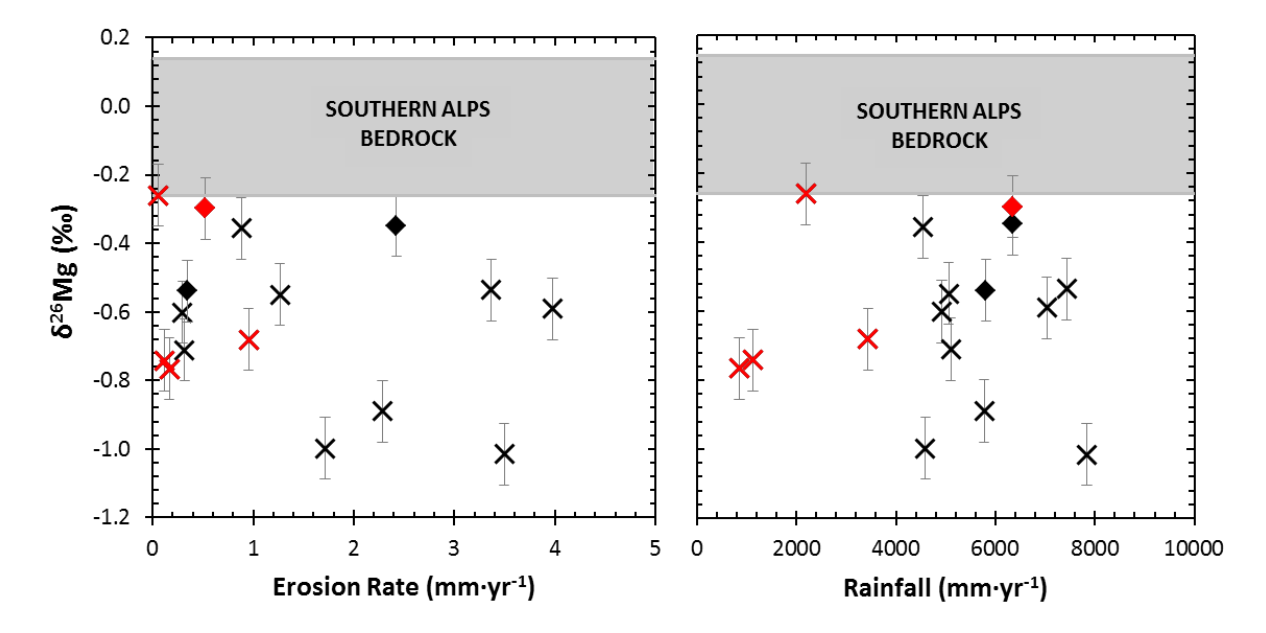


FIGURE 6.14: Erosion rate and rainfall against $\delta^{26}Mg$ values in the dissolved load of the Southern Alps. The crosses represent the non-glacial rivers and the diamonds represent the glacial rivers. The black symbols represent rivers west of the Main Divide and the red symbols represent rivers east of the Main Divide. Rainfall data are from NIWA (Tait et al., 2006) and the erosion rates were calculated from sediment yields measured by NIWA (Cox et al., 2012). The grey band represents the range of bedrock $\delta^{26}Mg$ values across the Southern Alps. The external reproducibility on the $\delta^{26}Mg$ values is 2σ .

relatively inhibited due to high rates of uplift and erosion in this region. This is likely to be due to the very high rainfall rates in the west (Griffiths and McSaveney, 1983; Henderson and Thompson, 1999), which would promote leaching and increase the potential for chemical weathering. Calculations have also shown that silicate chemical weathering rates are similar east and west of the Main Divide (see Section 4.4.6). In addition, secondary clays have been found in both eastern and western rivers (see Section 4.4.4), indicating that secondary mineral formation (incongruent weathering) has occurred on both sides of the Main Divide. This is in agreement with findings from Chapter 5 (see Section 5.4.3.2), which found little variation between the δ^7 Li value of rivers east and west of the Main Divide.

Although catchments to the east of the Main Divide generally have lower erosion rates and rainfall, the riverine δ^{26} Mg values appear to show little correlation with rainfall and erosion rate (Figure 6.14). High physical erosion rates should inhibit the formation of secondary alteration products, resulting in higher riverine δ^{26} Mg values. However, the highest erosion rates are in the west where rainfall is very high (up to 8 m/yr; Figure 6.14), which would increase the potential for chemical weathering. The relationships between riverine δ^{26} Mg value against erosion rate and rainfall are not linear, which suggests that climate has an indirect effect upon Mg isotopic fractionation. A similar conclusion was drawn for the effect of climate on Li isotopic fractionation (see Section 5.4.3.2).

6.4.2.4 Effect of Biotic Activity

The Mg content of vegetation is variable (Anderson et al., 1983; Black et al., 2006; Bi et al., 2007), and can deplete surface waters in light Mg and drive their values towards heavier values. Although, the decay and recycling of plant material may enrich surface waters in light Mg (Gosz et al., 1973), and drive isotopic compositions towards lighter values.

Generally, vegetation on the steep slopes of the Southern Alps is sparse (Wardle, 1964). Although, the amount of vegetation is higher to the east in the lowlands than it is in the west where slopes are steep and landslides are common (Wardle, 1964; Allen et al., 2011). Little variation was observed in δ^{26} Mg values in rivers east and west of the Main Divide (Figure 6.13). This indicates that either vegetation in the Southern Alps was too sparse to observe the effect of biota on Mg isotopic fractionation in the rivers, or that the effect observed between a low-vegetation area and a high-vegetation area in the Southern Alps was too small to be observed (i.e. the effect of biotic activity on Mg isotopic fractionation is small).

As no plant material from the Southern Alps was analysed in this study, the impact of biotic activity upon riverine δ^{26} Mg values cannot be ruled out. However, this effect is likely to be only minor due

to other, more dominant, controls upon riverine Mg isotopic fractionation. This is consistent with previous studies (e.g. Brenot et al., 2008).

6.4.2.5 Effect of Glaciation

The glacial river catchments of the Southern Alps experience very high physical weathering rates from glacial grinding, which is attributed to rapid advance/retreat of these warm-based maritime glaciers (Fitzharris et al., 1999). Precipiation is evenly distributed throughout the year in this region so that at high altitudes, substantial amounts of snow can be deposited all year round, which in conjunction with high summer solar radiation levels, results in a high amount of melt (Fitzharris et al., 1999).

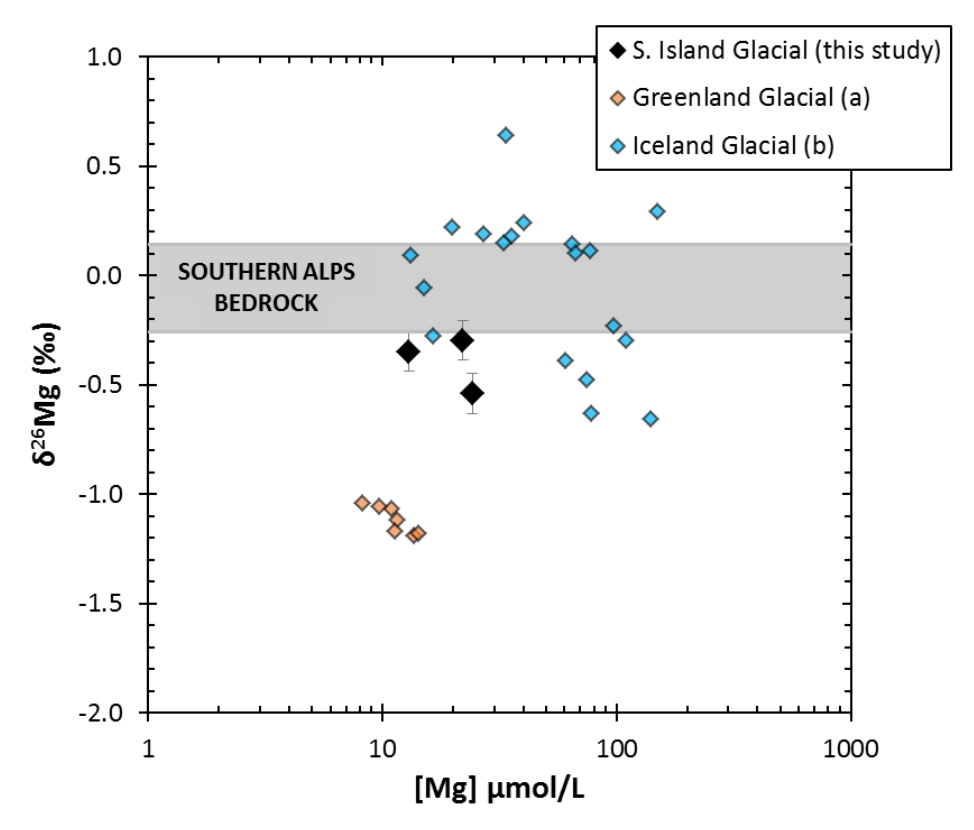


FIGURE 6.15: Mg concentration against δ^{26} Mg value of glacial river waters draining the Southern Alps, with comparison to published data. Data sourced from: ^a(Wimpenny et al., 2011) and ^b(Pogge von Strandmann et al., 2008). The grey band represents the range of bedrock δ^{26} Mg values across the Southern Alps. The external reproducibility on the δ^{26} Mg values from this study is 2σ .

As discussed previously, in the rivers draining the Southern Alps, secondary mineral formation is causing Mg isotopic fractionation, with heavy Mg retained in secondary minerals, resulting in lighter δ^{26} Mg values of rivers. However, the glacial rivers of the Southern Alps generally have heavier δ^{26} Mg values (average δ^{26} Mg = -0.40 ± 0.14‰) than non-glacial rivers (average δ^{26} Mg = -0.67 ± 0.41‰), and are thus less fractionated from the bedrock (average δ^{26} Mg = -0.13 ± 0.27‰; Figure 6.3).

Mechanical erosion is very high in these glacial rivers, which can inhibit secondary mineral formation, resulting in more congruent weathering (although XRD analysis has suggested that at least some secondary mineral formation is occurring). The reduced secondary mineral formation in glacial rivers can account for why the δ^{26} Mg value of glacial rivers is higher than that of non-glacial rivers.

Glacial rivers draining the Southern Alps have heavier δ^{26} Mg values (δ^{26} Mg = -0.54 to -0.30‰), than glacial rivers in Greenland (δ^{26} Mg = -1.19 to -1.04‰; Wimpenny et al., 2011), but glacial rivers from Iceland display a much larger range (δ^{26} Mg = -0.66 to +0.64‰; Pogge von Strandmann et al., 2008; Figure 6.15). Glacial rivers from Iceland display δ^{26} Mg values that range above and below the δ^{26} Mg average for Icelandic basalt (δ^{26} Mg_{Icelandic Basalt} = -0.84 to +0.53‰; Pogge von Strandmann et al., 2008). It was suggested that this was due to secondary mineral formation preferentially incorporating either the heavy Mg isotope or the light Mg isotope, depending on what mineral was being formed (Pogge von Strandmann et al., 2008). Glacial rivers from Greenland display δ^{26} Mg values are that lower than the δ^{26} Mg range shown for Greenland bedrock (δ^{26} Mg_{Greenland Bedrock} = -0.53 to -0.10; Wimpenny et al., 2011). Mineral saturation state modelling suggested that little secondary mineral formation was occurring in the glacial rivers of Greenland (Wimpenny et al., 2011). The light δ^{26} Mg value of the glacial dissolved load was instead attributed to preferential dissolution of carbonate minerals under the ice, which imparts a more negative δ^{26} Mg signal to the glacial river waters (Wimpenny et al., 2011).

The rivers draining the Southern Alps have an abundance of Ca^{2+} due to the dissolution of disseminated hydrothermal calcite present in the bedrock (see Section 4.4.5), which weathers very rapidly at ~ 10^4 - 10^5 times faster than plagioclase at neutral pH (Chou et al., 1989; Blum and Stillings, 1995). Glacial rivers in the Southern Alps have higher mechanical erosion rates than non-glacial rivers, resulting in a higher amount of calcite dissolution and producing high Ca/Na values (Figure 6.16). Carbonates usually have relatively low δ^{26} Mg values (Galy et al., 2002; Chang et al., 2004), and as they dissolve light Mg should be released into solution, lowering the δ^{26} Mg value of the rivers (Wimpenny et al., 2011). However, in the rivers draining the Southern Alps, as the Ca/Na ratio increases, the δ^{26} Mg value of the rivers becomes higher (Figure 6.16). This suggests that although Ca^{2+} from dissolved hydrothermal calcite is dominating the river chemistry of the Southern Alps, it is not influencing the δ^{26} Mg value of the rivers, which is likely due to the low Mg content of the calcite veins (Menzies, 2012). Therefore, it can be suggested that the dominant control upon Mg isotopic fractionation in the glacial rivers is also secondary mineral formation.

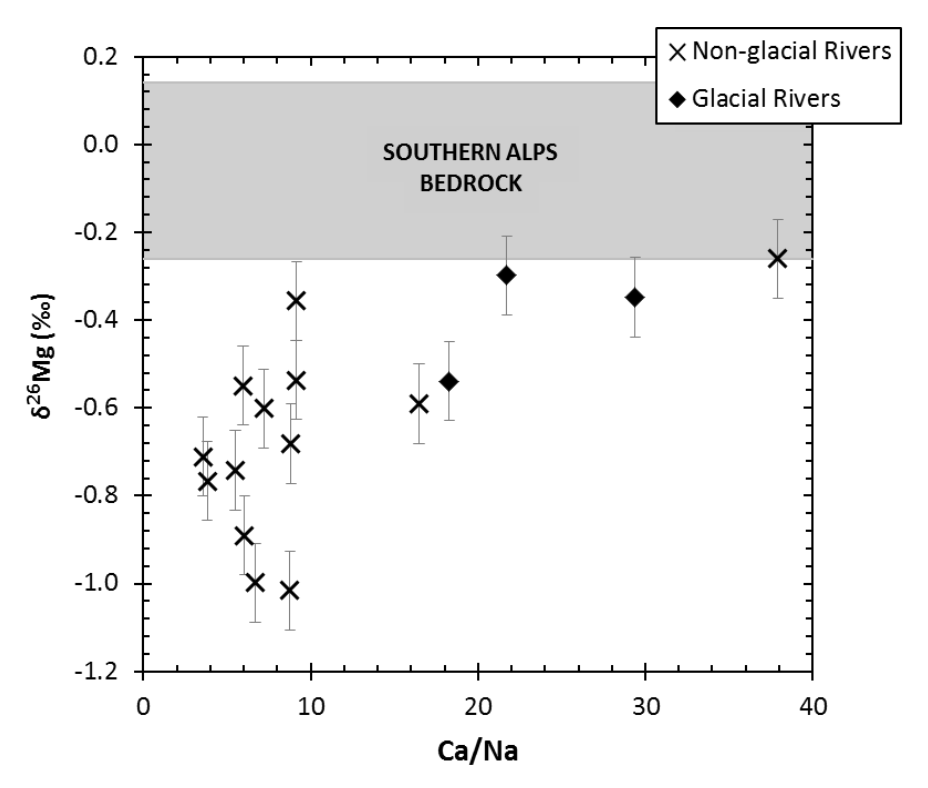


FIGURE 6.16: Molar Ca/Na ratio against $\delta^{26}Mg$ value of the rivers draining the Southern Alps. The grey band represents the range of bedrock $\delta^{26}Mg$ values across the Southern Alps. The external reproducibility on the $\delta^{26}Mg$ values is 2σ .

6.4.3 Mineral Saturation States

River water chemistry is strongly influenced by primary mineral dissolution and secondary mineral formation during weathering (Gislason and Arnorsson, 1993; Gislason et al., 1996; Sophocleous, 2002; Gislason et al., 2006; Maher et al., 2009; Zhu and Lu, 2009). Therefore, secondary mineral precipitation can potentially deplete surface waters in the elements derived from the dissolution of primary minerals, which consequently continue to dissolve (Pogge von Strandmann et al., 2010). Mineral saturation states are important with respect to magneisum, because during mineral synthesis, Mg is readily taken up into clays (Harder, 1972). Primary mineral dissolution in the Southern Alps is significantly affected by rapid uplift and subsequent rapid erosion (Jacobson and Blum, 2003), resulting in greatly enhanced physical weathering. High elevation through uplift has also led to the development of steep slopes (increasing the potential for landslides) and the formation of glaciers (leading to glacial grinding), which further enhance physical weathering.

Primary and secondary mineral saturation states were calculated using the geochemical modelling software Geochemist's Workbench, which estimates mineral stability (degree of oversaturation or undersaturation) in terms of Gibbs free energy (kJ), and the results are given in SI units. A more detailed description on how the mineral saturation states were calculated is given in Chapter 5.

The δ^{26} Mg signature of the dissolved load shows no relationship with SI values for the primary mineral biotite (Figure 6.17). Although primary mineral dissolution has been suggested to cause some Mg isotopic fractionation resulting in lower δ^{26} Mg values in solution (Tipper et al., 2006a; Wimpenny et al., 2010a), this effect is either not occurring or is too minor to observe in the Southern Alps. In addition, no correlation can be observed between the δ^{26} Mg value of the dissolved load and SI value of illite, kaolinite and smectite (secondary minerals) in the rivers draining the Southern Alps (Figure 6.17).

Previous work has been carried out to assess the behaviour of Mg isotopes during the formation and dissolution of clay minerals (Wimpenny et al., 2014) due to the uncertainty regarding the sense and magnitude of isotopic fractionation during secondary silicate mineral formation (Huang et al., 2012; Pogge von Strandmann et al., 2012), although it is generally suggested that secondary silicate minerals uptake heavy Mg (Tipper et al., 2006a; Pogge von Strandmann et al., 2008; Teng et al., 2010). Magnesium uptake into clays consists of two mechanisms: 1) structural substitution of Mg, such as Al3+ for Si4+ or Mg2+ for Al3+, by which Mg chemically bonds into the octahedral sheet (Odom, 1984; Drever, 1988; Merkel and Planer-Friedrich, 2008); 2) adsorbed Mg by electrostatic interactions into the interlayer and surface sites, which is weakly bonded and thus termed 'exchangable' (Odom, 1984; Drever, 1988; Strawn et al., 2004; Merkel and Planer-Friedrich, 2008). Acid-leaching experiments of clays (illite, montmorillonite and kaolinite) show that the clay residue is isotopically fractionated to heavier values than the unleached bulk clay, and the corresponding leachate is enriched in isotopically light Mg (Wimpenny et al., 2014). This was attributed to preferential dissolution along edge sites of the clay structure, suggesting that the isotopic signature of exchangable Mg is different to structurally-bound Mg, resulting in isotopic fractionation (Wimpenny et al., 2014). These results indicate that the structurally-bound Mg in the octahedral sheet of the clay minerals is isotopically higher than the exchangable Mg on the surface (Wimpenny et al., 2014).

Exchangable Mg would therefore drive bulk clay δ^{26} Mg signatures to isotopically lower values, resulting in the clay fraction from the Southern Alps river sands (δ^{26} Mg_{average} = -0.10‰) showing little variation compared to the Southern Alps bedrock (δ^{26} Mg_{average} = -0.16‰; Figure 6.4), as opposed to the clay fractionating to heavier δ^{26} Mg values. As exchangeable Mg is particularly labile, the isotopic composition of the exchangeable Mg likely reflects the fluid phase in which the clay last re-equilibrated (Wimpenny et al., 2014). In the case of the Southern Alps, this fluid phase would be the river waters.

To quantify the behaviour of Mg isotopes during clay formation, brucite was synthesised by Wimpenny et al. (2014), which showed that the solid became increasingly enriched in the heavy Mg isotope as the experiment continued, leaving the fluid phase enriched in light Mg. This is consistent with findings from this study, which indicate that preferential uptake of heavy Mg into the solid

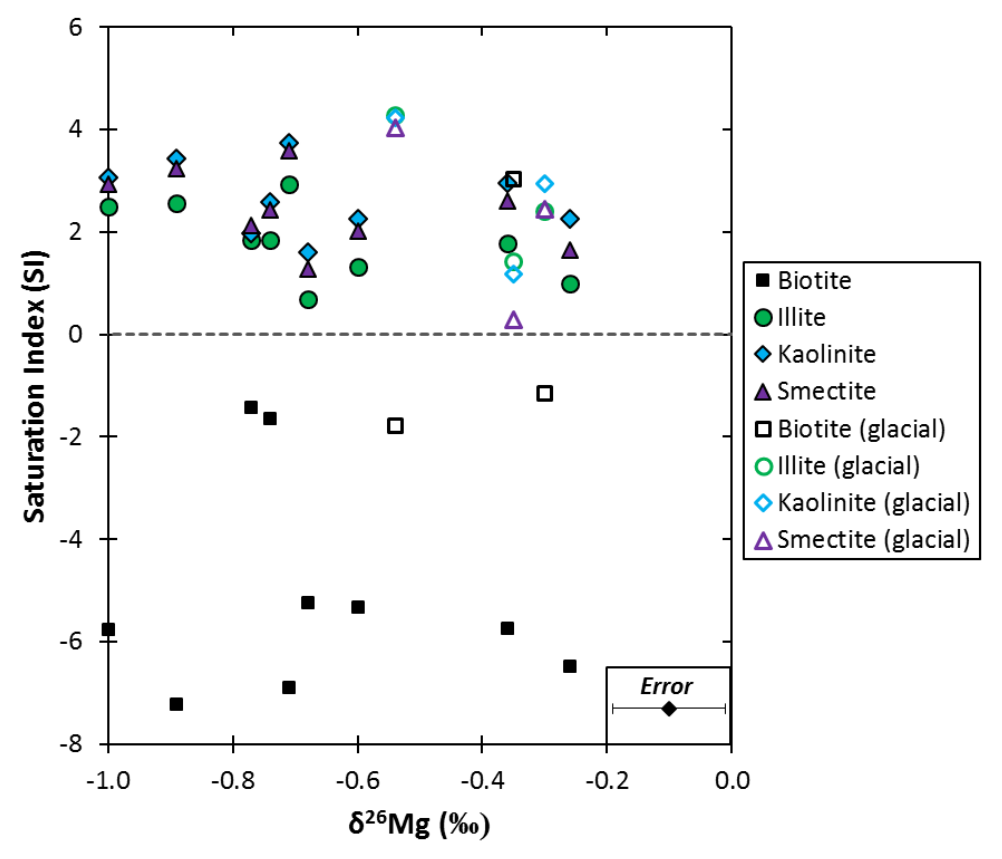


FIGURE 6.17: Saturation indices (SI) of biotite (primary mineral) and illite, kaolinite and smectite (secondary minerals) against δ^{26} Mg value of the dissolved load of the rivers draining the Southern Alps. The closed symbols represent the non-glacial rivers and the open symbols represent the glacial rivers. The external reproducibility of the δ^{26} Mg analyses is 2σ . The overall uncertainty on the saturation indices is 1-2 SI units (Stefansson and Gislason, 2001).

phase occurred during secondary silicate mineral formation, leaving the fluid phase (i.e. river waters) isotopically light.

No relationship can be observed between $\delta^{26}Mg$ value and the saturation index of calcite in the river waters draining the Southern Alps (Figure 6.18). This furthers the suggestion that the $\delta^{26}Mg$ composition of the Southern Alps rivers is controlled by secondary clay formation processes rather than carbonate precipitation in the form of calcite.

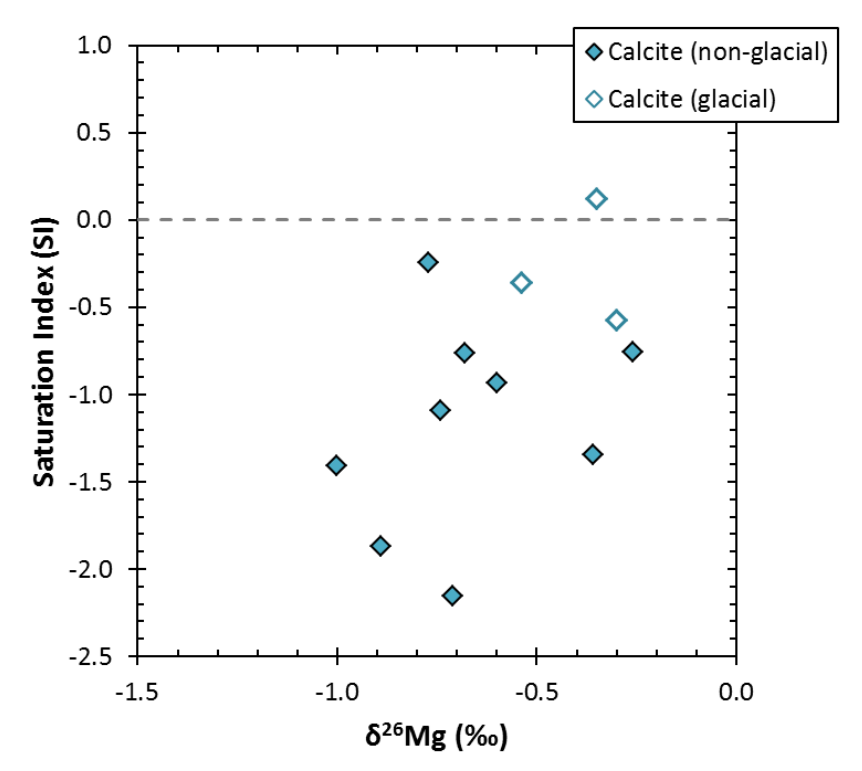


FIGURE 6.18: Saturation index (SI) of calcite against δ^{26} Mg value in the dissolved load of the river waters drainignt he Southern Alps. The overall uncertainty on these saturation indices is 0.5 SI units.

6.4.4 Assessing the Link between Riverine δ^{26} Mg and Silicate Weathering

The difference between the $\delta^{26}Mg$ signature of river waters and the $\delta^{26}Mg$ signature of suspended sediments ($\Delta^{26/24}Mg$) is given by:

$$\Delta^{26/24} Mg_{suspended-dissolved} = \delta^{26} Mg_{suspended} - \delta^{26} Mg_{dissolved}$$
 (Eq. 6.2)

 $\Delta^{26/24}$ Mg_{suspended-dissolved} is always >0 for rivers draining the Southern Alps, which indicates that 26 Mg is preferentially retained in secondary minerals while 24 Mg goes into solution. The average $\Delta^{26/24}$ Mg_{suspended-dissolved} for river waters draining the Southern Alps is $+0.49 \pm 0.4\%$, which is within range of published global river data (-0.12 to +1.05%; Pogge von Strandmann et al., 2008; Wimpenny et al., 2011; Tipper et al, 2012).

The isotopic fractionation factor (α) can be calculated from $\Delta^{26/24}$ Mg_{suspended-dissolved} values as follows:

$$\alpha = e^{\Delta/1000}$$
 (Eq. 6.3)

River water Mg isotopic fractionation factors (α) in the Southern Alps range from 1.0001-1.0009 ($\alpha_{average} = 1.0005$), which shows a good comparison to other studies examining incongruent weathering of silicate rocks ($\alpha = 1.00005$ to 1.00040; Teng et al., 2010b) and examining uptake of Mg during the formation of brucite ($\alpha = 1.0005$; Wimpenny et al., 2014).

On a plot of δ^{26} Mg_{dissolved} against δ^{26} Mg_{suspended}, the data from the Southern Alps plots within range of global data (Figure 6.19). Generally, rivers have consistently lighter δ^{26} Mg signatures than (and are therefore fractionated from) the suspended load (Wimpenny et al., 2011; Tipper et al., 2012; this study), but some rivers have heavier δ^{26} Mg signatures than the suspended load (Pogge von Strandmann et al., 2008).

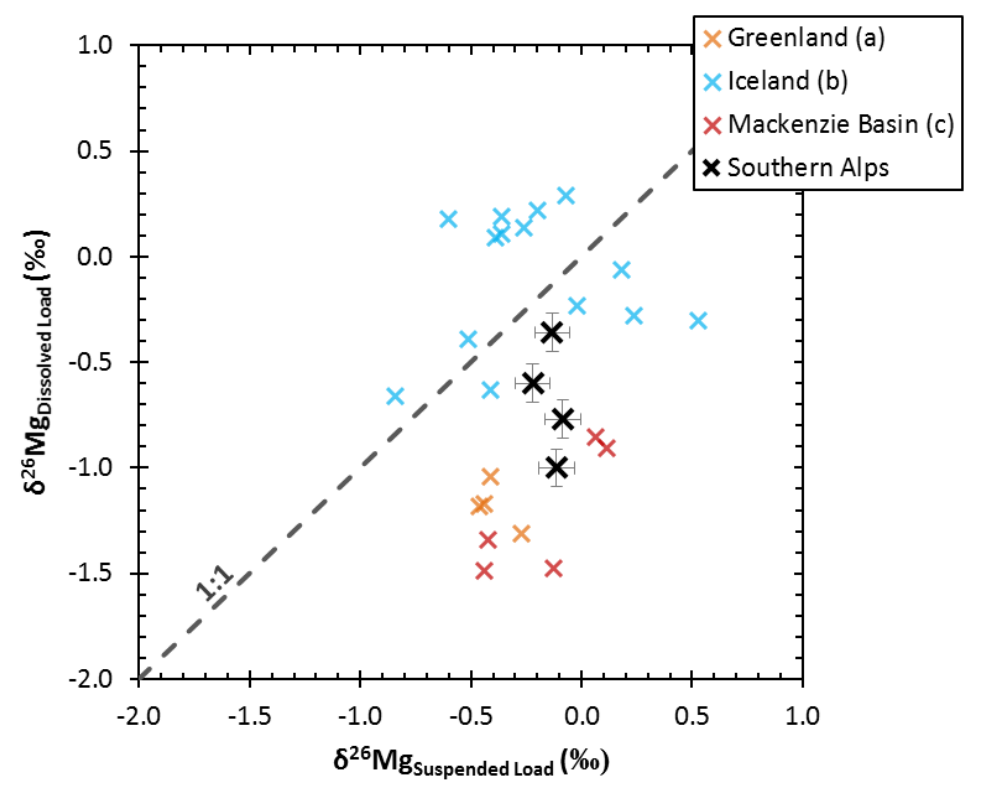


FIGURE 6.19: δ^{26} Mg value of the suspended load against the δ^{26} Mg value of the dissolved load of rivers draining the Southern Alps, with comparison to published global river data. Data sourced from: ^a(Wimpenny et al., 2011), ^b(Pogge von Strandmann et al., 2008), ^c(Tipper et al., 2012). The external reproducibility of the δ^{26} Mg analyses from this study is 2σ .

A decrease in silicate weathering intensity does not necessarily mean that a decrease in silicate weathering rate is observed (Wan et al., 2012). Chemical weathering intensity is defined as the degree of chemical depletion of silicate rocks (Wan et al., 2012). Chemical weathering rate is the lost amount of soluble mass per unit area per unit time of the bedrock due to chemical weathering (White and Blum, 1995). The chemical weathering rate is influenced by physical erosion, as high physical erosion rates result in the rapid production of fresh mineral surfaces, which potentially leads to rapid chemical weathering rates (West et al., 2005).

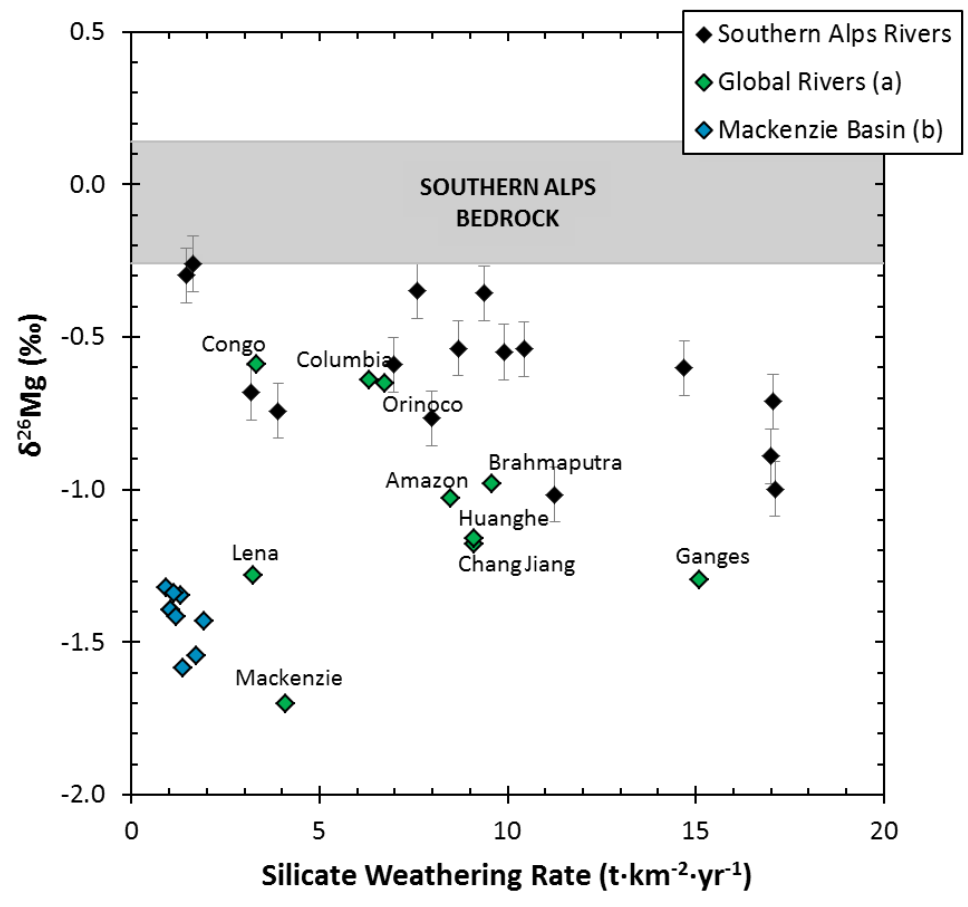


FIGURE 6.20: Silicate weathering rates estimated from runoff and flux of dissolved elements transported by rivers, against total $\delta^{26}Mg$ value of river waters. Data sourced from: $^a(Gaillardet\ et\ al.,\ 1999;\ Tipper\ et\ al.,\ 2006b),\ ^b(Millot\ et\ al.,\ 2003;\ Tipper\ et\ al.,\ 2012).$ The grey band represents the range of bedrock $\delta^{26}Mg$ values across the Southern Alps. The external reproducibility of the $\delta^{26}Mg$ analyses from this study is $2\sigma.$

There is some evidence for a relationship between silicate weathering rate and δ^{26} Mg value in the riverine dissolved load, although it should be noted that the δ^{26} Mg values represent silicate and carbonate weathering. Southern Alps calcite δ^{26} Mg values would be required to separate total δ^{26} Mg into silicate δ^{26} Mg and carbonate δ^{26} Mg. As silicate weathering rate increases, the riverine δ^{26} Mg value in the Southern Alps appears to become lighter ($R^2 = 0.35$; Figure 6.20). However, this possible weak correlation is almost within analytical uncertainty. Generally, global rivers follow the same trend, which include the Amazon, Ganges, Brahmaputra, Orinoco, Chang Jiang, Huanghe, Columbia and Congo. The rivers Lena (Siberia) and Mackenzie (North America) do not follow this trend and have light δ^{26} Mg values under low rates of silicate weathering (Figure 6.20). Lena and Mackenzie drain mixed lithologies and some of these rock formations are made up of carbonates (Spektor and Spektor, 2009; Millot et al., 2010). Carbonate rocks have light δ^{26} Mg signatures (Hippler et al., 2009) Wimpenny et al., 2011), which can likely explain why the Lena and Mackenzie rivers have lighter than expected δ^{26} Mg values. At very low silicate weathering rates ('supply-limited') there would be limited potential for chemical weathering and secondary mineral formation, but at very high silicate weathering rates ('kinetic-limited'), secondary mineral formation may become inhibited. As seen previously in Chapter 5 (Figure 5.16), the Southern Alps rivers are under a 'kinetic-limited' regime, and if mechanical erosion were to increase, secondary mineral formation may become inhibited and observed riverine δ^{26} Mg values would be higher and less fractionated from the bedrock.

The rivers draining the Southern Alps show a weak relationship between Mg/Na and δ^{26} Mg value in the dissolved load (R² = 0.46; Figure 6.21). As Mg/Na in the dissolved load increases, the riverine δ^{26} Mg value increases, which is consistent with the formation of secondary minerals. A positive correlation between Mg/Na and δ^{26} Mg value in the dissolved load would reflect the incorporation of heavy Mg into secondary minerals, whereas Na remains in solution. Little comparison can be made in this plot with global silicate river data (Tipper et al., 2006; Brenot et al., 2008; Pogge von Strandmann et al., 2008; Tipper et al., 2012; Lee et al., 2014). A relationship can also be observed between Li/Na and δ^7 Li (Chapter 5; Figure 5.23). The Na concentration in the dissolved load is generally at least 3 orders of magnitude higher than Li, and is therefore not as strongly affected by small amounts of secondary mineral formation (Liu et al., 2015). Mg and Na however have a ratio closer to 1:1, which could explain the poor correlation show in Figure 6.21.

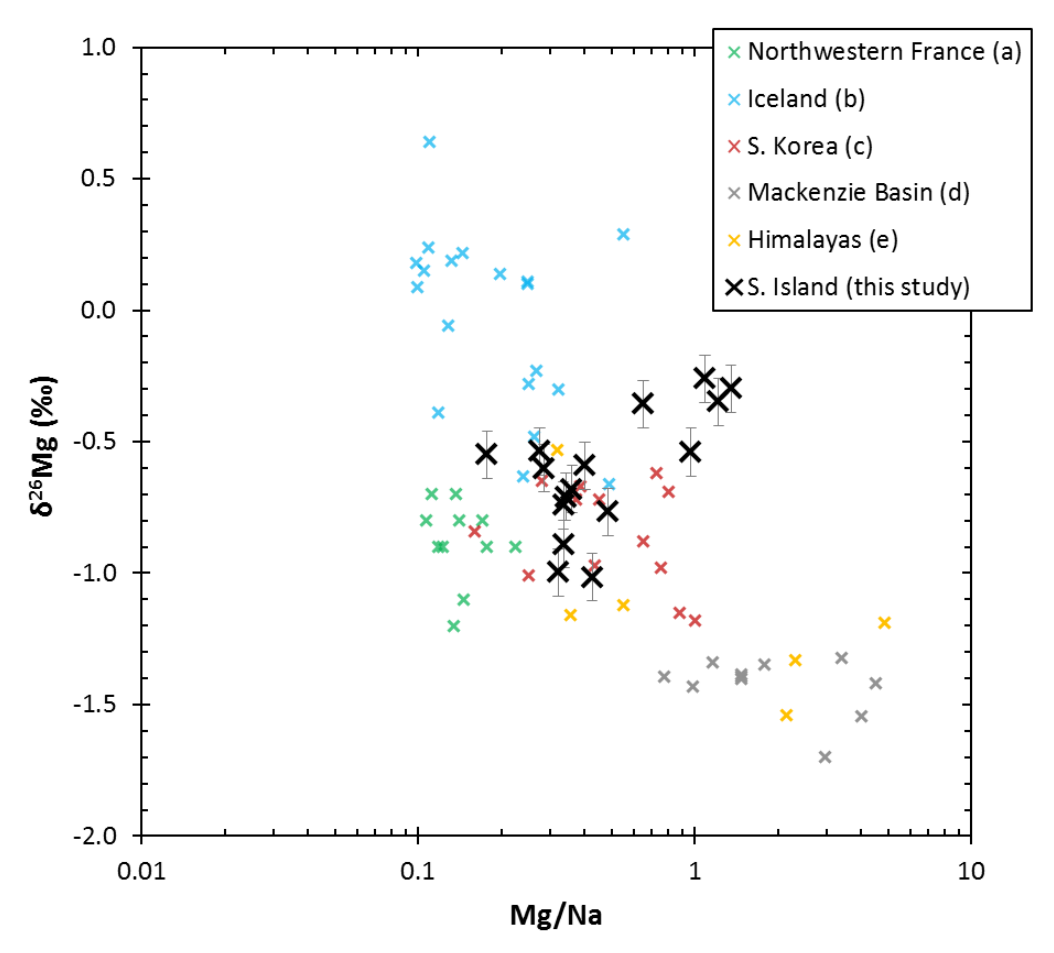


FIGURE 6.21: δ^{26} Mg value against Mg/Na in the dissolved load of the rivers draining the Southern Alps, with comparison to global published river data. Data sourced from: ^a(Brenot et al., 2008), ^b(Pogge von Strandmann et al., 2008), ^c(Lee et al., 2014), ^d(Tipper et al., 2012), ^e(Tipper et al., 2006). The external reproducibility of the δ^{26} Mg analyses from this study is 2σ .

There is no clear variation in riverine $\delta^{26}Mg$ value between rivers east and west of the Main Divide, and no correlation can be observed against erosion rate or amount of rainfall (Figure 6.13 and 6.14). This suggests that climate does not have a direct control upon riverine $\delta^{26}Mg$ values.

With this current dataset, it is apparent that it is difficult to assess to what extent the riverine δ^{26} Mg values are the result of Mg isotopic fractionation from primary mineral dissolution, secondary mineral formation, and biotic activity. In the Southern Alps it appears that secondary mineral formation is only fractionating river water δ^{26} Mg to lighter values, however in Iceland, surface waters are fractionated to heavier and lighter values depending upon the secondary minerals being formed (Pogge von Strandmann et al., 2008). Although this does highlight the importance of Mg isotopes as a tracer of chemical weathering processes, the complexities of the processes affecting Mg isotopic fractionation will make deciphering patterns of Mg isotopes in a weathering environment difficult.

More data and experiments are needed to determine what processes dominate Mg isotope fractionation, but we highlight the potential of using Mg isotopes as a tracer of weathering processes.

6.4.5 Behaviour of Mg vs. Li Isotopes during Weathering

With increasing degree of chemical weathering and formation of secondary minerals, the dissolved load δ^{26} Mg value should become lighter and the δ^7 Li value should become heavier, with regards to the bedrock isotopic values, if Li and Mg are coupled in their chemical behaviour during weathering (Horstman, 1957; Huh et al., 1998). This should result in a negative correlation between riverine δ^7 Li and δ^{26} Mg values. In rivers from Greenland, no correlation between δ^7 Li and δ^{26} Mg values in the dissolved load can be observed (Wimpenny et al., 2010b; Wimpenny et al., 2011). However, fractionation of riverine Li and Mg isotopes in Greenland rivers was not simply attributed to the formation of secondary clays. It was deduced that Li isotopic fractionation was due to the formation of Fe-oxyhydroxides (Wimpenny et al., 2010b), and light riverine δ^{26} Mg values were the result of carbonate dissolution (Wimpenny et al., 2011).

The Mackenzie rivers from Northwest Canada appear to show a positive correlation (Millot et al., 2010; Tipper et al., 2012), as do a small selection of global rives (Huh et al., 1998; Tipper et al., 2006b). This unexpected correlation was attributed to either mixing or process-related fractionation. Mixing between three different water bodies, with differing Li/Mg ratios, was suggested to reconcile this dataset (Tipper et al., 2012). Alternatively, various processes linked to clays, such as neoformation of clay, cation exchange or adsorption, were suggested as being important mechanisms of isotopic fractionation, and to reconcile the data in this study, either more than one process was occurring or one single process is kinetically-limited (Tipper et al., 2012). As for the positive correlation observed between the global rivers (Figure 6.22), this might not be representative of each

isotopic system. If multiple data points were observed for each of these large rivers, the correlation between δ^7 Li and δ^{26} Mg values may be positive or negative, depending on the relationship between these two isotopes in each individual weathering system.

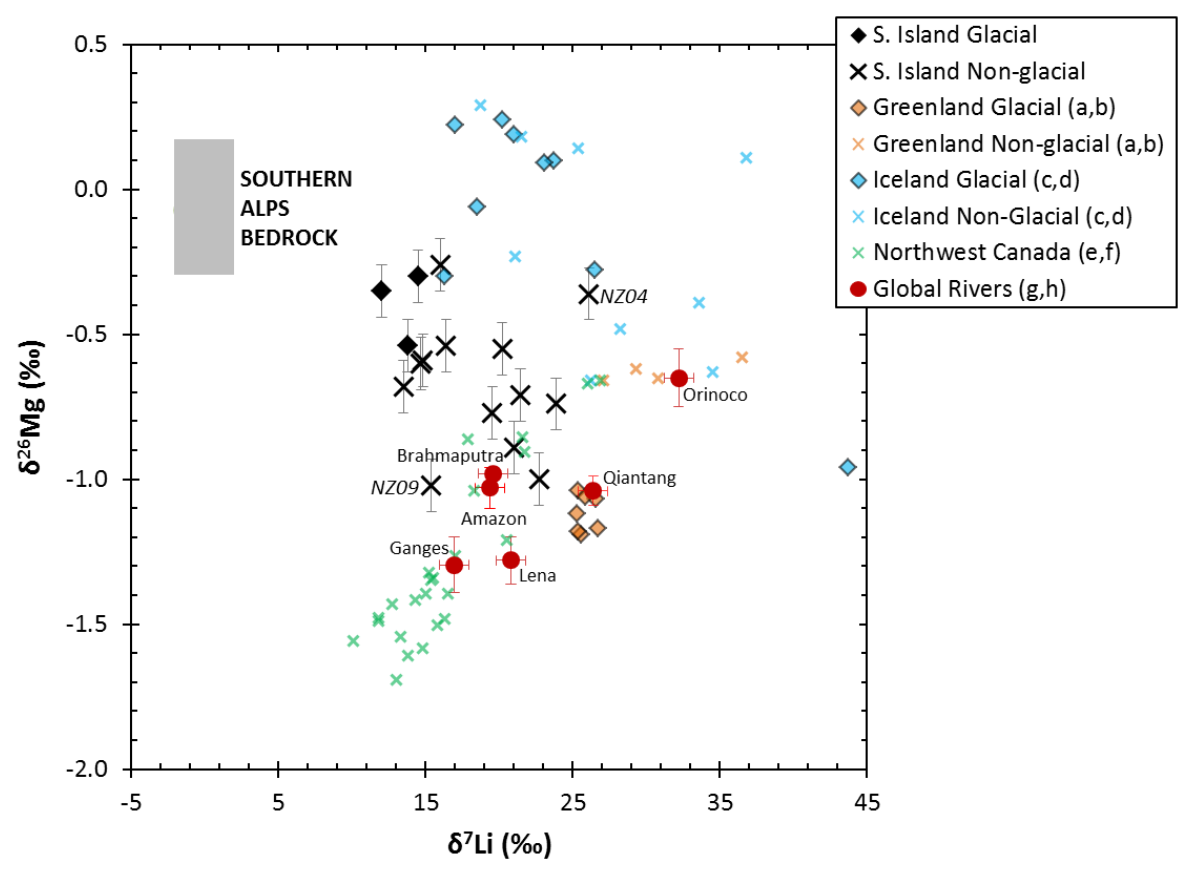


FIGURE 6.22: $\delta^7 \text{Li}$ value against $\delta^{26} \text{Mg}$ value in the dissolved load of the rivers draining the Southern Alps, with comparison to global river data. Data sourced from: $^a\text{(Wimpenny et al., 2010b)}$, $^b\text{(Wimpenny et al., 2011)}$, $^c\text{(Pogge von Strandmann et al., 2006)}$, $^d\text{(Pogge von Strandmann et al., 2008)}$, $^e\text{(Millot et al., 2010)}$, $^f\text{(Tipper et al., 2012)}$, $^g\text{(Huh et al., 1998)}$, $^b\text{(Tipper et al., 2006b)}$. The grey box represents the range of $\delta^7\text{Li}$ and $\delta^{26}\text{Mg}$ values for the Southern Alps bedrock. The external reproducibility of the $\delta^{26}\text{Mg}$ and $\delta^7\text{Li}$ (smaller than the data points) analyses is 2σ .

In contrast, there is some evidence for a negative correlation for Icelandic rivers (Pogge von Strandmann et al., 2006; Pogge von Strandmann et al., 2008), and rivers draining the Southern Alps (Figure 6.21), although two outliers from this trend have been identified ($R^2 = 0.35$, minus two outliers). The outlier from Thunder Creek (NZ04) has undergone a large amount of Li isotopic fractionation, but only minor Mg isotopic fractionation. The Li concentration in this river is 0.08 μ mol/L, much lower than the riverine average of 0.25 μ mol/L, which suggests that a large portion of the dissolved Li in this river has been lost to secondary mineral formation, resulting in a heavy δ^7 Li signature. In addition, the Mg concentration in this river (20.72 μ mol/L) is slightly higher than the riverine average of 18.22 μ mol/L suggesting that little dissolved Mg is being lost to secondary mineral formation in this river. The outlier from Sheil's Creek (NZ09) has undergone a large amount of Mg isotopic fractionation, while little Li isotopic fractionation has occurred. The Mg concentration

in this river is low (9.37 μ mol/L) compared to the riverine average of 18.22 μ mol/L, suggesting that a large portion of the dissolved Mg in this river has been lost to secondary mineral formation, resulting in a light δ^{26} Mg value. The Southern Alps rivers and Icelandic Rivers are affected by the primary dissolution of only one lithology, and therefore the effect of mixing upon the isotopic values can be ruled out. The Southern Alps rivers are also only affected by isotopic fractionation via secondary mineral formation in one direction, and so fractionation would be kinetically-limited.

The variations observed highlight the complexities associated with distinguishing mixing from processes inducing isotopic fractionation in stable isotopic data. Figure 6.22 also highlights the inherent variations that can be observed between different weathering environments, adding to the complexity of extrapolating local studies to global interpretations.

The rivers draining the Southern Alps show a relatively large range of δ^{26} Mg values (-1.02 to -0.26‰), whereas little isotopic heterogeneity can be observed in the bedrock of the Southern Alps (-0.26 to +0.14‰; Figure 6.3), therefore it is unlikely that mixing between source rocks is responsible for the Mg isotopic fractionation observed in the rivers. The riverine suspended particles, which contain a higher proportion of secondary alteration products, also show little Mg isotopic heterogeneity (-0.22 to -0.09 ‰; Figure 6.23), and are within range of bedrock δ^{26} Mg values. This indicates that multiple processes may be controlling Mg isotopic fractionation, e.g. mixing between

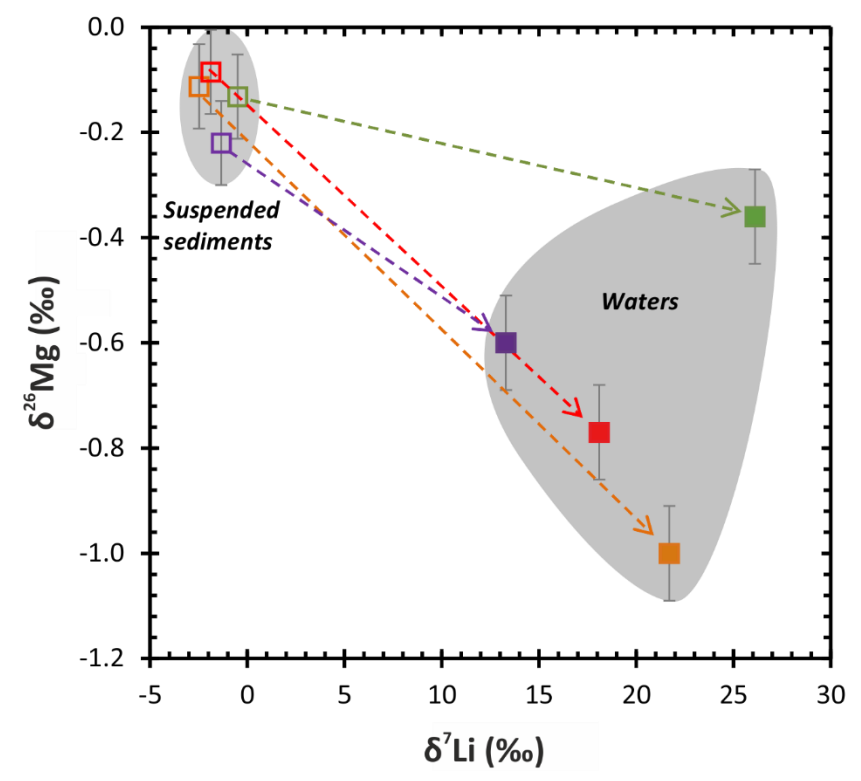


FIGURE 6.23: $\delta^7 Li$ value against $\delta^{26} Mg$ value in the dissolved load (filled symbols) and riverine suspended load (open symbols) of the rivers draining the Southern Alps. The arrows link corresponding suspended sediment and water samples of rivers as follows: red – Rakai, green – Thunder Creek, purple – Deception, orange – Wanganui Tributary. The external reproducibility of the $\delta^{26} Mg$ and $\delta^7 Li$ (smaller than the data points) analyses is 2σ .

source rocks, secondary mineral formation, and biotic activity. However, quantifying the exact impact of each of these processes would be very difficult with current data sets. We have determined that it is likely that secondary mineral formation is the dominant control upon Mg and Li isotopic fractionation, and there is evidence for a weak negative correlation between δ^7 Li and δ^{26} Mg values in the dissolved load of the rivers draining the Southern Alps.

6.5 Summary

- There is little variation in Mg concentration observed in the metasedimentary bedrock samples from the Southern Alps (5910-14700 $\mu g/g$), although a higher Mg concentration was observed in a metabasalts (52500 $\mu g/g$). Little variation is observed in δ^{26} Mg values of the bedrock samples (δ^{26} Mg = -0.26 to +0.14‰). Protolith lithology appears to have no effect upon the δ^{26} Mg value of the bedrock. Increasing metamorphic grade also appears to have little effect upon the δ^{26} Mg value of the bedrock.
- The suspended particulate material shows little/no variation in magnesium concentration or $\delta^{26} Mg$ signature. The mica mineral separates, river sands and riverine suspended loads are all within range of bedrock $\delta^{26} Mg$ values, although the riverine suspended load has a wider range of Mg concentration ([Mg]_{suspended load} = 2800-14000 $\mu g/g$; [Mg]_{bedrock} = 5900-53000 $\mu g/g$).
- Mica minerals are a major source of Mg in the bedrock (>80%), as they have high Mg concentrations (11300-59000 μ g/g). There is little difference in the range of δ^{26} Mg values of the bedrock (-0.26 to +0.14‰) and the mica mineral separates (-0.27 to -0.09‰), which suggests that the δ^{26} Mg signature of the bedrock is strongly influenced by the δ^{26} Mg signature of micas present in the bedrock.
- The rivers draining the Southern Alps are within range of Mg concentration and δ^{26} Mg values observed for global rivers in previously published work. However, the Southern Alps river waters are at the lower end of the Mg concentration range (7.21-69.3 μ mol/L), compared to rivers globally (8.28-580 μ mol/L). The river waters are also enriched in 24 Mg relative to the bedrock and weathering products (δ^{26} Mg_{dissolved} = -1.02 to -0.26%; δ^{26} Mg_{bedrock} = -0.26 to +0.14%).
- There is little isotopic heterogeneity between the lithological protoliths of the Southern Alps, yet riverine δ^{26} Mg values show a large range. Therefore, primary mineral dissolution may be causing some Mg isotopic fractionation, but the effect of this process is likely to be relatively minor.

- Secondary mineral formation during weathering is the dominant control on Mg isotopic fractionation in river waters draining the Southern Alps. XRD analyses have shown the presence of secondary clays (illite, kaolinite and smectite) in the Southern Alps rivers, and geochemical modelling of saturation states of these minerals shows that they are oversaturated (0 to +4) and have the potential to precipitate.
- Rainfall and erosion appear to have little impact upon the $\delta^{26}Mg$ value in rivers draining the Southern Alps. This suggests that climate does not have a direct control upon riverine $\delta^{26}Mg$ values.
- The glacial rivers of the Southern Alps generally have heavier δ^{26} Mg values (average δ^{26} Mg = -0.40 ± 0.14‰) than non-glacial rivers (average δ^{26} Mg = -0.67 ± 0.41‰), and are thus less fractionated from the bedrock (δ^{26} Mg_{bedrock} = -0.26 to +0.14‰). The glaciers in the Southern Alps are high velocity and are subject to high degrees of melting, leading to high levels of mechanical erosion and more congruent weathering by lowering the water-rock interaction time (inhibiting the formation of secondary minerals), resulting in heavier glacial river δ^{26} Mg values.
- Although calcite dissolution in the Southern Alps has resulted in an abundance of Ca^{2+} in the river waters, rivers with high Ca/Na do not have low $\delta^{26}Mg$ values. This suggests that the Mg concentration in hydrothermal calcite is low and that it has little influence upon the riverine $\delta^{26}Mg$ composition.
- A weak correlation can be observed between silicate weathering rate and riverine δ²⁶Mg value; as silicate weathering rate increases, the riverine δ²⁶Mg values become lighter. This in generally in agreement in major global rivers. The rivers of the Southern Alps are subject to a 'kinetic-limited' regime, and it is likely that if mechanical erosion were much higher, an increase in riverine δ²⁶Mg values would be observed as rivers become less fractionated from the bedrock.
- A weak relationship can be observed between Mg/Na and riverine δ^{26} Mg values, which is consistent with the formation of secondary minerals. A positive correlation between Mg/Na and δ^{26} Mg value in the dissolved load would reflect the incorporation of heavy Mg into secondary minerals, whereas Na remains in solution.
- The formation of secondary minerals during chemical weathering appears to be the dominant control upon Mg isotopic fractionation. However, the extent of the role of other processes fractionating Mg isotopes (primary mineral dissolution and biotic activity) is unknown, although it seems likely that the effects of these processes are minor.

• There is evidence for a weak negative correlation between δ²⁶Mg values and δ⁷Li values in the dissolved load of the rivers draining the Southern Alps, which highlights the coupling between Li and Mg isotopes in their chemical behaviour during weathering. However, not all studies display evidence for a negative correlation between these two isotopic systems, suggesting that the behaviour of these isotopes may vary between different weathering environments, which adds to the complexity of extrapolating local studies to global interpretations.

Li and Mg Isotope Fractionation in Warm Springs

7.1 Introduction

Due to the large relative mass difference between 6 Li and 7 Li, there are large differences in the lithium isotopic signature (δ^7 Li) of natural reservoirs. This means that lithium isotopes are effective tracers of weathering processes, as the isotopic compositions in solution are dependent on the isotopic composition of the material being weathered, and the secondary mineral reactions occurring. Generally, hydrothermal spring waters display a wide range of δ^7 Li values (Tomascak et al., 2003; Kısakűrek et al., 2005; Pogge von Strandmann et al., 2006; Pogge von Strandmann et al., 2010), which range from bedrock δ^7 Li values to heavier δ^7 Li values (Figure 1.9).

Surface water (i.e. river water) δ^7 Li compositions are controlled by the rate of Li release into solution by the dissolution of primary minerals and by the rate of Li removal from solution by secondary mineral precipitation. However, the warm springs of the Southern Alps are subject to higher temperatures, which may affect the minerals that are precipitated from solution and how Li isotopic fractionation occurs and to what extent. In order to better understand the processes occurring at depth, the δ^7 Li signatures of terrestrial hydrothermal spring waters need to be characterised, and the dominant processes controlling Li isotopic fractionation and the extent of fractionation need to be determined. In addition, the utility of Li isotopes for tracking fluid-rock interaction in a hydrothermal system will be assessed. In this chapter, the δ^7 Li composition of spring waters and spring suspended sediment collected from the Southern Alps, New Zealand, will be used to investigate processes occurring at depth.

7.2 Hydrothermal Fluid Flow in the Southern Alps

The Southern Alps mountain range has been subject to collisional tectonics and is presently undergoing rapid uplift, where advection of rock occurs faster than heat can be conducted laterally, which has produced a thermal anomaly (Koons, 1987). Rapid erosion effectively removes rock in the Southern Alps, which along with rapid uplift, has raised the brittle-ductile transition zone, which may lie only 6-8 km below the surface in the areas of highest uplift (Koons, 1987; Craw, 1997; Leitner et al., 2001; Sutherland et al., 2012). This has resulted in high geothermal gradients estimated between 40-200 °C/km in the upper crust (Allis et al., 1979; Koons, 1987; Allis and Shi, 1995; Shi et al., 1996; Craw, 1997; Batt and Braun, 1999; Toy et al., 2010). The Deep Fault Drilling Project (DFDP-1) drilled a ~150 m borehole at Gaunt Creek, and measured a geothermal gradient of 62.6 ± 2.1 °C/km (Sutherland et al., 2012). Although, recent findings from the DFDP-2 drilling project on the Alpine Fault have suggested that the geothermal gradient is >100 °C/km, and may even be as high as 140-150 °C/km in the upper 1 km of the crust (DFDP-2, unpublished data).

In the Southern Alps, evidence for fluid flow within the mountain range is shown by warm springs emanating up to 20 km south east of the Alpine Fault (Reyes et al., 2010; Menzies et al., 2014), the presence of hydrothermal veins (Craw, 1988; Holm et al., 1989; Jenkin et al., 1994; Campbell et al., 2004), and hydrothermally altered rocks (Warr and Cox, 2001; Boulton et al., 2012). The stable isotopic signatures (δD and $\delta^{18}O$) of the Southern Alps springs (Barnes et al., 1978; Jenkin et al., 1994; Upton et al., 1995; Reyes et al., 2010) indicate that meteoric waters are the dominant fluid source in the upper ~2 km of the crust (Menzies et al., 2014). At depths of more than 2 km, variability in δ^{18} O values in veins is thought to reflect fluid-rock interactions along different fluid flow paths (Menzies et al., 2014), instead of mixing between meteoric and metamorphic fluids (Jenkin et al., 1994). This is because deeper, ductilely deformed veins would be expected to have a higher proportion of metamorphic fluids (and higher δD values), whereas the opposite is measured (Menzies et al., 2014). Some vein samples appear to be deposited under lithostatic pressure, suggesting that surface-derived fluids may infiltrate down to the brittle-ductile transition zone (Jenkin et al., 1994). In addition, fluid flux calculations have shown that the input of meteoric water is at least two orders of magnitude higher than the estimated metamorphic water production (Menzies et al., 2014). This is likely due to the exceptionally high precipitation on the western side of the Main Divide, up to ~12 m of rainfall per year (Griffiths and McSaveney, 1983; Henderson and Thompson, 1999; Woods et al., 2006).

7.3 Methods

A detailed description of the methods used for the determination of lithium isotopic values is given in Chapter 3 (Section 3.5). In brief, Li was separated from the sample matrix using cation exchange

chromatography. Acid-cleaned PTFE columns were loaded with AG50W-X12 cation exchange resin to a height of 8.5 cm in 0.2 M TD HCl, and the Li fraction was eluted with 0.2 M TD HCl. Li isotopic analyses were carried out on a Thermo Scientific Neptune MC-ICP-MS at the National Oceanography Centre, Southampton. Both a CETAC Aridus IITM and a ThermoFinnigan stable introduction system (SIS) were used depending on the Li concentration in the samples. The Li isotopic values are expressed as δ^7 Li, the per mil (‰) deviation of the 7 Li/ 6 Li ratio from the international NIST standard LSVEC. To ensure that no isotopic fractionation occurred during column chemistry, LSVEC, IAPSO seawater and a series of rock reference materials (JB-2, BCR-2, JSl-1 and JSl-2) were passed through the cation exchange columns and analysed within each instrument analysis. The external reproducibility (2σ) of the of the δ^7 Li values of the fluid samples from this study is $\pm 0.61\%$, and $\pm 0.64\%$ for rock samples (Table 3.4).

Full details of the methods used to determine the Mg isotopic composition of the spring waters is given in Chapter 3 (Section 3.6). Briefly, Mg was separated from the sample matrix using cation exchange chromatography. Acid-cleaned PTFE columns were loaded with AG50W-X12 cation exchange resin to a height of 8.5 cm (in 0.8 M TD HNO₃), unwanted elements were discarded with a wash of 0.8 M TD HNO₃, and the complete Mg fraction was eluted with 2 M TD HNO₃. This column procedure was carried out twice on all samples and standards to ensure complete separation of Mg from all other elements. Mg isotopic analyses were carried out on a Thermo Scientific Neptune MC-ICP-MS, using a ThermoFinnigan sample introduction system (SIS), at the National Oceanography Centre, Southampton. The Mg isotopic values are expressed as δ^{26} Mg, the per mil (‰) deviation from the pure Mg standard DSM-3 (Dead Sea Magnesium). To ensure that no isotopic fractionation occurred during column chemistry, DSM-3, IAPSO and rock standards (JB-2, BCR-2 and JDo-1) were passed through the cation exchange columns and analysed within each analytical run (Table 3.7). The external reproducibility for the δ^{26} Mg and δ^{25} Mg analyses was determined by repeated analyses of standards that have well constrained Mg isotopic values in the literature, and is given as 2σ . The external reproducibility for the rock samples was determined by repeated analyses of JB-2 (n = 3), and is $\pm 0.08\%$ for δ^{26} Mg and $\pm 0.07\%$ δ^{25} Mg. The external reproducibility for the fluid samples was determined by repeated analyses of IAPSO (n = 7), and is $\pm 0.09\%$ for $\delta^{26}Mg$ and $\pm 0.06\%$ for δ^{25} Mg.

7.4 Results

As discussed in Chapter 5, the spring water samples ($\delta^7 \text{Li}_{\text{spring}} = +0.2 \text{ to } +10.8\%$) collected from the Southern Alps generally have $\delta^7 \text{Li}$ values that range from bedrock composition ($\delta^7 \text{Li}_{\text{bedrock}} = -1.6 \text{ to } +1.4\%$) to higher values, approaching river water compostion ($\delta^7 \text{Li}_{\text{river}} = +11.8 \text{ to } +26.1\%$; Figure 5.2).

As discussed in Chapter 6, the spring waters ($\delta^{26}Mg = -0.74$ to -0.39%) have $\delta^{26}Mg$ values that fall within range of river water values ($\delta^{26}Mg = -1.02$ to -0.26%), and are thus fractionated from the bedrock ($\delta^{26}Mg = -0.26$ to +0.14%; Figure 7.2).

7.4.1 Metasedimentary-hosted Springs

Spring waters from the metasedimentary-hosted hydrothermal system of the Southern Alps display a large range of δ^7 Li values (+0.2 to +10.8‰) and Li concentration (30.6-303 µmol/L). These values are similar to hydrothermal spring data (Figure 7.1) from the Mono Basin in California (δ^7 Li = +3.0 to +17‰; Tomascak et al., 2003), the Azores (δ^7 Li = +1.0‰; Pogge von Strandmann et al., 2010) and the Himalayas (δ^7 Li = +2.5‰; Kisakűrek et al., 2005).

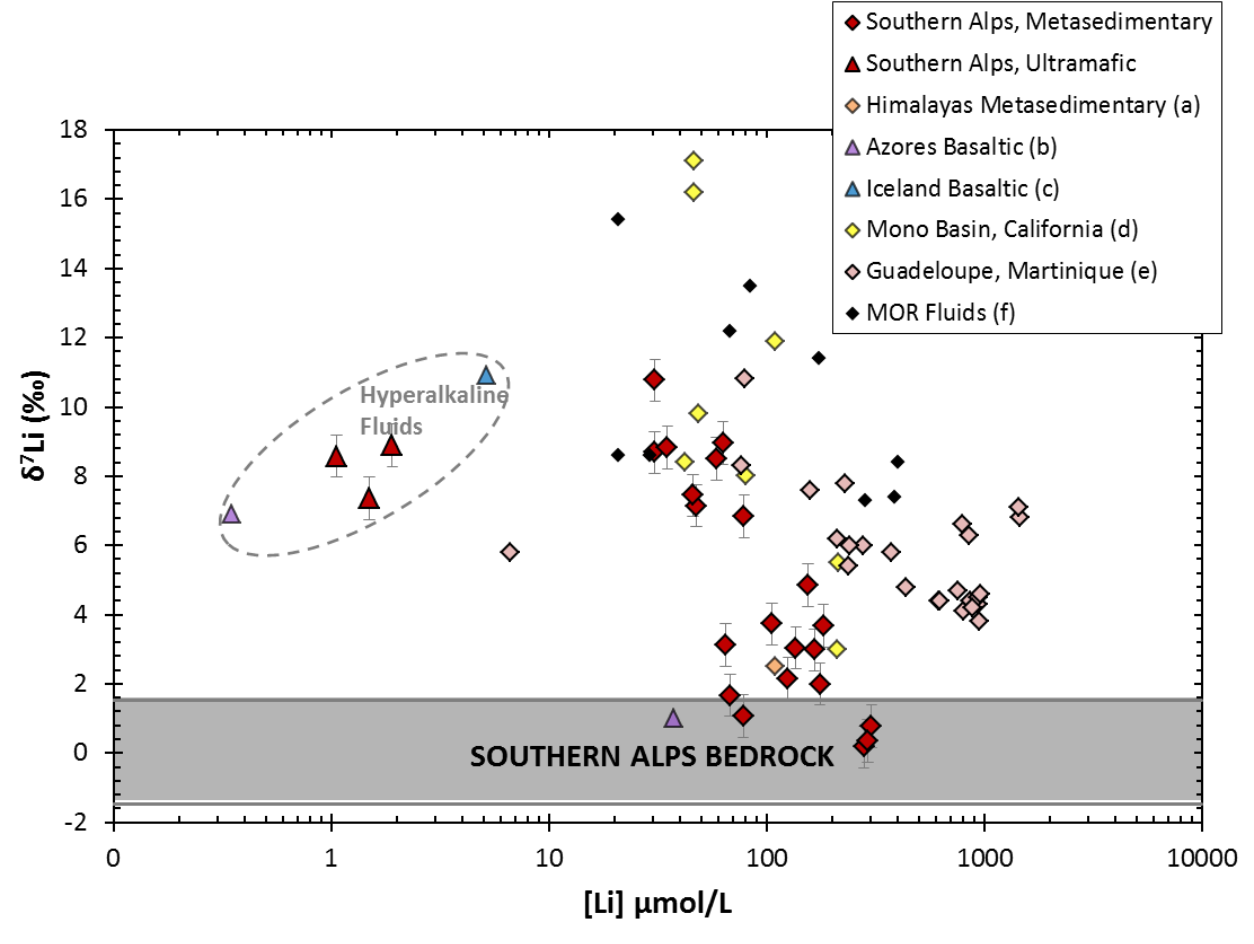


FIGURE 7.1: Lithium concentration against $\delta^7 Li$ value of the spring waters in the Southern Alps, with comparison to published data. Data sourced from: ^a(Kısakűrek et al., 2005), ^b(Pogge von Strandmann et al., 2010), ^c(Pogge von Strandmann et al., 2006), ^d(Tomascak et al., 2003), ^e(Millot et al., 2010b), ^f(Foustoukos et al., 2004). The grey band represents the range of bedrock $\delta^7 Li$ values across the Southern Alps. The external reproducibility of the $\delta^7 Li$ analyses from this study is 2σ .

Metasedimentary-hosted spring waters of the Southern Alps display a relatively small range of δ^{26} Mg values (-0.74 to -0.39‰) and Mg concentration (49-194 µmol/L) compared to hydrothermal spring water data from the literature (Figure 7.2). Himalayan springs have a wide range of δ^{26} Mg values (-0.87 to -0.05‰), and have higher Mg concentrations than the Southern Alps springs (798-4304 µmol/L; Tipper et al., 2008).

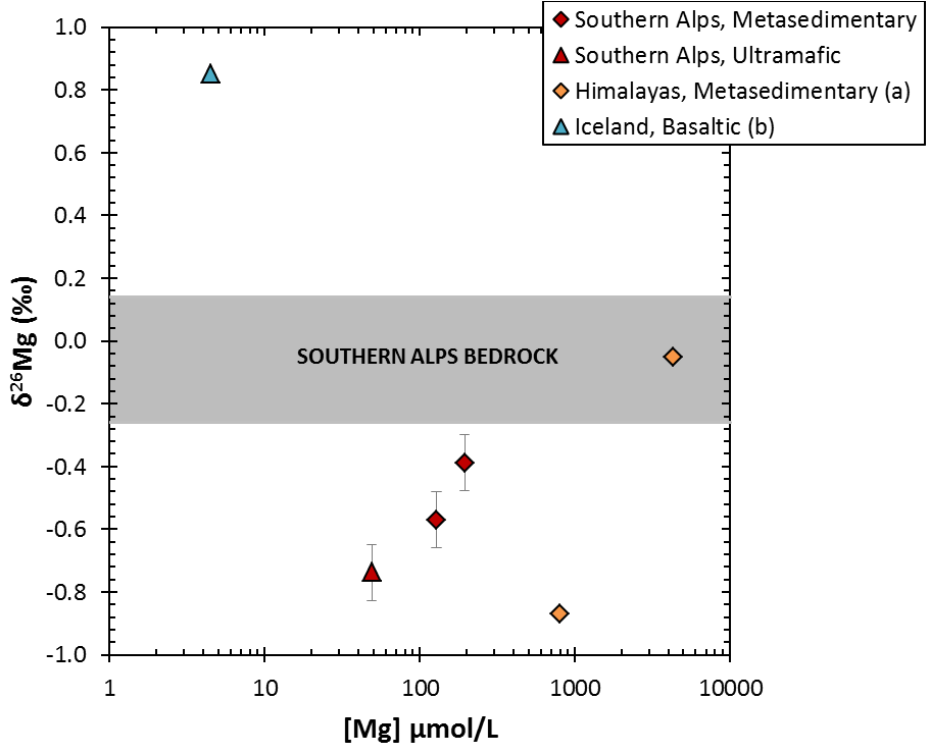


FIGURE 7.2: Magnesium concentration and $\delta^{26}Mg$ value of the spring waters in the Southern Alps, with comparison to published data. Data sourced from: ^a(Tipper et al., 2008), ^b(Pogge von Strandmann et al., 2008). The grey band represents the range of bedrock $\delta^{26}Mg$ values across the Southern Alps. The external reproducibility of the $\delta^{26}Mg$ analyses from this study is 2σ .

7.4.2 Ultramafic-hosted Springs

Ultramafic-hosted springs emanate from the Permian Dun Mountain Ophiolite Belt, which has been separated by ~460 km of strike-slip movement on the Alpine Fault (Norris et al., 1990; Sutherland, 1996). The springs have interacted with peridotites (Red Hills in the north and Cascade in the south), and are hyperalkaline, absorbing atmospheric CO₂ and precipitating calcite on emerging at the surface (Menzies, 2012).

The δ^7 Li values of the hyperalkaline spring waters range from +7.4‰ to +8.9‰ (Figure 7.1). These values are within range of the metasedimentary-hosted springs of the Southern Alps, but they are at the heavier end of this range. The Li concentration in the hyperalkaline springs is much lower (1.06-1.90 µmol/L) than the Li concentration range in the metasedimentary-hosted springs (30.6-303 µmol/L; Figure 7.1).

The ultramafic-hosted hyperalkaline hydrothermal springs from the Southern Alps plot relatively close to a hydrothermal fluid sample from the Azores ($\delta^7 \text{Li} = +6.9\%$; Pogge von Strandmann et al., 2010) and a fluid sample from Iceland ($\delta^7 \text{Li} = +10.9\%$; Pogge von Strandmann et al., 2006).

The δ^{26} Mg value of the hyperalkaline spring water from the Southern Alps (-0.74‰) is lower than the range of δ^{26} Mg values of the metasedimentary-hosted springs (-0.57 to -0.39‰; Figure 7.2). The Mg concentration in the hyperalkaline spring fluid is lower (49 µmol/L) than the Mg concentration in the metasedimentary-hosted springs (128-194 µmol/L). Although, the hyperalkaline fluids from the Southern Alps and Iceland (Pogge von Strandmann et al., 2008) have the lowest Mg concentrations, these fluids have very different δ^{26} Mg values (δ^{26} Mg_{Southern Alps} = -0.74‰; δ^{26} Mg_{Iceland} = +0.85‰; Pogge von Strandmann et al., 2008; Figure 7.2).

7.5 Discussion

7.5.1 Effect of Temperature

The temperature of the metasedimentary-hosted spring waters was measured as they were expelled at the surface (Menzies, 2012), but this is not representative of the fluid temperature at depth. Geothermometers can be constructed using major and trace element geochemistry to estimate the temperatures of the last equilibrium water-rock reactions (Truesdell, 1984). A silica geothermometer was used to estimate the temperatures at which the spring waters of the Southern Alps equilibrated with the bedrock (Menzies, 2012). Silica geothermometers are reliant upon the temperature dependence of quartz solubility (i.e. the concentration of SiO_2 in solution is higher at higher temperatures), which is unaffected by differences in local mineral suites, gas partial pressures and concentrations of the dissolved load (Fournier and Rowe, 1966; Fournier and Truesdell, 1970). Several geothermometers were calculated for the Southern Alps springs by Menzies (2012), and the silica geothermometer displayed the best relationship with measured sampling temperature ($R^2 = 0.74$). The silica geothermometer relies only on SiO_2 , which behaves more linearly than the alkali geothermometers (Menzies, 2012). The silica geothermometer assumes:

- 1. There is no steam loss; however, there is no evidence for steam loss from hydrothermal fluids in the Southern Alps.
- 2. There has been no precipitation of silica.
- 3. There has been no shallow level mixing of spring fluids with lower temperature infiltrating fluids, which would alter the sampling temperature and cause a decrease in estimated equilibration temperature (Menzies, 2012).

Therefore, the temperatures estimated from the silica geothermometer should be taken as a minimum equilibration temperature for spring waters in the Southern Alps (Menzies, 2012).

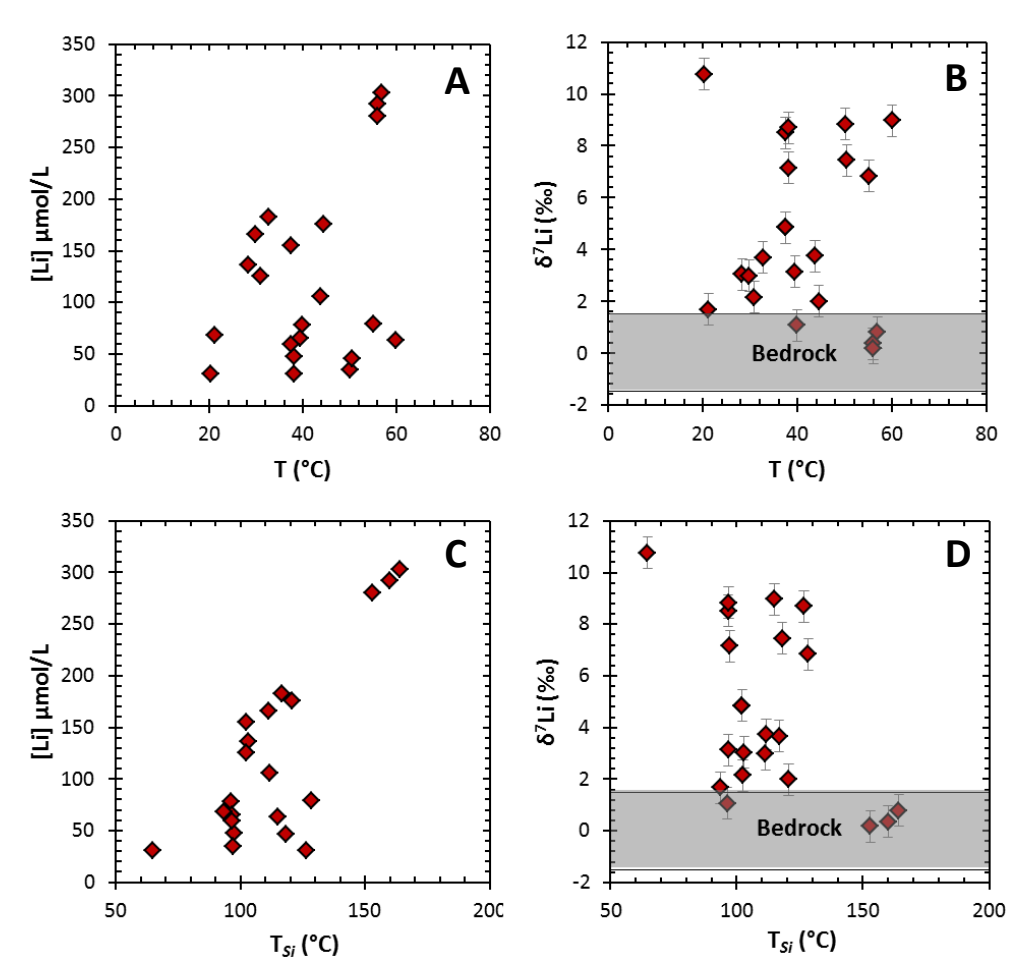


FIGURE 7.3: Measured fluid temperatures (T) of the spring waters against (A) Li concentration and (B) $\delta^7 \text{Li}$ value. Plots C and D show calculated silica equilibration temperature (T_{Si}) of the spring waters against Li concentration and $\delta^7 \text{Li}$ value. The grey band represents the range of bedrock $\delta^7 \text{Li}$ values across the Southern Alps. Calculations of T_{Si} are from Menzies (2012). The error on the T_{Si} values is estimated to be ± 10 °C. The external reproducibility of the $\delta^7 \text{Li}$ analyses is 2σ .

An increase in the concentration of dissolved Li in spring waters should be observed with increasing temperature due to increased rock dissolution at higher temperatures and increased uptake of lithium in weathering products at low temperatures (Fouillac and Michard, 1981). The measured temperature (T) of the hydrothermal spring waters shows no correlation with Li concentration or δ^7 Li value (Figure 7.3 A and B), but there is a weak relationship between silica equilibration temperature (T_{Si}) and Li concentration (Figure 7.3 C). However, this apparent positive correlation is skewed by samples from Welcome Flat, which display very high silica equilibration temperatures. A weak negative relationship can be observed between T_{Si} and δ^7 Li, however, again this relationship may be skewed by samples from Welcome Flat. Generally, the values with the highest T_{Si} values have δ^7 Li values closest to the bedrock, and the samples with the lowest T_{Si} values plot closest to river δ^7 Li values, which is broadly what would be expected. These findings are consistent with hydrothermal

inputs, which show a transition from net uptake of Li to net removal of Li, which occurs at ~150 °C (Seyfried et al., 1984; James et al., 2003).

7.5.2 Secondary Mineral Formation

As discussed in Chapter 5, a major control upon the $\delta^7 \text{Li}$ composition of river waters is Li isotopic fractionation during chemical weathering via secondary mineral formation. The spring waters emanating from the Southern Alps are generally fractionated from the bedrock to heavier values $(\delta^7 \text{Li}_{\text{springs}} = +0.2 \text{ to } +10.8\%; \delta^7 \text{Li}_{\text{bedrock}} = -1.6 \text{ to } +1.4\%)$, but the spring waters are less fractionated from the bedrock than the river waters draining the Southern Alps. Previous studies have shown that, along the Alpine Fault, secondary mineral assemblages that form under high temperature (chlorite and muscovite) conditions are different from those that form at low temperature (smectite, kaolinite and chlorite) conditions (Warr and Cox, 2001; Boulton et al., 2012).

Mineral saturation states can be calculated using the elemental chemistry of the metasedimentary-hosted spring waters to establish the secondary minerals that may form. These were calculated using the geochemical modelling software Geochemist's Workbench, which estimates mineral stability (degree of oversaturation or undersaturation) in terms of Gibbs free energy (kJ), and the results are given in SI (saturation indices) units. Further details on how the mineral saturation states were calculated is given in Chapter 5. Mineral saturation states were calculated using both the temperature measured upon sampling (T) and the silica equilibration temperature (T_{Si}). These two sets of conditions were used to assess the reactions occurring near the surface at lower temperature, and also reactions occurring at depth at higher temperature.

Illite, smectite and kaolinite are all secondary minerals that form in the Southern Alps rivers, according to geochemical modelling results (see Section 5.4.4). In the modelling results for the spring waters emanating from the Southern Alps, the SI values of the secondary minerals show a negative correlation with pH (Figure 7.4 A and B), indicating that these minerals become increasingly undersaturated with increasing pH, which is consistent with what is observed in the river waters. A weak negative relationship between measured temperature and SI values of illite, kaolinite and smectite can be observed (Figure 7.4 C), which indicates that secondary minerals are increasingly oversaturated at lower temperatures. However, no correlation can be observed between silica equilibration temperature and SI values (Figure 7.4 D). Modelling results using measured temperature values generally yield SI values of secondary minerals between ~0-4, which is similar to the results for the river waters. However, modelling results using silica equilibration temperatures (Tsi) are between -5 to 1. These results used a much higher fluid temperature, which resulted in undersaturated SI values of these secondary

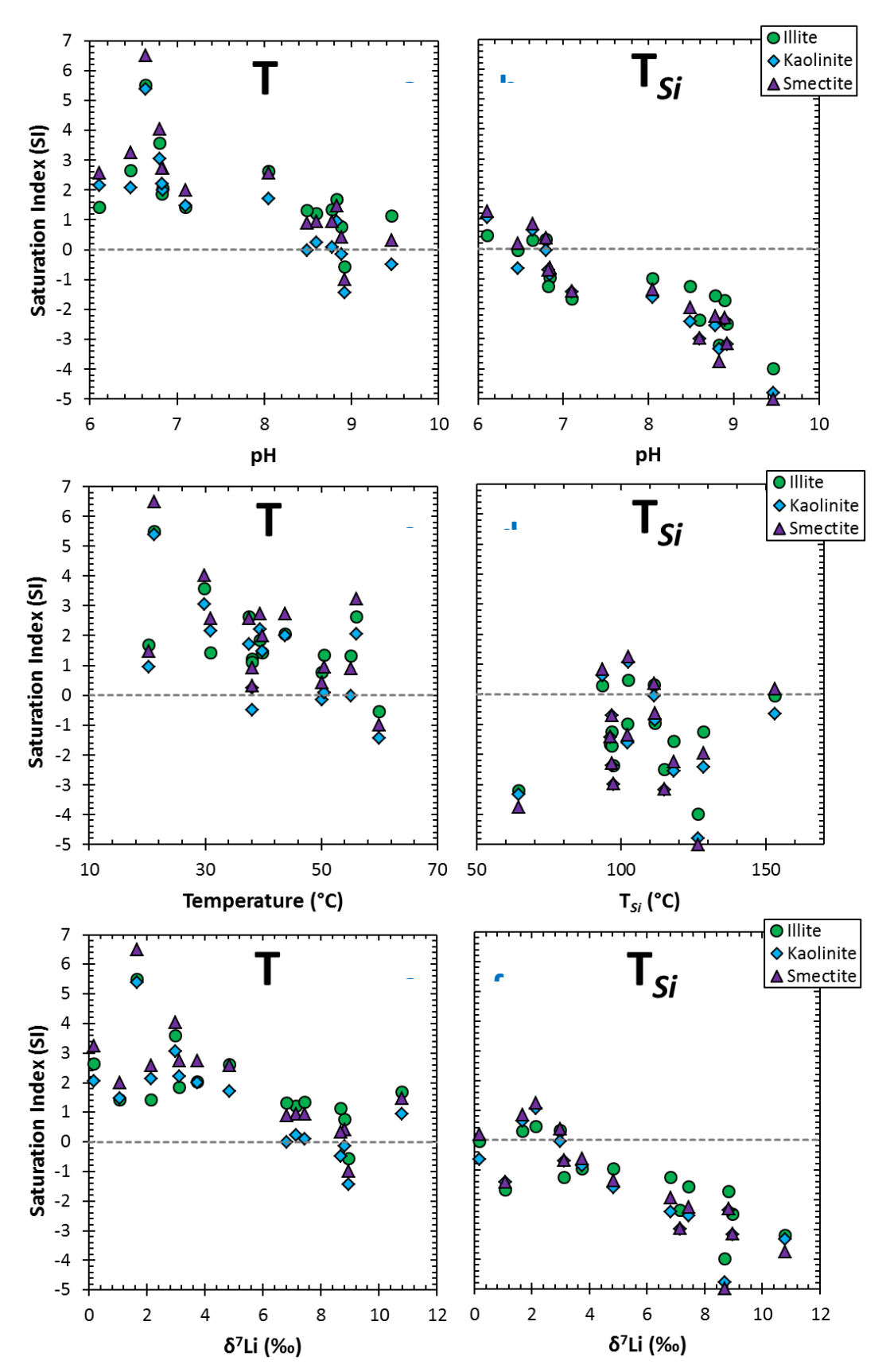


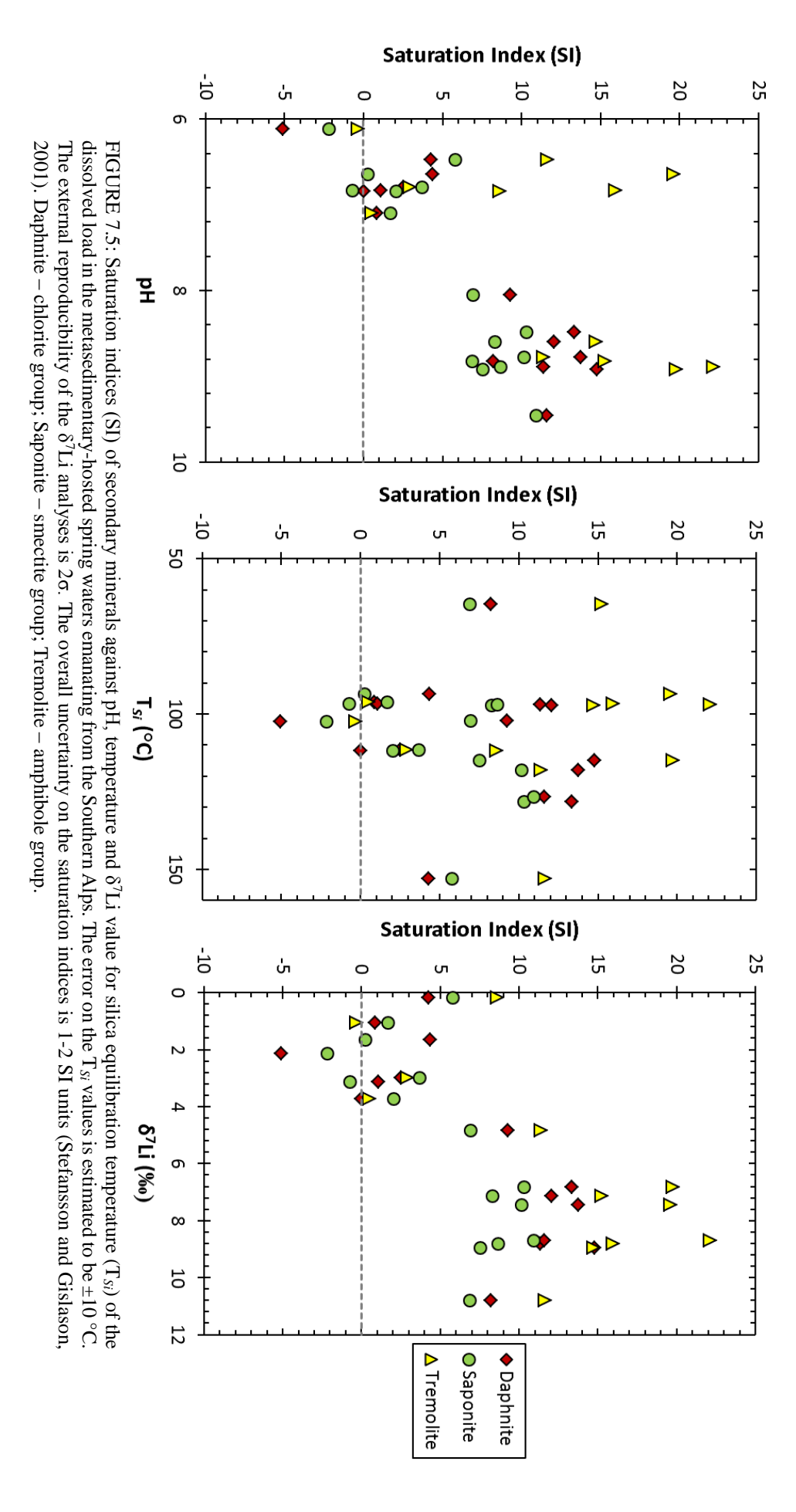
FIGURE 7.4: Saturation indices (SI) of secondary minerals against pH (A and B), temperature (C and D) and $\delta^7 \text{Li}$ value (E and F) for measured temperature (T) and silica equilibration temperature (T_{Si}) of the dissolved load in the metasedimentary-hosted spring waters emanating from the Southern Alps. The error on the T_{Si} values is estimated to be ± 10 °C. The external reproducibility of the $\delta^7 \text{Li}$ analyses is 2σ . The overall uncertainty on the saturation indices is 1-2 SI units (Stefansson and Gislason, 2001).

minerals. This would suggest that secondary clay minerals, such as illite, smectite and kaolinite, are unlikely to form at depth where the temperature is raised, but may be more likely to form as the spring waters approach the suface where temperature is lower. Previous studies have shown that smectite is not stable >150 °C and will only form under low temperature alteration (<120 °C) of muscovite or chlorite (Warr and Cox, 2001). A negative correlation can be observed between δ^7 Li value and SI value for both the geochemical model using measured temperature and the geochemical model using silica equilibration temperature (Figure 7.4 E and F). Although, the latter shows a stronger correlation. This is the opposite trend to what is observed for river waters, and the opposite of what would be expected. A positive correlation would suggest that as secondary minerals become increasingly oversaturated (i.e. SI values increased), the dissolved δ^7 Li value would also increase due to preferential uptake of 6 Li in secondary minerals (Huh et al., 2001). It is possible that at depth and under higher temperature conditions, different secondary minerals are forming which are controlling Li isotopic fractionation in these fluids.

Geochemical modelling results at silica equilibration temperatures (T_{Si}) are oversaturated in different minerals compared to results under measured temperature (T) conditions, which produce results similar to the river waters (see Section 5.4.4). Under silica equilibration temperatures (Figure 7.5), the most frequently observed oversaturated minerals are daphnite (chlorite group), saponite (smectite group) and tremolite (amphibole group), which are known to form through metasomatic processes and can be found along the Alpine Fault (Koons, 1981; Warr and Cox, 2001; Boulton et al., 2012).

The SI values of the secondary minerals daphnite and saponite under silica equilibration temperature conditions show a positive correlation with pH ($R^2 = \sim 0.8$; Figure 7.5), indicating that these minerals become increasingly oversaturated with increasing pH. No relationship can be observed between SI values for tremolite and pH. No relationship can be observed between temperature and SI value of secondary minerals formed under silica equilibration temperatures (Figure 7.5). This suggests that, over a certain temperature, the temperature of the Southern Alps springs at depth has little effect upon the oversaturation/undersaturation of this mineral assemblage.

The SI values of the secondary minerals formed under silica equilibration conditions show a weak positive relationship with δ^7 Li values in the dissolved load of the spring waters ($R^2 = 0.5$ -0.6; Figure 7.5). This is what would be expected, as 6 Li should be preferentially retained in the secondary alteration products (Huh et al., 2001). Therefore, the same process (secondary mineral formation) controlling Li isotopic fractionation in the river waters is occurring in the spring waters, but a different secondary mineral assemblage is formed under higher temperature conditions at depth.



175

7.5.3 Link between Spring Water δ^7 Li and Silicate Chemical Weathering

The difference between the δ^7 Li value of spring waters and the δ^7 Li value of the spring suspended sediments (Δ^7 Li) is given by:

$$\Delta^7 \text{Li}_{\text{suspended-dissolved}} = \delta^7 \text{Li}_{\text{suspended}} - \delta^7 \text{Li}_{\text{dissolved}}$$
 (Eq. 7.1)

In river waters, $\Delta^7 \text{Li}_{\text{suspended-dissolved}}$ is always <0, which indicates that ^6Li is preferentially retained in secondary minerals while ^7Li goes into solution (Huh et al., 1998; Huh et al., 2001). The average $\Delta^7 \text{Li}_{\text{suspended-dissolved}}$ for the spring waters emanating from the Southern Alps is -5.0‰, which is much closer to 0 than the average $\Delta^7 \text{Li}_{\text{suspended-dissolved}}$ for the river waters draining the Southern Alps (-20.5‰). Yet, this does indicate that ^6Li is generally preferentially retained in secondary minerals, while ^7Li goes into the spring water dissolved phase.

The isotopic fractionation factor (α) can be calculated from $\Delta^7 \text{Li}_{\text{suspended-dissolved}}$ values as follows:

$$\alpha = e^{\Delta/1000}$$
 (Eq. 7.2)

Spring water Li isotopic fractionation factors in the Southern Alps range from 0.989-1.000, suggesting that some springs are in equilibrium with the suspended load. The fractionation factors of the spring waters suggest that they are closer to equilibrium than the river waters draining the

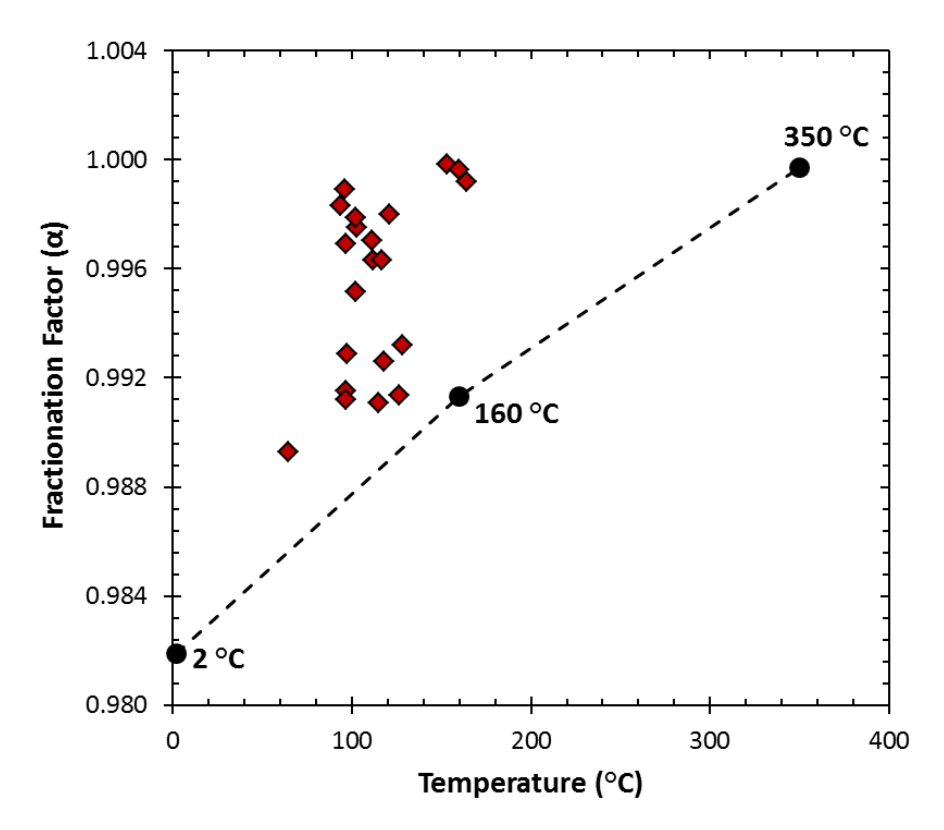


FIGURE 7.6: Silica equilibration temperature of the springs against the lithium isotopic fractionation factor (α). The α values at various temperatures are sourced from the literature: 2 °C (Chan et al., 1992), 160 °C (Magenheim et al., 1994), 350 °C (Chan and Edmond, 1988).

Southern Alps ($\alpha = 0.973$ -0.987; see Section 5.4.5). This is what would be expected, as the higher temperature of the spring waters would result in more fluid-rock interaction, and at higher temperature fractionation is lower (Chan et al., 1994). The lithium isotopic fractionation factors of the spring waters weakly follow the trend displayed by fractionation factors from the literature for various temperatures (Figure 7.6). Although, the springs from the Southern Alps tend to have a higher fractionation factor for any given temperature.

On a plot of δ^7 Li value of the metasedimentary-hosted spring dissolved load and δ^7 Li value of the metasedimentary-hosted spring suspended load, the data generally shows that the springs have consistently higher δ^7 Li values than the suspended load (Figure 7.7). However, a spring water sample from Welcome Flat plots just below the 1:1 line between δ^7 Li signatures of the spring water dissolved and suspended load. This spring has a positive Δ^7 Li_{suspended-dissolved} value of +0.2‰ and α = 1.000, which would suggest that no significant secondary mineral formation (other than carbonate) is occurring in this spring and that the fluid and suspended load are near equilibrium. The Welcome Flat spring flow rate is very vigorous and it carries a lot of rock debris, including travertine and calcite, and is also ~11 km from the Alpine Fault yet has the highest silica equilibration temperature measured of all springs (153 °C; Menzies, 2012). This may be due to either a higher geothermal gradient in this area or the fluids penetrate to greater crustal depths than other springs which may be aided by increased permeability. This may explain why this spring water is closer to equilibrium.

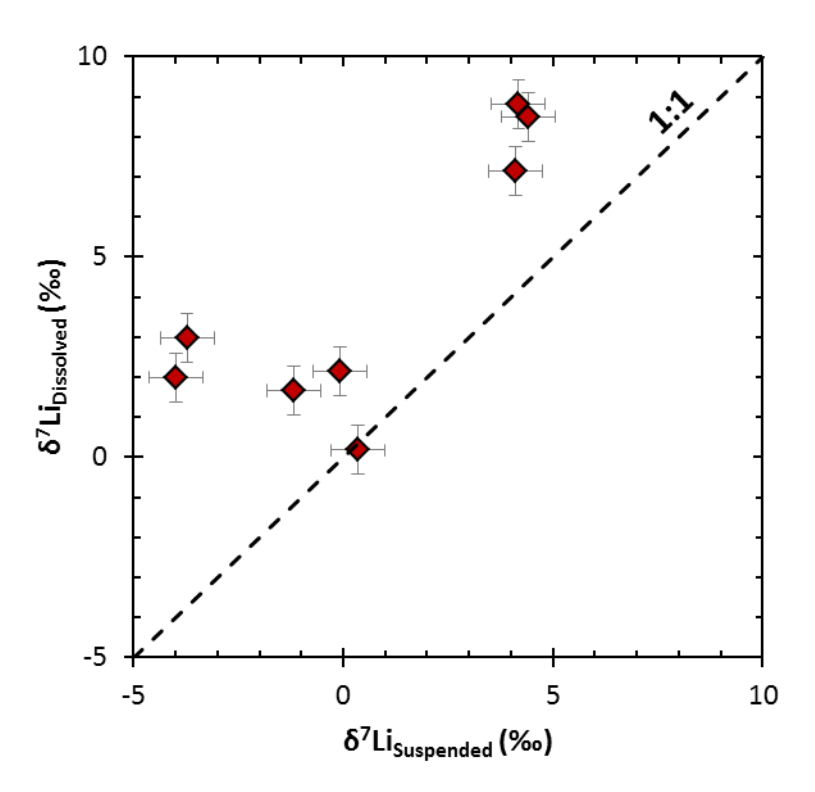


FIGURE 7.7: $\delta^7 Li$ value of the spring suspended load against the $\delta^7 Li$ value of the dissolved load of the metasedimentary-hosted spring waters emanating from the Southern Alps. The external reproducibility of the $\delta^7 Li$ analyses is 2σ .

It was established in Chapter 5 that the rivers draining the Southern Alps show a negative relationship between Li/Na and δ^7 Li value (Figure 5.23), which is consistent with global river data (Kısakűrek et al., 2005; Pogge von Strandmann et al., 2006; Vigier et al., 2009; Pogge von Strandmann et al., 2010; Liu et al., 2015). This reflects the incorporation of Li into secondary minerals, and implies that residence time in surface waters has a major effect upon the δ^7 Li signatures of rivers. However, in the metasedimentary-hosted spring waters emanating from the Southern Alps, no relationship can be observed between Li/Na and δ^7 Li value (Figure 7.8). This may suggest that Li isotopic fractionation via secondary mineral formation may not be the only factor controlling spring water δ^7 Li signatures, or that this mechanism of isotopic fractionation is more complex and variable at higher temperatures.

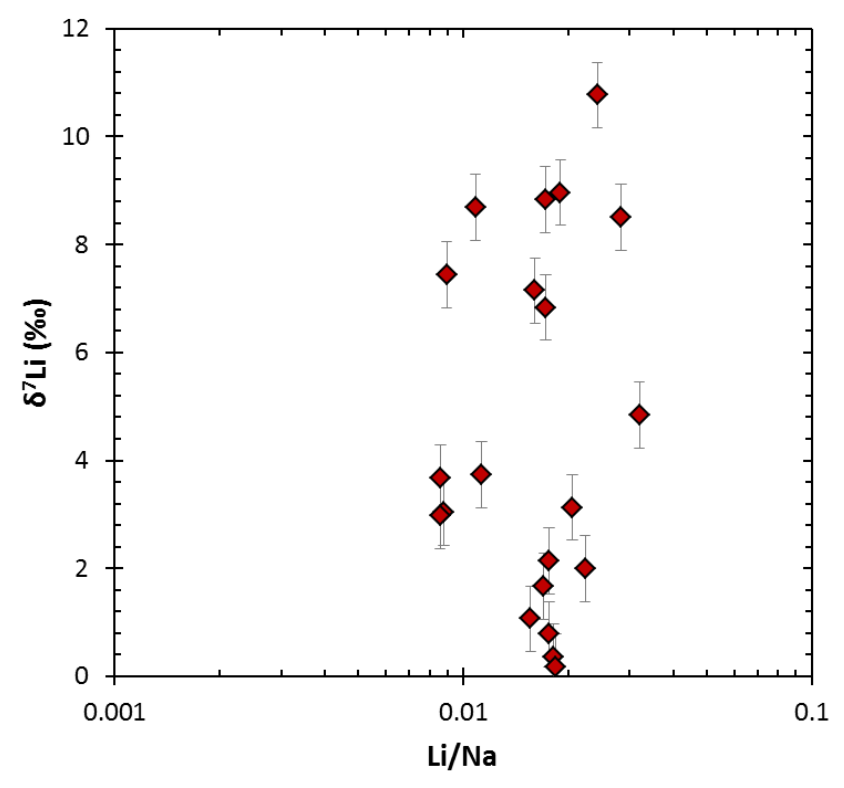


FIGURE 7.8: Li/Na against $\delta^7 Li$ value of the dissolved load of the metasedimentary-hosted spring waters emanating from the Southern Alps. The external reproducibility of the $\delta^7 Li$ analyses is 2σ .

7.5.4 Coupled Mg and Li Isotopes in Spring Waters

As chemical weathering intensity increases and more secondary minerals are formed, the dissolved load δ^{26} Mg value should become lighter and the δ^7 Li value should become heavier, in comparison to the bedrock isotopic values, if Li and Mg are coupled in their chemical behaviour during weathering (Horstman, 1957; Huh et al., 1998). This behaviour is appears to be observed for the spring waters emanating from the Southern Alps (Figure 7.9).

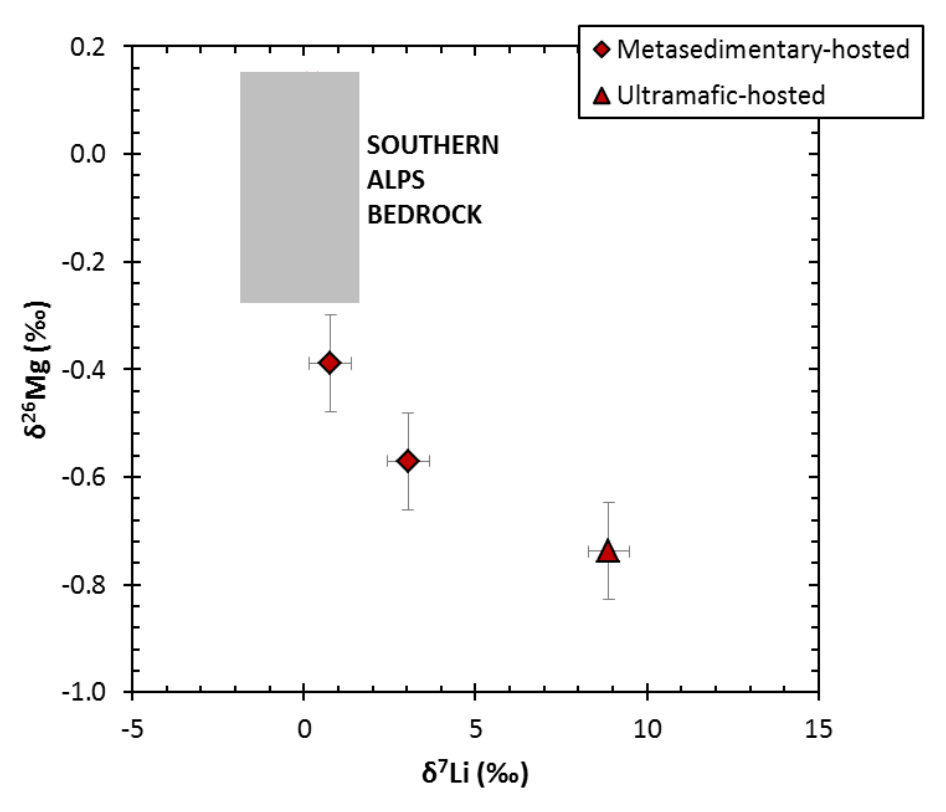


FIGURE 7.9: $\delta^7 Li$ value against $\delta^{26} Mg$ value in the dissolved load of the spring waters emanating from the Southern Alps, with comparison to the Southern Alps bedrock $\delta^7 Li$ and $\delta^{26} Mg$ values. The external reproducibility of the $\delta^7 Li$ and $\delta^{26} Mg$ analyses is 2σ .

7.6 Summary

- The metasedimentary-hosted springs emanating from the Southern Alps have $\delta^7 \text{Li} = +0.2$ to +10.8‰, higher than bedrock ($\delta^7 \text{Li} = -1.6$ to +1.4‰), but not as highly fractionated from the bedrock as the river waters draining the Southern Alps.
- δ^7 Li values of ultramafic-hosted hyperalkaline springs are within range of the metasedimentary-hosted springs, but they have much lower Li concentrations ([Li]_{ultramafic-hosted} = 1.06-1.90 μ mol/L; [Li]_{metasedimentary-hosted} = 30.6-303 μ mol/L).
- A weak negative relationship can be observed between T_{Si} and $\delta^7 Li$, where the values with the highest T_{Si} values have $\delta^7 Li$ values closest to the bedrock, and the samples with the lowest T_{Si} values plot closest to river $\delta^7 Li$ values.
- Mineral saturation states modelled using measured spring water temperature produce similar results to mineral saturation states modelled for the river waters draining the Southern Alps, and produce the same secondary mineral assemblage (illite, kaolinite and smectite) at similar SI values (0 to +4). However, modelling results using silica equilibration temperature yield SI

values that are much more undersaturated for the same secondary mineral assemblage (SI values = -5 to +1). This suggests that these secondary minerals are likely to form nearer the surface, but less likely to form at depth under higher temperature conditions.

- Geochemical modelling results produced using silica equilibration temperatures (T_{Si}) show that a different mineral assemblage is oversaturated in the springs at depth (daphnite, saponite and tremolite). These minerals show a weak positive correlation with δ^7 Li value, indicating that 6 Li is preferentially retained in these mineral phases.
- No correlation can be observed between Li/Na and δ^7 Li value for the spring waters, which suggests that secondary mineral formation may not be the only factor controlling Li isotopic fractionation and spring water δ^7 Li signatures, or that this mechanism of isotopic fractionation is more complex and variable at higher temperatures. However, a negative correlation can be observed between δ^7 Li and δ^{26} Mg values in the dissolved load of the springs, which would suggest that Li and Mg are coupled in their behaviour during secondary mineral formation at higher temperature in spring waters.

Conclusions and Further Work

8.1 Conclusions

8.1.1 Chemical Weathering and Atmospheric CO₂ Drawdown in the Southern Alps

Overall chemical dissolution rates, carbonate dissolution rates, and to a lesser extent silicate dissolution rates in the Southern Alps are relatively high compared to rates calculated for global rivers. Atmospheric CO₂ consumption rates attributed to carbonate dissolution are high compared to rivers globally, but atmospheric CO₂ consumption rates attributed to silicate dissolution are relatively low. This suggests that rapid uplift and erosion increases dissolution of carbonates disproportionately to the dissolution of silicates.

High total chemical dissolution rates and atmospheric CO₂ consumption rates attributed to carbonate weathering are likely to be the result of rapid uplift and erosion along with heavy rainfall west of the Main Divide. Yet, little difference can be observed in silicate dissolution rate east and west of the Main Divide, even though physical erosion is much higher in the west due to increased rates of uplift and rainfall. Atmospheric CO₂ consumption rates attributed to silicate dissolution are in fact higher east of the Main Divide, which indicates that although rapid uplift in the Southern Alps may accelerate chemical dissolution, it does not necessarily enhance the rate of long term atmospheric CO₂ consumption. The important implication of this finding is that periods of rapid uplift in the past (e.g. uplift of the Himalayas ~40 Ma) may not have directly resulted in increased drawdown of atmospheric CO₂ due in increased dissolution of silicates. This potentially calls into question the significance of continental silicate weathering as a major sink of atmospheric CO₂ in the global carbon cycle and the efficiency of this process in drawing CO₂ down from the atmosphere, which may be important to consider for carbon cycle modelling.

However, it should be noted that these calculations say little about the chemical weathering intensity, in terms of precipitation of secondary minerals during chemical weathering.

8.1.2 Li and Mg Isotopic Fractionation

The chemical weathering rates calculated for the Southern Alps are a measure of chemical dissolution. As shown in this study, the process that controls riverine δ^7 Li composition is the incorporation and adsorption of Li on or into newly formed or neo-formed secondary minerals. The chemical weathering rates calculated in Chapter 4 unfortunately do not provide a measure of secondary mineral formation.

The same can be said for riverine $\delta^{26}Mg$ composition, which is also dominantly controlled by fractionation via secondary mineral formation, which is demonstrated in this study. This would therefore explain why we observe little correlation when plotting these riverine isotopic values against silicate weathering rate. Silicate weathering rate is a measure of silicate chemical dissolution, whereas the extent of Li and Mg isotopic fractionation is a measure of secondary mineral precipitation processes.

A limitation at this stage in this field of research is that we are not yet able to discern between incorporation or adsorption of an element onto/into clays. It is likely that these processes would fractionate Li and Mg to different extents and at variable rates. Until we have a better understanding of the processes that occur during formation/neo-formation of clays during chemical weathering processes, we are limited in our interpretation of riverine $\delta^7 Li$ and $\delta^{26} Mg$ isotopic compositions.

8.1.3 Global Implications of δ^7 Li Values

A direct relationship between silicate dissolution rate and $\delta^7 \text{Li}$ value is not observed in the rivers draining the Southern Alps, which is consistent with values obtained for global rivers. Rather, the $\delta^7 \text{Li}$ signature of river waters appears to be controlled by the residence time of water-rock interaction, identified by sodium-normalised lithium ratio evolution in river waters. This relationship reflects the incorporation of Li into secondary minerals, whereas Na remains in solution, which makes Li isotopic fractionation a useful tracer of silicate precipitation of secondary minerals during chemical weathering.

The seawater δ^7 Li signature has risen during the Cenozoic. If it is assumed that this rise is primarily due to riverine input, the results from this study suggest that this increase may be related to tectonic uplift, which resulted in increased chemical dissolution due to the increase in physical erosion and

the decrease in weathering intensity. An increase in physical weathering increases the potential for secondary mineral formation during chemical weathering, raising the overall seawater $\delta^7 Li$ composition. Observations from this study also suggest that local climate (e.g. temperature and meteoric precipitation) appears to have at most only an indirect effect upon riverine $\delta^7 Li$ values, as secondary mineral precipitation is not affected by simply one factor.

The $\delta^7 \text{Li}$ composition of the warm springs is not as high as the river water $\delta^7 \text{Li}$ composition, but it is still fractionated to higher $\delta^7 \text{Li}$ values relative to the bedrock. This suggests that a process is cocurring that is fractionating these fluids, whereby ${}^6 \text{Li}$ is lost and ${}^7 \text{Li}$ remains in solution. We found that Li isotope fractionation in warm springs is also dominantly controlled by secondary mineral formation. Geochemical modelling of mineral saturation states suggests that a similar mineral assemblage to the river waters is formed in the spring waters near the surface. However, at depth and under higher temperature conditions a different mineral assemblage is produced, but the same relationship as rivers can be observed with the saturation indices of these minerals and spring water $\delta^7 \text{Li}$ values. This suggests that even at higher temperature and pressure conditions, the ${}^6 \text{Li}$ isotope is still preferentially retained in newly formed minerals and ${}^7 \text{Li}$ remains in solution. This can further our understanding of the extent of subsurface flud $\delta^7 \text{Li}$ fractionation, and geochemical modelling can give us an idea of the types of mineral assemblages that are likely to fractionate Li isotopes under high temperature and pressure conditions.

8.1.4 Global Implications of δ^{26} Mg Values

A weak correlation can be observed between silicate dissolution rate and riverine δ^{26} Mg value in the Southern Alps. As silicate dissolution rate increases, the riverine δ^{26} Mg values become lower, which is generally in agreement with major global rivers. We know that the rivers draining the Southern Alps are subject to a 'kinetic-limited' regime, and it is likely that if mechanical erosion were to increase, riverine δ^{26} Mg values would become higher as the rivers become less fractionated from the bedrock. This would occur as secondary mineral formation would be inhibited due to very high mechanical erosion rates.

The formation of secondary minerals during chemical weathering appears to be the dominant control upon Mg isotopic fractionation, as a weak relationship between riverine Mg/Na and δ^{26} Mg values can be observed, which is consistent with the formation of secondary minerals and Mg retention in the newly formed minerals. This would make Mg isotopic fractionation a useful tracer of silicate precipitation of secondary minerals during chemical weathering. However, the extent of the role of other processes fractionating riverine Mg isotopes, such as primary mineral dissolution and biotic activity, is unknown, although the results from this study indicate that the effects of these processes are minor. Observations from this study also suggest that local climate (e.g. temperature and meteoric

precipitation) appears to have at most only an indirect effect upon riverine δ^{26} Mg values, as secondary mineral precipitation is not affected by simply one factor.

The scope of using Mg isotopes as a tracer of past weathering is potentially limited by the fact that Mg is a major element. In the global Mg cycle, the Mg lost to clays via precipitation is likely to be minor compared to the Mg input into the oceans via continental chemical dissolution. In addition, riverine Mg isotopic fractionation appears to only be affected by secondary mineral precipitation, and is not strongly affected by silicate chemical dissolution. As riverine δ^{26} Mg values seem to be dominantly controlled by secondary mineral formation, how much is this fractionation telling us about past ocean δ^{26} Mg changes? Instead, these isotopic values tell us more about the efficiency of cation retention, i.e. the relative amounts of clays that form on the continents (the more clays formed, the less Mg in the oceans).

A limitation in using the Mg isotopic system in weathering studies is the similarity in the δ^{26} Mg composition of natural reservoirs, and hence the small amount of isotopic fractionation that occurs during chemical weathering. Differences between natural reservoirs sometimes falls within analytical uncertainty of the data points. Higher precision and accuracy on the MC-ICP-MS could greatly enhance the potential of the Mg isotopic system in studies such as this.

The lack of Mg isotopic variation between natural reservoirs in weathering systems likely explains why no variation is observed in a plot of seawater with depth. Due to the size and mixing in the oceans, it is likely that any change in the riverine δ^{26} Mg signal to the oceans is dominated by the oceanic δ^{26} Mg signal and not measurable at this stage.

8.1.5 Coupled Li and Mg Isotopic Systems

If riverine $\delta^7\text{Li}$ and $\delta^{26}\text{Mg}$ values are coupled in their behaviour during chemical weathering, a negative correlation should be observed, which represents an increasing degree of chemical weathering and secondary mineral formation. River data from the Southern Alps displays a weak negative correlation between these two isotopic systems, which is what should be expected. However, not all river studies display evidence for a negative correlation, suggesting that the behaviour of these isotopes may vary between different weathering environments, adding to the complexity of extrapolating local studies to global interpretations.

8.2 Further Work

8.2.1 Further Sample Collection

There is evidence for a relationship between groundwater (Tartare Tunnels) fluid chemistry and increasing tunnel overburden. As tunnel overburden increases, major anion and cation fluid concentrations generally increase. There is also evidence for a decrease in groundwater δ^7 Li value with increasing tunnel overburden, which suggests that weathering becomes more congruent with increasing water-rock interaction. Or it is possible that dissolution of secondary minerals is occurring and releasing 6 Li into solution, resulting in lower δ^7 Li of the tunnel fluids. However, only a limited number of groundwater samples were available for use in this study. Further groundwater sample collection should include more samples from the Tartare Tunnels, with varying distance into the tunnel. More samples would be needed to test the robustness of the above conclusions.

More river water samples, including suspended sediment and bedload samples, need to be collected on the eastern side of the Southern Alps. This would achieve a better overview of the effect of a lower rainfall and erosion rate regime on the fractionation of Li and Mg isotopes. The majority of the samples used in this study were collected along or near to the Alpine Fault. The rivers Haast and Rakai were used as representative river waters for the west and east of the Southern Alps. It could be beneficial to the understanding of Li isotope fractionation by carrying out river transect studies on these river localities, and observing the variation, if any, in isotopic fractionation from source to sink for these rivers. A small collection of rivers should also be collected in both winter and summer to observe the extent of seasonable variations in the rivers of the Southern Alps.

To get a complete overview of the weathering processes that are occurring in the Southern Alps, soil depth profiles should also be undertaken. Soils and their respective pore waters could be useful in determining the soil processes and interpreting the processes that control Li and Mg isotopic fractionation. This would be helpful in determining the secondary clays that form and constraining their behaviour during chemical weathering.

It was not possible in this project to calculate an isotopic correction for rain water input to the riverine $\delta^7 \text{Li}$ and $\delta^{26} \text{Mg}$ values. Therefore, it would be useful to collect large rain water samples east of the Southern Alps that can be concentrated to perform $\delta^7 \text{Li}$ and $\delta^{26} \text{Mg}$ analyses. By correcting for the isotoic rain water input, we would achieve more accurate riverine $\delta^7 \text{Li}$ and $\delta^{26} \text{Mg}$ values.

8.2.2 Investigation of the Adsorption of Li and Mg onto Clays

It is widely accepted that secondary mineral formation is the dominant control upon Li isotopic fractionation and a major control upon Mg isotopic fractionation in river waters, but it is still

relatively unclear as to how Li and Mg structurally substitute into certain clays. More experimental laboratory studies need to be carried out to assess the behaviour of Li and Mg during secondary mineral formation, as it is likely that different minerals will fractionate these isotopes at different rates and to variable extents. The findings from this study have shown that riverine Mg isotopes to fractionate in only one direction, however, a study of Icelandic rivers demonstrated the fractionation of riverine Mg isotopes to both heavier and lighter values. The determination of how Li and Mg isotopes behave with specific secondary minerals is fundamental in constraining the observed isotopic fractionation.

8.2.3 Identification and Potential Quantification of the Processes Fractionating Mg

Interpretation of riverine Mg isotopic fractionation is more complex than Li isotopic fractionation. Li isotopic fractionation during weathering is only significantly affected by secondary mineral formation. Whereas, with regards to Mg isotopic fractionation, evidence has shown that secondary mineral formation is the dominant control, although, other processes such as primary mineral dissolution and biotic activity, may also exert minor controls. In addition, both secondary mineral formation and biotic activity have been shown to isotopically fractionate Mg isotopes in both directions, releasing both the heavy and light isotope into solution. Quantifying the extent of these factors upon Mg isotopic fractionation is crucial for using Mg isotopes to accurately interpret a weathering system.

To further understand the processes controlling riverine $\delta^{26}Mg$ compositions, calcite (the major form of carbonate in the Southern Alps) $\delta^{26}Mg$ values would need to be determined. This would enable us to separate total $\delta^{26}Mg$ into silicate $\delta^{26}Mg$ and carbonate $\delta^{26}Mg$ values.

Appendix A

Methods

A.1 Preparation of Bedrock and Particulate Material

A.1.1 Rock Crushing

- 1. Rock samples were cut using a water-lubricated diamond saw and the surfaces were ground on a high speed diamond grinding lap to remove any weathered surfaces.
- Approximately 50 g of each sample was weighed, which was then washed with Milli-Q and placed into an ultrasonic bath for 10 minutes. This process was repeated until no more material was coming off of the samples.
- 3. The samples were then crushed using a hardened pure-iron fly-press, until the sample was in millimetre-sized chips. Care was taken not to touch the sample directly with the iron fly press, and to minimise contact between samples, clean sheets of paper were used for each sample.
- 4. Each sample was crushed to a fine powder ($<75 \mu m$) in a hardened pure-iron Tema pot to ensure homogeneity. The samples had to be powdered to this degree of fineness for maximum grainacid contact during acid digestion (Potts, 1987).
- 5. Each sample was then transferred to a clean and labelled sample pot.
- 6. The Tema pot was cleaned prior to use and between samples by grinding clean sand for 1 minute.

 The Tema pot was then cleaned with water and acetone with white roll.

A.1.2 Splitting of River Sand Samples

- 1. Before sieving, the samples had to be split to a reasonable size to fit in the sieves (~150-200 g).
- 2. The river sand samples were completely dried before splitting.

Appendix A

- The workbench was cleaned with acetone and paper was mosaicked to ensure no sample was lost
- 4. Some sample was poured over the split of 2 clean sheets in the middle of the table, trying to keep the sample as even on either side as possible, and then these splits were poured into separate labelled bags.
- 5. Splitting was repeated until the sample was a suitable size for sieving.
- Before splitting another sample, the workbench was cleaned with acetone and clean paper was used to mosaic the table.

A.1.3 Sieving River Sand Samples

- 1. A set of 6 sieves and a pan was cleaned: 2 mm (granules), 1 mm (very coarse sand), 0.5 mm (coarse sand), 0.25 mm (medium sand), 0.125 mm (fine sand), 0.0625 mm (very fine sand) and a pan (<0.0625; coarse silt).
- 2. The sample was accurately weighed before starting the sieving procedure.
- 3. The sieves were stacked so that the finest mesh is placed at the bottom of the stack, and the sample was placed into the uppermost sieve in ~50 g fractions.
- 4. The stack of sieves was shaken for 5 minutes in a circular motion, with occasional rapping of the stack of sieves on the workbench.
- 5. Each size fraction was decanted onto a piece of clean paper and then poured into labelled and weighed bottles.
- 6. The weight of the different size fractions was totalled and the loss of sample throughout this procedure was calculated.

The bulk sub-samples (<2 mm) and the fine sand samples (0.125 mm) were powdered using the Tema Procedure (Appendix A.1.1) and then digested using the HF-HNO₃-HCl method (Appendix A.1.7).

A.1.4 Separation of Clay from Coarse Silt Fraction (for ICP-MS Analysis)

- 1. Approximately 5 g of the coarse silt fraction was placed into a clean 100 ml glass beaker.
- 2. The beaker was filled to ~100 ml with Milli-Q water and stirred thoroughly with a glass rod.
- 3. This was left to settle for 3 hours, and then the water was poured off and the suspended material was placed into a plastic centrifuge tube.
- 4. The sample was centrifuged for 30 minutes.
- 5. The water was poured off and the clay fraction was dried down overnight on a hotplate set at 80 $^{\circ}$ C.

- 6. The clay residue was scraped out of the plastic centrifuge vials and placed into weighed and labelled vials.
- 7. The clay fractions were digested using the HF-HNO₃-HCl method (Appendix A.1.7).

A.1.5 Suspended Load Removal from Filters

The river water and spring water samples were filtered whilst they were sampled (Menzies, 2012). The particulate material that remained on the filters is the suspended load and this was removed using the following method.

- 1. The filters were placed in 30 ml Teflon vials and submerged in Milli-Q.
- 2. The vials were ultrasonicated for 2 hours until the material had re-suspended.
- 3. The filters were removed and rinsed with Milli-Q into the same Teflon pot to remove as much of the suspended load as possible. If a significant amount of material remained on the filter, then steps 1-3 were repeated.
- 4. The suspended load was dried down and digested using the HF-HNO₃-HCl method (Appendix A.1.7).

A.1.6 Mica Mineral Separate Picking

A range of different micas were selected (biotite, chlorite and muscovite) for picking from different bedrock samples. These rock samples were collected by Pitcairn (2004).

- 1. The sample vials were cleaned by ultrasonicating them in Milli-Q for 15 minutes and then drying in an oven overnight at <50 °C.
- 2. The picking tools and equipment (picking tool, razor blade, glass slide and petri dishes) were cleaned with ethanol and white roll.
- 3. A sample vial was labelled for 'pure' mica collection and another for discarded rock material.
- 4. A small amount of the crushed rock sample was poured onto the glass slide and the mica intended for collection was picked out.
- 5. Approximately 30 mg of mica was collected from each sample and then crushed using a mortar and pestle.
- 6. The mica mineral separates were digested using the HF-HNO₃-HCl method (Appendix A.1.7).

A.1.7 Dissolution of Bedrock and Particulate Material

1. Approximately 75 mg of each powdered rock sample (bedrock, bulk river sand fractions and fine river sand fractions) was accurately weighed and placed into a weighed acid-cleaned Teflon pot.

Appendix A

Little material was collected for the mica mineral separates and the clay river sand fraction, and so the whole sample was digested (after being accurately weighed again). The suspended load samples were kept in the same Teflon pots for digestion as the sample sizes were very small, and complete removal of all of the particulate material from inside of the Teflon vials would have been difficult. The weights of the suspended sediments were back-calculated after the digestion was complete.

- 2. 1 drop of 15M TD HNO₃ per 10 mg of powdered rock was added to make a slurry.
- 3. In a scrubbed fume cupboard, 0.75 ml of Aristar HF was added to each Teflon pot.
- 4. The lids were firmly screwed on and placed on a hotplate set at 130 °C for at least 12 hours.
- 5. The samples were removed from the hotplate and left to cool.
- 6. Once the Teflon pots were cool, the lids were removed (in a scrubbed fume cupboard) and checked to see that all of the sample has dissolved and then placed back on the hotplate with the lids removed, to wait for the samples to dry to incipient dryness (care was taken to not overdry).
- 7. If some undissolved sample was still present, then Steps 2-6 were repeated.
- 8. Once dry, the samples were carefully removed from the hotplate and sufficient 6M TD HCl was added to dissolve the sample (>2 ml).
- 9. The lids were firmly screwed on and placed on a hotplate set at 130 °C overnight to reflux until the sample had dissolved.
- 10. If undissolved sample remained, the sample was dried down and 6M TD HCl was added again and left to reflux. If undissolved material still remained, the samples were dried down and repeated attacks of 15M TD HNO₃ and 12M TD HCl were carried out.
- 11. Once fully dissolved in 6M TD HCl, the lids were removed and the samples were placed on a hotplate to dry, being careful not to overdry.
- 12. Once dry, sufficient 6M TD HCl was added and left to dissolve for at least 2 hours.
- 13. The samples were transferred to labelled and weighed acid-cleaned HDPE bottles and the Teflon pots were thoroughly rinsed with 6M TD HCl and Milli-Q to make the solution up to an approximate volume (~30 ml) and then re-weighed. The solution should be roughly 50:50 of 6M TD HCl and Milli-Q.

Dilution factors of the mother solutions were calculated (usually on the order of ~400). At least 1 laboratory blank accompanied each batch of samples, which underwent the same digestion procedure as the rock samples, but without the addition of any rock powder. A rock standard was also digested along with every batch of samples (usually JB-2 and/or BCR-2).

A.2 Elemental Analysis of Fluids

A.2.1 ICP-MS (Inductively-Coupled Plasma-Source Mass Spectrometry)

The ICP-MS data for the fluid samples reported in this study was conducted by Menzies (2012). These analyses were carried out on a Thermo X-Series II ICP-MS at NOC, Southampton. The river water and spring water samples were sub-sampled and diluted with Milli-Q to the desired concentration and spikes of In, Re and Be were added as well as 15M TD HNO₃ to give a final solution of 0.45M TD HNO₃. The rivers and springs were run undiluted for all elements other than Li and B. Li and B were run separately for the spring fluids due to very high concentrations, and these samples had dilution factors of 10-100 depending on the estimated Li or B concentration of the sample. Rainwater and a blank (Milli-Q) were concentrated ~40 times prior to analyses by ICP-MS, after which they were analysed in the same way as river waters and spring waters.

During analysis of Li and B in spring fluids, the external drift was monitored using a middle concentration standard every 10 samples. Synthetic standards were used in the analysis to calibrate the instrument. Blank wash solutions of 0.45M TD HNO₃ were run between samples for a minimum of 3 minutes. During the analysis of B in springs, the wash was monitored, and washing was continued until the counts per second were back to base levels. The international standard reference river water (SLRS-4) and an external river water standard (Sco2/15; Open University) (Wimpenny, 2008) were used to test for precision and accuracy during analyses of springs and rivers.

A.2.2 ICP-OES (Inductively-Coupled Plasma-Source Optical Emission Spectrometry)

The ICP-OES data for the fluid samples used in this study was conducted by Menzies (2012). Subsampled river waters were run undiluted and sub-sampled spring waters were diluted ~10 times with Milli-Q. The solutions were spiked with the appropriate volume of 15M TD HNO₃ to make a final solution of 0.45M TD HNO₃. Rainwater and a blank (Milli-Q) were concentrated by ~40 times prior to analyses by ICP-OES, after which they were analysed in the same way as river and spring waters.

Major elements in the spring fluids were analysed on a PerkinElmer Optima 4300 DV ICP-OES at NOC, Southampton. A blank and drift monitor (intermediate concentration standard) were run to assess drift. A wash of 0.45M TD HNO₃ was used between samples, which was taken up by an AS93plus random-access autosampler. The samples are fed into an argon plasma via a glass concentric nebuliser and open cyclonic spray chamber using an integral peristaltic pump. Light and atomic emissions from the plasma are measured axially and radially. The data are processed using the PerkinElmer software where peak sizes are measured and integrated, then calibrated to peak sizes

Appendix A

of known standard concentrations. The machine was calibrated using multi-element synthetic standards that bracket the expected maximum and minimum concentration in samples.

The international standard reference river water (SLRS-4) and an external river water standard (Sco2/15; Open University) (Wimpenny, 2008) were used to assess precision and accuracy. Internal precision was monitored by measuring each sample four times and calculating the percentage relative standard deviation (%RSD) which is expressed as the standard deviation of the mean as a percentage of the mean. Data with RSD of >10% were rejected. The precision and accuracy of these measurements are available in Menzies (2012).

A.2.3 IC (Ion Chromatography)

IC analyses of the fluid samples were conducted by Menzies (2012). Cl⁻, F⁻, SO₄²⁻ and Br⁻ in spring and river waters were measured on a Dionex ICS2500 ion chromatograph at NOC, Southampton.

The spring samples were diluted ~10 times with Milli-Q and the river waters were run undiluted. The results were calibrated using single element synthetic standards, and four standards of different concentrations (which bracketed the sample concentrations) were run per element. Between every 10 samples, washes of blank Milli-Q were used to rinse the system. During the run, samples were bracketed by 2 multi-element standards, which were used as external drift monitors. Accuracy was monitored using international groundwater standards BRC617 and BRC612 for Cl⁻, SO₄²⁻ and Br. These standards are not certified for F⁻, and so a synthetic standard was run to assess accuracy. The accuracy measured using BRC617 for Cl⁻ is lower than normal samples as the concentration was higher than the top standard during this run (Menzies, 2012). The precision was monitored by measuring the same multi-element synthetic standard multiple times as an unknown (Menzies, 2012).

A.3 Spring Contribution Calculations

Flow rate values for some of the springs sampled in this study (Table B.2 in Appendix B) were taken from Reyes et al. (2010), and discharge values for the Haast River were sourced from the National Institute of Water and Atmospheric Research Limited in Christchurch, New Zealand (NIWA). Most of the springs that had flow data and concentration data were found along or near the Alpine Fault, which is west of the Main Divide. Therefore, we used the Haast River as being representative of rivers on the west coast. Discharge data was not available for any other rivers west of the Main Divide, and so a minimum and maximum was taken from varying discharge rates between the years 2009-2011 (period when the spring water samples from this study were collected). A minimum

spring water input into river waters was calculated by using the highest measured discharge value for the Haast River and the spring with the lowest flow rate. A maximum spring water input into river waters was calculated by using the lowest measured discharge value for the Haast River and the spring with the highest flow rate.

Average river water and spring water values were used for the concentrations of each element due to the lack of spring flow rate and river discharge data. The total load in the rivers and springs for each element was calculated using the following equation:

Total Load
$$(mg/s)$$
 = Discharge (L/s) x Element Concentration (mg/L) (Eq. A.1)

The spring water input (calculated as a per cent of the total river water load) to the river waters was calculated using the following equation:

Spring Water Input (%) =
$$\frac{\text{Spring Load (mg/s)}}{\text{River Load (mg/s)}} \times 100$$
 (Eq. A.2)

TABLE A.1: Calculations of the minimum and maximum spring water contribution to river waters, given as a per cent of the total river water concentration.

		MINIMUM		MAXIMUM	
		Average River	Average Spring	Average River	Average Spring
Flow Rate	L/s	300000	0.02	10000	0.12
HCO ₃	mg/L	414	5880	414	5880
	mg/s	124000000	118	4140000	706
	%	0.000		0.017	
F	mg/L	0.05	2.72	0.05	2.72
	mg/s	15700	0.05	524	0.33
	%	0.000		0.062	
Cl	mg/L	1.15	81.2	1.15	81.2
	mg/s	346000	1.62	11500	9.75
	%	0.000		0.085	
Br	mg/L	0.00	0.26	0.00	0.26
	mg/s	976	0.01	33	0.03
	%	0.0	001	0.094	
SO ₄	mg/L	5.31	21.1	5.31	21.1
	mg/s	1590000	0.42	53100	2.53
	%	0.000		0.005	
Li	μg/L	1.73	834	1.73	834
	$\mu g/s$	520000	16.7	17300	100
	%	0.003		0.578	
В	$\mu g/L$	3.95	2940	3.95	2940.00
	$\mu g/s$	1190000	58.8	39500	353
	%	0.005		0.893	
Na	mg/L	1.32	186	1.32	186
	mg/s	397000	3.72	13200	22.3
	%	0.0	001	0.169	
Mg	mg/L	0.49	1.49	0.49	1.49
	mg/s	146000	0.03	4860	0.18
	%	0.000		0.004	
Al	$\mu g/L$	28.5	29.0	28.5	29.0
	$\mu g/s$	8550000	0.58	285000	3.47
	%	0.000		0.001	
Si	mg/L	1.84	31.2	1.84	31.2
	mg/s	551000	0.62	18400	3.74
	%	0.000		0.020	
K	mg/L	0.87	10.3	0.87	10.3
	mg/s	261000	0.21	8690	1.23
	%	0.000		0.014	
Ca	mg/L	8.39	23.4	8.39	23.4
	mg/s	2520000	0.47	84000	2.81
	%	0.0	000	0.0	003

TABLE A.1 Continued – Spring water input to rivers

		MINIMUM		MAXIMUM	
		Average River	Average Spring	Average River	Average Spring
Flow Rate	L/s	300000	0.02	10000	0.12
Mn	μg/L	0.87	67.2	0.87	67.2
	μg/s	261000	1.34	8690	8.06
	%	0.001		0.093	
Fe	μg/L	4.93	62.4	4.93	62.4
	$\mu g/s$	1480000	1.25	49300	7.49
	%	0.000		0.015	
Rb	μg/L	1.55	71.9	1.55	71.9
	$\mu g/s$	465000	1.44	15500	8.62
	%	0.000		0.056	
Sr	μg/L	48.3	482	48.3	482
	$\mu g/s$	14500000	9.64	483000	57.8
	%	0.0	000	0.012	
Cs	$\mu g/L$	0.04	68.2	0.04	68.2
	$\mu g/s$	12500	1.36	415	8.19
	%	0.0	011	1.9	973
Ba	μg/L	3.05	36.4	3.05	36.4
	$\mu g/s$	915000	0.73	30500	4.36
	%	0.000		0.014	
Y	ng/L	7.12	129	7.12	129
	ng/s	2140000	2.59	71200	15.5
	%	0.000		0.022	
La	ng/L	5.94	11.7	5.94	11.7
	ng/s	1780000	0.23	59400	1.41
	%	0.000		0.002	
Ce	ng/L	7.09	21.7	7.09	21.7
	ng/s	2130000	0.43	70900	2.61
	%	0.000		0.004	
Pr	ng/L	1.29	3.18	1.29	3.18
	ng/s	386000	0.06	12900	0.38
	%	0.000		0.003	
Nd	ng/L	5.27	14.0	5.27	14.0
	ng/s	1580000	0.28	52700	1.68
	%	0.0	000	0.0	003
Sm	ng/L	1.05	3.62	1.05	3.62
	ng/s	314000	0.07	10500	0.43
	%	0.000		0.004	
Eu	ng/L	0.26	1.19	0.26	1.19
	ng/s	77200	0.02	2570	0.14
	%	0.0	000	0.0	006

TABLE A.1 Continued – Spring water input to rivers

		MIN	IMUM	MAX	IMUM
		Average River	Average Spring	Average River	Average Spring
Flow Rate	L/s	300000	0.02	10000	0.12
Gd	ng/L	1.31	5.35	1.31	5.35
	ng/s	392000	0.11	13100	0.64
	%	0.0	000	0.0	005
Tb	ng/L	0.16	1.09	0.16	1.09
	ng/s	49400	0.02	1650	0.13
	%	0.0	000	0.0	008
Dy	ng/L	1.03	9.53	1.03	9.53
	ng/s	309000	0.19	10300	1.14
	%	0.0	000	0.0	011
Но	ng/L	0.24	2.67	0.24	2.67
	ng/s	71000	0.05	2370	0.32
	%	0.0	000	0.0	014
Er	ng/L	0.79	10.5	0.79	10.5
	ng/s	236000	0.21	7870	1.25
	%	0.0	000	0.0	016
Tm	ng/L	0.12	1.81	0.12	1.81
	ng/s	35600	0.04	1190	0.22
	%	0.0	000	0.0	018
Yb	ng/L	0.84	13.9	0.84	13.9
	ng/s	252000	0.28	8400	1.67
	%	0.0	000	0.0	020
Lu	ng/L	0.14	2.28	0.14	2.28
	ng/s	42600	0.05	1420	0.27
	%	0.0	000	0.0)19
Pb	ng/L	23.4	60.4	23.4	60.4
	ng/s	7010000	1.21	234000	7.24
	%	0.0	000	0.0	003
U	ng/L	22.7	6.65	22.7	6.65
	ng/s	6810000	0.13	227000	0.80
	%	0.0	000	0.0	000

A.4 Global Chemical Weathering and Atmospheric CO₂ Consumption Rates

Silicate and carbonate weathering rates along with atmospheric CO₂ consumption rates were calculated following Jacobsen et al. (2003) for major global rivers, using river chemistry data from Gaillardet et al. (1999b). Calculated values for some of the rivers were illogical, for example, some of the values were negative. These rivers either had high salinity (a high concentration of Na compared to Ca) or were affected by anthropogenic effects, or both. Therefore, only the major rivers that were least likely to be affected by anthropogenic effects and have low salinity were included for comparison to the data from this study.

TABLE A.2: Weathering rates and atmospheric CO₂ consumption rates for global rivers. The data for the New Zealand rivers is sourced from this study. The data for all other rivers is sourced from Gaillardet et al. (1999b).

River Basin A	Area R	Pundf	Z E	Z	Y	ع		•				***			
*			1	211	4	Ça	Mg	%	Ca_{sil}	Ca_{carb}	M_{chem}	W sil	$W_{\rm carb}$	$W_{ m sil\text{-}CO2}$	$W_{\rm carb-CO2}$
	$x 10^{5}$										$x 10^7$	x 10 ⁷	$x 10^7$	$x 10^4$	x 10 ⁵
	km² n	mm/yr	mg/L	ng/L	ng/L	ng/L	ng/L	ng/L	ng/L	ng/L	$\mathrm{g\cdot km^{-2}\cdot yr^{-1}}$	$g \cdot km^{-2} \cdot yr^{-1}$	$\mathrm{g\cdot km^{-2}\cdot yr^{-1}}$	mol·km ⁻² ·yr ⁻¹	mol·km ⁻² ·yr ⁻¹
New Zealand															
Haast 0.	0.01	2990	37.5	774	241	7085	504	1690	432	6654	3.10	0.90	2.10	6.40	5.60
Rakai 0.	0.03	801	39.1	3471	454	13257	1683	4112	1935	11321	1.80	0.80	1.00	7.70	2.80
N. America															
Mississippi 29	8.62	195	216	20793	1842	21209	15059	2114	11600	6096	1.19	0.71	0.48	11.3	1.18
	17.9	172	209	14355	999	22207	13865	832	8008	14199	0.89	0.41	0.48	6.87	1.19
Yukon 8.	.49	236	183	4915	793	19836	12137	2130	2742	17094	0.94	0.25	0.69	3.23	1.70
Columbia 6.	69:9	353	115	9439	716	11228	8476	2497	5266	5962	1.14	0.63	0.51	9.28	1.25
Nelson	1.3	79	236	30275	1509	20535	18803	383	16890	3645	0.56	0.39	0.18	99.9	0.43
Fraser 2.	2.20	509	92	5481	460	11053	6809	1515	3058	9662	1.25	0.54	0.72	7.77	1.77
	.23	487	145	4176	512	15096	8676	2114	2330	12766	1.52	0.44	1.07	5.66	2.65
S. America															
	1.1	1078	4	3480	537	3368	1522	1914	1941	1427	1.17	0.85	0.32	10.4	0.78
Parana 2	27.8	204	98	10048	2404	4317	3538	4743	5606	-1289	0.51	0.47	0.05	5.71	0.11
Orinoco	11.0	1032	25	2784	435	1622	1111	1748	1553	69	0.79	0.67	0.12	8.00	0.30
Tocantins 7.	7.57	491	42	3567	895	1347	3086	3212	1990	-643	0.59	0.47	0.12	4.88	0.29
	.40	604	09	5350	895	3693	4073	4161	2985	802	1.10	0.81	0.29	00.6	0.70
Europe															
	8.17	253	428	32146	1304	36753	45958	1148	17933	18820	2.97	1.33	1.64	22.6	4.01
	5.9	239	112	9831	999	10305	6254	2297	5484	4821	0.70	0.44	0.26	6.54	0.65
St. Lawrence 10	10.2	330	168	10396	895	18714	10163	999	5800	12914	1.35	0.59	92.0	9.55	1.88
	24.9	211	112	8526	460	10679	8640	1614	4756	5923	0.63	0.32	0.31	5.01	0.75
Magdalena 2.	2.35	1009	118	15703	1253	9357	5596	3495	8760	969	3.57	2.95	0.62	44.1	1.52
	6.6	135	126	10005	999	11602	8640	716	5581	6021	0.43	0.23	0.20	3.76	0.49
N. Dvina 3.	3.48	316	173	9439	999	18714	12179	632	5266	13448	1.32	0.51	0.81	8.30	2.00
Rhone 0.	96	565	339	21358	1381	44164	10985	1115	11915	32249	4.46	2.02	2.44	33.6	6.05
Po 0.	.70	<i>L</i> 99	354	31754	1969	38749	20160	1115	17715	21035	6.25	3.51	2.75	59.0	6.77
Elbe 1.	1.48	154	869	161686	17111	66745	27278	1115	90200	-23456	4.22	4.16	90.0	69.3	0.12
Dnepr 5.	5.04	103	274	26491	999	27571	17445	646	14779	12793	0.75	0.44	0.31	7.60	0.77
Kolima 6.	09:9	200	74	5307	1177	6737	4073	1115	2961	3776	0.37	0.21	0.16	2.95	0.39
Pechora 3.	3.24	404	70	5655	999	6487	4732	449	3155	3333	0.73	0.40	0.33	6.36	0.80
Khatanga 3.	3.64	234	96	18357	999	7810	6809	882	10241	-2431	0.79	0.71	0.09	12.0	0.20
Seine 0.	0.79	164	493	40106	3223	65497	15593	1764	22374	43123	2.07	1.11	96.0	18.3	2.39
Nemunas 0.	96:0	200	447	29884	999	43291	38223	999	16671	26619	2.25	0.96	1.30	16.6	3.19

River Basin	Area	Runoff	TDS	Na	K	Ca	M_g	Σ:	Ca_{sil}	Ca_{carb}	$W_{ m chem}$	$W_{ m sil}$	$W_{ m carb}$	$W_{ m sil ext{-}CO2}$	$W_{ m carb\text{-}CO2}$
	x 10 ⁵										$\times 10^7$	$\times 10^7$	$x 10^7$	$x 10^4 x 10^5$	$\times 10^{5}$
	km^2	mm/yr	m mg/L	ug/L	ug/L	ug/L	ug/L	ug/L	ug/L	ug/L	g·km ⁻² ·yr ⁻¹	$g \cdot \text{km}^{-2} \cdot \text{yr}^{-1}$	$g\cdot km^{-2}\cdot yr^{-1}$	mol·km ⁻² ·yr ⁻¹ mol·km ⁻² ·yr ⁻¹	mol·km ⁻² ·yr ⁻¹
Asia															
Changjiang	18.1	513	221	9657	921	24278	12014	1798	5387	18890	2.50	0.91	1.59	13.8	3.92
Xijiang	4.37	831	161	5089	793	20211	8146	2363	2839	17371	3.04	0.92	2.12	11.8	5.25
Brahmaputra	5.80	879	101	3958	2558	8733	6418	2164	2208	6525	2.09	0.96	1.14	9.69	2.80
Ganges	10.5	470	182	18139	1714	14472	10985	2130	10119	4352	2.23	1.51	0.72	23.7	1.77
Godavari	3.13	335	193	15312	1432	18838	4073	5859	8542	10296	1.52	1.04	0.48	14.3	1.19
Amur	18.6	185	55	5481	665	5564	3909	599	3058	2507	0.30	0.18	0.12	2.82	0.29
Huanghe	7.52	55	460	103093	2686	29318	34890	2130	57513	-28195	0.95	0.91	0.04	15.8	0.08
Shatt el Arab	5.41	85	400	58637	1969	32437	37235	1914	32712	-275	1.12	0.81	0.31	13.9	0.76
Hong He	1.20	1025	147	21010	972	9681	13701	2779	11721	-2040	4.93	3.74	1.20	60.0	2.89
Fly	0.61	2311	116	4393	281	13299	2962	2497	2451	10848	5.42	2.22	3.19	28.3	7.92
Sepik	0.79	1525	114	6612	256	9681	6789	3462	3689	5993	4.09	2.14	1.95	28.1	4.80
Purari	0.31	2749	126	6046	665	12850	4402	3828	3373	9477	7.64	3.82	3.82	46.3	9.44
Mahanadi	1.32	500	147	19270	972	6487	16087	2497	10750	-4263	2.27	1.67	0.59	26.8	1.42
Kikori	0.13	3035	177	2479	128	23280	6789	2214	1383	21896	10.6	1.88	8.71	20.9	21.6
Africa															
Limpopo	4.40	59	238	38975	3018	12051	20819	4910	21743	-9692	0.47	0.41	0.07	6.40	0.16
Congo-Zaire	37.0	324	35	4176	1100	1397	2427	2613	2330	-932	0.38	0.33	0.05	3.77	0.12
Zambese	13.3	77	80	10222	1253	6612	6953	4660	5703	909	0.23	0.17	0.06	2.19	0.15
Niger	12.0	128	59	3393	716	3443	3209	3878	1893	1550	0.19	0.13	0.06	1.21	0.15

TABLE A.2 Continued - Weathering rates and atmospheric CO₂ consumption rates

A.5 Erosion and Rainfall Rates

TABLE A.3: Sediment yield, erosion rates and rainfall values for the river localities analysed in this study.

Sample	Locality	Туре	Sediment Yield	Erosion Rate	Rainfall
	·	••	t∙km ⁻² ∙yr ⁻¹	mm∙yr ⁻¹	mm·yr ⁻¹
Eastern	Rivers				
NZ01	Franz Terminus	Glacial	6420	2.42	6350
NZ03	Fox Terminus	Glacial	917	0.35	5810
NZ04	Thunder Creek	Non-glacial	2340	0.88	4540
NZ19	Deception	Non-glacial	791	0.30	4920
NZ20	Wanganui	Non-glacial	4550	1.72	4590
NZ22	Gaunt Creek	Non-glacial	6050	2.28	5770
NZ26	Rpugh Creek	Non-glacial	844	0.32	5100
NZ09	Sheil's Creek	Non-glacial	9270	3.50	7840
NZ13	Smythe	Non-glacial	10500	3.96	7040
NZ14	Scone-Perth	Non-glacial	8930	3.37	7430
NZ16	Mungo	Non-glacial	3350	1.26	5060
Western	Rivers				
NZ27	Rakai	Non-glacial	436	0.16	856
NZ05	Chinaman's Bluff	Non-glacial	141	0.05	2190
NZ25	Potts	Non-glacial	308	0.12	1130
NZ07	Mingha	Non-glacial	2530	0.95	3440
NZ06	Hooker Terminus	Glacial	1390	0.52	6350

A.6 Mineral Saturation States

The thermodynamic modelling presented in this study was performed with the program SpecE8, which is part of the software package, The Geochemist's Workbench (Bethke, 2002). SpecE8 includes a thermodynamic database from the PHRQPITZ program (Plummer et al., 1988). The SI units are given in log Q/K, where Q is the ratio of component activities in the fluid, and K is the ratio of component activities if the fluid is in equilibrium with respect to the mineral of interest (Tosca, 2007).

• If **Q=K**:

Then SI=0, indicating mineral saturation, or equilibrium between a fluid and the mineral of interest.

• If **Q**<**K**:

Then SI is negative, and the fluid is undersaturated with respect to the mineral of interest.

• If **Q>K**:

Then SI is positive, and the fluid is supersaturated with respect to the mineral of interest.

The mineral saturation indices calculated for river waters and spring waters under different conditions are given in Tables A.3-A.6

TABLE A.4: River water primary and secondary mineral saturation indices calculated using the geochemical modelling software Geochemist's Workbench. To calculate these values, in situ pH and temperature measurements, and measured anion and cation concentrations were used.

				PRIMARY	SECONDARY	SECONDARY	SECONDARY
		pН	Temperature	Biotite	Illite	Kaolinite	Smectite
			℃	SI units	SI units	SI units	SI units
NZ01	Franz	9.0	3.0	3.02	1.42	1.17	0.29
NZ03	Fox	8.7	0.3	-1.79	4.28	4.22	4.02
NZ06	Hooker	8.7	5.0	-1.15	2.41	2.93	2.44
NZ19	Deception	7.9	14	-5.32	1.31	2.25	2.02
NZ20	Trib. Wanganui	7.8	10	-5.76	2.49	3.07	2.92
NZ22	Gaunt Creek	7.5	11	-7.21	2.57	3.44	3.23
NZ26	Rough Creek	7.5	11	-6.89	2.92	3.74	3.59
NZ04	Thunder Creek	7.9	11	-5.73	1.77	2.95	2.61
NZ07	Mingha	8.2	12	-5.23	0.70	1.61	1.27
NZ27	Trib. Rakai	8.3	15	-1.43	1.84	1.96	2.12
NZ05	Chinaman's Bluff	8.0	8.6	-6.49	1.00	2.26	1.65
NZ25	Potts	8.0	20	-1.64	1.84	2.59	2.44

TABLE A.5: Spring water primary and secondary mineral saturation indices calculated using the geochemical modelling software Geochemist's Workbench. To calculate these values, in situ pH and temperature (T) measurements, and measured anion and cation concentrations were used.

			S	ECONDARY	SECONDARY	SECONDARY
		pН	Temperature	Illite	Kaolinite	Smectite
			°C	SI units	SI units	SI units
HS41	Fox	6.8	30	3.58	3.05	4.04
HS40	Amythest	6.1	31	1.43	2.15	2.58
HS39	Hot Spring Flat	7.1	40	1.43	1.47	2.00
HS16	Morgon's Gorge	6.8	44	2.04	2.00	2.73
WF2	Welcome Flat	6.5	56	2.64	2.06	3.25
HS13	Scone	8.8	20	1.67	0.94	1.47
HS36	Smythe	8.6	38	1.21	0.23	0.93
HS15	Butler	6.8	40	1.85	2.21	2.73
BIV 1	Bivouac	6.6	21	5.51	5.39	6.50
HS17	Julia	8.9	60	-0.56	-1.44	-0.99
HS33	Mungo	8.9	50	0.76	-0.15	0.42
HS19	Horseshoe Flat	8.8	51	1.33	0.09	0.95
HS23	Wren Creek	8.5	55	1.31	-0.01	0.90
HS24	Haupiri	9.5	38	1.12	-0.49	0.33
HS26	Sylvia	8.1	38	2.62	1.72	2.58

TABLE A.6: Spring water primary and secondary mineral saturation indices calculated using the geochemical modelling software Geochemist's Workbench. To calculate these values, in situ pH, silica equilibration temperatures (T_{Si}), and measured anion and cation concentrations were used.

				SECONDARY	SECONDARY	SECONDARY
		pН	\mathbf{T}_{Si}	Illite	Kaolinite	Smectite
			°C	SI units	SI units	SI units
HS41	Fox	6.8	111	0.32	-0.05	0.36
HS40	Amythest	6.1	102	0.46	1.06	1.25
HS39	Hot Spring Flat	7.1	96	-1.68	-1.42	-1.42
HS16	Morgon's Gorge	6.8	112	-0.97	-0.87	-0.62
WF2	Welcome Flat	6.5	153	-0.06	-0.66	0.17
HS13	Scone	8.8	65	-3.22	-3.35	-3.76
HS36	Smythe	8.6	97	-2.37	-3.01	-2.98
HS15	Butler	6.8	97	-1.26	-0.70	-0.69
BIV 1	Bivouac	6.6	94	0.29	0.63	0.85
HS17	Julia	8.9	115	-2.50	-3.19	-3.15
HS33	Mungo	8.9	97	-1.73	-2.37	-2.31
HS19	Horseshoe Flat	8.8	118	-1.57	-2.55	-2.25
HS23	Wren Creek	8.5	128	-1.25	-2.43	-1.95
HS24	Haupiri	9.5	127	-4.00	-4.80	-5.00
HS26	Sylvia	8.1	102	-0.98	-1.61	-1.36

TABLE A.7: Spring water primary and secondary mineral saturation indices calculated using the geochemical modelling software Geochemist's Workbench. To calculate these values, in situ pH, silica equilibration temperatures (T_{Si}), and measured anion and cation concentrations were used.

				SECONDARY	SECONDARY	SECONDARY
		pН	\mathbf{T}_{Si}	Daphnite	Saponite-Mg	Tremolite
			°C	SI units	SI units	SI units
HS41	Fox	6.8	111	2.46	3.69	2.88
HS40	Amythest	6.1	102	-5.13	-2.15	-10.5
HS39	Hot Spring Flat	7.1	96	0.81	1.72	-0.36
HS16	Morgon's Gorge	6.8	112	-0.05	2.06	0.47
WF2	Welcome Flat	6.5	153	4.24	5.80	8.56
HS13	Scone	8.8	65	8.20	6.91	11.6
HS36	Smythe	8.6	97	12.0	8.30	15.2
HS15	Butler	6.8	97	1.05	-0.70	-5.76
BIV 1	Bivouac	6.6	94	4.31	0.29	-4.46
HS17	Julia	8.9	115	14.7	7.55	14.7
HS33	Mungo	8.9	97	11.3	8.66	15.9
HS19	Horseshoe Flat	8.8	118	13.7	10.2	19.6
HS23	Wren Creek	8.5	128	13.3	10.3	19.7
HS24	Haupiri	9.5	127	11.6	10.9	22.1
HS26	Sylvia	8.1	102	9.24	6.96	11.4

A.7 Lithium Isotope Method Ticksheet

			_
Lithium	Column	Procedure -	Data:

	Column Position	Tot	tal time = 9.	5hr	1	2	3	4	5	6	7	8	9	10
	Column ID													
	Sample ID													
	Sample Type													
	Clean	15ml	6M HCI	1hr45										
Precond	Rinse	8ml	MQ	1hr										
Prec	Eqilibrate	8ml	0.2M HCI	1hr										
	Check resin height	8.5cm	(in 0.2M H	CI)										
	Dissolve dried sample	200µl	0.2M HCI	5 mins	i									
oadina	Load	200µl	of sample											
Loa	Wash in	500µl	0.2M HCI	5mins										
	Wash in	500µl	0.2M HCI	5mins										
	Discard	22ml	0.2M HCI	2hr45										
_	COLLECT Li	18ml	0.2M HCI	2hr45										
ction	Vial ID													
Collection	Dry Li fraction on hot	olate												
	Clean	30ml	6M HCI	3hr30										
	Rinse	30ml	MQ	3hr30										

A.8 Magnesium Isotope Method Ticksheet

Magnesium Column Procedure - Date:

_		.ugoc	dulli Colullili		44.0		1		_	1	1		
	Column Position			1	2	3	4	5	6	7	8	9	10
	Column ID												
	Sample ID												
	Sample Type												
-:	Clean	4ml	6M HCI										
onc	Rinse	4ml	MQ										
Precond	Eqilibrate	4ml	0.8M HNO ₃										
14	Check resin height	8.5cm	(in 0.8M HNO ₃)									
	Dissolve dried sample	200μΙ	0.8M HNO ₃										
oading-	Load	200μΙ	of sample										
oa	Wash in	500µl	0.8M HNO ₃										
-	Wash in	500µl	0.8M HNO ₃										
<u>_</u>	Discard	50ml	0.8M HNO ₃										
ollection	COLLECT Mg	20ml	2M HNO ₃										
olle	Vial ID												
Ö	Dry Mg fraction on hot pl	late											
	Clean	25ml	6M HCI										
an	Rinse	8ml	MQ										
Clean	Clean	8ml	6M HCI										
	Rinse	8ml	MQ										

Appendix B

Data Tables for Fluid and Solid Phases

TABLE B.1: Chemical composition of river waters, groundwaters and rain waters from the Southern Alps. Li isotopic data from this study, and general information and elemental data are from Menzies (2012), except for rain waters east of the Main Divide, which are from Jacobsen et al. (2003). Bd = below detection, nd = not determined, TDS = total dissolved solids, P-P = Prehnite-Pumpellyite, P-Act = Prehnite-Actinolite, GS = Greenschist Facies, G-O Amph = garnet oligoclase Amphibolite Facies.

		Gro	oundwater (Tart	are Tunnels Flu	ids)
Sample ID		SP1	SP3	SP4	SP5
Sample Name		TT 279 m	TT 46m	TT 94.3m	TT 290m
Sampling Date		2009	2010	2010	2010
Easting		2283935	2283760	2283798	2283946
Northing		5753780	5753930	5753899	5753770
Туре		Groundwater	Groundwater	Groundwater	Groundwater
Catchment Litholo	ogy	Metasediment	Metasediment	Metasediment	Metasediment
Catchment Met. (G-O Amph	G-O Amph	G-O Amph	G-O Amph
δ^7 Li	% %	nd	25.9	23.4	17.1
δ^{26} Mg	%	nd	nd	nd	nd
δ^{25} Mg	‰	nd	nd	nd	nd
Temperature	°C	10.4	10.0	10.7	10.2
pН		7.14	6.79	7.92	7.16
Conductivity	S/m	0.09	0.07	0.12	0.03
Total Alkalinity	μeq/L	nd	666	123	666
TDS	mg/L	nd	67.1	19.4	85.6
F	μmol/L	2.47	1.58	1.21	2.86
Cl	μmol/L	68.0	64.0	53.0	67.8
Br	μmol/L	0.15	0.10	0.10	0.11
SO ₄	μmol/L	88.5	45.9	32.3	83.1
В	nmol/L	196	265	200	186
Na	μmol/L	123	104	72.6	123
Mg	μmol/L	78.7	45.3	11.9	74.1
Al	μmol/L	0.05	0.48	0.07	0.04
Si	μmol/L	172	115	72.6	157
K	μmol/L	73.7	49.4	20.5	79.2
Ca	μmol/L	574	277	53.4	561
Li	nmol/L	nd	154	81.8	553
Mn	nmol/L	1.07	3.11	6.02	1.38
Fe	nmol/L	18.7	61.9	14.7	9.22
Rb	nmol/L	3.92	4.28	15.2	3.97
Sr	nmol/L	599	326	102	585
Cs	nmol/L	bd	bd	bd	bd
Ba	nmol/L	91.9	60.7	27.6	86.7
Y	pmol/L	174	597	127	190
La	pmol/L	9.00	266	20.4	9.63
Ce	pmol/L	3.79	29.0	14.7	4.10
Pr	pmol/L	1.96	58.1	8.46	2.34
Nd	pmol/L	8.33	235	40.4	9.60
Sm	pmol/L	2.31	44.0	12.1	2.75
Eu	pmol/L	1.62	14.9	3.24	2.23
Gd	pmol/L	4.21	59.9	14.1	5.37
Tb	pmol/L	0.79	6.24	1.93	0.96
Dy	pmol/L	6.30	38.4	13.6	7.75
Ho	pmol/L	1.53	8.24	3.00	2.15
Er	pmol/L	5.18	25.2	11.2	7.66
Tm	pmol/L	0.72	3.29	1.82	1.10
Yb	pmol/L	5.43	21.3	15.5	8.29
	-	0.95	3.54	2.70	1.52
Lu Db	pmol/L				
Pb U	pmol/L pmol/L	46.8 49.0	94.6 11.3	1750 1.05	53.1 46.0

TABLE B.1 Continued – River water, rain water and groundwater

		Rivers West of Main Divide							
Sample ID		NZ01	NZ03	NZ09	NZ13	NZ14			
Sample Name		Franz Term	Fox Term	Sheil's Creek	Smythe	Scone-Perth			
_					-	River			
Sampling Date		2009	2009	2009	2011	2011			
Easting		2281166	2271885	2263063	2335060	2313303			
Northing		5747883	5740946	5726991	5775399	5756287			
Type		Glacial river	Glacial river		Non-glacial river	Non-glacial rive			
Catchment Litholo		Metasediment	Metasediment	Metasediment	Metasediment	Metasediment			
Catchment Met. (Grade	G-O Amph	G-O Amph	Biotite GS	Biotite GS	Chlorite GS			
δ ⁷ Li	‰	12.0	13.8	15.4	13.8	15.4			
δ^{26} Mg	‰	-0.35	-0.54	-1.02	-0.59	-0.54			
δ^{25} Mg	‰	-0.17	-0.28	-0.52	-0.30	-0.28			
Temperature	°C	1.90	0.30	nd	nd	nd			
рН		9.76	8.70	nd	nd	nd			
Conductivity	S/m	0.03	0.06	nd	nd	nd			
Total Alkalinity	μeq/L	217	506	nd	390	366			
TDS	mg/L	27.8	55.0	nd	43.3	39.2			
F	μmol/L	0.65	0.60	0.66	3.46	3.74			
Cl	μmol/L	25.1	26.2	28.9	27.2	28.4			
Br	μmol/L	bd	bd	bd	bd	0.03			
SO ₄	μmol/L	30.7	81.3	39.8	59.1	39.2			
В	nmol/L	71.0	143	212	121	877			
- Na	μmol/L	10.3	25.1	23.3	25.0	39.3			
Mg	μmol/L	11.9	23.0	9.37	9.46	10.2			
Al	μmol/L	3.94	3.41	0.25	0.89	0.70			
Si	μmol/L	11.2	22.2	40.9	29.7	36.9			
K	μmol/L	43.5	46.2	41.0	11.1	7.34			
Ca	μmol/L	174	264	117	236	206			
Li	nmol/L	246	349	191	134	312			
Mn	nmol/L	26.4	35.4	4.39	33.4	12.8			
Fe	nmol/L	26.4	29.6	51.2	238	192			
Rb	nmol/L	33.6	28.8	40.3	8.35	4.10			
Sr	nmol/L	475	867	156	675	757			
Cs	nmol/L	0.29	0.28	1.46	0.12	0.09			
Ba	nmol/L	9.92	17.5	64.1	10.4	10.3			
Y	pmol/L	7.91	10.3	104	42.7	44.1			
La	pmol/L	24.9	16.1	38.3	16.5	12.9			
Ce	pmol/L	35.3	21.6	31.5	32.9	23.6			
Pr	pmol/L	5.02	2.66	10.0	4.50	3.29			
Nd	pmol/L	18.0	10.3	40.6	18.4	13.7			
Sm	pmol/L	2.31	1.00	8.92	4.09	2.49			
Eu	pmol/L	0.41	0.17	2.32	0.86	0.90			
Gd	pmol/L	1.73	1.39	10.1	4.73	3.13			
Tb	pmol/L	0.30	0.15	1.20	0.58	0.49			
Dy	pmol/L	0.56	0.73	7.05	3.87	3.09			
Ho	pmol/L	0.16	0.14	1.87	0.85	0.70			
Er	pmol/L	0.43	0.57	6.00	2.93	2.70			
Tm	pmol/L	0.13	0.08	1.06	0.42	0.32			
Yb	pmol/L	0.43	0.35	7.93	3.26	2.37			
Lu	pmol/L	0.02	0.13	1.44	0.49	0.44			
Pb	pmol/L	33.8	29.0	183	261	290			
U	pmol/L	55.4	201	3.60	146	93.1			

TABLE B.1 Continued – River water, rain water and groundwater

			River	s West of Main I	Divide	
Sample ID		NZ16	NZ19	NZ20	NZ22	NZ26
Sample Name		Mungo	Deception River	Trib Wanganui	Gaunt Creek	Rough Creek
		I I I I I I I I I I I I I I I I I I I	Deception ruver	The Wanganan		riough Croon
Sampling Date		2011	2011	2011	2011	2011
Easting		2362267	2395906	2317321	2293366	2253890
Northing		5795650	5823070	5779321	5758836	5732496
Type			Non-glacial river	Non-glacial river		Non-glacial river
Catchment Litholo	ogy	Metasediment	Metasediment	Metasediment	Metasediment	Metasediment
Catchment Met. C	Grade	P-Act	P-P	G-O Amph	G-O Amph	G-O Amph
δ^7 Li	‰	18.8	13.3	21.7	19.6	20.0
δ^{26} Mg	‰	-0.55	-0.60	-1.00	-0.89	-0.71
δ^{25} Mg	‰	-0.29	-0.32	-0.53	-0.45	-0.38
Temperature	°C	nd	13.7	10.4	10.5	11.4
pН		nd	7.94	7.80	7.49	7.49
Conductivity	S/m	nd	0.04	0.01	0.01	nd
Total Alkalinity	μeq/L	293	504	376	306	233
TDS	mg/L	30.0	52.8	41.5	38.7	29.1
F	μmol/L	3.50	4.57	3.95	4.22	4.03
Cl	μmol/L	31.5	39.1	46.4	43.7	47.3
Br	μmol/L	0.03	0.06	bd	0.05	0.05
SO ₄	μmol/L	9.23	44.2	25.6	50.8	18.2
В	nmol/L	577	612	92.9	107	103
Na	μmol/L	43.0	62.0	45.9	45.5	49.5
Mg	μmol/L	7.21	16.7	13.9	14.5	16.0
Al	μmol/L	0.40	0.40	0.39	0.32	0.50
Si	μmol/L	50.8	74.4	72.5	71.6	77.3
K	μmol/L	3.87	9.37	45.0	45.4	37.7
Ca	μmol/L	147	256	176	158	101
Li	nmol/L	158	572	203	259	134
Mn	nmol/L	1.09	4.17	8.54	3.86	4.57
Fe	nmol/L	29.7	50.0	43.3	64.7	66.9
Rb Sr	nmol/L nmol/L	3.51 442	7.46 744	38.1 204	51.1 257	43.9 139
Cs	nmol/L	0.08	0.31	0.56	0.45	0.46
Ba	nmol/L	3.42	16.2	55.6	35.5	69.1
Y Y	pmol/L	18.1	10.2	147	196	166
La	pmol/L	4.83	47.1	40.7	34.4	41.0
Ce	pmol/L	4.36	38.9	24.7	31.1	51.5
Pr	pmol/L	1.06	9.91	10.1	9.20	10.0
Nd	pmol/L	5.05	42.9	43.1	40.5	39.2
Sm	pmol/L	1.02	8.75	8.29	11.2	8.99
Eu	pmol/L	0.23	1.92	2.65	4.35	2.65
Gd	pmol/L	1.60	11.3	10.5	12.7	12.3
Tb	pmol/L	0.17	1.37	1.49	2.26	1.47
Dy	pmol/L	1.03	8.23	10.1	14.4	11.4
Но	pmol/L	0.28	1.82	2.34	3.30	3.04
Er	pmol/L	1.04	5.03	8.65	10.9	10.9
Tm	pmol/L	0.14	0.58	1.46	1.69	1.56
Yb	pmol/L	0.94	3.63	11.4	11.7	12.3
Lu	pmol/L	0.15	0.60	2.01	1.92	2.15
Pb	pmol/L	38.6	67.6	19.3	29.0	19.3
U	pmol/L	124	88.6	14.4	9.75	2.63

TABLE B.1 Continued – River water, rain water and groundwater

				Rivers East of	f Main Divide	
Sample ID		NZ04	NZ06	NZ07	NZ27	NZ05
Sample Name		Thunder Creek	Hooker Term	Mingha	Trib of Rakai	Chinaman's
Sumple I turne		Thander Creek	Hooker Tellin	TVIIII GIRC	River	Bluff/Dart River
Sampling Date		2009	2009	2009	2011	2011
Easting		2218613	2276200	2396030	2381992	2142277
Northing		5678977	5720205	5802900	5761869	5600803
Туре		Non-glacial river	Glacial river	Non-glacial river	Non-glacial river	
Catchment Lithole	ogv	Metasediment	Metasediment	Metasediment	Metasediment	Metasediment
Catchment Met. (Chlorite GS	P-P	Biotite GS	P-P	P-P
δ^7 Li	%	26.1	14.5	13.5	18.1	16.0
δ^{26} Mg	‰	-0.36	-0.30	-0.68	-0.77	-0.26
δ^{25} Mg	‰	-0.19	-0.16	-0.35	-0.41	-0.14
· ·						
Temperature	°C	10.6	5.00	12.3	14.8	8.60
pH	C /	7.86	8.68	8.21	8.27	8.01
Conductivity	S/m	0.04	0.04	0.05	0.08	0.07
Total Alkalinity	μeq/L	368	359	442	899	571
TDS	mg/L	37.3	37.9	48.8	39.1	86.3
F	μmol/L	1.01	0.64	1.24	6.56	0.92
Cl Pro	μmol/L	30.7	25.2	30.1	35.4	28.2
Br	μmol/L	bd 22.6	bd 43.2	bd	bd	bd 126
SO ₄	μmol/L	22.6	43.2	64.5	61.0	126
B	nmol/L	167	377	659	689	170
Na	μmol/L	33.7	15.7	47.7	151	16.4
Mg	μmol/L	20.7	20.1	16.2	69.3	16.9
Al	μmol/L	0.55	2.34	0.31	0.43	0.37
Si K	μmol/L	53.5	27.1 12.6	71.4 6.84	146 11.6	37.9 10.1
	μmol/L	6.17 177	12.6 196	6.84 241	331	357
Ca Li	μmol/L nmol/L	77.1	230	430	463	134
Mn	nmol/L	7.94	3.75	1.07	11.6	57.4
Fe	nmol/L	79.0	81.8	22.8	11.0	38.7
Rb	nmol/L	4.50	4.21	6.40	7.07	4.02
Sr	nmol/L	325	1060	723	966	711
Cs	nmol/L	0.14	0.09	0.25	0.29	0.07
Ba	nmol/L	12.1	8.11	17.2	8.37	11.0
Y	pmol/L	141.33	12.4	88.1	91.3	11.7
La	pmol/L	161.56	13.6	68.0	55.2	17.7
Ce	pmol/L	189.15	22.2	52.6	76.9	21.5
Pr	pmol/L	28.00	3.04	13.3	12.7	2.96
Nd	pmol/L	100.53	10.7	52.7	56.3	9.58
Sm	pmol/L	14.63	1.86	10.4	11.4	1.04
Eu	pmol/L	3.13	0.40	1.73	2.18	0.18
Gd	pmol/L	17.95	2.24	12.0	12.2	1.69
Tb	pmol/L	1.89	0.25	1.42	1.54	0.14
Dy	pmol/L	11.08	1.58	7.23	9.14	0.86
Ho	pmol/L	2.42	0.32	1.64	1.85	0.17
Er	pmol/L	8.67	0.83	4.64	5.53	0.61
Tm	pmol/L	1.41	0.11	0.64	0.76	0.16
Yb	pmol/L	8.18	0.74	3.59	5.00	0.94
Lu	pmol/L	1.37	0.07	0.56	0.73	0.21
Pb	pmol/L	337.84	96.5	33.8	135	48.3
U	pmol/L	23.72	249	192	1880	95.3

TABLE B.1 Continued – River water, rain water and groundwater

			West Coast Rain	East Co	ast Rain
Sample ID		NZ25	WCR	Rain 1	Rain 2
Sample Name		Potts River	Karangarua Rain		
Sampling Date		2011	2010	2003	2003
Easting East		2344581	2010	2003	2003
Northing		5734788			
Type		Non-glacial river	Rain	Rain	Rain
Catchment Litholo	nav	Metasediment	Kan	Kani	Каш
Catchment Met. (P-P			
$\frac{\text{catchine it iviet.}}{\delta^7 \text{Li}}$	%	22.9	nd	nd	nd
δ^{26} Mg	‰	-0.74	nd		
				nd	nd
δ^{25} Mg	‰	-0.40	nd	nd	nd
Temperature	°C	19.6	nd	nd	nd
pН		8.00	6.32	nd	nd
Conductivity	S/m	0.02	0.00	nd	nd
Total Alkalinity	μeq/L	384	278	nd	nd
TDS	mg/L	65.6	nd	nd	nd
F	μmol/L	4.35	bd	bd	bd
Cl	μmol/L	26.5	bd	9.10	11.2
Br	μmol/L	bd	bd	bd	bd
SO_4	μmol/L	27.5	bd	11.5	14.7
В	nmol/L	875	bd	bd	bd
Na	μmol/L	50.6	0.35	6.96	7.26
Mg	μmol/L	16.0	0.33	0.55	1.03
Al	μmol/L	1.69	0.00	bd	bd
Si	μmol/L	96.0	0.14	1.61	4.49
K	μmol/L	9.22	0.12	7.08	7.61
Ca	μmol/L	160	4.22	2.34	4.01
Li	nmol/L	101	bd	nd	nd
Mn	nmol/L	36.6	0.00	nd	nd
Fe	nmol/L	279	17.4	nd	nd
Rb	nmol/L	4.52	0.00	bd	bd
Sr	nmol/L	323	3.08	nd	960
Cs	nmol/L	0.07	bd	bd	bd
Ba	nmol/L	6.55	0.00	bd	bd
Y	pmol/L	94.4	bd	bd	bd
La	pmol/L	91.3	bd	bd	bd
Ce	pmol/L	151	bd	bd	bd
Pr	pmol/L	20.3	bd	bd	bd
Nd	pmol/L	83.3	bd	bd	bd
Sm	pmol/L	15.1	bd	bd	bd
Eu	pmol/L	3.03	bd	bd	bd
Gd	pmol/L	17.3	bd	bd	bd
Tb	pmol/L	1.87	bd	bd	bd
Dy	pmol/L	11.1	bd	bd	bd
Но	pmol/L	2.05	bd	bd	bd
Er	pmol/L	5.81	bd	bd	bd
Tm	pmol/L	0.72	bd	bd	bd
Yb	pmol/L	4.89	bd	bd	bd
Lu	pmol/L	0.71	bd	bd	bd
Pb	pmol/L	183	bd	bd	bd
U	pmol/L	133	bd	bd	bd

TABLE B.2: Chemical composition of spring water samples from the Southern Alps. Li isotopic data from this study, and general information and elemental data are from Menzies (2012). Flow rate was measured in 2010 by Reyes et al. (2010). Bd = below detection, nd = not determined, TDS = total dissolved solids, P-P = Prehnite-Pumpellyite, P-Act = Prehnite-Actinolite, GS = Greenschist Facies, G-O Amph = garnet oligoclase Amphibolite Facies. T_{Si} = silica equilibration temperature calculated by Menzies (2012).

			Fox		Amy	thest
Sample ID		HS5	HS22	HS41	HS9	HS40
Sampling Date		2009	2010	2011	2009	2011
Easting		2268935	2268935	2268935	2317214	2317210
Northing		5742959	5742975	5742959	5779300	5779292
Distance from Alp	oine Fault (m)	377	377	377	1200	1200
Host Lithology		Metasediment	Metasediment	Metasediment	Metasediment	Metasediment
Host Met. Grade		G-O Amph				
Flow Rate (L/min))	nd	nd	nd	2.0	2.0
δ^7 Li	‰	3.04	3.67	2.98	2.00	2.14
δ^{26} Mg	‰	-0.57	nd	nd	nd	nd
δ^{25} Mg	‰	-0.30	nd	nd	nd	nd
T	°C	28.3	32.7	29.8	44.5	30.9
Tsi	°C	103	117	29.8 111	121	102
pH	C	6.72	6.77	6.80	5.77	6.11
Conductivity	S/m	1.46	1.92	1.80	0.57	0.80
Total Alkalinity	s/m μeg/L	9500	18400	1.80	nd	3110
TDS	μεq/L mg/L	nd	nd	44100	nd	16400
F	mg/L μmol/L	nd	323	304	142	72.0
Cl	μmol/L	nd	6340	5932	4730	4540
Br	μmol/L	nd	5.62	5.06	5.05	4.91
SO ₄	μmol/L	nd	bd	17.0	60.8	52.6
B	μmol/L	250	340	311	165	156
Na	μmol/L	15500	21200	19300	7870	7130
Mg	μmol/L	128	158	144	48.1	63.8
Al	μmol/L	1.76	0.26	0.37	0.55	0.34
Si	μmol/L	858	1100	1020	1160	844
K	μmol/L	429	626	574	380	290
Ca	μmol/L	776	966	913	477	392
Li	μmol/L	136	182	166	176	126
Mn	nmol/L	1450	1730	1950	1270	503
Fe	nmol/L	6400	1900	953	485	543
Rb	nmol/L	1260	1700	2010	1370	1450
Sr	nmol/L	5320	7040	6300	2270	2420
Cs	nmol/L	629	857	945	852	1040
Ba	nmol/L	149	161	169	95.4	140
Y	pmol/L	3180	nd	nd	150	780
La	pmol/L	297	nd	nd	42.7	78.7
Ce	pmol/L	499	nd	nd	73.8	88.8
Pr	pmol/L	71.4	nd	nd	9.28	22.1
Nd	pmol/L	298	nd	nd	34.8	108
Sm	pmol/L	69.0	nd	nd	7.32	26.7
Eu	pmol/L	19.6	nd	nd	2.02	8.50
Gd	pmol/L	84.2	nd	nd	7.58	38.7
Tb	pmol/L	17.3	nd	nd	1.43	5.11
Dy	pmol/L	148	nd	nd	7.97	38.5
Но	pmol/L	41.9	nd	nd	1.83	11.0
Er	pmol/L	164	nd	nd	6.55	46.1
Tm	pmol/L	29.7	nd	nd	1.11	8.29
Yb	pmol/L	240	nd	nd	8.51	71.5
Lu	pmol/L	42.5	nd	nd	1.87	16.9
Pb	pmol/L	310	80.6	bd	396	980
U	pmol/L	11.2	6.52	7.68	54.4	67.8

TABLE B.2 Continued – Spring waters

		Hot Springs	Morgon's		Welcome Flat	
		Flat	Gorge			
Sample ID		HS39	HS16	HS6	HS28	WF2
Sampling Date		2011	2010	2009	2010	2011
Easting		2319283	2325180	2263608	2263608	2263645
Northing		5776317	5784018	5726340	5726340	5726380
Distance from Al	oine Fault (m)	5000	1800	11000	11000	11000
Host Lithology	pine Tuait (iii)	Metasediment	Metasediment	Metasediment	Metasediment	Metasediment
Host Met. Grade		G-O Amph	G-O Amph	Biotite GS	Biotite GS	Biotite GS
Flow Rate (L/min		nd	nd	nd	nd	nd
$\frac{1000 \text{ Rate} (271111)}{\delta^7 \text{Li}}$	/	1.07	3.73	0.78	0.36	0.18
δ^{26} Mg	‰	nd	nd	-0.39	nd	nd
δ^{1} Mg		-	-			
o Mg	‰	nd	nd	-0.21	nd	nd
T	°C	39.9	43.7	56.9	56.0	56.1
Tsi	°C	96.2	112	164	160	153
pН		7.10	6.84	6.29	6.46	6.47
Conductivity	S/m	0.56	0.91	nd	2.10	2.04
Total Alkalinity	μeq/L	3550	6270	nd	nd	16900
TDS	mg/L	11400	22400	nd	nd	41200
F	μmol/L	98.9	56.8	67.5	64.6	67.8
Cl	μmol/L	1480	4810	4340	4160	3880
Br	μmol/L	1.46	4.98	4.57	4.32	4.18
SO_4	μmol/L	85.3	50.2	9.51	bd	11.1
В	μmol/L	51.6	90.2	578	553	517
Na	μmol/L	5000	9400	17200	16100	15200
Mg	μmol/L	25.1	32.9	194	191	177
Al	μmol/L	0.14	0.16	0.02	0.26	0.10
Si	μmol/L	737	1010	2120	2430	2350
K	μmol/L	152	221	711	663	630
Ca	μmol/L	339	579	1650	2230	2060
Li	μmol/L	78.1	106	303	292	280
Mn	nmol/L	776	2400	4460	3990	4380
Fe	nmol/L	369	303	29.0	451	1700
Rb	nmol/L	434	460	2670	1990	2500
Sr	nmol/L	2760	7320	21000	20700	19100
Cs	nmol/L	327	199	1320	1180	1380
Ba	nmol/L	139	139	1280	1280	1170
Y	pmol/L	289	8310	nd	3330	4700
La	pmol/L	6.51	192	nd	11.5	14.3
Ce	pmol/L	12.2	344	nd	22.3	16.8
Pr	pmol/L	1.89	53.1	nd	3.26	3.22
Nd	pmol/L	9.00	241	nd	14.4	17.9
Sm	pmol/L	2.48	83.2	nd	5.27	5.62
Eu	pmol/L	1.31	44.2	nd	2.14	4.04
Gd	pmol/L	5.75	150	nd	18.4	24.1
Tb	pmol/L	1.12	39.2	nd	4.78	7.47
Dy	pmol/L	10.5	350	nd	63.7	96.0
Но	pmol/L	3.31	93.4	nd	25.0	35.4
Er	pmol/L	15.1	354	nd	118	155
Tm	pmol/L	2.73	63.2	nd	20.8	26.5
Yb	pmol/L	23.4	453	nd	168	200
Lu	pmol/L	4.71	67.0	nd	27.7	32.2
Pb	pmol/L	29.0	35.7	25.1	74.8	bd
U	pmol/L	0.48	25.4	22.8	28.3	24.4

TABLE B.2 Continued – Spring waters

		Scone	Smythe	Butler	Bivouac	Deception
Sample ID		HS13	HS36	HS15	BIV 1	HS7
Sampling Date		2010	2011	2010	2011	2009
Easting		2313250	2335054	2300990	2263683	2398075
Northing		5756250	5775404	5753397	5726351	5818850
Distance from Alp	ine Fault (m)	16500	14500	12000	11000	3500
Host Lithology	me raun (m)	Metasediment	Metasediment	Metasediment	Metasediment	Metasedimen
Host Met. Grade		Chlorite GS	Biotite GS	Chlorite GS	Biotite GS	P-P
Flow Rate (L/min)		nd	2.0	nd	nd	3.4
riow Kate (L/IIIII) δ ⁷ Li	‰	10.77	7.14	3.13	1.67	8.51
δ^{26} Mg	‰	nd	nd	nd	nd	nd
δ^{25} Mg	‰	nd	nd	nd	nd	nd
Γ	°C	20.3	38.1	39.5	21	37.5
Tsi	°C	64.7	97.3	96.7	94	96.7
рH		8.83	8.60	6.83	6.64	9.01
Conductivity	S/m	0.14	0.33	0.33	0.55	0.20
Total Alkalinity	μeq/L	996	2180	2980	1510	nd
ГDS	mg/L	3280	7100	7830	8290	nd
7	μmol/L	46.0	107	110	17.7	92.6
CI	μmol/L	301	739	411	1120	100
Br	umol/L	0.24	0.84	0.50	1.14	17.5
SO_4	μmol/L	198	277	185	8.44	361
В	μmol/L	87.8	317	228	121	77.6
Na	μmol/L	1270	2960	3160	3990	2080
Иg	μmol/L	9.87	4.94	12.8	65.8	9.46
Al	μmol/L	0.60	0.87	0.18	0.54	2.30
Si	μmol/L	336	755	733	694	705
K	μmol/L	26.2	65.4	125	181	26.8
Ca	μmol/L	146	121	223	724	142
Li	μmol/L	30.7	47.6	64.8	68.0	58.9
Mn	nmol/L	75.9	67.8	305	1850	55.0
Fe	nmol/L	117	258	911	6640	333
Rb	nmol/L	12.4	120	299	639	32.8
Sr	nmol/L	940	2210	4680	5240	746
Cs	nmol/L	bd	35.2	197	353	8.68
es Ba	nmol/L	6.99	12.6	67.6	390	13.0
Y Y	pmol/L	142	12.0	123	3400	247
La	pmol/L	41.5	20.0	22.6	167	119
					297	
Ce Pr	pmol/L pmol/L	40.7 11.3	46.4 5.75	41.2 5.96	44.1	231 28.0
Nd	pmol/L	45.4	25.2	24.9	202	111
Nu Sm	pmol/L	11.2	5.68	5.49	51.7	21.3
sm Eu	-	11.2	1.53	1.50	18.9	4.34
eu Gd	pmol/L					I .
sa Fb	pmol/L	11.0	7.08	6.98 1.01	87.1 18.3	26.1 3.02
	pmol/L	1.68	1.15			
Dy	pmol/L	9.59	8.12	5.65	165	20.3
Ho E	pmol/L	2.30	2.02	1.55	43.4	4.13
Er Dan	pmol/L	6.51	7.70	5.47	161	12.7
Гm Vb	pmol/L	0.88	1.10	0.93	26.1	1.74
Yb	pmol/L	5.64	9.00	6.60	191	11.5
Lu	pmol/L	0.81	1.62	1.31	27.8	1.65
Pb U	pmol/L pmol/L	265 25.2	386 33.8	219 26.8	19.3 3.21	314 23.2

TABLE B.2 Continued – Spring waters

		Julia	Mungo	Horseshoe	Wren Creek	Haupiri
			_	Flat		_
Sample ID		HS17	HS33	HS19	HS23	HS24
Sampling Date		2010	2011	2010	2010	2011
Easting		2381488	2362267	2467948	2359051	2409417
Northing		5811227	5795650	5846280	5803087	5837839
Distance from Alp	oine Fault (m)	7000	14000	950	7000	7500
Host Lithology		Metasediment	Metasediment	Metasediment	Metasediment	Metasediment
Host Met. Grade		P-P	P-Act	P-P	Biotite GS	Chlorite GS
Flow Rate (L/min))	7.3	1.7	nd	5.1	1.3
δ^7 Li	%	8.96	8.83	7.45	6.83	8.69
δ^{26} Mg	‰	nd	nd	nd	nd	nd
δ^{25} Mg	‰	nd	nd	nd	nd	nd
Т	°C	60.0	50.1	50.5	55.1	38.1
Tsi	°C	115	96.9	30.3 118	128	38.1 127
pH	C	8.92	8.89	8.78	8.49	9.46
Conductivity	S/m	0.54	0.02	0.36	0.47	9.46 0.16
Total Alkalinity	μeq/L	2680	1700	3960	2610	2450
TDS	μεq/L mg/L	8200	5040	11700	10800	7090
F	mg/L μmol/L	252	77.4	255	353	7090 171
r Cl	μπο/L μmol/L	113	147	632	1660	104
Br	μmol/L	0.13	0.16	0.71	2.14	0.11
SO ₄	μmol/L	939	323	648	366	332
B	μmol/L	289	198	811	176	109
Na	μmol/L	3320	2030	5130	4570	2820
Mg	μmol/L	0.41	2.06	3.29	4.94	1.23
Al	μmol/L	2.06	4.18	2.82	1.42	2.47
Si	μmol/L	1070	748	1140	1385	1310
K	μmol/L	51.8	29.1	54.1	116	44.7
Ca	μmol/L	30.2	62.4	110	109	31.7
Li	μmol/L	63.1	35.0	46.0	78.7	30.6
Mn	nmol/L	11.1	8.81	13.4	224	17.7
Fe	nmol/L	641	75.0	338	383	446
Rb	nmol/L	62.4	42.5	64.7	371	92.7
Sr	nmol/L	522	563	932	793	329
Cs	nmol/L	38.8	12.2	1.20	333	49.9
Ba	nmol/L	6.77	2.84	116	15.0	4.73
Y	pmol/L	279	70.8	386	88.9	216
La	pmol/L	106	25.9	163	22.9	92.9
Ce	pmol/L	251	63.4	304	49.3	193
Pr	pmol/L	30.3	6.96	44.7	6.32	27.0
Nd	pmol/L	124	29.9	191	24.8	108
Sm	pmol/L	25.6	6.06	44.2	5.35	25.8
Eu	pmol/L	6.07	2.27	9.05	1.09	5.81
Gd	pmol/L	27.4	8.86	41.8	6.53	24.1
Tb	pmol/L	4.10	0.97	6.80	0.99	3.82
Dy	pmol/L	25.8	6.45	36.6	7.16	24.0
Но	pmol/L	5.31	1.45	7.24	1.76	4.46
Er	pmol/L	15.0	4.89	19.2	5.37	11.7
Tm	pmol/L	2.03	0.74	2.37	0.75	1.75
Yb	pmol/L	13.5	5.17	12.4	5.69	10.0
Lu	pmol/L	2.14	0.90	1.69	0.86	1.16
Pb	pmol/L	628	391	450	102	234
U	pmol/L	45.8	53.4	15.0	1.65	23.4

TABLE B.2 Continued – Spring waters

		Sylvia	Red Hills		Cascade	
Sample ID		HS26	RHS	HS2	HS20	CS1
Sampling Date		2011	2011	2009	2010	2011
Easting		2459588	2508726	2147665	2147665	2147430
Northing		5857249	5943895	5657965	5657965	5657698
Distance from Alp	nine Fault (m)	4500	3943693	3037903	3037903	3037098
Host Lithology	me raun (m)	Metasediment	Ultramafic	Ultramafic	Ultramafic	Ultramafic
Host Met. Grade		P-P	P-P	P-P	P-P	P-P
Flow Rate (L/min)		1.2	nd	13	13	13
$\frac{\text{Flow Rate (L/IIIII)}}{\delta^7 \text{Li}}$	%	4.84	7.35	nd	8.89	nd
δ L1 δ ²⁶ Mg						
0 Mg	‰	nd	nd	nd	-0.74	nd
δ^{25} Mg	‰	nd	nd	nd	-0.39	nd
T	°C	37.5	10.6	17.1	16.7	16.4
Tsi	°C	102	nd	nd	nd	nd
pН		8.05	11.8	11.6	11.5	11.5
Conductivity	S/m	0.63	0.61	nd	0.48	0.45
Total Alkalinity	μeq/L	5040	1.93	nd	1.05	1.54
TDS	mg/L	11300	nd	nd	nd	3440
F	μmol/L	186	0.00	nd	0.28	1.54
Cl	μmol/L	312	706	nd	1350	1390
Br	μmol/L	0.30	1.02	nd	1.36	1.47
SO_4	μmol/L	27.9	bd	nd	bd	0.25
В	μmol/L	281	0.18	0.36	0.37	0.31
Na	μmol/L	4830	432	1560	1460	1470
Mg	μmol/L	11.5	4.94	15.3	49.0	37.0
Al	μmol/L	1.13	bd	0.09	0.03	0.07
Si	μmol/L	798	1.07	2.30	13.2	13.1
K	μmol/L	116	14.5	31.5	34.3	31.7
Ca	μmol/L	178	1130	528	362	498
Li	μmol/L	155	1.49	2.09	1.90	1.92
Mn	nmol/L	140	1.06	6.90	5.86	8.32
Fe	nmol/L	204	bd	64.5	333	430
Rb	nmol/L	95.2	2.35	6.76	6.20	7.02
Sr	nmol/L	4380	184	246	459	250
Cs	nmol/L	bd	0.07	bd	bd	0.21
Ba	nmol/L	206	5.53	23.5	8.58	16.6
Y	pmol/L	384	0.16	8.41	4.87	14.9
La	pmol/L	97.1	0.42	8.50	2.01	3.07
Ce	pmol/L	217	0.51	14.3	4.47	5.42
Pr	pmol/L	31.3	0.06	1.73	0.62	0.84
Nd	pmol/L	137	0.15	5.81	2.81	3.34
Sm	pmol/L	31.9	bd	0.75	1.16	1.26
Eu	pmol/L	7.07	0.01	0.13	0.12	0.33
Gd	pmol/L	36.8	0.07	1.55	0.55	1.30
Tb	pmol/L	4.98	bd	0.17	0.09	0.25
Dy	pmol/L	31.3	bd	0.84	0.70	1.42
Но	pmol/L	6.25	bd	0.06	0.11	0.34
Er	pmol/L	15.7	0.06	0.30	0.38	0.90
Tm	pmol/L	1.96	0.01	0.01	0.03	0.15
Yb	pmol/L	11.9	bd 0.01	0.30	0.42	0.94
Lu	pmol/L	1.75	0.01	0.00	0.07	0.14
Pb	pmol/L	595	145	174	531	917
U	pmol/L	86.3	0.50	1.04	0.13	0.88

TABLE B.2 Continued – Spring waters

				Cas	cade		
Sample ID		CS2	CS3	CS4	CS5	CS6	CS7
Sampling Date		2011	2011	2011	2011	2011	2011
Easting		2147430	2147430	2147430	2147430	2147430	2147430
Northing		5657698	5657698	5657698	5657698	5657698	5657698
Distance from Al	pine Fault (m)						
Host Lithology		Ultramafic	Ultramafic	Ultramafic	Ultramafic	Ultramafic	Ultramafic
Host Met. Grade		P-P	P-P	P-P	P-P	P-P	P-P
Flow Rate (L/min))	13	13	13	13	13	13
δ^7 Li	‰	8.58	nd	nd	nd	nd	nd
δ^{26} Mg	‰	nd	nd	nd	nd	nd	nd
δ^{25} Mg	‰	nd	nd	nd	nd	nd	nd
<u> </u>							
T	°C	13.8	13.7	13.2	13.9	13.9	15.6
Tsi	°C	nd	nd	nd	nd	nd	nd
pН	G /	10.8	10.7	10.2	10.4	9.67	11.3
Conductivity	S/m	0.19	0.18	0.16	0.16	0.15	0.30
Total Alkalinity	μeq/L	0.91	0.91	0.78	0.84	0.72	0.83
TDS	mg/L	2080	2020	1960	1940	1860	nd
F	μmol/L	0.91	0.91	0.78	0.84	0.72	0.83
Cl	μmol/L	757	730	713	705	681	937
Br	μmol/L	0.89	0.73	0.88	0.84	bd 2.02	0.93
SO ₄	μmol/L	1.94	2.12	2.17	2.67	2.83	bd
В	μmol/L	0.23	0.23	0.25	0.23	0.24	0.24
Na	μmol/L	837	811	787	777	740	983
Mg	μmol/L	160	161	158	160	160	47.0
Al	μmol/L	0.10	0.09	0.11	0.11	0.12	0.16
Si	μmol/L	72.7	73.0	71.5	71.6	70.6	12.6
K	μmol/L	19.3	18.6	19.0	18.2	17.7	29.8
Ca	μmol/L	272	260	244	244	227	396
Li	μmol/L	1.06	1.02	1.00	0.97	0.91	1.35
Mn	nmol/L	6.23	6.46	6.43	7.28	5.55	11.0
Fe	nmol/L	264	253	234	258	172	541
Rb Sr	nmol/L nmol/L	4.19	4.08 136	4.07 132	3.85	3.67	5.98 194
Cs	nmol/L	142			129	120	
Ba	nmol/L	0.14 9.48	0.13 9.23	0.17 10.0	0.16 8.69	0.31 8.10	0.14 13.8
Ба Y		25.5	48.0	16.3	41.8	44.8	21.0
La	pmol/L pmol/L	4.40	6.03	3.15	7.03	14.2	3.91
Ce	-	7.37	11.9	6.87	12.7	23.9	8.18
Pr	pmol/L pmol/L	1.14	1.64	1.02	1.84	3.52	1.03
Nd	pmol/L	4.72	6.89	3.72	7.56	14.55	4.45
Sm	pmol/L	0.87	1.40	0.87	1.93	2.92	1.02
Eu	pmol/L	0.87	0.46	0.87	0.36	0.64	0.32
Gd	pmol/L	1.48	2.42	1.23	3.13	3.97	1.85
Tb	pmol/L	0.20	0.33	0.15	0.42	0.48	0.22
Dy	pmol/L	1.33	2.97	1.34	3.20	3.39	1.57
Ho	pmol/L	0.37	0.58	0.23	0.59	0.64	0.37
Er	pmol/L	1.45	2.11	1.09	1.95	2.03	1.37
Tm	pmol/L	0.19	0.28	0.14	0.35	0.26	0.22
Yb	pmol/L	1.42	1.88	0.14	1.96	1.85	1.26
Lu	pmol/L	0.28	0.25	0.14	0.26	0.25	0.26
Pb	pmol/L	468	483	2027	483	241	48.3
U	pmol/L	0.57	0.72	2.05	1.23	1.29	0.58

TABLE B.3: Major and trace element concentrations of bedrock of the Southern Alps. Li isotopic data and major element data from this study, and trace element data are from Pitcairn (2004). P-P = Prehnite-Pumpellyite, P-Act = Prehnite-Actinolite, GS = Greenschist Facies, G-O Amph = garnet-oligoclase Amphibolite Facies, GW = greywacke, psam = Psammite, pel = pelite, QFS = quartzofeld-spathic, MB = metabasalts.

Sample ID C47 A63 A89 B30 Locality PortersPass Hawea Hawea Hawea Sampling Date 2004 2004 2004 2004 Easting 2409656 2213000 2210700 2207200 Northing 5766383 5626000 5631500 5633200 Lithology GW psam pel QFS	A18 Nevis Bluff 2004 2195000 5567000 MB	A22 Nevis Bluff 2004 2195000
Sampling Date 2004 2004 2004 2004 Easting 2409656 2213000 2210700 2207200 Northing 5766383 5626000 5631500 5633200	2004 2195000 5567000 MB	2004 2195000
Easting 2409656 2213000 2210700 2207200 Northing 5766383 5626000 5631500 5633200	2195000 5567000 MB	2195000
Northing 5766383 5626000 5631500 5633200	5567000 MB	
Northing 5766383 5626000 5631500 5633200	5567000 MB	
8	MB	5567000
		MB
Met. Grade None P-P Lower GS GS	GS	GS
Temperature °C 100 200 300 400	400	400
	0.72	
		-0.69
$\delta^{26} Mg$ % -0.19 -0.22 nd nd	nd	-0.13
$\delta^{25} Mg$ % -0.08 -0.11 nd nd	nd	-0.03
Na μg/g 27700 27200 23600 26300	14900	3030
Mg μg/g 9920 7030 15800 8110	42800	52500
Al μg/g 80100 72800 75100 80300	54600	69500
P μg/g 604 345 659 456	2680	2360
K μg/g 24000 17100 17900 25700	13200	11000
Ca μg/g 14800 14600 26000 16000	51100	56200
Ti μg/g 3290 4040 4310 3460	17600	21700
Fe μg/g 30000 30700 41300 28200	76400	107000
Li µg/g 40.7 37.2 46.6 51.4	715	02.2
166	74.5	92.2
V μg/g 84.2 94.1 125 76.0 Cr μg/g 49.4 35.0 160 38.1	177	251
100	196	613
Co μg/g 9.60 10.5 15.2 8.00	33.3	53.2
Ni μg/g 18.1 13.6 38.1 18.5	123	218
Cu μg/g 14.3 14.0 28.7 16.1	21.6	73.6
Zn μg/g 63.5 66.0 78.9 67.3	131	178
Rb μg/g 88.4 74.3 80.6 111	45.0	41.9
Sr μg/g 408 350 270 291	131	305
Y μg/g 24.2 22.1 27.6 21.6	27.8	35.3
Zr μg/g 172 292 161 169	263	304
Nb μg/g 9.68 9.51 8.86 8.77	57.4	60.8
Mo μg/g 0.84 0.51 0.71 0.65	2.09	0.51
Sn μg/g 2.37 3.27 2.80 3.17	2.51	2.38
Sb $\mu g/g$ 0.22 0.62 0.32 0.76	0.31	0.53
Te μg/g 1.00 1.00 1.00 1.42	3.08	1.66
Cs $\mu g/g$ 3.24 2.80 4.40 4.77	2.92	1.81
Ba μg/g 687 514 501 737	167	106
La µg/g 27.6 27.3 24.4 25.5	38.8	44.0
Ce $\mu g/g$ 52.9 56.7 52.7 50.7	86.4	96.4
$\frac{1}{2}$ Pr $\frac{1}{2}$ \frac	10.6	12.0
Nd μg/g 25.3 24.8 24.1 22.7	41.2	47.3
Sm $\mu g/g$ 5.02 4.62 4.99 4.39	8.02	9.56
Eu $\mu g g$ 1.10 1.09 1.16 1.03	2.37	3.08
Gd $\mu g/g$ 1.10 1.05 1.10 1.03 Gd 4.13 3.96 4.72 3.74	7.45	8.79
, , ,	0.92	1.13
166	5.00	6.31
, , , ,		
Ho μg/g 0.66 0.70 0.85 0.65	0.89	1.13
Er μg/g 1.97 2.05 2.47 1.89	2.29	3.01
Tm μg/g 0.28 0.32 0.37 0.29	0.34	0.40
Yb μg/g 1.82 2.20 2.30 1.94	1.97	2.52
Lu μg/g 0.27 0.33 0.34 0.28	0.27	0.37
Hf μg/g 6.30 6.53 4.48 2.00	7.32	2.00
Ta μg/g 0.56 0.59 0.57 0.56	4.16	4.50
W μg/g 1.09 1.16 1.05 0.97	0.18	0.38
Hg $\mu g/g$ 0.08 0.04 0.02 0.02	0.00	0.01
Tl μg/g 0.62 0.35 0.40 0.62	0.22	0.23
Pb μg/g 19.9 14.8 13.5 13.3	3.48	12.4
Th μg/g 11.2 15.5 8.79 12.8	8.90	6.22
U μg/g 2.50 3.23 1.05 2.23	1.76	2.01

TABLE B.3 Continued – Bedrock

		Caples Terrar	ne		Alpine Schist	
Sample ID	A4	B92	B64	C72	C70	C66
Locality	Rongaher	e Glenorchy	Remarks	Pleasant Flat	Haast	Haast
Sampling Date	2004	2004	2004	2004	2004	2004
Easting	2237000	2155000	2180400	2219700	2223100	2222500
Northing	5463000	5560500	5564400	5681300	5686300	5686700
Lithology	pel	pel	psam	QFS	QFS	QFS
Met. Grade	P-P	Lower GS	Lower GS	GS	GS	Biotite GS
Temperature °C	200	300	300	400	400	500
δ^7 Li	-0.41	-0.69	-1.48	-0.92	-0.45	-1.57
δ^{26} Mg %	nd	-0.23	nd	-0.06	-0.13	-0.07
δ^{25} Mg	nd	-0.10	nd	-0.02	-0.05	-0.02
Na μg	/g 30300	21100	25500	41700	35400	23100
Mg μg		14000	13000	7470	5910	14700
Al μg	/g 742300	99800	71700	78400	84000	121000
P μg	/g 331	604	720	327	141	732
\mathbf{K} µg		27000	15500	9530	23800	48700
Ca µg	/g 16800	26400	23000	13300	4280	8170
Ti μg		5210	3900	3190	3330	6390
Fe μg	/g 28000	49300	37400	27800	22500	47100
Li μg	/g 33.3	48.1	37.9	35.9	28.2	75.6
V µg		161	96.0	67.8	63.7	166
Cr µg	•	112	44.8	26.3	31.9	155
Co µg		10.9	12.8	8.80	7.50	16.1
Ni μg		11.4	20.4	9.50	12.3	26.5
Cu µg		32.2	5.46	9.71	10.3	25.1
Zn μg		90.9	77.4	56.6	49.2	111
Rb μg		112	60.7	39.2	95.5	221
Sr μg	/g 186	403	227	224	100	212
Y μg	/g 25.9	26.7	27.0	17.2	22.1	41.2
Zr μg	/g 182	177	135	192	324	333
Nb μg		9.39	6.00	6.62	9.65	16.6
Mo μg		0.73	0.35	0.25	0.39	0.87
Sn µg		1.65	3.32	1.68	3.02	3.30
Sb μg		1.37	0.19	0.19	0.09	0.23
Te μg		1.34	1.00	1.00	2.78	1.33
Cs µg		5.86	3.37	1.93	3.59	8.36
Ba μg		658	393	280	579	1130
La µg		22.0	17.7	26.1	32.6	42.0
Ce µg		51.8	40.1	53.2	65.8	91.0
Pr μg	/g 4.92	6.01	5.04	6.42	7.72	10.4
Nd μg	/g 18.6	23.4	19.8	23.4	27.2	38.9
Sm µg		4.93	4.36	4.36	5.01	7.79
Eu µg		1.21	1.08	1.05	1.10	1.68
Gd μg. Tb μg.		4.50 0.64	4.39	3.87	4.22	6.85 1.00
		4.12	0.65 4.13	0.52	0.60 3.53	6.04
Dy μg. Ho μg.		0.80	0.84	3.10 0.63	3.33 0.70	1.21
Ho μg Er μg		2.37	2.46	1.88	2.00	3.59
Tm μg	-	0.36	0.41	0.30	0.31	0.53
Yb μg	-	2.31	2.35	1.78	2.05	3.42
Lu µg	-	0.33	0.36	0.28	0.30	0.49
Hf µg	-	7.73	2.00	13.0	11.2	7.07
Ta µg		0.74	0.52	0.46	0.64	1.19
W μg	-	0.96	0.76	0.72	0.97	1.59
Hg µg		0.01	0.01	0.01	0.00	0.00
TI µg		0.47	0.27	0.18	0.51	1.15
Pb μg	-	17.3	7.82	17.2	14.5	7.80
Th µg	-	11.4	7.81	12.2	12.2	22.2
U µg	-	2.63	1.33	3.22	2.63	4.01

TABLE B.3 Continued – Bedrock

				Alpine Schist		
Sample ID		C68	C54	C61	C56	C59
Locality		Haast	Haast	Haast	Haast	Haast
Sampling Date		2004	2004	2004	2004	2004
Easting		2222900	2200900	2215300	2200900	2208700
Northing		5686500	5688800	5688100	5688800	5687900
Lithology		QFS	QFS	QFS	QFS	QFS
Met. Grade		Biotite GS	Garnet GS	Garnet GS	G-O Amph	G-O Amph
Temperature °C		500	550	550	600	600
δ^7 Li	% o	-0.42	0.15	0.69	0.25	1.39
δ^{26} Mg	‰	nd	nd	nd	0.14	-0.26
δ^{25} Mg	‰	nd	nd	nd	0.09	-0.12
Na	μg/g	36900	37800	29300	30300	26500
Mg	μg/g μg/g	6050	11300	18800	9140	8220
Al	μg/g μg/g	64200	99300	95200	86000	82200
P.		356	454	1080	470	493
	μg/g					
K Co	μg/g	13600	25500	21000	22200 17300	27600
Ca T:	μg/g	18400	27100	25600		17200
Ti E-	μg/g	2240	4860	7670	3410	2990
Fe	μg/g	26400	39900	59600	30800	24100
Li	μg/g	21.6	47.5	61.6	38.9	34.0
V	μg/g	51.4	116	146	81.1	80.4
Cr	μg/g	36.5	48.4	106	185	28.3
Co	μg/g	8.50	11.3	20.8	8.70	8.00
Ni	μg/g	12.9	15.4	49.0	11.1	9.93
Cu	μg/g	8.07	16.6	8.51	14.2	8.83
Zn	μg/g	43.9	69.2	125	71.7	63.2
Rb	μg/g	50.2	107	105	106	128
Sr	μg/g	375	494	282	267	349
Y	μg/g	46.1	24.1	31.6	22.2	20.0
- Zr	μg/g	189	296	223	186	212
Nb	μg/g	21.3	9.77	17.0	11.3	9.68
Mo	μg/g	1.54	0.30	0.62	0.74	0.51
Sn	μg/g μg/g	1.20	2.11	2.49	1.72	1.87
Sb	μg/g	0.22	0.12	0.09	0.00	0.00
Te	μg/g μg/g	1.00	1.00	0.99	1.31	1.00
Cs		1.64	4.89	5.51	5.29	5.66
Cs Ba	μg/g	521	4.89	3.51	3.29 486	704
	μg/g					31.3
La Co	μg/g	104	26.2	28.7	31.2	
Ce D	μg/g	236	55.5	65.4	66.8	64.2
Pr NJ	μg/g	25.9	6.55	7.80	7.57	7.20
Nd S	μg/g	86.9	24.0	30.1	28.0	25.8
Sm E	μg/g	16.8	4.68	6.33	5.17	4.55
Eu	µg/g	4.79	1.23	1.45	1.10	1.06
Gd	µg/g	14.2	4.29	6.23	4.48	4.00
Гb	µg/g	1.64	0.60	0.88	0.61	0.54
Dy	μg/g	8.64	3.80	5.40	3.72	3.21
Ho	μg/g	1.44	0.77	1.06	0.74	0.65
Er 	μg/g	3.61	2.27	3.09	2.09	1.77
Tm	µg/g	0.47	0.32	0.45	0.30	0.28
Yb	μg/g	2.77	2.21	2.97	1.97	1.70
Lu	μg/g	0.35	0.31	0.44	0.27	0.24
Hf	μg/g	9.07	11.4	5.82	4.33	3.04
Та	μg/g	0.38	0.92	1.15	1.10	0.86
\mathbf{W}	μg/g	1.57	0.41	0.24	0.69	1.20
Hg	μg/g	0.00	0.00	0.00	0.00	0.00
TĬ	μg/g	0.24	0.55	0.68	0.61	0.71
Pb	μg/g	11.4	18.6	24.9	24.6	19.5
Th	μg/g	57.0	14.9	14.8	15.3	13.0
U	μg/g	1.29	3.35	3.10	3.08	2.71

TABLE B.4: Major and trace element concentrations of mica mineral separates picked from bedrock of the Southern Alps. GS = Greenschist Facies, G-O Amph = garnet oligoclase Amphibolite Facies, QFS = quartzofeldspathic, MB = metabasalts.

Sample ID		C50	C56	C58	C66	C77	C77
Mica Mineral		Biotite	Biotite	Biotite	Chlorite	Muscovite	Biotite
Locality		Haast	Haast	Haast	Haast	Haast	Haast
Sampling Date		2004	2004	2004	2004	2004	2004
Easting		2281204	2200900	2200900	2222500	2200900	2200900
Northing		5746989	5688800	5688800	5686700	5688800	5688800
Lithology		QFS	QFS	Metabasalt	QFS	QFS	QFS
Met. Grade		Garnet GS	G-O Amph	G-O Amph	Biotite GS	Garnet GS	Garnet GS
δ^7 Li	‰	0.74	-0.89	0.13	-2.46	-0.97	-0.48
δ^{26} Mg	‰	nd	nd	nd	-0.27	-0.23	-0.09
δ^{25} Mg	‰	nd	nd	nd	-0.28	-0.27	-0.18
Na	μg/g	1650	878	1640	1990	6600	3220
Mg	μg/g	56800	54600	69400	59000	11300	45900
Al	μg/g	107000	98400	106000	119000	142000	98700
P	μg/g	117	0.69	99.7	71.0	92.5	82.9
K	μg/g	86400	88700	89400	12000	82800	84400
Ca	μg/g	1240	67.5	5260	1390	3660	2630
Ti	μg/g	8780	11700	10900	1020	4980	15200
Fe	μg/g	165000	165000	160000	219000	33900	151000
	,	250	2.12	102	106	60.0	15.6
Li	μg/g	259	242	192	186	68.8	176
Sc	μg/g	20.8	23.5	22.9	7.08	50.0	28.7
V	μg/g	260	288	460	128	310	325
Cr	μg/g	68.6	78.0	221	57.0	110	92.1
Co	μg/g	42.8	44.9	74.8	40.7	6.66	40.8
Ni	μg/g	61.8	44.7	131	63.7	5.21	47.7
Cu	μg/g	21.4	10.1	13.0	502	11.0	37.9
Zn	μg/g	465	482 521	351	838	54.9	306
Rb	μg/g	586 16.2	7.13	426 68.8	56.8 31.1	214 106	417 47.5
Sr Y	μg/g	5.53	5.05		3.88	21.5	
zr	μg/g μg/g	1.02	0.47	13.4 6.17	0.73	1.27	11.6 1.03
Nb	μg/g μg/g	31.2	41.0	7.55	1.95	12.4	20.8
Mo	μg/g μg/g	11.7	31.7	136	101	224	72.4
Sn	μg/g	6.33	4.62	2.21	2.51	8.00	3.51
Cs	μg/g	46.5	32.5	32.3	3.10	6.86	31.8
Ba	μg/g	798	921	1510	256	2200	1000
La	μg/g	4.65	8.43	4.74	4.31	27.7	13.3
Ce	μg/g	10.1	17.5	11.8	9.23	60.2	28.5
Pr	μg/g	1.19	2.06	1.81	1.09	7.24	3.45
Nd	μg/g	4.45	7.47	8.75	4.13	27.7	13.2
Sm	μg/g	0.90	1.41	2.60	0.83	5.57	2.67
Eu	μg/g	0.18	0.25	0.64	0.18	1.23	0.62
Gd	μg/g	0.79	1.16	3.08	0.76	4.73	2.32
Tb	μg/g	0.12	0.17	0.47	0.11	0.71	0.35
Dy	μg/g	0.77	0.95	2.70	0.68	4.07	2.05
Но	μg/g	0.19	0.18	0.51	0.14	0.78	0.40
Er	μg/g	0.63	0.46	1.27	0.38	2.09	1.12
Tm	μg/g	0.10	0.06	0.16	0.06	0.30	0.16
Yb	μg/g	0.68	0.34	0.90	0.34	1.92	1.04
Lu	μg/g	0.09	0.04	0.11	0.04	0.28	0.15
Hf	μg/g	0.03	0.02	0.19	0.03	0.06	0.04
Ta	μg/g	1.82	2.48	0.07	0.16	0.63	1.58
Pb	μg/g	8.13	5.06	6.88	29.5	10.4	8.22
Th	μg/g	1.84	3.70	0.87	1.76	11.9	5.87
U	μg/g	0.38	0.77	0.25	0.31	2.79	1.33

TABLE B.5: Major and trace element concentrations of river sand size fractions from rivers draining the Southern Alps. P-P = Prehnite Pumpellyite, P-Act = Prehnite-Actinolite, GS = Greenschist Facies, G-O Amph = garnet oligoclase Amphibolite Facies.

-				Bulk River Sand		
Sample ID		RS04	RS05	RS06	RS08	RS09
Locality		Thunder Creek	Chinaman's Bluff	Hooker Terminus	Sheil's Creek	Copland
		Falls				
Sampling Date		2009	2011	2009	2009	2263608
Easting		2218613	2142277	2276200	2263063	5726340
Northing		5678977	5600803	5720205	5726991	11000
Lithology		Metasediment	Metasediment	Metasediment	Metasediment	Metasediment
Met. Grade		Chlorite GS	P-Act	P-P	Biotite GS	Biotite GS
δ ⁷ Li	‰	-0.29	-0.92	-0.05	-1.50	-0.72
δ^{26} Mg	‰	-0.06	-0.11	-0.22	-0.21	nd
δ^{25} Mg	% o	-0.02	-0.05	-0.10	-0.09	nd
Na	μg/g	23000	34900	23200	24000	18200
Mg	μg/g	8660	9580	9880	10500	10600
Al	μg/g	70400	87400	78600	80300	75300
P	μg/g	567	1650	738	717	762
K	μg/g	19300	13900	25800	22100	26000
Ca	μg/g	11100	23900	16300	15200	14300
Ti	μg/g	3360	4480	3950	5010	5550
Fe	µg/g	36800	43900	36600	43600	42000
Li	µg/g	43.3	38.8	39.2	42.2	41.9
Sc	μg/g	10.1	21.8	11.1	12.1	13.5
\mathbf{V}	μg/g	77.1	120	87.2	98.9	105
Cr	μg/g	105	95.1	79.5	131	142
Co	μg/g	7.28	10.9	9.56	11.2	9.95
Ni	μg/g	9.18	14.2	13.9	15.6	15.4
Cu	μg/g	16.5	33.2	17.8	24.0	16.9
Zn	μg/g	64.2	69.8	68.0	84.7	74.7
Rb	μg/g	85.3	61.1	117	105	121
Sr	μg/g	245	422	374	313	322
Y	μg/g	18.3	33.4	24.2	21.3	25.8
Zr	μg/g	17.2	10.4	21.0	2.26	8.50
Nb	μg/g	7.21	8.84	10.5	13.3	13.2
Mo	μg/g	384	434	316	479	635
Sn	μg/g	1.90	2.45	2.32	3.07	2.58
Cs	μg/g	4.33	3.20	4.65	5.43	5.36
Ba	μg/g	432	292	625	535	617
La	μg/g	23.4	34.7	37.1	28.6	38.3
Ce	μg/g	50.1	78.0	76.7	61.9	80.9
Pr	μg/g	5.91	9.23	8.83	7.18	9.31
Nd	μg/g	22.1	36.0	32.8	27.3	34.6
Sm	μg/g	4.38	7.54	6.22	5.43	6.62
Eu	μg/g	0.95	1.73	1.33	1.21	1.38
Gd	μg/g	3.78	6.76	5.12	4.67	5.46
Tb	μg/g	0.57	1.02	0.76	0.70	0.82
Dy	μg/g	3.34	5.94	4.35	3.96	4.63
Ho E	μg/g	0.65	1.16	0.83	0.75	0.90
Er	µg/g	1.78	3.08	2.22	1.94	2.40
Tm Vb	μg/g	0.25	0.41	0.32	0.27	0.34
Yb	μg/g	1.45	2.42	2.00	1.59	2.11
Lu	μg/g	0.18	0.29	0.28	0.21	0.28
Hf To	μg/g	0.60	0.37	0.73	0.07	0.29
Ta	μg/g	0.62	0.78	0.90	1.01	1.12
Pb	μg/g	15.3	17.0	19.3	21.7	16.2
Th	µg/g	9.11	11.7	10.9	10.4	12.7
U	μg/g	1.71	2.28	2.04	2.02	2.28

TABLE B.5 Continued – River sand size fractions

				Fine River Sand		
Sample ID		RS04	RS05	RS06	RS08	RS09
Locality		Thunder Creek		Hooker Terminus	Sheil's Creek	Copland
•		Falls				1
Sampling Date		2009	2011	2009	2009	2263608
Easting		2218613	2142277	2276200	2263063	5726340
Northing		5678977	5600803	5720205	5726991	11000
Lithology		Metasediment	Metasediment	Metasediment	Metasediment	Metasediment
Met. Grade		Chlorite GS	P-Act	P-P	Biotite GS	Biotite GS
δ^7 Li	‰	0.08	-0.59	1.52	-1.22	-0.11
$\delta^{26}{ m Mg}$	‰	-0.13	-0.22	-0.23	-0.12	nd
$\delta^{25} Mg$	‰	-0.06	-0.10	-0.11	-0.04	nd
Na	μg/g	24900	37900	20900	19300	18500
Mg	μg/g	9610	10700	7570	12400	8300
Al	μg/g	80600	91900	62800	69200	64400
P	μg/g	602	997	538	430	642
K	μg/g	23000	16600	19700	18800	18000
Ca	μg/g	15900	16500	12400	12400	15700
Ti	μg/g	4370	3960	3370	4670	7870
Fe	μg/g	42400	45500	27300	52000	40400
Li	μg/g	45.3	43.3	29.4	46.3	29.7
Sc	μg/g	13.7	15.1	8.21	9.56	11.7
V	μg/g	97.4	104	64.0	95.3	81.7
Cr	μg/g	271	109	47.8	390	139
Co	μg/g	8.82	11.0	6.92	14.1	8.92
Ni	μg/g	13.0	16.7	9.26	22.2	13.1
Cu	μg/g	21.0	26.7	13.1	32.0	20.0
Zn	μg/g	75.0	77.6	49.4	101	59.5
Rb	μg/g	103	72.9	91.6	107	80.6
Sr	μg/g	361	280	285	248	338
Y	μg/g	25.6	22.8	17.7	14.7	26.3
Zr	μg/g	17.2	10.6	15.0	2.43	5.99
Nb	μg/g	10.5	7.38	8.07	12.3	16.0
Mo	μg/g	1010	549	249	1310	509
Sn	μg/g	2.49	1.97	1.75	2.15	2.08
Cs	μg/g	5.10	3.76	3.67	6.17 396	3.60 429
Ba	μg/g	512 38.0	349 25.3	465 27.0	396 18.8	429 44.4
La Ce	μg/g	79.9	55.8	55.7	40.2	90.8
Pr	μg/g μg/g	9.01	6.58	6.47	4.72	10.1
Nd	μg/g μg/g	33.0	25.2	24.1	17.9	36.5
Sm	μg/g μg/g	6.26	5.15	4.55	3.57	6.55
Eu	μg/g	1.34	1.16	0.98	0.81	1.36
Gd	μg/g	5.13	4.51	3.72	3.07	5.28
Tb	μg/g	0.78	0.69	0.56	0.47	0.78
Dy	μg/g	4.56	4.07	3.19	2.70	4.56
Но	μg/g	0.89	0.80	0.61	0.52	0.91
Er	μg/g	2.38	2.16	1.65	1.37	2.53
Tm	μg/g	0.33	0.30	0.24	0.18	0.36
Yb	μg/g	1.96	1.79	1.48	1.09	2.26
Lu	μg/g	0.25	0.22	0.21	0.14	0.29
Hf	μg/g	0.62	0.35	0.50	0.08	0.25
Ta	μg/g	0.93	0.38	0.71	0.83	1.44
Pb	μg/g	18.8	13.0	15.5	18.8	16.2
Th	μg/g	12.8	9.04	7.38	6.76	14.7
U	μg/g	2.35	1.63	1.39	1.28	2.01

TABLE B.5 Continued – River sand size fractions

			Clay Fraction	of River Sand	
Sample ID		RS04	RS06	RS08	RS09
Locality			Hooker Terminus	Sheil's Creek	Copland
Locality		Falls	HOOKET TEITIMUS	Shell's Creek	Copiana
Sampling Date		2009	2009	2009	2263608
Easting		2218613	2276200	2263063	5726340
Northing		5678977	5720205	5726991	11000
Lithology		Metasediment	Metasediment	Metasediment	Metasediment
Met. Grade		Chlorite GS	P-P	Biotite GS	Biotite GS
$\frac{\delta^7 \text{Li}}{\delta^7 \text{Li}}$	%	0.10	-0.46	-2.57	-1.88
δ^{26} Mg	‰	-0.07	-0.08	-0.15	nd
δ^{25} Mg	%	-0.07	-0.02	-0.07	nd
Na	μg/g	8380	11600	4930	42700
Mg	μg/g	15800	21000	8210	6300
Al	μg/g	95600	124000	41400	33900
P	μg/g	949	588	2130	98100
K	μg/g	44300	62400	14300	15100
Ca	μg/g	7900	11500	5200	3530
Ti	μg/g	5020	5140	6080	2770
Fe	µg/g	69100	72900	48200	26300
Li	μg/g	90.3	87.9	81.9	50.8
Sc	μg/g	11.6	15.9	17.6	9.27
\mathbf{v}	μg/g	168	168	194	101
Cr	μg/g	148	103	155	75.5
Co	μg/g	47.8	41.2	83.9	27.5
Ni	μg/g	87.4	52.7	133	51.1
Cu	μg/g	528	155	412	249
Z n	μg/g	257	256	230	145
Rb	μg/g	246	261	192	163
Sr	μg/g	125	276	194	108
Y	μg/g	16.5	24.7	21.0	11.6
Z r	μg/g	54.2	43.6	5.14	43.4
Nb	μg/g	11.1	13.3	18.3	7.79
Mo	μg/g	3240	737	3340	2350
Sn	μg/g	27.3	5.61	11.4	9.13
Cs	μg/g	16.4	17.5	16.2	14.1
Ba	μg/g	1220	1420	1990	837
La	μg/g	15.0	21.7	20.0	14.9
Ce	μg/g	32.3	48.6	46.2	31.5
Pr	μg/g	3.83	5.63	5.17	3.69
Nd	μg/g	14.8	22.0	19.8	13.9
Sm	μg/g	3.04	4.64	4.01	2.71
Eu	μg/g	0.66	1.14	0.93	0.56
Gd Tb	μg/g	2.79	4.33 0.69	3.58 0.58	2.31 0.35
Dy	μg/g	0.45 2.77	4.28	0.58 3.49	2.05
Ho	μg/g μg/g	0.58	4.28 0.86	0.72	0.41
Er	µg∕g µg∕g	1.66	2.40	2.14	1.16
Tm	μg/g μg/g	0.25	0.34	0.34	0.18
Yb	μg/g μg/g	1.62	2.19	2.44	1.19
Lu	μg/g μg/g	0.22	0.30	0.36	0.18
Hf	μg/g μg/g	0.96	1.35	0.15	1.08
Ta	μg/g	0.54	1.13	1.39	0.61
Pb	μg/g	368	157	183	131
Th	μg/g	8.03	10.8	7.64	6.66
U	μg/g	1.60	2.25	1.65	2.80
	100	1.00		2.00	

TABLE B.6: Major and trace element concentrations of the riverine and spring water suspended load from rivers draining the Southern Alps. P-P = Prehnite Pumpellyite, P-Act = Prehnite-Actinolite, GS = Greenschist Facies, G-O Amph = garnet oligoclase Amphibolite Facies.

				Riverine		
Sample ID		NZ04	NZ07	NZ19	NZ20	NZ22
Locality		Thunder Creek	Mingha	Deception River	Trib Wanganui	Gaunt Creek
Locality		Thunder Creek	Miligia	Deception River	THE Wanganui	Gaulii Creek
Sampling Date		2009	2009	2011	2011	2011
Easting		2218613	2396030	2395905.7	2317320.9	2293366
Northing		5678977	5802900	5823070	5779321.1	5758836
Lithology		Metasediment	Metasediment	Metasediment	Metasediment	Metasediment
Met. Grade		Chlorite GS	Biotite GS	P-P	G-O Amph	G-O Amph
$\frac{\text{Niet. Grade}}{\delta^7 \text{Li}}$	% o	-0.50	0.67	-1.34	-2.48	-1.94
δ L1 δ ²⁶ Mg	%o	-0.30	nd	-0.22	-2.46 -0.11	-1.94 nd
δ^{10} Mg						
_	‰	-0.05	nd	-0.09	-0.06	nd
Na	μg/g	22100	5450	5640	7800	10100
Mg	μg/g	14400	4040	2740	4810	6900
Al	μg/g	97100	22100	22400	30700	52400
P	μg/g	617	301	161	374	511
K	μg/g	38800	9920	9820	11200	21000
Ca	μg/g	12700	5560	3610	5030	5380
Ti	μg/g	3390	981	764	1350	1760
Fe	µg/g	41100	9780	8380	14100	21000
Li	μg/g	51.1	12.6	12.8	18.1	29.4
Sc	μg/g	10.3	3.08	3.19	5.20	7.94
V	μg/g	108	28.7	26.9	44.0	71.6
Cr	μg/g	62.6	41.9	14.7	23.0	39.2
Co	μg/g	12.9	4.51	3.29	5.24	7.3
Ni	μg/g	22.9	9.65	6.05	9.85	15.3
Cu	μg/g	25.5	19.4	10.2	11.4	22.5
Zn	μg/g	117	64.1	111	43.6	76.1
Rb	μg/g	178	35.1	37.6	45.4	80.1
Sr	μg/g	270	76.9	62.5	89.7	114
Y	μg/g	15.0	4.86	5.39	7.91	10.9
Zr	μg/g	7.13	4.74	6.82	0.86	0.67
Nb	μg/g	6.37	2.36	2.44	3.53	5.80
Mo	μg/g	0.24	0.32	0.20	0.14	0.23
Sn	μg/g	2.93	1.47	1.12	1.38	2.63
Cs	μg/g	7.37	2.14	3.48	4.19	4.20
Ba	μg/g	940	184	157	210	454
La	μg/g	18.0	5.78	6.44	10.4	21.8
Ce	μg/g	39.6	12.2	13.6	21.4	46.7
Pr	μg/g	4.61	1.46	1.62	2.53	5.43
Nd	μg/g	17.2	5.54	6.25	9.45	20.2
Sm	μg/g	3.47	1.10	1.25	1.95	3.97
Eu	μg/g	0.75	0.23	0.26	0.41	0.78
Gd	μg/g	2.86	1.02	1.00	1.67	3.28
Tb	μg/g	0.44	0.15	0.16	0.26	0.48
Dy	μg/g	2.57	0.88	0.93	1.49	2.40
Но	μg/g	0.50	0.17	0.19	0.29	0.40
Er	μg/g	1.34	0.46	0.46	0.73	0.98
Tm	μg/g	0.19	0.06	0.07	0.10	0.13
Yb	μg/g	1.16	0.39	0.45	0.62	0.74
Lu	μg/g	0.15	0.05	0.06	0.08	0.09
Hf	μg/g	0.29	0.16	0.22	0.04	0.03
Ta	μg/g	0.23	0.14	0.10	0.00	0.41
Pb	μg/g	24.4	11.9	8.19	10.1	13.7
Th	μg/g	7.08	1.99	2.38	3.32	7.85
U	μg/g	1.22	0.36	0.51	0.73	1.44

TABLE B.6 Continued – Riverine and spring water suspended load

		Divonino		Cnuinca		
Cl- ID		Riverine NZ27	1107	Springs	11020	DIV. 1
Sample ID			HS7	HS9	HS30	BIV-1
Locality		Trib of Rakai				
		River	Deception	Amythest	Deception	Bivouac
Sampling Date		2011	2009	2009	2011	2011
Easting		2381992.3	2398075	2317214	2398075	2263683
Northing		5761868.5	5818850	5779300	5818850	5726351
Lithology		Metasediment	Metasediment	Metasediment	Metasediment	Metasediment
Met. Grade		P-P	P-P	G-O Amph	P-P	Biotite GS
δ^7 Li	% o	-1.88	4.42	-3.99	nd	-1.17
δ^{26} Mg	‰	-0.09	nd	nd	nd	nd
δ^{25} Mg	% o	-0.02	nd	nd	nd	nd
Na	μg/g	8350	23400	21100	9200	5370
Mg	μg/g	7550	3680	11500	3750	446
Al	μg/g	46100	30700	80200	33700	2450
P	μg/g	611	424	460	532	106
K	μg/g	16600	17200	30500	14500	1550
Ca	μg/g	12600	6590	7800	3650	2430
Ti	μg/g	2130	1330	2480	1300	68.2
Fe	μg/g	22000	11000	33000	12700	14000
Li	μg/g	28.7	119	56.7	56.9	25.5
Sc	μg/g	7.11	4.08	9.55	4.39	0.65
V	μg/g	60.1	33.2	87.4	36.6	5.96
Cr	μg/g	35.4	19.3	52.6	22.0	1.63
Co	μg/g	10.1	3.84	8.69	5.69	1.56
Ni	μg/g	13.5	11.6	18.4	8.56	1.24
Cu	μg/g	24.7	36.5	26.4	15.2	12.8
Zn	μg/g	101	129	82.0	65.7	17.1
Rb	μg/g	74.6	58.0	140	61.9	4.45
Sr	μg/g	145	108	221	91.0	53.6
Y Zr	μg/g	14.0 32.4	9.25 21.8	14.4 2.58	9.70 20.5	11.2 0.41
Nb	μg/g	5.89	3.86	6.81	4.28	0.41
Mo	μg/g	0.52	0.29	0.25	0.41	0.13
Sn	µg∕g µg∕g	1.99	2.25	2.40	1.93	1.55
Cs	μg/g	8.65	10.5	29.9	11.1	3.18
Ba	μg/g	325	239	684	246	40.9
La	μg/g	17.5	12.6	17.7	13.0	2.10
Ce	μg/g	36.5	26.4	37.7	27.6	4.43
Pr	μg/g	4.29	3.11	4.45	3.16	0.57
Nd	μg/g	16.1	11.4	16.7	11.6	2.35
Sm	μg/g	3.21	2.16	3.38	2.27	0.59
Eu	μg/g	0.66	0.43	0.74	0.44	0.19
Gd	μg/g	2.69	1.79	2.89	1.88	0.82
Tb	μg/g	0.41	0.28	0.43	0.28	0.17
Dy	μg/g	2.40	1.64	2.55	1.63	1.24
Но	μg/g	0.47	0.31	0.50	0.33	0.30
Er	μg/g	1.31	0.84	1.33	0.92	1.02
Tm	μg/g	0.19	0.12	0.19	0.14	0.17
Yb	μg/g	1.26	0.80	1.16	0.90	1.16
Lu	μg/g	0.19	0.11	0.15	0.13	0.17
Hf	μg/g	1.00	0.65	0.12	0.65	0.01
Ta	μg/g	0.48	0.01	0.48	0.00	0.00
Pb	μg/g	24.3	11.6	22.4	16.3	2.70
Th	μg/g	6.28	3.86	6.66	4.55	0.15
U	μg/g	2.30	0.85	1.30	1.01	0.06

TABLE B.6 Continued – Riverine and spring water suspended load

		I		Contract		
Commis ID		11022	11024	Springs	11040	110 41
Sample ID		HS33	HS34	HS36	HS40	HS41
Locality						
		Mungo	Wren Creek	Smythe	Amythest	Fox
Sampling Date		2011	2011	2011	2011	2011
Easting		2362267	2359051	2335054	2317210	2268935
Northing		5795650	5803087	5775404	5779292	5742959
Lithology		Metasediment	Metasediment	Metasediment	Metasediment	Metasediment
Met. Grade		P-Act	Biotite GS	Chlorite GS	G-O Amph	G-O Amph
δ^7 Li	‰	4.18	nd	4.11	-0.07	-3.72
δ^{26} Mg	‰	nd	nd	nd	nd	nd
δ^{25} Mg	‰	nd	nd	nd	nd	nd
Na	μg/g	4490	5450	7200	28400	55400
Mg	μg/g	817	356	1530	8450	29600
Al	μg/g	4660	807	10300	63000	138000
P	μg/g	648	1240	345	762	1850
K	μg/g	3420	1560	4940	21500	69400
Ca	μg/g	0.00	0.00	1610	8990	27200
Ti	μg/g	178	33.2	405	2100	8150
Fe	μg/g	1900	408	4750	26200	124000
	100					
Li	μg/g	22.9	25.5	26.3	70.5	189
Sc	μg/g	0.57	0.18	1.36	7.76	24.8
\mathbf{V}	μg/g	6.74	1.37	9.57	63.7	241
Cr	μg/g	4.39	1.09	7.54	37.2	143
Co	μg/g	2.10	0.49	2.95	8.65	26.9
Ni	μg/g	8.40	0.50	4.02	19.3	54.3
Cu	μg/g	6.87	12.2	18.9	59.1	72.4
Zn	μg/g	15.8	25.0	37.4	80.5	252
Rb	μg/g	9.13	4.11	17.5	88.4	314
Sr	μg/g	27.2	10.1	76.3	234	442
Y	μg/g	0.90	0.23	2.83	16.4	71.8
Zr	μg/g	0.46	0.20	0.68	2.95	3.48
Nb	μg/g	0.49	0.12	1.10	6.30	22.4
Mo	μg/g	0.46	0.33	0.40	0.25	0.72
Sn	μg/g	0.42	0.71	0.72	2.08	105
Cs	μg/g	2.12	4.02	2.20	16.3	81.1
Ba	μg/g	32.4	5.63	76.8	394	1304
La	μg/g	0.90	0.26	3.59	19.8	38.0
Ce	μg/g	1.86	0.50	7.06	40.9	81.3
Pr	μg/g	0.23	0.05	0.81	4.93	9.83
Nd	μg/g	0.84	0.18	2.94	18.6	37.4
Sm	μg/g	0.16	0.01	0.53	3.68	7.81
Eu Gd	μg/g	0.03 0.14	0.00 0.01	0.12	0.77 3.11	1.87
Tb	μg/g	0.14	0.00	0.46 0.07	0.48	7.58 1.29
Dy	µg∕g µg∕g	0.03	0.04	0.45	2.77	8.59
Ho	μg/g μg/g	0.17	0.01	0.43	0.54	2.02
Er	μg/g μg/g	0.09	0.03	0.05	1.47	6.78
Tm	μg/g μg/g	0.09	0.00	0.23	0.22	1.16
Yb	μg/g μg/g	0.01	0.00	0.03	1.40	8.38
Lu	μg/g μg/g	0.07	0.00	0.23	0.19	1.42
Hf	μg/g μg/g	0.01	0.01	0.03	0.15	0.14
Ta	μg/g	0.03	0.00	0.04	0.29	1.70
Pb	μg/g	6.25	1.77	7.71	43.9	35.8
Th	μg/g μg/g	0.32	0.07	0.82	6.26	14.1
U	μg/g μg/g	0.09	0.03	0.17	1.30	2.74
	ME/ E	0.07	0.05	0.17	1.50	۷./+

TABLE B.6 Continued – Riverine and spring water suspended load

Sample ID Locality			Springs	Hvn	eralkaline Spri	ings
New Network Plat 2011 20	Sample ID				_	_
Sampling Date 2011 2018726 2508726	_		VV1 2	C52	CSO	ICID-1
Sampling Date 2011 2011 2011 2011 2011 2011 2020 2508726 2508768 25087698 2508726 2508726 25087698 2508726 250872	Locality		XX 1	C 1 .	C 1.	D. 1111
Easting 2263645 5726380 5147430 2508726 5726380 Metasediment Peridotite Perido	G P D					
Northing S726380 S657698 S657698 S943895 Lithology Metasediment Biotite GS P-Act P-Act P-Pact Flat Solution P-Act P-Act P-Pact Flat Solution P-Act P-Act P-Pact Flat Solution P-Act P-Pact Flat Solution P-Act P-Pact Flat Solution P-Act P-Pact Flat Solution P-Act P-Pact Flat P-Pact						
Metasediment Peridotite	_					
Met. Grade Bioine GS P-Act P-Act P-P δ²Li % 0.35 nd nd nd nd δ²Mg % nd nd nd nd nd nd δ²Mg % nd nd <t< th=""><th></th><th></th><th></th><th></th><th></th><th></th></t<>						
δ*Isi ‰ 0.35 nd <						
8 ²⁶ Mg % nd nd <th< th=""><th></th><th></th><th></th><th>P-Act</th><th>P-Act</th><th>P-P</th></th<>				P-Act	P-Act	P-P
8 ²⁵ Mg % nd nd <th< th=""><th></th><th>‰</th><th>0.35</th><th>nd</th><th>nd</th><th>nd</th></th<>		‰	0.35	nd	nd	nd
Na	δ^{26} Mg	‰	nd	nd	nd	nd
Mg	δ^{25} Mg	% o	nd	nd	nd	nd
Al	Na	μg/g	37800	1800	1580	154
P	Mg	μg/g	1370	4510	1710	149000
P μg/g 1020 51.1 64.4 40.7 K μg/g 54200 1030 477 119 Ca μg/g 37100 3620 1180 129000 Ti μg/g 144 46.7 60.1 51.7 Fe μg/g 161 1.54 1.24 1.87 Sc μg/g 1.83 0.47 0.32 2.16 V μg/g 7.76 1.55 1.96 4.98 Cr μg/g 2.52 3.30 1.11 9.58 Ni μg/g 1.68 844 91.1 97.2 Cu μg/g 2.31 22.6 23.9 13.9 Rb μg/g 2.31 22.6 23.9 13.9 Rb μg/g 29.2 1.03 1.08 0.59 Sr μg/g 29.2 1.03 1.08 0.59 Sr μg/g 783 3.81 3.1	Al	μg/g	4260	657	542	1220
K μg/g 54200 1030 477 119 Ca μg/g 37100 3620 1180 129000 Ti μg/g 144 46.7 60.1 51.7 Fe μg/g 153000 2830 1080 33000 Li μg/g 161 1.54 1.24 1.87 Sc μg/g 1.83 0.47 0.32 2.16 V μg/g 7.76 1.55 1.96 4.98 Cr μg/g 3.74 20.2 6.43 128 Co μg/g 2.52 3.30 1.11 9.58 Ni μg/g 2.68 844 91.1 97.2 Cu μg/g 2.08 10.4 5.63 3.24 Zn μg/g 20.8 10.4 5.63 3.24 Zn μg/g 29.2 1.03 1.08 0.59 Sr μg/g 29.2 1.03	P		1020	51.1	64.4	40.7
Ca µg/g 37100 3620 1180 129000 Ti µg/g 144 46.7 60.1 51.7 Fe µg/g 153000 2830 1080 33000 Li µg/g 161 1.54 1.24 1.87 Sc µg/g 1.83 0.47 0.32 2.16 V µg/g 7.76 1.55 1.96 4.98 Cr µg/g 3.74 20.2 6.43 128 Co µg/g 2.52 3.30 1.11 9.58 Ni µg/g 2.52 3.30 1.11 9.58 Ni µg/g 2.52 3.30 1.11 9.58 Ni µg/g 2.31 22.6 23.9 13.9 Rb µg/g 23.1 22.6 23.9 13.9 Rb µg/g 23.1 22.6 23.9 13.9 Rb µg/g 783 3.81 <t< th=""><th>K</th><th></th><th>54200</th><th>1030</th><th></th><th></th></t<>	K		54200	1030		
Ti μg/g 144 46.7 60.1 51.7 Fe μg/g 153000 2830 1080 33000 Li μg/g 161 1.54 1.24 1.87 Sc μg/g 1.83 0.47 0.32 2.16 V μg/g 7.76 1.55 1.96 4.98 Cr μg/g 3.74 20.2 6.43 128 Co μg/g 2.52 3.30 1.11 9.58 Ni μg/g 1.68 844 91.1 97.2 Cu μg/g 2.08 10.4 5.63 3.24 Zn μg/g 23.1 22.6 23.9 13.9 Rb μg/g 29.2 1.03 1.08 0.59 Sr μg/g 783 3.81 3.14 15.3 Y μg/g 64.6 0.33 0.33 0.28 Zr μg/g 0.40 3.25 1.2						
Te						
Sc μg/g 1.83 0.47 0.32 2.16 V μg/g 7.76 1.55 1.96 4.98 Cr μg/g 3.74 20.2 6.43 128 Co μg/g 2.52 3.30 1.11 9.58 Ni μg/g 2.52 3.30 1.11 9.58 Ni μg/g 2.08 10.4 5.63 3.24 Zn μg/g 23.1 22.6 23.9 13.9 Rb μg/g 29.2 1.03 1.08 0.59 Sr μg/g 29.2 1.03 1.08 0.59 Sr μg/g 64.6 0.33 0.33 0.28 Zr μg/g 0.53 0.10 0.13 0.08 Nb μg/g 0.53 0.10 0.13 0.08 Nb μg/g 0.23 0.04 0.35 0.03 Nb μg/g 0.89 0.60 0						
Sc μg/g 1.83 0.47 0.32 2.16 V μg/g 7.76 1.55 1.96 4.98 Cr μg/g 3.74 20.2 6.43 128 Co μg/g 2.52 3.30 1.11 9.58 Ni μg/g 2.52 3.30 1.11 9.58 Ni μg/g 2.08 10.4 5.63 3.24 Zn μg/g 23.1 22.6 23.9 13.9 Rb μg/g 29.2 1.03 1.08 0.59 Sr μg/g 29.2 1.03 1.08 0.59 Sr μg/g 64.6 0.33 0.33 0.28 Zr μg/g 0.53 0.10 0.13 0.08 Nb μg/g 0.53 0.10 0.13 0.08 Nb μg/g 0.23 0.04 0.35 0.03 Nb μg/g 0.89 0.60 0	Ti	ug/g	161	1.54	1 24	1.87
V με/g 3.74 20.2 6.43 128 Co με/g 2.52 3.30 1.11 9.58 Ni με/g 1.68 844 91.1 97.2 Cu με/g 2.3.1 22.6 23.9 13.9 Rb με/g 29.2 1.03 1.08 0.59 Sr με/g 783 3.81 3.14 15.3 Y με/g 64.6 0.33 0.33 0.28 Y με/g 0.53 0.10 0.13 0.08 Mo με/g 0.53 0.10 0.13 0.08 Mo με/g 0.63 0.04 0.35 0.03 Sn με/g 31.1 0.09 0.11 0.07 Ba με/g 31.1 0.09 0.11 0.07 Ba με/g 673 4.53 4.62 3.45 La με/g 7.50 0.31 0.28 0.28 Ce με/g 15.4 0.56 0.57 0.56 Pr με/g 9.57 0.27 0.24 0.26 Sm με/g 9.57 0.27 0.24 0.26 Sm με/g 0.93 0.00 0.00 0.00 Gd με/g 0.93 0.00 0.00 0.01 Gd με/g 0.93 0.00 0.00 0.01 Dy με/g 0.93 0.00 0.00 0.00 Fr με/g 0.93 0.00 0.00 0.00 Th με/g 0.92 0.00 0.00 0.00 0.00 Th με/g 0.92 0.00 0.00 0.00 0.00 Th με/g 0.92 0.00 0.00 0.00 0.00 Th με/g 0.89 0.00 0.00 0.00 0.00 Th με/g 0.92 0.00 0.00 0.00 0.00 Th με/g 0.93 0.00 0.00 0.00 0.00 Th με/g 0.93 0.00 0.00 0.00 0.00 Th με/g 0.93 0.00 0.00 0.00 0.00 Th με/g 0.92 0.00 0.00 0.00 0.00						
Cr με/g 3.74 20.2 6.43 128 Co με/g 2.52 3.30 1.11 9.58 Ni με/g 1.68 844 91.1 9.72 Cu με/g 20.8 10.4 5.63 3.24 Zn με/g 20.8 10.4 5.63 3.24 Zn με/g 29.2 1.03 1.08 0.59 Sr με/g 783 3.81 3.14 15.3 Y με/g 64.6 0.33 0.33 0.28 Xr με/g 0.40 3.25 1.21 0.89 Nb με/g 0.53 0.10 0.13 0.08 Mo με/g 0.53 0.10 0.13 0.08 Mo με/g 0.53 0.01 0.03 0.03 Sn με/g 0.89 0.60 0.44 0.15 Cs με/g 31.1 0.09 0.1						
Co μg/g 2.52 3.30 1.11 9.58 Ni μg/g 1.68 844 91.1 97.2 Cu μg/g 20.8 10.4 5.63 3.24 Zn μg/g 23.1 22.6 23.9 13.9 Rb μg/g 29.2 1.03 1.08 0.59 Sr μg/g 783 3.81 3.14 15.3 Y μg/g 64.6 0.33 0.33 0.28 Zr μg/g 0.40 3.25 1.21 0.89 Nb μg/g 0.53 0.10 0.13 0.08 Mo μg/g 0.53 0.10 0.13 0.08 Sn μg/g 0.53 0.10 0.13 0.08 Nb μg/g 0.53 0.10 0.13 0.08 Nb μg/g 0.53 0.04 0.35 0.03 La μg/g 0.89 0.60 0.						
Ni μg/g 1.68 844 91.1 97.2 Cu μg/g 20.8 10.4 5.63 3.24 Zn μg/g 23.1 22.6 23.9 13.9 Rb μg/g 29.2 1.03 1.08 0.59 Sr μg/g 783 3.81 3.14 15.3 Y μg/g 64.6 0.33 0.33 0.28 Zr μg/g 0.40 3.25 1.21 0.89 Nb μg/g 0.53 0.10 0.13 0.08 Mo μg/g 0.89 0.60 0.44 0.15 Cs μg/g 31.1 0.09 0.11 0.07 Ba μg/g 673 4.53 4.62 3.45 La μg/g 7.50 0.31 0.28 0.28 Ce μg/g 15.4 0.56 0.57 0.56 Pr μg/g 9.57 0.27 0.2						
Cu µg/g 20.8 10.4 5.63 3.24 Zn µg/g 23.1 22.6 23.9 13.9 Rb µg/g 29.2 1.03 1.08 0.59 Sr µg/g 783 3.81 3.14 15.3 Y µg/g 64.6 0.33 0.33 0.28 Zr µg/g 0.40 3.25 1.21 0.89 Nb µg/g 0.53 0.10 0.13 0.08 Mo µg/g 0.23 0.04 0.35 0.03 Sn µg/g 0.89 0.60 0.44 0.15 Cs µg/g 31.1 0.09 0.11 0.07 Ba µg/g 7.50 0.31 0.28 0.28 Ce µg/g 15.4 0.56 0.57 0.56 Pr µg/g 2.90 0.03 0.03 0.03 0.05 Eu µg/g 2.90 0.						
Zn µg/g 23.1 22.6 23.9 13.9 Rb µg/g 29.2 1.03 1.08 0.59 Sr µg/g 783 3.81 3.14 15.3 Y µg/g 64.6 0.33 0.33 0.28 Zr µg/g 0.40 3.25 1.21 0.89 Nb µg/g 0.53 0.10 0.13 0.08 Mo µg/g 0.23 0.04 0.35 0.03 Sn µg/g 0.89 0.60 0.44 0.15 Cs µg/g 31.1 0.09 0.11 0.07 Ba µg/g 673 4.53 4.62 3.45 La µg/g 7.50 0.31 0.28 0.28 Ce µg/g 15.4 0.56 0.57 0.56 Pr µg/g 2.11 0.06 0.07 0.07 Nd µg/g 9.57 0.27 0.2						
Rb μg/g 29.2 1.03 1.08 0.59 Sr μg/g 783 3.81 3.14 15.3 Y μg/g 64.6 0.33 0.33 0.28 Zr μg/g 0.40 3.25 1.21 0.89 Nb μg/g 0.53 0.10 0.13 0.08 Mo μg/g 0.23 0.04 0.35 0.03 Sn μg/g 0.89 0.60 0.44 0.15 Cs μg/g 31.1 0.09 0.11 0.07 Ba μg/g 673 4.53 4.62 3.45 La μg/g 7.50 0.31 0.28 0.28 Ce μg/g 15.4 0.56 0.57 0.56 Pr μg/g 2.57 0.27 0.24 0.26 Sm μg/g 2.95 0.03 0.03 0.05 Eu μg/g 4.76 0.03 0.						
Sr μg/g 783 3.81 3.14 15.3 Y μg/g 64.6 0.33 0.33 0.28 Zr μg/g 0.40 3.25 1.21 0.89 Nb μg/g 0.53 0.10 0.13 0.08 Mo μg/g 0.23 0.04 0.35 0.03 Sn μg/g 0.89 0.60 0.44 0.15 Cs μg/g 31.1 0.09 0.11 0.07 Ba μg/g 673 4.53 4.62 3.45 La μg/g 7.50 0.31 0.28 0.28 Ce μg/g 15.4 0.56 0.57 0.56 Pr μg/g 2.51 0.06 0.07 0.07 Nd μg/g 9.57 0.27 0.24 0.26 Sm μg/g 2.90 0.03 0.03 0.05 Eu μg/g 0.93 0.00 0.						
Y μg/g 64.6 0.33 0.33 0.28 Zr μg/g 0.40 3.25 1.21 0.89 Nb μg/g 0.53 0.10 0.13 0.08 Mo μg/g 0.23 0.04 0.35 0.03 Sn μg/g 0.89 0.60 0.44 0.15 Cs μg/g 31.1 0.09 0.11 0.07 Ba μg/g 673 4.53 4.62 3.45 La μg/g 7.50 0.31 0.28 0.28 Ce μg/g 15.4 0.56 0.57 0.56 Pr μg/g 2.11 0.06 0.07 0.07 Nd μg/g 9.57 0.27 0.24 0.26 Sm μg/g 2.90 0.03 0.03 0.03 Eu μg/g 1.05 0.00 0.00 0.01 Gd μg/g 0.93 0.00 0						
Zr µg/g 0.40 3.25 1.21 0.89 Nb µg/g 0.53 0.10 0.13 0.08 Mo µg/g 0.23 0.04 0.35 0.03 Sn µg/g 0.89 0.60 0.44 0.15 Cs µg/g 31.1 0.09 0.11 0.07 Ba µg/g 673 4.53 4.62 3.45 La µg/g 673 4.53 4.62 3.45 La µg/g 7.50 0.31 0.28 0.28 Ce µg/g 15.4 0.56 0.57 0.56 Pr µg/g 9.57 0.27 0.24 0.26 Sm µg/g 9.57 0.27 0.24 0.26 Sm µg/g 1.05 0.00 0.00 0.01 Gd µg/g 4.76 0.03 0.03 0.05 Tb µg/g 0.93 0.00 0.						
Nb μg/g 0.53 0.10 0.13 0.08 Mo μg/g 0.23 0.04 0.35 0.03 Sn μg/g 0.89 0.60 0.44 0.15 Cs μg/g 31.1 0.09 0.11 0.07 Ba μg/g 673 4.53 4.62 3.45 La μg/g 7.50 0.31 0.28 0.28 Ce μg/g 15.4 0.56 0.57 0.56 Pr μg/g 2.11 0.06 0.07 0.07 Nd μg/g 9.57 0.27 0.24 0.26 Sm μg/g 2.90 0.03 0.03 0.05 Eu μg/g 1.05 0.00 0.00 0.01 Gd μg/g 4.76 0.03 0.03 0.05 Tb μg/g 0.93 0.00 0.00 0.01 Dy μg/g 5.79 0.03						
Mo μg/g 0.23 0.04 0.35 0.03 Sn μg/g 0.89 0.60 0.44 0.15 Cs μg/g 31.1 0.09 0.11 0.07 Ba μg/g 673 4.53 4.62 3.45 La μg/g 7.50 0.31 0.28 0.28 Ce μg/g 15.4 0.56 0.57 0.56 Pr μg/g 2.11 0.06 0.07 0.07 Nd μg/g 9.57 0.27 0.24 0.26 Sm μg/g 9.57 0.27 0.24 0.26 Sm μg/g 2.90 0.03 0.03 0.03 0.05 Eu μg/g 1.05 0.00 0.00 0.01 0.01 Gd μg/g 4.76 0.03 0.03 0.03 0.05 Tb μg/g 0.93 0.00 0.00 0.01 0.01 <t< th=""><th></th><th></th><th></th><th></th><th></th><th></th></t<>						
Sn µg/g 0.89 0.60 0.44 0.15 Cs µg/g 31.1 0.09 0.11 0.07 Ba µg/g 673 4.53 4.62 3.45 La µg/g 7.50 0.31 0.28 0.28 Ce µg/g 15.4 0.56 0.57 0.56 Pr µg/g 2.11 0.06 0.07 0.07 Nd µg/g 9.57 0.27 0.24 0.26 Sm µg/g 9.57 0.27 0.24 0.26 Sm µg/g 2.90 0.03 0.03 0.03 0.05 Eu µg/g 1.05 0.00 0.00 0.01 0.01 Gd µg/g 4.76 0.03 0.03 0.03 0.05 Tb µg/g 0.93 0.00 0.00 0.01 0.01 Dy µg/g 7.24 0.05 0.06 0.04 <t< th=""><th></th><th></th><th></th><th></th><th></th><th></th></t<>						
Cs μg/g 31.1 0.09 0.11 0.07 Ba μg/g 673 4.53 4.62 3.45 La μg/g 7.50 0.31 0.28 0.28 Ce μg/g 15.4 0.56 0.57 0.56 Pr μg/g 2.11 0.06 0.07 0.07 Nd μg/g 9.57 0.27 0.24 0.26 Sm μg/g 0.03 0.03 0.03 0.05 Eu μg/g 1.05 0.00 0.00 0.00 0.01 Gd μg/g 0.93 0.00 0.00 0.00 0.01 Dy μg/g 7.24 0.05 0.06 0.04 Ho μg/g						
Ba μg/g 673 4.53 4.62 3.45 La μg/g 7.50 0.31 0.28 0.28 Ce μg/g 15.4 0.56 0.57 0.56 Pr μg/g 2.11 0.06 0.07 0.07 Nd μg/g 2.11 0.06 0.07 0.07 Nd μg/g 9.57 0.27 0.24 0.26 Sm μg/g 9.57 0.27 0.24 0.26 Sm μg/g 2.90 0.03 0.03 0.05 Eu μg/g 1.05 0.00 0.00 0.01 Gd μg/g 4.76 0.03 0.03 0.05 Tb μg/g 0.93 0.00 0.00 0.01 Dy μg/g 7.24 0.05 0.06 0.04 Ho μg/g 5.79 0.03 0.03 0.03 Tm μg/g 0.24 0.00						
La μg/g 7.50 0.31 0.28 0.28 Ce μg/g 15.4 0.56 0.57 0.56 Pr μg/g 2.11 0.06 0.07 0.07 Nd μg/g 9.57 0.27 0.24 0.26 Sm μg/g 2.90 0.03 0.03 0.03 0.05 Eu μg/g 1.05 0.00 0.00 0.01 0.01 Gd μg/g 4.76 0.03 0.03 0.03 0.05 Tb μg/g 0.93 0.00 0.00 0.01 0.01 Dy μg/g 7.24 0.05 0.06 0.04 0.01 Ho μg/g 5.79 0.03 0.03 0.03 0.03 Tm μg/g 0.92 0.00 0.00 0.00 0.00 Yb μg/g 0.89 0.00 0.00 0.00 Hf μg/g 0.01 0.01						
$ \begin{array}{cccccccccccccccccccccccccccccccccccc$						
Pr μg/g 2.11 0.06 0.07 0.07 Nd μg/g 9.57 0.27 0.24 0.26 Sm μg/g 2.90 0.03 0.03 0.05 Eu μg/g 1.05 0.00 0.00 0.01 Gd μg/g 4.76 0.03 0.03 0.05 Tb μg/g 0.93 0.00 0.00 0.01 Dy μg/g 7.24 0.05 0.06 0.04 Ho μg/g 1.78 0.01 0.01 0.01 Er μg/g 5.79 0.03 0.03 0.03 Tm μg/g 0.92 0.00 0.00 0.00 Yb μg/g 0.89 0.00 0.00 0.00 Hf μg/g 0.03 0.03 0.03 0.03 Ta μg/g 0.01 0.01 0.04 0.00 Pb μg/g 0.49 0.09 <th< th=""><th></th><th></th><th></th><th></th><th></th><th></th></th<>						
$\begin{array}{c ccccccccccccccccccccccccccccccccccc$						
$\begin{array}{c ccccccccccccccccccccccccccccccccccc$						
$ \begin{array}{c ccccccccccccccccccccccccccccccccccc$						
$ \begin{array}{cccccccccccccccccccccccccccccccccccc$						
$ \begin{array}{c ccccccccccccccccccccccccccccccccccc$						
$\begin{array}{c ccccccccccccccccccccccccccccccccccc$						
Ho μg/g 1.78 0.01 0.01 0.01 Er μg/g 5.79 0.03 0.03 0.03 Tm μg/g 0.92 0.00 0.00 0.00 Yb μg/g 6.24 0.03 0.03 0.03 Lu μg/g 0.89 0.00 0.00 0.00 Hf μg/g 0.03 0.06 0.03 0.03 Ta μg/g 0.01 0.01 0.04 0.00 Pb μg/g 3.36 17.4 2.13 1.14 Th μg/g 0.49 0.09 0.06 0.08						
$\begin{array}{c ccccccccccccccccccccccccccccccccccc$	-					
$\begin{array}{c ccccccccccccccccccccccccccccccccccc$						
$ \begin{array}{c ccccccccccccccccccccccccccccccccccc$						
$ \begin{array}{c ccccccccccccccccccccccccccccccccccc$						
$ \begin{array}{c ccccccccccccccccccccccccccccccccccc$						
$ \begin{array}{c ccccccccccccccccccccccccccccccccccc$						
Pb μg/g 3.36 17.4 2.13 1.14 Th μg/g 0.49 0.09 0.06 0.08		μg/g				
Th $\mu g/g$ 0.49 0.09 0.06 0.08	Ta	μg/g	0.01	0.01	0.04	0.00
Th μg/g 0.49 0.09 0.06 0.08		μg/g			2.13	
	Th		0.49	0.09	0.06	0.08
	U		0.09	0.01	0.01	0.02

TABLE B.7: Major element concentrations of the bedrock, mica mineral separates, river sand size fractions, riverine suspended sediments and spring suspended sediments from the Southern Alps in Wt. %. Major element data for the bedrock from Pitcairn (2004). P-P = Prehnite Pumpellyite, P-Act = Prehnite-Actinolite, GS = Greenschist Facies, G-O Amph = garnet oligoclase Amphibolite Facies, GW = greywacke, psam = Psammite, pel = pelite, QFS = quartzofeldspathic, MB = metabasalts.

Major Elements (Wt. %)

Sample	Location	Lithology	Met. Grade	TiO ₂	Al ₂ O ₃	Fe_2O_3	MgO	CaO	Na ₂ O	K ₂ O	P ₂ O ₅	CIA
Bedrock												
C47	Porters Pass	Greywacke	None	0.58	15.3	4.65	1.50	1.58	3.83	2.83	0.13	65.0
A63	Hawea	Psammite	P-P	0.72	14.5	4.72	1.10	1.73	3.98	2.10	0.11	65.0
A4	Rongahere	Pelite	Lower GS	0.62	14.6	4.35	1.29	1.79	4.37	2.62	0.09	62.4
A89	Hawea	QFS	Chlorite GS	0.79	15.0	6.24	2.61	3.00	3.46	2.31	0.16	63.2
B92	Glenorchy	Metabasalt	Chlorite GS	0.92	20.1	7.27	2.29	2.75	3.02	3.29	0.17	6.89
B64	Remarks	Metabasalt	Chlorite GS	0.70	13.8	5.64	1.97	2.57	3.62	1.83	0.20	63.3
A18	Nevis Bluff	Pelite	P-P	2.95	10.7	10.8	6.85	6.57	2.20	1.66	0.65	50.7
A22	Nevis Bluff	Pelite	Lower GS	3.78	13.7	15.3	8.64	7.11	0.41	1.45	0.61	60.4
B30	Hawea	Psammite	Lower GS	0.61	16.0	4.41	1.29	1.56	3.78	3.05	0.11	9.59
C72	Pleas ant Flat	QFS	Chlorite GS	0.56	14.7	4.39	1.06	1.32	5.84	1.11	0.09	64.1
C70	Haast	QFS	Chlorite GS	0.63	15.9	3.51	98.0	0.51	4.95	2.76	0.08	6.59
C66	Haast	QFS	Biotite GS	1.11	23.6	7.15	2.40	1.01	3.09	5.94	0.22	70.1
C68	Haast	QFS	Biotite GS	0.40	12.0	4.02	0.88	1.91	5.18	1.61	0.13	58.0
C54	Haast	QFS	Garnet GS	0.83	18.6	5.73	1.66	2.52	5.06	2.97	0.12	63.8
C61	Haast	QFS	Garnet GS	1.33	18.1	8.45	2.95	2.74	3.98	2.67	0.27	8.59
C56	Haast	QFS	G-O Amph	09.0	16.7	4.41	1.38	1.85	4.29	2.67	0.14	65.4
C59	Haast	QFS	G-O Amph	0.56	16.3	3.94	1.38	1.79	3.76	3.46	0.13	64.3
Mica Mineral Separates	eparates											
C50 (biotite)	Haast	QFS	Garnet GS	1.46	40.4	47.3	9.41	0.17	0.44	20.8	0.05	65.3
C56 (biotite)	Haast	QFS	G-O Amph	1.95	37.2	47.3	9.05	0.01	0.24	21.4	0.00	63.2
C58 (biotite)	Haast	Metabasalt	G-O Amph	1.82	40.1	45.8	11.5	0.74	0.44	21.5	0.05	63.8
C66 (chlorite)	Haast	QFS	Biotite GS	0.17	45.1	62.5	87.6	0.19	0.54	2.91	0.03	92.5
C77 (musc.)	Haast	QFS	Garnet GS	0.83	53.8	69.6	1.88	0.51	1.78	20.0	0.04	70.7
C77 (biotite)	Haast	QFS	Garnet GS	2.54	37.3	43.3	7.60	0.37	0.87	20.3	0.04	63.4

TABLE B.7 Continued – Solid phase major element concentrations in Wt. %

							Major Elements	nts (Wt. %)				
Sample	Location	Lithology	Met. Grade	$\mathrm{Ti}\mathrm{O}_2$	Al_2O_3	$\mathrm{Fe_2O_3}$	MgO	CaO	Na ₂ O	K ₂ O	P ₂ O ₅	CIA
Bulk River Sand	d											
RS04	Thunder Creek	Metasediment	Chlorite GS	0.56	26.6	10.5	1.44	1.55	6.19	4.64	0.26	68.2
RS05	Chinaman's Bluff	Metasediment	P-P	0.75	33.0	12.5	1.59	3.35	9.40	3.36	0.75	67.2
RS06	Hooker Glacier	Metasediment	P-P	0.66	29.7	10.5	1.64	2.28	6.27	6.21	0.34	66.8
RS08	Sheil's Creek	Metasediment	Biotite GS	0.84	30.3	12.5	1.73	2.12	6.46	5.32	0.33	68.6
RS09	Copland	Metasediment	Biotite GS	0.93	28.5	12.0	1.75	2.00	4.91	6.26	0.35	68.4
Fine River Sand	l											
RS04	Thunder Creek	Metasediment	Chlorite GS	0.73	30.5	12.1	1.59	2.22	6.71	5.55	0.28	67.8
RS05	Chinaman's Bluff	Metasediment	P-P	0.66	34.7	13.0	1.77	2.31	10.2	3.99	0.46	67.8
RS06	Hooker Glacier	Metasediment	P-P	0.56	23.7	7.80	1.26	1.74	5.62	4.74	0.25	66.2
RS08	Sheil's Creek	Metasediment	Biotite GS	0.78	26.2	14.9	2.06	1.73	5.21	4.53	0.20	69.5
RS09	Copland	Metasediment	Biotite GS	1.31	24.3	11.6	1.38	2.20	5.00	4.35	0.29	67.8
Clay Fraction of River Sand	f River Sand											
RS04	Thunder Creek	Metasediment	Chlorite GS	0.84	36.1	19.8	2.62	1.11	2.26	10.7	0.44	72.0
RS06	Hooker Glacier	Metasediment	P-P	0.86	46.8	20.8	3.48	1.60	3.13	15.0	0.27	70.3
RS08	Sheil's Creek	Metasediment	Biotite GS	1.01	15.7	13.8	1.36	0.73	1.33	3.45	0.98	74.0
RS09	Copland	Metasediment	Biotite GS	0.46	12.8	7.52	1.05	0.49	11.5	3.65	45.0	45.0
Riverine Suspended Load	nded Load											
NZ04	Thunder Creek	Metasediment	Chlorite GS	0.56	36.7	11.8	2.39	1.78	5.95	9.35	0.28	68.2
NZ07	Mingha	Metasediment	Biotite GS	0.16	8.35	2.80	0.67	0.78	1.47	2.39	0.14	64.3
NZ19	Deception	Metasediment	P-P	0.13	8.46	2.39	0.45	0.50	1.52	2.37	0.07	65.8
NZ20	Wanganui	Metasediment	G-O Amph	0.22	11.6	4.03	0.80	0.70	2.10	2.70	0.17	67.8
NZ22	Gaunt Creek	Metasediment	G-O Amph	0.29	19.8	6.00	1.14	0.75	2.71	5.06	0.23	69.9
NZ27	Rakaia	Metasediment	P-P	0.35	17.4	6.30	1.25	1.77	2.25	4.00	0.28	68.5

TABLE B.7 Continued – Solid phase major element concentrations in Wt. %

Major Elements (Wt. %)

Sample	Location	Lithology	Met. Grade	TiO_2	Al ₂ O ₃	Fe ₂ O ₃	MgO	CaO	Na ₂ O	K2O	P_2O_5	CIA
Spring Suspended Load	ed Load											
HS7	Deception	Metasediment	P-P	0.22	11.6	3.14	0.61	0.92	6.30	4.14	0.19	50.5
HS9	Amythest	Metasediment	G-O Amph	0.41	30.3	9.44	1.90	1.09	5.69	7.34	0.21	68.2
HS30	Deception	Metasediment	P-P	0.22	12.7	3.64	0.62	0.51	2.48	3.49	0.24	66.3
HS33	Mungo	Metasediment	P-Act	0.03	1.76	0.54	0.14	0.00	1.21	0.82	0.30	46.4
HS34	Wren Creek	Metasediment	Biotite GS	0.01	0.30	0.12	90:0	0.00	1.47	0.38	0.57	14.2
HS 36	Smythe	Metasediment	Chlorite GS	0.07	3.91	1.36	0.25	0.23	1.94	1.19	0.16	53.8
HS 40	Amythest	Metasediment	G-O Amph	0.35	23.8	7.48	1.40	1.26	7.65	5.17	0.35	62.8
HS41	Fox	Metasediment	G-O Amph	1.36	52.3	35.5	4.92	3.80	14.9	16.7	0.85	59.6
BIV-1	Bivouac	Metasediment	Biotite GS	0.01	0.93	4.01	0.07	0.34	1.45	0.37	0.05	30.0
WF2	Welcome Flat	Metasediment	Biotite GS	0.02	1.61	43.7	0.23	5.20	10.2	1.30	0.47	8.8
CS2	Cascade	Peridotite	P-Act	0.01	0.25	0.81	0.75	0.51	0.49	0.25	0.02	16.7
CS6	Cascade	Peridotite	P-Act	0.01	0.20	0.31	0.28	0.17	0.42	0.12	0.03	22.5
RHS-1	Red Hills	Peridotite	P-P	0.01	0.46	9.42	24.7	18.0	0.04	0.03	0.02	2.5

Appendix C

Electronic Data Tables

This is an electronic appendix containing EXCEL spreadsheets of geochemical data presented in this thesis.

- Acimovic, Z., Pavlovic, L., Trumbulovic, L., Andric, L. & Stamatovic, M. 2003. Synthesis and characterization of the cordierite ceramics from nonstandard raw materials for application in foundry. Materials Letters, 57, 2651-2656.
- Adams, C. J., Bishop, D. G. & Gabites, J. E. 1985. Potassium-argon age studies of a low-grade, progressively metamorphosed greywacke sequence, Dansey Pass, South Island, New Zealand. Journal of the Geological Society, 142, 339-349.
- Adams, J. 1980. Contemporary uplift and erosion of the Southern Alps, New Zealand. Geological Society of America Bulletin, 91, 1-114.
- Ahn, J. H. & Peacor, D. R. 1987. Kaolinitization of biotite: TEM data and implications for an alteration mechanism. American Mineralogist, 72, 353-356.
- Albarède, F. & Beard, B. 2004. Analytical methods for non-traditional isotopes. Reviews in Mineralogy and Geochemistry, 55, 113-152.
- Albarède, F. & Michard, A. 1986. Transfer of continental Mg, S, O, and U to the mantle through hydrothermal alteration of the oceanic crust. Chemical Geology, 57, 1-15.
- Allen, S. K., Cox, S. C. & Owens, I. F. 2011. Rock avalanches and other landslides in the central Southern Alps of New Zealand: a regional study considering possible climate change impacts. Landslides, 8, 33-48.
- Allis, R. G. & Shi, Y. 1995. New insights to temperature and pressure beneath the central Southern Alps, New Zealand. New Zealand Journal of Geology and Geophysics, 38, 585-592.

- Allis, R. G., Henley, R. W. & Carman, A. F. 1979. The thermal regime beneath the Southern Alps. In: Walcott, R. I., Cresswell, M. M. (eds). The Origin of the Southern Alps. Bulletin Royal Society of New Zealand, 18, 79-85.
- Alt, J. C. & Teagle, D. 1999. The uptake of carbon during alteration of ocean crust. Geochimica et Cosmochimica Acta, 63, 1527-1535.
- Amiotte-Suchet, P., Probst, J.-L. & Ludwig, W. 2003. Worldwide distribution of continental rock lithology: Implications for the atmospheric/soil CO₂ uptake by continental weathering and alkalinity river transport to the oceans. Global Biogeochemical Cycles, 17, 1-14.
- Anbeek, C. 1994. Comment on "Change in surface area and dissolution rates during hornblende dissolution at pH 4.0" by H. Zhang, P. R. Bloom, and E. A. Nater. Geochimica et Cosmochimica Acta, 58, 1849-1850.
- Anderson, J. M., Proctor, J. & Vallack, H. W. 1983. Ecological studies in four contrasting lowland rain forests in Gunung Mulu National Park, Sarawak. Journal of Ecology, 71, 503-527.
- Anderson, R. S. & Anderson, S. P. 2010. Geomorphology: The Mechanics and Chemistry of Landscapes. Cambridge University Press, Cambridge.
- Anderson, S. P., Drever, J. I. & Humphrey, N. F. 1997. Chemical weathering in glacial environments. Geology, 25, 399.
- Asmerom, Y., Jacobsen, S. B., Knoll, A. H., Butterfield, N. J. & Swett, K. 1991. Strontium isotopic variations of Neoproterozoic seawater: Implications for crustal evolution. Geochimica et Cosmochimica Acta, 55, 2883-2894.
- Atkinson, B. K. & Meredith, P. G. 1981. Stress corrosion cracking of quartz: a note on the influence of chemical environment. Tectonophysics, 77, T1-T11.
- Bach, W. & Humphris, S. E. 1999. Relationship between the Sr and O isotope compositions of hydrothermal fluids and the spreading and magma-supply rates at oceanic spreading centers. Geology, 27, 1067-1070.
- Bahr, D. B., Pfeffer, W. T., Sassolas, C. & Meier, M. F. 1998. Response time of glaciers as a function of size and mass balance: 1. Theory. Journal of Geophysical Research, 103, 9777-9782.
- Bailey, S. W. 1980. Structures of layer silicates. Crystal Structures of Clay Minerals and their X-ray Identification, 5, 1-123.
- Banfield, J. F. & Barker, W. W. 1994. Direct observation of reactant-product interfaces formed in natural weathering of exsolved, defective amphibole to smectite: Evidence for episodic,

- isovolumetric reactions involving structural inheritance. Geochimica et Cosmochimica Acta, 58, 1419-1429.
- Banfield, J. F., Barker, W. W., Welch, S. A. & Taunton, A. 1999. Biological impact on mineral dissolution: Application of the lichen model to understanding mineral weathering in the rhizosphere. Proceedings of the National Academy of Sciences, 96, 3404-3411.
- Banfield, J. F., Ferruzzi, G. G., Casey, W. H. & Westrich, H. R. 1995. HRTEM study comparing naturally and experimentally weathered pyroxenoids. Geochimica et Cosmochimica Acta, 59, 19-31.
- Banfield, J. F., Jones, B. F. & Veblen, D. R. 1991a. An AEM-TEM study of weathering and diagenesis, Abert Lake, Oregon: I. Weathering reactions in the volcanics. Geochimica et Cosmochimica Acta, 55, 2781-2793.
- Banfield, J. F., Jones, B. F. & Veblen, D. R. 1991b. An AEM-TEM study of weathering and diagenesis, Abert Lake, Oregon: II. Diagenetic modification of the sedimentary assemblage. Geochimica et Cosmochimica Acta, 55, 2795-2810.
- Barnes, I., Downes, C. J. & Hulston, J. R. 1978. Warm springs, South Island, New Zealand, and their potentials to yield laumontite. American Journal of Science, 278, 1412-1427.
- Barrell, D. J. A. 2011. Quaternary glaciers of New Zealand. Quaternary Science Reviews, 15, 1047-1064.
- Batt, G. E. & Braun, J. 1999. The tectonic evolution of the Southern Alps, New Zealand: insights from fully thermally coupled dynamical modelling. Geophysical Journal International, 136, 403-420.
- Batt, G. E., Baldwin, S. L., Cottam, M. A., Fitzgerald, P. G., Brandon, M. T. & Spell, T. L. 2004. Cenozoic plate boundary evolution in the South Island of New Zealand: New thermochronological constraints. Tectonics, 23, 1-17.
- Bayon, G., Vigier, N., Burton, K. W., Jean Carignan, A. B., Etoubleau, J. & Chu, N.-C. 2006. The control of weathering processes on riverine and seawater hafnium isotope ratios. Geology, 34, 433-436.
- Beaumont, C. P., Fullsack, P. & Hamilton, J. 1992. Erosional control of active compressional orogens. In: McClay, K. R. (eds). Thrust Tectonics. New York, Chapman and Hall, pp 1-18.
- Beavan, J., Moore, M., Pearson, C., Henderson, M., Parsons, B., Bourne, S., England, P., Walcott, D., Blick, G., Darby, D. & Hodgkinson, K. 1999. Crustal deformation during 1994–1998 due

- to oblique continental collision in the central Southern Alps, New Zealand, and implications for seismic potential of the Alpine fault. Journal of Geophysical Research, 104, 25233-25255.
- Berner, E. K. & Berner, R. A. 2012. Global Environment: Water, Air and Geochemical Cycles. Princeton University Press.
- Berner, E. K. & Berner, R. A. 1996. Global Environment. Prentice Hall, New York.
- Berner, R. A. & Kothavala, Z. 2001. GEOCARB III: A revised model of atmospheric CO₂ over Phanerozoic time. American Journal of Science, 301, 182-204.
- Berner, R. A. 2004. A model for calcium, magnesium and sulphate in seawater over Phanerozoic time. American Journal of Science, 304, 438-453.
- Berner, R., A., Lasaga, A., C. & Garrels, R., M. 1983. The carbonate-silicate geochemical cycle and its effects on atmospheric carbon dioxide over the past 100 million years. American Journal of Science, 283, 641-683.
- Berryman, K. R., Cochran, U. A., Clark, K. J., Biasi, G. P., Langridge, R. M. & Villamor, P. 2012b. Major earthquakes occur regularly on an isolated plate boundary fault. Science, 336, 1690-1693.
- Berryman, K., Cooper, A., Norris, R., Villamor, P., Sutherland, R., Wright, T., Schermer, E., Langridge, R. & Biasi, G. 2012a. Late Holocene rupture history of the Alpine Fault in South Westland, New Zealand. Bulletin of the Seismological Society of America, 102, 620-638.
- Bethke, C. M. 2002. The Geochemist's Workbench, Release 4.0, A User's Guide to Rxn, Act2, Tact, React, and GtPlot. University of Illinois, Urbana, IL.
- Bi, E. B., Vigier, N., Poszwa, A. & Brenot, A. 2007. Compared Mg isotope compositions of plants, rocks and waters. . Geochimica et Cosmochimica Acta, 71, A106.
- Bickle, M. J. 1996. Metamorphic decarbonation, silicate weathering and the long-term carbon cycle. Terra Nova, 8, 270-276.
- Bindeman, I. N., Davis, A. M. & Drake, M. J. 1998. Ion microprobe study of plagioclase-basalt partition experiments at natural concentration levels of trace elements. Geochimica et Cosmochimica Acta, 62, 1175-1193.
- Birsoy, R. 2002. Formation of sepiolite-palygorskite and related minerals from solution. Clays and Clay Minerals, 50, 736-745.

- Biscaye, P. E. 1965. Mineralogy and sedimentation of recent deep-sea clay in the Atlantic Ocean and adjacent seas and oceans. Geological Society of America Bulletin, 76, 803-831.
- Bishop, D. G. 1972. Progressive metamorphism from Prehnite-Pumpellyite to Greenschist Facies in the Dansey Pass area, Otago, New Zealand. Geological Society of America Bulletin, 83, 3177-3198.
- Bishop, D. G. 1985. Provisional terrane map of South Island, New Zealand.
- Black, J. R., Yin, Q.-Z. & Casey, W. H. 2006. An experimental study of magnesium-isotope fractionation in chlorophyll-a photosynthesis. Geochimica et Cosmochimica Acta, 70, 4072-4079.
- Blättler, C. L., Jenkyns, H. C., Reynard, L. M. & Henderson, G. M. 2011. Significant increases in global weathering during Oceanic Anoxic Events 1a and 2 indicated by calcium isotopes. Earth and Planetary Science Letters, 309, 77-88.
- Blum, A. E. & Stillings, L. L. 1995. Feldspar dissolution kinetics. Reviews in Mineralogy and Geochemistry, 31, 291-351.
- Bluth, G., J. S. & Kump, L., R. 1994. Lithological and climatological controls of river chemistry. Geochimica et Cosmochimica Acta, 58, 2341-2359.
- Bolou-Bi, E. B., Poszwa, A., Leyval, C. & Vigier, N. 2010. Experimental determination of magnesium isotope fractionation during higher plant growth. Geochimica et Cosmochimica Acta, 74, 2523-2537.
- Bolou-Bi, E. B., Vigier, N., Brenot, A. & Poszwa, A. 2009. Magnesium isotope compositions of natural reference materials. Geostandards and Geoanalytical Research, 33, 95-109.
- Boulton, C., Carpenter, B. M., Toy, V. & Marone, C. 2012. Physical properties of surface outcrop cataclastic fault rocks, Alpine Fault, New Zealand. Geochemistry Geophysics Geosystems, 13, 1-13.
- Bouman, C., Elliott, T. & Vroon, P. Z. 2004. Lithium inputs to subduction zones. Chemical Geology, 212, 59-79.
- Bourdon, B., Tipper, E. T., Fitoussi, C. & Stracke, A. 2010. Chondritic Mg isotope composition of the Earth. Geochimica et Cosmochimica Acta, 74, 5069-5083.
- Bragg, W. L. 1933. The Crystalline State. London, Bell.

- Brantley, S., L. & Chen, Y. 1995. Chemical weathering rates of pyroxenes and amphiboles. Reviews in Mineralogy and Geochemistry, 31, 119-172.
- Bray, A. M., Chan, L. H. & Von Damm, K. L. 2001. Constancy of the Li-isotopic signature in midocean ridge hydrothermal fluids: Evidence for equilibrium control. Eos Transcripts, American Geophysical Union.
- Brenan, J. M., Ryerson, F. J. & Shaw, H. F. 1998. The role of aqueous fluids in the slab-to-mantle transfer of boron, beryllium, and lithium during subduction: Experiments and models. Geochimica et Cosmochimica Acta, 62, 3337-3347.
- Brenot, A., Cloquet, C., Vigier, N., Carignan, J. & France-Lanord, C. 2008. Magnesium isotope systematics of the lithologically varied Moselle river basin, France. Geochimica et Cosmochimica Acta, 72, 5070-5089.
- Broecker, W. S. & Peng, T. H. 1982. Tracers in the Sea. Lamont-Doherty Geological Observatory, Palisades, New York.
- Brooker, R. A., James, R. H. & Blundy, J. D. 2004. Trace elements and Li isotope systematics in Zabargad peridotites: evidence of ancient subduction processes in the Red Sea mantle. Chemical Geology, 212, 179-204.
- Bryant, C. J., Mcculloch, M. T. & Bennett, V. C. 2003. Impact of matrix effects on the accurate measurement of Li isotope ratios by inductively coupled plasma mass spectrometry (MC-ICP-MS) under ?cold? plasma conditions. Journal of Analytical Atomic Spectrometry, 18, 734-737.
- Bull, W. B. & Brandon, M. T. 1998. Lichen dating of earthquake-generated regional rockfall events, Southern Alps, New Zealand. GSA Bulletin, 110, 60-84.
- Bull, W. B. & Cooper, A. F. 1986. Uplifted marine terraces along the Alpine Fault, New Zealand. Science, 234, 1225-1228.
- Campbell, J. R., Craw, D., Frew, R., Horton, T. & Chamberlain, C. P. 2004. Geochemical signature of orogenic hydrothermal activity in an active tectonic intersection zone, Alpine Fault, New Zealand. Mineralium Deposita, 39, 437-451.
- Canadell, J. G., Le Quere, C., Raupach, M. R., Field, C. B., Buitenhuis, E. T., Ciais, P., Conway, T. J., Gillett, N. P., Houghton, R. A. & Marland, G. 2007. Contributions to accelerating atmospheric CO₂ growth from economic activity, carbon intensity, and efficiency of natural sinks. Proceedings of the National Academy of Sciences, 104, 18866-18870.

- Cande, S. C. & Stock, J. M. 2004. Pacific-Antarctic-Australia motion and the formation of the Macquarie Plate. Geophysical Journal International, 157, 399-414.
- Carson, M. A. & Kirkby, M. J. 1972. Hillslope Form and Process. Cambridge University Press, Cambridge.
- Chakrabarti, R. & Jacobsen, S. B. 2009. A combined silicon and magnesium isotopic study of bulk meteorites and the Earth. In: 40th Lunar and Planetary Science Conference, 2089 (abstract).
- Chamberlain, C. P., Waldbauer, J. R. & Jacobson, A. D. 2005. Strontium, hydrothermal systems and steady-state chemical weathering in active mountain belts. Earth and Planetary Science Letters, 238, 351-366.
- Chamberlain, C. P., Poage, M. A., Craw, D. & Reynolds, R. C. 1999. Topographic development of the Southern Alps recorded by the isotopic composition of authigenic clay minerals, South Island, New Zealand. Chemical Geology, 155, 279-294.
- Chan, L. H. & Edmond, J. M. 1988. Variation of lithium isotope composition in the marine environment: A preliminary report. Geochimica et Cosmochimica Acta, 52, 1711-1717.
- Chan, L. H. & Frey, F. A. 2003. Lithium isotope geochemistry of the Hawaiian plume: results from the Hawaii Scientific Drilling Project and Koolau volcano. Geochemistry, Geophysics, Geosystems, 4, 1-20.
- Chan, L. H. & Kastner, M. 2000. Lithium isotopic compositions of pore fluids and sediments in the Costa Rica subduction zone: implications for fluid processes and sediment contribution to the arc volcanoes. Earth and Planetary Science Letters, 183, 275-290.
- Chan, L. H., Alt, J. C. & Teagle, D. a. H. 2002. Lithium and lithium isotope profiles through the upper oceanic crust: a study of seawater-basalt exchange at ODP Sites 504B and 896A. Earth and Planetary Science Letters, 201, 187-201.
- Chan, L. H., Edmond, J. M., Thompson, A. B. & Gillis, K. 1992. Lithium isotopic composition of submarine basalts: implications for the lithium cycle in the oceans. Earth and Planetary Science Letters, 108, 151-160.
- Chan, L. H., Gieskes, J. M., You, C. F. & Edmond, J. M. 1994. Lithium isotope geochemistry of sediments and hydrothermal fluids of the Guaymas Basin, Gulf of California. Geochimica et Cosmochimica Acta, 58, 4443-4454.

- Chan, L. H., Edmond, J. M. & Thompson, G. 1993. A lithium isotope study of hot springs and metabasalts from Mid-Ocean Ridge Hydrothermal Systems. Journal of Geophysical Research, 98, 9653-9659.
- Chan, L. H., Leeman, W. P. & Plank, T. 2006. Lithium isotopic composition of marine sediments. Geochemistry, Geophysics, Geosystems, 7, 1-25.
- Chang, H., An, Z., Wu, F., Jin, Z., Liu, W. & Song, Y. 2013. A Rb/Sr record of the weathering response to environmental changes in westerly winds across the Tarim Basin in the late Miocene to the early Pleistocene. Palaeogeography, Palaeoclimatology, Palaeoecology, 386, 364-373.
- Chang, V. T. C., Makishima, A., Belshaw, N. S. & O'nions, R. K. 2003. Purification of Mg from low-Mg biogenic carbonates for isotope ratio determination using multiple collector ICP-MS. Journal of Analytical Atomic Spectrometry, 18, 296-301.
- Chang, V. T. C., Williams, R. J. P., Makishima, A., Belshawl, N. S. & O'nions, R. K. 2004. Mg and Ca isotope fractionation during CaCO₃ biomineralisation. Biochemical and Biophysical Research Communications, 323, 79-85.
- Chen, J., Wang, F., Xia, X. & Zhang, L. 2002. Major element chemistry of the Changjiang (Yangtze River). Chemical Geology, 187, 231-255.
- Chen, T.-Y., Li, G., Frank, M. & Ling, H.-F. 2013. Hafnium isotope fractionation during continental weathering: Implications for the generation of the seawater Nd-Hf isotope relationships. Geophysical Research Letters, 40, 916-920.
- Chetelat, B., Liu, C. Q., Gaillardet, J., Wang, Q. L., Zhao, Z. Q., Liang, C. S. & Xiao, Y. K. 2009. Boron isotopes geochemistry of the Changjiang basin rivers. Geochimica et Cosmochimica Acta, 73, 6084-6097.
- Chinn, T. 1995. Glacier fluctuations in the Southern Alps of New Zealand determined from snowline elevations. Arctic and Alpine Research, 187-198.
- Chinn, T. 2001. Distribution of the glacial water resources of New Zealand. Journal of Hydrology (NZ), 40, 139-187.
- Choi, M. S., Ryu, J.-S., Lee, S.-W., Shin, H. S. & Lee, K.-S. 2012. A revisited method for Mg purification and isotope analysis using cool-plasma MC-ICP-MS. Journal of Analytical Atomic Spectrometry, 27, 1955-1959.

- Chopra, R., Richter, F. M., Bruce Watson, E. & Scullard, C. R. 2012. Magnesium isotope fractionation by chemical diffusion in natural settings and in laboratory analogues. Geochimica et Cosmochimica Acta, 88, 1-18.
- Chou, L., Garrels, R., M. & Wollast, R. 1989. Comparative study of the kinetics and mechanisms of dissolution of carbonate minerals. Chemical Geology, 78, 269-282.
- Clarke, B. A. & Burbank, D. W. 2011. Quantifying bedrock-fracture patterns within the shallow subsurface: Implications for rock mass strength, bedrock landslides, and erodibility. Journal of Geophysical Research, 116, 1-22.
- Cooper, A. F. & Kostro, F. 2006. A tectonically uplifted marine shoreline deposit, Knights Point, Westland, New Zealand. New Zealand Journal of Geology and Geophysics, 49, 203-216.
- Cooper, A. F., Barreiro, B. A., Kimbrough, D. L. & Mattinson, J. M. 1987. Lamprophyre dike intrusion and the age of the Alpine Fault, New Zealand. Geology, 15, 941-944.
- Cox, S. C. & Findlay, R. H. 1995. The Main Divide Fault Zone and its role in formation of the Southern Alps, New Zealand. New Zealand Journal of Geology and Geophysics, 38, 489-499.
- Cox, S. C. & Rattenbury, M. S. 2006. The QMAP dataset and an example of its application in modelling gold prospectivity in New Zealand.
- Cox, S. C. & Sutherland, R. 2007. Regional geological framework of South Island, New Zealand, and its significance for understanding the active plate boundary. In: Okaya, D., Stern, T., Davey, F. (eds). A Continental Plate Boundary: Tectonics at South Island, New Zealand. Geophysical Monograph Series, 175, 19-46.
- Cox, S. C., Stirling, M. W., Herman, F., Gerstenberger, M. & Ristau, J. 2012. Potentially active faults in the rapidly eroding landscape adjacent to the Alpine Fault, central Southern Alps, New Zealand. Tectonics, 31, 1-24.
- Craw, D. 1984a. Ferrous-iron-bearing vermiculite-smectite series formed during alteration of chlorite to kaolinite, Otago Schist, New Zealand. Clay Minerals, 19, 509-520.
- Craw, D. 1984b. Lithologic variations in Otago Schist, Mt Aspiring area, northwest Otago, New Zealand. New Zealand Journal of Geology and Geophysics, 27, 151-166.
- Craw, D. 1988. Shallow-level metamorphic fluids in a high uplift rate metamorphic belt; Alpine Schist, New Zealand. Journal of Metamorphic Geology, 6, 1-16.
- Craw, D. 1994. Contrasting alteration mineralogy at an unconformity beneath auriferous terrestrial sediments, central Otago, New Zealand. Sedimentary Geology, 92, 17-30.

- Craw, D. 1997. Fluid inclusion evidence for geothermal structure beneath the Southern Alps, New Zealand. New Zealand Journal of Geology and Geophysics, 40, 43-52.
- Craw, D. 2002. Geochemistry of late metamorphic hydrothermal alteration and graphitization of host rock, Macraes gold mine, Otago Schist, New Zealand. Chemical Geology, 191, 257-275.
- Craw, D., Windle, S. J. & Angus, D. F. 1999. Gold mineralization without quartz veins in a ductile-brittle shear zone, Macraes Mine, Otago Schist, New Zealand. Mineralium Deposita, 34, 382-394.
- Dauphas, N., Teng, F. Z. & Arndt, N. T. 2010. Magnesium and iron isotopes in 2.7 Ga Alexo komatiites: mantle signatures, no evidence for Soret diffusion, and identification of diffusive transport in zoned olivine. Geochimica et Cosmochimica Acta, 74, 3274-3291.
- Davies, J. P., Clarke, B. A., Whiter, J. T. & Cunningham, R. J. 2001. Factors influencing the structural deterioration and collapse of rigid sewer pipes. Urban Water, 3, 73-89.
- De La Rocha, C. L., Brzezinski, M. A. & Deniro, M. J. 2000. A first look at the distribution of the stable isotopes of silicon in natural waters. Geochimica et Cosmochimica Acta, 64, 2467-2477.
- De Villiers, S., Dickson, J. a. D. & Ellam, R. M. 2005. The composition of the continental river weathering flux deduced from seawater Mg isotopes. Chemical Geology, 216, 133-142.
- Decarreau, A., Vigier, N., Pálková, H., Petit, S., Vieillard, P. & Fontaine, C. 2012. Partitioning of lithium between smectite and solution: An experimental approach. Geochimica et Cosmochimica Acta, 85, 314-325.
- Deer, W. A. & Zussman, J. 2003. Rock-Forming Minerals. Geological Society of London.
- Deer, W. A., Howie, R. A. & Zussman, J. 1992. An Introduction to the Rock-Forming Minerals. Volume 2. Hong Kong, Longman Scientific & Technical.
- Delaney, M. L. & Boyle, E. A. 1986. Lithium in foraminiferal shells: implications for high-temperature hydrothermal circulation fluxes and oceanic crustal generation rates. Earth and Planetary Science Letters, 80, 91-105.
- Demets, C., Gordon, R. C., Argus, D. F. & Stein, S. 1994. Effect of recent revisions to the geomagnetic time scale on estimates of current plate motions. Geophysical Research Letters, 21, 2191-2194.
- Dennen, W. H. 1966. Stoichiometric substitution in natural quartz. Geochimica et Cosmochimica Acta, 30, 1235-1241.

- Dennen, W. H. 1967. Trace elements in quartz as indicators of provenance. Geological Society of America Bulletin, 78, 125-130.
- Derry, L. A., Brasier, M. D., Corfield, R. M., Rozanov, A. Y. & Zhuravlev, A. Y. 1994. Sr and C isotopes in Lower Cambrian carbonates from the Siberian craton: A paleoenvironmental record during the 'Cambrian explosion'. Earth and Planetary Science Letters, 128, 671-681.
- Derry, L. A., Kaufman, A. J. & Jacobsen, S. B. 1992. Sedimentary cycling and environmental change in the Late Proterozoic: Evidence from stable and radiogenic isotopes. Geochimica et Cosmochimica Acta, 56, 1317-1329.
- Derry, L. A., Keto, L. S., Jacobsen, S. B., Knoll, A. H. & Swett, K. 1989. Sr isotopic variations in Upper Proterozoic carbonates from Svalbard and East Greenland. Geochimica et Cosmochimica Acta, 53, 2331-2339.
- Derry, L. A., Kurtz, A. C., Ziegler, K. & Chadwick, O. A. 2005. Biological control of terrestrial silica cycling and export fluxes to watersheds. Nature, 433, 728-731.
- Dessert, C., Dupré, B., François, L. M., Schott, J., Gaillardet, J., Chakrapani, G. & Bajpai, S. 2001. Erosion of Deccan Traps determined by river geochemistry: impact on the global climate and the ⁸⁷Sr/⁸⁶Sr ratio of seawater. Earth and Planetary Science Letters, 188, 459-474.
- Dessert, C., Dupré, B., Gaillardet, J., François, L. M. & Allègre, C. J. 2003. Basalt weathering laws and the impact of basalt weathering on the global carbon cycle. Chemical Geology, 202, 257-273.
- Dickson, J. a. D. 2002. Fossil Echinoderms As Monitor of the Mg/Ca Ratio of Phanerozoic Oceans. Science, 298, 1222-1224.
- Dixon, J. B. & Weed, S. B. 1989. Palygorskite and sepiolite group minerals. In: Dixon, J. B., Weed, S. B., Dinauer, R. C. (eds). Minerals in Soil Environments. Soil Science Society of America, pp 829-872.
- Dixon, J. L., Heimsath, A. M. & Amundson, R. 2009. The critical role of climate and saprolite weathering in landscape evolution. Earth Surface Processes and Landforms, 34, 1507-1521.
- Dove, P. M. 1995. Kinetic and thermodynamic controls on silica reactivity in weathering environments. Reviews in Mineralogy and Geochemistry, 31, 235-290.
- Drever, J. I. 1988. The Geochemistry of Natural Waters. Prentice Hall, New Jersey.

- Drever, J. I. & Maynard, B. 1988. Geochemical cycles the continental crust and the oceans. In: Gregor, C. B., Garrels, R. M., Mackenzie, F. T., Maynard, J. B. (eds). Chemical Cycles in the Evolution of the Earth. Wiley Interscience, New York, pp 15-54.
- Drever, J. I. 1974. The magnesium question. In: Goldberg, E. (eds). The Sea. Wiley-Interscience, New York, pp 337-358.
- Drever, J. I. 1994. The effect of land plants on weathering rates of silicate minerals. Geochimica et Cosmochimica Acta, 58, 2325-2332.
- Edmond, J. M. 1992. Himalayan tectonics, weathering processes, and the strontium isotope record in marine limestones. Science, 258, 1594-1597.
- Edmond, J. M., Palmer, M. R., Measures, C., Brown, E. T. & Huh, Y. 1996. Fluvial geochemistry of the eastern slope of the northeastern Andes and its foredeep in the drainage of the Orinoco in Columbia and Venezuela. Geochimica et Cosmochimica Acta, 60, 2949-2976.
- Elderfield, H. & Schultz, A. 1996. Mid-ocean ridge hydrothermal fluxes and the chemical composition of the ocean. Annual Review of Earth and Planetary Sciences, 24, 191-224.
- Elliott, T., Jeffcoate, A. & Bouman, C. 2004. The terrestrial Li isotope cycle: light-weight constraints on mantle convection. Earth and Planetary Science Letters, 220, 231-245.
- Elliott, T., Thomas, A., Jeffcoate, A. & Niu, Y. 2006. Lithium isotope evidence for subduction-enriched mantle in the source of mid-ocean-ridge basalts. Nature, 443, 565-568.
- English, N. B., Quade, J., Decelles, P. G. & Garzione, C. N. 2000. Geologic control of Sr and major element chemistry in Himalayan Rivers, Nepal. Geochimica et Cosmochimica Acta, 64, 2549-2566.
- Evans, M. J., Derry, L. A., Anderson, S. P. & France-Lanord, C. 2001. Hydrothermal source of radiogenic Sr to Himalayan rivers. Geology, 29, 803-806.
- Fitzharris, B., Hay, J. E. & Jones, P. D. 1992. Behaviour of New Zealand glaciers and atmospheric circulation changes over the past 130 years. The Holocene, 2, 97-106.
- Fitzharris, B., Lawson, W. & Owens, I. 1999. Research on glaciers and snow in New Zealand. Progress in Physical Geography, 23, 469-500.
- Fleming, C. A. 1969. The Mesozoic of New Zealand: Chapters in the history of the Circum-Pacific Mobile Belt: 22nd William Smith Lecture. Quarterly Journal of the Geological Society, 125, 125-170.

- Fordham, A. W. 1990. Formation of trioctahedral illite from biotite in a soil profile over granite gneiss. Clays and Clay Minerals, 38, 187-195.
- Foster, G. L., Pogge von Strandmann, P. A. E. & Rae, J. W. B. 2010. Boron and magnesium isotopic composition of seawater. Geochemistry, Geophysics, Geosystems, 11, 1-10.
- Fouillac, C. & Michard, G. 1981. Sodium/lithium ratio in water applied to geothermometry of geothermal reservoirs. Geothermics, 10, 55-70.
- Fournier, R. O. & Rowe, J. J. 1966. Estimation of underground temperatures from the silica content of water from hot springs and wet-steam wells. American Journal of Science, 264, 685-697.
- Fournier, R. O. & Truesdell, A. H. 1970. Chemical indicators of subsurface temperature applied to hot spring waters of Yellowstone National Park, Wyoming, U.S.A. Geothermics, 2, 529-535.
- Foustoukos, D. I., James, R. H., Berndt, M. E. & Seyfried, W. E. 2004. Lithium isotopic systematics of hydrothermal vent fluids at the Main Endeavour Field, Northern Juan de Fuca Ridge. Chemical geology, 212, 17-26.
- France-Lanord, C., Evans, M., Hurtrez, J.-E. & Riotte, J. 2003. Annual dissolved fluxes from Central Nepal rivers: budget of chemical erosion in the Himalayas. Comptes Rendus Geoscience, 335, 1131-1140.
- Gabet, E. J. & Mudd, S. M. 2009. A theoretical model coupling chemical weathering rates with denudation rates. Geology, 37, 151-154.
- Gaillardet, J., Dupré, B. & Allègre, C. J. 1995. A global geochemical mass budget applied to the Congo Basin rivers: Erosion rates and continental crust composition. Geochimica et Cosmochimica Acta, 59, 3469-3485.
- Gaillardet, J., Dupré, B. & Allègre, C. J. 1999a. Geochemistry of large river suspended sediments: silicate weathering or recycling tracer? Geochimica et Cosmochimica Acta, 63, 4037-4051.
- Gaillardet, J., Dupré, B., Allègre, C. J. & Negrel, P. 1997. Chemical and physical denudation in the Amazon River Basin. Chemical Geology, 142, 141-173.
- Gaillardet, J., Dupré, B., Louvat, P. & Allègre, C. J. 1999b. Global silicate weathering and CO₂ consumption rates deduced from the chemistry of large rivers. Chemical Geology, 159, 3-30.
- Gaillardet, J., Viers, J. & Dupré, B. 2003. Trace elements in river waters. Treatise on Geochemistry, 5, 225-272.

- Galy, A. & France-Lanord, C. 1999. Weathering processes in the Ganges-Brahmaputra basin and the riverine alkalinity budget. Chemical Geology, 159, 31-60.
- Galy, A. & O'Nions, R. K. 2000. Is there a CHUR for Mg? Goldschmidt Conference Abstracts 2000, 424.
- Galy, A., Bar-Matthews, M., Halicz, L. & O'Nions, R. K. 2002. Mg isotopic composition of carbonate: insight from speleothem formation. Earth and Planetary Science Letters, 201, 105-115.
- Galy, A., France-Lanord, C. & Derry, L. A. 1999. The strontium isotopic budget of Himalayan rivers in Nepal and Bangladesh. Geochimica et Cosmochimica Acta, 63, 1905-1925.
- Galy, A., Yoffe, O., Janney, P. E., Williams, R. W., Cloquet, C., Alard, O., Halicz, L., Wadhwa, M., Hutcheon, I. D., Ramon, E. & Carignan, J. 2003. Magnesium isotope heterogeneity of the isotopic standard SRM980 and new reference materials for magnesium-isotope-ratio measurements. Journal of Analytical Atomic Spectrometry, 18, 1352-1356.
- Gardner, L. R., Kheoruenromne, I. & Chen, H. S. 1981. Geochemistry and mineralogy of an unusual diabase saprolite near Columbia, South Carolina. Clays and Clay Minerals, 29, 184-190.
- Gellatly, A. F., Chinn, T. & Rothlisberger, F. 1988. Holocene glacier variations in New Zealand: A review. Quaternary Science Reviews, 7, 227-242.
- Georg, R. B., Reynolds, B. C., West, A. J., Burton, K. W. & Halliday, A. N. 2007. Silicon isotope variations accompanying basalt weathering in Iceland. Earth and Planetary Science Letters, 261, 476-490.
- Gerlach, T. M. 1991. Present-day CO₂ Emissions from Volcanoes. EOS, Transactions, Americal Geophysical Union 72, 249.
- Giletti, B. J. & Shanahan, T. M. 1997. Alkali diffusion in plagioclase feldspar. Chemical Geology, 139, 3-20.
- Gislason, S. R. & Arnorsson, S. 1993. Dissolution of primary basaltic minerals in natural waters: saturation state and kinetics. Chemical Geology, 105, 117-135.
- Gislason, S. R., Arnorsson, S. & Armannsson, H. 1996. Chemical weathering of basalt in southwest Iceland: Effects of runoff, age of rocks and vegetative/glacial cover. American Journal of Science, 296, 837-907.
- Gislason, S. R., Oelkers, E. H. & Snorrason, Á. 2006. Role of river-suspended material in the global carbon cycle. Geology, 34, 49-52.

- Goldsmith, S. T., Carey, A. E., Johnson, B. M., Welch, S. A., Lyons, W. B., Mcdowell, W. H. & Pigott, J. S. 2010. Stream geochemistry, chemical weathering and CO₂ consumption potential of andesitic terrains, Dominica, Lesser Antilles. Geochimica et Cosmochimica Acta, 74, 85-103.
- Gordeev, V. V. & Siderov, I. S. 1993. Concentrations of major elements and their outflow into the Laptev Sea by the Lena River. Marine Chemistry, 43, 33-45.
- Gosz, J. R., Likens, G. E. & Bormann, F. H. 1973. Nutrient release from decomposing leaf and branch litter in the Hubbard Brook Forest, New Hampshire. Ecological Monographs, 43, 173-191.
- Goudie, A. S. & Viles, H. A. 2012. Weathering and the global carbon cycle: Geomorphological perspectives. Earth-Science Reviews, 113, 59-71.
- Grapes, R. H. & Watanabe, T. 1984. Al-Fe (super 3+) and Ca-Sr (super 2+) epidotes in metagreywacke-quartzofeldspathic schist, Southern Alps, New Zealand. American Mineralogist, 69, 490-498.
- Grapes, R. H. & Watanabe, T. 1992. Metamorphism and uplift of the Alpine Schist in the Franz Josef-Fox glacier area of the Southern Alps, New Zealand. Journal of Metamorphic Geology, 10, 171-180.
- Grapes, R. H. 1995. Uplift and exhumation of Alpine Schist, Southern Alps, New Zealand: Thermobarometric constraints. New Zealand Journal of Geology and Geophysics, 38, 525-533.
- Gray, D. R. & Foster, D. A. 2004. ⁴⁰Ar/³⁹Ar thermochronologic constraints on deformation, metamorphism and cooling/exhumation of a Mesozoic accretionary wedge, Otago Schist, New Zealand. Tectonophysics, 385, 181-210.
- Griffiths, G. A. & Mcsaveney, M. J. 1983. Distribution of mean annual precipitation across some steepland regions of New Zealand. New Zealand Journal of Science, 26, 197-209.
- Gruber, S. & Haeberli, W. 2007. Permafrost in steep bedrock slopes and its temperature-related destabilization following climate change. Journal of Geophysical Research, 112, 1-10.
- Gussone, N., Eisenhauer, A., Heuser, A., Dietzel, M., Bock, B., Böhm, F., Spero, H. J., Lea, D. W., Bijma, J. & Nägler, T. F. 2003. Model for kinetic effects on calcium isotope fractionation (δ⁴⁴Ca) in inorganic aragonite and cultured planktonic foraminifera. Geochimica et Cosmochimica Acta, 67, 1375-1382.

- Hales, T. C. & Roering, J. J. 2005. Climate-controlled variations in scree production, Southern Alps, New Zealand. Geology, 33, 701-704.
- Hallet, B., Hunter, L. & Bogen, J. 1996. Rates of erosion and sediment evacuation by glaciers: A review of field data and their implications. Global and Planetary Change, 12, 213-235.
- Han, G. & Liu, C.-Q. 2004. Water geochemistry controlled by carbonate dissolution: a study of the river waters draining karst-dominated terrain, Guizhou Province, China. Chemical Geology, 204, 1-21.
- Handler, M. R., Baker, J. A., Schiller, M., Bennett, V. C. & Yaxley, G. M. 2009. Magnesium stable isotopic composition of Earth's upper mantle. Earth and Planetary Science Letters, 282, 306-313.
- Hansen, J., Sato, M., Kharecha, P., Beerling, D. J., Berner, R. A., Masson-Delmotte, V., Pagani, M., Raymo, M. E., Royer, D. L. & Zachos, J. C. 2008. Target atmospheric CO₂: Where should humanity aim? Open Atmospheric Science Journal, 2, 217-231.
- Harder, H. 1972. The role of magnesium in the formation of smectite minerals. Chemical Geology, 10, 31-39.
- Hardie, L. A. 1996. Secular variation in seawater chemistry: An explanation for the coupled secular variation in the mineralogies of marine limestones and potash evaporites over the past 600 m.y. Geology, 24, 279-283.
- Hartmann, J., Jansen, N., Dürr, H. H., Kempe, S. & Köhler, P. 2009. Global CO₂-consumption by chemical weathering: What is the contribution of highly active weathering regions? Global and Planetary Change, 69, 185-194.
- Harvey, P. K. 1989. Automated X-ray fluorescence in geochemical exploration. X-ray fluorescence analysis in the geological sciences, advances in methodology. Geological Association of Canada, Short Courses, 7, 221-257.
- Hathorne, E. & James, R. 2006. Temporal record of lithium in seawater: A tracer for silicate weathering? Earth and Planetary Science Letters, 246, 393-406.
- Hayes, J. M. & Waldbauer, J. R. 2006. The carbon cycle and associated redox processes through time. Philosophical Transactions of the Royal Society B: Biological Sciences, 361, 931-950.
- Henderson, R. D. & Thompson, S. M. 1999. Extreme rainfalls in the Southern Alps of New Zealand. Journal of Hydrology (NZ), 38, 309-330.

- Henderson, R. D. 1993. Extreme storm rainfalls in the Southern Alps, New Zealand. In: Extreme Hydrological Events: Precipitation, Floods and Droughts. Proceedings of the Yokohama Symposium, July 1993, 213.
- Herman, F., Anderson, B. & Leprince, S. 2011. Mountain glacier velocity variation during a retreat/advance cycle quantified using sub-pixel analysis of ASTER images. Journal of Glaciology, 57, 197-207.
- Heydemann, A. 1969. Tables. In: Wedepohl, K. H. (eds). Handbook of Geochemistry, Chapter 12. Springer, Berlin, pp 376-412.
- Hicks, D. M., Hill, J. & Shankar, U. 1996. Variation of suspended sediment yields around New Zealand: the relative importance of rainfall and geology. Erosion and Sediment Yield: Global and Regional Perspectives (Proceedings of the Exeter Symposium), 236, 149-156.
- Higgins, J. A. & Schrag, D. P. 2015. The Mg isotopic composition of Cenozoic seawater evidence for a link between Mg-clays, seawater Mg/Ca, and climate. Earth and Planetary Science Letters, 416, 73-81.
- Hilley, G. E. & Porder, S. 2008. A framework for predicting global silicate weathering and CO₂ drawdown rates over geologic time-scales. Proceedings of the National Academy of Sciences, 105, 16855-16859.
- Hindshaw, R. S., Reynolds, B. C., Wiederhold, J. G., Kretzschmar, R. & Bourdon, B. 2011. Calcium isotopes in a proglacial weathering environment: Damma glacier, Switzerland. Geochimica et Cosmochimica Acta, 75, 106-118.
- Hippler, D., Buhl, D., Witbaard, R., Richter, D. K. & Immenhauser, A. 2009. Towards a better understanding of magnesium-isotope ratios from marine skeletal carbonates. Geochimica et Cosmochimica Acta, 73, 6134-6146.
- Hoefs, J. & Sywall, M. 1997. Lithium isotope composition of Quaternary and Tertiary biogene carbonates and a global lithium isotope balance. Geochimica et Cosmochimica Acta, 61, 2679-2690.
- Holland, H. D. 1978. The Chemistry of the Atmosphere and Oceans. Wiley, New York.
- Holm, D. K., Norris, R. & Craw, D. 1989. Brittle and ductile deformation in a zone of rapid uplift: central Southern Alps, New Zealand. Tectonics, 8, 153-168.
- Hornberger, G. M., Scanlon, T. M. & Raffensperger, J. P. 2001. Modelling transport of dissolved silica in a forested headwater catchment: the effect of hydrological and chemical time scales

- on hysteresis in the concentration-discharge relationship. Hydrological Processes, 15, 2029-2038.
- Horstman, E. L. 1957. The distribution of lithium, rubidium and caesium in igneous and sedimentary rock. Geochimica et Cosmochimica Acta, 12, 1-28.
- Hovius, N., Stark, C. P. & Allen, P. A. 1997. Sediment flux from a mountain belt derived by landslide mapping. Geology, 25, 231-234.
- Howarth, J. D., Fitzsimons, S. J., Norris, R. J. & Jacobsen, G. E. 2012. Lake sediments record cycles of sediment flux driven by large earthquakes on the Alpine fault, New Zealand. Geology, 40, 1091-1094.
- Hren, M., Chamberlain, C., Hilley, G., Blisniuk, P. & Bookhagen, B. 2007. Major ion chemistry of the Yarlung Tsangpo–Brahmaputra river: Chemical weathering, erosion, and CO₂ consumption in the southern Tibetan plateau and eastern syntaxis of the Himalaya. Geochimica et Cosmochimica Acta, 71, 2907-2935.
- Huang, F., Glessner, J., Ianno, A., Lundstrom, C. & Zhang, Z. 2009. Magnesium isotopic composition of igneous rock standards measured by MC-ICP-MS. Chemical Geology, 268, 15-23.
- Huang, F., Zhang, Z., Lundstrom, C. C. & Zhi, X. 2011. Iron and magnesium isotopic compositions of peridotite xenoliths from Eastern China. Geochimica et Cosmochimica Acta, 75, 3318-3334.
- Huang, K.-F., You, C.-F., Liu, Y.-H., Wang, R.-M., Lin, P.-Y. & Chung, C.-H. 2010. Low-memory, small sample size, accurate and high-precision determinations of lithium isotopic ratios in natural materials by MC-ICP-MS. Journal of Analytical Atomic Spectrometry, 25, 1019-1024.
- Huang, K.-J., Teng, F.-Z., Wei, G.-J., Ma, J.-L. & Bao, Z.-Y. 2012. Adsorption- and desorption-controlled magnesium isotope fractionation during extreme weathering of basalt in Hainan Island, China. Earth and Planetary Science Letters, 359-360, 73-83.
- Huh, Y. & Edmond, J. M. 1999. The fluvial geochemistry of the rivers of Eastern Siberia: III. Tributaries of the Lena and Anabar draining the basement terrain of the Siberian Craton and the Trans-Baikal Highlands. Geochimica et Cosmochimica Acta, 63, 967-987.
- Huh, Y. 2003. Chemical weathering and climate a global experiment: A review. Geosciences Journal, 7, 277-288.

- Huh, Y., Chan, L. H. & Edmond, J. M. 2001. Lithium isotopes as a probe of weathering processes: Orinoco River. Earth and Planetary Science Letters, 194, 189-199.
- Huh, Y., Chan, L. H., Zhang, L. & Edmond, J. M. 1998a. Lithium and its isotopes in major world rivers: Implications for weathering and the oceanic budget. Geochimica et Cosmochimica Acta, 62, 2039-2051.
- Huh, Y., Chan, L. H. & Chadwick, O. A. 2004. Behaviour of lithium and its isotopes during weathering of Hawaiian basalt. Geochemistry, Geophysics, Geosystems, 5, 1-22.
- Huh, Y., Panteleyev, G., Babich, D., Zaitsev, A. & Edmond, J. M. 1998b. The fluvial geochemistry of the rivers of Eastern Siberia: II. Tributaries of the Lena, Omoloy, Yana, Indigirka, Kolyma, and Anadyr draining the collisional/accretionary zone of the Verkhoyansk and Cherskiy ranges. Geochimica et Cosmochimica Acta, 62, 2053-2075.
- Hulston, J. R. & Thode, H. G. 1965. Variations in the S³³, S³⁴, and S³⁶ contents of meteorites and their relation to chemical and nuclear effects. Journal of Geophysical Research, 70, 3475-3484.
- Immenhauser, A., Buhl, D., Richter, D., Niedermayr, A., Riechelmann, D., Dietzel, M. & Schulte,
 U. 2010. Magnesium-isotope fractionation during low-Mg calcite precipitation in a limestone
 cave Field study and experiments. Geochimica et Cosmochimica Acta, 74, 4346-4364.
- Jacobsen, B., Yin, Q.-Z., Moynier, F., Amelin, Y., Krot, A. N., Nagashima, K., Hutcheon, I. D. & Palme, H. 2008. ²⁶Al-²⁶Mg and ²⁰⁷Pb-²⁰⁶Pb systematics of Allende CAIs: Canonical solar initial ²⁶Al/²⁷Al ratio reinstated. Earth and Planetary Science Letters, 272, 353-364.
- Jacobsen, S. B. & Kaufman, A. J. 1999. The Sr, C and O isotopic evolution of Neoproterozoic seawater. Chemical Geology, 161, 37-57.
- Jacobson, A. D. & Blum, J. D. 2003. Relationship between mechanical erosion and atmospheric CO₂ consumption in the New Zealand Southern Alps. Geology, 31, 865-868.
- Jacobson, A. D., Blum, J. D., Chamberlain, C., Craw, D. & Koons, P. O. 2003. Climatic and tectonic controls on chemical weathering in the New Zealand Southern Alps. Geochimica et Cosmochimica Acta, 67, 29-46.
- James, R. & Palmer, M. R. 2000. The lithium isotope composition of international rock standards. Chemical Geology, 166, 319-326.

- Janoušek, V., Erban, V., Holub, F. V., Magna, T., Bellon, H., Mlčoch, B., Wiechert, U. & Rapprich,V. 2010. Geochemistry and genesis of behind-arc basaltic lavas from eastern Nicaragua.Journal of Volcanology and Geothermal Research, 192, 232-256.
- Jeffcoate, A. B., Elliott, T., Kasemann, S. A., Ionov, D., Cooper, K. & Brooker, R. 2007. Li isotope fractionation in peridotites and mafic melts. Geochimica et Cosmochimica Acta, 71, 202-218.
- Jenkin, G. R. T., Craw, D. & Fallick, A. E. 1994. Stable isotopic and fluid inclusion evidence for meteoric fluid penetration into an active mountain belt; Alpine Scist, New Zealand. Journal of Metamorphic Geology, 12, 429-444.
- Jochum, K. P., Nohl, U., Herwig, K., Lammel, E., Stoll, B. & Hofmann, A. W. 2005. GeoReM: A new geochemical database for reference materials and isotopic standards. Geostandards and Geoanalytical Research, 29, 333-338.
- Jochum, K. P., Stoll, B., Herwig, K., Willbold, M., Hofmann, A. W., Amini, M., Aarburg, S., Abouchami, W., Hellebrand, E., Mocek, B., Raczek, I., Stracke, A., Alard, O., Bouman, C., Becker, S., Dücking, M., Brätz, H., Klemd, R., De Bruin, D., Canil, D., Cornell, D., De Hoog, C.-J., Dalpé, C., Danyushevsky, L., Eisenhauer, A., Gao, Y., Snow, J. E., Groschopf, N., Günther, D., Latkoczy, C., Guillong, M., Hauri, E. H., Höfer, H. E., Lahaye, Y., Horz, K., Jacob, D. E., Kasemann, S. A., Kent, A. J. R., Ludwig, T., Zack, T., Mason, P. R. D., Meixner, A., Rosner, M., Misawa, K., Nash, B. P., Pfänder, J., Premo, W. R., Sun, W. D., Tiepolo, M., Vannucci, R., Vennemann, T., Wayne, D. & Woodhead, J. D. 2006. MPI-DING reference glasses for in situ microanalysis: New reference values for element concentrations and isotope ratios. Geochemistry, Geophysics, Geosystems, 7, 1-44.
- John, T., Gussone, N., Podladchikov, Y. Y., Bebout, G. E., Dohmen, R., Halama, R., Klemd, R., Magna, T. & Seitz, H.-M. 2012. Volcanic arcs fed by rapid pulsed fluid flow through subducting slabs. Nature Geoscience, 5, 489-492.
- Kadko, D., Baross, J. & Alt, J. C. 1995. The magnitude and global implications of hydrothermal flux. Geophysical Monograph, 91, 446-466.
- Kamp, P. J. J. & Tippett, J. M. 1993. Dynamics of Pacific Plate crust in the South Island (New Zealand) zone of oblique continent-continent convergence. Journal of Geophysical Research: Solid Earth, 98, 16105-16118.
- Kamp, P. J. J. 1986. The mid-Cenozoic Challenger Rift System of western New Zealand and its implications for the age of Alpine Fault inception. Geological Society of America Bulletin, 97, 255-281.

- Kamp, P. J. J. 1997. Paleogeothermal gradient and deformation style, Pacific front of the Southern Alps Orogen: Constraints from fission track thermochronology. Tectonophysics, 271, 37-58.
- Kamp, P. J. J., Green, P. F. & White, S. H. 1989. Fission track analysis reveals character of collisional tectonics in New Zealand. Tectonics, 8, 169-195.
- Kaufman, A. J., Jacobsen, S. B. & Knoll, A. H. 1993. The Vendian record of Sr and C isotopic variations in seawater: Implications for tectonics and paleoclimate. Earth and Planetary Science Letters, 120, 409-430.
- Kaufman, A. J., Knoll, A. H., Semikhatov, M. A., Grotzinger, J. P., Jacobsen, S. B. & Adams, W. 1996. Integrated chronostratigraphy of Proterozoic-Cambrian boundary beds in the western Anabar region, northern Siberia. Geological Magazine, 133, 509-533.
- Keech, A. R., West, A. J., Pett-Ridge, J. C. & Henderson, G. M. 2013. Evaluating U-series tools for weathering rate and duration on a soil sequence of known ages. Earth and Planetary Science Letters, 374, 24-35.
- Kısakűrek, B., James, R. H. & Harris, N. B. W. 2005. Li and δ⁷Li in Himalayan rivers: Proxies for silicate weathering? Earth and Planetary Science Letters, 237, 387-401.
- Koons, P. O. & Henderson, C. M. 1995. Geodetic analysis of model oblique collision and comparison to the Southern Alps of New Zealand. New Zealand Journal of Geology and Geophysics, 38, 545-552.
- Koons, P. O. 1981. A study of natural and experimental metasomatic assemblages in an ultramafic-quartzfeldspathic metasomatic system from the Haast Schist, South Island, New Zealand. Contributions to Mineralogy and Petrology, 78, 189-195.
- Koons, P. O. 1987. Some thermal and mechanical consequences of rapid uplift: an example from the Southern Alps, New Zealand. Earth and Planetary Science Letters, 86, 307-319.
- Koons, P. O. 1989. The topographical evolution of collisional mountain belts: a numerical look at the Southern Alps, New Zealand. Science, 289, 1041-1069.
- Koons, P. O. 1990. Two-sided orogen: Collision and erosion from the sandbox to the Southern Alps, New Zealand. Geology, 18, 679-682.
- Koons, P. O. 1994. Three-dimensional critical wedges: Tectonics and topography in oblique collisional orogens. Journal of Geophysical Research, 99, 12301-12315.

- Korup, O. 2004. Geomorphic implications of fault zone weakening: Slope instability along the Alpine Fault, South Westland to Fiordland. New Zealand Journal of Geology and Geophysics, 47, 257-267.
- Korup, O., McSaveney, M. J. & Davies, T. R. H. 2004. Sediment generation and delivery from large historic landslides in the Southern Alps, New Zealand. Geomorphology, 61, 189-207.
- Košler, J., Magna, T., Mlčoch, B., Mixa, P., Nývlt, D. & Holub, F. V. 2009. Combined Sr, Nd, Pb and Li isotope geochemistry of alkaline lavas from northern James Ross Island (Antarctic Peninsula) and implications for back-arc magma formation. Chemical Geology, 258, 207-218.
- Krauskopf, K. 1967. Introduction to Geochemistry. McGraw-Hill, New York.
- Krishnaswami, S., Trivedi, J. R., Sarin, M. M., Ramesh, R. & Sharma, K. K. 1992. Strontium isotopes and rubidium in the Ganges-Brahmaputra river system: Weathering in the Himalaya, fluxes to the Bay of Bengal and contributions to the evolution of oceanic ⁸⁷Sr/⁸⁶Sr. Earth and Planetary Science Letters, 109, 243-253.
- Kronenberg, A. K. 1994. Hydrogen speciation and chemical weakening of quartz. Reviews in Mineralogy and Geochemistry, 29, 123-176.
- Kump, L., R., Brantley, S., L. & Arthur, M. A. 2000. Chemical weathering, atmospheric CO₂, and climate. Annual Review of Earth and Planetary Sciences, 28, 611-667.
- Lamb, S. H. & Bibby, H. M. 1989. The last 25 Ma of rotational deformation in part of the New Zealand plate-boundary zone. Journal of Structural Geology, 11, 473-492.
- Landis, C. A. & Coombs, D. S. 1967. Metamorphic belts and orogenesis in Southern New Zealand. Tectonophysics, 4, 501-518.
- Lasaga, A. C., Soler, J. M., Ganor, J., Timothy, E. B. & Kathryn, L. N. 1994. Chemical weathering rate laws and global geochemical cycles. Geochimica et Cosmochimica Acta, 58, 2361-2386.
- Le Fort, P. 1975. Himalayas: The collided range. Present knowledge of the continental arc. American Journal of Science, 275-A, 1-44.
- Lee, S.-W., Ryu, J.-S. & Lee, K.-S. 2014. Magnesium isotope geochemistry in the Han River, South Korea. Chemical Geology, 364, 9-19.
- Lehner, F. K. 1986. Comments on "Noncohesive critical Coulomb wedges: An exact solution" by F. A. Dahlen. Journal of Geophysical Research, 91, 793-796.

- Leitner, B., Eberhart-Phillips, D., Anderson, H. & Nabelek, J. L. 2001. A focused look at the Alpine fault, New Zealand: Seismicity, focal mechanisms, and stress observations. Journal of Geophysical Research, 106, 2193-2220.
- Lemarchand, D. & Gaillardet, J. 2006. Transient features of the erosion of shales in the Mackenzie basin (Canada), evidences from boron isotopes. Earth and Planetary Science Letters, 245, 174-189.
- Lemarchand, E., Chabaux, F., Vigier, N., Millot, R. & Pierret, M.-C. 2010. Lithium isotope systematics in a forested granitic catchment (Strengbach, Vosges Mountains, France). Geochimica et Cosmochimica Acta, 74, 4612-4628.
- Levasseur, S., Birck, J.-L. & Allègre, C. J. 1999. The osmium riverine flux and the oceanic mass balance of osmium. Earth and Planetary Science Letters, 174, 7-23.
- Li, W., Chakraborty, S., Beard, B. L., Romanek, C. S. & Johnson, C. M. 2012. Magnesium isotope fractionation during precipitation of inorganic calcite under laboratory conditions. Earth and Planetary Science Letters, 333-334, 304-316.
- Little, T. A., Wightman, R., Holcombe, R. J. & Hill, M. 2007. Transpression models and ductile deformation of the lower crust of the Pacific Plate in the central Southern Alps, a perspective from structural geology. In: Okaya, D., Stern, T., Davey, F. (eds). A Continental Plate Boundary: Tectonics at South Island, New Zealand. Geophysical Monograph Series, 175, 271-288.
- Liu, X.-M., Rudnick, R. L., Mcdonough, W. F. & Cummings, M. L. 2013. Influence of chemical weathering on the composition of the continental crust: Insights from Li and Nd isotopes in bauxite profiles developed on Columbia River Basalts. Geochimica et Cosmochimica Acta, 115, 73-91.
- Liu, X.-M., Wanner, C., Rudnick, R. L. & Mcdonough, W. F. 2015. Processes controlling δ^7 Li in rivers illuminated by study of streams and groundwaters draining basalts. Earth and Planetary Science Letters, 409, 212-224.
- Livingstone, D. A. 1963. Chemical Composition of Rivers and Lakes. US Government Printing Office.
- Lorenz, J. C., Teufel, L. W. & Warpinski, N. R. 1991. Regional fractures 1: A mechanism for the formation of regional fractures at depth in flat-lying reservoirs (1). AAPG Bulletin, 75, 1714-1737.

- Louvat, P. & Allègre, C. J. 1997. Present denudation rates on the island of Réunion determined by river geochemistry: Basalt weathering and mass budget between chemical and mechanical erosions. Geochimica et Cosmochimica Acta, 61, 3645-3669.
- Lowenstein, T. K. 2001. Oscillations in Phanerozoic Seawater Chemistry: Evidence from Fluid Inclusions. Science, 294, 1086-1088.
- Mackenzie, F. T. & Garrels, R., M. 1966. Chemical mass balance between rivers and oceans. American Journal of Science, 264.
- Mackinnon, T. C. 1983. Origin of the Torlesse terrane and coeval rocks, South Island, New Zealand. Geological Society of America Bulletin, 94, 967-985.
- Magenheim, A. J., Spivack, A. J., Alt, J. C., Bayhurst, G., Chan, L. H., Zuleger, E. & Gieskes, J. M. 1994. 13. Borehole fluid chemistry in hole 504B, Leg137: formation water or in-situ reaction? Proceedings of the Ocean Drilling Program, Scientific Results, 137/140, 141-152.
- Magna, T., Wiechert, U. & Halliday, A. N. 2006. New constraints on the lithium isotope compositions of the Moon and terrestrial planets. Earth and Planetary Science Letters, 243, 336-353.
- Magna, T., Wiechert, U., Stuart, F. M., Halliday, A. N. & Harrison, D. 2011. Combined Li–He isotopes in Iceland and Jan Mayen basalts and constraints on the nature of the North Atlantic mantle. Geochimica et Cosmochimica Acta, 75, 922-936.
- Maher, K., Steefel, C. I., White, A. F. & Stonestrom, D. A. 2009. The role of reaction affinity and secondary minerals in regulating chemical weathering rates at the Santa Cruz Soil Chronosequence, California. Geochimica et Cosmochimica Acta, 73, 2804-2831.
- Maréchal, J. C., Dewandel, B. & Subrahmanyam, K. 2004. Use of hydraulic tests at different scales to characterize fracture network properties in the weathered-fractured layer of a hard rock aquifer. Water Resources Research, 40, 1-32.
- Marschall, H. R., Pogge Von Strandmann, P. a. E., Seitz, H.-M., Elliott, T. & Niu, Y. 2007. The lithium isotopic composition of orogenic eclogites and deep subducted slabs. Earth and Planetary Science Letters, 262, 563-580.
- Martin, J.-M. & Meybeck, M. 1979. Elemental mass-balance of material carried by major world rivers. Marine Chemistry, 7, 173-206.
- Matsuhisa, Y., Goldsmith, J. R. & Clayton, R. N. 1978. Mechanisms of hydrothermal crystallisation of quartz and 250 °C and 15 kbar. Geochimica et Cosmochimica Acta, 42, 173-182.

- Matsuoka, N. 2001. Direct observation of frost wedging in alpine bedrock. Earth Surface Processes and Landforms, 26, 601-614.
- Mcarthur, J. M., Howarth, R. J. & Bailey, T. R. 2001. Strontium isotope stratigraphy: LOWESS Version 3: Best fit to the marine Sr-isotope curve for 0-509 Ma and accompanying look-up table for deriving numerical age. The Journal of Geology, 109, 155-170.
- Mcsaveney, M. J. 2002. Recent rockfalls and rock avalanches in Mount Cook national park, New Zealand. Catastrophic Landslides: Effects, Occurrence, and Mechanisms, 15, 35-70.
- Menzies, C. D. 2012. Fluid flow associated with the Alpine Fault, South Island, New Zealand (PhD). University of Southampton, UK.
- Menzies, C. D., Teagle, D. A. H., Craw, D., Cox, S. C., Boyce, A. J., Barrie, C. D. & Roberts, S. 2014. Incursion of meteoric waters into the ductile regime in an active orogen. Earth and Planetary Science Letters, 399, 1-13.
- Meredith, K., Moriguti, T., Tomascak, P., Hollins, S. & Nakamura, E. 2013. The lithium, boron and strontium isotopic systematics of groundwaters from an arid aquifer system: Implications for recharge and weathering processes. Geochimica et Cosmochimica Acta, 112, 20-31.
- Merkel, B. & Planer-Friedrich, B. 2008. Groundwater Geochemistry: A Practical Guide to Modelling of Natural and Aquatic Systems. Springer Verlag.
- Meunier, A., Lanson, B. & Beaufort, D. 2000. Vermiculitization of smectite interfaces and illite layer growth as a possible dual model for illite-smectite illitization in diagenetic environments: a synthesis. Clay Minerals, 35, 573-586.
- Meybeck, M. 1980. Pathways of major elements from land to ocean through rivers. In: Martin, J-M., Burton, J. D., Eisma, D. (eds). Proceedings of the Review and Workshop on River Inputs to Ocean System, Rome. Food and Agricultural Organization of the United Nations, 18-30.
- Meybeck, M. 1987. Global chemical weathering of surficial rocks estimated from river dissolved loads. American Journal of Science, 287, 401-428.
- Meybeck, M. 2003. Global occurrence of major elements in rivers. In: Holland, H. D., Turekian, K. K. (eds). Treatise on Geochemistry. Permamon, Oxford, pp 207-223.
- Millero, F. J. 2006. Chemical Oceanography. 3rd Edition. CRC Press.
- Millot, R., Gaillardet, J. É., Dupré, B. & Allègre, C. J. 2003. Northern latitude chemical weathering rates: clues from the Mackenzie River Basin, Canada. Geochimica et Cosmochimica Acta, 67, 1305-1329.

- Millot, R., Gaillardet, J. É, Dupré, B. & Allègre, C. J. 2002. The global control of silicate weathering rates and the coupling with physical erosion: new insights from rivers of the Canadian Shield. Earth and Planetary Science Letters, 196, 83-98.
- Millot, R., Guerrot, C. & Vigier, N. 2004. Accurate and high-precision measurement of lithium isotopes in two reference materials by MC-ICP-MS. Geostandards and Geoanalytical Research, 28, 153-159.
- Millot, R., Vigier, N. & Gaillardet, J. 2010a. Behaviour of lithium and its isotopes during weathering in the Mackenzie Basin, Canada. Geochimica et Cosmochimica Acta, 74, 3897-3912.
- Millot, R., Scaillet, B. & Sanjuan, B. 2010b. Lithium isotopes in island arc geothermal systems: Gaudeloupe, Martinique (French West Indies) and experimental approach. Geochimica et Cosmochimica Acta, 74, 1832-1871.
- Ming-Hui, H., Stallard, R. F. & Edmond, J. M. 1982. Major ion chemistry of some large Chinese rivers. Nature, 298, 550-553.
- Misra, S. & Froelich, P. N. 2012. Lithium isotope history of Cenozoic seawater: Changes in silicate weathering and reverse weathering. Science, 335, 818-823.
- Molnar, P. & England, P. 1990. Late Cenozoic uplift of mountain ranges and global climate change: chicken or egg? Nature, 346, 29-34.
- Molnar, P., Atwater, T., Mammerickx, J. & Smith, S. M. 1975. Magnetic anomalies, bathymetry and the tectonic evolution of the South Pacific since the Late Cretaceous. Geophysical Journal of the Royal Astronomical Society, 40, 383-420.
- Moore, D. M. & Reynolds, R. C. 1997. X-ray Diffraction and the Identification and Analysis of Clay Minerals: Second Edition. Oxford University Press, Inc.
- Moore, J., Jacobson, A. D., Holmden, C. & Craw, D. 2013. Tracking the relationship between mountain uplift, silicate weathering, and long-term CO₂ consumption with Ca isotopes: Southern Alps, New Zealand. Chemical Geology, 341, 110-127.
- Moriguti, T. & Nakamura, E. 1998a. Across-arc variation of Li isotopes in lavas and implications for crust/mantle recycling at subduction zones. Earth and Planetary Science Letters, 163, 167-174.
- Moriguti, T. & Nakamura, E. 1998b. High-yield lithium separation and the precise isotopic analysis for natural rock and aqueous samples. Chemical Geology, 145, 91-104.
- Mortimer, N. & Roser, B. P. 1992. Geochemical evidence for the position of the Caples-Torlesse boundary in the Otago Schist, New Zealand. Journal of the Geological Society, 149, 967-977.

- Mortimer, N. 1993. Jurassic tectonic history of the Otago Schist, New Zealand. Tectonics, 12, 237-244.
- Mortimer, N. 2000. Metamorphic discontinuities in orogenic belts: example of the garnet-biotitealbite zone in the Otago Schist, New Zealand. International Journal of Earth Science, 89, 295-306.
- Mortimer, N. 2004. New Zealand's Geological Foundations. Gondwana Research, 7, 261-272.
- Mortimer, N., Gans, P., Calvert, A. & Walker, N. 1999a. Geology and thermochronology of the east edge of the Median Batholith (Median Tectonic Zone): a new perspective on Permian to Cretaceous crustal growth in New Zealand. Island Arc, 8, 404-425.
- Mortimer, N., Tulloch, A. J., Spark, R. N., Walker, N. W., Ladley, E., Allibone, A. & Kimbrough, D. L. 1999b. Overview of the Median Batholith, New Zealand: a new interpretation of the geology of the Median Tectonic Zone and adjacent rocks. Journal of African Earth Sciences, 29, 257-268.
- Mosley, M. P. & Pearson, C. P. 1997. Hydrological extremes and climate in New Zealand. In: Mosley, M. P. and Pearson, C. P. (eds). Floods and Droughts: the New Zealand Experience. New Zealand, New Zealand Hydrological Society, pp 1-14.
- Moulton, K. L. & Berner, R. A. 1998. Quantification of the effect of plants on weathering: studies in Iceland. Geology, 26, 895-898.
- Moulton, K. L., West, J. A. & Berner, R. A. 2000. Solute flux and mineral mass balance approaches to the quantification of plant effects on silicate weathering. American Journal of Science, 300, 539-570.
- Munhoven, G. 2002. Glacial-interglacial changes of continental weathering: estimates of the related CO₂ and HCO₃⁻ variations and their uncertainties. Global and Planetary Change, 33, 155-176.
- Murphy, M. J., Strandmann, P. a. E. P. V., Porcelli, D. & Ingri, J. 2014. Li isotope behaviour in the low salinity zone during estuarine mixing. Procedia Earth and Planetary Science, 10, 204-207.
- Muttik, N., Kirsimäe, K., Newsom, H. E. & Williams, L. B. 2011. Boron isotope composition of secondary smectite in suevites at the Ries crater, Germany: Boron fractionation in weathering and hydrothermal processes. Earth and Planetary Science Letters, 310, 244-251.
- Nagy, K. L. 1995. Dissolution and precipitation of kinetics of sheet silicates. Reviews in Mineralogy and Geochemistry, 31, 173-233.

- Nagy, K. L., Steefel, C. I., Blum, A. E. & Lasaga, A. C. 1990. Dissolution and precipitation kinetics of kaolinite: Initial results at 80 °C with application to porosity evolution in a sandstone. AAPG Special Volumes, 85-101.
- Négrel, P., Millot, R., Brenot, A. & Bertin, C. 2010. Lithium isotopes as tracers of groundwater circulation in a peat land. Chemical Geology, 276, 119-127.
- Négrel, P., Millot, R., Guerrot, C., Petelet-Giraud, E., Brenot, A. & Malcuit, E. 2012. Heterogeneities and interconnections in groundwaters: Coupled B, Li and stable-isotope variations in a large aquifer system (Eocene Sand aquifer, Southwestern France). Chemical Geology, 296-297, 83-95.
- Nesbitt, H. W. & Young, G. M. 1982. Early Proterozoic climates and plate motions inferred from major element chemistry of lutites. Nature, 299, 715-717.
- Nesbitt, H. W. & Young, G. M. 1989. Formation and diagenesis of weathering profiles. The Journal of Geology, 129-147.
- Nishio, Y. & Nakai, S. 2002. Accurate and precise lithium isotopic determinations of igneous rock samples using multi-collector inductively coupled plasma mass spectrometry. Analytica Chimica Acta, 456, 271-281.
- Nishio, Y., Okamura, K., Tanimizu, M., Ishikawa, T. & Sano, Y. 2010. Lithium and strontium isotopic systematics of waters around Ontake volcano, Japan: Implications for deep-seated fluids and earthquake swarms. Earth and Planetary Science Letters, 297, 567-576.
- Norris, R. J. & Cooper, A. F. 2000. Late Quaternary slip rates and slip partitioning on the Alpine Fault, New Zealand. Journal of Structural Geology, 23, 507-520.
- Norris, R. J., Koons, P. O. & Cooper, A. F. 1990. The obliquely-convergent plate boundary in the South Island of New Zealand: implications for ancient collision zones. Journal of Structural Geology, 12, 715-725.
- Odom, I. E. 1984. Smectite clay minerals: properties and uses. Philosophical Transactions of the Royal Society of London. Series A, Mathematical and Physical Sciences., 311, 391-409.
- Oi, T., Kawada, K., Hosoe, M. & Kakihana, H. 1991. Fractionation of lithium isotopes in cation-exchange chromatography. Separation Science and Technology, 26, 1353-1375.
- Oliver, L., Harris, N., Bickle, M., Chapman, H., Dise, N. & Horstwood, M. 2003. Silicate weathering rates decoupled from the ⁸⁷Sr/⁸⁶Sr ratio of the dissolved load during Himalayan erosion. Chemical Geology, 201, 119-139.

- Olson, J. E. 1993. Joint pattern development: Effects of subcritical crack growth and mechanical crack interaction. Journal of Geophysical Research, 98, 12251-12265.
- O'Neil, J. R. 1986. Theoretical and experimental aspects of isotope fractionation. In: Valley, J. W., Taylor, H. P., O'Neil, J. R. (eds). Stable Isotopes in High Temperature Geological Processes. Reviews in Mineralogy, Volume 6, Mineralogical Society of America, Washington, DC, pp 1-40.
- Opfergelt, S., Georg, R. B., Delvaux, B., Cabidoche, Y. M., Burton, K. W. & Halliday, A. N. 2012. Mechanisms of magnesium isotope fractionation in volcanic soil weathering sequences, Guadeloupe. Earth and Planetary Science Letters, 341-344, 176-185.
- Ota, Y., Pillans, B., Berryman, K., Beu, A., Fujimori, T., Miyauchi, T., Berger, G., Beu, A. G. & Climo, F. M. 2010. Pleistocene coastal terraces of Kaikoura Peninsula and the Marlborough coast, South Island, New Zealand. New Zealand Journal of Geology and Geophysics, 39, 51-73.
- Palmer, M. R. & Edmond, J. M. 1989. The strontium isotope budget of the modern ocean. Earth and Planetary Science Letters, 92, 11-26.
- Palmer, M. R. & Edmond, J. M. 1992. Controls over the strontium isotope composition of river water. Geochimica et Cosmochimica Acta, 56, 2099-2111.
- Penniston-Dorland, S. C., Bebout, G. E., Pogge Von Strandmann, P. a. E., Elliott, T. & Sorensen, S. S. 2012. Lithium and its isotopes as tracers of subduction zone fluids and metasomatic processes: Evidence from the Catalina Schist, California, USA. Geochimica et Cosmochimica Acta, 77, 530-545.
- Peucker-Ehrenbrink, B. & Ravizza, G. 2000. The marine osmium isotope record. Terra Nova, 12, 205-219.
- Peucker-Ehrenbrink, B. & Ravizza, G. 2012. Osmium isotope stratigraphy. In: Gradstein, F. M., Ogg, J. G., Schmitz, M. D. (eds). The Geologic Time Scale Chapter 8. Cambridge University Press, Cambridge.
- Pistiner, J. S. & Henderson, G. M. 2003. Lithium-isotope fractionation during continental weathering processes. Earth and Planetary Science Letters, 214, 327-339.
- Pitcairn, I. 2004. Sources of fluids and metals in orogenic gold deposits: the Otago Schists, New Zealand (PhD). University of Southampton, UK.

- Plummer, L. N., Parkhurst, D. L., Fleming, G. W. & Dunkle, S. A. 1988. A computer program incorporating Pitzer's equations for calculation of geochemical reactions in brines. Water-Resources Investigations Report (USGS), 1-315.
- Pogge Von Strandmann, P. A. E. & Henderson, G. M. 2015. The Li isotope response to mountain uplift. Geology, 43, 67-70.
- Pogge Von Strandmann, P. A. E., Burton, K. W., James, R. H., Van Calsteren, P. & Gislason, S. R. 2010. Assessing the role of climate on uranium and lithium isotope behaviour in rivers draining a basaltic terrain. Chemical Geology, 270, 227-239.
- Pogge Von Strandmann, P. A. E., Burton, K. W., James, R. H., Van Calsteren, P., Gíslason, S. R. & Mokadem, F. 2006. Riverine behaviour of uranium and lithium isotopes in an actively glaciated basaltic terrain. Earth and Planetary Science Letters, 251, 134-147.
- Pogge Von Strandmann, P. A. E., Burton, K. W., James, R. H., Van Calsteren, P., Gislason, S. R. & Sigfússon, B. 2008. The influence of weathering processes on riverine magnesium isotopes in a basaltic terrain. Earth and Planetary Science Letters, 276, 187-197.
- Pogge Von Strandmann, P. A. E., Elliott, T., Marschall, H. R., Coath, C., Lai, Y.-J., Jeffcoate, A. B. & Ionov, D. A. 2011. Variations of Li and Mg isotope ratios in bulk chondrites and mantle xenoliths. Geochimica et Cosmochimica Acta, 75, 5247-5268.
- Pogge Von Strandmann, P. A. E., Opfergelt, S., Lai, Y.-J., Sigfússon, B., Gislason, S. R. & Burton, K. W. 2012. Lithium, magnesium and silicon isotope behaviour accompanying weathering in a basaltic soil and pore water profile in Iceland. Earth and Planetary Science Letters, 339-340, 11-23.
- Pogge Von Strandmann, P. A. E., Porcelli, D., James, R. H., Van Calsteren, P., Schaefer, B., Cartwright, I., Reynolds, B. C. & Burton, K. W. 2014. Chemical weathering processes in the Great Artesian Basin: Evidence from lithium and silicon isotopes. Earth and Planetary Science Letters, 406, 24-36.
- Pollard, D. D. & Aydin, A. 1988. Progress in understanding jointing over the past century. Geological Society of America Bulletin, 100, 1181-1204.
- Porder, S., Hilley, G. E. & Chadwick, O. A. 2007. Chemical weathering, mass loss, and dust inputs across a climate by time matrix in the Hawaiian Islands. Earth and Planetary Science Letters, 258, 414-427.
- Potts, P. J. 1987. A Handbook of Silicate Rock Analysis. London, Blackie Academic and Professional, Chapman and Hall.

- Probst, J.-L., Nkounkou, R.-R., Krempp, G., Bricquet, J.-P., Thiebaux, J.-P. & Olivry, J.-C. 1992. Dissolved major elements exported by the Congo and the Ubangi rivers during the period 1987-1989. Journal of Hydrology, 135, 237-257.
- Qiu, L., Rudnick, R. L., Ague, J. J. & Mcdonough, W. F. 2011. A lithium isotopic study of subgreenschist to greenschist facies metamorphism in an accretionary prism, New Zealand. Earth and Planetary Science Letters, 301, 213-221.
- Qiu, L., Rudnick, R. L., Mcdonough, W. F. & Merriman, R. J. 2009. Li and δ^7 Li in mudrocks from the British Caledonides: Metamorphism and source influences. Geochimica et Cosmochimica Acta, 73, 7325-7340.
- Ra, K. & Kitagawa, H. 2007. Magnesium isotope analysis of different chlorophyll forms in marine phytoplankton using multi-collector ICP-MS. Journal of Analytical Atomic Spectrometry, 22, 817-821.
- Raymo, M. E. & Ruddiman, W. F. 1992. Tectonic forcing of late Cenozoic climate. Nature, 359, 117-122.
- Reed, J. J. 1964. Mylonites, cataclasites, and associated rocks along the Alpine Fault, South Island, New Zealand. New Zealand Journal of Geology and Geophysics, 7, 645-684.
- Renshaw, C. E. & Pollard, D. D. 1994. Numerical simulation of fracture set formation: A fracture mechanics model consistent with experimental observations. Journal of Geophysical Research, 99, 9359-9372.
- Reyes, A. G., Christenson, B. W. & Faure, K. 2010. Sources of solutes and heat in low-enthalpy mineral waters and their relation to tectonic setting, New Zealand. Journal of Volcanology and Geothermal Research, 192, 117-141.
- Richter, F. M., Rowley, D. B. & Depaolo, D. J. 1992. Sr isotope evolution of seawater: the role of tectonics. Earth and Planetary Science Letters, 109, 11-23.
- Riebe, C. S., Ferrier, K. L., Hahm, W. J. & Kirchner, J. W. 2011. Supply-limited and kinetic-limited chemical erosion. Goldschmidt Conference Abstracts.
- Riebe, C. S., Kirchner, J. W. & Finkel, R. C. 2004. Erosional and climatic effects on long-term chemical weathering rates in granitic landscapes spanning diverse climate regimes. Earth and Planetary Science Letters, 224, 547-562.
- Riebe, C. S., Kirchner, J. W., Granger, D. E. & Finkel, R. C. 2001. Strong tectonic and weak climatic control of long-term chemical weathering rates. Geology, 29, 511.

- Rimstidt, J. D. & Dove, P. M. 1986. Mineral/solution reaction rates in a mixed flow reactor: Wollastonite hydrolysis. Geochimica et Cosmochimica Acta, 50, 2509-2516.
- Riotte, J., Chabaux, F., Benedetti, M., Dia, A., Gérard, M., Boulègue, J. & Etamé, J. 2003. Uranium colloidal transport and origin of the ²³⁴U–²³⁸U fractionation in surface waters: new insights from Mount Cameroon. Chemical Geology, 202, 365-381.
- Robinson, L. F., Henderson, G. M., Hall, L. & Matthews, I. 2004. Climatic control of riverine and seawater uranium-isotope ratios. Science, 305, 851-854.
- Roser, B. P. & Korsch, R. J. 1986. Determination of tectonic setting of sandstone-mudstone suites using SiO₂ content and K₂O/Na₂O ratio. The Journal of Geology, 94, 635-650.
- Røyne, A., Jamtveit, B., Mathiesen, J. & Malthe-Sørenssen, A. 2008. Controls on rock weathering rates by reaction-induced hierarchical fracturing. Earth and Planetary Science Letters, 275, 364-369.
- Rudnick, R. L., Tomascak, P. B., Njo, H. B. & Gardner, L. R. 2004. Extreme lithium isotopic fractionation during continental weathering revealed in saprolites from South Carolina. Chemical Geology, 212, 45-57.
- Ryan, J. G. & Kyle, P. R. 2004. Lithium abundance and lithium isotope variations in mantle sources: insights from intraplate volcanic rocks from Ross Island and Marie Byrd Land (Antarctica) and other oceanic islands. Chemical Geology, 212, 125-142.
- Sarin, M. M., Krishnaswami, S., Dilli, K., Somayajulu, B. L. K. & Moore, W. S. 1989. Major ion chemistry of the Ganga-Brahmaputra river system: weathering processes and fluxes to the Bay of Bengal. Geochimica et Cosmochimica Acta, 53, 997-1009.
- Schiller, M., Baker, J. A. & Bizzarro, M. 2010. ²⁶Al–²⁶Mg dating of asteroidal magmatism in the young Solar System. Geochimica et Cosmochimica Acta, 74, 4844-4864.
- Schmitt, A.-D., Stille, P. & Vennemann, T. 2003. Variations of the 44 Ca/ 40 Ca ratio in seawater during the past 24 million years: evidence from δ^{44} Ca and δ^{18} O values of Miocene phosphates. Geochimica et Cosmochimica Acta, 67, 2607-2614.
- Scholz, F., Hensen, C., De Lange, G. J., Haeckel, M., Liebetrau, V., Meixner, A., Reitz, A. & Romer, R. L. 2010. Lithium isotope geochemistry of marine pore waters Insights from cold seep fluids. Geochimica et Cosmochimica Acta, 74, 3459-3475.

- Seitz, H.-M., Brey, G. P., Lahaye, Y., Durali, S. & Weyer, S. 2004. Lithium isotopic signatures of peridotite xenoliths and isotopic fractionation at high temperature between olivine and pyroxenes. Chemical Geology, 212, 163-177.
- Seitz, H.-M., Zipfel, J., Brey, G. P. & Ott, U. 2012. Lithium isotope compositions of chondrules, CAI and a dark inclusion from Allende and ordinary chondrites. Earth and Planetary Science Letters, 329-330, 51-59.
- Selvaraj, K. & Chen, C.-T. A. 2006. Moderate chemical weathering of subtropical Taiwan: Constraints from solid-phase geochemistry of sediments and sedimentary rocks. The Journal of Geology, 114, 101-116.
- Sephton, M. A., James, R. & Bland, P. A. 2004. Lithium isotope analyses of inorganic constituents from the Murchison meteorite. The Astrophysical Journal, 612, 588-591.
- Shannon, R. D. 1976. Revised effective ionic radii and systematic studies of interatomic distances in halides and chalcogenides. Acta Crystallographica, A32, 751-767.
- Shaul, O. 2002. Magnesium transport and function in plants: the tip of the iceberg. Biometals, 15, 309-323.
- Shi, Y., Allis, R. G. & Davey, F. 1996. Thermal modelling of the Southern Alps, New Zealand. Pure and Applied Geophysics, 146, 469-501.
- Shulmeister, J., Goodwin, I., Renwick, J., Harle, K., Armand, L., Mcglone, M. S., Cook, E., Dodson, J., Hesse, P. P., Mayewski, P. & Curran, M. 2004. The Southern Hemisphere westerlies in the Australasian sector over the last glacial cycle: a synthesis. Quaternary International, 118-119, 23-53.
- Sims, A. 2013. Shallow fluid movement in the hanging wall of the Alpine Fault (Msc). University of Otago, Dunedin, New Zealand.
- Sleep, N. H. & Zahnle, K. 2001. Carbon dioxide cycling and implications for climate on ancient Earth. Journal of Geophysical Research, 106, 1373-1399.
- Sophocleous, M. 2002. Interactions between groundwater and surface water: the state of the science. Hydrogeology Journal, 10, 52-67.
- Spektor, V. B. & Spektor, V. V. 2009. Karst processes and phenomena in the perennially frozen carbonate rocks of the middle Lena River basin. Permafrost and Periglacial Processes, 20, 71-78.

- Spooner, E. T. C. 1976. The strontium isotopic composition of seawater, and seawater-oceanic crust interaction. Earth and Planetary Science Letters, 31, 167-174.
- Stallard, R. F. & Edmond, J. M. 1981. Geochemistry of the Amazon 1. Precipitation Chemistry and the Marine Contribution to the Dissolved Load at the Time of Peak Discharge. Journal of Geophysical Research, 86, 9844-9858.
- Stallard, R. F. & Edmond, J. M. 1983. Geochemistry of the Amazon 2. The influence of geology and weathering environment on the dissolved load. Journal of Geophysical Research, 88, 9671-9688.
- Stallard, R. F. 1980. Major element geochemistry of the Amazon River system (PhD). Massachusetts Institute of Technology, USA.
- Stefansson, A. & Gislason, S. R. 2001. Chemical weathering of basalts, Southwest Iceland: effect of rock crystallinity and secondary minerals on chemical fluxes to the ocean. American Journal of Science, 301, 513-556.
- Stoffyn-Elgi, P. & Mackenzie, F., T. 1984. Mass balance of dissolved lithium in the oceans. Geochimica et Cosmochimica Acta, 48, 859-872.
- Strawn, D. G., Palmer, N. E., Furnare, L. J., Goodell, C., Amonette, J. E. & Kukkadapu, R. K. 2004. Copper sorption mechanisms on smectites. Clays and Clay Minerals, 52, 321-333.
- Strelow, F. W. E., Rethemeyer, R. & Bothma, C. J. C. 1965. Ion exchange selectivity scales for cations in nitric acid and sulphuric acid media with a sulfonated polystyrene resin. Analytical Chemistry, 37, 106-111.
- Sutherland, R. 1996. Transpressional development of the Australia-Pacific boundary through southern South Island, New Zealand: Constraints from Miocene-Pliocene sediments, Waiho-1 borehole, South Westland. New Zealand Journal of Geology and Geophysics, 39, 251-264.
- Sutherland, R., Berryman, K. & Norris, R. 2006. Quaternary slip rate and geomorphology of the Alpine fault: Implications for kinematics and seismic hazard in southwest New Zealand. Geological Society of America Bulletin, 118, 464-474.
- Sutherland, R., Davey, F. & Beavan, J. 2000. Plate boundary deformation in South Island, New Zealand, is related to inherited lithospheric structure. Earth and Planetary Science Letters, 177, 141-151.
- Sutherland, R., Eberhart-Phillips, D., Harris, R. A., Stern, T., Beavan, J., Ellis, S., Henrys, S., Cox, S. C., Norris, R., Berryman, K., Townend, J., Bannister, S., Pettinga, J., Leitner, B., Wallace,

- L., Little, T. A., Cooper, A. F., Yetton, M. & Stirling, M. 2007. Do great earthquakes occur on the Alpine Fault in central South Island, New Zealand? In: Okaya, D., Stern, T., Davey, F. (eds). A Continental Plate Boundary: Tectonics at South Island, New Zealand. Geophysical Monograph Series, 175, 235-251.
- Sutherland, R., Toy, V. G., Townend, J., Cox, S. C., Eccles, J. D., Faulkner, D. R., Prior, D. J., Norris,
 R. J., Mariani, E., Boulton, C., Carpenter, B. M., Menzies, C. D., Little, T. A., Hasting, M.,
 De Pascale, G. P., Langridge, R. M., Scott, H. R., Lindroos, Z. R., Fleming, B. & Kopf, A. J.
 2012. Drilling reveals fluid control on architecture and rupture of the Alpine fault, New
 Zealand. Geology, 40, 1143-1146.
- Tait, A., Henderson, R., Turner, R. & Zheng, X. 2006. Thin plate smoothing spline interpolation of daily rainfall for New Zealand using a climatological rainfall surface. International Journal of Climatology, 26, 2097-2115.
- Tang, Y.-J., Zhang, H.-F., Nakamura, E. & Ying, J.-F. 2010. Multistage melt/fluid-peridotite interactions in the refertilized lithospheric mantle beneath the North China Craton: constraints from the Li–Sr–Nd isotopic disequilibrium between minerals of peridotite xenoliths. Contributions to Mineralogy and Petrology, 161, 845-861.
- Taylor, A. & Blum, J. D. 1995. Relation between soil age and silicate weathering rates determined from the chemical evolution of a glacial chronosequence. Geology, 23, 979.
- Taylor, T. I. & Urey, H. C. 1938. Fractionation of the lithium and potassium isotopes by chemical exchange with zeolites. Journal of Chemical Physics, 6, 429-438.
- Telang, S. A., Pocklington, R., Naidu, A. S., Romankevich, E. A., Gitelson, I. I. & Gladyshev, M. I. 1991. Carbon and mineral transport in major North American, Russian arctic, and Siberian rivers: the St Lawrence, the Mackenzie, the Yukon, the arctic Alaskan rivers, the arctic basin rivers in the Soviet Union, and the Yenisei. Biogeochemistry of Major World Rivers, 42, 75-104.
- Telus, M., Dauphas, N., Moynier, F., Tissot, F. L. H., Teng, F.-Z., Nabelek, P. I., Craddock, P. R. & Groat, L. A. 2012. Iron, zinc, magnesium and uranium isotopic fractionation during continental crust differentiation: The tale from migmatites, granitoids, and pegmatites. Geochimica et Cosmochimica Acta, 97, 247-265.
- Teng, F. Z., McDonough, W. F., Rudnick, R. L., Dalpé, C., Tomascak, P. B., Chappell, B. W. & Gao, S. 2004. Lithium isotopic composition and concentration of the upper continental crust. Geochimica et Cosmochimica Acta, 68, 4167-4178.

- Teng, F. Z., McDonough, W. F., Rudnick, R. L. & Wing, B. 2007a. Limited lithium isotopic fractionation during progressive metamorphic dehydration in metapelites: A case study from the Onawa contact aureole, Maine. Chemical Geology, 239, 1-12.
- Teng, F. Z., Li, W.-Y., Ke, S., Marty, B., Dauphas, N., Huang, S., Wu, F.-Y. & Pourmand, A. 2010a. Magnesium isotopic composition of the Earth and chondrites. Geochimica et Cosmochimica Acta, 74, 4150-4166.
- Teng, F. Z., Li, W.-Y., Rudnick, R. L. & Gardner, L. R. 2010b. Contrasting lithium and magnesium isotope fractionation during continental weathering. Earth and Planetary Science Letters, 300, 63-71.
- Teng, F. Z., Wadhwa, M. & Helz, R. T. 2007b. Investigation of magnesium isotope fractionation during basalt differentiation: Implications for a chondritic composition of the terrestrial mantle. Earth and Planetary Science Letters, 261, 84-92.
- Thomas, M. F. 1994. Geomorphology in the Tropics. Wiley, Chichester.
- Tipper, E. T., Calmels, D., Gaillardet, J., Louvat, P., Capmas, F. & Dubacq, B. 2012. Positive correlation between Li and Mg isotope ratios in the river waters of the Mackenzie Basin challenges the interpretation of apparent isotopic fractionation during weathering. Earth and Planetary Science Letters, 333-334, 35-45.
- Tipper, E. T., Gaillardet, J., Louvat, P., Capmas, F. & White, A. F. 2010. Mg isotope constraints on soil pore-fluid chemistry: Evidence from Santa Cruz, California. Geochimica et Cosmochimica Acta, 74, 3883-3896.
- Tipper, E. T., Bickle, M., Galy, A., West, A., Pomies, C. & Chapman, H. 2006a. The short term climatic sensitivity of carbonate and silicate weathering fluxes: Insight from seasonal variations in river chemistry. Geochimica et Cosmochimica Acta, 70, 2737-2754.
- Tipper, E. T., Galy, A. & Bickle, M. 2006b. Riverine evidence for a fractionated reservoir of Ca and Mg on the continents: Implications for the oceanic Ca cycle. Earth and Planetary Science Letters, 247, 267-279.
- Tipper, E. T., Galy, A. & Bickle, M. 2008a. Calcium and magnesium isotope systematics in rivers draining the Himalaya-Tibetan-Plateau region: Lithological or fractionation control? Geochimica et Cosmochimica Acta, 72, 1057-1075.
- Tipper, E. T., Galy, A., Gaillardet, J., Bickle, M., Elderfield, H. & Carder, E. 2006c. The magnesium isotope budget of the modern ocean: Constraints from riverine magnesium isotope ratios. Earth and Planetary Science Letters, 250, 241-253.

- Tipper, E. T., Louvat, P., Capmas, F., Galy, A. & Gaillardet, J. 2008b. Accuracy of stable Mg and Ca isotope data obtained by MC-ICP-MS using the standard addition method. Chemical Geology, 257, 65-75.
- Tomascak, P. B. & Langmuir, C. H. 1999. Lithium isotope variability in MORB. Eos, 80, F1086-F1087.
- Tomascak, P. B. 2004. Developments in the understanding and application of lithium isotopes in the Earth and planetary sciences. Reviews in Mineralogy and Geochemistry, 55, 153-195.
- Tomascak, P. B., Carlson, R. W. & Shirey, S. B. 1999a. Accurate and precise determination of Li isotopic compositions by multi-collector sector ICP-MS. Chemical Geology, 158, 145-154.
- Tomascak, P. B., Hemming, N. G. & Hemming, S. R. 2003. The lithium isotopic composition of waters of the Mono Basin, California. Geochimica et Cosmochimica Acta, 67, 601-611.
- Tomascak, P. B., Langmuir, C. H., Le Roux, P. J. & Shirey, S. B. 2008. Lithium isotopes in global mid-ocean ridge basalts. Geochimica et Cosmochimica Acta, 72, 1626-1637.
- Tomascak, P. B., Tera, F., Helz, R. T. & Walker, R. J. 1999b. The absence of lithium isotope fractionation during basalt differentiation: New Measurements by multicollector sector ICP-MS. Geochimica et Cosmochimica Acta, 63, 907-910.
- Tonkin, P. J. & Basher, L. R. 1990. Soil-stratigraphic techniques in the study of soil and landform evolution across the Southern Alps, New Zealand. Geomorphology, 3, 547-575.
- Tosca, N. J. 2007. The formation and stability of saline minerals at the Martian surface. ProQuest, MI, USA.
- Toy, V. G., Craw, D., Cooper, A. F. & Norris, R. J. 2010. Thermal regime in the central Alpine Fault zone, New Zealand: Constraints from microstructures, biotite chemistry and fluid inclusion data. Tectonophysics, 485, 178-192.
- Tranter, M. 2003. Geochemical weathering in glacial and proglacial environments. In: Drever, J. I., Holland, H. D., Turekian, K. K. (eds). Treatise on Geochemistry, Volume 5. Elsevier, pp 189-205.
- Truesdell, A. H. 1984. Chemical geothermometers for geothermal exploration. In: Fluid-mineral equilibria in hydrothermal systems. Reviews in Economic Geology, 1, 31-43.
- Turekian, K. K. & Wedepohl, K. H. 1961. Distribution of the elements in some major units of the Earth's crust. Geological Society of America Bulletin, 72, 175-192.

- Upton, P., Koons, P. O. & Chamberlain, C. P. 1995. Penetration of deformation-driven meteoric water into ductile rocks: Isotopic and model observations from the Southern Alps, New Zealand. New Zealand Journal of Geology and Geophysics, 38, 535-543.
- Van De Flierdt, T., Frank, M., Lee, D.-C. & Halliday, A. N. 2002. Glacial weathering and the hafnium isotope composition of seawater. Earth and Planetary Science Letters, 201, 639-647.
- Vance, D. & Burton, K. W. 1999. Neodymium isotopes in planktonic foraminifera: a record of the response of continental weathering and ocean circulation rates to climate change. Earth and Planetary Science Letters, 173, 365-379.
- Vance, D., Teagle, D. A. H. & Foster, G. L. 2009. Variable Quaternary chemical weathering fluxes and imbalances in marine geochemical budgets. Nature, 458, 493-496.
- Velbel, M. A. 1985. Geochemical mass balances and weathering rates in forested watersheds of the Southern Blue Ridge. American Journal of Science, 285, 904-930.
- Velbel, M. A. 1993. Temperature dependence of silicate weathering in nature: How strong a negative feedback on long-term accumulation of atmospheric CO₂ and global greenhouse warning? Geology, 21, 1059-1062.
- Viers, J., Dupré, B., Braun, J., Deberdt, S., Angeletti, B., Ngoupayou, J. N. & Michard, A. 2000. Major and trace element abundances, and strontium isotopes in the Nyong basin rivers (Cameroon): constraints on chemical weathering process and elements transport mechanisms in humid tropical environments. Chemical Geology, 169, 211-241.
- Vigier, N., Burton, K. W., Gislason, S. R., Rogers, N. W., Duchene, S., Thomas, L., Hodge, E. & Schaefer, B. 2006. The relationship between riverine U-series disequilibria and erosion rates in a basaltic terrain. Earth and Planetary Science Letters, 249, 258-273.
- Vigier, N., Decarreau, A., Millot, R., Carignan, J., Petit, S. & France-Lanord, C. 2008. Quantifying Li isotope fractionation during smectite formation and implications for the Li cycle. Geochimica et Cosmochimica Acta, 72, 780-792.
- Vigier, N., Gislason, S. R., Burton, K. W., Millot, R. & Mokadem, F. 2009. The relationship between riverine lithium isotope composition and silicate weathering rates in Iceland. Earth and Planetary Science Letters, 287, 434-441.
- Vorontsov, A. Y. & Lin, N. G. 1966. Rubidium and lithium in the grabitoids of the Bugul'min complex. Geokhimiya, 11, 1377-1384.

- Walcott, R. I. 1998. Modes of oblique compression: Late Cenozoic tectonics of the South Island of New Zealand. Review of Geophysics, 36, 1-26.
- Waldbauer, J. R. & Chamberlain, C. 2005. Influence of uplift, weathering and base cation supply on past and future CO₂ levels. In: Ehleringer, J. R., Cerling, T. E., Dearing, M. D. (eds). A History of Atmopsheric CO₂ and its Effects on Plants, Animals, and Ecosystems. Springer. Ecological Studies, 177, 166-184.
- Walder, J. S. & Hallet, B. 1986. The physical basis of frost weathering: toward a more fundamental and unified perspective. Arctic and Alpine Research, 18, 27-32.
- Walker, J., C.G., Hays, P. B. & Kasting, J. F. 1981. A negative feedback mechanism for the long-term stabilization of Earth's surface temperature. Journal of Geophysical Research, 86, 9776-9782.
- Wallmann, K. 2001. Controls on the Cretaceous and Cenozoic evolution of seawater composition, atmospheric CO₂ and climate. Geochimica et Cosmochimica Acta, 65, 3005-3025.
- Wan, S., Clift, P. D., Li, A., Yu, Z., Li, T. & Hu, D. 2012. Tectonic and climatic controls on long-term silicate weathering in Asia since 5 Ma. Geophysical Research Letters, 39, 1-5.
- Wanner, C., Sonnenthal, E. L. & Liu, X.-M. 2014. Seawater δ⁷Li: A direct proxy for global CO₂ consumption by continental silicate weathering? Chemical Geology, 381, 154-167.
- Wardle, P. 1964. Facets of the distribution of forest vegetation in New Zealand. New Zealand Journal of Botany, 2, 352-366.
- Warr, L. N. & Cox, S. C. 2001. Clay mineral transformations and weakening mechanisms along the Alpine Fault, New Zealand. In: Holdsworth, R. E., Strachan, R. A., Magloughlin, J. F. (eds). The Nature and Tectonic Significance of Fault Zone Weakening. The Geological Society of London. Geological Society Special Publications, 186, 85-101.
- Weaver, C. E. & Beck, K. C. 1972. Vertical variability in the attapulgite mining area. Proceedings of Seventh Forum on Geology of Industrial Minerals, 17, 51-90.
- Wedepohl, K. H. 1995. The composition of the continental crust. Geochimica et Cosmochimica Acta, 59, 1217-1232.
- Wegmann, M., Gudmundsson, G. H. & Haeberli, W. 1998. Permafrost changes in rock walls and the retreat of Alpine Glaciers: a thermal modelling approach. Permafrost and Periglacial Processes, 8, 23-33.

- West, A., Galy, A. & Bickle, M. 2005. Tectonic and climatic controls on silicate weathering. Earth and Planetary Science Letters, 235, 211-228.
- Weston, R. E. 1999. Anomalous or mass-dependent isotope effects. Chemical Reviews, 99, 2115-2136.
- Wheat, C. G. & Mottl, M., J. 2000. Composition of pore and spring waters from Baby Bare: Global implications of geochemical fluxes from a ridge flank hydrothermal system. Geochimica et Cosmochimica Acta, 64, 629-642.
- White, A. F. & Brantley, S. L. 2003. The effect of time on the weathering of silicate minerals: why do weathering rates differ in the laboratory and field? Chemical Geology, 202, 479-506.
- White, A. F. & Brantley, S. L. 1995a. Chemical weathering rates of silicate minerals: An overview. Reviews in Mineralogy and Geochemistry, 31, 1-22.
- White, A. F., Blum, A. E., Bullen, T. D., Vivit, D. V., Schulz, M. S. & Fitzpatrick, J. 1999. The effect of temperature on experimental and natural chemical weathering rates of granitoid rocks. Geochimica et Cosmochimica Acta, 63, 3277-3291.
- White, A. F., Blum, A. E., Schulz, M. S., Vivit, D. V., Stonestrom, D. A., Larsen, M., Murphy, S. F. & Eberl, D. 1998. Chemical weathering in a tropical watershed, Luquillo Mountains, Puerto Rico: I. Long-term versus short-term weathering fluxes. Geochimica et Cosmochimica Acta, 62, 209-226.
- White, A. F. & Blum, A., E. 1995b. Effects of climate on chemical weathering in watersheds. Geochimica et Cosmochimica Acta, 59, 1729-1747.
- White, W., M. 2013. Geochemistry. Wiley-Blackwell, UK.
- Whitehouse, I. E. & Griffiths, G. A. 1983. Frequency and hazard of large rock avalanches in the central Southern Alps, New Zealand. Geology, 11, 331-334.
- Whitehouse, I. E. 1986. Geomorphology of a compressional plate boundary, Southern Alps, New Zealand. International Geomorphology, 897-924.
- Wiechert, I. E. & Halliday, A. N. 2007. Non-chondritic magnesium and the origins of the inner terrestrial planets. Earth and Planetary Science Letters, 256, 360-371.
- Wightman, R. & Little, T. A. 2007. Deformation of the Pacific Plate above the Alpine Fault ramp and its relationship to expulsion of metamorphic fluids: an array of backshears. In: Okaya, D., Stern, T., Davey, F. (eds). A Continental Plate Boundary: Tectonics at South Island, New Zealand. Geophysical Monograph Series, 175, 177-205.

- Williams, P. W., King, D. N. T., Zhao, J. X. & Collerson, K. D. 2005. Late Pleistocene to Holocene composite speleothem ¹⁸O and ¹³C chronologies from South Island, New Zealand did a global Younger Dryas really exist? Earth and Planetary Science Letters, 230, 301-317.
- Williams, S. N., Schaefer, S. J., Calvache, M. L. & Lopez, D. 1992. Global carbon dioxide emission to the atmosphere by volcanoes. Geochimica et Cosmochimica Acta, 56, 1765-1770.
- Wimpenny, J. 2008. Chemical weathering and erosional transport in an ancient shield terrain (PhD). The Open University, UK.
- Wimpenny, J., Burton, K. W., James, R. H., Gannoun, A., Mokadem, F. & Gíslason, S. R. 2011. The behaviour of magnesium and its isotopes during glacial weathering in an ancient shield terrain in West Greenland. Earth and Planetary Science Letters, 304, 260-269.
- Wimpenny, J., Colla, C. A., Yin, Q.-Z., Rustad, J. R. & Casey, W. H. 2014. Investigating the behaviour of Mg isotopes during the formation of clay minerals. Geochimica et Cosmochimica Acta, 128, 178-194.
- Wimpenny, J., Gíslason, S. R., James, R. H., Gannoun, A., Pogge Von Strandmann, P. A. E. & Burton, K. W. 2010a. The behaviour of Li and Mg isotopes during primary phase dissolution and secondary mineral formation in basalt. Geochimica et Cosmochimica Acta, 74, 5259-5279.
- Wimpenny, J., James, R. H., Burton, K. W., Gannoun, A., Mokadem, F. & Gíslason, S. R. 2010b. Glacial effects on weathering processes: New insights from the elemental and lithium isotopic composition of West Greenland rivers. Earth and Planetary Science Letters, 290, 427-437.
- Wolery, T. J. & Sleep, N. H. 1976. Hydrothermal circulation and geochemical flux at mid-ocean ridges. The Journal of Geology, 84, 249-275.
- Wolery, T. J. & Sleep, N. H. 1988. Chemical Cycles in the Evolution of the Earth. Wiley International, New York.
- Wombacher, F., Eisenhauer, A., Heuser, A. & Weyer, S. 2009. Separation of Mg, Ca and Fe from geological reference materials for stable isotope ratio analyses by MC-ICP-MS and double-spike TIMS. Journal of Analytical Atomic Spectrometry, 24, 627-636.
- Wood, B. L. 1963. Structure of the Otago schists. New Zealand Journal of Geology and Geophysics, 6, 641-680.
- Woods, R., Hendrikx, J., Henderson, R. D. & Tait, A. 2006. Estimating mean flow of New Zealand rivers. Journal of Hydrology (NZ), 45, 95-110.

- Wunder, B., Meixner, A., Romer, R. L. & Heinrich, W. 2005. Temperature-dependent isotopic fractionation of lithium between clinopyroxene and high-pressure hydrous fluids. Contributions to Mineralogy and Petrology, 151, 112-120.
- Xie, Z. & Walther, J. V. 1992. Incongruent dissolution and surface area of kaolinite. Geochimica et Cosmochimica Acta, 56, 3357-3363.
- Yang, W., Teng, F-Z. & Zhang, H-F. 2009. Chondritic magnesium isotopic composition of the terrestrial mantle; a case study of peridotite xenoliths from the North China craton. Earth and planetary Science Letters, 288, 475-482.
- You, C. F. & Chan, L. H. 1996. Precise determination of lithium isotopic composition in low concentration natural samples. Geochimica et Cosmochimica Acta, 60, 909-915.
- You, C. F., Chan, L. H., Spivack, A. J. & Gieskes, J. M. 1995. Lithium, boron, and their isotopes in sediments and pore waters of Ocean Drilling Program Site 808, Nankai Trough: Implications for fluid expulsion in accretionary prisms. Geology, 23, 37-40.
- Young, E. D. & Galy, A. 2004. The isotope geochemistry and cosmochemistry of magnesium. Reviews in Mineralogy and Geochemistry, 55, 197-230.
- Young, E. D., Galy, A. & Nagahara, H. 2002. Kinetic and equilibrium mass-dependent isotope fractionation laws in nature and their geochemical and cosmochemical significance. Geochimica et Cosmochimica Acta, 66, 1095-1104.
- Young, E. D., Tonui, E., Manning, C. E., Schauble, E. A. & Macris, C. 2009. Spinel-olivine magnesium isotope thermometry in the mantle and implications for the Mg isotopic composition of Earth. Earth and Planetary Science Letters, 288, 524-533.
- Zane, A., Sassi, R. & Guidotti, C. V. 1998. New data on metamorphic chlorite as a petrogenetic indicator mineral, with special regard to Greenschist Facies rocks. The Canadian Mineralogist, 36, 713-726.
- Zhang, H., Bloom, P. R. & Nater, E. A. 1993. Change in surface area and dissolution rates during hornblende dissolution at pH 4.0. Geochimica et Cosmochimica Acta, 57, 1681-1689.
- Zhang, J., Letolle, R., Martin, J.-M., Jusserand, C. & Mouchel, J. M. 1990. Stable oxygen isotope distribution in the Huanghe (Yellow River) and the Changjiang (Yangtze River) estuarine systems. Continental Shelf Research, 10, 369-384.

- Zhang, L., Chan, L. H. & Gieskes, J. M. 1998. Lithium isotope geochemistry of pore waters from Ocean Drilling Program Sites 918 and 919, Irminger Basin. Geochimica et Cosmochimica Acta, 62, 2437-2450.
- Zhu, C. & Lu, P. 2009. Alkali feldspar dissolution and secondary mineral precipitation in batch systems: 3. Saturation states of product minerals and reaction paths. Geochimica et Cosmochimica Acta, 73, 3171-3200.
- Zobrist, J. & Stumm, W. 1981. River Inputs to Ocean Systems. SCOR/UNEP/UNESCO Workshop, Rome.